

# Molybdenum *para*-Terphenyl Diphosphine Complexes

Thesis by  
Joshua Alan Buss

In Partial Fulfillment of the Requirements  
for the Degree of Doctor of Philosophy

CALIFORNIA INSTITUTE OF TECHNOLOGY  
Division of Chemistry and Chemical Engineering  
Pasadena, California  
2018  
(Defended on March 12<sup>th</sup> 2018)



*To my family*

*for their unyielding love and support*

## ACKNOWLEDGEMENTS

Although synthetically I have pursued it avidly, science is not done in a vacuum. I owe my development as an academic, an experimentalist, and a person to an incredible collection of mentors, labmates, friends, and family members, without whom, I would not be where I am today.

First, I must thank my advisor, Prof. Theodor Agapie. You did not woo me into your group with keg stands or foosball prowess, but I knew well before coming to Caltech that I wanted to work with you. You may not remember, but we first met during lunch after you gave a seminar in Claremont. I was preparing for a talk on my senior thesis research and you asked me to present it to you. In a crowded and boisterous dining hall, you demonstrated interest in my work before I was even admitted to graduate school. We engaged in a discourse that day that has continued for the past six years. Your enthusiasm and excitement for science bolsters my own and that propagation of avidity has been a constant positive in our interactions. I can honestly say that you have pushed me harder than anyone has, but I do not resent it. In consistently setting a high bar, you have also helped me achieve more than I thought I could. I am grateful for your criticism, your attention to detail, your rigor, and your occasional encouragement; you taught me to be a better scientist.

Along with Theo, many Caltech professors have been extremely influential. To my committee, Profs. Jonas Peters, Greg Fu, and Harry Gray, thank you for your feedback and support. It is difficult to receive criticism from all of you, only because of the tremendous respect I have for each of you. I feel very strongly that each of you is invested in my success, and for that, I could not be more fortunate nor more grateful. Jonas, thank you for instructing me to resist the urge to be “intellectually lazy.” Those words still haunt me, and in doing so, likely motivate me exactly as you intended. Greg, I am in awe of your attention to detail and I hope that some of that rubbed off on me in the course of

our meetings. Thank you for your guidance in selecting a post doc. Harry, thank you for both asking tough questions and bringing a little bit of comic relief. Your continued passion for science is inspiring.

Occasionally, when finding myself on the second floor of Noyes, I would hear “Hot Damn!” or “Yee-Haw!” resound out of one of the labs. Tracing the source of the noise, it was inevitably Prof. John Bercaw, standing in front of his high vacuum line, holding a flashlight up to a reaction flask—an investigator in many senses of the word. John, your impact on my education at Caltech has been second only to Theo’s. Thank you for teaching me organometallics and for always being willing to discuss challenging experiments or diagnose vacuum line problems. You are truly an incredible source of knowledge. I also appreciate that after many years, you still derive such excitement and fascination out of synthesis, it is admirable. Please tell Scout I am sorry I scolded her for being in the men’s room.

When I first joined the Agapie group, I had never encountered a collection of people so hard working, intelligent, and creative. Maddy, Emily, Sibó, Paul, Sandy, Jacob, Davide, Guy, Justin, Kyle, Dave, and Po-Heng, thank you for welcoming me into the group and putting up with my endless stream of questions. Emily, I could not have asked for a better mentor. Your synthetic expertise, drive, and intellect are phenomenal; from the start, I tried to emulate you: #honoraryasiangirl. Sibó, I remember you reluctantly helping me at 3 am, making my very first batch of P2. Thanks for your patience! I am grateful to you both for also getting me into hiking in the Sierras. We had some incredible trips, even though I was worried you weren’t going to make it back down Whitney. Sandy and Kyle, thanks for introducing me to dumplings, Korean BBQ, and all sorts of other tasty eats. Guy, Kyle, and Davide, thanks for helping me get some exercise out of lab, whether it be basketball, soccer, or the occasional ski trip. Dave, to whom I will always be “Chesty,” it was great catching up at the GRC.

Since this original cohort, I have overlapped with a number of phenomenal people. Marcus, you have been my partner in crime for so long now I think we are almost codependent. Thank you for putting up with my peculiarities, for calling me out when needed, and for being an astonishing baker. You aren't the reason I am getting fat, but I will certainly let you take the credit. I think we would both agree that you haven't always been the bay and boxmate that I have wanted, but you have always been the one that I needed and I deserved. Naoki! It has been a real pleasure getting to be a (small) part of your development as a synthetic organometallic chemist. It has been an even greater pleasure getting to become your friend. I wasn't too sure about you when you started—breaking all of my NMR standard capillaries didn't help—but I couldn't have been more wrong. You, Marcus, and Marco made lab infinitely more enjoyable. To the younger members of the group, I look forward to seeing how your projects evolve. Nate, keep asking the tough questions. The high vac line is your baby now. Treat her well.

Outside of the direct confines of the group, there have been exceptional mentors and friends, too many to properly thank. Aaron, Wes, Oliver, Jon, JR, Trevor, Cowper, Tanvi, Marc, Ben, Chalkley, Gael, Kareem, Javier, Jillian, Brian, Bryan, Julian, Beau, and Paul, are all top-notch people and I am glad I got to know you all. I was lucky to have a big friend group outside of Caltech. Matt, Sasi, Chandana, Emma, Teo, Carly, and Rishabh, I can't thank you enough for your friendship and support!

Two important people need mentioning. Prof. Anna Wenzel at Claremont got me started in original research. My first project in her group was a total bust, but her enthusiasm and positive reinforcement made it seem like a success. She taught me, first hand, how to use a Schlenk line and interpret an NMR, I owe her so much. Likewise, my first foray into organometallic chemistry came under the supervision of Prof. Mike Heinekey. Mike, thank you for everything. You provided me with an invaluable foundation in synthetic transition metal chemistry and channeled my ambition into cool

side-projects like glassblowing and refractory synthesis. Both you and Anna have been advocates for me throughout my short career and I cannot thank you both enough.

Caltech has top notch facilities, in no small part, due to the people running them. Dr. Dave VanderVelde, thank you for your patience with my many NMR questions and your willingness to always help me tackle a problem. Dr. Paul Oyala, thank you for your tireless help with EPR. Dr. Mike Takase, I am grateful for your suggestions solving structures and your reluctance to let me use SQUEEZE. And, of course, Larry. Larry I can't thank you enough for not only bending over backwards to help me with my research but for also being a friend. I never made that workbench, but discussing construction projects or gardening or your squirrel problem was always a great distraction from the grind.

Last, but certainly not least, I would like to thank my family. Mom, Dad, thank you for everything. You have helped me, supported me, cared for me, and brightened my day, unconditionally, since the start. I know that will never change. Mom, you have always played an active role in my education. At times, too active; but, I know you have only ever meant well. Don't worry, I am looking after my "rocks." Dad, thank you for all you have taught me, how to fix things, how to deal with adversity, and even the commutative law. You are the kind of father I hope to one day become. Etta, I have never met a woman as strong as you. Thank you for telling me the truth, even when it isn't what I want to hear, and for always being there, no matter what. Yaneli, te amo. I am so incredibly blessed to have you in my life. Your love and support means the world and I am so excited to see what adventures we will have and what memories we will make. Tulum? Thank you all for encouraging me to follow my dreams, this is only possible because of you.

## PREFACE

Parts of this thesis have been adapted from both published articles, and those that are currently in preparation, that I have co-authored:

The following articles will be reproduced, in part, with permission from the American Chemical Society:

Joshua A. Buss and Theodor Agapie “Mechanism of Molybdenum Mediated Carbon Monoxide Deoxygenation and Coupling: Mono- and Dicarbyne Complexes Precede C-O Bond Cleavage and C-C Bond Formation” *J. Am. Chem. Soc.*, **2016**, *138*, 16466-16477.

Joshua A. Buss, Guy A. Edouard, Christine Cheng, Jade Shi, and Theodor Agapie “Molybdenum Catalyzed Ammonia Borane Dehydrogenation: Oxidation State Specific Mechanisms” *J. Am. Chem. Soc.* **2014**, *136*, 11272-11275.

The following article will be reproduced, in part, with permission from Nature Publishing Group:

Joshua A. Buss and Theodor Agapie “Four-electron deoxygenative reductive coupling of carbon monoxide at a single metal site” *Nature*, **2016**, *529*, 72-75.

The following article will be reproduced, in part, with permission from Wiley-VHC:

Joshua A. Buss, Paul H. Oyala, and Theodor Agapie. “Terminal Molybdenum Phosphides with d-Electrons: Radical Character Promotes Coupling Chemistry” *Angew. Chem. Int. Ed.*, **2017**, *56*, 14502-14506.



## RESPECTIVE CONTRIBUTIONS

Parts of the work described in this dissertation are the result of scientific collaborations, without which, the reported studies would not have been possible.

In Chapter 2, the initial synthesis and structural characterization of complex **2** was reported by Jade Shi. Optimization of this metalation and subsequent elaboration of **2** to compounds **3** and **4**, was conducted by Dr. Guy Edouard. Christine Cheng first synthesized and characterized N<sub>2</sub> adduct **5**.

In Chapter 4, work on related phenol/phenoxide asymmetric terphenyl ligands by Dr. Siti Riduan provided a basis for the CO coupling studies from both diene **3** and monophosphine **9**.

Christine Cheng collaborated once more, as part of the work discussed in Chapter 5, reporting the synthesis and structure of nitride azide complex **2**.

In Chapters 6 and 8, visiting scholars and post doctoral researchers assisted with the advancement of the presented science. Using the dinuclear phosphide complexes as a starting point, Yohei Ueda and Dr. Masa Hirahara prepared complexes **10**, **11** and **12**. Yohei obtained structural verification of dication **11** and Masa has conducted spectroscopic studies, including isotopic labeling. The pK<sub>a</sub> measurements, EPR characterization, and electrochemistry, were all carried out by Masa. He obtained the reported solid-state structure of complex **12**.

All of the work in Chapter 8 on the CO<sub>2</sub> hydrogenation catalysis was conducted by Dr. Naoki Shida. Save for an initial proof-of-principle experiment with formic acid, the

dehydrogenation catalysis is also entirely his work. He prepared and structurally characterized complex **5**, and has been conducting the mechanistic investigations providing insight into the operative pathways of these processes.

Dr. Paul Oyala collected and fit all of the CW and pulse EPR data presented in this thesis, save for the CW spectrum of complex **11** in Chapter 6. Dr. Dave VanderVelde was invaluable for his assistance with NMR spectroscopy, and the X-ray diffraction studies presented herein would not have been possible without the expertise and assistance of Dr. Mike Takase and Larry Henling.

## ABSTRACT

This dissertation describes studies exploring the coordination chemistry and reactivity of molybdenum complexes bearing a flexible and redox non-innocent *para*-terphenyl diphosphine ligand. Within this context, transformations relevant to energy storage and conversion, fundamental structure function studies, and unusual group transfer reactivity are presented.

Chapter 2 accounts the ability of Mo *para*-terphenyl diphosphine complexes to catalyze extensive ammonia borane dehydrogenation, releasing greater than two equiv. of hydrogen (H<sub>2</sub>). Initially believed to be a frontrunner as a high energy density H<sub>2</sub> storage medium, AB is a Lewis acid/base adduct that features both hydridic B–H bond and protic N–H bonds. As a highly reactive molecule, the controlled dehydrogenation of AB, accessing  $\geq 2$  of the 3 stored equiv. of H<sub>2</sub>, is uncommon. We disclose a catalytic system, utilizing an earth-abundant metal, that is capable of such reactivity. The mechanism by which the catalysis proceeds is dependent on the oxidation state of the precatalyst, with Mo<sup>II</sup> proceeding through a II/IV cycle and Mo<sup>0</sup> proceeding through a 0/II cycle. Several Mo hydride complexes were characterized in conjunction with this work. Importantly, the ability of the *para*-terphenyl diphosphine ancillary ligand to support a range of Mo oxidation states and coordination numbers was established, a feature that provides a foundation for the work presented in subsequent chapters.

In Chapter 3, new features of the *para*-terphenyl diphosphine ligand were discovered, namely facilitation of electron loading that subsequently leads to small molecule functionalization and cleavage. From the Mo dicarbonyl complex described in Chapter 2, stepwise reduction affords Mo<sup>0</sup>, Mo<sup>-II</sup>, and Mo<sup>-III</sup> compounds, all of which were characterized both structurally and by a variety of spectroscopies. The latter two

complexes were demonstrated to react with silyl electrophiles, instigating deoxygenative reductive coupling of the bound CO ligands to a metal-free  $C_2O_1$  fragment. This remarkable four-electron process was studied in detail, characterizing twelve different reaction intermediates, including rare examples of bis(siloxy)carbyne, terminal carbide, and mixed dicarbyne motifs. The cleavage of a bound carbon monoxide (CO), subsequent coupling, and spontaneous product release was an unprecedented sequence of chemical transformations, the detailed mechanistic study of which provides valuable precedent for catalyses for the conversion of  $C_1$  oxygenates to multicarbon products.

Chapter 4 discusses continuations of this work in an attempt to model Fischer-Tropsch catalysis with higher fidelity. To this end, the silyl electrophiles used in the fundamental studies in Chapter 3 needed to be replaced with protons. Addition of protons to the super-reduced Mo complexes resulted in formal arene hydrogenation; no evidence for C–O functionalization was obtained. These diene-linked complexes; however, provided an opportunity to explore how the nature of the basal  $\pi$ -system effects CO catenation chemistry and ultimately led to the preparation of a Mo-bound  $C_3O_3$  unit derived entirely from CO. Reactivity with protons was likewise explored for downstream intermediates. Carbide protonation yields a stable methylidyne carbonyl complex, that, upon treatment with hydride, forms a methylidene. Comparison to a silyl-bearing model system suggests that subsequent carbene carbonylation affords enthenone.

Chapter 5 and 6 focus on the synthesis and reactivity of Mo(IV) terminal pnictogen complexes isoelectronic to the carbyne and carbide complexes prepared in Chapters 3 and 4. Chapter 5 describes successful N–C bond formation through  $N^-$  transfer to CO from a  $Mo^{II}$  anionic nitride precursor. In Chapter 6, the first example of a terminal transition metal phosphide with d-electrons was prepared via a  $4 e^-$  oxidative group

transfer. This species can undergo a single-electron oxidation, providing, at low temperatures, an unstable Mo(V) phosphide cation that studied extensively by CW and pulse EPR techniques. Upon warming, P–P bond formation is evidenced by chemical trapping and characterization of coupling byproducts. Related phosphinidene (Mo=PR), phosphide (Mo-PR<sub>2</sub>), and dinuclear  $\mu$ -phosphido compounds are also reported. In a collaboration with Mr. Yohei Ueda and Dr. Masa Hirahara these complexes were explored for proton reduction reactivity. Isotopic labeling suggests formation of a dinuclear  $\mu$ -phosphinidene upon treatment with acid, and a bimetallic hydride  $\mu$ -phosphide was accessed from reaction with hydride.

The final chapters of this dissertation are focused on the reduction of carbon dioxide (CO<sub>2</sub>). Chapter 7 presents a fundamental study involving Lewis acid (LA) additives, that demonstrates the importance of kinetic stabilization, and not just thermodynamic activation, in productive small molecule functionalization chemistry. Upon addition of LAs, well-defined adducts are formed with Mo-bound CO<sub>2</sub>. Protonation results in C–O bond cleavage, utilizing two electrons from the metal center to reduce CO<sub>2</sub> to CO and H<sub>2</sub>O. Though the degree of CO<sub>2</sub> activation trends well as a function of Lewis acidity, the residence time of the bound CO<sub>2</sub>, reported via the rate of CO<sub>2</sub> self-exchange, is shown to correlate to the degree of C–O scission. Chapter 8 looks at CO<sub>2</sub> reactivity with E–H bonds, describing first stoichiometric reactivity with silanes. In this system, CO<sub>2</sub> is reduced to CO and silanol; mechanistic studies suggest a pathway that involves oxygen atom transfer to silane from a transient Mo oxo. In a collaboration with Dr. Naoki Shida, CO<sub>2</sub> hydrogenation was explored, with demonstration of bidirectional catalysis in addition to detailed studies investigating the elementary steps of both formate formation and formic acid dehydrogenation.



## TABLE OF CONTENTS

<b>Dedication</b>	<b>iii</b>
<b>Acknowledgements</b>	<b>iv</b>
<b>Preface</b>	<b>viii</b>
<b>Respective Contributions</b>	<b>ix</b>
<b>Abstract</b>	<b>xi</b>
<b>Table of Contents</b>	<b>xv</b>
<b>List of Figures</b>	<b>x</b>
<b>List of Schemes</b>	<b>-</b>
<b>List of Tables</b>	<b>-</b>
<b>Chapter 1</b>	<b>1</b>
General Introduction	
<b>Chapter 2</b>	<b>11</b>
<b>Molybdenum Catalyzed Ammonia Borane Dehydrogenation: Oxidation State Specific Mechanisms</b>	
Abstract	12
Introduction	13
Results and Discussion	14
Conclusions	22
Experimental Section	23
References	53
<b>Chapter 3</b>	<b>56</b>
<b>Four-Electron Deoxygenative Reductive Coupling of Carbon Monoxide at a Single Metal Site</b>	
Abstract	57
Introduction	59
Results and Discussion	65
Conclusions	97
Experimental Section	99
References	166
<b>Chapter 4</b>	<b>171</b>
<b>Toward Molecular Fischer-Tropsch: The Role of Protons and Hydrides in Mo Mediated CO Catenation</b>	
Abstract	172
Introduction	173
Results and Discussion	175
Conclusions	193
Experimental Section	194
References	209

<b>Chapter 5</b>	<b>212</b>
<b>A Low-Valent Anionic Molybdenum Nitride: Synthesis, Electronic Structure, and Group Transfer</b>	
Abstract	213
Introduction	214
Results and Discussion	216
Conclusions	224
Experimental Section	225
References	241
<b>Chapter 6</b>	<b>244</b>
<b>Terminal Molybdenum Phosphides with d-Electrons and Structurally Related MoPR, MoPR<sub>2</sub>, and MoPMo Motifs</b>	
Abstract	245
Introduction	246
Results and Discussion	247
Conclusions	263
Experimental Section	264
References	305
<b>Chapter 7</b>	<b>310</b>
<b>Tying Down Metal-Bound Small Molecules: Proton Induced C–O Bond Cleavage of CO<sub>2</sub> Facilitated by Lewis Acid Coordination</b>	
Abstract	311
Introduction	312
Results and Discussion	314
Conclusions	322
Experimental Section	323
References	345
<b>Chapter 8</b>	<b>348</b>
<b>Bimodal CO<sub>2</sub> Reduction at Low-Valent Mo Terphenyl Diphosphine Complexes</b>	
Abstract	349
Introduction	350
Results and Discussion	352
Conclusions	364
Experimental Section	365
References	376
<b>Appendix A</b>	<b>379</b>
<b>Open-Shell Mo(V) Nitrides and Alkyldynes: Does Radical Character Dictate Coupling Chemistry?</b>	
Abstract	380



Introduction	381
Results and Discussion	383
Conclusions	391
Experimental Section	392
References	394
<b>Appendix B</b>	<b>396</b>
<b>Terphenyl Diphosphine Molybdenum Complexes Bearing a Central Phenol: Towards Bifunctional Catalysis</b>	
Abstract	397
Introduction	398
Results and Discussion	399
Conclusions	405
Experimental Section	406
References	409
<b>Appendix C</b>	<b>411</b>
<b>Nuclear Magnetic Resonance Spectra for Characterization of Isolated and <i>in situ</i> Generated Complexes</b>	
Chapter 2	412
Chapter 3	419
Chapter 4	435
Chapter 5	444
Chapter 6	454
Chapter 7	464
Chapter 8	470
<b>About the Author</b>	<b>475</b>
<b>Curriculum Vitae</b>	<b>476</b>

## LIST OF FIGURES

**Note:** Figures listed below correspond to those included in the main text of each Chapter. Remaining figures can be found in the respective Experimental Sections.

### Chapter 1

- Figure 1.1.** 4  
Prior examples of M-arene interactions observed in solution and the solid-state.
- Figure 1.2.** 5  
Qualitative and calculated orbital depictions of  $\eta^2$  and  $\eta^6$  metal-arene interactions.
- Figure 1.3.** 6  
Teraryl diphosphine ligands bearing functionalized redox-active central arene motifs.

### Chapter 2

- Figure 2.1.** 15  
Solid-state structures of **2-5** and **7-8**.
- Figure 2.2.** 17  
Eudiometry of AB dehydrogenation catalyzed by **4**, **5**, and **11**.

### Chapter 3

- Figure 3.1.** 66  
X-ray crystal structures of **2**, **3**, and **4**.
- Figure 3.2.** 68  
ATR IR Spectra of **1**, **1-<sup>13</sup>C**O, **2**, **2-<sup>13</sup>C**O, **3**, and **3-<sup>13</sup>C**O.
- Figure 3.3.** 71  
NMR spectroscopic data for terminal carbide complex **7**.
- Figure 3.4.** 76  
Variable Temperature <sup>13</sup>C{<sup>1</sup>H} and <sup>31</sup>P{<sup>1</sup>H} NMR Spectra of **9-<sup>13</sup>C**.
- Figure 3.5.** 77  
Solid state structure of bis(siloxy)acetylene complex **10**.
- Figure 3.6.** 78  
Solid state structures of silyl carbyne isomers **7** and **11**.
- Figure 3.7.** 81  
Kinetic data supporting C–O bond cleavage is zeroth order in silyl electrophile.
- Figure 3.8.** 91  
Calculated valence molecular orbitals of models of **7**, **9**, **15**, and **10**.
- Figure 3.9.** 95  
Solid-state structures for monocarbonyl complexes **16** and **17**.

### Chapter 4

<b>Figure 4.1.</b>	173
Schematic representation of a plausible mechanism for CO reduction and coupling in the industrial FT process.	
<b>Figure 4.2.</b>	176
Solid-state structures of <b>2</b> and <b>3</b> .	
<b>Figure 4.3.</b>	178
Solid-state structure of <b>5</b> .	
<b>Figure 4.4.</b>	181
CO catenation from bis(siloxy)acetylene adducts <b>12</b> and <b>5</b> .	
<b>Figure 4.5.</b>	182
Experimental and simulated partial $^{13}\text{C}\{^1\text{H}\}$ and $^{31}\text{P}\{^1\text{H}\}$ NMR spectra of <b>15</b> .	
<b>Figure 4.6.</b>	182
Truncated preliminary solid-state structure of <b>15</b> .	
<b>Figure 4.7.</b>	185
Proton and 2D NMR data for a reaction mixture comprised primarily of Mo carbene carbonyl complex <b>17</b> - $^{13}\text{C}$ .	
<b>Figure 4.8.</b>	186
Solid-state structure of Mo(0) TMS ketene adduct <b>18</b> .	
<b>Figure 4.9.</b>	188
Solid-state structure of terminal methylidyne <b>19</b> .	
<b>Figure 4.10.</b>	190
Solid-state structure of terminal phosphoranylidene ketene <b>22</b> .	
<b>Figure 4.11.</b>	193
Schematic representation of carbide hydrogenation and subsequent C–C coupling in FT chemistry.	
<b>Chapter 5</b>	
<b>Figure 5.1.</b>	214
Envisioned extension of $\text{C}\equiv\text{C}$ bond forming methodology to $\text{C}\equiv\text{N}$ bond construction based on prior reports of nitride/CO coupling.	
<b>Figure 5.2.</b>	217
Solid state structures of <b>2</b> , <b>4</b> , and <b>5</b> .	
<b>Figure 5.3.</b>	220
Qualitative MO diagram and selected calculated valence MOs depicting the Mo/nitride bonding in <b>5</b> .	
<b>Chapter 6</b>	
<b>Figure 6.1.</b>	246
<b>Figure 6.1.</b> Classes of previously reported terminal phosphide complexes.	
<b>Figure 6.2.</b>	247
Solid-state structure of <b>2</b> .	
	249

<b>Figure 6.3.</b>	Qualitative MO energy diagram and selected calculated valence MOs depicting the Mo/phosphide bonding in <b>2</b> .	
<b>Figure 6.4.</b>	Experimental and simulated X-band CW EPR spectra of <b>3</b> .	251
<b>Figure 6.5.</b>	Solid-state structures of <b>6</b> and <b>7</b> .	255
<b>Figure 6.6.</b>	Solid-state structures of <b>8</b> and <b>9</b> .	257
<b>Figure 6.7.</b>	Synthesis of dinuclear Mo complexes bearing bridging phosphinidene and phosphido ligands.	259
<b>Figure 6.8.</b>	X-band CW EPR spectrum of a 2Me-THF glass of <b>11</b> .	260
<b>Figure 6.9.</b>	Synthesis and solid-state structure of phosphide hydride complex <b>12</b> .	262
<b>Chapter 7</b>		
<b>Figure 7.1.</b>	Solid-state structure and schematic representation of the CO <sub>2</sub> -bound NiFe-CODH active site.	312
<b>Figure 7.2.</b>	Solid-state structures of Mo(0) complexes <b>2</b> , <b>3</b> , and <b>4</b> .	315
<b>Figure 7.3.</b>	ATR IR Spectra of Mo(0) N <sub>2</sub> complex, <b>1</b> , and its B(C <sub>6</sub> F <sub>5</sub> ) <sub>3</sub> adduct, <b>3</b> .	316
<b>Figure 7.4.</b>	ATR IR Spectra of isotopologs <b>2/2-<sup>13</sup>C</b> and <b>4/4-<sup>13</sup>C</b> .	317
<b>Figure 7.5.</b>	CO <sub>2</sub> Activation as a function of Lewis acidity.	319
<b>Chapter 8</b>		
<b>Figure 8.1.</b>	Synthesis and solid-state structure of carboxylate hydride complex <b>5</b> .	353
<b>Figure 8.2.</b>	Synthesis and solid-state structure of carboxylate hydride complex <b>5</b> .	354
<b>Figure 8.3.</b>	Synthesis and solid-state structure of <b>11</b> .	358
<b>Appendix A</b>		
<b>Figure A.1.</b>	Solid state structures of nitrides <b>1</b> and <b>3</b> .	384
<b>Figure A.2.</b>	A) X-band CW-EPR spectra of nitride <b>4</b> generated with natural abundance N and 50% <sup>15</sup> N. B) Pseudomodulated Q-band ESE-EPR spectra of nitride <b>4</b> generated with natural abundance N and 50% <sup>15</sup> N.	384

<b>Figure A.3.</b>	385
X-band Davies ENDOR of nitride <b>4</b> generated with natural abundance N	
<b>Figure A.4.</b>	386
Q-band Davies ENDOR of nitride <b>4</b> generated with natural abundance N	
<b>Figure A.5.</b>	387
Field-dependent Q-band Davies ENDOR of nitride <b>4</b> generated with natural abundance N and 50% $^{15}\text{N}$ .	
<b>Figure A.6.</b>	388
Field-dependent Q-band HYSORE of nitride <b>4</b> generated with natural abundance N and 50% $^{15}\text{N}$ .	
<b>Figure A.7.</b>	389
Partial $^{13}\text{C}\{^1\text{H}\}$ and $^{31}\text{P}\{^1\text{H}\}$ NMR spectra following the oxidation of terminal carbide <b>6-<math>^{13}\text{C}</math></b> .	
<b>Appendix B</b>	
<b>Figure B.1.</b>	398
Literature examples of metal-ligand bifunctional catalysts	
<b>Figure B.2.</b>	400
Preliminary solid-state structure and relevant metrical parameters for Mo(0) $\text{N}_2$ adduct, <b>1</b> .	
<b>Figure B.3.</b>	401
Small molecule reactivity from putative $\eta^6$ -phenol Mo $\text{N}_2$ adduct <b>3</b> .	
<b>Figure B.4.</b>	403
Solid-state structure of <b>7</b> .	
<b>Appendix C</b>	
<b>Note:</b> Appendix C contains the characterization NMR spectra for the complexes reported in this dissertation (Figures C.1. – C.174); a complete list of which is impractical.	

## LIST OF SCHEMES

<b>Chapter 2</b>	
<b>Scheme 2.1.</b>	14
Synthesis of Mo <i>para</i> -terphenyl diphosphine complexes.	
<b>Scheme 2.2.</b>	20
Proposed mechanism for MoII-initiated catalytic AB dehydrogenation.	
<b>Scheme 2.3.</b>	21
Proposed mechanism for Mo <sup>0</sup> -initiated catalytic AB dehydrogenation.	
<b>Chapter 3</b>	
<b>Scheme 3.1.</b>	65
Stepwise reduction of <i>para</i> -terphenyl diphosphine supported Mo dicarbonyl complexes.	
<b>Scheme 3.2.</b>	69
Deoxygenative coupling of CO to a C <sub>2</sub> O <sub>1</sub> fragment.	
<b>Scheme 3.3.</b>	70
Trimethylsilyl alkylidyne desilylation to terminal carbide <b>7</b> and subsequent resilylation to carbyne <b>8</b> .	
<b>Scheme 3.4.</b>	73
<sup>4</sup> Pr <sub>3</sub> SiCl addition to dianion <b>3</b> . Product distribution, as determined by <sup>31</sup> P{ <sup>1</sup> H} NMR spectroscopy, is shown in brackets.	
<b>Scheme 3.5.</b>	74
Me <sub>3</sub> SiCl addition to dianion <b>3</b> .	
<b>Scheme 3.6.</b>	80
Mechanistic possibilities (Paths 1-5, in blue) for the elementary reaction step of C–O bond cleavage from dicarbyne <b>9</b> .	
<b>Scheme 3.7.</b>	82
End-product distributions in isotopic labeling studies of the C–O bond cleavage step.	
<b>Scheme 3.8.</b>	86
<i>In situ</i> generation and silylation of terminal carbide <b>8</b> .	
<b>Scheme 3.9.</b>	87
Synthesis of mixed dicarbyne complexes and subsequent C–C bond formation.	
<b>Scheme 3.10.</b>	89
Crossover-type experiments from <b>8/8-<sup>13</sup>C</b> and <b>1/1-<sup>13</sup>C</b> .	
<b>Scheme 3.11.</b>	94
Envisioned synthetic cycle for four-electron CO reductive coupling.	
<b>Chapter 4</b>	
<b>Scheme 4.1.</b>	175
Addition of protons to dianion <b>1</b> .	
<b>Scheme 4.2.</b>	177

Reduction and electrophilic quenching of diene dicarbonyl <b>3</b> to give bis(siloxy)acetylene adduct <b>5</b> .	
<b>Scheme 4.3.</b>	180
Regioselectivity comparison for electrophile-induced C–C coupling and C–O cleavage in a series of Mo dicarbonyl complexes.	
<b>Scheme 4.4.</b>	183
Envisioned synthetic cycle for formation of silylated dihydroxy acrolein or dihydroxy cyclopentenone from three molecules of CO.	
<b>Scheme 4.5.</b>	184
Sequential reduction and electrophile addition and concerted hydride addition prompting C–C bond formation from <b>16</b> .	
<b>Scheme 4.6.</b>	185
Possible mechanistic pathways for hydride addition to and C–C coupling from trimethylsilyl alkylidyne precursor <b>16-<sup>13</sup>C</b> .	
<b>Scheme 4.7.</b>	187
Terminal methylidyne synthesis from acid addition to terminal carbide <b>8</b> .	
<b>Scheme 4.8.</b>	189
Terminal methyldene intermediate observed prior to P–C bond formation upon hydride addition to <b>19</b> .	
<b>Scheme 4.9.</b>	190
Sequential CO insertion and C–P bond formation leading to phosphoranylidene ketene complexes <b>22</b> and <b>23</b> .	
<b>Scheme 4.10.</b>	191
Synthesis of carbonyl complex <b>24</b> from methyldene intermediate <b>C</b> .	
<b>Chapter 5</b>	
<b>Scheme 5.1.</b>	216
Synthesis of Mo(IV) terminal nitrido complexes.	
<b>Scheme 5.2.</b>	219
Anionic nitride synthesis and N <sup>-</sup> group transfer reactivity.	
<b>Scheme 5.3.</b>	222
Possible mechanisms for cyanate anion formation from <b>5-Na</b> and CO.	
<b>Chapter 6</b>	
<b>Scheme 6.1.</b>	247
Synthesis of terminal phosphide <b>2</b> .	
<b>Scheme 6.2.</b>	252
Oxidation-induced phosphide coupling.	
<b>Scheme 6.3.</b>	254
Synthesis of Mo dimethylamino phosphinidene <b>6</b> and phosphide <b>7</b> complexes.	
<b>Scheme 6.4.</b>	256
Synthesis of $\mu$ -phosphide complexes <b>8</b> and <b>9</b> .	
<b>Scheme 6.5.</b>	261

Thermochemical square scheme for HAT from  $\mu$ -phosphinidene **10**.

<b>Chapter 7</b>	
<b>Scheme 7.1.</b>	314
CO <sub>2</sub> binding and LA adduct formation at low-valent Mo.	
<b>Scheme 7.2.</b>	317
Acid-induced C–O bond cleavage of Mo-bound LA-adducted CO <sub>2</sub> .	
<b>Scheme 7.3.</b>	320
Proposed mechanism for proton-induced CO <sub>2</sub> cleavage from <b>4</b> .	
<b>Chapter 8</b>	
<b>Scheme 8.1.</b>	352
Small-molecule binding equilibria and stoichiometric CO <sub>2</sub> hydrogenation at low-valent Mo.	
<b>Scheme 8.2.</b>	354
Proposed catalytic cycle for CO <sub>2</sub> hydrosilylation from precatalyst <b>2</b> .	
<b>Scheme 8.3.</b>	355
CO <sub>2</sub> cleavage in the presence (A) and absence (B) of silane.	
<b>Scheme 8.4.</b>	357
Plausible mechanisms for the formation of <b>7</b> from <b>6</b> and CO <sub>2</sub> .	
<b>Scheme 8.5.</b>	358
Formic acid protonation of N <sub>2</sub> adduct <b>1</b> .	
<b>Scheme 8.6.</b>	360
Plausible mechanisms for FA dehydrogenation from <b>4</b> .	
<b>Scheme 8.7.</b>	361
Independent synthetic routes to hydride cation <b>15</b> .	
<b>Scheme 8.8.</b>	362
Stoichiometric reactions of <b>4</b> with LA (left), base (down), and both (right).	
<b>Scheme 8.9.</b>	363
Plausible catalytic cycle for CO <sub>2</sub> hydrogenation from <b>4</b> .	
<b>Appendix A</b>	
<b>Scheme A.1</b>	381
Terminal Mo(V) phosphide coupling.	
<b>Scheme A.2</b>	383
Synthesis of Mo(IV) and Mo(V) nitride chloride complexes.	
<b>Scheme A.3</b>	389
<i>In situ</i> oxidation of terminal carbide <b>6</b> .	
<b>Appendix B</b>	
<b>Scheme B.1</b>	399
Synthesis of <b>P2<sup>OH</sup></b> -supported Mo(0) N <sub>2</sub> adducts.	
<b>Scheme B.2</b>	403
Synthesis of Mo tricarbonyl anion <b>7</b> .	



## LIST OF TABLES AND CHARTS

<b>Chapter 2</b>	
<b>Table 2.1.</b>	18
Mo-based homogeneous precatalysts for AB dehydrogenation in comparison to precatalysts reported to release $\geq 2.0$ equiv. of H <sub>2</sub> .	
<b>Table 2.2.</b>	49
Crystal and refinement data for complexes <b>2-5</b> and <b>7-8</b> .	
<b>Chapter 3</b>	
<b>Chart 3.1.</b>	61
Select examples reporting reductive CO functionalization.	
<b>Table 3.1.</b>	122
Dynamic NMR fit parameters for carbyne exchange in <b>9-<sup>13</sup>C</b> .	
<b>Table 3.2.</b>	153
Optimized gas-phase single-point energies for variants of <b>8</b> and <b>11</b> .	
<b>Table 3.3.</b>	153
Comparison of experimental and calculated spectroscopic data for <b>2</b> , <b>7-11</b> , and <b>15</b> .	
<b>Table 3.4.</b>	154
Comparison of experimental and calculated spectroscopic data for <b>2</b> , <b>7-11</b> , and <b>15</b> .	
<b>Table 3.5.</b>	156
Crystal and refinement data for complexes <b>2-4</b> and <b>8</b> .	
<b>Table 3.6.</b>	157
Crystal and refinement data for complexes <b>10</b> , <b>11</b> , <b>16</b> , and <b>17</b> .	
<b>Chapter 4</b>	
<b>Table 4.1.</b>	203
Crystal and refinement data for complexes <b>2</b> , <b>3</b> , and <b>5</b> .	
<b>Table 4.1.</b>	204
Crystal and refinement data for complexes <b>9</b> , <b>18</b> , <b>19</b> , and <b>22</b> .	
<b>Chapter 5</b>	
<b>Table 5.1</b>	235
Comparison of experimental and calculated structural metrics and <b>5</b> .	
<b>Table 5.2</b>	237
Crystal and refinement data for complexes <b>2</b> , <b>4</b> , & <b>5</b> .	
<b>Chapter 6</b>	
<b>Table 6.1.</b>	248
Selected bond metrics [ $\text{\AA}$ ] for phosphides <b>2</b> and <b>3</b> .	
<b>Table 6.2.</b>	286
Absolute values of hyperfine coupling parameters for <b>3</b> .	

<b>Table 6.3.</b>	295
Comparison of experimental and calculated structural metrics for <b>2</b> and <b>3</b> .	
<b>Table 6.4.</b>	295
Computed Mulliken spin densities and experimental isotropic hyperfine coupling constants for <b>3</b> .	
<b>Table 6.5.</b>	298
Crystal and refinement data for complexes <b>2 – 4</b> and <b>6 – 9</b> .	
<b>Chapter 7</b>	
<b>Table 7.1.</b>	319
CO <sub>2</sub> adduct activation, exchange rates, and C–O bond cleavage selectivities as a function of LA.	
<b>Table 7.2.</b>	329
Lewis Acid acceptor number determination.	
<b>Table 7.3.</b>	332
Compiled NMR data for Lewis acid adducts of <b>3</b> .	
<b>Table 7.4.</b>	333
Inversion recovery experiments for and equilibrium mixture of <b>1-<sup>15</sup>N/2-<sup>13</sup>C</b> .	
<b>Table 7.5.</b>	336
CO <sub>2</sub> Exchange rate as a function of LA identity.	
<b>Table 7.6.</b>	341
Crystal and refinement data for complexes <b>2 - 4, 6, &amp; 7</b> .	
<b>Chapter 8</b>	
<b>Table 8.1.</b>	319
Preliminary catalytic screening for FA dehydrogenation.	
<b>Table 8.2.</b>	329
Catalytic data for formic acid dehydrogenation.	
<b>Table 8.3.</b>	374
Crystal and refinement data for complexes <b>5, 6<sup>PhH</sup>, and 11</b> .	
<b>Appendix A</b>	
<b>Table 8.1.</b>	387
EPR fit parameters for nitrides <b>4/4-<sup>15</sup>N</b> .	



## CHAPTER 1

### General Introduction

***“Simplicity is the ultimate sophistication”***

~Clare Boothe Luce

Simple small molecules, such as CO<sub>2</sub>, CO, N<sub>2</sub>, H<sub>2</sub>, CH<sub>4</sub>, and O<sub>2</sub> provide the underpinnings for numerous chemistries practiced on tremendous global scales—indeed in that sense, they prove to be anything but “small” and “simple.” From biological processes like photosynthesis and cellular respiration, responsible for the oxygen we breathe and the energy that powers our cells, to large-scale industrial processes such as Haber-Bosch and Fischer-Tropsch, that feed our planet and fuel our cars, these molecules are integral feedstocks and reagents. Significant effort in chemical research is devoted to harnessing the reactivity of these species; control of their chemistry has the potential to address many concerns threatening societal sustainability.<sup>1</sup>

Though plentiful, many small molecules are inert. They feature strong chemical bonds, the manipulation of which is both kinetically unfavorable and thermodynamically demanding.<sup>2</sup> Moreover, the chemistries of these molecules frequently require the controlled transfer of multiple redox equivalents, in concert with the transfer of multiple protons.<sup>1a,3</sup> This presents a litany of challenges we face as organometallic chemists pursuing small molecule activation: i) How can we engineer metal complexes capable of binding and activating these molecules? ii) How can we engender the types of reactivity we desire? iii) How can we control said reactivity and make it selective for the product(s) of interest?

Looking at these problems, it is apparent that Nature has the advantage. Through complex protein architectures, channels usher reagents in and products out of intricately designed active sites in which multiple metal centers are poised to distribute redox loading, activate substrates, and control reactivity.<sup>4</sup> Management of proton delivery, through proximal basic moieties, and environmental conditions, through hydrophobicity/philicity, adds an additional level of regulation. In this sense, it is not surprising that biological machinery is capable of such remarkable transformations *nor* is

it unexpected that many enzyme active sites prove unreactive once removed from their parent protein.

Attempted mimicry of biological systems has resulted in ever-increasing complexity in molecular organometallic chemistry. Ligand scaffolds premeditated to include hydrogen bonding networks,<sup>5</sup> undergo redox reactivity in concert with the supported metal center,<sup>6</sup> and coordinate multiple metals in close proximity (both homo- and hetero-multimetallic)<sup>7</sup> are all topical. These designs allow for the stabilization of unique motifs, the transfer of multiple protons and electrons, and achievement of unprecedented reactivity. The idea of devising and assembling a secondary coordination sphere in homogenous metal complexes is now commonplace.

This dissertation describes small molecule activation chemistry at a series of *para*-terphenyl diphosphine supported Mo complexes. These compounds demonstrate that arenes are capable of imbuing a number of desirable ligand properties, including hemilability, redox non-innocence, and electronic variability.<sup>8</sup> Though metal-arene interactions have been a known entity in organometallic chemistry since the synthesis of bis(benzene)chromium,<sup>9</sup> very few studies have investigated the nuances of chelation enforced metal-arene binding. Prior to work from our group, literature precedent had shown that arene ligands could act as hemilabile donors capable of unmasking coordinatively unsaturated reactive metal fragments,<sup>10</sup> stabilizing reaction intermediates,<sup>11</sup> and even altering reactivity (Figure 1.1).<sup>12</sup> In this sense, incorporation of an arene donor in a ligand platform seems alluring.

Initially intended to support multiple metal centers between a rigid aromatic spacer,<sup>13</sup> the *para*-terphenyl diphosphine ligand's wide bite angle was found to likewise be viable for supporting monometallic species, giving rise to an atypical "pincer-like" chelate with a central arene  $\pi$ -system in lieu of an anionic donor. This work focusses on the chemistry of Mo complexes in this coordination environment. Early studies (Chapter 2) disclose

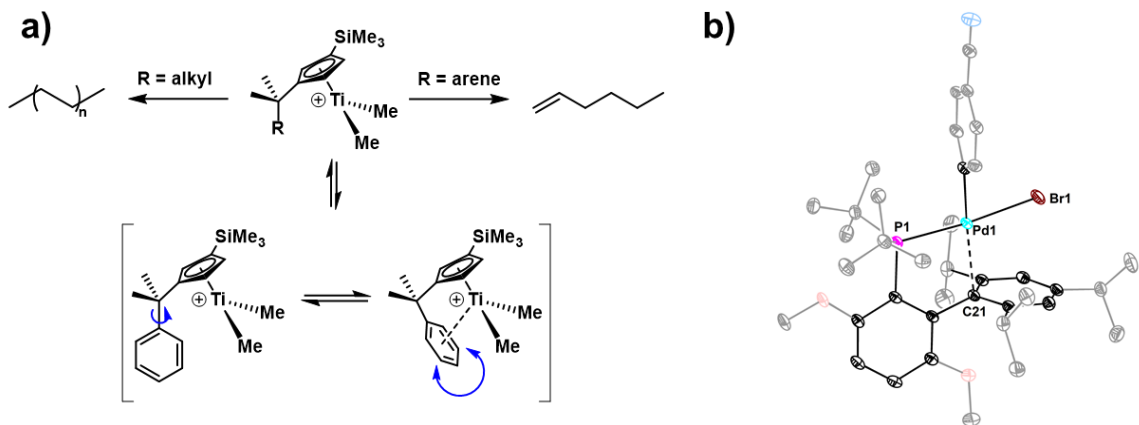


**Figure 1.1.** Prior examples of M-arene interactions observed in solution (a)<sup>12d</sup> and the solid-state (b)<sup>11a</sup>.

Mo-arene interaction changes as a function of metal oxidation state and coordination number in the greater context of H<sub>2</sub> storage. Both  $\eta^2$  and  $\eta^6$  metal-arene binding is observed, evidenced by solution NMR spectroscopy and demonstrated in the solid-state via metrical perturbations of the central ring. This flexible binding provides access to Mo complexes with one to three additional donors, spanning four formal oxidation states (from +4 to 0). Subsequent work expands the accessible redox-state range from Mo(V) to Mo(-III)! The latter Chapters of this thesis describe how these electrons (Chapters 3 and 5) and holes (Chapter 6, Appendix A) afford access to unusual molecular motifs and, perhaps more importantly, imparts them with atypical reactivity. Some work has been conducted looking at how variations of the basal  $\pi$ -system effect reactivity (Chapter 4), but clearly significantly more work in this area remains to be done.

The protean behavior of arene donors must be, in no small part, attributed to the electronics of metal-arene binding.<sup>8</sup> Complexes with hapticities ranging from  $\eta^0$  to  $\eta^6$  have been well-characterized; not only does this reveal (or occupy) coordination sites at the metal, but the electronic structure of these binding modes varies markedly. Contrast, for instance, an  $\eta^2$  and an  $\eta^6$  metal-arene interaction (Figure 1.2.). In the former, an occupied C–C  $\pi$ -bonding orbital acts as a  $\sigma$ -donor and a  $\pi^*$  orbital of the same C–C bond is a  $\pi$ -acceptor. This allows for favorable “push-pull” interactions with trans coordinated  $\pi$ -

basic ligands, as is observed in Mo(IV) and Mo(V) terminal pnictogen complexes. In an  $\eta^6$  binding mode, the arene serves primarily as a  $\delta$ -acid, with the metal-based orbitals being energetically well-matched to arene  $\pi$ -system antibonding configurations with  $\delta$ -symmetry with respect to the metal. Notably, if the frame of reference is held constant, the metal d-orbitals that interact with the arene change as a function of binding mode— $d(yz)$  for  $\eta^2$  and  $d(xy)/d(x^2-y^2)$  for  $\eta^6$ .

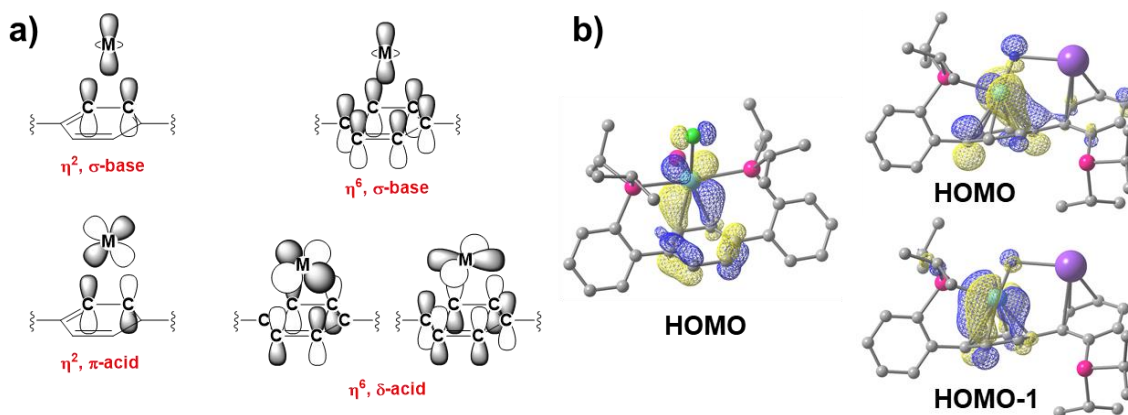


**Figure 1.2.** Qualitative (a) and calculated (b) orbital depictions of  $\eta^2$  and  $\eta^6$  metal-arene interactions. The DFT structures depict a Mo(IV) phosphide complex (b, left) and the two-electron reduced nitrogen congener (b, right).

Another beneficial feature discovered for the central arene is its role as an electron reservoir. The cleavage of small molecule substrates (such as  $N_2$  ( $6e^-$ ),  $CO$  ( $6e^-$ ), and  $O_2$  ( $4e^-$ )) requires multiple redox equivalents, making these transformations challenging to enact at a single metal center. Stepwise addition of electrons is possible, but can require traversing through high energy intermediates. We found that at sufficiently reducing potentials, the metal-arene interaction allows for significant delocalization of reducing equivalents into the ring, adopting cyclohexyldienyldianionic character.<sup>14</sup> This storage of charge facilitates the complete cleavage of  $CO$  to a rare example of a terminal transition metal carbide (Chapter 3). In conjunction with redox non-innocence, the elasticity of the arene ligand, able to support both low-valent Mo complexes capable of  $CO$  activation ( $\eta^6$  binding or reduced arene), and high-valent Mo complexes resulting from  $C-O$  cleavage



( $\eta^2$  or  $\eta^0$  binding), is paramount to the observed reactivity—deoxygenation and coupling of two molecules of CO to a metal-free oxyacetylene fragment.

It would be remiss of me not to mention projects that were conducted in the group in concert with the pursuit of this thesis research, many of which instigated ideas that are borne out in the present work. Expanding on these concepts of ligand non-innocence, functionalization of the central benzene to a motif prone to proton coupled electron transfer, such as catechol<sup>15</sup> and *para*-hydroquinone,<sup>16</sup> was achieved by Dr. Justin Henthorn and Dr. Kyle Horak (Figure 1.3.). Their exploration of these modified arenes as a source of electrons and protons for small molecule reduction is intimately related to concepts conveyed throughout this dissertation. From the catechol diphosphine scaffold, installation of a proximal Lewis acid was studied by Dr. Sibö Lin and Dr. Henthorn.<sup>15b</sup> Cooperative small molecule activation, a concept that was very influential to work presented here (Chapter 7), was established by these coworkers. Insightful discussions about the similarities and, often more critically, the differences of these systems were pivotal to gaining an understanding of the chemistry of P-arene-P chelates.

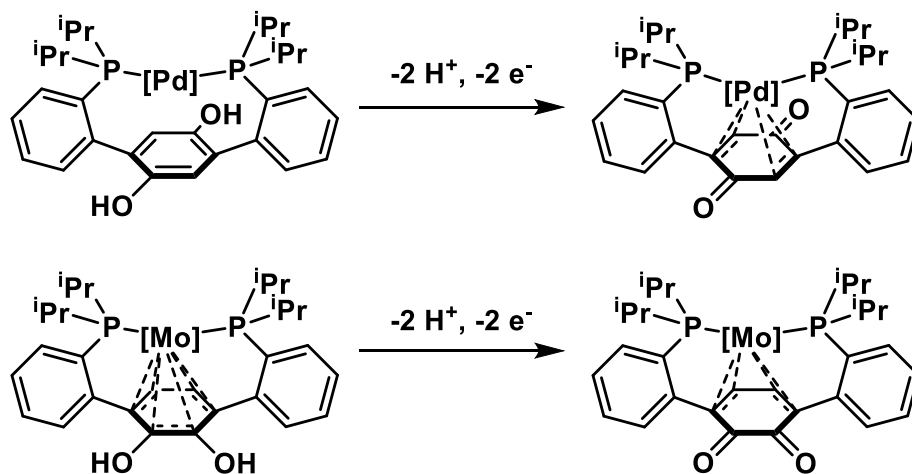


**Figure 1.3.** Teraryl diphosphine ligands bearing functionalized redox-active central arene motifs.

Overall, this work establishes the versatility of metal-arene interactions in the chemical transformations of small molecules, including binding and activation ( $H_2$ , Chapter 2; CO,

Chapter 3; CO<sub>2</sub>, Chapter 7), cleavage (CO, Chapter 3; CO<sub>2</sub>, Chapters 7 and 8), and group transfer of the resulting fragments (Chapters 3, 4, 5, 6, 8). The arene interactions provide sufficient reactivity to enact these challenging multi-electron transformations, while simultaneously conveying appropriate stability to observe and characterize reactive intermediates.

## REFERENCES

- (1) a) Meyer, F.; Tolman, W. B. *Inorg. Chem.* **2015**, *54*, 5039; b) Milani, B.; Licini, G.; Clot, E.; Albrecht, M. *Dalton Trans.* **2016**, *45*, 14419; c) Crutchley, R. J. *Coord. Chem. Rev.* **2017**, *334*, 1.
- (2) Jia, H.-P.; Quadrelli, E. A. *Chem. Soc. Rev.* **2014**, *43*, 547.
- (3) a) Weinberg, D. R.; Gagliardi, C. J.; Hull, J. F.; Murphy, C. F.; Kent, C. A.; Westlake, B. C.; Paul, A.; Ess, D. H.; McCafferty, D. G.; Meyer, T. J. *Chem. Rev.* **2012**, *112*, 4016; b) Huynh, M. H. V.; Meyer, T. J. *Chem. Rev.* **2007**, *107*, 5004.
- (4) Holm, R. H.; Kennepohl, P.; Solomon, E. I. *Chem. Rev.* **1996**, *96*, 2239.
- (5) a) Gordon, Z.; Drummond, M. J.; Matson, E. M.; Bogart, J. A.; Schelter, E. J.; Lord, R. L.; Fout, A. R. *Inorg. Chem.* **2017**, *56*, 4852; b) Ford, C. L.; Park, Y. J.; Matson, E. M.; Gordon, Z.; Fout, A. R. *Science* **2016**, *354*, 741; c) Matson, E. M.; Park, Y. J.; Fout, A. R. *J. Am. Chem. Soc.* **2014**, *136*, 17398; d) Hill, E. A.; Weitz, A. C.; Onderko, E.; Romero-Rivera, A.; Guo, Y.; Swart, M.; Bominaar, E. L.; Green, M. T.; Hendrich, M. P.; Lacy, D. C.; Borovik, A. S. *J. Am. Chem. Soc.* **2016**, *138*, 13143; e) Shook, R. L.; Peterson, S. M.; Greaves, J.; Moore, C.; Rheingold, A. L.; Borovik, A. S. *J. Am. Chem. Soc.* **2011**, *133*, 5810; f) MacBeth, C. E.; Golombek, A. P.; Young, V. G.; Yang, C.; Kuczera, K.; Hendrich, M. P.; Borovik, A. S. *Science* **2000**, *289*, 938; g) Dahl, E. W.; Dong, H. T.; Szymczak, N. K. *Chem. Commun.* **2018**, *54*, 892; h) Dahl, E. W.; Szymczak, N. K. *Angew. Chem. Int. Ed.* **2016**, *55*, 3101; i) Moore, C. M.; Szymczak, N. K. *Chem. Sci.* **2015**, *6*, 3373; j) Creutz, S. E.; Peters, J. C. *Chem. Sci.* **2017**, *8*, 2321.
- (6) a) Lyaskovskyy, V.; de Bruin, B. *ACS Catalysis* **2012**, *2*, 270; b) Luca, O. R.; Crabtree, R. H. *Chem. Soc. Rev.* **2013**, *42*, 1440.
- (7) a) Venkateswara Rao, P.; Holm, R. H. *Chem. Rev.* **2004**, *104*, 527; b) Sartorel, A.; Bonchio, M.; Campagna, S.; Scandola, F. *Chem. Soc. Rev.* **2013**, *42*, 2262; c) Cooper, B. G.; Napoline, J. W.; Thomas, C. M. *Catalysis Reviews* **2012**, *54*, 1; d) Berry, J. F.; Lu, C. C. *Inorg. Chem.* **2017**, *56*, 7577; e) de Ruiter, G.; Thompson, N. B.; Lionetti, D.; Agapie, T. *J. Am. Chem. Soc.* **2015**, *137*, 14094; f) Lionetti, D.; Day, M. W.; Agapie, T. *Chem. Sci.* **2013**, *4*, 785; g) Tsui, E. Y.; Tran, R.; Yano, J.; Agapie, T. *Nat. Chem.* **2013**, *5*, 293; h) Kanady, J. S.; Tsui, E. Y.; Day, M. W.; Agapie, T. *Science* **2011**, *333*, 733; i) Tsui, E. Y.; Day, M. W.; Agapie, T. *Angew. Chem. Int. Ed.* **2011**, *50*, 1668; j) Hernández Sánchez, R.; Betley, T. A. *J. Am. Chem. Soc.* **2015**, *137*, 13949; k) Zhao, Q.; Betley, T. A. *Angew. Chem. Int. Ed.* **2011**, *50*, 709; l) Powers, T. M.; Fout, A. R.; Zheng, S.-L.; Betley, T. A. *J. Am. Chem. Soc.* **2011**, *133*, 3336; m) Zhao, Q.; Harris, T. D.; Betley, T. A. *J. Am. Chem. Soc.* **2011**, *133*, 8293.
- (8) Muetterties, E. L.; Blecke, J. R.; Wucherer, E. J.; Albright, T. *Chem. Rev.* **1982**, *82*, 499.
- (9) a) Fischer, E. O.; Fritz, H. P. In *Advances in Inorganic Chemistry and Radiochemistry*; Emeléus, H. J., Sharpe, A. G., Eds.; Academic Press: 1959; Vol. 1, p 55; b) Jellinek, F. *Nature* **1960**, *187*, 871.
- (10) a) Werner, H. *Dalton Trans.* **2003**, 3829; b) Dugan, T. R.; Sun, X.; Rybak-Akimova, E. V.; Olatunji-Ojo, O.; Cundari, T. R.; Holland, P. L. *J. Am. Chem. Soc.* **2011**, *133*, 12418; c) Singewald, E. T.; Shi, X.; Mirkin, C. A.; Schofer, S. J.; Stern, C. L. *Organometallics* **1996**, *15*, 3062; d) Nesmeyanov, A. N.; Krivykh, V. V.; Rybinskaya, M. I. *J. Organomet. Chem.* **1979**, *164*, 159; e) Montag, M.; Leitus, G.; Shimon, L. J. W.; Ben-David, Y.; Milstein, D. *Chem. Eur. J.* **2007**, *13*, 9043; f) Braunstein, P.; Naud, F. *Angew. Chem. Int. Ed.* **2001**, *40*, 680.

- (11) a) Su, M.; Buchwald, S. L. *Angew. Chem. Int. Ed.* **2012**, *51*, 4710; b) Maimone, T. J.; Milner, P. J.; Kinzel, T.; Zhang, Y.; Takase, M. K.; Buchwald, S. L. *J. Am. Chem. Soc.* **2011**, *133*, 18106; c) Barder, T. E.; Biscoe, M. R.; Buchwald, S. L. *Organometallics* **2007**, *26*, 2183.
- (12) a) Otten, E.; Meetsma, A.; Hessen, B. *J. Am. Chem. Soc.* **2007**, *129*, 10100; b) Deckers, P. J. W.; Hessen, B.; Teuben, J. H. *Angew. Chem. Int. Ed.* **2001**, *40*, 2516; c) Blok, A. N. J.; Budzelaar, P. H. M.; Gal, A. W. *Organometallics* **2003**, *22*, 2564; d) Otten, E.; Batinas, A. A.; Meetsma, A.; Hessen, B. *J. Am. Chem. Soc.* **2009**, *131*, 5298.
- (13) a) Horak, K. T.; VanderVelde, D. G.; Agapie, T. *Organometallics* **2015**, *34*, 4753; b) Horak, K. T.; Lin, S.; Rittle, J.; Agapie, T. *Organometallics* **2015**, *34*, 4429; c) Horak, K. T.; Velian, A.; Day, M. W.; Agapie, T. *Chem. Commun.* **2014**, *50*, 4427; d) Lin, S.; Herbert, D. E.; Velian, A.; Day, M. W.; Agapie, T. *J. Am. Chem. Soc.* **2013**, *135*, 15830; e) Velian, A.; Lin, S.; Miller, A. J. M.; Day, M. W.; Agapie, T. *J. Am. Chem. Soc.* **2010**, *132*, 6296.
- (14) a) Cassani, M. C.; Gun'ko, Y. K.; Hitchcock, P. B.; Lappert, M. F.; Laschi, F. *Organometallics* **1999**, *18*, 5539; b) Sattler, A.; Parkin, G. *J. Am. Chem. Soc.* **2012**, *134*, 2355.
- (15) a) Henthorn, J. T.; Agapie, T. *Inorg. Chem.* **2016**, *55*, 5337; b) Henthorn, J. T.; Lin, S.; Agapie, T. *J. Am. Chem. Soc.* **2015**, *137*, 1458.
- (16) Horak, K. T.; Agapie, T. *J. Am. Chem. Soc.* **2016**, *138*, 3443.



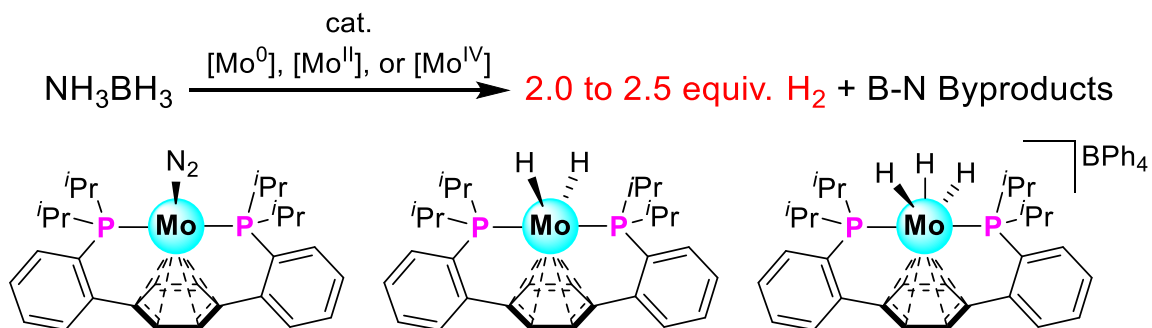
## CHAPTER 2

### Molybdenum Catalyzed Ammonia Borane Dehydrogenation: Oxidation State Specific Mechanisms

This work was published in part as:

*J. Am. Chem. Soc.* **2014**, *136*, 11272.

## ABSTRACT



Though numerous catalysts for the dehydrogenation of ammonia borane (AB) are known, those that release greater than 2 equivalents (equiv.) of  $\text{H}_2$  are uncommon. Herein, we report the synthesis of Mo complexes supported by a *para*-terphenyl diphosphine ligand, displaying metal-arene interactions. Both a  $\text{Mo}^0$   $\text{N}_2$  complex and a  $\text{Mo}^{\text{II}}$  bis(acetonitrile) complex exhibit high levels of AB dehydrogenation, releasing over 2.0 equiv. of  $\text{H}_2$ . The reaction rate, extent of dehydrogenation and reaction mechanism vary as a function of the precatalyst oxidation state. Several Mo hydrides ( $\text{Mo}^{\text{II}}(\text{H})_2$ ,  $[\text{Mo}^{\text{II}}(\text{H})]^+$ , and  $[\text{Mo}^{\text{IV}}(\text{H})_3]^+$ ) relevant to AB chemistry were characterized.

## GENERAL INTRODUCTION

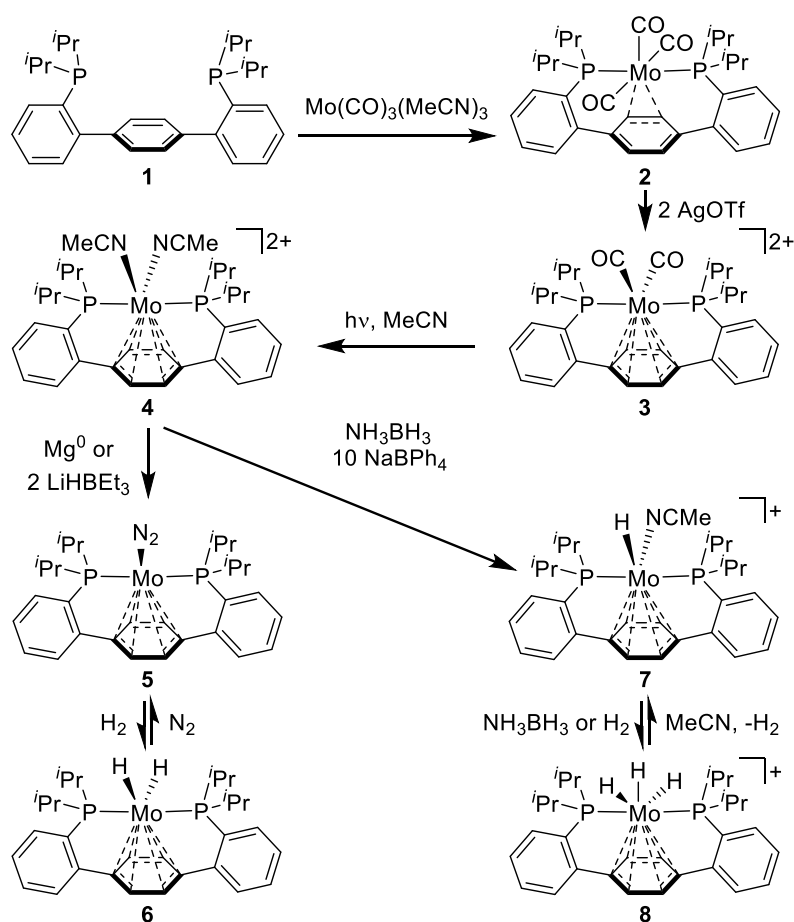
There has been significant interest in transitioning from petroleum-based fuels to a “hydrogen economy,” with respect to both green energy and increased energy security.<sup>1</sup> A limitation to the implementation of hydrogen (H<sub>2</sub>) in transportation is its low energy density and complications arising from compressed gas storage.<sup>1b,2</sup> Numerous forms of chemical H<sub>2</sub> storage from metal hydrides<sup>1b</sup> to metal organic frameworks<sup>3</sup> have been explored. A forerunner in this field is ammonia borane (AB, NH<sub>3</sub>BH<sub>3</sub>), a compound with a substantial gravimetric storage capability of 19.6 wt % H<sub>2</sub> when dehydrogenated through the third equivalent (equiv.).<sup>4</sup> AB shows promise for reversible H<sub>2</sub> storage, with work towards efficient regeneration ongoing.<sup>5</sup>

Various AB dehydrogenation catalysts, including frustrated Lewis pairs<sup>6</sup> and ionic liquids,<sup>7</sup> have been investigated. Metal-based catalysts show the most potential for controlling both the rate and extent of H<sub>2</sub> release,<sup>2</sup> and have demonstrated high activities in the cases of Ir,<sup>8</sup> Ru,<sup>9</sup> and Pd.<sup>10</sup> Extensive H<sub>2</sub> release is less common due to NH<sub>2</sub>BH<sub>2</sub> oligomerization,<sup>11</sup> but examples are known for Ni (*ca.* 2.7 equiv.),<sup>12</sup> Fe (*ca.* 1.7 equiv.),<sup>13</sup> Pd (*ca.* 2.0 equiv.),<sup>10</sup> Rh (*ca.* 2.0 equiv.),<sup>14</sup> and Ru (*ca.* 2.3 equiv.) (Table 2.1).<sup>15</sup> These catalysts either employ expensive metals (Ru<sup>15</sup> and Pd<sup>10</sup>) or suffer from instability (Pd,<sup>10</sup> Fe,<sup>13</sup> and Ni<sup>16</sup>). We report here the first examples of AB dehydrogenation catalysts based on Mo, an abundant and inexpensive metal. Our systems have demonstrated distinct behavior dependent on oxidation state, with isolated Mo<sup>0</sup>, Mo<sup>II</sup>, and Mo<sup>IV</sup> complexes capable of releasing over 2 equiv. of H<sub>2</sub> from AB under moderate conditions.



## RESULTS AND DISCUSSION

Transition metal complexes supported by *para*-terphenyl diphosphine **1** (Scheme 2.1) have been studied for new types of reactivity.<sup>17</sup> Mo complexes ligated by diphosphine **1** were targeted to take advantage of the pendant arene acting as a versatile and hemilabile ligand for supporting different metal oxidation states and binding modes. Heating **1** in the presence of  $\text{Mo}(\text{CO})_3(\text{MeCN})_3$ , cleanly afforded the Mo *para*-terphenyl diphosphine complex **2** (Scheme 2.1). Through single crystal X-ray diffraction (XRD) analysis,  $\eta^2$ -arene binding was observed with partial disruption of aromaticity in the central ring (Figure 2.1).



**Scheme 2.1.** Synthesis of Mo *para*-Terphenyl Diphosphine Complexes

Targeting open Mo coordination sites, decarbonylation was pursued. Oxidation of **2** with two equivalents of silver trifluoromethanesulfonate liberated one of the carbonyl ligands, increasing the hapticity of the Mo-arene interaction and maintaining an 18-electron

configuration at the metal. Dicarbonyl **3** exhibits a uniform elongation of the arene C–C bonds in the solid state (Figure 2.1), consistent with  $\eta^6$ -binding. Irradiation of **3** with UV light at  $-78\text{ }^\circ\text{C}$  in the presence of acetonitrile afforded a deep purple complex lacking C–O stretching bands in the IR spectrum. XRD confirmed complete decarbonylation to the  $\eta^6$ -bis(acetonitrile) complex **4** (Figure 2.1). Stirring **4** vigorously over  $\text{Mg}^0$  under an  $\text{N}_2$  atmosphere afforded the  $\text{Mo}^0$  dinitrogen complex, **5** (Scheme 2.1). The same species can be accessed upon treatment of **4** with  $\text{LiHBEt}_3$ , albeit in lower yield. The  $^1\text{H}$  NMR spectrum displayed two central arene signals at 4.3 and 4.0 ppm, suggesting a *pseudo-C<sub>s</sub>* symmetric structure in solution, similar to the solid-state. The average C–C distances ( $\text{Å}$ ) in **5** (2.254(1)) are shorter than in **3** (2.378(2)) and **4** (2.312(2)), consistent with increased  $\delta$ -backbonding from  $\text{Mo}^0$  compared to  $\text{Mo}^{\text{II}}$  (Figure 2.1).<sup>18</sup> The N–N IR stretching frequency,  $2020\text{ cm}^{-1}$ , is similar to previously characterized  $(\text{C}_6\text{H}_5\text{Me})\text{Mo}(\text{PPh}_3)_2\text{N}_2$  ( $2000\text{ cm}^{-1}$ ).<sup>19</sup> Compounds **2-5** demonstrate the ability of diphosphine **1** to support Mo in multiple binding modes and oxidation states.

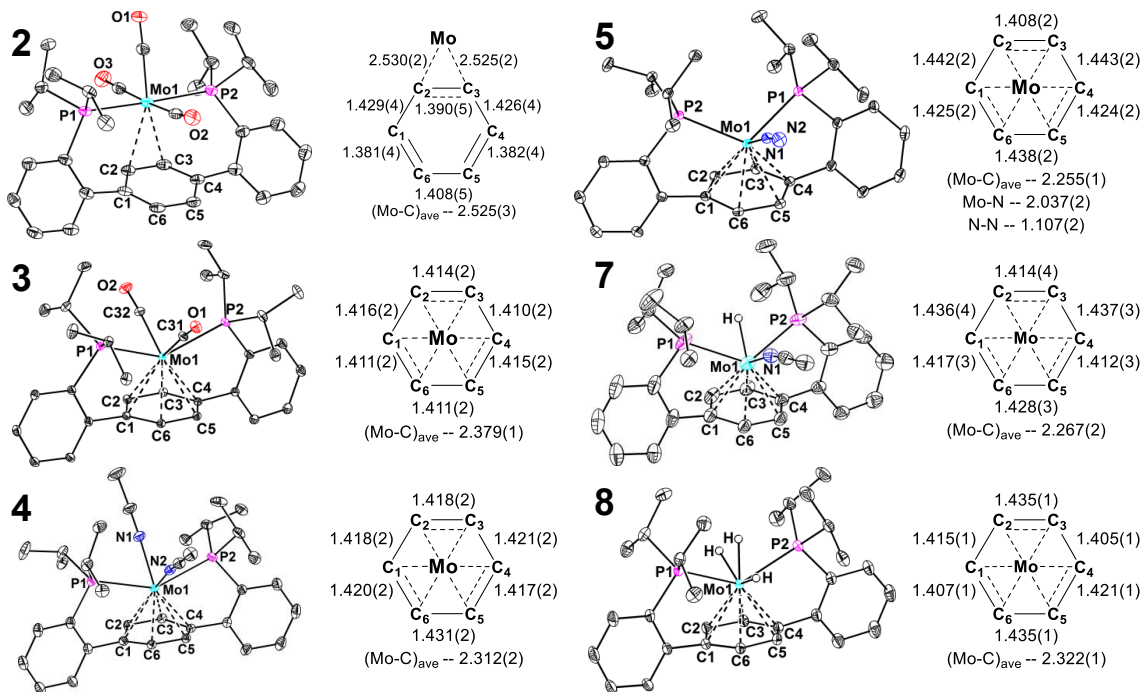


**Figure 2.1.** Solid-state structures of **2-5** and **7-8**. Selected bond distances are reported in  $\text{Å}$ . Solvent molecules counteranions, and select hydrogen atoms are omitted for clarity.

With precedent for base-metal catalysts effecting extensive  $\text{H}_2$  release,<sup>12</sup> the reactivity of

complex **5** with AB was tested. Addition of 1 equiv. of AB led to partial conversion to a new species over several hours at room temperature. Although X-ray quality crystals have not been obtained, the  $^1\text{H}$  NMR spectrum for this compound displays a single central arene signal at 4.81 ppm, indicating pseudo- $C_{2v}$  symmetry, and a triplet at -4.10 ppm integrating to two protons, consistent with a Mo dihydride, **6**. Complex **6** was independently synthesized via addition of  $\text{H}_2$  to complex **5**. Under excess  $\text{N}_2$ , **6** quantitatively reverts to **5**, suggesting **6** as an intermediate in the  $\text{LiHBEt}_3$ -induced formation of **5** from **4**. The  $T_1(\text{min})$  (78 ms, 233 K,  $\text{C}_7\text{D}_8$ , 500MHz; Figure 2.4) of **6** is inconsistent with a dihydrogen complex ( $T_1(\text{min})$  *ca.* 20 ms), but is shorter than a typical dihydride relaxation, suggesting intermediate character.<sup>20</sup> The hydride-deuteride isotopolog, **6-HD**, displays coupling ( $J_{\text{HD}}=10.75$  Hz, Figure 2.5) consistent with an H–D distance of 1.25<sup>21</sup> to 1.36<sup>22</sup> Å, further supporting this assignment. The Mo center in **6** is more electron rich than that of a similar Mo-dihydrogen complex bearing arene and CO ligands,<sup>20b</sup> facilitating conversion toward a dihydride structure.

Extending this stoichiometric reaction to a catalytic system, a 0.25 M AB solution in diglyme was treated with 5 mol % **5** at 70 °C and gas evolution was monitored via eudiometry (Figure 2.11). This system produced 2.5 equiv. of  $\text{H}_2$  within 15 h, with the first 2 equiv. liberated in 6.5 h (Figure 2.2). Such extensive  $\text{H}_2$  release, 2.5 equiv., is rare.<sup>12</sup> Dehydrogenation attempts with  $\text{Mo}^0$  powder showed no change from the uncatalyzed control and in the presence of elemental mercury, catalysis still proceeds (Figure 2.11),<sup>23</sup> consistent with homogeneous catalysis.<sup>24</sup> Analysis of the final reaction mixture by  $^{11}\text{B}$  NMR spectroscopy showed a broad signal at 30 ppm corresponding to polyborazylene (PB),<sup>11,25</sup> in agreement with production of >2 equiv. of  $\text{H}_2$ .

Other  $\text{Mo}^0$  complexes were tested for AB dehydrogenation activity for comparison (Table 2.1). Bis(dinitrogen) complex **9** proved ineffective, releasing less  $\text{H}_2$  than the control and instead forming the stable tetrahydride complex  $\text{Mo}(\text{dppe})_2(\text{H})_4$ .<sup>26</sup> The  $\mu\text{-N}_2$  dimer, **10**,<sup>27</sup> showed similar dehydrogenation activity to **5**, though ultimately provided less  $\text{H}_2$  (Figure 2.13).

Reports

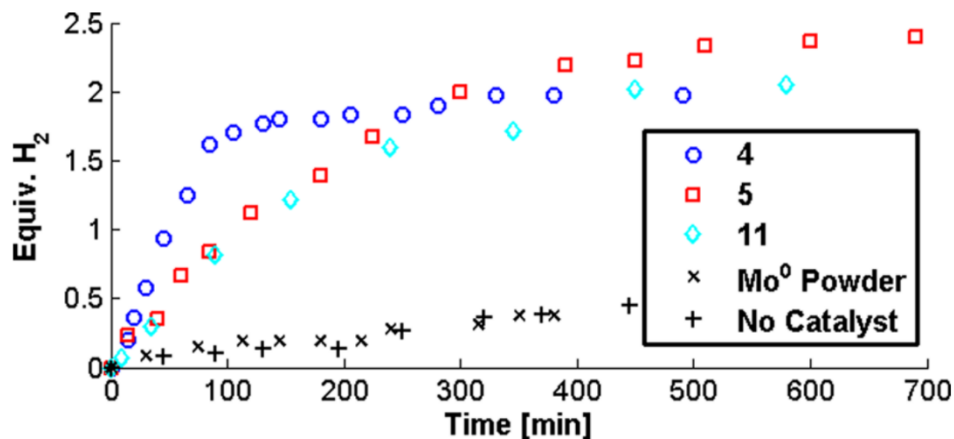


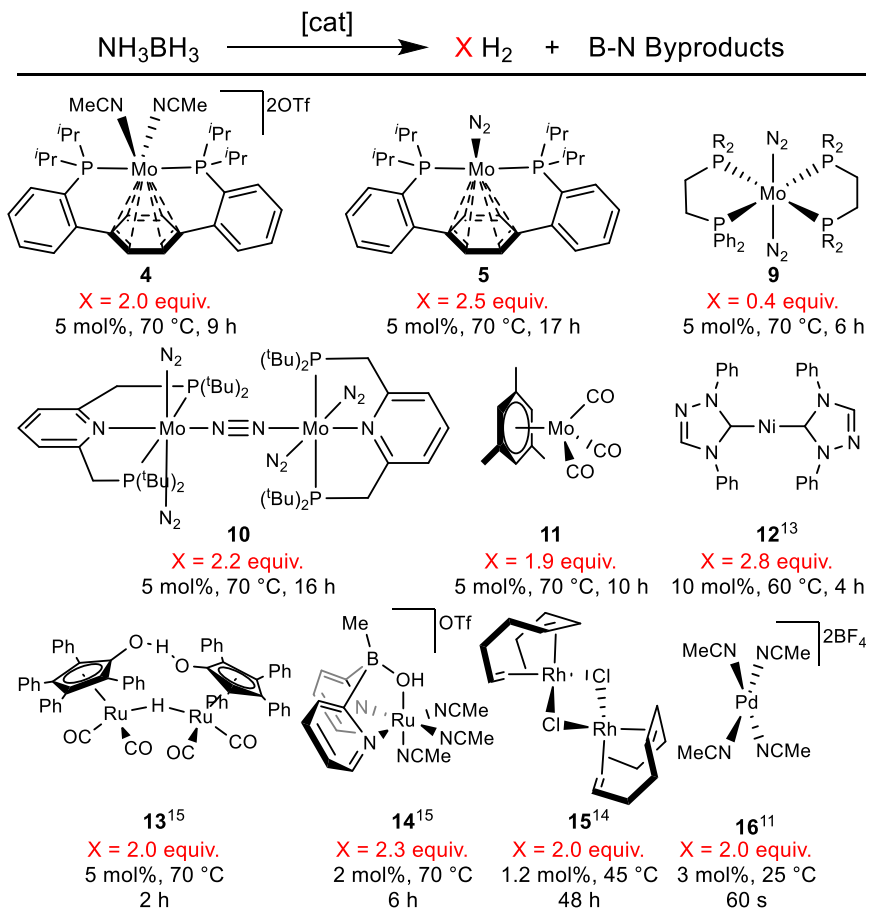
**Figure 2.2.** Eudiometry of AB dehydrogenation catalyzed by **4**, **5**, and **11**. Mo<sup>0</sup> powder and catalyst-free controls are included for reference.

of efficient dehydrogenative coupling of amino boranes by group 6 metal carbonyls under thermo- or photolytic conditions<sup>28</sup> prompted the investigation of tricarbonyl **11**,<sup>29</sup> which demonstrated a similar initial rate of AB dehydrogenation to **5**, but yielded less H<sub>2</sub> (Figure 2.2). Overall, precatalyst **5** is superior to other Mo<sup>0</sup> species in terms of rate and extent of AB dehydrogenation (Table 2.1).

For comparison, catalytic trials were performed with Mo<sup>II</sup> compound **4** under the aforementioned conditions, resulting in the release of 2 equiv. of H<sub>2</sub> in 8.5 h (Figure 2.2). Though complex **4** provided less extensive H<sub>2</sub> release, the initial rate was significantly faster than that of **5**. Similar to **5**, addition of elemental mercury had no effect on the rate of dehydrogenation (Figure 2.11). The Mo oxidation state (Mo<sup>0</sup> vs. Mo<sup>II</sup>) significantly affects the efficacy of the dehydrogenation catalysis, a phenomenon also observed for Fe-based systems.<sup>13</sup>

Interest in the disparate rate and extent of H<sub>2</sub> release catalyzed by **4** and **5** prompted a closer investigation of their respective reactivity. Monitoring stoichiometric reactions of **4** with AB at 70 °C by <sup>31</sup>P NMR spectroscopy showed the formation of a single new species with a peak at 92 ppm. <sup>1</sup>H NMR spectroscopy displayed two central arene signals suggesting pseudo-C<sub>s</sub> symmetry and a triplet with a relative integration of one at -0.5 ppm, consistent with a Mo monohydride (Scheme 2.1). XRD analysis confirmed the structure as a cationic Mo<sup>II</sup> hydride, **7**, with an acetonitrile ligand completing the metal coordination sphere (Figure 2.1).

**Table 2.1.** Mo-based homogeneous precatalysts for AB dehydrogenation in comparison to precatalysts reported to release  $\geq 2.0$  equiv. of  $H_2$ .

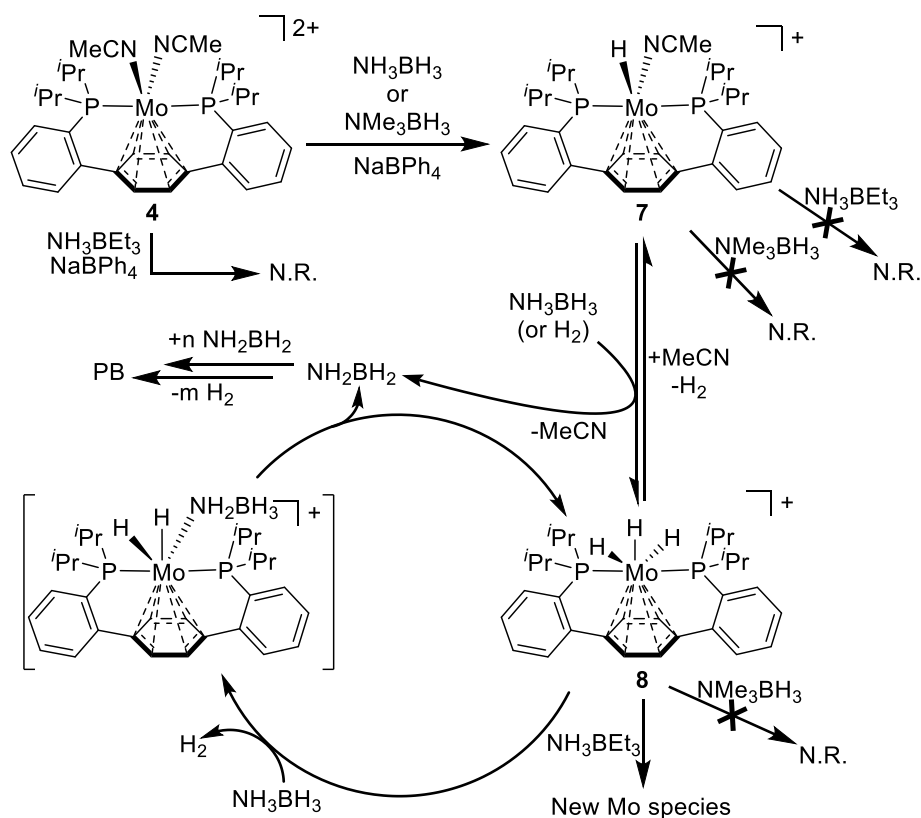


Treatment of **7** with AB resulted in partial conversion to another species (Scheme 2.1). The  $^1H$  NMR spectrum of the mixture showed a new hydridic triplet at -4.6 ppm, integrating to three protons with respect to a single central arene peak at 5.6 ppm, suggesting a more oxidized and symmetric complex: a  $Mo^{IV}$  trihydride cation, **8**. Selective  $^1H$  decoupling of the  $^{31}P$  NMR spectrum and independent synthesis via treating **7** with  $H_2$  further supported this assignment. The hydridic resonance of **8** has a  $T_1(\text{min})$  of 235 ms at 223 K ( $CD_2Cl_2$ , 500 MHz; Figure 2.4), on the order of reported  $Mo(H)_3$  complexes, indicating classical trihydride character.<sup>20g,20h,30</sup> Precipitation in the absence of acetonitrile allows for the isolation of **8**. Acetonitrile promotes  $H_2$  loss and the formation of **7**, with an equilibrium constant ( $K_{eq}$ ) of 0.3 at 25 °C, as determined from solution concentrations.

Both hydrides **7** and **8** were observed in catalytic AB dehydrogenation by **4**, within 20

minutes, via  $^{31}\text{P}$  NMR spectroscopy. Consumption of AB was observed in the  $^{11}\text{B}$  NMR spectrum concurrent with initial appearance of new signals at -20 and -12 ppm (B-(cyclohexyl)aminoborohydride, BCDB, Figure 2.7)<sup>11</sup> followed by two resonances near 30 ppm appearing after 45 min (borazine and PB).<sup>25,25,31</sup> These observations suggest generation of  $\text{NH}_2\text{BH}_2$  as a dehydrogenation intermediate on the way to borazine and PB.<sup>11,25</sup> The formation of  $\text{NH}_2\text{BH}_2$  was corroborated by cyclohexene trapping (Figure 2.7). Catalysis in the presence of excess cyclohexene afforded a major peak by  $^{11}\text{B}$  NMR spectroscopy at 47 ppm, assigned to the hydroborylation product.<sup>11</sup>

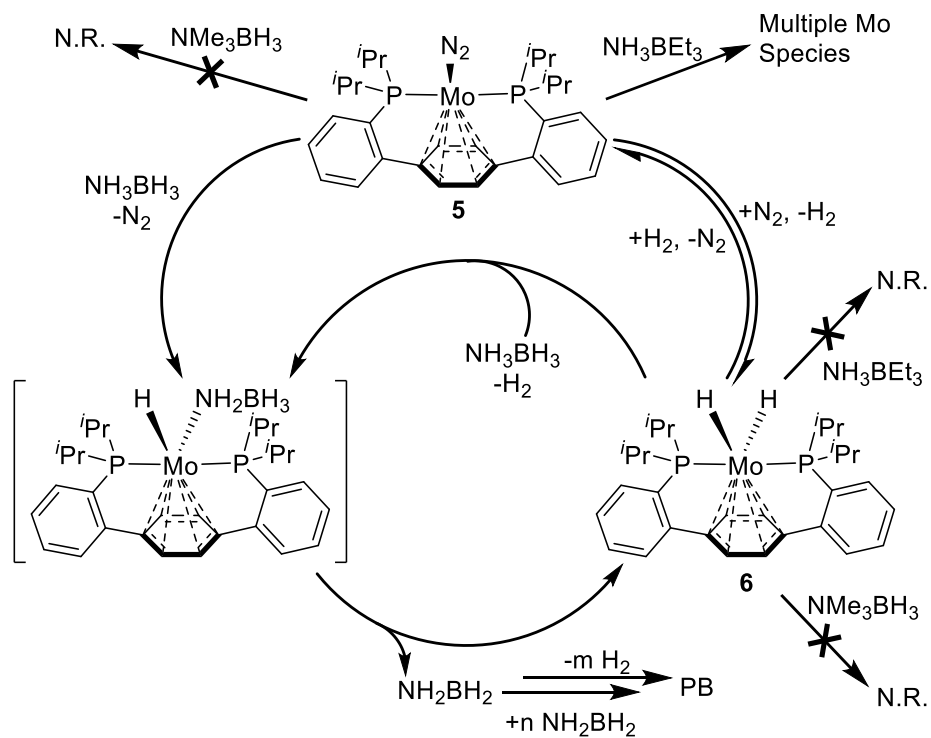
The terminus of activation was investigated using substituted amine-borane adducts.<sup>9c</sup> Compound **4** reacts with  $\text{NMe}_3\text{BH}_3$  to form **7** (Scheme 2.2) and not with  $\text{Et}_3\text{BNH}_3$ , suggesting B–H activation as an initial step. This is reminiscent of the reaction of **4** with  $\text{LiHBEt}_3$  (Scheme 2.1). Reactions of the isolated monohydride with these AB analogs at 70 °C showed no change after 12 h even in the presence of excess substrate, providing no insight as to the site of reactivity with AB. Analogous experiments with **8** (Scheme 2.2) show reaction with  $\text{Et}_3\text{BNH}_3$ , but not  $\text{NMe}_3\text{BH}_3$ , in agreement with protic N–H hydrogens reacting with  $\text{Mo}^{\text{IV}}$ –H moieties. Catalytic trials with **4**, **7**, and **8** show that all are kinetically competent. Monitoring the rate of AB consumption by  $^{11}\text{B}$  NMR showed first-order kinetics through three half-lives. Isotope effects of 1.7, 1.6, and 3.3 were determined for  $\text{ND}_3\text{BH}_3$ ,  $\text{NH}_3\text{BD}_3$ , and  $\text{ND}_3\text{BD}_3$ , respectively (Figure 2.22). Though this may be consistent with  $\text{H}_2$  evolution as the rate determining step, the observed equilibrium between **8** and  $\text{H}_2$  and potential H/D scrambling complicate the interpretation of these data. A mechanism consistent with the present findings involves initiation from precatalyst **4** to generate  $\text{Mo}^{\text{II}}$ -monohydride **7**. Reaction of **7** with AB leads to  $\text{Mo}^{\text{IV}}$ -trihydride **8** and  $\text{NH}_2\text{BH}_2$  which can undergo further dehydrogenation events.<sup>11</sup> Subsequently, activation of AB can occur directly at the N terminus with subsequent release of  $\text{H}_2$  or via initial  $\text{H}_2$  release followed by reaction with AB.



**Scheme 2.2.** Proposed mechanism for Mo<sup>II</sup>-initiated catalytic AB dehydrogenation.

Similar studies of the catalytic behavior of **5** demonstrated the formation of **6** and disappearance of **5** within minutes. The <sup>11</sup>B NMR spectrum showed the consumption of AB and the appearance of the intermediate BCDB. Borazine and PB were observed, in accordance with dehydrogenation past one equivalent. Unlike complex **4**, precatalyst **5** reacts with Et<sub>3</sub>BNH<sub>3</sub>, albeit not cleanly. Complex **6**, isolated under argon, did not react with either terminus blocked substrate but did demonstrate AB dehydrogenation catalysis. Kinetics of cycle consistent with these results involves reaction of **5** with AB via oxidative addition of an N–H bond (Scheme 2.3). Dihydride **6** may be accessible via β-hydride elimination, releasing NH<sub>2</sub>BH<sub>2</sub>. Complex **6** could eliminate H<sub>2</sub> followed by reaction with AB. Alternatively, **6** may react with AB directly and release H<sub>2</sub>. In both instances, one equiv. of H<sub>2</sub> is generated in an on-metal process, with the remainder derived from dehydrooligomerization of NH<sub>2</sub>BH<sub>2</sub>. Although NH<sub>2</sub>BH<sub>2</sub> is generated from both **4** and **5**, the difference in dehydrogenation extent is presently not well understood. It may be due to further metal-based reactivity of AB

dehydrogenation products, in accordance with disparate byproduct distributions.



**Scheme 2.3.** Proposed mechanism for Mo<sup>0</sup>-initiated catalytic AB dehydrogenation.



## CONCLUSION

In summary, a series of Mo complexes have been shown to effectively catalyze the extensive dehydrogenation of AB, releasing *ca.* 2 equiv. of H<sub>2</sub> in four cases. The Mo<sup>0</sup> compound **5** is a rare example of a transition metal precatalyst capable of dehydrogenating AB through 2.5 equiv. of H<sub>2</sub>. These well-defined systems supported by the *para*-terphenyl diphosphine ligand, **1**, have been studied mechanistically and exhibit different reaction pathways as a function of metal oxidation state. A series of isolated Mo-hydrides (Mo<sup>II</sup>(H)<sub>2</sub>, [Mo<sup>II</sup>(H)]<sup>+</sup>, and [Mo<sup>IV</sup>(H)<sub>3</sub>]<sup>+</sup>) were found to support catalysis for the dehydrogenation of AB. Elucidation of the respective mechanisms and investigation of additional Mo-based AB dehydrogenation catalysts is ongoing.

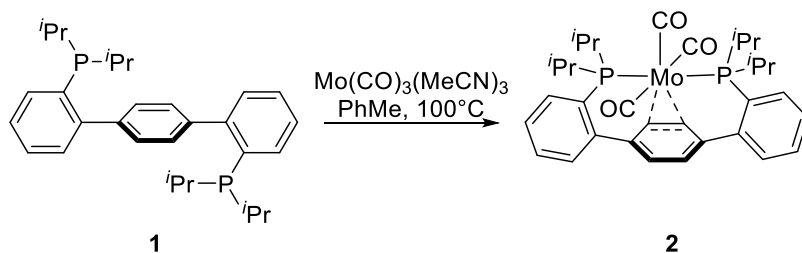
## EXPERIMENTAL SECTION

### *General Considerations*

Unless otherwise specified, all operations were carried out in an MBraun drybox under a nitrogen atmosphere or using standard Schlenk and vacuum line techniques. Solvents for air- and moisture-sensitive reactions were dried over sodium benzophenone ketyl, calcium hydride, or by the method of Grubbs.<sup>32</sup> Deuterated solvents were purchased from Cambridge Isotope Laboratories and vacuum transferred from sodium benzophenone ketyl ( $C_6D_6$ ) or calcium hydride ( $CD_3CN$  and  $CD_2Cl_2$ ). All solvents, once dried and degassed, were stored under inert atmosphere over 4 Å molecular sieves. Ammonia borane and all amino-borane analogs were sublimed prior to use and stored at  $-35\text{ }^\circ\text{C}$  unless noted otherwise. Magnesium turnings were oven dried prior to use. All other compounds were used as received. Diphosphine **1**,<sup>17d</sup>  $Mo(CO)_3(MeCN)_3$ ,<sup>33</sup> **9**,<sup>26</sup> **10**,<sup>27</sup> **11**,<sup>29</sup>  $ND_3BH_3$ ,  $NH_3BD_3$ ,  $ND_3BD_3$ <sup>12</sup> and  $NH_3BEt_3$ <sup>9a</sup> were prepared and purified according to literature procedures.  $Mo(CO)_6$  was purchased from Strem Chemicals, Inc. Diethylene glycol dimethyl ether (diglyme) was purchased from TCI America. Silver trifluoromethanesulfonate (triflate) was purchased from Alfa Aesar. Magnesium turnings were purchased from Fischer Scientific. Ammonia borane,  $LiHBEt_3$  (Superhydride), sodium tetraphenyl borate, dimethylamine borane, and trimethylamine borane were all purchased from Sigma Aldrich.  $H_2$  and  $D_2$  gases were purchased from American Air Liquide and Cambridge Isotope Laboratories, respectively. HD was prepared according to a previously reported procedure<sup>34</sup> and purified via passage through a  $-196\text{ }^\circ\text{C}$  cold trap prior to use.  $^1H$ ,  $^{13}C$ , and  $^{31}P$  NMR spectra were recorded on Varian Mercury 300 MHz, Varian 400 MHz, or Varian INOVA-500 spectrometers with shifts reported in parts per million (ppm).  $^{11}B$  NMR spectra were recorded for samples prepared in quartz NMR tubes, using a Varian 400 MHz spectrometer equipped with a quartz probe insert.  $^1H$  and  $^{13}C\{^1H\}$  NMR spectra are referenced to residual solvent peaks.<sup>35</sup>  $^{31}P$  and  $^{11}B$  chemical shifts are referenced to external 85%  $H_3PO_4$  (0 ppm) and  $NaBPh_4$  (-7.26 ppm) standards,

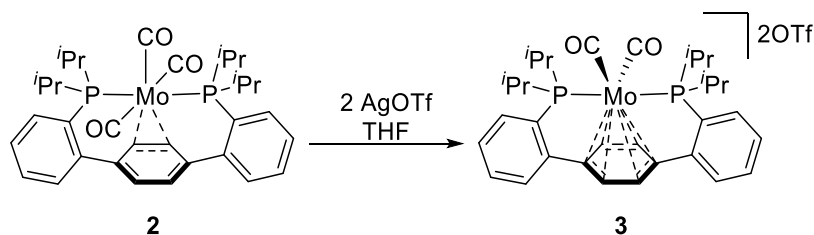
respectively. IR spectra were obtained as solution samples using a CaF<sub>2</sub> window cell on a Thermo Scientific Nicolet 6700 FT-IR spectrometer. Photolyses were conducted using an Oriol Instruments arc lamp housing and a Newport Corporation 200 W Hg/Xe arc lamp set to a current of 8 A. During irradiation, samples were cooled with a dry ice/acetone bath. Elemental analysis was conducted by Robertson Microлит Laboratories, Inc. (Ledgewood, NJ).

### Synthesis of **2**



Addition of Mo(CO)<sub>3</sub>(MeCN)<sub>3</sub> (1.43 g, 4.75 mmol) to a clear solution of **1** (2.05 g, 4.32 mmol) in toluene (50 mL) resulted in a yellow/green heterogeneous mixture. Following heating to 100 °C and stirring for 12 h, the mixture became a deep orange homogenous solution. The volatiles were removed *in vacuo*. The resulting orange solids were collected and washed with cold hexanes (2 x 15 mL). Residual volatiles were removed under reduced pressure to yield **2** (2.54 g, 3.81 mmol, 88 %). X-ray quality crystals were grown from vapor diffusion of pentane into a saturated THF solution of **2**. <sup>1</sup>H NMR (500 MHz, CD<sub>2</sub>Cl<sub>2</sub>, 25 °C) δ: 7.86 (m, 2H, aryl-*H*), 7.53 (m, 6H, aryl-*H*), 6.52 (br s, 4H, central arene-*H*), 2.75 (br s, 4H, CH(CH<sub>3</sub>)<sub>2</sub>), and 1.09-1.23 (br s, 24H, CH(CH<sub>3</sub>)<sub>2</sub>). <sup>13</sup>C {<sup>1</sup>H} NMR (101 MHz, CD<sub>2</sub>Cl<sub>2</sub>, 25 °C) δ: 221.15 (t, *J* = 10.19 Hz, Mo-CO), 213.75 (t, *J* = 8.87 Hz, Mo-CO), 148.80 (t, *J* = 6.90 Hz, aryl-C), 139.99 (t, *J* = 2.74, central arene-C), 131.23 (s, aryl-CH), 131.02 (t, *J* = 9.41 Hz, aryl-C), 129.90 (s, aryl-CH), 129.35 (s, aryl-CH), 128.34 (s, aryl-CH), 33.83 (br s, CH(CH<sub>3</sub>)<sub>2</sub>), 19.88 (s, CH(CH<sub>3</sub>)<sub>2</sub>), and 19.43 (s, CH(CH<sub>3</sub>)<sub>2</sub>). <sup>31</sup>P {<sup>1</sup>H} NMR (121 MHz, C<sub>6</sub>D<sub>6</sub>, 25 °C) δ: 51.01. IR (CaF<sub>2</sub> window, C<sub>6</sub>H<sub>6</sub>, cm<sup>-1</sup>) ν<sub>CO</sub>: 2298.5, 2192.8. Anal. Calcd. for **2** C<sub>33</sub>H<sub>40</sub>MoO<sub>3</sub>P<sub>2</sub> (%): C, 61.68; H, 6.27. Found: C, 61.43; H, 5.99.

*Synthesis of 3*

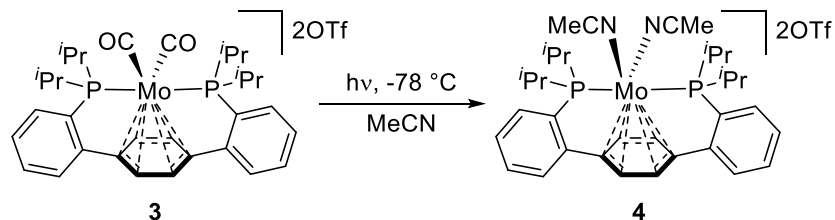


To a rapidly stirring solution of **2** (1.17 g, 1.82 mmol) in THF (50 mL), a solution of AgOTf (1.00 g, 3.83 mmol) in THF (35 mL) was added dropwise. With each drop, an immediate darkening of the solution was observed. Complete addition of the silver solution led to a persistent purple/brown mixture, which was stirred at room temperature for 3 h. The volatiles were removed under reduced pressure to yield green/brown solids. These solids were collected on a fritted glass funnel and washed with THF (3 x 10 mL). The solid residue was extracted into MeCN (30 mL), filtered through Celite, and the resulting yellow solution was dried *in vacuo*. The yellow solids were dissolved in minimal MeCN and filtered through celite once more.<sup>‡</sup> Et<sub>2</sub>O was added to the filtrate which was then cooled to -35 °C. The precipitate was collected via vacuum filtration, providing **3** (1.16 g, 1.26 mmol, 69 %) as yellow microcrystals. X-ray quality crystals were obtained from vapor diffusion of diethyl ether into a saturated MeCN solution of **3**. <sup>1</sup>H NMR (300 MHz, CD<sub>3</sub>CN, 25 °C) δ: 7.93 (m, 2H, aryl-*H*), 7.83 (m, 6H, aryl-*H*), 7.15 (s, 4H, central arene-*H*), 3.35 (m, 4H, CH(CH<sub>3</sub>)<sub>2</sub>), and 1.29-1.44 (m, 24H, CH(CH<sub>3</sub>)<sub>2</sub>). <sup>13</sup>C{<sup>1</sup>H} NMR (101 MHz, CD<sub>3</sub>CN, 25 °C) δ: 219.03 (s, Mo-CO), 141.32 (dd, *J* = 7.58, 5.79, aryl-C), 137.69 (t, *J* = 3.93 Hz, central arene-C), 134.64 (s, aryl-CH), 133.93 (dd, *J* = 47.74, 8.22, aryl-C), 133.83 (s, aryl-CH), 132.12 (t, *J* = 3.07 Hz, aryl-CH), 128.58 (t, *J* = 5.70 Hz, aryl-CH), 122.07 (q, *J* = 320.73 Hz, F<sub>3</sub>CSO<sub>3</sub><sup>-</sup>), 104.72 (s, central arene-CH), 28.97 (q, *J* = 11.67 Hz, CH(CH<sub>3</sub>)<sub>2</sub>), 18.47 (s, CH(CH<sub>3</sub>)<sub>2</sub>), and 18.07 (s, CH(CH<sub>3</sub>)<sub>2</sub>). <sup>31</sup>P{<sup>1</sup>H} NMR (121 MHz,

<sup>‡</sup> Omission of this second filtration step resulted in a less-soluble yellow/orange impurity noticed when employing **3** in the preparation of **4**.

CD<sub>3</sub>CN, 25 °C)  $\delta$ : 75.05. IR (CaF<sub>2</sub> window, C<sub>6</sub>H<sub>6</sub>, cm<sup>-1</sup>)  $\nu_{\text{CO}}$ : 2025.2, 1986.4. Anal. Calcd. for **3** C<sub>34</sub>H<sub>40</sub>F<sub>6</sub>MoO<sub>8</sub>P<sub>2</sub>S<sub>2</sub> (%): C, 44.74; H, 4.42. Found: C, 44.65; H, 4.49.

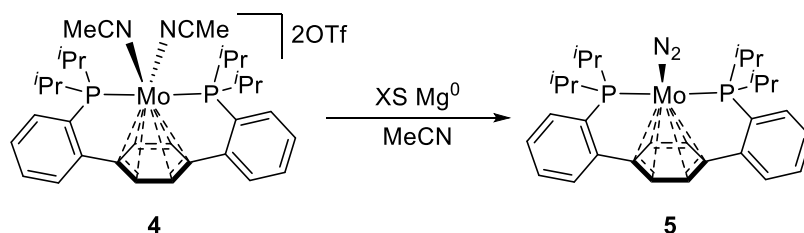
### Synthesis of **4**



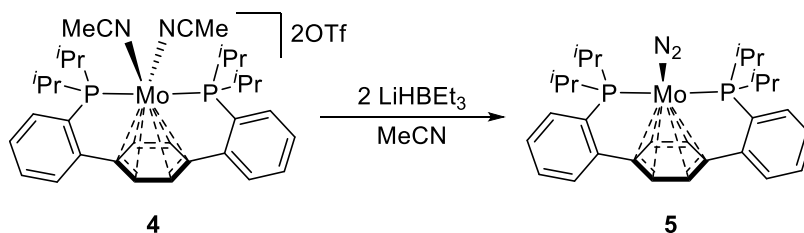
A bright yellow acetonitrile (20 mL) solution of **3** (533 mg, 0.583 mmol) was transferred to a quartz Schlenk tube, charged with a stir bar. The tube was degassed via three freeze-pump-thaw cycles and then, while stirring, irradiated with a 200 W Hg/Xe lamp at -78 °C for 2 h. The evolution of bubbles was observed and the solution steadily darkened to deep red. The flask was degassed as above and photolysis continued. With continued irradiation, the solution darkened to a deep purple color that glowed intensely under the UV light. This degas/irradiation process was continued until aliquots of the solution showed no presence of **3** or the putative monocarbonyl species by <sup>31</sup>P NMR (75.05 and 68.62 ppm, respectively). The total irradiation time was dependent on lamp age, frequency of degassing, and solution concentration, varying from 12 h to several days. Upon complete conversion, volatiles were removed under reduced pressure, providing deep purple solids. These solids were collected on a fritted funnel and washed with THF until the filtrate was colorless. The purple microcrystalline product was collected (528 mg, 0.565 mmol, 97 %). Crystals suitable for X-ray diffraction were obtained from vapor diffusion of Et<sub>2</sub>O into a saturated MeCN solution of **4**. <sup>1</sup>H NMR (300 MHz, CD<sub>3</sub>CN, 25 °C)  $\delta$ : 7.62-7.72 (m, 6H, aryl-*H*), 7.51-7.52 (m, 2H, aryl-*H*), 5.59 (t, 4H, *J* = 2.2 Hz, central arene-*H*), 2.86-2.93 (m, 4H, CH(CH<sub>3</sub>)<sub>2</sub>), 2.72 (m, 6H, NC(CH<sub>3</sub>)), and 1.25-1.31 (m, 24H, CH(CH<sub>3</sub>)<sub>2</sub>). <sup>13</sup>C{<sup>1</sup>H} NMR (126 MHz, CD<sub>3</sub>CN, 25 °C)  $\delta$ : 145.36 (t, *J* = 10.51 Hz, aryl-C), 143.35 (s, NCCH<sub>3</sub>), 133.44 (s, aryl-CH), 132.35 (s, aryl-CH), 130.60 (dd, *J* = 62.25, 23.73, aryl-C), 130.57 (s, aryl-CH), 127.48 (s, aryl-CH), 123.39 (s, Mo- CNCH<sub>3</sub>), 122.15 (q, *J* =

318.51,  $F_3CSO_3^-$ ), 120.50 (s, central arene-C), 88.90 (s, central arene-CH), 25.74 (t,  $J = 9.77$  Hz,  $CH(CH_3)_2$ ), 18.67 (s,  $CH(CH_3)_2$ ), 17.86 (s,  $CH(CH_3)_2$ ), 7.03 (s, Mo-NCCH<sub>3</sub>) and 6.52 (m, Mo-NCCH<sub>3</sub>).  $^{31}P\{^1H\}$  NMR (121 MHz, CD<sub>3</sub>CN, 25 °C)  $\delta$ : 63.35. Anal. Calcd. for **4** C<sub>36</sub>H<sub>46</sub>F<sub>6</sub>MoN<sub>2</sub>O<sub>6</sub>P<sub>2</sub>S<sub>2</sub> (%): C, 46.06; H, 4.94; N, 2.98. Found: C, 45.09; H, 4.77; N, 3.25.

### Synthesis of **5**

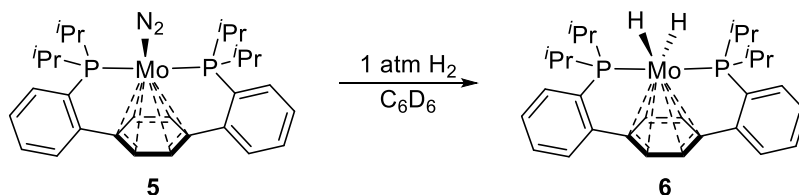


A deep purple solution of **4** (225 mg, 0.241 mmol) in MeCN (4 mL) was portioned into four 20 mL scintillation vials, each charged with a stir bar and an excess of magnesium turnings (3-5 g/vial). The solution was stirred at room temperature for 8 h, during which time it lightened to a green/brown heterogeneous mixture. The mixtures were filtered through celite. Each vial was rinsed with MeCN (2 x 1.5 mL) and each rinse was likewise filtered. The insoluble material was extracted in benzene and dried *in vacuo*, providing a brown/green residue. This residue was extracted with benzene and filtered through celite once more. The brown filtrate solution was lyophilized, yielding **5** as a red/brown powder (108 mg, 0.184 mmol, 76 %). X-ray quality crystals were grown by either vapor diffusion of pentane into a saturated toluene solution of **5** at -35 °C or by chilling a saturated hexanes solution of **5** (-35 °C).



In an alternate synthesis, a 20 mL scintillation vial was charged with **4** (370 mg, 0.396 mmol), MeCN (15 mL), and a stir bar. Stirring was initiated, and 1.0 M LiHBET<sub>3</sub> in THF (0.80 mL, 0.792 mmol) was added to the purple solution dropwise. An immediate color change to reddish-brown was observed. Stirring continued for 12 h, furnishing a green/brown suspension. Volatiles were removed under reduced pressure affording brown solids. The solids were extracted with benzene (10 mL) and filtered. The filtrate was lyophilized, giving **5** as a red/brown powder (63 mg, 0.107 mmol, 27 %). <sup>1</sup>H NMR (300 MHz, C<sub>6</sub>D<sub>6</sub>, 25 °C) δ: 7.48-7.50 (m, 2H, aryl-*H*), 7.23-7.27 (m, 2H, aryl-*H*), 7.02-7.09 (m, 4H, aryl-*H*), 4.26 (s, 2H, central arene-*H*), 3.99 (s, 2H, central arene-*H*), 2.38-2.50 (m, 2H, CH(CH<sub>3</sub>)<sub>2</sub>), 2.20-2.31 (m, 2H, CH(CH<sub>3</sub>)<sub>2</sub>), and 0.94-1.27 (m, 24H, CH(CH<sub>3</sub>)<sub>2</sub>). <sup>13</sup>C {<sup>1</sup>H} NMR (101 MHz, C<sub>6</sub>D<sub>6</sub>, 25 °C) δ: 150.23-150.84 (m, aryl-C), 130.50 (s, aryl-CH), 128.21 (s, aryl-CH), 126.62 (s, aryl-CH), 126.06 (s, central arene-C), 97.47 (s, central arene-C), 82.04 (s, central arene-CH), 75.29 (s, central arene-CH), 29.71 (br t, *J* = 6.20, CH(CH<sub>3</sub>)<sub>2</sub>), 28.17 (br t, *J* = 5.33, CH(CH<sub>3</sub>)<sub>2</sub>), 21.14 (br t, *J* = 5.06, CH(CH<sub>3</sub>)<sub>2</sub>), 19.85 (br t, *J* = 4.31, CH(CH<sub>3</sub>)<sub>2</sub>), 19.59 (s, CH(CH<sub>3</sub>)<sub>2</sub>), and 19.16 (s, CH(CH<sub>3</sub>)<sub>2</sub>). <sup>31</sup>P {<sup>1</sup>H} NMR (121 MHz, C<sub>6</sub>D<sub>6</sub>, 25 °C) δ: 76.72. IR (CaF<sub>2</sub> window, C<sub>6</sub>H<sub>6</sub>, cm<sup>-1</sup>) ν<sub>N-N</sub>: 2020.2. Anal. Calcd. for **5** C<sub>30</sub>H<sub>40</sub>MoN<sub>2</sub>P<sub>2</sub> (%): C, 61.43; H, 6.87; N, 4.78. Found: C, 61.40; H, 6.67; N, 3.68.

### Synthesis of **6**



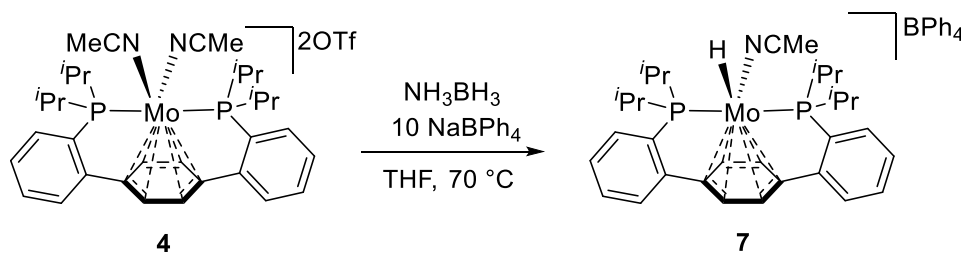
A J. Young NMR tube was charged with a brown/red solution of **5** (20 mg, 0.034 mmol) in C<sub>6</sub>D<sub>6</sub> (0.7 mL). The solution was degassed via three freeze-pump-thaw cycles. The headspace was backfilled with H<sub>2</sub> gas, enacting an immediate reddening of the solution. The NMR tube was mechanically rotated for 15 min, providing a red solution of **6**. Isolation and recrystallization of **6** is hampered by its conversion back to **5** in the presence

of N<sub>2</sub>. <sup>1</sup>H NMR (300 MHz, C<sub>6</sub>D<sub>6</sub>, 25 °C) δ: 7.44-7.48 (m, 2H, aryl-*H*), 6.97-7.11 (m, 6H, aryl-*H*), 4.81 (t, 4H, *J* = 3.17 Hz, central arene-*H*), 2.12-2.24 (m, 4H, CH(CH<sub>3</sub>)<sub>2</sub>), 1.23-1.30 (m, 12H, CH(CH<sub>3</sub>)<sub>2</sub>), 0.92-0.99 (m, 12H, CH(CH<sub>3</sub>)<sub>2</sub>), and -4.10 (t, 1H, *J* = 35.8 Hz, Mo-*H*). <sup>13</sup>C{<sup>1</sup>H} NMR (126 MHz, C<sub>6</sub>D<sub>6</sub>, 25 °C) δ: 150.20-150.55 (m, aryl-*C*), 147.38-147.73 (m, aryl-*C*), 128.34 (s, aryl-CH), 126.45 (s, aryl-CH), 94.38 (s, central arene-*C*), 74.40 (s, central arene-CH), 75.29 (s, central arene-CH), 30.05 (t, *J* = 9.71, CH(CH<sub>3</sub>)<sub>2</sub>), 20.27 (s, CH(CH<sub>3</sub>)<sub>2</sub>), and 19.49 (s, CH(CH<sub>3</sub>)<sub>2</sub>). <sup>31</sup>P{<sup>1</sup>H} NMR (121 MHz, C<sub>6</sub>D<sub>6</sub>, 25 °C) δ: 89.70.

### Synthesis of **6-HD**

The hydride-deuteride isotopolog can be prepared analogously utilizing H-D gas rather than H<sub>2</sub> gas. This gave rise to a 3:5:2 mixture of **6-H<sub>2</sub>**:**6-HD**:**6-D<sub>2</sub>**. Integration of the hydridic resonances is omitted. <sup>1</sup>H NMR (400 MHz, C<sub>6</sub>D<sub>6</sub>, 25 °C) δ: 7.45-7.47 (m, 2H, aryl-*H*), 7.16-7.06 (m, 2H, aryl-*H*), 6.96-7.02 (m, 2H, aryl-*H*), 4.81 (br t, 4H, *J* = 2.52 Hz, central arene-*H*), 2.12-2.24 (m, 4H, CH(CH<sub>3</sub>)<sub>2</sub>), 1.24-1.30 (m, 12H, CH(CH<sub>3</sub>)<sub>2</sub>), 0.93-0.98 (m, 12H, CH(CH<sub>3</sub>)<sub>2</sub>), -4.10 (t, *J* = 33.9 Hz, **6-H<sub>2</sub>** Mo-*H*), -4.12 (tt, *J*<sub>HD</sub> = 10.8 Hz, *J*<sub>HP</sub> = 34.0 Hz, **6-HD** Mo-*H*). <sup>31</sup>P{<sup>1</sup>H} NMR (162 MHz, C<sub>6</sub>D<sub>6</sub>, 25 °C) δ: 89.70 (s, **6-H<sub>2</sub>**), 89.44 (t, *J*<sub>DP</sub> = 4.3 Hz, **6-HD**), and 89.04 (q, *J*<sub>DP</sub> = 4.4 Hz, **6-D<sub>2</sub>**).

### Synthesis of **7**

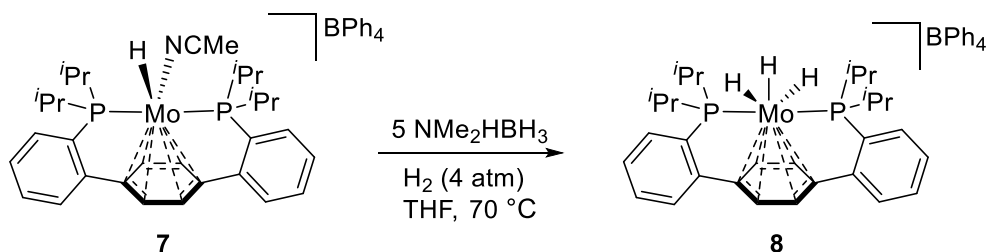


To a Schlenk tube charged with **4** (142 mg, 0.152 mmol), NaBPh<sub>4</sub> (107 mg, 0.313 mmol), and a stir bar, a THF (7 mL) solution of AB (5.0 mg, 0.162 mmol) in was added. The purple/brown suspension was heated to 70 °C with stirring for 4 h, providing a



homogeneous orange solution. Volatiles were removed *in vacuo*, furnishing an orange powder. DCM (3 mL) was added and the powder was filtered through a Celite plug. Volatiles were again removed and the resulting residue was crystallized via pentane vapor diffusion into a concentrated THF solution. Generally additional recrystallizations were conducted to fully remove the B–N reaction byproducts, providing pure **7** as X-ray quality red/orange blades (89 mg, 0.097 mmol, 64 %).  $^1\text{H}$  NMR (400 MHz,  $\text{CD}_2\text{Cl}_2$ , 25 °C)  $\delta$ : 7.30-7.56 (m, 8H, aryl-*H*), 7.01 (br s, 8H, B- $\text{C}_6\text{H}_5$ ), 7.01 (br s, 8H, B- $\text{C}_6\text{H}_5$ ), 6.86 (br s, 4H, B- $\text{C}_6\text{H}_5$ ), 5.20 (br s, 2H, central arene-*H*), 4.26-4.23 (m, 2H, central arene-*H*), 2.66-2.79 (m, 2H,  $\text{CH}(\text{CH}_3)_2$ ), 2.54-2.67 (m, 2H,  $\text{CH}(\text{CH}_3)_2$ ), 1.93 (s, 3H,  $\text{NCCH}_3$ ), 1.19-1.37 (m, 12H,  $\text{CH}(\text{CH}_3)_2$ ), 0.94-1.02 (m, 12H,  $\text{CH}(\text{CH}_3)_2$ ), and -0.56 (t, 1H,  $J = 76.74$  Mo-*H*).  $^{13}\text{C}\{^1\text{H}\}$  NMR (101 MHz,  $\text{CD}_2\text{Cl}_2$ , 25 °C)  $\delta$ : 163.69-165.16 (q,  $J = 49.90$  Hz, B-*C*), 147.43 (d,  $J = 25.04$  Hz, aryl-*C*), 141.01 (d,  $J = 29.00$ , aryl-*C*), 136.25 (s, B- $\text{C}_6\text{H}_5$ ), 131.25 (s, aryl-*CH*), 130.73 (s, aryl-*CH*), 128.54 (br d,  $J = 4.33$  Hz, aryl-*CH*), 127.61 (d,  $J = 12.21$ , aryl-*CH*), 126.07 (s, B- $\text{C}_6\text{H}_5$ ), 124.93 (s, Mo- $\text{CNCH}_3$ ), 122.14 (s, B- $\text{C}_6\text{H}_5$ ), 106.54 (s, central arene-*C*), 80.32 (s, central arene-*CH*), 30.83 (d,  $J = 30.01$  Hz,  $\text{CH}(\text{CH}_3)_2$ ), 26.61 (d,  $J = 23.60$ ,  $\text{CH}(\text{CH}_3)_2$ ), 20.18 (s,  $\text{CH}(\text{CH}_3)_2$ ), 19.35 (s,  $\text{CH}(\text{CH}_3)_2$ ), 18.92 (s,  $\text{CH}(\text{CH}_3)_2$ ), 18.20 (s,  $\text{CH}(\text{CH}_3)_2$ ), and 4.65 (s, Mo- $\text{CNCH}_3$ ).  $^{31}\text{P}\{^1\text{H}\}$  NMR (162 MHz,  $\text{CD}_2\text{Cl}_2$ , 25 °C)  $\delta$ : 91.47. Anal. Calcd. for **7**·DCM  $\text{C}_{57}\text{H}_{66}\text{BCl}_2\text{MoNP}_2$  (%): C, 68.14; H, 6.62; N, 1.39. Found: C, 68.57; H, 6.70; N, 1.93.

### Synthesis of **8**



THF (5 mL) was added to a thick-walled Schlenk tube charged with **7** (102 mg, 0.110 mmol),  $\text{Me}_2\text{NHBH}_3$  (53 mg, 0.832 mmol), and a stir bar. The solution was degassed by a

single freeze-pump-thaw cycle. The orange homogeneous solution was frozen and the headspace was backfilled with *ca.* 4 atm of H<sub>2</sub> gas. Once at room temperature, the flask was placed in a 70 °C oil bath for 16 h with stirring. During this time, a color change to pale yellow was observed. Pentane (50 mL) was carefully added via cannula,<sup>‡</sup> causing the precipitation of pale yellow solids. The solids were collected via vacuum filtration and washed with Et<sub>2</sub>O (2 x 5 mL). The remaining solids were extracted with DCM (2 x 3 mL), giving a vibrant yellow filtrate. Volatiles were removed *in vacuo*, giving a mixture of yellow and white solids. Crystallization via pentane vapor diffusion into a concentrated THF solution removed the B–N reaction byproducts, providing pure **8** as X-ray quality crystalline yellow plates. <sup>1</sup>H NMR (300 MHz, CD<sub>2</sub>Cl<sub>2</sub>, 25 °C) δ: 7.37-7.59 (m, 8H, aryl-*H*), 7.32 (br s, 8H, B-aryl-*H*), 7.01 (br t, 8 H, *J* = 6.50, B-aryl-*H*), 6.68 (br t, 4H, *J* = 6.60, B-aryl-*H*), 5.56 (s, 4H, central arene-*H*), 2.43-2.54 (m, 4H, CH(CH<sub>3</sub>)<sub>2</sub>), 1.24-1.31 (m, 12H, CH(CH<sub>3</sub>)<sub>2</sub>), 0.97-1.03 (m, 12H, CH(CH<sub>3</sub>)<sub>2</sub>), and -4.64 (t, 3H, *J* = 29.72 Mo-*H*). <sup>13</sup>C{<sup>1</sup>H} NMR (101 MHz, CD<sub>2</sub>Cl<sub>2</sub>, 25 °C) δ: 165.13-166.61 (q, *J* = 49.44 Hz, B-C), 143.89 (br d, *J* = 4.19 Hz, aryl-C), 143.65 (d, *J* = 15.99 Hz, aryl-C), 137.82 (s, B-C<sub>6</sub>H<sub>5</sub>), 133.34 (s, aryl-CH), 132.33 (br s, central arene-C), 131.84 (s, aryl-CH), 131.70 (br s, aryl-CH), 127.96-128.08 (m, aryl-CH), 127.51 (s, B-C<sub>6</sub>H<sub>5</sub>), 123.63 (s, B-C<sub>6</sub>H<sub>5</sub>), 91.16 (s, central arene-CH), 31.97 (d, *J* = 32.95, CH(CH<sub>3</sub>)<sub>2</sub>), 20.90 (s, CH(CH<sub>3</sub>)<sub>2</sub>), and 20.53 (s, CH(CH<sub>3</sub>)<sub>2</sub>). <sup>31</sup>P{<sup>1</sup>H} NMR (121 MHz, CD<sub>2</sub>Cl<sub>2</sub>, 25 °C) δ: 97.70.

#### *Reaction of 8 with D<sub>2</sub>*

A mixture of the isotopologs can be prepared via addition of 7 equiv. of D<sub>2</sub> (as measured by calibrated gas bulb) to a degassed CD<sub>2</sub>Cl<sub>2</sub> solution of **8**. Unlike the dihydride **6**, the isotopologs of **8** are not resolved in the <sup>31</sup>P{<sup>1</sup>H} NMR and as such, their relative ratio is unknown. Integration of the hydridic resonances is omitted. <sup>1</sup>H NMR (400 MHz, CD<sub>2</sub>Cl<sub>2</sub>,

---

<sup>‡</sup> CAUTION: Pressure builds up over the course of the reaction.

25 °C)  $\delta$ : 7.39-7.59 (m, 8H, aryl-*H*), 7.31 (br s, 8H, B-aryl-*H*), 7.00 (br t, 8 H,  $J = 6.50$ , B-aryl-*H*), 6.86 (br t, 4H,  $J = 6.82$ , B-aryl-*H*), 5.56 (s, 4H, central arene-*H*), 2.43-2.54 (m, 4H, CH(CH<sub>3</sub>)<sub>2</sub>), 1.26-1.30 (m, 12H, CH(CH<sub>3</sub>)<sub>2</sub>), 0.99-1.02 (m, 12H, CH(CH<sub>3</sub>)<sub>2</sub>), and -4.76 to -4.57 (tm,  $J_{HP} = 34.77$ , Mo-*H*). <sup>31</sup>P{<sup>1</sup>H} NMR (162 MHz, CD<sub>2</sub>Cl<sub>2</sub>, 25 °C)  $\delta$ : 96.64-96.80 (m).

#### *Reactivity with AB Analogs*

In a typical reaction, the Mo complex under investigation (**4-8**, 0.025 mmol) and the AB analog (NH<sub>3</sub>BEt<sub>3</sub> or NMe<sub>3</sub>BH<sub>3</sub>, 0.125 mmol) were dissolved in THF. The resulting solution was transferred to a quartz J. Young NMR tube. In the case of precatalyst **4**, NaBPh<sub>4</sub> (17 mg, 0.050 mmol) was also added to the reaction mixture to aid in solubilizing the dication. The reactions were heated to 70 °C and monitored via <sup>31</sup>P NMR spectroscopy.

#### *Time Resolved AB Dehydrogenation Experiments*

In a typical reaction, a solution of catalyst (**4** or **8**, 0.010 mmol) and AB (2.3 mg, 0.075 mmol) in diglyme (0.500 mL) was transferred to quartz J. Young NMR tube. NaBPh<sub>4</sub> (6.8 mg, 0.020 mmol) was added in reactions with **4** to aid in solubilizing the dication as well as acting as an internal standard for <sup>11</sup>B NMR experiments. The reactions were placed in a Varian 400 MHz NMR spectrometer preheated to 70 °C. Successive <sup>11</sup>B and <sup>31</sup>P{<sup>1</sup>H} NMR spectra were recorded. See figures 2.7-2.8.

#### *NH<sub>2</sub>BH<sub>2</sub> Trapping Experiments*

In a typical reaction, a quartz J. Young NMR tube was charged with precatalyst (**4** or **5**, 0.020 mmol), AB (1.2 mg, 0.040 mmol), and diglyme (0.5 mL). Cyclohexene (61  $\mu$ L, 0.600 mmol) was added via microsyringe and the tube was sealed and placed in a Varian 400 MHz NMR spectrometer preheated to 70 °C. Successive <sup>11</sup>B and <sup>31</sup>P{<sup>1</sup>H} NMR spectra were recorded. See figures 2.9-2.10.

*Eudiometric Measurement Details*

In a typical run, a 2 mL Schlenk tube was charged with precatalyst (0.0125 mmol), AB (7.7 mg, 0.250 mmol), diglyme (1 mL) and a stir bar. The Schlenk tube was sealed and attached to the eudiometer depicted in Figure 2.3. The tubing attached to the Schlenk tube was evacuated and backfilled with N<sub>2</sub> (x3). Under positive N<sub>2</sub> pressure, the flask was opened to the burette, causing immediate bubbling. Once the pressure had equilibrated, the Schlenk tube was quickly opened and closed to alleviate positive pressure remaining from the drybox. Once bubbling stopped, the initial volume was recorded. The Schlenk tube was submerged in a 70 °C oil bath, with stirring, and opened. Gas evolution was monitored over time.

Precatalysts **5**, **9**, and **11**, formed homogeneous solutions under the above described conditions. Complex **4** proved only slightly soluble in diglyme, but rapidly formed a homogeneous red/orange solution upon heating the in the presence of AB. In case of **4**, **5**, and **11**, homogeneity was maintained until the majority of the H<sub>2</sub> had been liberated, at which point the forming solids were assumed to be dehydrogenation byproducts (namely PB). Experiments utilizing complex **9** remained homogeneous throughout the 6.5 h experiment. Diglyme solutions of complex **10** appeared to remain homogeneous, but at the employed concentrations, the deep green solution proved too darkly colored to be certain.

For catalyst reusability reactions, following a run set up as described above, the 3-way valve was used to place the reaction vessel under positive N<sub>2</sub> pressure. The Teflon tap was removed and additional dry AB was added with a backflow of N<sub>2</sub>. The Schlenk tube was sealed, the pressure in the eudiometer allowed to equalize, and H<sub>2</sub> evolution measurement resumed.

Catalyst reuse was first explored using conditions analogous to those employed for single-use dehydrogenation measurements. In a typical run, a 2 mL Schlenk tube was charged with precatalyst (0.017 mmol), AB (10.5 mg, 1.62 mmol), diglyme (1.00 mL) and

a stir bar. The Schlenk tube was sealed and attached to the eudiometer as described above. The Schlenk tube was submerged in a 70 °C oil bath, with stirring, and opened. Gas evolution was monitored over time. Every 4 h (for complex **4**) or 6 h (for complex **5**), an additional charge of AB (10.5 mg, 1.62 mmol) was added with N<sub>2</sub> counter pressure. Turnover number was calculated from the moles of H<sub>2</sub> produced and system weight percent hydrogen was determined according to the following formula:<sup>15a</sup>

$$\left( \frac{\text{Theor. Wt. Yield H}_2}{\text{Wt. AB} + \text{Wt. Diglyme} + \text{Wt. Precatalyst}} \right) * \left( \frac{\text{Tot. H}_2 \text{ Collected}}{\text{Theor. H}_2 \text{ Content}} \right) * 100\% = \text{System Wt. \% H}_2$$

In an attempt to increase the system weight percent, conditions similar to those reported by Williams and coworkers were used.<sup>15a</sup> In a typical reaction, a 2 mL Schlenk tube was charged with precatalyst (0.0017 mmol), AB (50.0 mg, 1.62 mmol), diglyme (0.100 mL) and a stir bar, providing a slurry comprised of *ca.* 16 M AB. The Schlenk tube was sealed and attached to the eudiometer as described above. The Schlenk tube was submerged in a 70 °C oil bath, with stirring, and opened. Gas evolution was monitored over time. Every 6 h, an additional charge of 50 mg of AB and 0.100 mL of diglyme was added with N<sub>2</sub> counter pressure. Turnover number and system weight percent hydrogen were calculated as before.

The effect of H<sub>2</sub>O and methanol on dehydrogenation catalysis was determined as follows. In a typical reaction, a 2 mL Schlenk tube was charged with precatalyst (0.017 mmol), AB (10.5 mg, 1.62 mmol), diglyme (1.00 mL) and a stir bar. The Schlenk tube was sealed and attached to the eudiometer as described above. With a backflow on N<sub>2</sub>, the Teflon pin was removed and replaced with a rubber septum. Degassed H<sub>2</sub>O or MeOH (2 μL) was added via microsyringe. The septum was removed and the Teflon pin replaced. The 3-way valve was turned to connect the reaction vessel and the upturned burette and following pressure equilibration, the Schlenk tube was submerged in a 70 °C oil bath, with stirring, and opened. Gas evolution was monitored over time. Alternatively, unpurified

(benchtop) AB was used in lieu of sublimed AB in the absence of added water as described above.

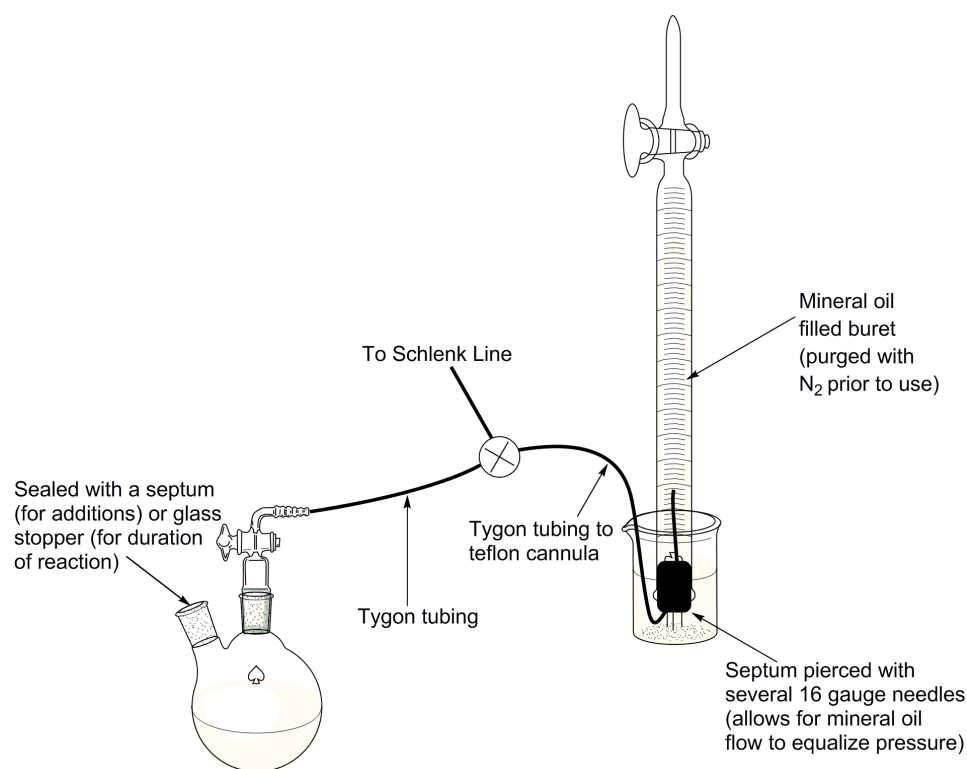


**Figure 2.3.** Schematic for the eudiometer apparatus used for ammonia borane dehydrogenation reactions. Note that rather than a 2-neck round bottom flask as depicted above, a Teflon valve Schlenk tube was used for all reported reactions.

#### *Reaction Kinetics Measurements*

In a typical reaction, a quartz J. Young NMR tube was charged with precatalyst (**4** or **5**, 0.009 mmol), AB (5.6 mg, 0.180 mmol),  $NaBPh_4$  (30.8 mg, 0.09 mmol) and diglyme (0.5 mL). Tube was sealed<sup>‡</sup> and placed in a Varian 400 MHz NMR spectrometer preheated to 70 °C.  $^{11}B$  NMR spectra were recorded as an array utilizing the pre-acquisition delay mechanism in Agilent's Vnmrj software. Relative AB concentration was determined via integration of the AB resonance with respect to  $NaBPh_4$ .

<sup>‡</sup> CAUTION: Pressure builds up over the course of the reaction.

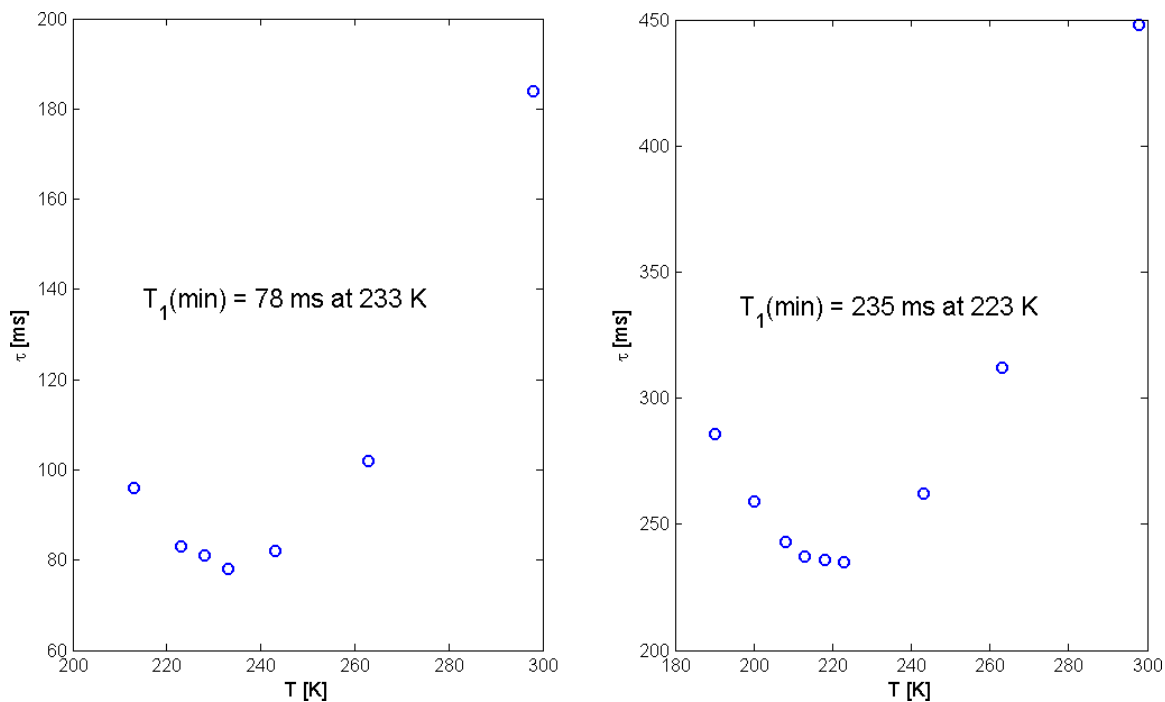


**Figure 2.4.** Plots of  $T_1$  vs.  $T$  for **6** (left) and **8** (right).

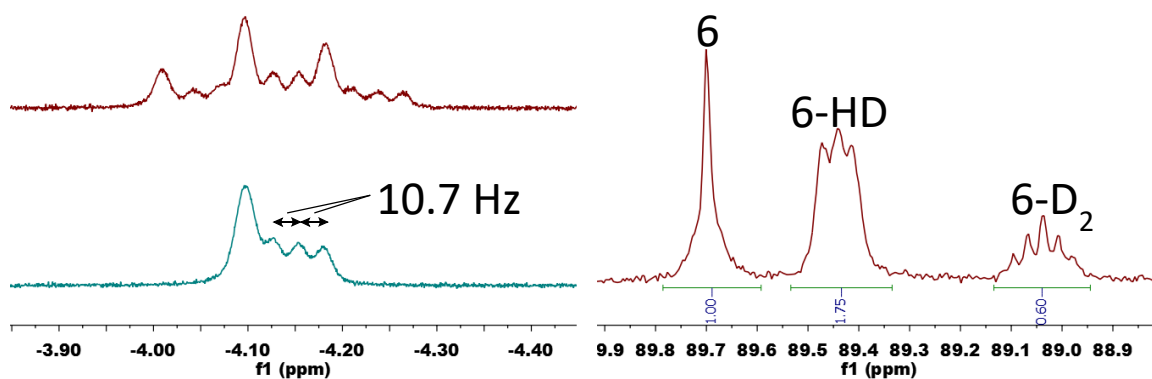


**Figure 2.5.** Partial  $^1\text{H}$  (top left, 400 MHz,  $\text{C}_6\text{D}_6$ ),  $^1\text{H}\{^{31}\text{P}\}$  (bottom left, 400 MHz,  $\text{C}_6\text{D}_6$ ), and  $^{31}\text{P}\{^1\text{H}\}$  (right, 162 MHz,  $\text{C}_6\text{D}_6$ ) NMR spectra of a mixture of **6**, **6-HD**, and **6-D<sub>2</sub>**. The observed  $J_{\text{HD}}$  of 10.7 Hz is consistent with a contracted Mo dihydride complex.<sup>21-22</sup>

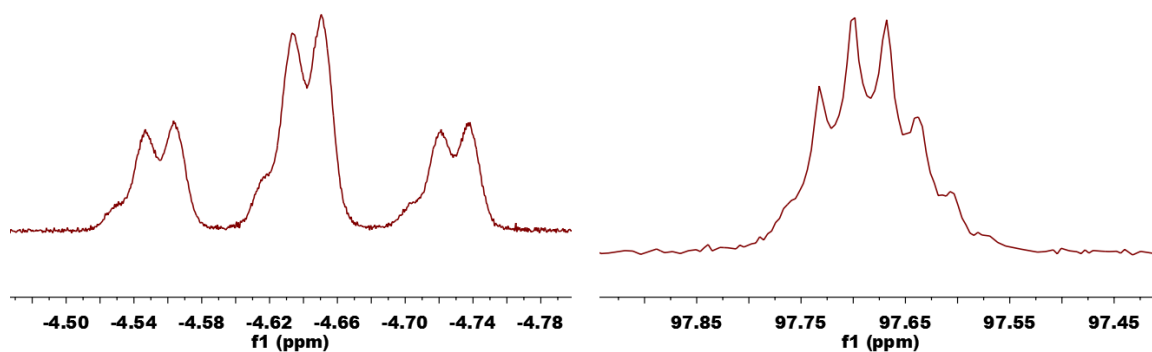


**Figure 2.6.** Partial  $^1\text{H}$  (left, 400 MHz,  $\text{CD}_2\text{Cl}_2$ ) and  $^{31}\text{P}\{^1\text{H}\}$  (right, 162 MHz,  $\text{CD}_2\text{Cl}_2$ ) NMR spectra of **8** following treatment with ca. 7 equiv. of  $\text{D}_2$ . Unresolved isotopologue resonances have been reported for other classical Mo trihydride complexes.<sup>20g</sup>

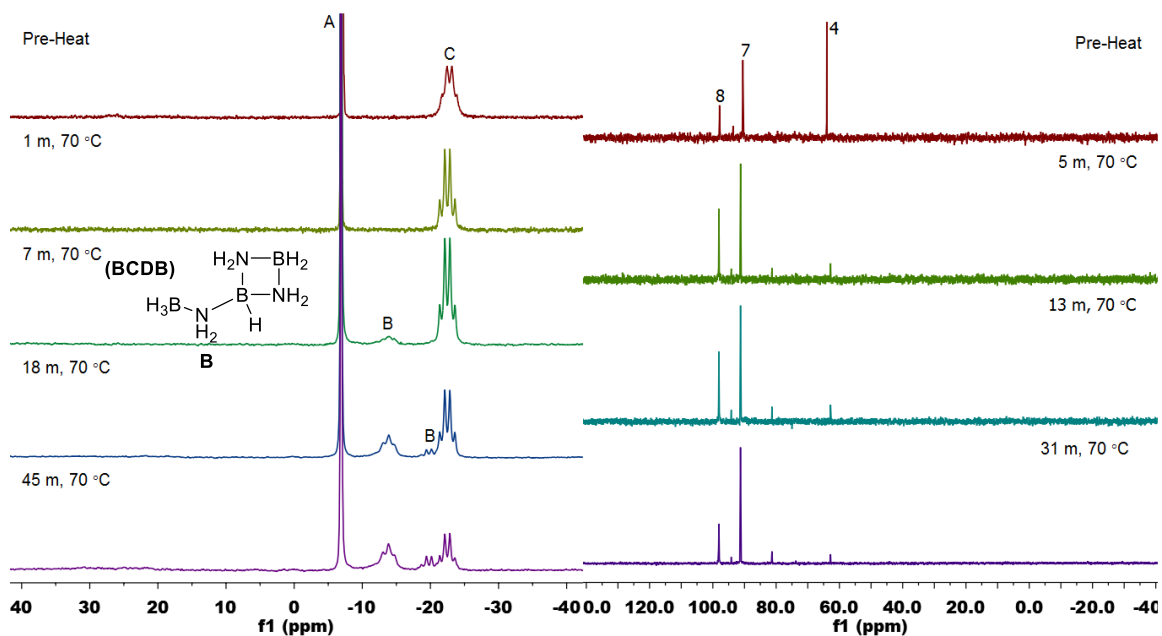


**Figure 2.7.**  $^{11}\text{B}$  (left) and  $^{31}\text{P}\{^1\text{H}\}$  (right) NMR spectra (128 and 162 MHz respectively, diglyme) of AB dehydrogenation by **4**. In the  $^{11}\text{B}$  NMR spectra, the internal  $\text{NaBPH}_4$  standard (**A**) and AB (**C**) were initially observed. Over 45 mins, AB was consumed with concomitant generation of BCDB (**B**, inset). The  $^{31}\text{P}\{^1\text{H}\}$  NMR spectrum shows formation of **8** and **7** from **4**, even prior to heating.



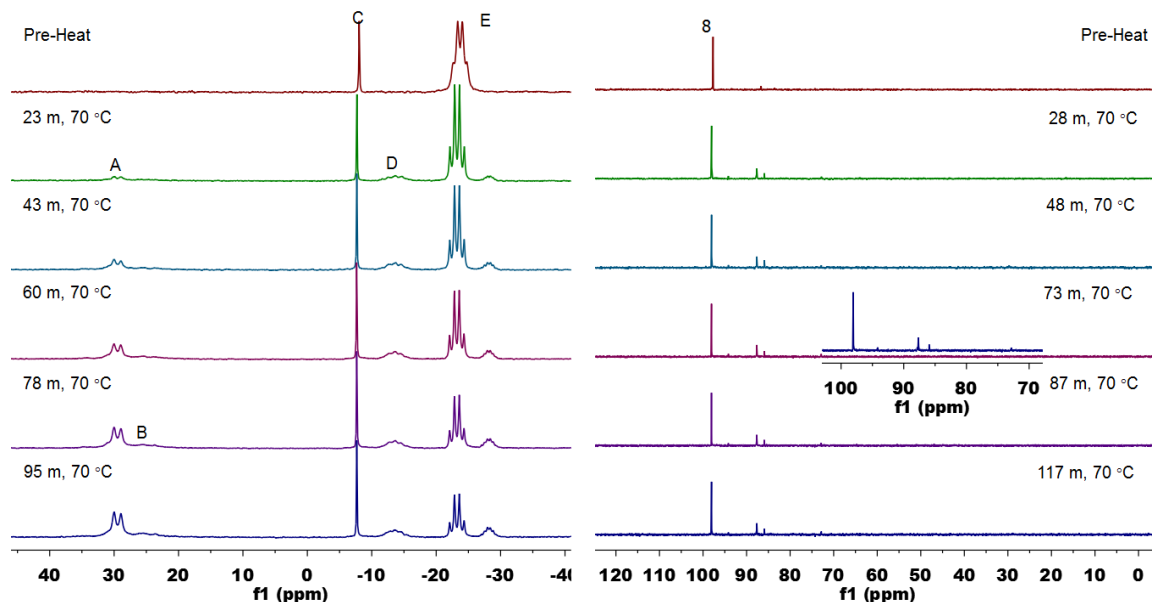


**Figure 2.8.**  $^{11}\text{B}$  (left) and  $^{31}\text{P}\{^1\text{H}\}$  (right) NMR spectra (128 and 162 MHz respectively, diglyme) of AB dehydrogenation by **8**. In the  $^{11}\text{B}$  NMR spectra, borazine (**A**) and PB (**B**) grow in with time. The formation of BCBD (**D**) is observed with the concomitant consumption of AB (**E**). A resonance for the  $\text{BPh}_4^-$  counterion of **8** is also observed. The  $^{31}\text{P}\{^1\text{H}\}$  NMR spectrum shows formation of several species (see inset), with the most prominent starting to form prior to heating.

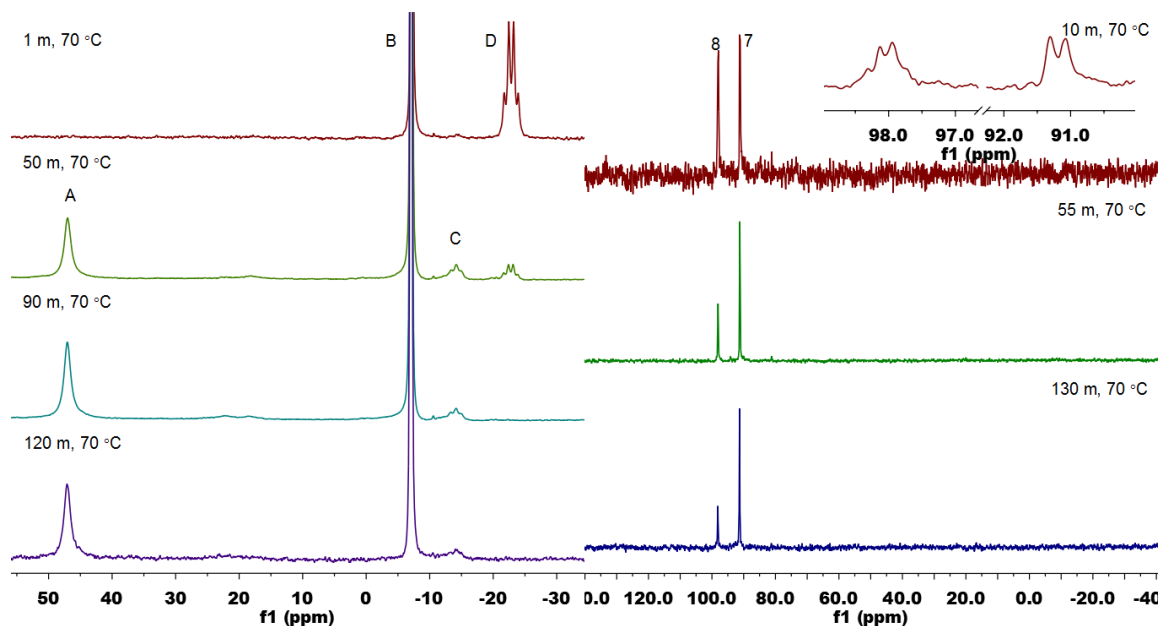


**Figure 2.9.**  $^{11}\text{B}$  (left) and  $^{31}\text{P}$  (right) NMR spectra (128 and 162 MHz respectively, diglyme) of AB dehydrogenation by **4** in the presence of cyclohexene and the internal standard  $\text{NaBPh}_4$  (**B**). The formation of the hydroborylation product  $\text{H}_2\text{NB}(\text{Cy})_2$  (**A**) is observed, along with consumption of AB (**D**). Some BCDB (**C**) was also generated. The selectively coupled  $^{31}\text{P}$  NMR spectrum (top left) shows that **4** is consumed completely within 10 m, furnishing **7** (doublet) and **8** (quartet). Subsequent  $^{31}\text{P}$  NMR spectra were proton decoupled to increase the signal to noise ratio.

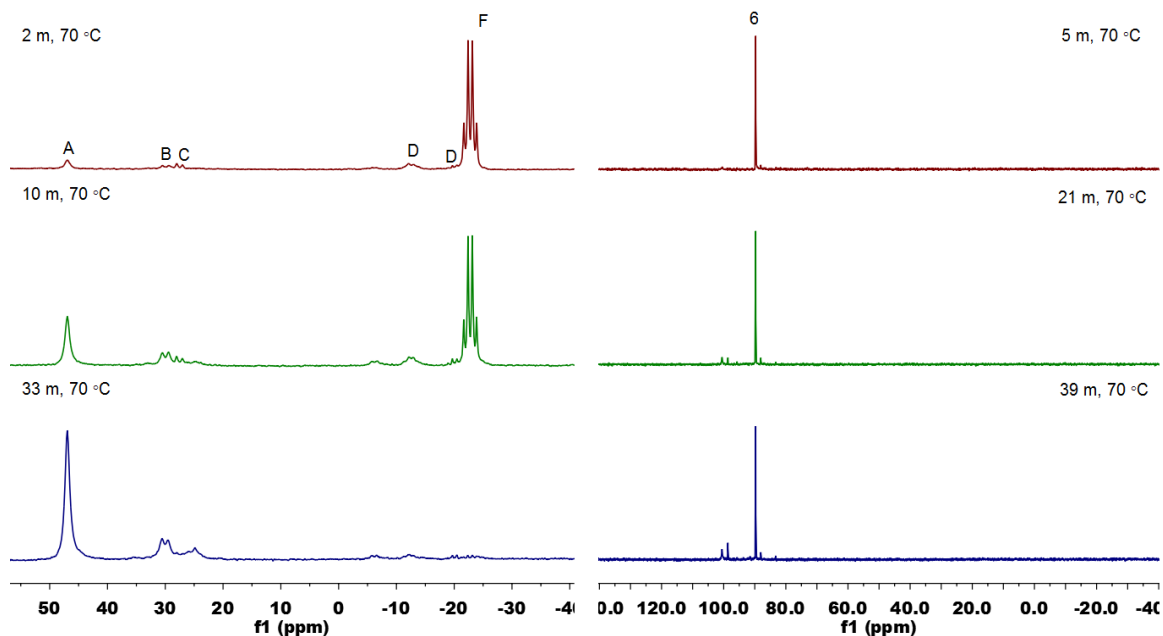


**Figure 2.10.**  $^{11}\text{B}$  (left) and  $^{31}\text{P}\{^1\text{H}\}$  (right) NMR spectra (128 and 162 MHz respectively, diglyme) of AB dehydrogenation by **5** in the presence of cyclohexene. The formation of the hydroborylation product  $\text{H}_2\text{NB}(\text{Cy})_2$  (**A**) is observed, along with consumption of AB (**F**). Some BCDB (**D**), borazine (**B**), and PB (**C**) were also generated. The  $^{31}\text{P}\{^1\text{H}\}$  NMR shows that **5** is consumed completely within 5 m, and **6** is the major species throughout the reaction.

#### Endiometric Data

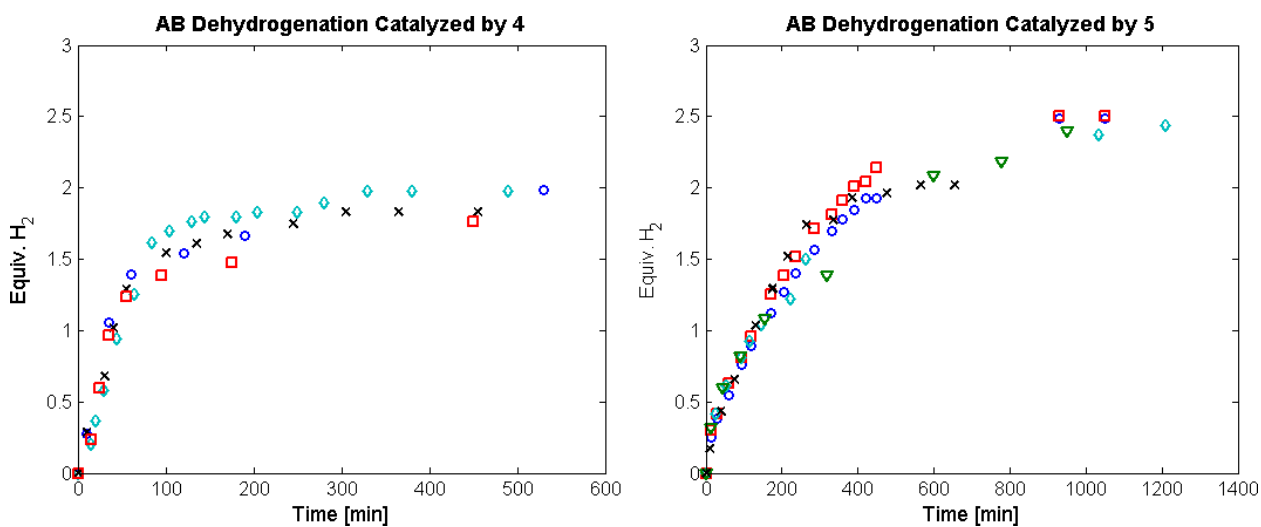


**Figure 2.11.** Hydrogen evolution measurements for **4** (left) and **5** (right). Addition of elemental mercury was observed to have no effect on the rate of catalysis (black x's). Mercury addition did lessen the extent of dehydrogenation catalysis from precatalyst **5**.

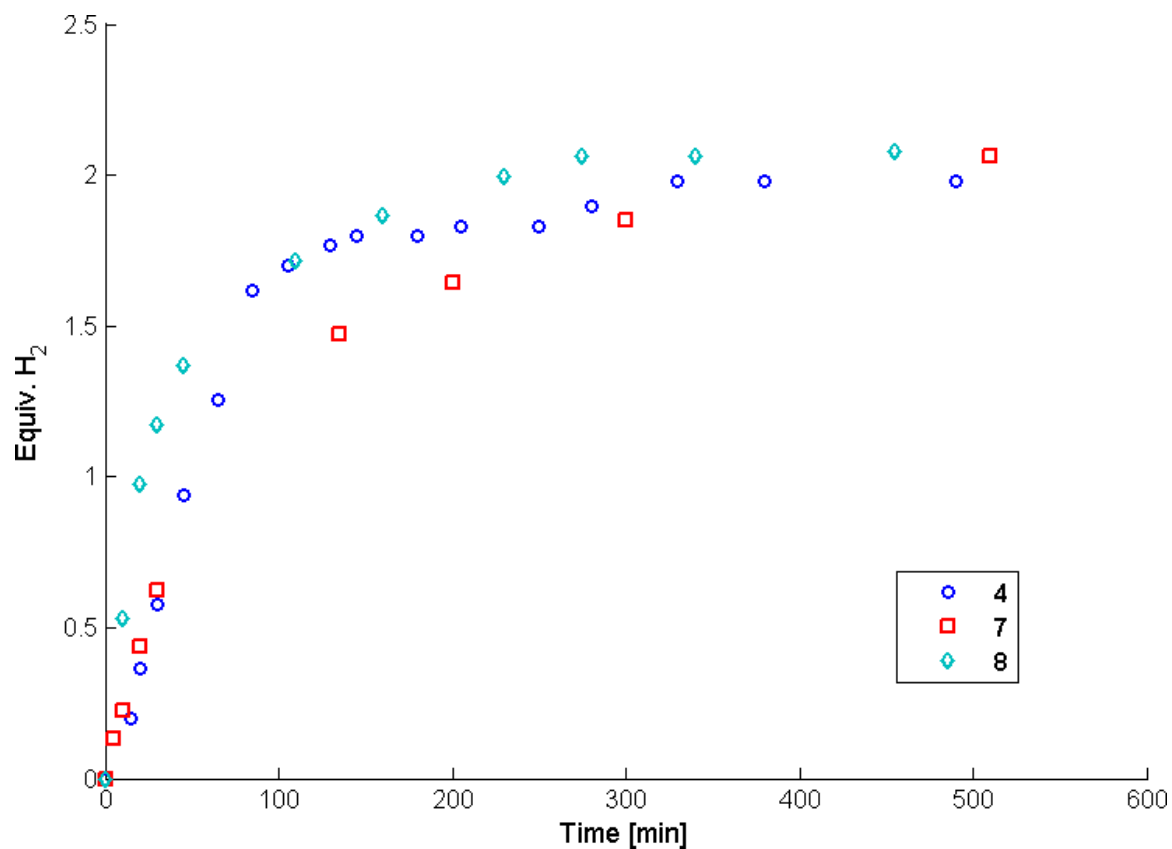


Figure 2.12. Eudiometric measurements displaying the kinetic competence of 4, 7, and 8.

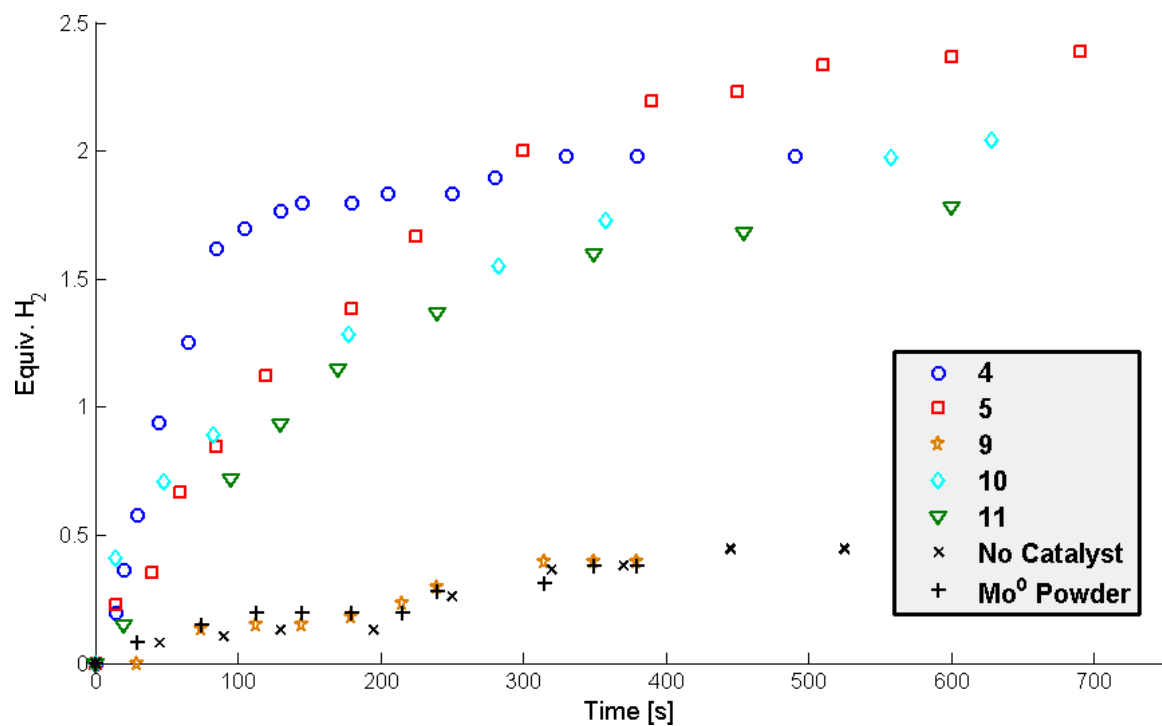
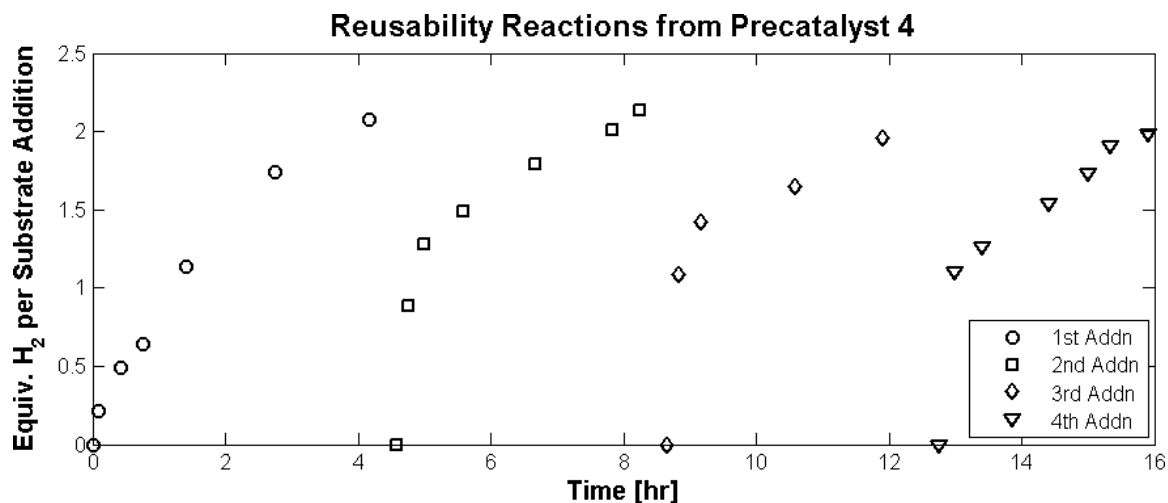
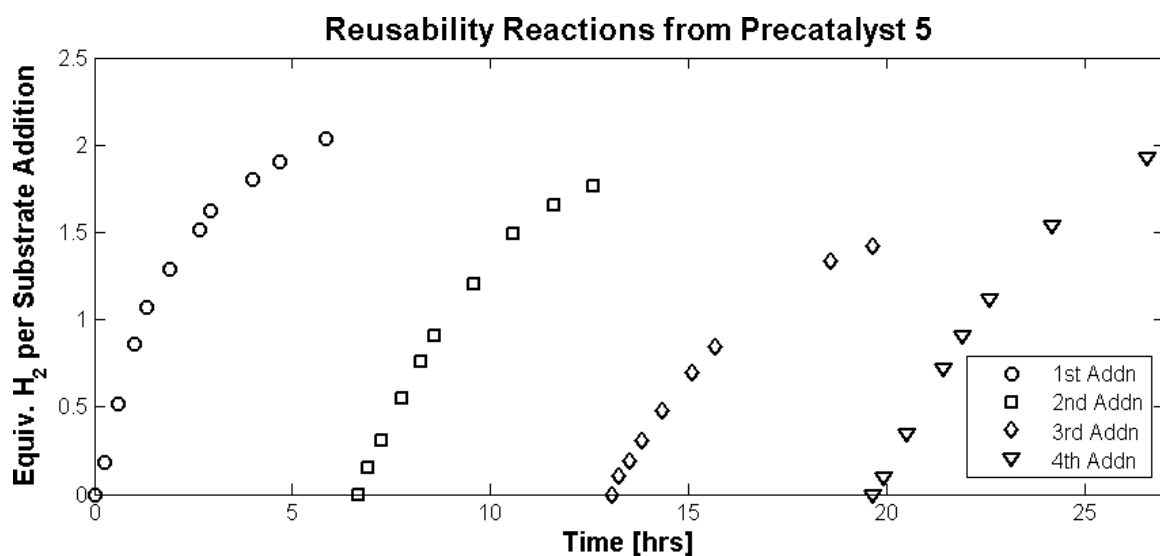


Figure 2.13. Hydrogen evolution profiles for Mo catalyzed AB dehydrogenation. Control reactions with AB in the absence of a catalyst and in the presence of Mo<sup>0</sup> powder are included for reference.



**Figure 2.14.** Multiple substrate additions to the reaction of AB with 5 mol % **4**. No decrease in the rate or extent of catalysis is observed over four sequential *ca.* 4 hour experiments. A total of 2.0 equiv. of H<sub>2</sub> per AB molecule were released, indicating 274 turnovers. This corresponds to the liberation of 0.80 system wt. % H<sub>2</sub> (out of a possible 1.18 %).



**Figure 2.15.** Multiple substrate additions to the reaction of AB with 5 mol % **5**. A slight decrease in the extent of catalysis is observed for the second and third addition. A total of 1.8 equiv. of H<sub>2</sub> per AB molecule were released, indicating 143 turnovers. This corresponds to the liberation of 0.52 system wt. % H<sub>2</sub> (out of a possible 0.88 %).

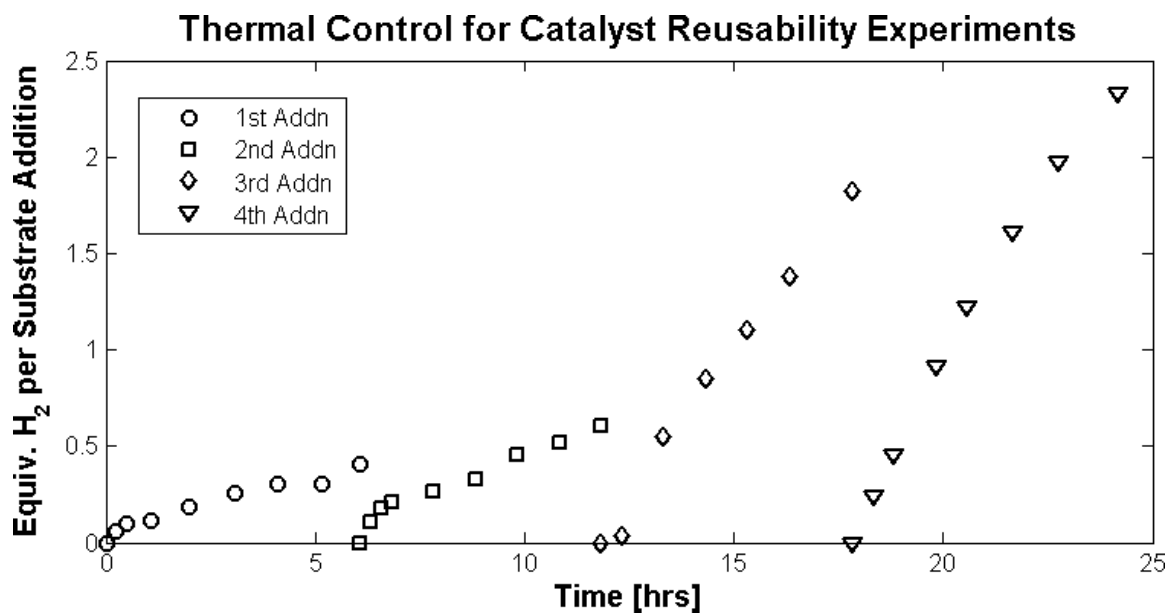


**Figure 2.16.** Multiple substrate additions to the thermal control reaction of heating *ca.* 0.25 M AB solutions in diglyme. No decrease in the rate or extent of catalysis is observed over four sequential *ca.* 4 hour experiments. A total of 1.25 equiv. of H<sub>2</sub> per AB was collected, a significant decrease from the catalyzed systems (2.04 equiv. for **4** and 1.78 equiv. for **5**, respectively).

During the control, the marked difference in the rate of dehydrogenation observed between the first and latter two additions of AB is attributed to the second-order decomposition process for thermal dehydrogenation.<sup>25,36</sup> As the concentration of AB increases with subsequent substrate additions, thermal dehydrogenation becomes more kinetically viable, leading to rapid H<sub>2</sub> release in the third and fourth runs.

The system weight percent H<sub>2</sub> released from the above systems is low in comparison to reported values;<sup>11,9c,15a</sup> however, this is largely a manifestation of the concentration of AB in solution. The majority (93 %) of the system weight can be attributed to the solvent. To attempt to increase system weight percent H<sub>2</sub>, dehydrogenation was attempted at higher AB concentrations and lower catalyst loadings.

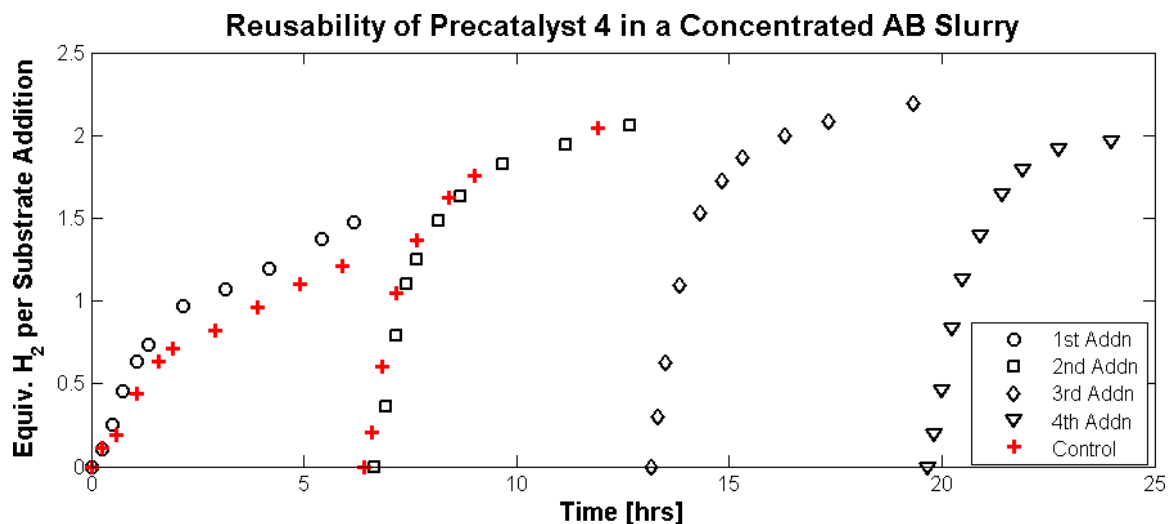


**Figure 2.17.** Multiple substrate additions to 0.1 mol % **4** in a *ca.* 16 M slurry of AB. The thermal control (identical conditions sans catalyst) is overlaid in red. Although a slight deviation between the catalyzed run and the control is observed for the first addition, no difference is observed following the second addition. Notably, this system achieves 4.4 wt. % H<sub>2</sub> release. The similarity of the catalyzed and control experiments eliminates the ability to attribute dehydrogenation activity to **4** under these conditions.

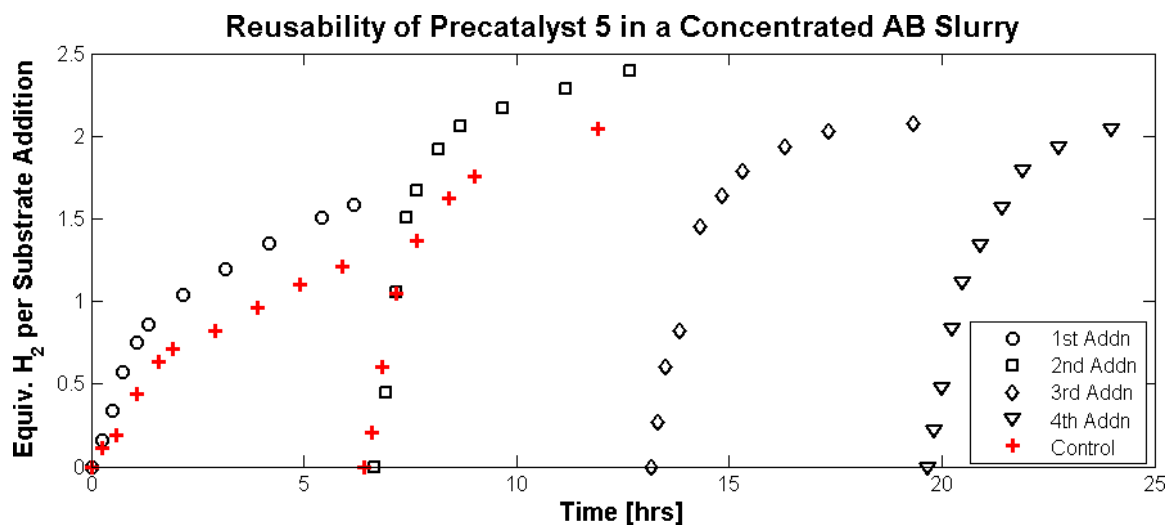


**Figure 2.18.** Multiple substrate additions to 0.1 mol % **5** in a *ca.* 16 M slurry of AB. The thermal control (identical conditions sans catalyst) is overlaid in red. Only a slight deviation between the catalyzed run and the control is observed. Notably, this system achieves 4.5 wt. % H<sub>2</sub> release. The similarity of the catalyzed and control experiments eliminates the ability to attribute dehydrogenation activity to **5** under these conditions.

Under concentrated AB conditions, little difference was observed between catalyzed and uncatalyzed experiments. This is attributable to thermal dehydrogenation processes dominating at high [AB]. With low catalyst loading (0.1 mol %), these conditions fail to

lend insight into the role of the catalyst but further optimization of the catalyzed systems for both precatalysts **4** and **5** is underway. Corroborating the concentration dependence of thermally induced, solution state AB dehydrogenation, rapid H<sub>2</sub> release is observed even after the first substrate addition under these more concentrated conditions. The increase from 1.5 equiv. to 2.0 equiv. released in control runs 1 and 2 is attributed to the presence of reactive dehydrogenation intermediates and improved stirring resulting from doubling the volume of diglyme. Presumably, solid-state thermal dehydrogenation is also playing a role in these slurry reactions.<sup>37</sup>

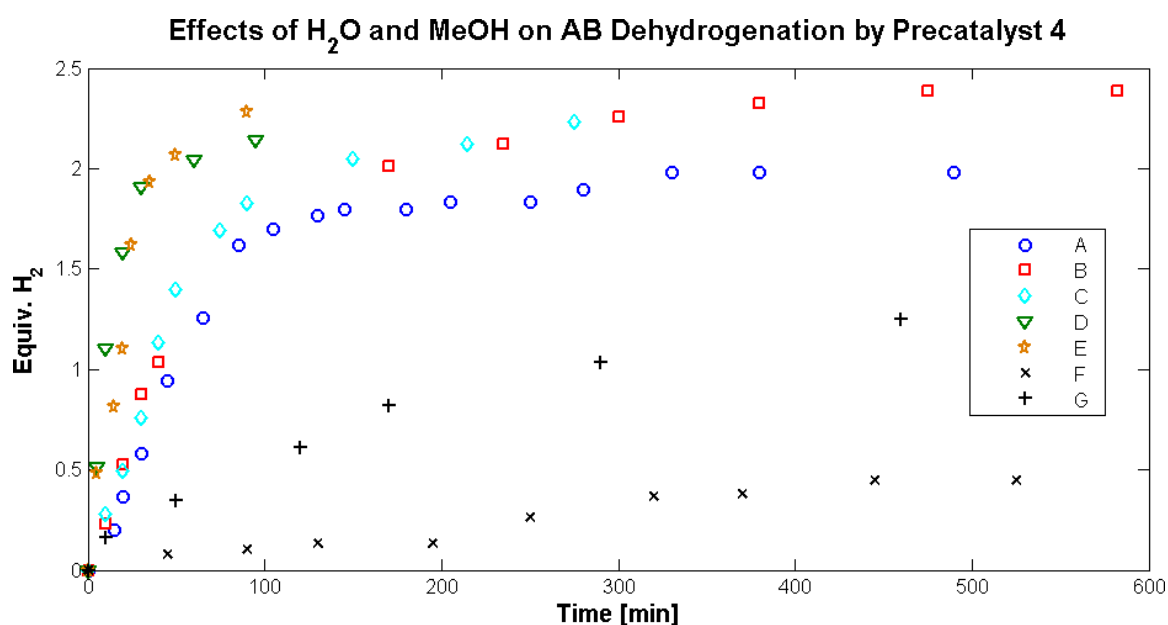


**Figure 2.19.** Hydrogen evolution profiles for reactions of precatalyst **4** with dry AB (A), AB and water (B-D), and AB and methanol (E). Control reactions with dry AB (F) and AB with water added (G) are included for comparison.

A significant disparity in the rate and extent of hydrogen evolution was observed when using sublimed AB (A) and unpurified AB (B). This rate increase was attributed to water, as sublimed AB that was later exposed to air showed a similar H<sub>2</sub> evolution profile to unpurified AB (C). Addition of 50 mol % H<sub>2</sub>O to dehydrogenation experiments resulted in a significant rate increase, releasing over 2 equiv. of H<sub>2</sub> in 1 h (D). A similar effect was observed with the addition of 20 mol % methanol, again resulting in a significant increase to the rate and extent of dehydrogenation. Addition of 50 mol % H<sub>2</sub>O to an AB solution lacking catalyst also leads

to a greater extent of H<sub>2</sub> release (G). Though hydrolysis<sup>2,4b,38</sup> and acid catalysis<sup>17b,4b,39</sup> are established methods for the dehydrogenation of AB, the resulting B–O bonds likely preclude facile recyclability and therefore these systems were not studied further. Though little effect was observed for the source of AB utilized with precatalyst **5**, reported experiments use rigorously purified AB unless stated otherwise. Control experiments (with AB and **4**) were run on each batch of substrate to ensure consistency.

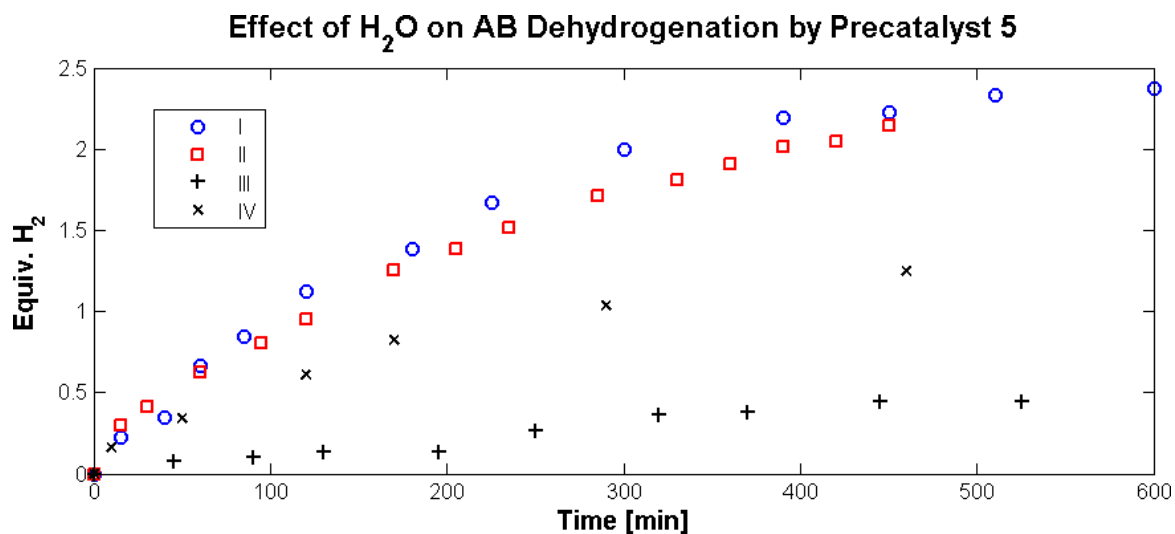


**Figure 2.20.** Hydrogen evolution profiles for reactions of precatalyst **5** with dry AB (I) and AB and water (II). Control reactions with dry AB (III) and AB with water added (IV) are included for comparison.



## Kinetic Data

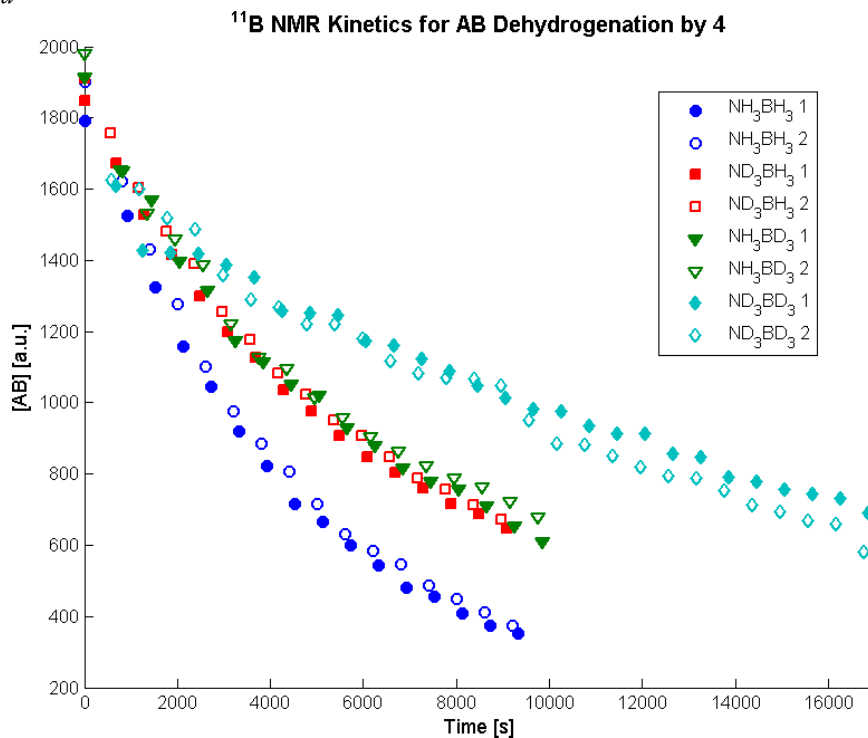


**Figure 2.21.** Relative concentration vs. time plots for reactions of AB isotopologs with catalytic 4 as monitored by  $^{11}\text{B}$  NMR spectroscopy.

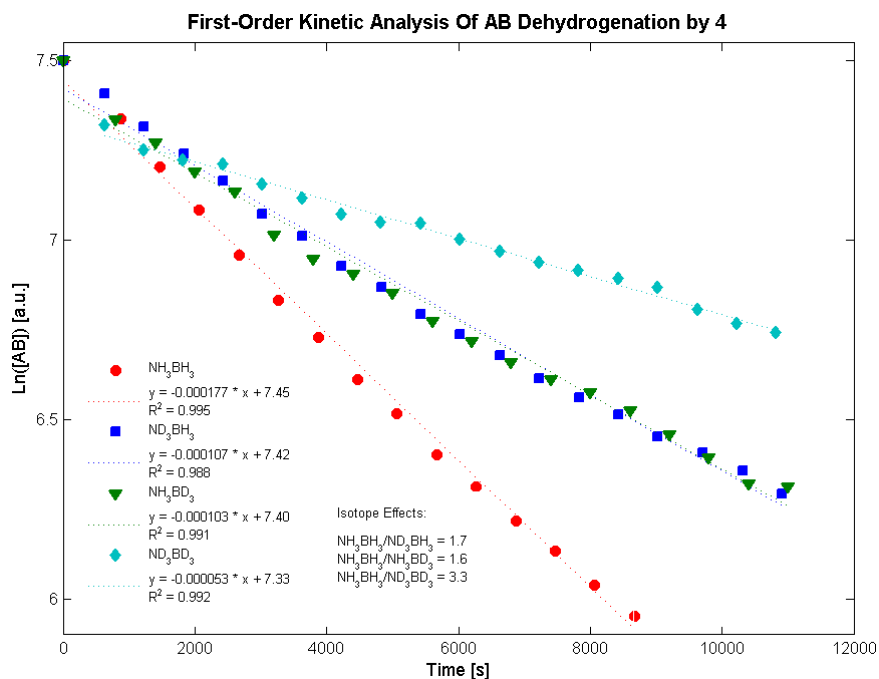


**Figure 2.22.** Log plot of [AB] vs. time with catalytic 4 as monitored by  $^{11}\text{B}$  NMR spectroscopy. Isotope effects were calculated from the ratios of the respective slopes and are reported in the inset.

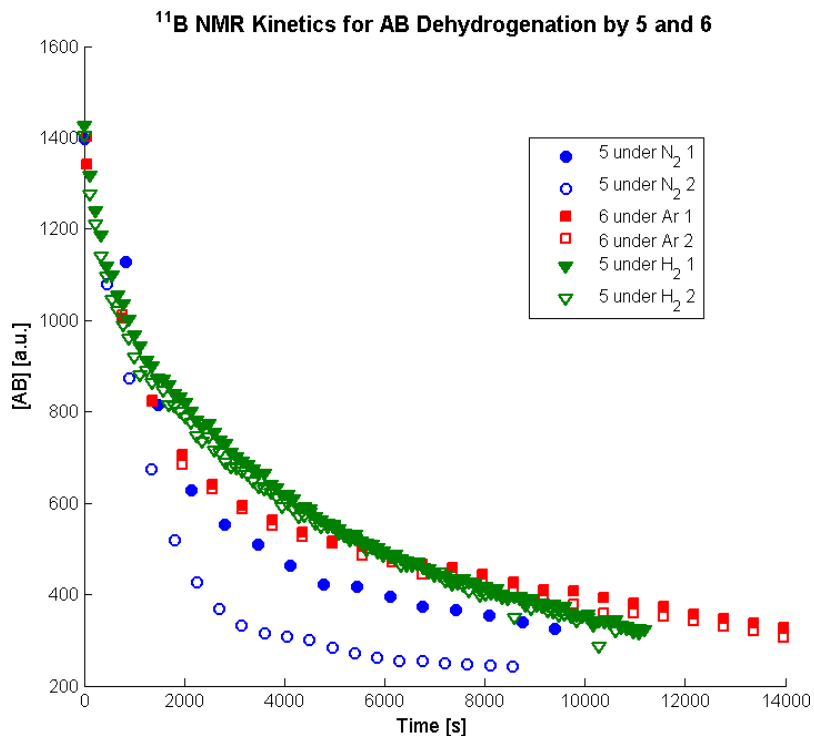


**Figure 2.23.** Relative concentration vs. time plots for reactions of AB with catalytic **5** and **6** as monitored by  $^{11}\text{B}$  NMR spectroscopy.

Analysis of the dehydrogenation kinetics for **5** showed neither first- nor second-order behavior. The possibility of the equilibrium between **5** and **6** ( $[\text{H}_2]$  increases with time) affecting the rate of the reaction was ruled out via measuring kinetics from isolated **6** (red squares). Addition of 1 atm of  $\text{H}_2$  to precatalyst **5** prior to heating demonstrated *pseudo*-first-order kinetics. This is consistent with product ( $\text{H}_2$ ) inhibition, but further experimentation is required to confirm this hypothesis.

#### *Crystallographic Information*

CCDC deposition numbers 804890, 1008197, 1008330-1008331, and 1008356-1008357 contain the supplementary crystallographic data for this paper. These data can be obtained free of charge from The Cambridge Crystallographic Data Centre via [www.ccdc.cam.ac.uk/data\\_request/cif](http://www.ccdc.cam.ac.uk/data_request/cif).

**Refinement Details**—In each case, crystals were mounted on a glass fiber or nylon loop using Paratone oil, then placed on the diffractometer under a nitrogen stream. Low temperature (100 K) X-ray data were obtained on a Bruker APEXII CCD based

diffractometer (Mo sealed X-ray tube,  $K_{\alpha} = 0.71073 \text{ \AA}$ ) or a Bruker SMART CCD based diffractometer (Mo sealed X-ray tube,  $K_{\alpha} = 0.71073 \text{ \AA}$ ). All diffractometer manipulations, including data collection, integration, and scaling were carried out using the Bruker APEXII software.<sup>40</sup> Absorption corrections were applied using SADABS.<sup>41</sup> Space groups were determined on the basis of systematic absences and intensity statistics and the structures were solved by direct methods using XS<sup>42</sup> or by intrinsic phasing using XT (incorporated into SHELXTL) and refined by full-matrix least squares on  $F^2$ . All non-hydrogen and hydride atoms were refined using anisotropic displacement parameters. Non-hydride hydrogen atoms were placed in the idealized positions and refined using a riding model. The structure was refined (weighed least squares refinement on  $F^2$ ) to convergence. Graphical representation of structures with 50% probability thermal ellipsoids was generated using Diamond visualization software.<sup>43</sup>

**Table 2.2.** Crystal and refinement data for complexes **2-5** and **7-8**.

	<b>2</b>	<b>3</b>	<b>4</b>	<b>5</b>	<b>7</b>	<b>8</b>
CCDC Number <sup>44</sup>	804890	1008197	1008330	1008356	1008331	1008357
Empirical formula	C <sub>33</sub> H <sub>40</sub> MoO <sub>3</sub> P <sub>2</sub>	C <sub>34</sub> H <sub>40</sub> F <sub>6</sub> MoO <sub>8</sub> P <sub>2</sub> S <sub>2</sub>	C <sub>36.67</sub> H <sub>46</sub> F <sub>6</sub> MoN <sub>2.33</sub> O <sub>6</sub> P <sub>2</sub> S <sub>2</sub>	C <sub>30</sub> H <sub>40</sub> MoN <sub>2</sub> P <sub>2</sub>	C <sub>56</sub> H <sub>64</sub> BMoNP <sub>2</sub>	C <sub>58</sub> H <sub>71</sub> BMoOP <sub>2</sub>
Formula weight	642.53	912.66	951.42	586.52	919.77	952.83
T (K)	100	100	100	100	100	100
<i>a</i> , Å	12.9284(7)	12.7866(6)	32.0444(10)	8.9892(3)	12.7883(6)	11.1314(5)
<i>b</i> , Å	12.6055(6)	16.4447(7)	32.0444(10)	23.8655(7)	16.1757(7)	17.1403(8)
<i>c</i> , Å	19.2797(9)	17.5292(7)	21.1665(9)	12.7797(4)	23.2443(10)	26.9594(12)
$\alpha$ , °	90	90	90	90	90	90
$\beta$ , °	100.020(2)	91.785(2)	90	94.7145(16)	101.250(2)	94.544(2)
$\gamma$ , °	90	90	120	90	90	90
Volume, Å <sup>3</sup>	3094.1(3)	3684.1(3)	18822.7(14)	2732.37(15)	4715.9(4)	5127.6(4)
Z	4	4	18	4	4	4
Crystal system	Monoclinic	Monoclinic	Trigonal	Monoclinic	Monoclinic	Monoclinic
Space group	P 2 <sub>1</sub> /c	P 2 <sub>1</sub> /n	R3c	P 2 <sub>1</sub> /c	P 2 <sub>1</sub> /c	P 2 <sub>1</sub> /c
<i>d</i> <sub>calc</sub> , g/cm <sup>3</sup>	1.379	1.645	1.511	1.426	1.295	1.234
$\theta$ range, °	2.44 to 30.54	1.698 to 45.424	2.059 to 43.500	1.707 to 45.535	1.544 to 39.298	1.409 to 45.385
$\mu$ , mm <sup>-1</sup>	0.559	0.637	0.563	0.619	0.384	0.357
Abs. Correction	Semi-empirical	Semi-empirical	Semi-empirical	Semi-empirical	Semi-empirical	Semi-empirical
GOF	1.631	1.130	1.056	1.111	1.120	1.092
<i>R</i> <sub>1</sub> , <sup>a</sup> <i>wR</i> <sub>2</sub> <sup>b</sup> [I>2 $\sigma$ (I)]	0.0313, 0.0313	0.0464, 0.1251	0.0371, 0.0855	0.0493, 0.0951	0.0731, 0.1417	0.0448, 0.1007
Diffractometer	APEXII	APEXII	APEXII	SMART	APEXII	APEXII

<sup>a</sup>  $R_1 = \sum ||F_o| - |F_c|| / \sum |F_o|$ . <sup>b</sup>  $wR_2 = [\sum [w(F_o^2 - F_c^2)^2] / \sum [w(F_o^2)^2]]^{1/2}$ .

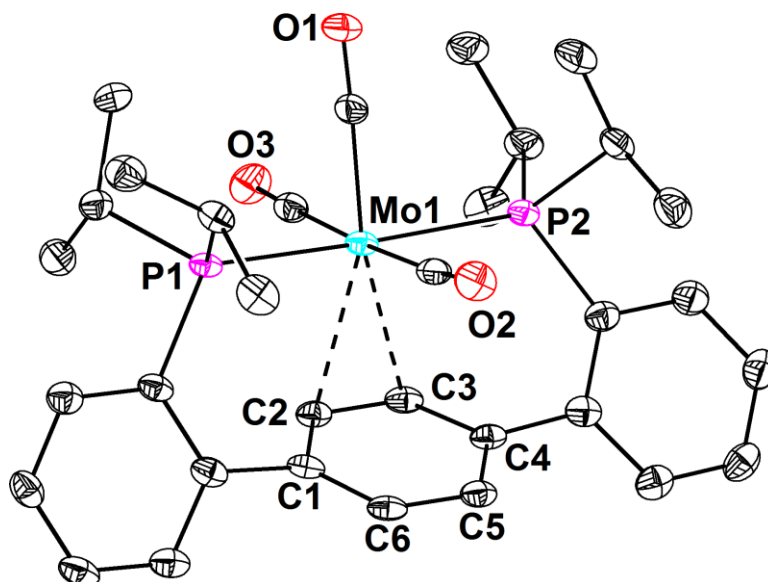


**Figure 2.24.** Structural drawing of **2** with 50% probability ellipsoids. Co-crystallized toluene and hydrogen atoms are omitted for clarity.

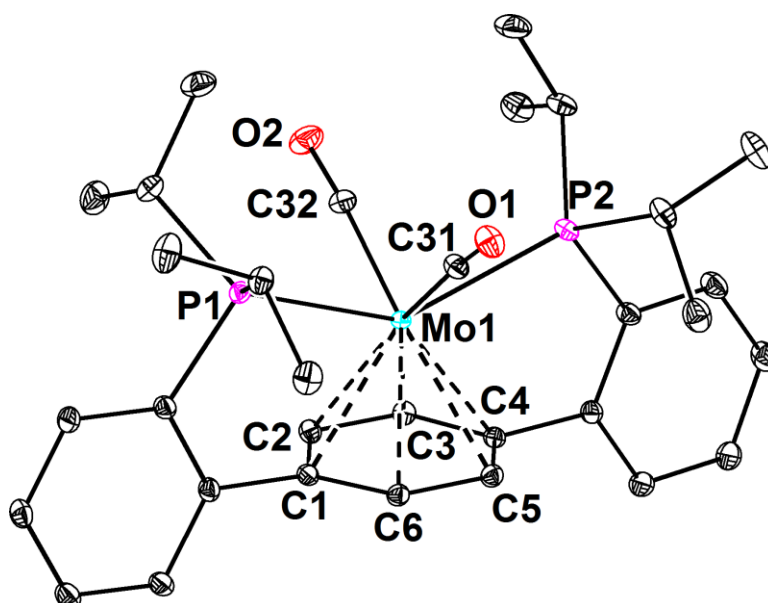


**Figure 2.25.** Structural drawing of **3** with 50% probability ellipsoids. Outer-sphere triflate ions and hydrogen atoms are omitted for clarity.

**Special refinement details for 3**— The crystal was twinned by a 180 degree rotation about the *a* axis. An HKLF 5 file was generated with the TwinRotMat option in PLATON. The twin ratio refined to 0.82:0.18.

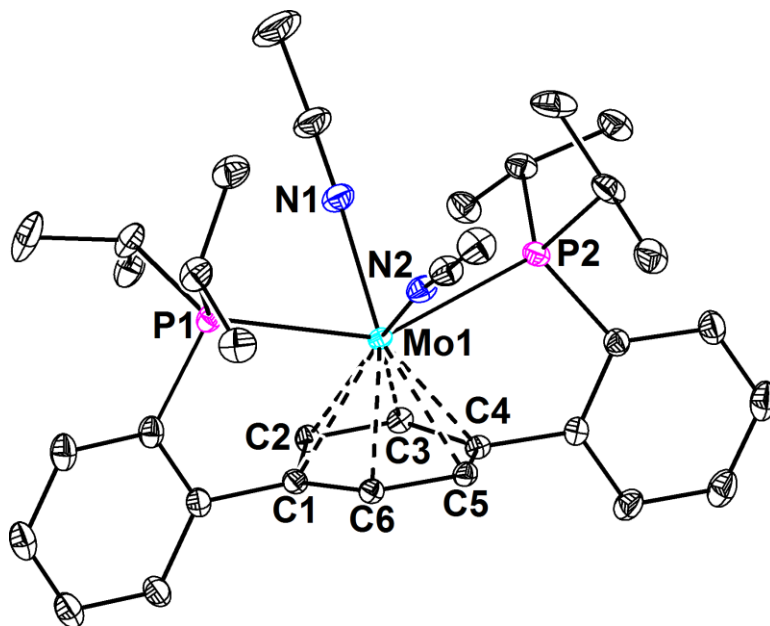


**Figure 2.26.** Structural drawing of 4 with 50% probability ellipsoids. Co-crystallized acetonitrile, outer-sphere triflate ions and hydrogen atoms are omitted for clarity.

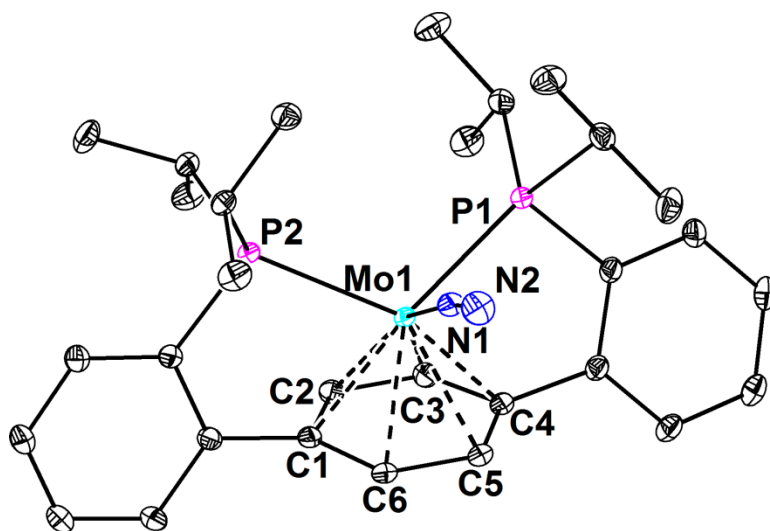


**Figure 2.27.** Structural drawing of 5 with 50% probability ellipsoids. Hydrogen atoms are omitted for clarity.

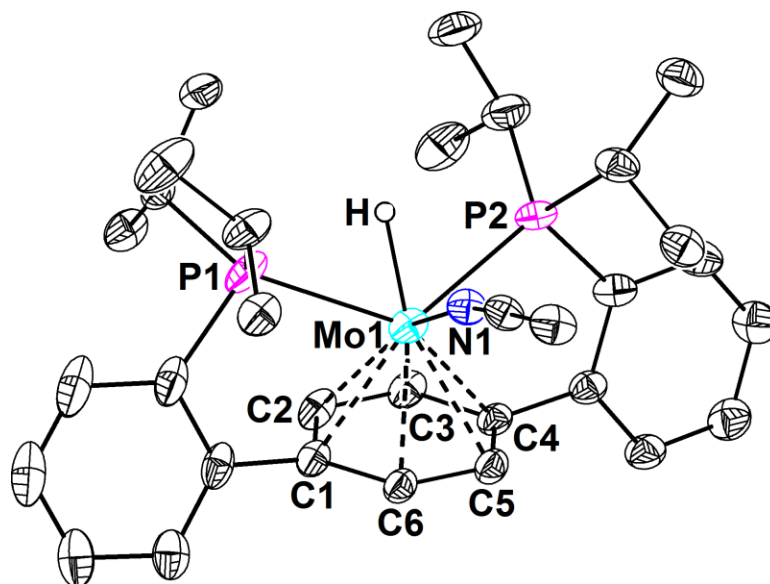


**Figure 2.28.** Structural drawing of **7** with 50% probability ellipsoids. Outer-sphere tetraphenylborate molecule and hydrogen atoms (except for the hydride) are excluded for clarity.

**Special refinement details for 7**—The ligand isopropyl groups were positionally disordered and satisfactorily modeled as approximately a 70:30 mixture using “PART” cards in SHELX.

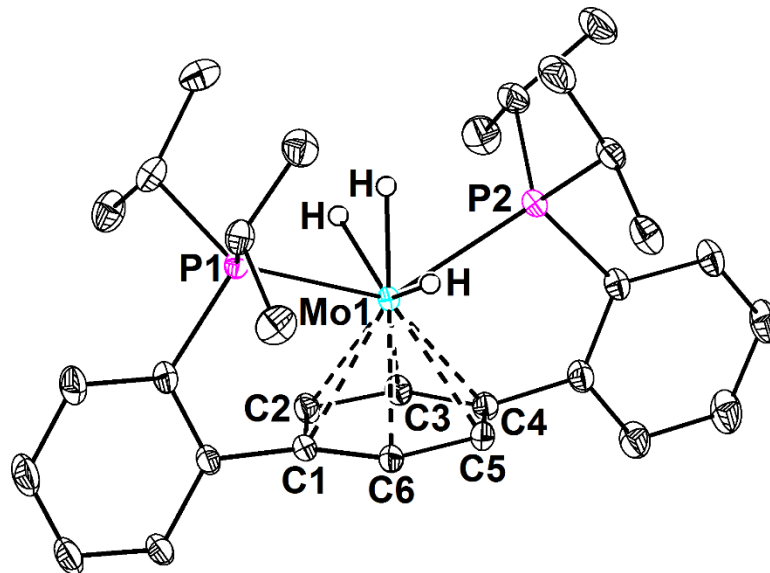


**Figure 2.29.** Structural drawing of **8** with 50% probability ellipsoids. A co-crystallized THF molecule and hydrogen atoms (except the hydrides) are omitted for clarity.

## REFERENCES

- (1) a) Satyapal, S.; Petrovic, J.; Read, C.; Thomas, G.; Ordaz, G. *Catal. Today* **2007**, *120*, 246; b) Schlapbach, L.; Züttel, A. *Nature* **2001**, *414*, 353.
- (2) Hamilton, C. W.; Baker, R. T.; Staubitz, A.; Manners, I. *Chem. Soc. Rev.* **2009**, *38*, 279.
- (3) Murray, L. J.; Dinca, M.; Long, J. R. *Chem. Soc. Rev.* **2009**, *38*, 1294.
- (4) a) Staubitz, A.; Robertson, A. P. M.; Manners, I. *Chem. Rev.* **2010**, *110*, 4079; b) Stephens, F. H.; Pons, V.; Baker, R. T. *Dalton Trans.* **2007**, 2613.
- (5) a) Carter, T. J.; Wang, J. Y.; Szymczak, N. K. *Organometallics* **2014**, *33*, 1540; b) Carter, T. J.; Kampf, J. W.; Szymczak, N. K. *Angew. Chem. Int. Ed.* **2012**, *51*, 13168; c) Sutton, A. D.; Burrell, A. K.; Dixon, D. A.; Garner, E. B.; Gordon, J. C.; Nakagawa, T.; Ott, K. C.; Robinson, P.; Vasiliu, M. *Science* **2011**, *331*, 1426.
- (6) Miller, A. J. M.; Bercaw, J. E. *Chem. Commun.* **2010**, *46*, 1709.
- (7) a) Himmelberger, D. W.; Yoon, C. W.; Bluhm, M. E.; Carroll, P. J.; Sneddon, L. G. *J. Am. Chem. Soc.* **2009**, *131*, 14101; b) Bluhm, M. E.; Bradley, M. G.; Butterick, R.; Kusari, U.; Sneddon, L. G. *J. Am. Chem. Soc.* **2006**, *128*, 7748.
- (8) Denney, M. C.; Pons, V.; Hebden, T. J.; Heinekey, D. M.; Goldberg, K. I. *J. Am. Chem. Soc.* **2006**, *128*, 12048.
- (9) a) Marziale, A. N.; Friedrich, A.; Klopsch, I.; Drees, M.; Celinski, V. R.; Guenne, J. S. A. D.; Schneider, S. *J. Am. Chem. Soc.* **2013**, *135*, 13342; b) Mal, S. S.; Stephens, F. H.; Baker, R. T. *Chem. Commun.* **2011**, *47*, 2922; c) Blaquiere, N.; Diallo-Garcia, S.; Gorelsky, S. I.; Black, D. A.; Fagnou, K. *J. Am. Chem. Soc.* **2008**, *130*, 14034.
- (10) Kim, S. K.; Han, W. S.; Kim, T. J.; Kim, T. Y.; Nam, S. W.; Mitoraj, M.; Piekos, L.; Michalak, A.; Hwang, S. J.; Kang, S. O. *J. Am. Chem. Soc.* **2010**, *132*, 9954.
- (11) Pons, V.; Baker, R. T.; Szymczak, N. K.; Heldebrant, D. J.; Linehan, J. C.; Matus, M. H.; Grant, D. J.; Dixon, D. A. *Chem. Commun.* **2008**, 6597.
- (12) Keaton, R. J.; Blacquiere, J. M.; Baker, R. T. *J. Am. Chem. Soc.* **2007**, *129*, 1844.
- (13) Baker, R. T.; Gordon, J. C.; Hamilton, C. W.; Henson, N. J.; Lin, P. H.; Maguire, S.; Murugesu, M.; Scott, B. L.; Smythe, N. C. *J. Am. Chem. Soc.* **2012**, *134*, 5598.
- (14) Jaska, C. A.; Temple, K.; Lough, A. J.; Manners, I. *J. Am. Chem. Soc.* **2003**, *125*, 9424.
- (15) a) Conley, B. L.; Guess, D.; Williams, T. J. *J. Am. Chem. Soc.* **2011**, *133*, 14212; b) Conley, B. L.; Williams, T. J. *Chem. Commun.* **2010**, *46*, 4815; c) Lu, Z. Y.; Conley, B. L.; Williams, T. J. *Organometallics* **2012**, *31*, 6705.
- (16) Zimmerman, P. M.; Paul, A.; Zhang, Z. Y.; Musgrave, C. B. *Angew. Chem. Int. Ed.* **2009**, *48*, 2201.
- (17) a) Horak, K. T.; Velian, A.; Day, M. W.; Agapie, T. *Chem. Commun.* **2014**, *50*, 4427; b) Lin, S. B.; Herbert, D. E.; Velian, A.; Day, M. W.; Agapie, T. *J. Am. Chem. Soc.* **2013**, *135*, 15830; c) Lin, S. B.; Day, M. W.; Agapie, T. *J. Am. Chem. Soc.* **2011**, *133*, 3828; d) Velian, A.; Lin, S. B.; Miller, A. J. M.; Day, M. W.; Agapie, T. *J. Am. Chem. Soc.* **2010**, *132*, 6296; e) Herbert, D. E.; Lara, N. C.; Agapie, T. *Chem. Eur. J.* **2013**, *19*, 16453.
- (18) King, W. A.; DiBella, S.; Lanza, G.; Khan, K.; Duncalf, D. J.; Cloke, F. G. N.; Fragalà, I. L.; Marks, T. J. *J. Am. Chem. Soc.* **1996**, *118*, 627.
- (19) Green, M. L. H.; Silverthorn, W. *J. Chem. Soc. Dalton Trans.* **1973**, 301.
- (20) a) Crabtree, R. H. *Acc. Chem. Res.* **1990**, *23*, 95; b) Egbert, J. D.; Heinekey, D. M. *Organometallics* **2010**, *29*, 3387; c) Kubas, G. J.; Ryan, R. R.; Unkefer, C. J. *J. Am. Chem. Soc.* **1987**, *109*, 8113; d) Matthews, S. L.; Heinekey, D. M. *J. Am. Chem. Soc.* **2006**, *128*, 2615; e) Matthews, S. L.; Pons, V.; Heinekey, D. M. *J. Am. Chem. Soc.* **2005**, *127*, 850; f) Morris, R. H.; Earl, K. A.; Luck, R. L.; Lazarowich, N. J.; Sella, A. *Inorg. Chem.* **1987**, *26*, 2674; g) Janak, K.



- E.; Shin, J. H.; Parkin, G. J. *Am. Chem. Soc.* **2004**, *126*, 13054; h) Desrosiers, P. J.; Cai, L. H.; Lin, Z. R.; Richards, R.; Halpern, J. J. *Am. Chem. Soc.* **1991**, *113*, 4173.
- (21) Grundemann, S.; Limbach, H. H.; Buntkowsky, G.; Sabo-Etienne, S.; Chaudret, B. *J. Phys. Chem. A* **1999**, *103*, 4752.
- (22) Gelabert, R.; Moreno, M.; Lluch, J. M.; Lledos, A.; Pons, V.; Heinekey, D. M. *J. Am. Chem. Soc.* **2004**, *126*, 8813.
- (23) Widegren, J. A.; Finke, R. G. *J. Mol. Catal. A: Chem.* **2003**, *198*, 317.
- (24) Catalyst reuse experiments demonstrated that precatalyst **5** shows negligible loss of activity over four consecutive dehydrogenation runs (Figure 2.15).
- (25) Shaw, W. J.; Linehan, J. C.; Szymczak, N. K.; Heldebrant, D. J.; Yonker, C.; Camaioni, D. M.; Baker, R. T.; Autrey, T. *Angew. Chem. Int. Ed.* **2008**, *47*, 7493.
- (26) Archer, L. J.; George, T. A. *Inorg. Chem.* **1979**, *18*, 2079.
- (27) Arashiba, K.; Miyake, Y.; Nishibayashi, Y. *Nat. Chem.* **2011**, *3*, 120.
- (28) Kawano, Y.; Uruichi, M.; Shimoi, M.; Taki, S.; Kawaguchi, T.; Kakizawa, T.; Ogino, H. *J. Am. Chem. Soc.* **2009**, *131*, 14946.
- (29) Pidcock, A.; Smith, J. D.; Taylor, B. W. *J. Chem. Soc. A* **1967**, 872.
- (30) a) Abugideiri, F.; Fettingner, J. C.; Pleune, B.; Poli, R.; Bayse, C. A.; Hall, M. B. *Organometallics* **1997**, *16*, 1179; b) Luo, X. L.; Crabtree, R. H. *Inorg. Chem.* **1990**, *29*, 2788.
- (31) Fazen, P. J.; Remsen, E. E.; Beck, J. S.; Carroll, P. J.; McGhie, A. R.; Sneddon, L. G. *Chem. Mater.* **1995**, *7*, 1942.
- (32) Pangborn, A. B.; Giardello, M. A.; Grubbs, R. H.; Rosen, R. K.; Timmers, F. J. *Organometallics* **1996**, *15*, 1518.
- (33) Tate, D. P.; Knipple, W. R.; Augl, J. M. *Inorg. Chem.* **1962**, *1*, 433.
- (34) Wender, I.; Friedel, R. A.; Orchin, M. *J. Am. Chem. Soc.* **1949**, *71*, 1140.
- (35) Fulmer, G. R.; Miller, A. J. M.; Sherden, N. H.; Gottlieb, H. E.; Nudelman, A.; Stoltz, B. M.; Bercaw, J. E.; Goldberg, K. I. *Organometallics* **2010**, *29*, 2176.
- (36) Wang, J. S.; Geanangel, R. A. *Inorg. Chim. Acta* **1988**, *148*, 185.
- (37) Baitalow, F.; Baumann, J.; Wolf, G.; Jaenicke-Rossler, K.; Leitner, G. *Thermochim. Acta* **2002**, *391*, 159.
- (38) a) Diwan, M.; Diakov, V.; Shafirovich, E.; Varma, A. *Int. J. Hydrogen Energ.* **2008**, *33*, 1135; b) Chandra, M.; Xu, Q. *J. Power Sources* **2006**, *156*, 190.
- (39) a) Stephens, F. H.; Baker, R. T.; Matus, M. H.; Grant, D. J.; Dixon, D. A. *Angew. Chem. Int. Ed.* **2007**, *46*, 746; b) Kelly, H. C.; Marriott, V. B. *Inorg. Chem.* **1979**, *18*, 2875; c) Kelly, H. C.; Marchello, F. R.; Giusto, M. B. *Inorg. Chem.* **1964**, *3*, 431.
- (40) APEX2, Version 2 User Manual, M86-E01078, Bruker Analytical X-ray Systems, Madison, WI, June 2006.
- (41) Sheldrick, G.M. "SADABS (version 2008/1): Program for Absorption Correction for Data from Area Detector Frames", University of Göttingen, 2008.
- (42) Sheldrick, G.M. *Acta Cryst.*, **2008**, *A64*, 112.
- (43) Brandenburg, K. (1999). DIAMOND. Crystal Impact GbR, Bonn, Germany.
- (44) Crystallographic data have been deposited at the CCDC, 12 Union Road, Cambridge CB2 1EZ, UK and copies can be obtained on request, free of charge, by quoting the publication citation and the respective deposition numbers.



## CHAPTER 3

### Four-Electron Deoxygenative Reductive Coupling of Carbon Monoxide at a Single Metal Site

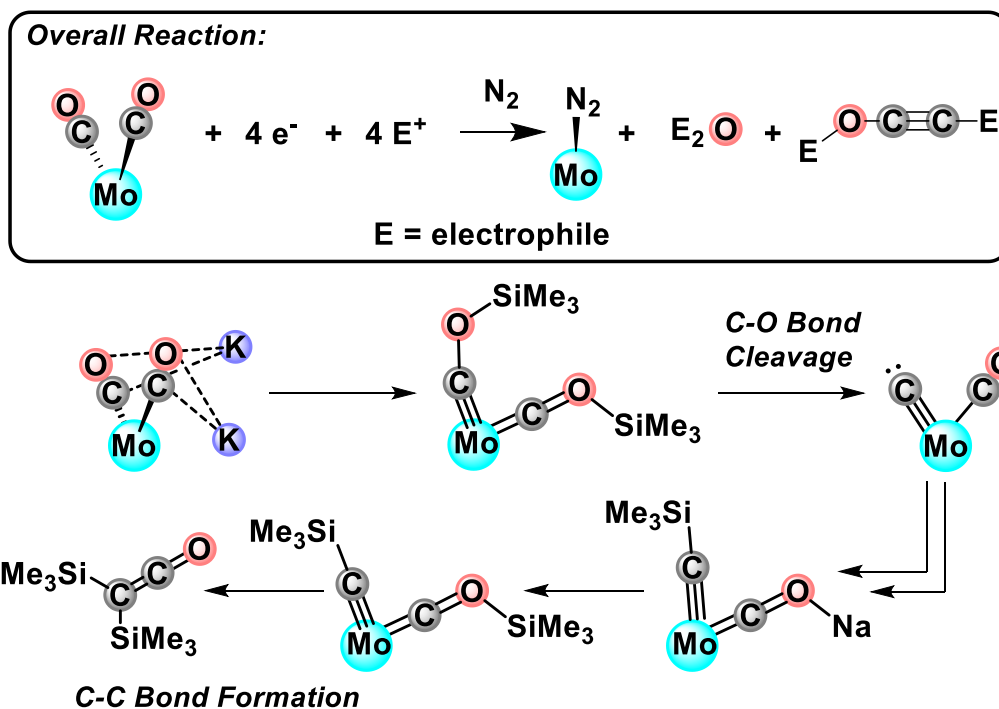
This work was published in part as:

*Nature* **2016**, 529, 72.

&

*J. Am. Chem. Soc.* **2016**, 138, 16466

## ABSTRACT



The conversion of carbon dioxide ( $\text{CO}_2$ ) to synthetic fuels is of significant interest in the context of renewable energy. While homogeneous and heterogeneous catalysts convert  $\text{CO}_2$  to carbon monoxide ( $\text{CO}$ ) and other  $\text{C}_1$  products, deoxygenative coupling of  $\text{CO}$  to value-added  $\text{C}_{\geq 2}$  products is challenging and mechanistically poorly understood. Herein, we describe mechanistic investigations of a previously reported system for the four-electron coupling of  $\text{CO}$ . A molybdenum dicarbonyl moiety has been characterized spanning six formal oxidation states by leveraging the coordinative flexibility and redox noninnocence of a terphenyl diphosphine ligand scaffold. Metal-arene interactions allow the ligand core to act as an electron reservoir, supporting di- and trianionic complexes. Treating these highly reduced compounds with silyl electrophiles ultimately releases a four-electron reduced  $\text{C}_2\text{O}_1$  fragment resulting from  $\text{C}-\text{O}$  bond cleavage and  $\text{C}-\text{C}$  coupling. The formation of a bis(siloxy) complex precedes  $\text{C}-\text{O}$  bond cleavage. At  $-78\text{ }^\circ\text{C}$ , over days,  $\text{C}-\text{C}$  coupling is observed without  $\text{C}-\text{O}$  cleavage. This two-electron reduced  $\text{C}_2\text{O}_2$  coupling product was isolated, and its reactivity is consistent with irreversible formation. However, upon warming to  $0\text{ }^\circ\text{C}$ ,  $\text{C}-\text{O}$  cleavage is observed from

the dicarbyne complex; kinetics and isotopic labeling are most consistent with a mechanism involving siloxide loss as the elementary step. Both independent synthesis and low temperature spectroscopic studies support carbide intermediacy in the CO deoxygenative coupling pathway, the first demonstration of such a functionality in a homogenous CO coupling reaction. The kinetic product of C–O bond scission displays a silylcarbyne coordinated *cis* with respect to the central arene moiety, suggesting that this is the position of the carbide ligand directly following C–O cleavage. The thermodynamic product displays a silylcarbyne *trans* versus the central arene. Reduction of Mo(IV) CO adducts of carbide and silylcarbyne species at -78 °C allowed for the observation of reduced silylcarbyne/CO and mixed silylcarbyne/siloxycarbyne complexes. Upon warming, both of these silylcarbynes undergo C–C bond formation, releasing the organic fragments and demonstrating that the multiple bonded terminal Mo≡C moiety is an intermediate on the path to deoxygenated, C–C coupled products. The electronic structures of Mo carbide and carbyne species were investigated computationally. Overall, the present studies provide detailed insight into the mechanism by which CO is cleaved and coupled at a single metal site.

## GENERAL INTRODUCTION

Utilization of oxygenated  $C_1$  feedstocks for the generation of liquid fuels is of interest in the context of environmental concerns regarding the rise of atmospheric carbon dioxide ( $CO_2$ ) levels and geopolitical constraints on the availability of reduced carbon reserves.<sup>1</sup> Mimicking photosynthetic carbon fixation, electrocatalytic reduction of  $CO_2$  to multicarbon products, using reducing equivalents generated from solar energy, has the potential to convert an inexpensive and abundant precursor into high energy density hydrocarbons.<sup>2</sup> Formation of deoxygenated  $C_{\geq 2}$  products from  $CO_2$  is rare, and occurs via initial conversion to carbon monoxide (CO).<sup>3</sup> While many homo- and heterogeneous catalysts convert  $CO_2$  to CO, the mechanism of which is currently a topic of significant interest,<sup>2,3</sup> examples of deoxygenative coupling of CO to  $C_2$  products are sparse and their mechanism is largely unknown.

The molybdenum and vanadium homologs of nitrogenase are capable of CO catenation to hydrocarbons at ambient temperature and pressure, utilizing ATP hydrolysis, electrons from dithionite, and protons.<sup>4</sup> Ethylene is the major carbon-containing product of these reactions, with trace formation of higher alkanes (up to  $C_4$ ). Though the mechanism of CO coupling in nitrogenases has been studied both experimentally<sup>5</sup> and *in silico*,<sup>6</sup> insight remains limited, and just recently has binding of CO to the molybdenum congener been characterized structurally.<sup>7</sup>

Electrocatalytic reduction of CO to  $C_{\geq 2}$  species has been developed, but is restricted to Cu catalysts.<sup>8</sup> In this case, monodeoxygenation is primarily observed; methanol formation accounts for the majority of the converted CO. Industrially, Fisher-Tropsch chemistry uses  $H_2$  as the source of electrons and protons to catalyze CO coupling at high temperatures and pressures on a variety of metal surfaces.<sup>9</sup> Detection of surface-bound species in these heterogeneous systems is challenging, but both electrocatalytic and Fischer-Tropsch coupling chemistries are proposed to occur via adsorbed  $C_1$  intermediates.<sup>3,8-9</sup>

Molecular systems have been studied extensively for mechanistic insight into the elementary steps of CO coupling chemistry. For decades, the alkali metal mediated reduction of CO to dianionic salts—croconate, rhodizonate,<sup>10</sup> and ethynediolate<sup>11</sup>—has been known, but relatively

few transition metal complexes mediate direct CO reductive coupling. Early investigations of the reduction of chromium hexacarbonyl to the pentacarbonyl dianion proceeded without the liberation of gas; the CO is instead coupled to give disodium ethynediolate.<sup>12</sup> Though it is uncertain if this process is indeed metal-mediated,<sup>13</sup> bound acetylenediolate fragments have been invoked as intermediates in the multi-electron reduction of several homoleptic metal carbonyls.<sup>13-14</sup>

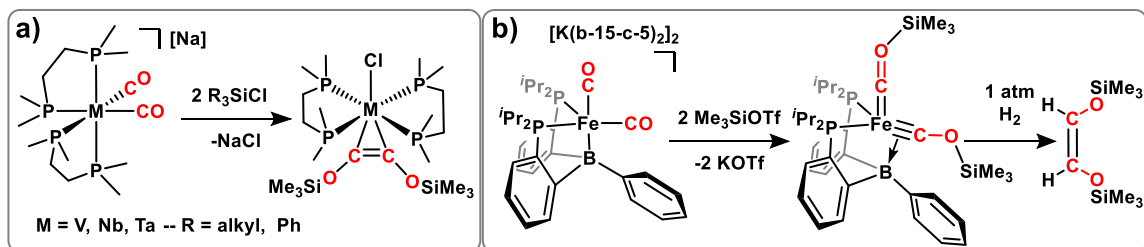
The reaction of electrophiles with reduced metal carbonyl complexes has proven an apt strategy for enacting C–C coupling. Bimolecular catenation of four CO molecules results when  $\text{Na}_2\text{Fe}(\text{CO})_4$  is treated with  $\text{Me}_3\text{SiBr}$ , providing a tetrakis(trimethylsiloxy)-metallacyclopentane moiety supported by two Fe centers.<sup>15</sup> The addition of silyl chlorides to monoanionic dicarbonyl complexes of group 5 metals results in the formation of bound bis(siloxy)acetylene units (Chart 3.1., a).<sup>16</sup> Importantly, the *cis*-bis(siloxy)ethylene can be liberated with addition of an overpressure of hydrogen gas (100 psi) or hydrogenation catalysts.<sup>16b,16d</sup> More recently, the proposed precursor to C–C coupling in these systems, a silylated dicarbyne complex,<sup>16e</sup> has been synthesized and structurally characterized on a bis(phosphino)borane supported iron center (Chart 3.1., b).<sup>17</sup> This dicarbyne releases the four-electron reduced, C–C coupled olefinic fragment rapidly, under mild conditions (1 atm  $\text{H}_2$ ).

Iron and rhodium complexes are known to enact CO catenation without the addition of electrophiles or strong reductants. Under an atmosphere of CO, a high-spin Fe trispyrrolide anion undergoes concomitant oxidative fragmentation of the ligand and coupling of two CO molecules to an oxalyl-pyrrole motif.<sup>18</sup> Porphyrin supported Rh complexes couple bound CO through a 17-electron metalloorganic radical to a related diketone product, the bridging 1,2-ethanedionyl linkage.<sup>19</sup> In this system, the bent CO ligand, with significant radical character on C, facilitates one-electron reactivity at the carbonyl carbon.<sup>20</sup>

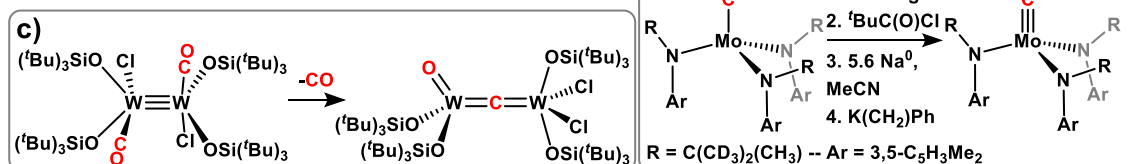
Under reducing conditions, oxophilic metal centers have been shown to reduce, couple, and

Chart 3.1. Select examples reporting reductive CO functionalization.<sup>‡</sup>

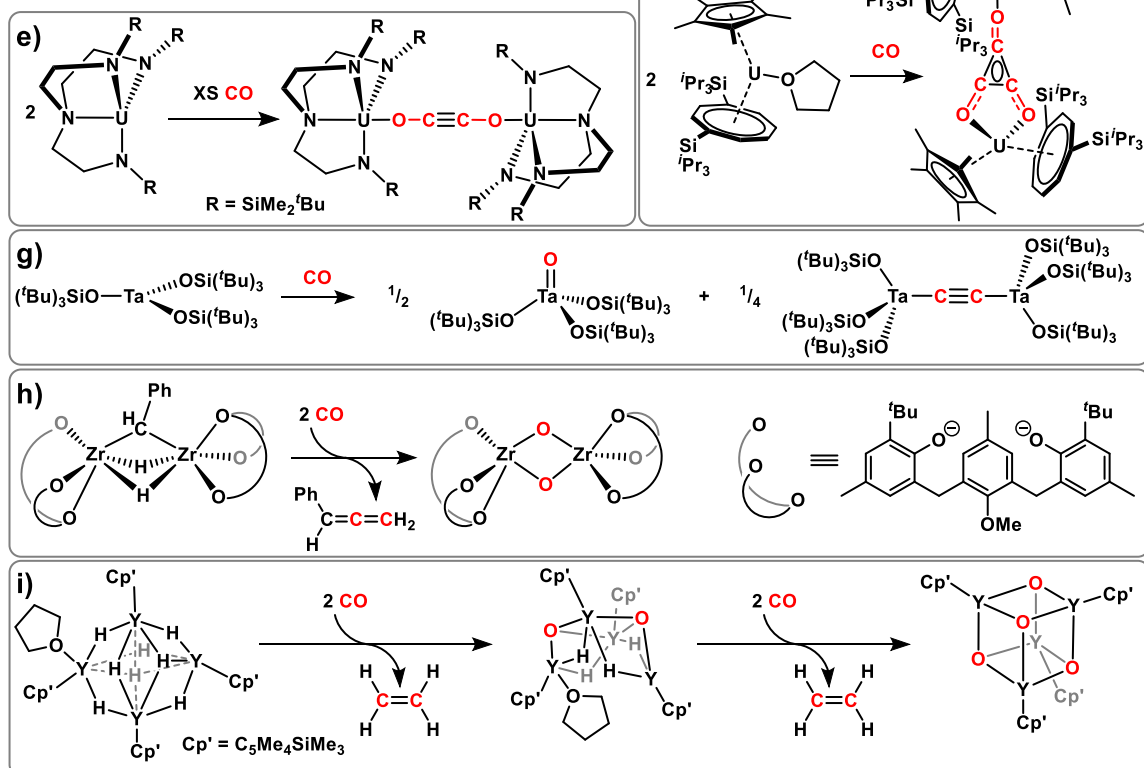
## 1) CO Coupling Without Deoxygenation



## 2) CO Deoxygenation Without Coupling



## 3) CO Coupling Driven by Strong M-O Bond Formation



<sup>‡</sup>Different strategies have been employed to reduce CO with transition and rare earth metals, ranging from electrophilic functionalization (**a**<sup>16b</sup>, **b**<sup>17</sup>, and **d**<sup>21</sup>) to leveraging formation of strong M–O bonds (**c**<sup>22</sup>, **e**<sup>23</sup>, **f**<sup>24</sup>, **g**<sup>25</sup>, **h**<sup>26</sup>, and **i**<sup>27</sup>). Reductive catenation of CO to hydrocarbons can be envisioned to proceed through elementary steps established by these systems, namely: *i*) C–O bond cleavage (**c**, **d**, **h**, and **i**), *ii*) C–C bond formation (**a**, **b**, **e**, **f**, **g**, **h**, and **i**), and *iii*) Organic product release (**b**, **e**, **h**, and **i**).



deoxygenate CO, driven by the strength of the metal-O interaction. Zirconocene dicarbonyl complexes react with dihydrogen to form a methoxide hydride adduct.<sup>28</sup> Subsequent protonolysis with HCl results in stoichiometric methanol formation. Three-coordinate Ta complexes, bearing bulky silox ligands, cleave CO to generate a monomeric Ta(V) oxo and an acetylide bridged dimer, in a two to one stoichiometry, both completely cleaving the C–O bond of CO and demonstrating C–C coupling (Chart 3.1., g).<sup>25,29</sup> A related complex, bearing a W≡W bond, utilizes the electrons in the M–M bond and the stability of the W oxo to cleave CO to a bridging carbide (Chart 3.1., c).<sup>22</sup>

Highly-reducing low-valent lanthanide complexes perform the reductive homologation of CO, with the resulting organic oxygenates stabilized by Ln–O bonds.<sup>30</sup> U(III) complexes provide electrons for the reductive oligomerization of CO to the delatate and squarate dianions (Chart 3.1., f).<sup>24,31</sup> In the presence of CO and H<sub>2</sub>, these complexes generate a methoxide ligand that can be liberated upon treatment with Me<sub>3</sub>SiOTf (OTf = trifluoromethanesulfonate).<sup>32</sup> Under a limiting stoichiometry of CO, in the absence of hydrogen, an yne diolate complex is formed, bridging two U centers.<sup>31b</sup> A related U(III) system forms this bridging dihydroxyacetylene and further demonstrates release of the free organic upon treatment with silyl iodides, facilitating a synthetic cycle for the formation of C<sub>2</sub>O<sub>2</sub> building blocks from CO (Chart 3.1., e).<sup>23</sup>

Insertion of CO into early transition metal hydride bonds is a complementary reduction strategy, forming both C–H bonds and stable M–O interactions.<sup>28b</sup> CO addition to a solution of a binuclear Ta hydride complex affords a bridging formyl motif that undergoes C–O bond cleavage when treated with phosphine.<sup>33</sup> A ditantalum hydride anion mediates the head-to-head catenation of six CO molecules, providing a [C<sub>6</sub>O<sub>6</sub>]<sup>8-</sup> unit supported by four Ta centers.<sup>34</sup> Dizirconium hydrides bearing similar aryloxy ligands facilitate a synthetic cycle for the formation of a phenylallene fragment in which two of the carbon atoms are derived from CO (Chart 3.1., h).<sup>35</sup> This remarkable system accomplishes C–O bond cleavage, C–C bond formation, and allene release between two metal centers. Hydride reduction of CO ligands to

bridging acetylenes<sup>36</sup> and ethylene<sup>27</sup> (Chart 3.1., i) is likewise known for multinuclear clusters.

Carbonyl insertion is not unique to early transition metal hydrides. CpMoMe(CO)<sub>3</sub> reacts with an external source of hydride to initially form an anionic formyl complex that rearranges to the hydrido acyl species.<sup>37</sup> Addition of benzyl bromide liberates acetaldehyde. Sequential Lewis acid-assisted metal-formyl generation, activation, and alkyl insertion have been demonstrated on rhenium,<sup>38</sup> achieving a complex C–C bond forming reaction in a single step. However, this transformation does not induce deoxygenation of the CO moieties, and the resulting Lewis-acid-oxygen interaction proves too stable, prohibiting further reactivity.

Many mechanistic proposals for the Fischer-Tropsch process invoke C–O bond cleavage prior to C–C coupling.<sup>9</sup> Complete bond breaking transformations of diatomic small molecule substrates at a single metal center present a significant challenge in homogeneous model chemistry, as four or more electrons are often required (*e.g.* dinitrogen (N<sub>2</sub>), six electrons; dioxygen, four electrons; CO, six electrons). A handful of molecular complexes bearing bridging<sup>22,39</sup> and terminal carbides<sup>21,40</sup> have been synthesized from CO (Chart 3.1., d), overcoming the strong C≡O triple bond (257 kcal/mol).<sup>41</sup> Elaboration of these carbides with electrophiles provides alkylidynes,<sup>21,40a</sup> motifs that have been shown to undergo C–C bond formation with CO ligands.<sup>42</sup>

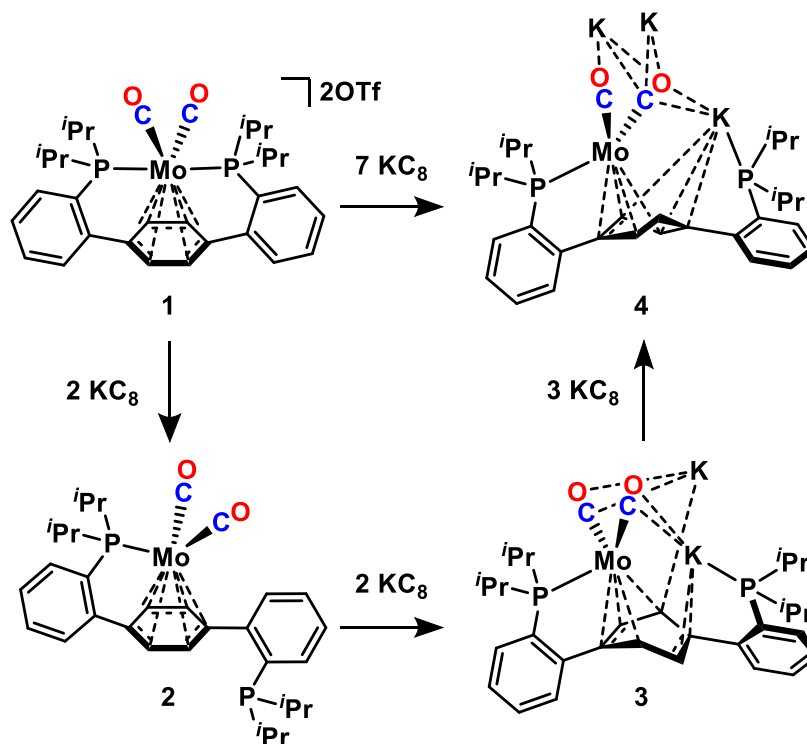
Although several modes of activation, cleavage, and coupling of CO have been demonstrated (Chart 3.1.), never before have these steps, C–O scission, C–C coupling, and product release, been concatenated to generate free C<sub>2</sub>O<sub>1</sub> fragments. Taking this into consideration, the nature of the envisioned intermediates in deoxygenative CO coupling scheme varies significantly. Prior to C–O cleavage, reduced, electron rich metal centers prone to activate CO are necessary. Following cleavage, the products and logical coupling precursors are more oxidized complexes bearing metal-ligand multiple bonds. To facilitate access to this broad range of potential intermediates, a labile ligand set with the propensity for diverse binding modes was employed. The terphenyl-diphosphine ligand architecture has been demonstrated to undergo changes in central arene coordination mode as a function of the

oxidation state and primary coordination sphere of the metal<sup>23-25</sup>. Furthermore, the requirement for numerous reducing equivalents can be satisfied by storage in the arene<sup>27</sup> in concert with oxidation state changes at the metal. Herein, we describe the four-electron deoxygenative coupling of two CO ligands to a C<sub>2</sub>O<sub>1</sub> product. Additionally, detailed mechanistic insight into the C–O bond cleavage and C–C bond formation steps is provided, interrogating the elementary steps of this complex multi-electron reaction sequence. Additionally, structural, computational, and reactivity studies are used to evaluate the advantageous design elements of the supporting ligand for the observed chemistry, as well as its limitations.

## RESULTS AND DISCUSSION

### *Mo Dicarbonyl Complexes Spanning Six Formal Oxidation States*

The Mo<sup>II</sup>-dicarbonyl complex, **1**,<sup>23</sup> discussed in chapter 2 of this dissertation, can be reduced in a stepwise fashion with KC<sub>8</sub>, K<sup>0</sup>, or K[C<sub>10</sub>H<sub>8</sub>] to generate formal Mo<sup>0</sup> (**2**), Mo<sup>-II</sup> (**3**), and Mo<sup>-III</sup> (**4**) species (Scheme 3.1). The change in ligand binding mode in the solid state upon electron loading is notable (Figure 3.1.). Compound **1** displays coordination of both phosphine arms and an η<sup>6</sup>-arene interaction corresponding to a formal 18 e<sup>-</sup> count.<sup>43</sup> Upon two-electron reduction, one phosphine arm dissociates, maintaining the δ-acidic η<sup>6</sup> metal arene interaction and the 18 e<sup>-</sup> count.<sup>44</sup> The M–C and C–O bond distances for these complexes, at 2.004(1) and 1.140(2) for **1** and 1.969(1) and 1.164(1) for **2**, respectively, show a slight increase in Mo to CO backbonding upon reduction. The Mo-arene interaction strengthens, as manifested by both slightly shorter Mo–C<sub>arene</sub> bonds and elongated C–C contacts around the ring.



**Scheme 3.1.** Stepwise reduction of *para*-terphenyl diphosphine supported Mo dicarbonyl complexes.

Further reduction to **3** leads to the formation of a potassium bridged dinuclear cluster—

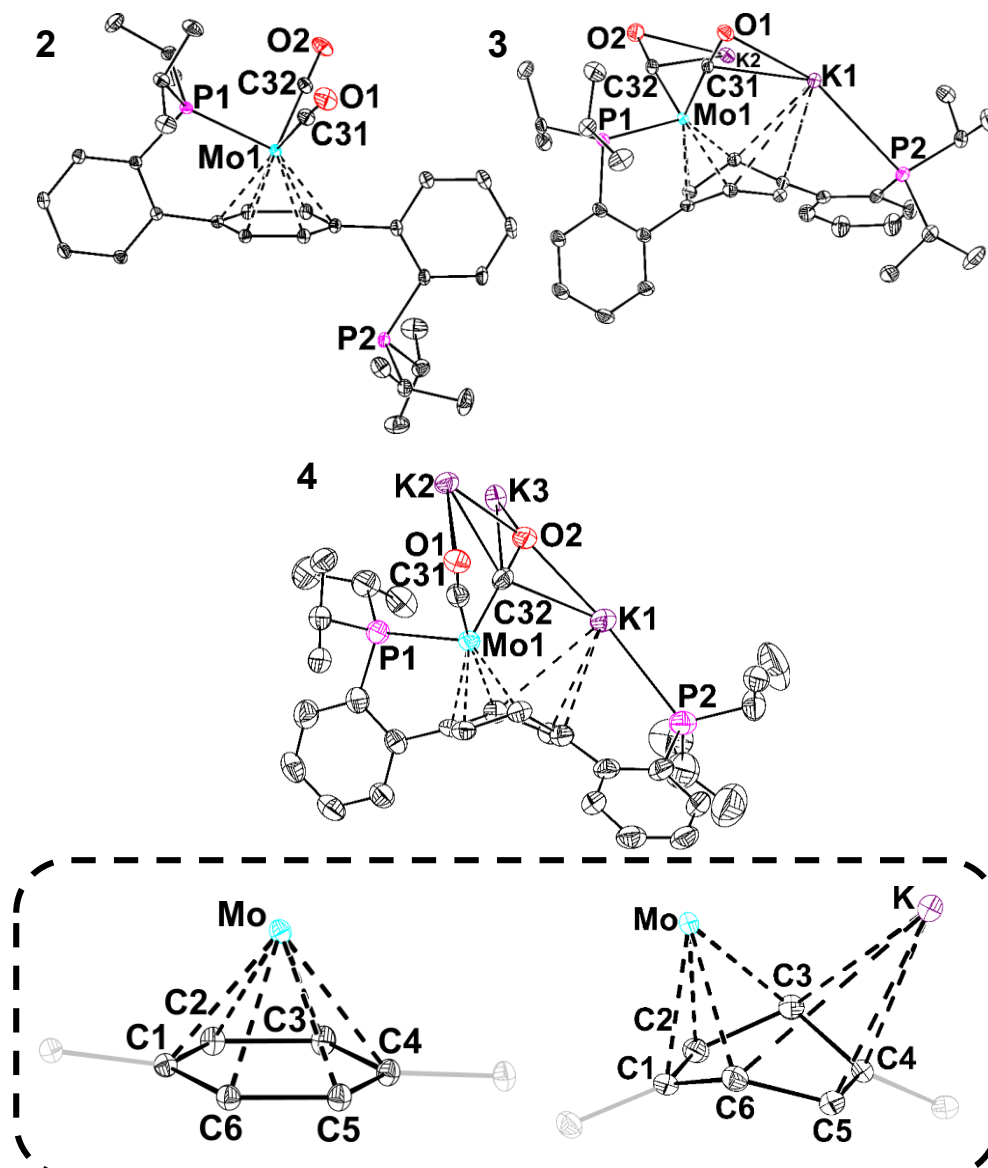


**Figure 3.1.** X-ray crystal structures of **2**, **3**, and **4**. Anisotropic displacement ellipsoids are represented at the 50% probability level. Co-crystallized solvent molecules, K-bound THF molecules, and hydrogen atoms are omitted for clarity.

two Mo(CO)<sub>2</sub> units are bridged by four potassium ions. The potassium cations display interactions with the carbonyl ligands, the dangling phosphine arm, the central arenes of the terphenyl backbone, and solvating THF molecules. Significant distortion of the central arene from planarity is observed, with an angle of 46.2° between the C<sub>1</sub>–C<sub>2</sub>–C<sub>5</sub>–C<sub>6</sub> and C<sub>2</sub>–C<sub>3</sub>–C<sub>4</sub>–C<sub>5</sub> planes. This deplanarization, as well as localization of short C–C contacts between C<sub>1</sub> and C<sub>2</sub> (1.395(3) Å) and C<sub>4</sub> and C<sub>5</sub> (1.365(3) Å), is consistent with partial cyclohexadienyldianionic character.<sup>45</sup> Notably, the dianion shows Mo–CO (1.915(2) Å) and C–O (1.210(3) Å) bond

metrics that are significantly contracted and elongated, respectively, from the neutral species. These structural parameters indicate further activation of the CO ligands by  $\pi$ -backbonding.

Trianion **4** likewise adopts a polynuclear structure—a  $\text{Mo}_4\text{K}_{12}$  tetramer—in the solid state. Two disparate  $\text{K}_3\text{Mo}(\text{CO})_2$  subunits are observed. One is quite similar in structure to dianion **3**, with an  $\eta^4$  metal-arene interaction, a deplanarization of the central arene ring of  $43.7^\circ$ , and short Mo–C (1.903(6) Å) and long C–O (1.226(7) Å) contacts. The second subunit has antifaceal phosphines, one coordinating Mo and the other K, on opposite faces of the central ring (Figure 3.42.). This arene ring, which interacts with Mo in an  $\eta^3$  fashion and displays two cation- $\pi$  interactions with the K counter ions,<sup>46</sup> is more planar ( $\angle(\text{C}_1\text{--}\text{C}_2\text{--}\text{C}_3)(\text{C}_1\text{--}\text{C}_3\text{--}\text{C}_4\text{--}\text{C}_6) = 34.8^\circ$ ). Contrasting the metal-arene interactions in **3** and **4- $\eta^4$** , the  $\eta^3$ -bound subunit of **4** displays single long (C<sub>3</sub>–C<sub>4</sub>) and short (C<sub>5</sub>–C<sub>6</sub>) contacts. The Mo center is poised closer to the ring carbons which have metrics most consistent with delocalized M-allyl character.<sup>47</sup> The Mo–C and C–O distances are comparable in both the  $\eta^3$  and  $\eta^4$ -bound components.

The increased C–O bond activation observed in the solid state is also borne out in solution.  $^{13}\text{C}$ O enriched isotopologs were prepared and showed a significant downfield shift of the labeled resonances in the  $^{13}\text{C}\{^1\text{H}\}$  nuclear magnetic resonance (NMR) spectra upon reduction—219.0, 228.5, and 263.8/245.7 ppm for **1- $^{13}\text{C}$** , **2- $^{13}\text{C}$** , and **3- $^{13}\text{C}$** , respectively.<sup>48</sup> The  $^{31}\text{P}$  NMR resonance corresponding to the Mo-bound phosphine arm(s) similarly moves downfield upon reduction, 75.1 to 92.3 to 104.6 ppm.

Infrared (IR) spectroscopy corroborated increased activation of the CO ligands in the more reduced complexes (Figure 3.2.). The IR spectrum of dication **1** showed two stretches at 2044 and 1989  $\text{cm}^{-1}$ . Reduction to **2** attenuated the CO stretching frequencies to 1887 and 1832  $\text{cm}^{-1}$ . Further reduction redshifts the frequencies by over 200  $\text{cm}^{-1}$ —to 1657 and 1570  $\text{cm}^{-1}$ —stretches that now resemble those of C–O double bonds. Even at these low frequencies, these resonances can be unequivocally assigned to the carbonyl ligands; the signals for **3- $^{13}\text{C}$**  at 1621 and 1534  $\text{cm}^{-1}$  differ from those of **3** by the values calculated applying a simple reduced mass oscillator model. This is likewise the case for the **1/1- $^{13}\text{C}$**  and **2/2- $^{13}\text{C}$**  isotopolog pairs. The IR

stretches for **4** could not be confidently assigned, even with isotopic labeling; the features in the IR spectrum were below  $1550\text{ cm}^{-1}$  and were undiscernible from supporting phosphine ligand stretches near  $1450\text{ cm}^{-1}$ .

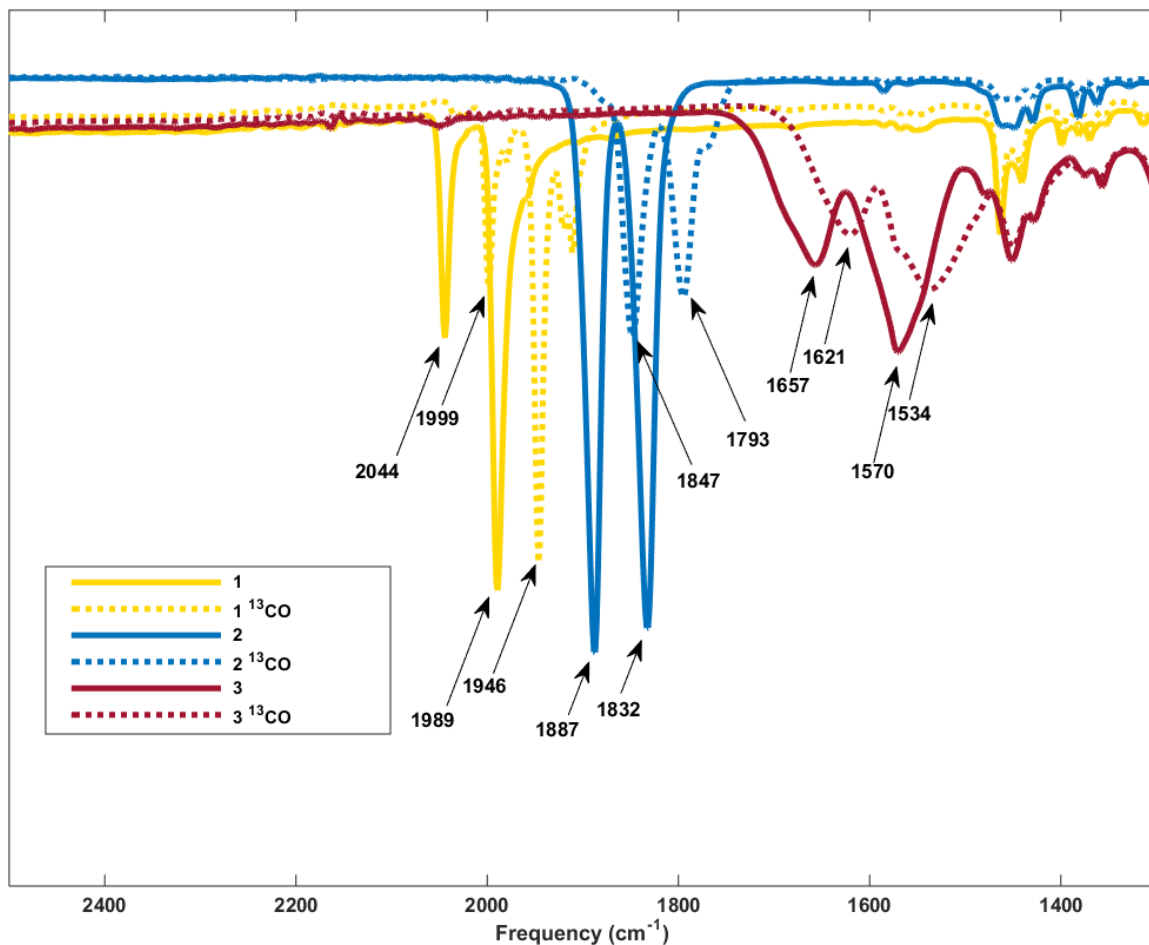
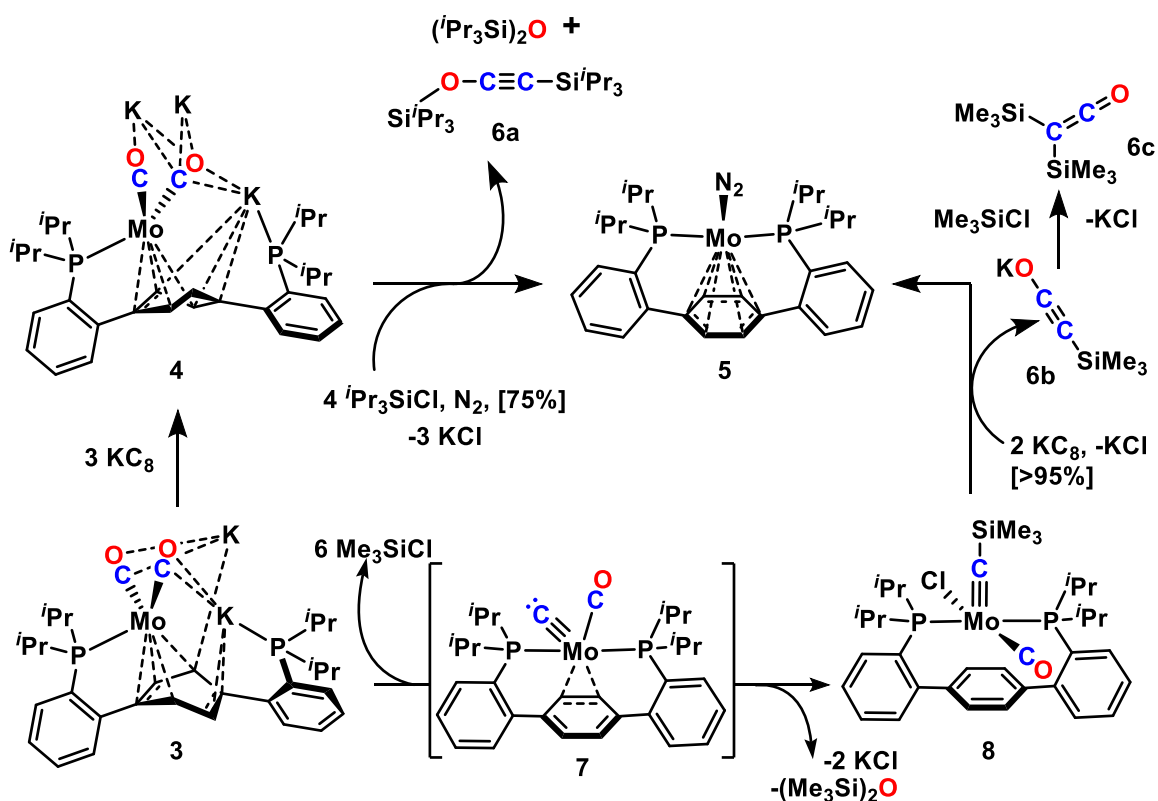


**Figure 3.2.** ATR IR Spectra of **1**,  $1\text{-}^{13}\text{CO}$ , **2**,  $2\text{-}^{13}\text{CO}$ , **3**, and  $3\text{-}^{13}\text{CO}$ , showing increased Mo–CO backbonding upon sequential reduction. The difference in the stretching frequency of the  $^{12}\text{C}$  and  $^{13}\text{C}$  isotopologs matches well with values calculated using the respective reduced masses. The CO stretches for **4** and  $4\text{-}^{13}\text{CO}$  were intractable, overlapping with ligand stretches near  $1450\text{ cm}^{-1}$ .

#### *Reactions of Polyanionic Mo Carbonyl Complexes with Silyl Electrophiles*

Given the strong CO activation, electrophilic functionalization was explored. Under an  $\text{N}_2$  atmosphere, treatment of **4** with excess  ${}^t\text{Pr}_3\text{SiCl}$  leads to the formation of the reported  $\text{N}_2$  complex **5**<sup>23</sup> as the major metal containing product (75% by  ${}^{31}\text{P}\{^1\text{H}\}$  NMR spectroscopy), in addition to partial oxidation to **2** (Scheme 3.1.). Comparison to

authentic samples confirmed  $(i\text{Pr}_3\text{Si})_2\text{O}$  (GC/MS) and the  $\text{C}_2\text{O}_1$  fragment **6a** ( $^{13}\text{C}\{^1\text{H}\}$  NMR spectroscopy) as the organic byproducts in the transformation of **4** to **5** (Figure 3.10). This remarkable reaction encompasses a trianionic metal complex demonstrating a high degree of CO activation, cleavage of the strong C–O bond, formation of a C≡C bond, and spontaneous release of the coupling product from the metal center. These features distinguish the present system from reported examples of transition metal mediated CO coupling which lead to two electron reduced products or prove resilient to dissociation of the formed organic fragment from the metal center.



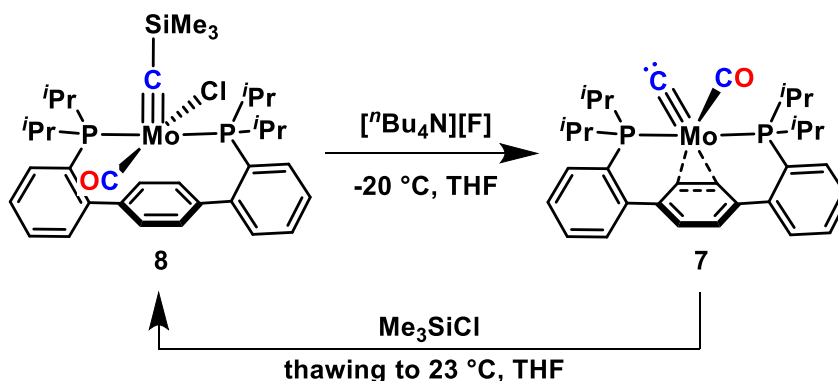
**Scheme 3.2.** Deoxygenative coupling of CO to a  $\text{C}_2\text{O}_1$  fragment.

Balancing this reaction, however, reveals that an additional reducing equivalent is required beyond the three stored in complex **4**. The generation of **2** suggests that **4** may be acting as a sacrificial reductant. Addition of  $i\text{Pr}_3\text{SiCl}$  to the less reduced compound **3**



lowers the yield of coupling products (50% by  $^{31}\text{P}\{^1\text{H}\}$  NMR spectroscopy) and increases observed oxidation to **2**, consistent with this hypothesis. Performing the reaction in the presence of an additional electron in the form of  $\text{K}[\text{C}_{10}\text{H}_8]$  leads to >90% conversion of **4** to **5** as measured by NMR spectroscopy, with no oxidation to **2** and instead minor decomposition to free phosphine accounting for the remaining material.

Anticipating that a smaller silyl electrophile may allow for the observation of reaction intermediates, a thawing tetrahydrofuran solution of dianion **3** was treated with excess  $\text{Me}_3\text{SiCl}$ . The silylcarbyne complex **8** was formed cleanly (Scheme 3.2.), suggested by an alkylidyne resonance at 355.9 ppm in the  $^{13}\text{C}\{^1\text{H}\}$  NMR spectrum and confirmed by single crystal XRD (Figure 3.6., left). To support the higher oxidation state Mo center in **8**, the ligand adapts a *pseudo*-square pyramidal coordination environment with no metal-arene interaction.  $(\text{Me}_3\text{Si})_2\text{O}$  was observed in the reaction mixture by  $^{13}\text{C}\{^1\text{H}\}$  NMR spectroscopy, accounting for the cleaved O atom. The formation of **8** from **3** represents a complete scission of the  $\text{C}\equiv\text{O}$  bond, a six-electron transformation. This conversion is accomplished in high yield, without additional reducing equivalents, due to the ability of the supporting ligand to facilitate the storage of multiple electrons.



**Scheme 3.3.** Trimethylsilyl alkylidyne desilylation to terminal carbide **7** and subsequent resilylation to carbyne **8**.

Formation of deoxygenated **7** suggests an intermediate terminal Mo carbide complex, **8**, generated after loss of silyl ether. To probe the viability of this proposal, **8** was targeted by independent synthesis (Scheme 3.3.). Low temperature (-20 °C) desilylation of **7** with  ${}^n\text{Bu}_4\text{NF}$  results in clean conversion to a new complex with a peak in the  ${}^{13}\text{C}\{^1\text{H}\}$  NMR spectrum at 546.2 ppm (Figure 3.3.). This chemical shift is diagnostic for terminal carbide species<sup>20,28</sup> and indicates that such moiety is accessible in the present system, even though examples of neutral metal carbides are exceedingly rare<sup>29,30</sup> and unprecedented for Mo. Treatment of **8** with  $\text{Me}_3\text{SiCl}$  leads to the formation of **7** upon warming, demonstrating the feasibility of the carbide as an intermediate in the mechanism of the formation of **7** from **3** (Scheme 3.3.).

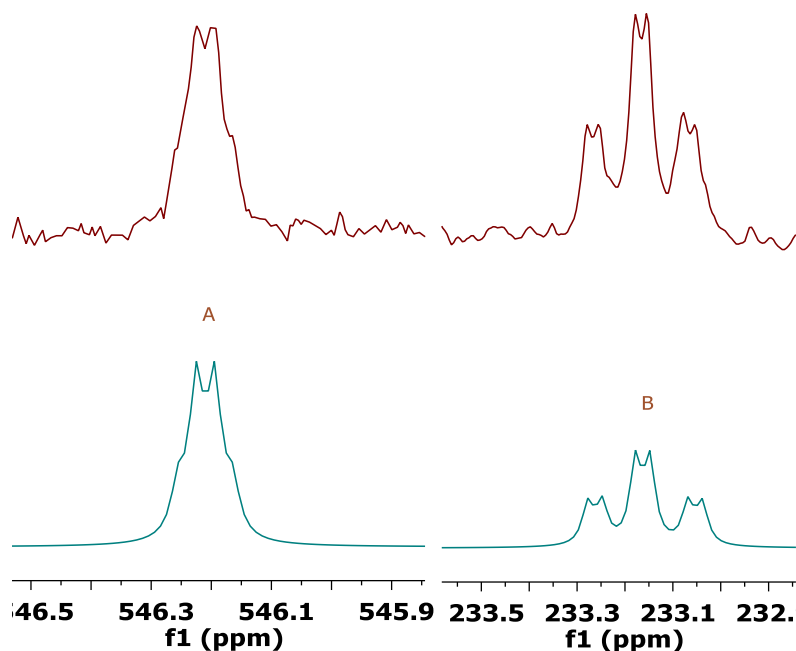


**Figure 3.3.** NMR spectroscopic data for terminal carbide complex **7**. (Top) A highly downfield shifted resonance in the  ${}^{13}\text{C}\{^1\text{H}\}$  NMR spectrum (100 MHz, 25 °C,  $\text{THF-}d_8$ ) of **8** indicated a terminal carbide moiety. (Bottom) Spectral simulation agrees with the resolved  ${}^2J_{CC}$  and  ${}^2J_{PC}$  coupling observed experimentally.

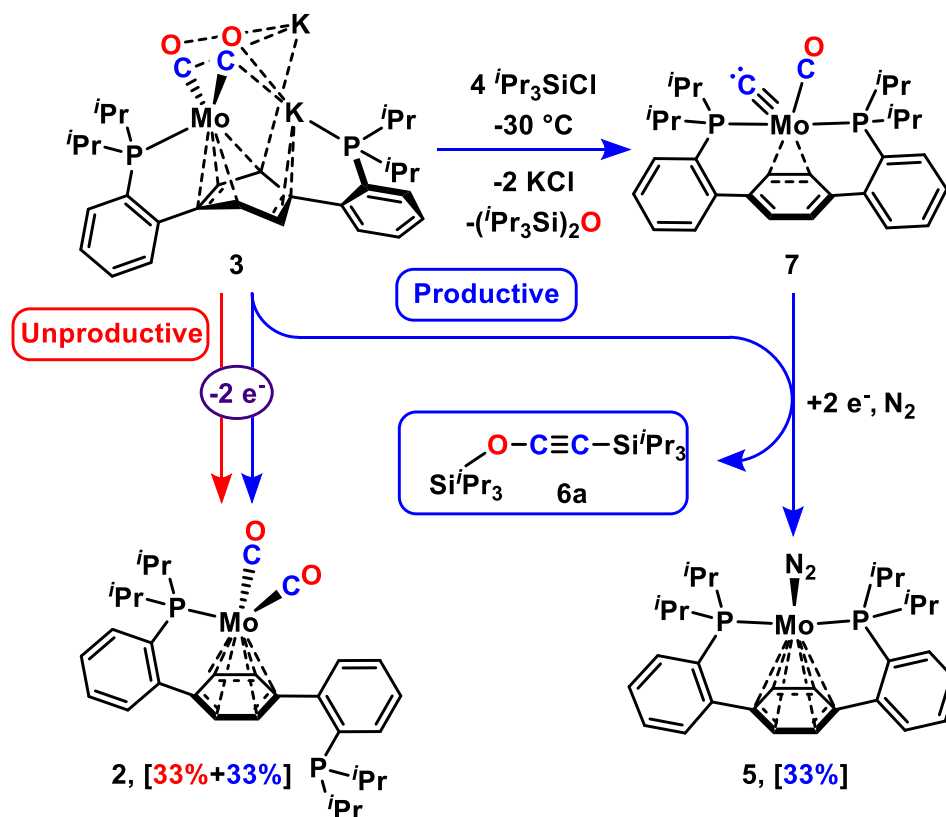
Recognizing that silylcarbyne **8** incorporates both C–Si and C–O linkages, we looked to explore C–C bond formation from this species. Treatment with two equivalents of Na[C<sub>10</sub>H<sub>8</sub>] in the presence of N<sub>2</sub> leads to quantitative formation of **5** and an unbound C<sub>2</sub>O<sub>1</sub> fragment (**6b**, Scheme 3.2.). Subsequent addition of Me<sub>3</sub>SiCl provides bis(trimethylsilyl)ketene **6c**. This sequence demonstrates the ability of **7** to undergo reductive C–C coupling followed by dissociation of the partially deoxygenated C<sub>2</sub> unit from Mo when provided with extra electrons. An additional reducing equivalent is pre-loaded in the system when starting from the trianion **4**, resulting directly in coupling chemistry.

#### *Variable Temperature NMR Studies of Electrophilic Quenching*

With a feasible reaction pathway pieced together (Scheme 3.2.), additional mechanistic information was sought via VT NMR spectroscopic studies. Reactions of dianion **3** with both small and large silyl electrophiles were monitored at low temperature in an attempt to spectroscopically characterize reaction intermediates. A solution of <sup>13</sup>CO enriched dianion **3** (**3-<sup>13</sup>C**) was treated with four equiv. of <sup>31</sup>P<sub>3</sub>SiCl at -78 °C (Scheme 3.4.). No reaction was observed at this temperature by <sup>31</sup>P{<sup>1</sup>H} or <sup>13</sup>C{<sup>1</sup>H} NMR spectroscopy. Warming the sample to -30 °C resulted in the appearance of carbide **7-<sup>13</sup>C**, as a minor species, as indicated by the characteristic low-field carbidic resonance at 547.2 ppm in the <sup>13</sup>C{<sup>1</sup>H} NMR spectrum (Figure 3.12.). Concomitant formation of oxyacetylene **6a**, dinitrogen adduct **5**, and dicarbonyl **2-<sup>13</sup>C** were observed by coupling doublets at 108.3 and 25.2 ppm (<sup>1</sup>J(C,C) = 167.7 Hz) in the <sup>13</sup>C{<sup>1</sup>H} NMR spectrum, a <sup>31</sup>P{<sup>1</sup>H} resonance at 76.4 ppm, and by <sup>13</sup>C{<sup>1</sup>H} (229.9 ppm, d, <sup>2</sup>J(P,C) = 11.1 Hz) and <sup>31</sup>P{<sup>1</sup>H} (95.9 ppm, t, <sup>2</sup>J(P,C) = 11.2 Hz) NMR spectroscopy, respectively. Further warming of the solution resulted in complete conversion to the Mo(0)-N<sub>2</sub> complex **5**, oxidized dicarbonyl **2-<sup>13</sup>C**—in a *ca.* 1:2 ratio (by <sup>31</sup>P{<sup>1</sup>H} NMR)—and the C<sub>2</sub>O<sub>1</sub> organic fragment, **6a**.

These data support the intermediacy of carbide **7** in the reaction sequence. No other intermediates were detected.

The observed reactivity is consistent with multiple reaction pathways from dianion **3**-<sup>13</sup>C (Scheme 3.4). Productive CO reduction chemistry involves carbonyl silylation and C–O bond cleavage, providing carbide **7**-<sup>13</sup>C and (<sup>i</sup>Pr<sub>3</sub>Si)<sub>2</sub>O. The intermediate Mo(IV) complex **7**-<sup>13</sup>C is

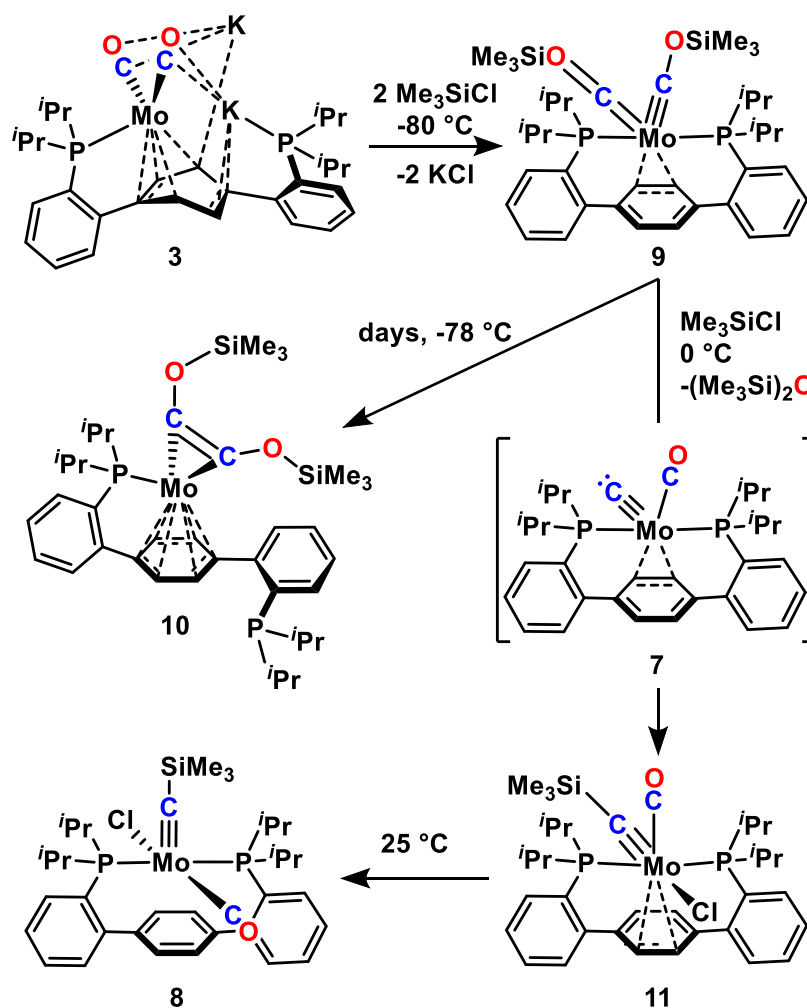


**Scheme 3.4.** <sup>i</sup>Pr<sub>3</sub>SiCl addition to dianion **3**. Product distribution, as determined by <sup>31</sup>P{<sup>1</sup>H} NMR spectroscopy, is shown in brackets.

envisioned to react with an equimolar amount of **3**-<sup>13</sup>C, which serves as a sacrificial two-electron reductant. This two-electron oxidation of **3**-<sup>13</sup>C leads to Mo(0) dicarbonyl complex **2**-<sup>13</sup>C. Reduction of **7**-<sup>13</sup>C by two electrons coupled with silylation forms the C<sub>2</sub>O<sub>1</sub> species, **6a**-<sup>13</sup>C, and Mo(0)-N<sub>2</sub> complex **5**. The four electrons required for the conversion of two molecules of CO to **6a**-<sup>13</sup>C are provided by two equivalents of dianion **3**-<sup>13</sup>C, forming equimolar amounts of the Mo(0) complexes **5** and **2**-<sup>13</sup>C (depicted in blue in Scheme 3.4).

The product ratio of **2** and **5** suggests additional unproductive redox chemistry from

dianion  $3\text{-}^{13}\text{C}$ , likely involving reduction of electrophile (depicted in red in Scheme 3.4.). Though the same products are observed when either dianion  $3\text{-}^{13}\text{C}$  or trianion  $4\text{-}^{13}\text{C}$  is treated with  ${}^i\text{Pr}_3\text{SiCl}$  at low temperature, the latter reacts quantitatively (in reducing equivalents) toward CO deoxygenative coupling chemistry to form the desired products **5** and **6a** (75% conversion, by  ${}^{31}\text{P}\{^1\text{H}\}$  NMR).<sup>40b</sup> The quantitative reactivity of trianion  $4\text{-}^{13}\text{C}$  suggests that fully pre-loading the complex with electrons promotes C–O reduction chemistry and disfavors unproductive outer-sphere redox, an important feature for designing highly selective systems.



**Scheme 3.5.**  $\text{Me}_3\text{SiCl}$  addition to dianion **3**.

The addition of the smaller silyl electrophile,  $\text{Me}_3\text{SiCl}$ , to dianion  $3\text{-}^{13}\text{C}$  was likewise

investigated via low temperature NMR spectroscopy. Thawing a frozen THF solution of **3-<sup>13</sup>C** and Me<sub>3</sub>SiCl to -80 °C resulted in the observation of a triplet at 63.8 ppm (<sup>2</sup>J(C,P) = 17.32 Hz) in the <sup>31</sup>P{<sup>1</sup>H} NMR spectrum, consistent with a Mo diphosphine complex with the two phosphine arms related by symmetry, indicating that the free phosphine arm in **3-<sup>13</sup>C** rebinds the Mo center following silyl chloride addition. Two broad resonances, 285.8 and 275.8 ppm, were present in the <sup>13</sup>C{<sup>1</sup>H} NMR spectrum (Figure 3.4.). These downfield shifted signals are similar to reported siloxycarbyne complexes,<sup>17,49</sup> suggesting formation of dicarbyne **9-<sup>13</sup>C** (Scheme 3.5.).<sup>50</sup> Though, to the best of our knowledge, bis(siloxycarbyne) complexes have not been reported for Mo, the bis(aminocarbyne) motif is known for both Mo and W.<sup>51</sup> The aminocarbyne carbon atoms resonate further upfield in the range of 250-280 ppm.<sup>51a,51b,51d</sup>

The *pseudo*-square pyramidal coordination geometry of **9-<sup>13</sup>C** is proposed with two ≡<sup>13</sup>COSiMe<sub>3</sub> moieties in distinct chemical environments, *trans* and *cis* with respect to the central arene (Figure 3.4., right), accounting for the resonances observed in the <sup>13</sup>C{<sup>1</sup>H} NMR spectrum at -80 °C. Warming **9-<sup>13</sup>C** to -20 °C results in coalescence of the <sup>13</sup>C resonances to a broad signal at 281.9 ppm, consistent with two Mo≡<sup>13</sup>COSiMe<sub>3</sub> fragments involved in a fast exchange process on the NMR time scale. This fluxionality is attributed to ring-slipping of the η<sup>2</sup>-arene interaction, interconverting the axial and equatorial alkylidyne. Cooling the sample to -100 °C returns the disparate signals, and resolves each as a broad triplet (284.9 and 276.0 ppm). These resolved resonances show no <sup>1</sup>J(C,C), demonstrating a lack of a C–C bond and further supporting the dicarbyne assignment. The <sup>2</sup>J(P,C) data from <sup>31</sup>P{<sup>1</sup>H} NMR spectroscopy also support this exchange process (Figure 3.4.).

The spectrum collected at -100 °C, where the carbyne moieties are under the slow exchange limit, was simulated; modeling the exchange dynamics up to -20 °C provided rates for the carbyne exchange (Figure 3.4.). The Eyring equation was used to calculate the activation parameters of this process giving ΔG<sup>‡</sup> = 9.4 ± 0.4 kcal/mol at -40 °C (Table 3.1.), which is in

reasonable agreement with the estimated value from the approximate coalescence temperature ( $\Delta G^\ddagger = 9.9$  kcal/mol,  $T_c = -40$  °C). The calculated activation parameters are  $\Delta H^\ddagger = 6.6 \pm 0.4$  kcal/mol and  $\Delta S^\ddagger = -12 \pm 2$  e.u. (Figure 3.13). The large and negative  $\Delta S^\ddagger$  is consistent with

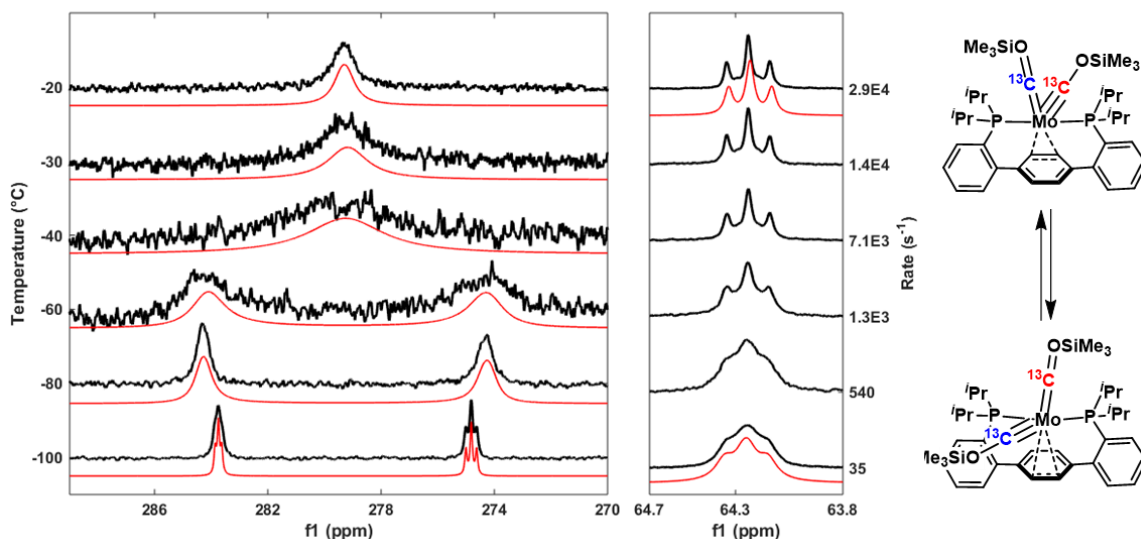


**Figure 3.4.** Variable Temperature  $^{13}\text{C}\{^1\text{H}\}$  (left) and  $^{31}\text{P}\{^1\text{H}\}$  (right) NMR Spectra of **9**- $^{13}\text{C}$  (only select regions of spectra are shown, for clarity). Sample temperature (in °C) and the calculated rate of exchange for the carbyne carbons (in  $\text{s}^{-1}$ ) are shown on the vertical axes. Experimental spectra and iteratively fit simulations are represented with black and red lines, respectively.

a non-dissociative process with a highly ordered transition state, likely required by the steric constraints of shifting of the two carbyne ligands in the terphenyl diphosphine cleft without phosphine arm dissociation

Crystallization of bis(siloxycarbyne) **9** was attempted at low temperature. Slow evaporation of liquid butane furnished maroon single crystals of a new complex bearing two silylated CO moieties as well as a carbon-carbon triple bond—bis(siloxy)acetylene complex **10** (Figure 3.5.). The solid-state structure of **10** is similar to that of other bis(siloxy)acetylene complexes of tantalum, niobium, and vanadium, with a short  $\text{C}_{31}\text{--C}_{32}$  distance (1.332(2) Å), an acute  $\text{C}_{31}\text{--Mo--C}_{32}$  angle (38.0°), and long  $\text{C}_{31/32}\text{--O}_{1/2}$  distances (1.367(2) Å).<sup>16a,16c,16d,16g-j</sup> The Mo center adopts an  $\eta^6$  metal-arene interaction, again dissociating one of the *trans*-spanning phosphine

donors.

The NMR data for  $10\text{-}^{13}\text{C}$  corroborate the conservation of a monophosphine coordination environment in solution, with resonances at 86.7 and -6.8 ppm for the Mo-bound and free phosphines, respectively. The  $^{13}\text{C}\{^1\text{H}\}$  NMR spectrum shows a single doublet for the acetylene

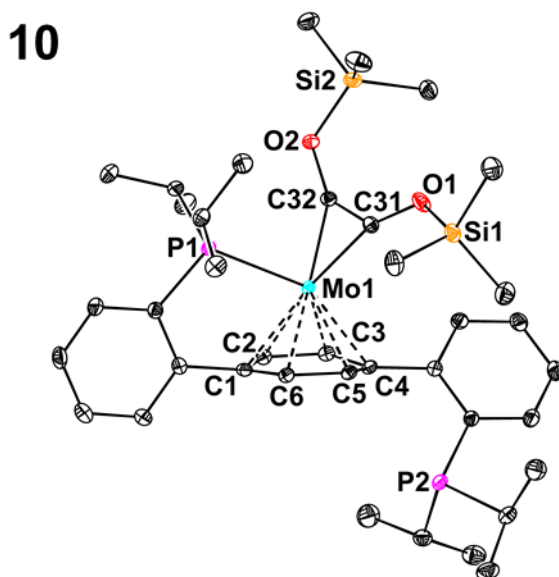


**Figure 3.5.** Solid state structure of bis(siloxy)acetylene complex **10** with anisotropic displacement ellipsoids shown at the 50% probability level. Hydrogen atoms are omitted for clarity. Selected bond lengths [Å] and angles [°]: Mo<sub>1</sub>–C<sub>arene</sub>(ave.) 2.280(2), Mo<sub>1</sub>–C<sub>31</sub> 2.054(1), Mo<sub>1</sub>–C<sub>32</sub> 2.032(1), C<sub>1</sub>–C<sub>2</sub> 1.424(2), C<sub>2</sub>–C<sub>3</sub> 1.427(2), C<sub>3</sub>–C<sub>4</sub> 1.430(2), C<sub>4</sub>–C<sub>5</sub> 1.430(2), C<sub>5</sub>–C<sub>6</sub> 1.426(2), C<sub>6</sub>–C<sub>1</sub> 1.428(2), C<sub>31</sub>–O<sub>1</sub> 1.362(2), C<sub>32</sub>–O<sub>2</sub> 1.368(2), C<sub>31</sub>–C<sub>32</sub> 1.332(2), ∠C<sub>31</sub>–Mo<sub>1</sub>–C<sub>32</sub> 38.02(6).

carbons at 207.9 ppm ( $^2J(\text{C},\text{P}) = 19.9$  Hz), despite their asymmetry in the solid-state. Holding complex  $9\text{-}^{13}\text{C}$  at -78 °C shows slow conversion to  $10\text{-}^{13}\text{C}$  by  $^{13}\text{C}\{^1\text{H}\}$  NMR spectroscopy, providing a route to a metal-bound two-electron reduced CO coupling product. Importantly, structurally characterized **10** furnishes indirect evidence for proposed dicarbyne **9**; dicarbyne complexes are demonstrated intermediates in the formation of C<sub>2</sub>O<sub>2</sub> fragments from CO.<sup>16b,16e,17</sup>

Studies at higher temperatures (-78 °C to room temperature) indicate that compound **10** does not show C–O cleavage chemistry in the presence of excess Me<sub>3</sub>SiCl; no reaction is observed under these conditions. To probe if the formation of **10** is indeed irreversible, *in situ* reduction was conducted. Treating a THF solution of  $10\text{-}^{13}\text{CO}$  with two equiv. of [Na][C<sub>10</sub>H<sub>8</sub>]



at -78 °C resulted in the formation of an intractable mixture as evidenced by  $^{13}\text{C}\{^1\text{H}\}$  and  $^{31}\text{P}\{^1\text{H}\}$  NMR (Figure 3.14.). Even upon warming, no  $^{13}\text{C}$  resonances consistent with C–O cleavage chemistry from **10** were observed, consistent with **10** being off-path to 4 e<sup>-</sup> reductive coupling chemistry.

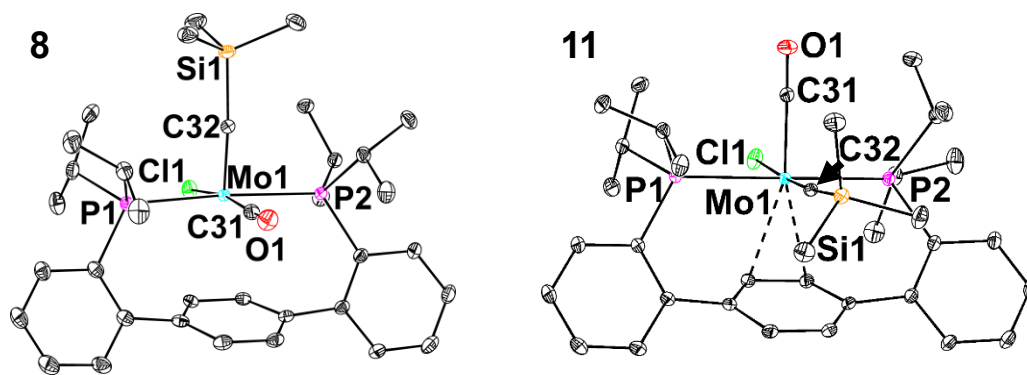


**Figure 3.6.** Solid state structures of silyl carbyne isomers **7** and **11**. Anisotropic displacement ellipsoids are represented at the 50% probability level. Hydrogen atoms are omitted for clarity.

Toward accessing silyl carbyne **8**, and ultimately four-electron reduced CO coupling fragments, a THF solution of **9**- $^{13}\text{C}$  was warmed -10 °C, evidencing slow formation of a new intermediate. A broad resonance in the  $^{31}\text{P}\{^1\text{H}\}$  NMR spectrum at 41.9 ppm supported the formation of a more oxidized Mo center. Signals in the  $^{13}\text{C}\{^1\text{H}\}$  NMR spectrum at 344.9 and 241.9 ppm are consistent with silyl carbyne<sup>52</sup> and carbonyl ligands, respectively. Low temperature crystallization (-35 °C) provided single-crystals suitable for solid-state analysis, confirming this intermediate, **11**, as a stereoisomer of **8** (Scheme 3.5.). Contrasting the *pseudo*-square pyramidal geometry of **8**, **11** adopts a *pseudo*-octahedral geometry with a clear  $\eta^2$  metal-arene interaction; the Mo–C<sub>arene</sub> contacts average 2.52 Å compared to 2.82 Å in **11**. The Mo–C<sub>32</sub> distances are similar between the alkylidyne isomers (1.795(1) Å for **11**, 1.767(2) Å for **8**), with both being consistent with Mo–C triple bonds.<sup>52a,52b,53</sup>

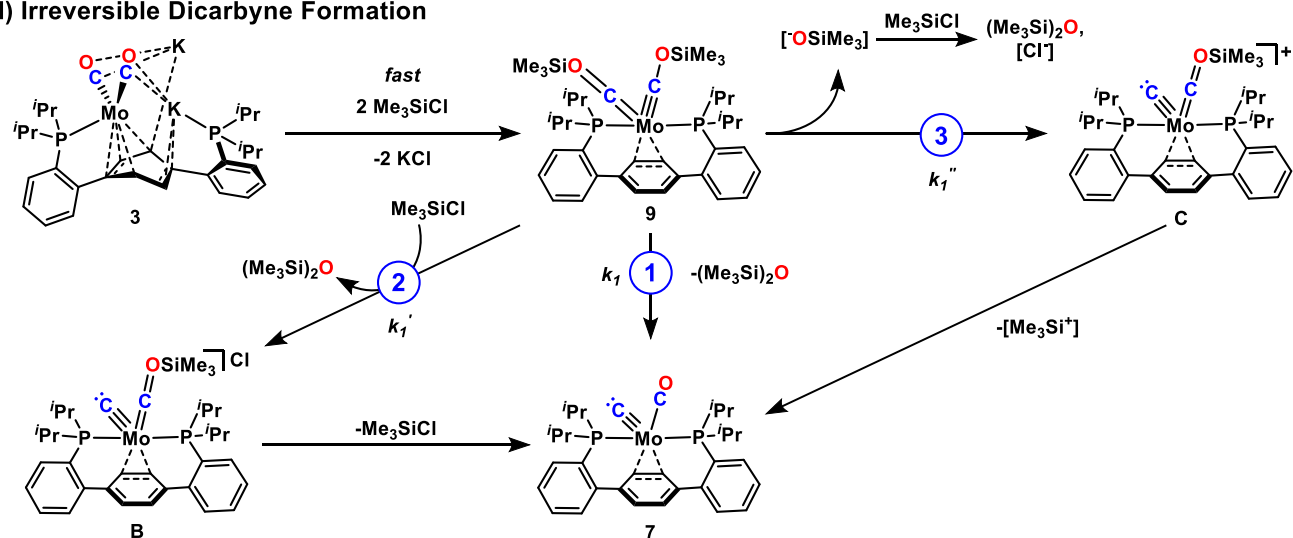
Warming samples of **11** resulted in conversion, within *ca.* 1 h, to **8** at 25 °C by  $^{31}\text{P}\{^1\text{H}\}$  NMR spectroscopy (Figure 3.15.). These data suggest that **11** is the kinetic product of carbide silylation. The *cis* geometry of the silyl carbyne moiety versus the central arene

supports the proposed *pseudo*-square pyramidal geometry for **7** (Schemes 3.3. and 3.5.). From **7**, electrophilic attack on the carbide followed by chloride coordination on the back-side of the molecule (as drawn) provides **11**. Although isomerization could occur in the six-coordinate complex by twists of trigonal faces of the octahedron, the rigidity of the terphenyl framework makes this mechanism unlikely.<sup>54</sup> It is proposed that dissociation of a ligand (chloride or phosphine) facilitates rearrangement to the thermodynamic product, **8**, where the alkylidyne is now located *trans* to the arene ring, a sterically preferred coordination geometry (Table 3.2.).

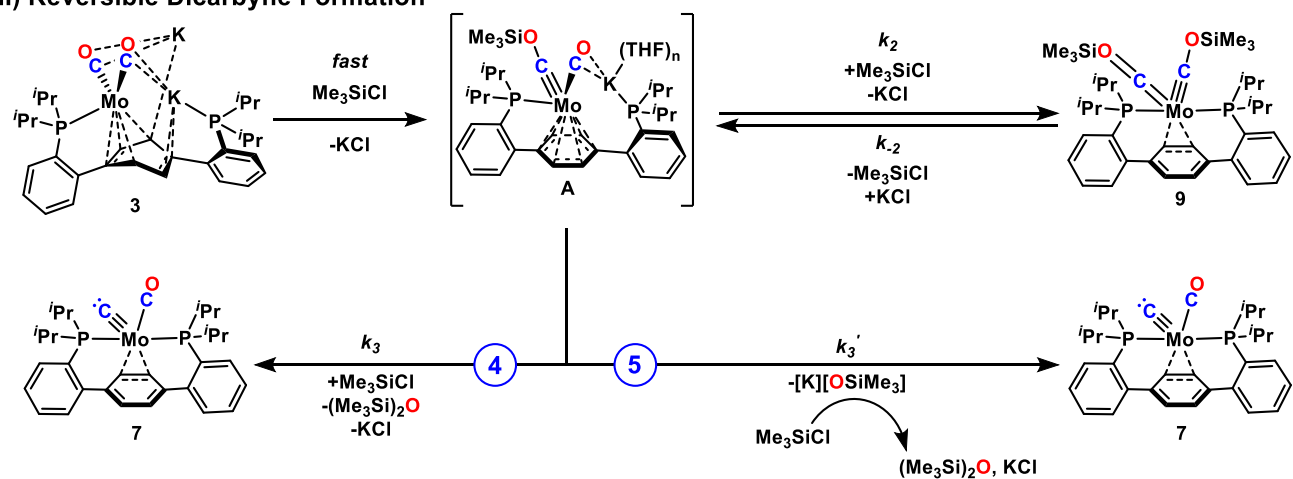
#### *Mechanistic Investigation of C–O Bond Cleavage*

From dicarbyne **9**, there are several envisioned pathways by which C–O bond cleavage could provide carbide **7** and hexamethyldisiloxane (Scheme 3.6., Paths 1-5). This reaction proceeds to completion in the course of *ca.* 2 h at 0 °C, to provide a mixture of **11** and **8**, without the spectroscopic observation of additional intermediates. If C–O bond cleavage proceeds from **9**, three pathways are envisioned. Intramolecular silyl ether formation—nucleophilic attack of a siloxide oxygen on the silyl group of the other siloxycarbyne ligand—would provide carbide **7** directly (Scheme 3.6., Path 1). Alternatively, external silyl electrophile attack on the siloxy carbyne oxygen could induce C–O bond cleavage to form a presumably highly unstable carbide/carbene complex, **B** (Scheme 3.6., Path 2). Silyl chloride elimination from this species would yield carbide **7**; subsequent silyl migration and chloride association would provide silyl alkylidyne **11**. C–O bond cleavage could also proceed from dicarbyne **9** via siloxide anion ( $\text{Me}_3\text{SiO}^-$ ) dissociation, generating a cationic siloxycarbyne/carbide intermediate, **C** (Scheme 3.6., Path 3). This species could react with the released  $\text{Me}_3\text{SiO}^-$  to generate  $(\text{Me}_3\text{Si})_2\text{O}$ , or lose  $\text{Me}_3\text{Si}^+$  (or  $\text{Me}_3\text{SiCl}$  upon attack by  $\text{Cl}^-$ —under the reaction conditions, chloride anions are necessarily present in solution) which would undergo metal-free reaction with  $\text{Me}_3\text{SiO}^-$  to generate the observed  $(\text{Me}_3\text{Si})_2\text{O}$ .

## I) Irreversible Dicarbyne Formation



## II) Reversible Dicarbyne Formation



**Scheme 3.6.** Mechanistic possibilities (Paths 1-5, in blue) for the elementary reaction step of C–O bond cleavage from dicarbyne **9**.

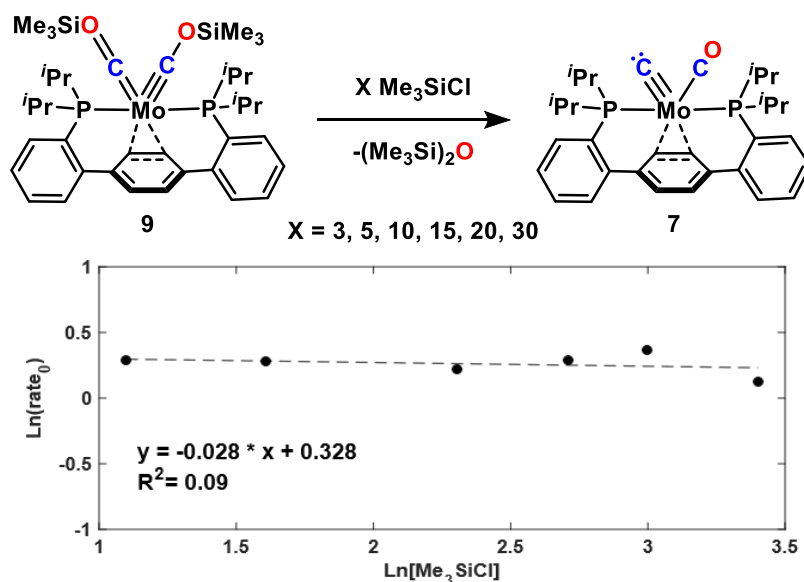
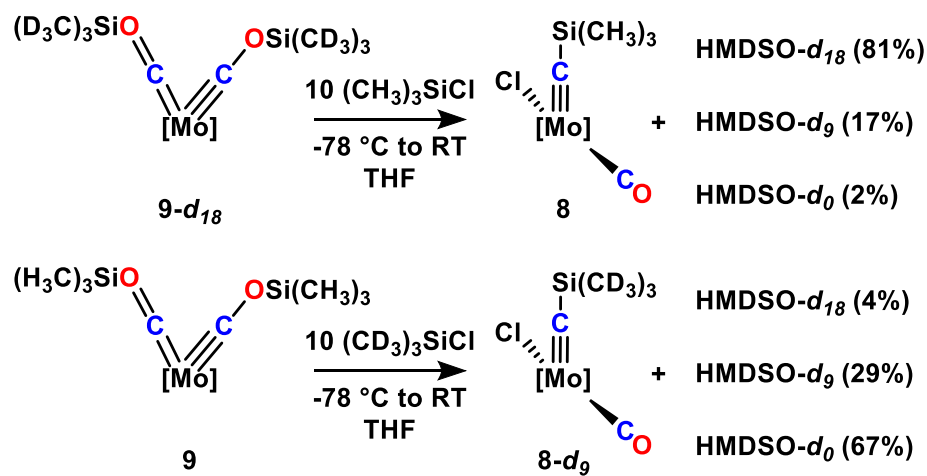


**Figure 3.7.** Kinetic data supporting C–O bond cleavage is zeroth order in silyl electrophile.

Both kinetics and isotopic labeling were employed to aid in experimentally evaluating these mechanistic possibilities. Kinetic analysis of the consumption of dicarbonyne **9**-<sup>13</sup>C and formation of silyl carbynes **11**-<sup>13</sup>C and **8**-<sup>13</sup>C at 0 °C (as at this temperature, carbide **7**-<sup>13</sup>C is silylated rapidly (*vide infra*)) shows that the rate of C–O bond cleavage is independent of electrophile concentration (Figures 3.7. and 3.18.). A zeroth order reaction in Me<sub>3</sub>SiCl is consistent with two of these mechanistic scenarios (Eq. 1-3); Path 2 is expected to show first order rate dependence on silyl electrophile concentration. Isotopic labeling studies invalidate both Paths 1 and 2. Condensing two equiv. of Me<sub>3</sub>SiCl-*d*<sub>9</sub> onto a frozen THF solution of dianion **3**-<sup>13</sup>C and allowing the mixture to thaw to -78 °C generated deuterated **9**-<sup>13</sup>C-*d*<sub>18</sub>. This dicarbonyne complex was warmed to room temperature in the presence of an excess of (CH<sub>3</sub>)<sub>3</sub>SiCl, facilitating C–O bond cleavage, and the end products were analyzed by both NMR spectroscopy and GC/MS. The major hexamethyldisiloxane (HMDSO) isotopolog observed was HMDSO-*d*<sub>18</sub> (81%, Scheme 3.7.). Incorporation of at least one (CH<sub>3</sub>)<sub>3</sub>Si group (as was observed in 19% of the product disiloxanes) excludes an intramolecular cleavage event (Scheme 3.6., I, Path 1). Electrophilic attack by external silyl electrophile, as in Path 2, can likewise be ruled out; if operative, this pathway would provide exclusively HMDSO-*d*<sub>9</sub>. These

results are further supported by the complementary experiment of warming  $9\text{-}^{13}\text{C}$  in an excess of  $(\text{CD}_3)_3\text{SiCl}$  (Scheme 3.7.).



**Scheme 3.7.** End-product distributions in isotopic labeling studies of the C–O bond cleavage step. The *para*-terphenyldiphosphine ligand is omitted for brevity. Endproduct isotopolog distributions were determined by GC/MS.

A siloxide dissociation pathway (Scheme 3.6., I, Path 3) is both zeroth order in silyl electrophile (Eq. 3) and accounts for the generation of all three HMDSO isotopologs. From  $9\text{-}^{13}\text{C}\text{-}d_{18}$ , the liberated siloxide anion could react with the proximal silyl group of cation **C** (giving HMDSO- $d_{18}$ ) or it could react off-metal with the excess  $\text{Me}_3\text{SiCl}$  (giving HMDSO- $d_9$ ). The preference for HMDSO- $d_{18}$  is potentially a consequence of the high local concentration of **C**, which is expected to be a strong silylating agent. The formation of HMDSO- $d_0$ , albeit in a small amount, is more convoluted as it requires a silyl group exchange. A control reaction demonstrates that  $\text{Me}_3\text{SiO}^-$  undergoes substitution chemistry with disiloxane, even in the presence of excess silyl electrophile (Figure 3.25.). Such a side reaction accounts for the formation of the observed HMDSO- $d_0$  from the deuterio dicarbyne. Assuming dicarbyne formation is irreversible, this pathway is the most consistent with both the reaction kinetics and labeling studies and cannot be ruled out based on the experimental data.

However, formation of dicarbyne **9** need not be irreversible (Scheme 3.6., II). Either a fast pre-equilibrium or rate limiting trimethylsilyl dissociation may precede C–O bond cleavage,

via carbyne anion **A**. Anionic carbyne **A** can be envisioned to act as a precursor to C–O bond cleavage; electrophilic attack by external silyl chloride (Scheme 3.6., II, Path 4) or siloxide dissociation (Scheme 3.6., II, Path 5) would both result in direct generation of carbide **7**.

Although a fast pre-equilibrium followed by reaction of **A** with external Me<sub>3</sub>SiCl (Scheme 3.6., II, Path 5) would be overall zeroth order in electrophile (Eq. 4a), such a process can be ruled out by the isotopic labeling studies. Any pathway involving a fast pre-equilibrium would scramble the silyl electrophile label statistically, which is not observed either spectroscopically during the course of the reaction (<sup>2</sup>H NMR, Figure 3.23.) or in the end product isotopolog distributions (Scheme 3.7.). Rate-limiting formation of **A** is likewise consistent with the observed reaction kinetics (Eqs. 6 and 7a). Further information was sought through direct studies of species **A**. Species **A** can be generated at low temperatures as part of a mixture, when using limiting amounts of electrophile. Careful addition of a single equiv. of Me<sub>3</sub>SiCl to dianion **3**-<sup>13</sup>C at -78 °C provides a mixture of **3**-<sup>13</sup>C, dicarbyne **9**-<sup>13</sup>C, and a third species. This new species displays <sup>13</sup>C{<sup>1</sup>H} NMR resonances at 263.6 and 232.8 ppm, chemical shifts consistent with siloxycarbyne and carbonyl ligands, respectively. The <sup>31</sup>P{<sup>1</sup>H} NMR spectrum shows signals at 97.7 and -2.8 ppm, supporting the tentative assignment of this new species as anionic carbyne **A** (Figure 3.26.). Addition of a second equiv. of silyl electrophile to this mixture yields dicarbyne **9**-<sup>13</sup>C almost quantitatively, consistent with **A** being a partially silylated species. Warming a mixture of **3**-<sup>13</sup>C, **A**, and **9**-<sup>13</sup>C to -50 °C demonstrates complete consumption of complex **A** by <sup>13</sup>C{<sup>1</sup>H} and <sup>31</sup>P{<sup>1</sup>H} NMR spectroscopies, the characteristic resonances of **3**-<sup>13</sup>C and **9**-<sup>13</sup>C persist at these temperatures. Anionic carbyne/CO adduct **A** forms a mixture of C–O cleaved products (Figure 3.27.), as indicated by the characteristic low-field <sup>13</sup>C{<sup>1</sup>H} NMR signals for silyl carbynes **8** and **11**, as well as mixed dicarbyne **15** (*vide infra*), observed upon exhaustively silylating this reaction mixture at -78 °C. These data are consistent with C–O bond cleavage occurring

more readily from anionic carbyne **A** than neutral dicarbyne **9**, though C–O scission occurring from both complexes at 0 °C cannot be ruled out conclusively.

Though the end-product isotopolog distribution in a rate limiting silyl dissociation mechanism is convoluted by a dependence on the relative rates of C–O bond cleavage from **A** and resilylation of **A** to provide isotopologs of **9**, *in situ* <sup>2</sup>H NMR spectroscopy is more consistent with C–O scission by siloxide dissociation (Path 5) than external electrophile attack (Path 4). From **9**, no <sup>2</sup>H incorporation is observed in the metal complex during the course of the reaction with (CD<sub>3</sub>)<sub>3</sub>SiCl (Figure 3.23.), consistent with C–O bond cleavage being faster than resilylation at 0 °C. If formation of carbide **7** proceeded from **A** via external silyl electrophile attack (Path 4), HMDSO-*d*<sub>0</sub> would be formed starting from either **9** or **9-d**<sub>18</sub>, inconsistent with the experimental data (Scheme 3.7.). Moreover, this reactivity pathway fails to account for the HMDSO-*d*<sub>0</sub> and HMDSO-*d*<sub>18</sub> observed from **9-d**<sub>18</sub> and **9**, respectively. A siloxide dissociation pathway (Scheme 3.6., Path 5) is most consistent with the observed end-products, with off-metal substitution chemistry facilitating the formation of all three HMDSO isotopologs.

We therefore favor Path 5, a reaction mechanism in which silyl dissociation from dicarbyne **9** is rate limiting, providing anionic carbyne **A**, the precursor to C–O cleavage. At 0 °C, siloxide dissociates from this electron-rich species more rapidly than resilylation can occur—consistent with both spectroscopic studies and the observed reaction kinetics—providing carbide **7** and siloxide anion. As indicated above, direct siloxide dissociation from **9** (Path 3) is also a viable mechanism for carbide formation. The observation of C–O bond cleavage at lower temperature when starting from **A** is notable, and offers a method to facilitate selective deoxygenation chemistry, avoiding non-deoxygenative C–C coupling, by limiting electrophile concentration. These studies

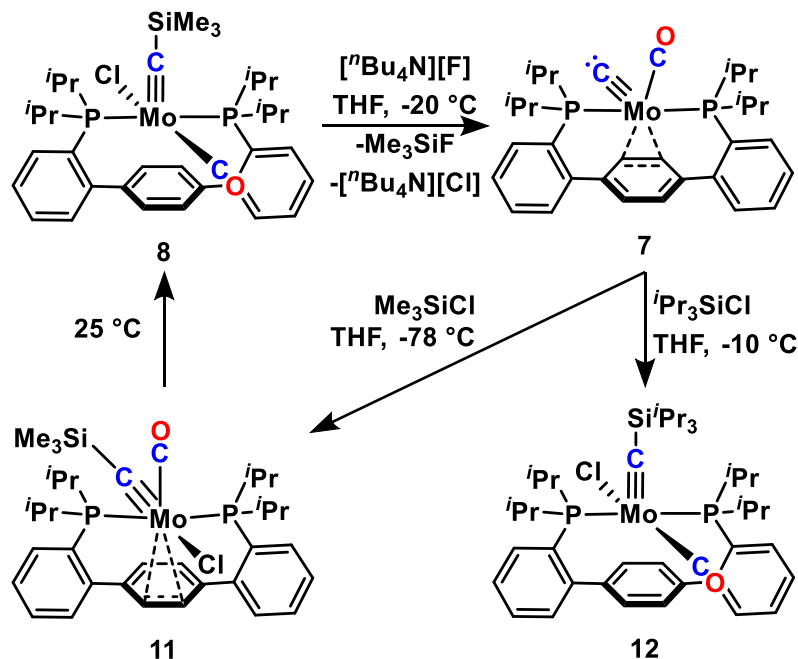
provide detailed mechanistic insight for an unprecedented observation of the elementary reaction step(s) of C–O bond cleavage to form a terminal transition metal carbide.

#### *Mechanistic Interrogation of C–C Bond Formation*

**7-<sup>13</sup>C** is a spectroscopically observed intermediate in the addition of <sup>t</sup>Pr<sub>3</sub>SiCl to dianion **3-<sup>13</sup>C** *en route* to **5** and **6a** (Scheme 3.5). It is a proposed intermediate in the formation of trimethylsilyl alkylidyne **11** from dicarbyne **9** (Scheme 3.8). The addition of both electrophiles to independently prepared **7-<sup>13</sup>C** was investigated at low temperature.

Treating a frozen THF solution of carbide **7-<sup>13</sup>C** with one equiv. of Me<sub>3</sub>SiCl resulted, upon warming to -78 °C, in complete disappearance of the carbidic resonance at 546.3 ppm and the growth in of the upfield shifted silylcarbyne resonances of **11-<sup>13</sup>C** (*ca.* 75% by <sup>31</sup>P{<sup>1</sup>H} NMR integration) and **8-<sup>13</sup>C** (*ca.* 25% by <sup>31</sup>P{<sup>1</sup>H} NMR integration) at 344.9 and 355.9 ppm, respectively (Scheme 3.8). These data support the hypothesis that **7-<sup>13</sup>C** is a precursor to silyl alkylidynes **11** and **8** (*vide supra*). In contrast, addition of <sup>t</sup>Pr<sub>3</sub>SiCl to a frozen THF solution of carbide **7-<sup>13</sup>C** did not show any conversion of starting material upon thawing to -78 °C. The spectroscopic features of **7-<sup>13</sup>C** persist in the <sup>13</sup>C{<sup>1</sup>H} NMR spectrum up to -10 °C, at which temperature slow conversion to the triisopropylsilyl alkylidyne complex **12-<sup>13</sup>C** (Scheme 3.8), is observed. Consistent with formation of this silyl carbyne are the upfield shifted resonance at 34.4 ppm in the <sup>31</sup>P{<sup>1</sup>H} NMR spectrum, and resonances at 360.8 and 250.8 ppm in the <sup>13</sup>C{<sup>1</sup>H} NMR spectrum. The stability of the carbide up to -10 °C in the presence of this bulky silyl electrophile is consistent with its spectroscopic detection in reactions of dianion **3-<sup>13</sup>C** with <sup>t</sup>Pr<sub>3</sub>SiCl. However, formation of organic **6a** proceeds below this temperature when treating either anions **3** or **4** with <sup>t</sup>Pr<sub>3</sub>SiCl, ruling out the intermediacy of isopropyl analogs of **8** and **11** at low temperatures. Based on this reactivity, coupling may occur from carbide **7-<sup>13</sup>C** directly, which prompted investigation of reduction prior to silylation.

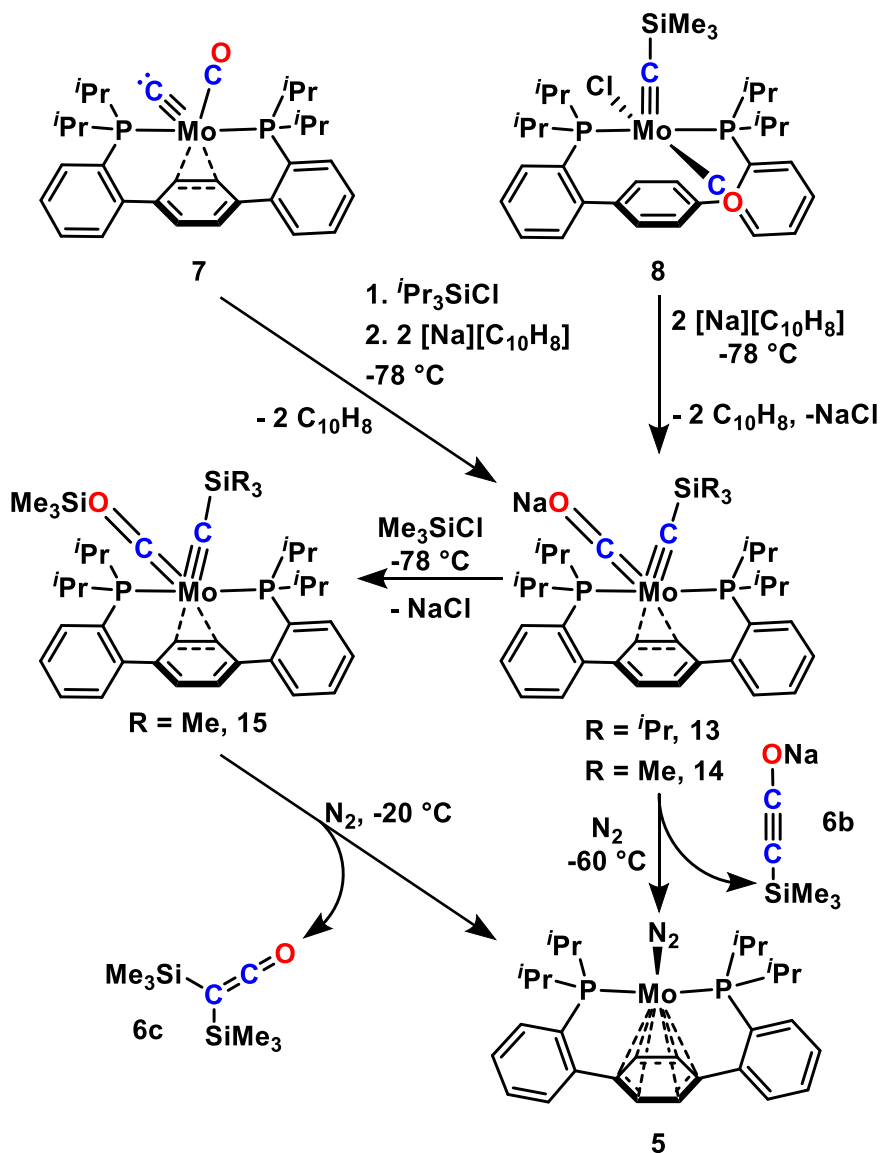




**Scheme 3.8.** *In situ* generation and silylation of terminal carbide **8**.

Reduction of carbide **7** in the presence of silyl electrophiles was targeted. One equiv. of  $\text{Pr}_3\text{SiCl}$  was added to *in situ* generated carbide **7**-<sup>13</sup>C at -78 °C, resulting in no change to the <sup>13</sup>C{<sup>1</sup>H} or <sup>31</sup>P{<sup>1</sup>H} NMR spectra (Figure 3.30.). Two equiv. of [Na][C<sub>10</sub>H<sub>8</sub>], as a solution in THF, were then added at low temperature. The <sup>13</sup>C{<sup>1</sup>H} and <sup>31</sup>P{<sup>1</sup>H} NMR spectra showed new broad resonances at 327.8 and 58.2 ppm, respectively. Expecting two resonances for the isotopically enriched nuclei in the <sup>13</sup>C NMR spectrum (given the chemically inequivalent C–Si and C–O motifs), the sample was cooled to -100 °C, resulting in further broadening, but maintenance of a single signal. Warming the sample to -60 °C resolved two broad <sup>13</sup>C resonances at 327.9 and 327.0 ppm, again in the chemical shift range of Mo alkyldynes. The product of carbide reduction in the presence of  $\text{Pr}_3\text{SiCl}$  was tentatively assigned as silyl carbyne/oxycarbyne **13**-<sup>13</sup>C (Scheme 3.9.).

Independent synthesis of the trimethylsilyl variant (**14**) was targeted via reduction of silyl carbyne **8**-<sup>13</sup>C (Scheme 3.9.). Treatment with two equiv. of [Na][C<sub>10</sub>H<sub>8</sub>] at -78 °C demonstrated formation of a new species with broad resonances at 330.8 and 58.5 ppm in the <sup>13</sup>C{<sup>1</sup>H} and <sup>31</sup>P{<sup>1</sup>H} NMR spectra, respectively. The chemical shift differences between these resonances



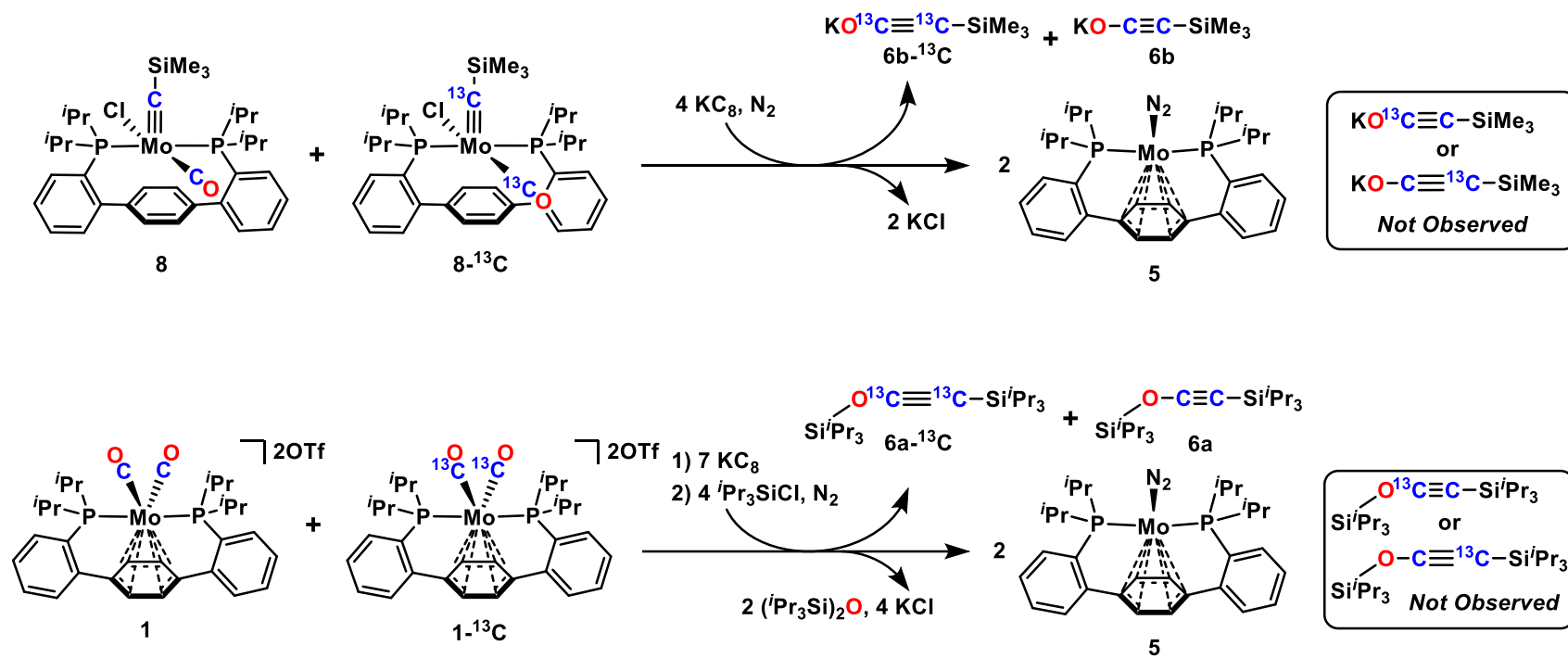
**Scheme 3.9.** Synthesis of mixed dicarbyne complexes and subsequent C–C bond formation. and those assigned to  $13\text{-}^{13}\text{C}$  are small, supporting assignment as the mixed carbyne  $14\text{-}^{13}\text{C}$  (Scheme 3.9.). Cooling the sample to  $-100^\circ\text{C}$  resolved two broad triplets in the  $^{13}\text{C}\{^1\text{H}\}$  NMR—that with the larger  $^2J(\text{C},\text{P})$  (19.3 Hz) being shifted further downfield. Warming the sample to  $-60^\circ\text{C}$  likewise showed two resonances, now with the peak displaying the larger  $^2J(\text{C},\text{P})$  (21.4 Hz) moving further upfield (Figure 3.31.). The lack of C–C coupling in the  $^{13}\text{C}\{^1\text{H}\}$  NMR spectrum supports the dicarbyne motif, and rules out silylated oxyacetylide or ketenylidene structures. Additional analysis of the temperature dependent fluxionality was

inhibited by the narrow temperature range at which the complex is stable.

Warming either **13-<sup>13</sup>C** or **14-<sup>13</sup>C** above -60 °C under N<sub>2</sub> resulted in conversion of the Mo species to dinitrogen complex **5**, and the growth in of a pair of doublets in the <sup>13</sup>C{<sup>1</sup>H} NMR spectrum—131.3 and 5.9 ppm, <sup>1</sup>J(C,C) = 139.6 Hz—consistent with formation of sodium silyl ethynolate, **6b** (Scheme 3.9).<sup>55</sup> As reported previously,<sup>56</sup> addition of a small silyl electrophile to the trimethylsilyl ethynolate yielded disilyl ketene, **6c** (<sup>13</sup>C{<sup>1</sup>H} δ = 167.5 and 1.1 ppm, <sup>1</sup>J(C,C) = 82.3 Hz), the thermodynamically preferred isomer of the disilylated C<sub>2</sub>O<sub>1</sub> product.

To gain further support for the proposed structures of anions **13-<sup>13</sup>C** and **14-<sup>13</sup>C**, silylation of the oxycarbyne fragment of **14-<sup>13</sup>C** was attempted at low temperature, targeting a mixed silyl/siloxy dicarbyne, **15-<sup>13</sup>C** (Scheme 3.9). Treating a solution of **14-<sup>13</sup>C** with Me<sub>3</sub>SiCl at -78 °C resulted in two new resonances in the <sup>13</sup>C{<sup>1</sup>H} NMR spectrum at 378.9 and 283.7 ppm, assigned to the silyl- and siloxycarbyne resonances of **15-<sup>13</sup>C**, respectively. The <sup>31</sup>P{<sup>1</sup>H} NMR spectrum of **15-<sup>13</sup>C** displays a broad apparent triplet at 56.8 ppm at -80 °C, lacking resolution necessary to assign two <sup>2</sup>J(P,C) coupling constants. Warming the sample to -20 °C resulted in resolution of this <sup>31</sup>P resonance to a doublet of doublets—<sup>2</sup>J(P,C) = 18.3 and 13.4 Hz—consistent with the proposed mixed dicarbyne structure of **15-<sup>13</sup>C**. The <sup>13</sup>C{<sup>1</sup>H} NMR signals likewise were resolved as triplets, coupling the *trans*-spanning <sup>31</sup>P nuclei. Upon warming further, growth of dinitrogen complex **5** was observed as a singlet at 76.4 ppm in <sup>31</sup>P NMR spectrum. Concurrently, resonances in the <sup>13</sup>C{<sup>1</sup>H} NMR showed formation of metal-free bis(trimethylsilyl)ketene **6c**.

Crossover experiments were performed to determine if the C–C bond forming step is unimolecular, both starting from silyl carbyne **8** and from a one-pot reduction and silylation of dicarbonyl dication **1** (Scheme 3.10.). A 1:1 mixture of **8** and **8-<sup>13</sup>C** was exposed to the conditions leading to C–C bond formation (Scheme 3.10.). The organic fragment was interrogated by <sup>13</sup>C NMR spectroscopy for the presence of **6b** with a single <sup>13</sup>C enriched position. Only **6b-<sup>13</sup>C** (displaying two <sup>13</sup>C enriched positions) is observed, consistent with



Scheme 3.10. Crossover-type experiments from  $8/8\text{-}^{13}\text{C}$  and  $1/1\text{-}^{13}\text{C}$ .

intramolecular C–C bond formation. Formation of silyl ethynolates directly from mixed dicarbynes **13** and **14** indicates that the C–C bond is formed via reductive elimination of two cofacial carbyne ligands. Similarly, in the one-pot reduction and silylation of a mixture of **1** and **1-<sup>13</sup>C**, only **6a-<sup>13</sup>C** is observed.

Though coupling of carbyne and CO ligands to form substituted oxyacetylenes is known,<sup>42c,57</sup> these reactions involve electrophile addition at oxygen after C–C bond formation with ketenyl complexes as established reaction intermediates.<sup>42b,57-58</sup> In contrast, complexes **13-15** demonstrate that in the present system, C–C bond formation occurs following functionalization at oxygen.

### *Computational Studies*

With myriad complexes bearing Mo–C multiple bonds in a variety of coordination environments, calculations were performed to investigate the electronic structures of these molecules. Revised TPSS exchange and correlation functionals<sup>59</sup> were employed at the LANL2DZ<sup>60</sup> level of theory. The diisopropylphosphine and trimethylsilyl moieties were modeled as dimethylphosphine and silyl groups, respectively, unless noted otherwise. The optimized geometries of the computed structures agree well with experimentally determined solid-state parameters established by single-crystal XRD (for **2**, **8**, **10**, and **11**, Table 3.4). To further test the validity of the calculated structures, CO stretching frequencies and <sup>13</sup>C NMR shifts (GIAO)<sup>61</sup> were computed. The trends observed experimentally are matched well computationally (Table 3.3).

As a rare example of a terminal transition metal carbide,<sup>21,40a,62</sup> the electronic structure of **7** is of particular interest. The highest occupied molecular orbital (HOMO) is non-bonding with

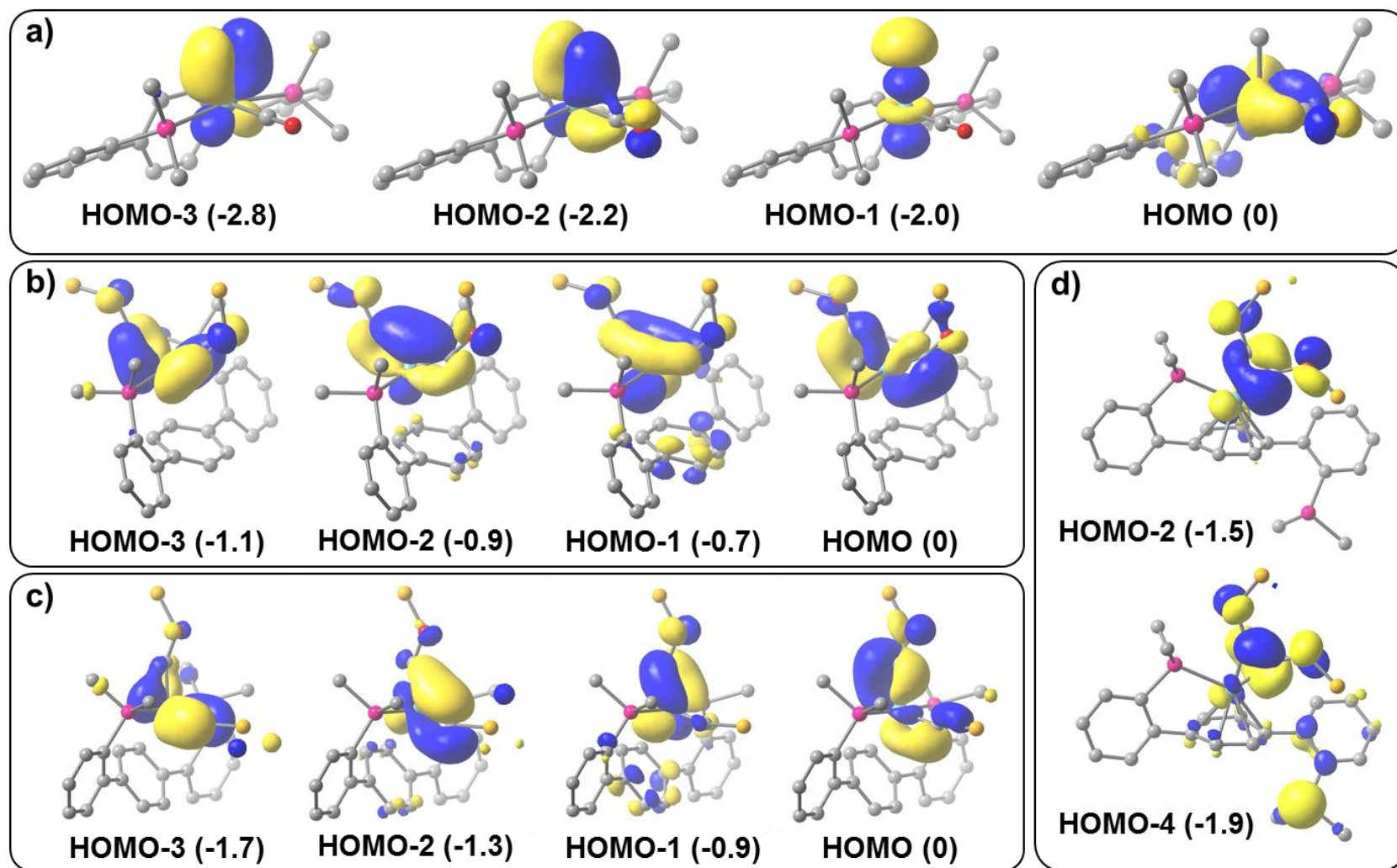


**Figure 3.8.** Calculated valence molecular orbitals of models of **7** (a), **9** (b), **15** (c), and **10** (d). Orbital energies (relative to the HOMO) in eV are given in parentheses. Isosurfaces are displayed at the  $0.04 \text{ e}/\text{\AA}^3$  level.

respect to the carbide ligand and has stabilizing contributions from the  $\pi$ -acidic antibonding orbitals of both the central arene and the CO (Figure 3.8., a). The  $\eta^2$  metal-arene interaction is supported experimentally; the arene  $^1\text{H}$  and  $^{13}\text{C}$  resonances of the metal-bound arene fragment show a distinct upfield shift (6.5 and 86.2 ppm, respectively), evidencing donation of electron density from Mo into an arene  $\pi^*$  orbital. The Mo-carbide  $\pi$ -bonds show contributions from the metal  $d_{xz}$  and  $d_{yx}$  orbitals and C  $p_x$  and  $p_y$  orbitals (Figure 3.8., a, HOMO-2 and HOMO-3). The Mo-carbide  $\sigma$ -bond is slightly higher in energy (HOMO-1) with primarily C  $p_z$  character and contribution from a metal-based orbital of  $d_{z^2}$  parentage. These results, in conjunction with natural population analysis, support a strong formal  $\text{Mo}\equiv\text{C}$  triple bond and agree well with computations for neutral Ru and Fe carbide complexes.<sup>63</sup>

The electronic structure of transition metal dicarbyne complexes has been studied extensively in the context of CO coupling.<sup>64</sup> The optimized structure of dicarbyne **9** shows short Mo–C distances of 1.850 Å, consistent with the proposed dicarbyne assignment. The Mo–C distance to the nearest arene carbons averages 2.593 Å, in agreement with the weak M-arene interaction inferred in solution from  $^1\text{H}$  and  $^{13}\text{C}\{^1\text{H}\}$  NMR spectroscopies. The four highest energy occupied molecular orbitals of **9** are composed of Mo d and C–O  $\pi^*$  orbitals (Figure 3.8., b). Four orbitals have  $\pi$  contributions to the Mo–C bonds, in two orthogonal pairs. The HOMO-1 and HOMO-2, with metal orbital contributions of  $d_{xz}$  and  $d_{yx}$  parentage, show considerable in-phase orbital overlap between the carbyne carbons, akin to calculations performed for adjacent cylindrical  $\pi$ -interacting ligands on the unique face of a capped trigonal prism.<sup>64a</sup>

The frontier molecular orbitals of mixed dicarbyne **15** (Figure 3.8., c) are quite similar to **9** (Figure 3.8., b), again demonstrating significant in-phase orbital overlap between the carbyne C atoms. Contraction of the C–Mo–C angle, as would be expected in the reaction coordinate for formation of a C–C bond from either **9** or **15**, would stabilize these orbitals (for instance, they become the C–C  $\pi$ -bonds of the alkyne fragment in **10**, Figure 3.8., d), an electronic justification for the observed C–C bond formation from these intermediates.<sup>64b,65</sup> All of these

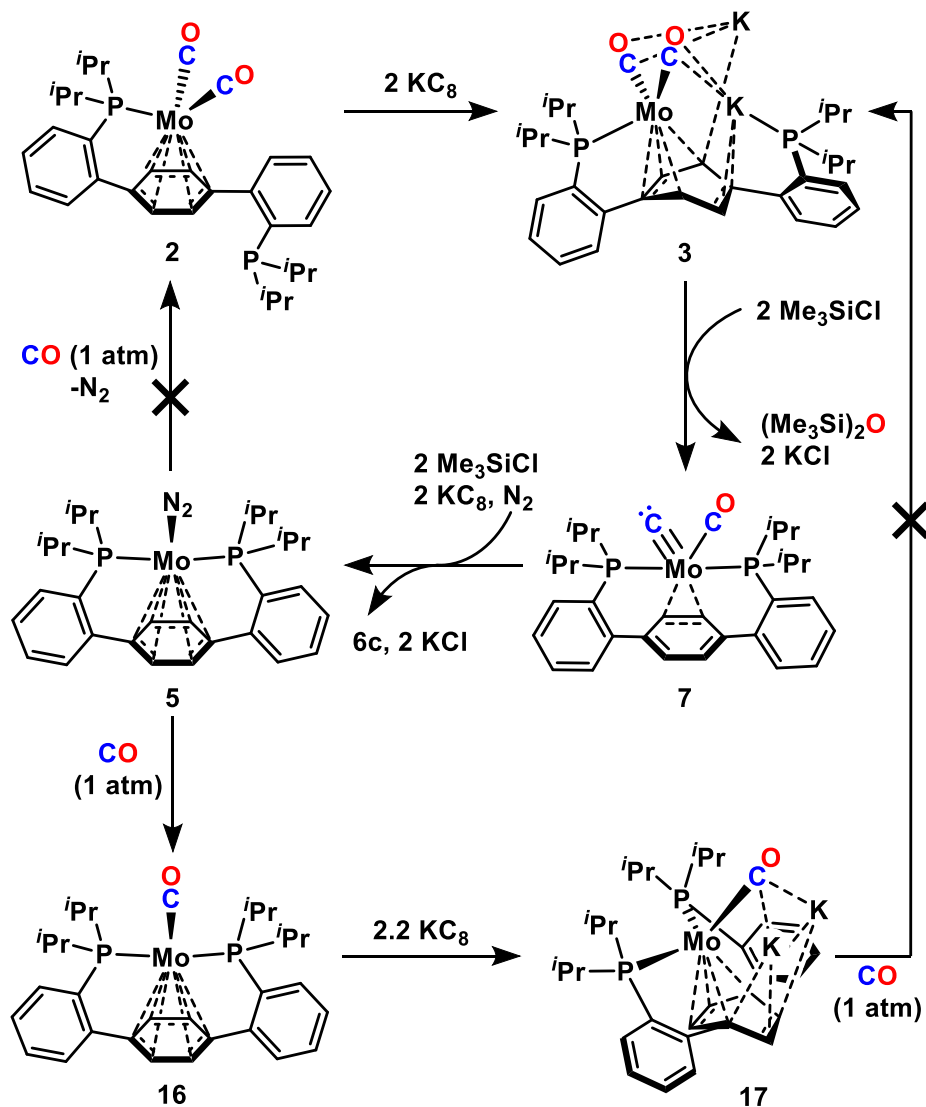
orbitals are comparable to those calculated for model systems for carbyne-carbyne coupling—a hypothetical tungsten dicarbyne<sup>64b,64c</sup> and an isolated iron diphosphine dicarbyne.<sup>17</sup>

#### *Efforts Toward a Synthetic Cycle for Silylated C<sub>2</sub>O<sub>1</sub> Fragments from CO*

Having characterized a number of potential intermediates, a synthetic cycle for the conversion of two CO molecules to a metal-free C<sub>2</sub>O<sub>1</sub> product was pursued (Scheme 3.11.). Starting from **2**, reduction to **3**, C–O cleavage to give **7**, and C–C coupling—with organic product release—to give **5**, have all been demonstrated. All that remains is recarbonylation to close the cycle. Dinitrogen complex **5** was treated with an atmosphere of CO gas, resulting not in the regeneration of **2**, but rather in the formation of monocarbonyl **16**. Phosphine arm dissociation from **16** does not proceed, even in the presence of excess CO. Neutral Mo(0) carbonyl **16** has spectroscopic features similar to isoelectronic **5**. The two central arene resonances in the <sup>1</sup>H NMR spectrum are shifted considerably upfield, 4.60 and 4.59 ppm, consistent with a strong η<sup>6</sup> metal-arene interaction. The <sup>31</sup>P{<sup>1</sup>H} NMR spectrum has a single resonance at 81.6 ppm in a similar range to both Mo(0) complexes **5** and **2**. The IR spectrum of **16** has a single sharp feature at 1786 cm<sup>-1</sup> that redshifts, as expected, to 1744 cm<sup>-1</sup> for isotopolog **16-<sup>13</sup>C**. The <sup>13</sup>C{<sup>1</sup>H} NMR spectrum shows a downfield resonance at 242.6 ppm for the carbonyl carbon, indicating more Mo–CO backbonding in monocarbonyl **16** than in dicarbonyl **2**. Despite being more electron rich, **16** may be reduced. Addition of 2.2 equiv. of KC<sub>8</sub> to a THF solution of **16** resulted in a color change to deep red. <sup>31</sup>P{<sup>1</sup>H} NMR spectroscopy showed a single resonance at 114.1 ppm, consistent with formation of two-electron reduced **17** (Scheme 3.11.). The carbonyl carbon of **17-<sup>13</sup>CO** is highly deshielded, resonating at 258.5 ppm in the <sup>13</sup>C{<sup>1</sup>H} NMR spectrum, a chemical shift similar to that observed for the CO ligands in **3**. Also akin to dianion **3**, **17** demonstrates very low CO stretching frequencies. The IR spectrum shows a broad CO stretch at 1507 cm<sup>-1</sup> that redshifts to 1459 cm<sup>-1</sup> upon <sup>13</sup>C incorporation, a value in relatively close agreement with that calculated for a simple



reduced mass oscillator. These spectroscopic features support a significant degree of backbonding into the CO ligand, again demonstrating the importance of metal-ligand covalency in stabilizing these extremely reduced molecules.



**Scheme 3.11.** Envisioned synthetic cycle for four-electron CO reductive coupling.

The structures of **16** and **17** were corroborated by single-crystal XRD analysis (Figure 3.9). The metal-arene interaction slips from  $\eta^6$  to  $\eta^4$  upon reduction, analogously to the dicarbonyl complexes. Dianion **17** crystallizes as dinuclear  $\text{Mo}_2\text{K}_4$  cluster with three K atoms, displaying interactions with the CO ligands and terphenyl  $\pi$ -systems, poised between the ligated Mo centers. The fourth  $\text{K}^+$  ion is coordinated to the back-side of one of the central arene rings

and is solvated by four THF molecules. The central arene rings are puckered with a  $47.8^\circ$  angle between the  $C_1-C_2-C_3-C_4$  and  $C_4-C_5-C_6-C_1$  planes, demonstrating delocalization of the reducing equivalents into the ligand. The solid state metrics also corroborate carbonyl ligand stabilization of the highly reduced metal center—the Mo–C bonds contract significantly from 18 (1.948(2) Å) to 19 (1.886(5) Å); the C–O bonds necessarily elongate (1.177(2) to 1.240(5) Å).

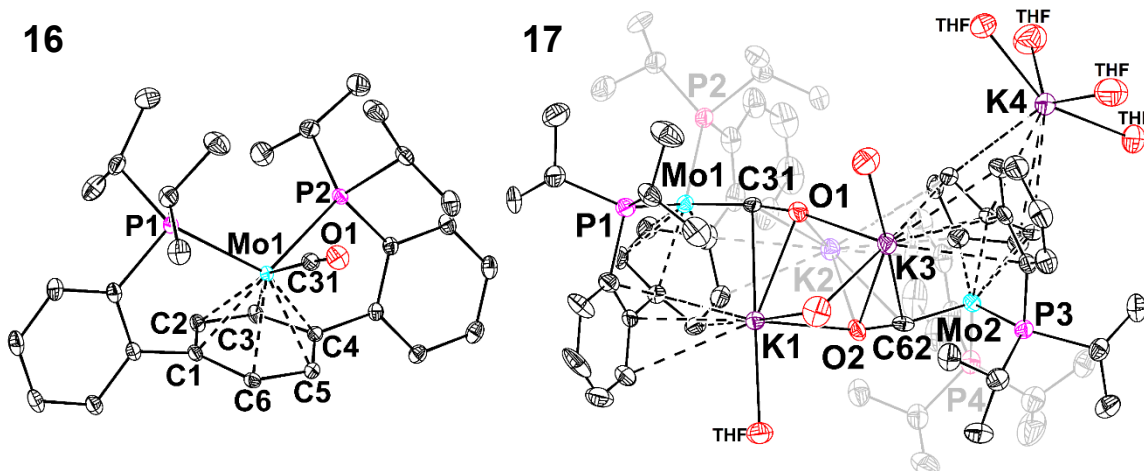


**Figure 3.9.** Solid-state structures for monocarbonyl complexes **16** and **17**. Anisotropic displacement ellipsoids are shown at the 50% probability level. The carbon atoms of K-bound THF molecules and hydrogen atoms have been omitted for clarity. Selected bond lengths [Å]: **16** Mo<sub>1</sub>–C<sub>arene</sub>(ave.) 2.281(2), Mo<sub>1</sub>–C<sub>31</sub> 1.948(2), C<sub>1</sub>–C<sub>2</sub> 1.439(2), C<sub>2</sub>–C<sub>3</sub> 1.393(2), C<sub>3</sub>–C<sub>4</sub> 1.444(2), C<sub>4</sub>–C<sub>5</sub> 1.425(2), C<sub>5</sub>–C<sub>6</sub> 1.427(2), C<sub>6</sub>–C<sub>1</sub> 1.422(2), C<sub>31</sub>–O<sub>1</sub> 1.177(2); **17** Mo<sub>1</sub>–C<sub>arene</sub>(ave.) 2.284(5), Mo<sub>1</sub>–C<sub>31</sub> 1.886(5), C<sub>1</sub>–C<sub>2</sub> 1.486(6), C<sub>2</sub>–C<sub>3</sub> 1.337(7), C<sub>3</sub>–C<sub>4</sub> 1.507(6), C<sub>4</sub>–C<sub>5</sub> 1.474(6), C<sub>5</sub>–C<sub>6</sub> 1.381(6), C<sub>6</sub>–C<sub>1</sub> 1.475(6), C<sub>31</sub>–O<sub>1</sub> 1.240(5).

With both solid-state and spectroscopic support for a highly activated CO ligand, **17** was treated with a variety of electrophiles. Unfortunately, even at low temperature, **17** exclusively undergoes outer-sphere electron transfer, returning oxidation product **16** in reactions with either acids or silyl electrophiles. In an attempt to both moderate the reduction potential of **17** and generate **3**, a species known to undergo electrophilic functionalization at the carbonyl oxygens, carbonylation was targeted. Addition of an atmosphere of CO gas resulted in no change, even over the course of days, aside from slow oxidation back to **16**. Anticipating that the intercalated potassium atoms may be prohibiting CO binding to Mo, **17**-<sup>13</sup>CO was treated with an excess of benzo-15-crown-5, resulting in a significant broadening of the <sup>31</sup>P and <sup>13</sup>C

resonances. Addition of 1 atmosphere of  $^{13}\text{CO}$  resulted in significant oxidation to **16- $^{13}\text{CO}$** , a color change to deep green, and formation of a colorless precipitate. It is possible that introduction of CO and crown leads to oxocarbon dianion formation; there is precedent for metal-free coupling of this type under similar conditions.<sup>66</sup> Whether or not this is the operative oxidation pathway, regeneration of the desired species (**3- $^{13}\text{CO}$** ) was not achieved.

## CONCLUSION

Crystallography, isotopic labeling, kinetics, spectroscopy, and computation have provided insight into the mechanism by which Mo-bound CO molecules can be cleaved and coupled to a C<sub>2</sub>O<sub>1</sub> product at a single metal center supported by a terphenyl diphosphine ligand. When dianion **3** is treated with Me<sub>3</sub>SiCl, a bis(siloxycarbyne) complex is formed, the first example of Mo supporting such a motif. This species can either undergo C–C coupling—forming a bis(siloxy)acetylene adduct of Mo, a two electron CO coupling product—or it can undergo C–O cleavage. Kinetics and isotopic labeling studies are consistent with two mechanisms, one involving rate determining siloxide dissociation, the second silyl electrophile dissociation followed by fast siloxide loss. An anionic Mo-siloxycarbyne/CO species indeed undergoes C–O cleavage at low temperatures and demonstrates that scission of this bond is more facile from a mono- rather than bis-silylated species.

The carbide resulting from C–O bond cleavage is trapped rapidly in the presence of excess electrophile at the temperatures required to break the C–O bond, giving a *pseudo*-octahedral silylalkylidyne complex. Further warming results in rearrangement to the thermodynamic product, a sterically preferred five-coordinate isomer lacking a metal-arene interaction. Reduction of this species at low temperature provides evidence for a mixed dicarbyne, which undergoes C–C bond formation at temperatures as low as -60 °C, releasing the silylethynolate fragment and binding dinitrogen to give the final product **5**.

Combined, the findings above provide valuable insight into the use of coordinatively flexible, redox noninnocent ligand scaffolds for multi-electron small molecule transformations. The adaptive binding of the arene plays a central role in the stabilization of unique molecular motifs throughout the reaction scheme—ranging from an extremely reducing trianion to high-valent molybdenum complexes bearing Mo–C multiple bonds: dicarbyne, carbide, and alkylidyne complexes. Phosphine arm hemilability is likewise critical for accessing the highly reduced species. Work to tune the selectivity and expand

the scope of this reductive functionalization chemistry to other electrophiles and small molecule substrates is ongoing.

This work establishes a series of design elements for monometallic complexes for applications toward multi-electron bond breaking and bond making small molecule transformations. A supporting ligand capable of storing reducing equivalents in a pendant arene facilitates the activation and cleavage of the strong C–O bond to generate an intermediate Mo-carbide. C–C coupling is facilitated by silylation and reduction. This combination of bond breaking, bond forming, and organic product release is unprecedented for a homogeneous system. An adaptive coordination environment is instrumental in supporting the diverse moieties characterized in this work. The transformations observed here provide precedent relevant to the conversion chemistry of oxygenated C<sub>1</sub> feedstocks to partially deoxygenated C<sub>2</sub> products, showcasing multi-electron reactions at a single metal site.

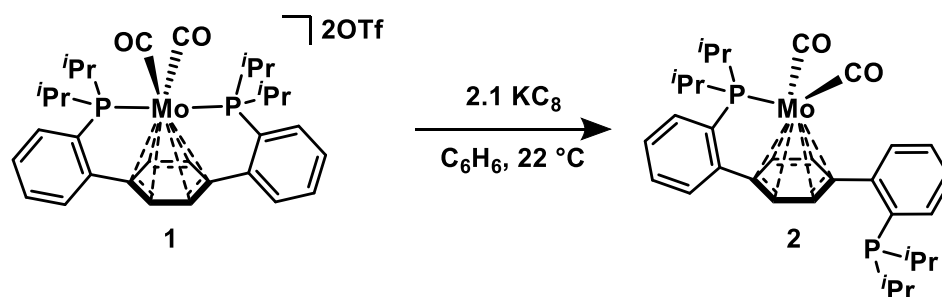
## EXPERIMENTAL SECTION

### *General Considerations*

Unless otherwise specified, all operations were carried out in an MBraun drybox under a nitrogen atmosphere or using standard Schlenk and vacuum line techniques. Pre-reduced Teflon-coated stir bars (prepared via stirring a Na[C<sub>10</sub>H<sub>8</sub>] solution overnight followed by rinsing three times with THF) were utilized in any stirred reaction in which KC<sub>8</sub>, K[C<sub>10</sub>H<sub>8</sub>], Na[C<sub>10</sub>H<sub>8</sub>], **3**, or **4** were employed as reagents. Solvents for air- and moisture-sensitive reactions were dried over sodium benzophenone ketyl, calcium hydride, or by the method of Grubbs.<sup>67</sup> Deuterated solvents were purchased from Cambridge Isotope Laboratories and vacuum transferred from sodium benzophenone ketyl. Solvents, once dried and degassed, were vacuum transferred directly prior to use or stored under inert atmosphere over 4 Å molecular sieves. Dicarbonyl dication **1**,<sup>43</sup> P<sub>2</sub>Mo(MeCN)<sub>2</sub><sup>2OTf</sup>,<sup>43</sup> potassium graphite (KC<sub>8</sub>),<sup>68</sup> (*Z*)-((2-bromovinyl)oxy)triisopropylsilane,<sup>69</sup> and tetrabutylammonium fluoride (tBu<sub>4</sub>NF)<sup>70</sup> were prepared and purified according to literature procedures. Unless indicated otherwise, all other chemicals were utilized as received. Silver trifluoromethanesulfonate (triflate), graphite (325 mesh), *n*-butyl lithium (2.5 M in hexanes), and trimethylsilyl chloride (dried over CaH<sub>2</sub> and distilled prior to use) were purchased from Alfa Aesar. Sodium tetraphenyl borate (dried under vacuum at 50 °C, 12h), naphthalene (sublimed under reduced pressure at 40 °C), potassium metal, diisopropyl amine (dried over CaH<sub>2</sub> and distilled prior to use), hexafluorobenzene (dried over CaH<sub>2</sub> and distilled prior to use), and tetrabutylammonium cyanide (dried under vacuum at 40 °C, 12h) were all purchased from Sigma Aldrich. <sup>13</sup>CO gas was purchased from Monsanto Research. Triisopropylsilyl chloride (dried over CaH<sub>2</sub> and distilled prior to use) was purchased from Oakwood Chemicals. <sup>1</sup>H, <sup>13</sup>C{<sup>1</sup>H}, and <sup>31</sup>P{<sup>1</sup>H} NMR spectra were recorded on Varian Mercury 300 MHz, Varian 400 MHz, Bruker Ascend 400 MHz (equipped with a Prodigy Cryoprobe), or Varian INOVA-500 spectrometers with shifts reported in parts per million (ppm). <sup>1</sup>H and <sup>13</sup>C{<sup>1</sup>H} NMR spectra are referenced to

residual solvent peaks.  $^{71}\text{P}\{^1\text{H}\}$  chemical shifts are referenced to an external 85%  $\text{H}_3\text{PO}_4$  (0 ppm) standard. Multiplicities are abbreviated as follows: s = singlet, d = doublet, dd = doublet of doublets, t = triplet, vt = virtual triplet, sext = sextet, sept d = septet of doublets, m = multiplet, and br = broad. Fourier transform infrared ATR spectra were collected from thin films or powders on a Thermo Scientific Nicolet iS5 Spectrometer with a diamond ATR crystal (utilized iD5 ATR insert). Elemental analysis was conducted by Robertson Microlit Laboratories, Inc. (Ledgewood, NJ) or Midwest Microlabs, LLC (Indianapolis, IN).

### Synthesis of **2**

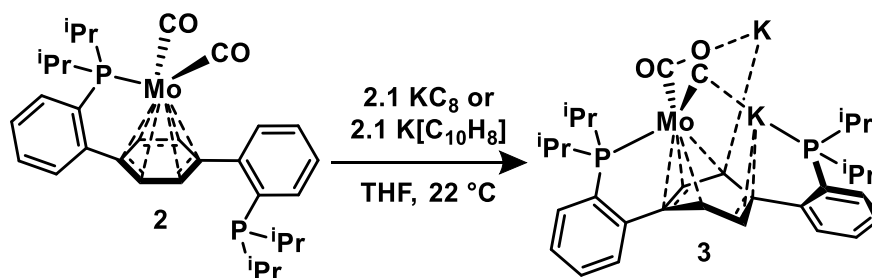


To a vigorously stirring suspension of **1** (200 mg, 0.217 mmol) in  $\text{C}_6\text{H}_6$  (10 mL), solid  $\text{KC}_8$  (62 mg, 0.456 mmol) was added in a single portion, resulting in an immediate darkening of the mixture. Stirring continued for 30 minutes at which time the solution was filtered through a Celite plug. The deep yellow filtrate was lyophilized, providing **2** as a yellow powder (120 mg, 0.195 mmol, 90 %). Diffusion of pentane into a saturated  $\text{C}_6\text{H}_6$  solution of **2** provided single crystals suitable for X-ray diffraction.  $^1\text{H}$  NMR (400 MHz,  $\text{C}_6\text{D}_6$ , 25 °C)  $\delta$ : 7.98-8.03 (m, 1H, aryl-*H*), 7.24-7.29 (m, 1H, aryl-*H*), 7.01-7.07 (m, 2H, aryl-*H*), 6.86-6.96 (m, 4H, aryl-*H*), 5.41 (d,  $J = 5.66$  Hz, 2H, central arene-*H*), 4.52 (dd,  $J = 6.11$ , 1.87 Hz, 2H, central arene-*H*), 2.18-2.30 (m, 2H,  $\text{CH}(\text{CH}_3)_2$ ), 1.83-1.94 (sept d,  $J = 6.97$ , 1.90 Hz, 2H,  $\text{CH}(\text{CH}_3)_2$ ), 1.18 (dd,  $J = 16.54$ , 6.84 Hz, 6H,  $\text{CH}(\text{CH}_3)_2$ ), 1.03 (dd,  $J = 14.87$ , 7.05 Hz, 6H,  $\text{CH}(\text{CH}_3)_2$ ), 0.91 (dd,  $J = 8.73$ , 6.98 Hz, 6H,  $\text{CH}(\text{CH}_3)_2$ ), 0.87 (t,  $J = 7.19$  Hz, 6H,  $\text{CH}(\text{CH}_3)_2$ ).  $^{13}\text{C}\{^1\text{H}\}$  NMR (101 MHz,  $\text{C}_6\text{D}_6$ , 25 °C)  $\delta$ : 228.5 (d,  $J = 11.63$  Hz, CO), 147.11 (d,  $J = 27.80$  Hz, aryl-C), 146.60 (d,  $J = 21.84$  Hz, aryl-C), 145.89 (d,  $J =$

27.80 Hz, aryl-C), 136.21 (d,  $J = 21.64$  Hz, aryl-C), 135.97 (d,  $J = 4.73$  Hz, aryl-C), 131.78 (d,  $J = 3.44$  Hz, aryl-C), 129.37 (d,  $J = 1.06$  Hz, aryl-C), 129.34 (d,  $J = 2.13$  Hz, aryl-C), 129.20 (s, aryl-C), 127.47 (s, aryl-C), 127.34 (s, aryl-C), 127.23 (s, aryl-C), 123.54 (d,  $J = 3.54$  Hz, central arene-C), 108.53 (dd,  $J = 9.33, 3.35$  Hz, central arene-C), 92.30 (dd,  $J = 5.52, 1.35$  Hz, central arene-C), 82.34 (d,  $J = 2.21$  Hz, central arene-C), 28.57 (d,  $J = 21.46$ , CH(CH<sub>3</sub>)<sub>2</sub>), 25.27 (d,  $J = 14.89$ , CH(CH<sub>3</sub>)<sub>2</sub>), 20.71 (d,  $J = 19.85$ , CH(CH<sub>3</sub>)<sub>2</sub>), 19.97 (d,  $J = 10.94$ , CH(CH<sub>3</sub>)<sub>2</sub>), 18.97 (d,  $J = 6.06$ , CH(CH<sub>3</sub>)<sub>2</sub>), 18.87 (d,  $J = 0.99$ , CH(CH<sub>3</sub>)<sub>2</sub>). <sup>31</sup>P{<sup>1</sup>H} NMR (162 MHz, C<sub>6</sub>D<sub>6</sub>, 25 °C)  $\delta$ : 92.33 (s, Mo-P), -7.32 (s). IR (THF cast thin film, cm<sup>-1</sup>)  $\nu_{\text{CO}}$ : 1887, 1832. Anal. Calcd. for **2** C<sub>32</sub>H<sub>40</sub>MoO<sub>2</sub>P<sub>2</sub> (%): C, 62.54; H, 6.56; N, 0.00 Found: C, 62.75; H, 6.68; N, <0.02.

**2**-<sup>13</sup>CO was prepared analogously starting from **1**-<sup>13</sup>CO; the enhanced resonance in the <sup>13</sup>C{<sup>1</sup>H} NMR spectrum is the doublet at 228.5 ppm and the <sup>31</sup>P{<sup>1</sup>H} NMR signal at 92.33 ppm is split into a triplet ( $J = 11.46$  Hz). IR (THF cast thin film, cm<sup>-1</sup>)  $\nu_{13\text{CO}}$ : 1847, 1793.

### Synthesis of **3**



Method A (KC<sub>8</sub>): To a stirring yellow solution of **2** in THF, KC<sub>8</sub> was added as a solid in a single portion, resulting in an immediate color change to dark red. Stirring continued for 10 minutes, at which time the mixture was filtered through a Celite plug. The burgundy filtrate was dried *in vacuo*, providing a tacky residue. Trituration with hexanes and removal of the volatiles under reduced pressure gave **3** as a red powder. X-ray quality crystals of **3** were obtained via chilling a saturated THF/pentane (3:1) mixture of **3** (-35 °C).

Method B (K[C<sub>10</sub>H<sub>8</sub>]): To a stirring yellow solution of **2** in THF, a deep green K[C<sub>10</sub>H<sub>8</sub>] solution in THF was added dropwise. With added reductant, the yellow color gave way



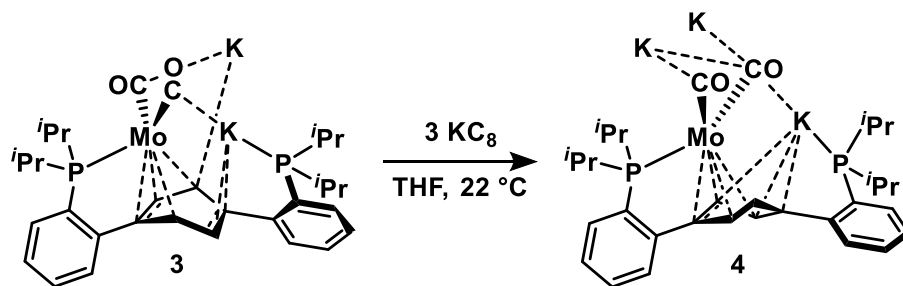
to a persistent deep red. Following complete addition, stirring continued for 45 minutes, at which time volatiles were removed *in vacuo*. The resulting red residue was triturated with hexanes and dried. Addition of hexanes suspended the red solids, which were collected on a fritted funnel. Washing of the filter cake with a mixture of hexanes and benzene (1:1) and collection of the solids provided **3** as a red powder.

Due to the extreme air and moisture sensitivity of **3**, its preparation is recommended in small batches. All samples of **3** were stored in the solid state at -35 °C.

$^1\text{H}$  NMR (400 MHz,  $\text{THF-}d_8$ , 25 °C)  $\delta$ : 7.17 (br s, 2H, aryl-*H*), 7.04 (br s, 2H, aryl-*H*), 6.86-6.93 (br m, 2H, aryl-*H*), 6.64 (br s, 1H, aryl-*H*), 6.36 (br s, 1H, central arene-*H*), 5.62-5.70 (br m, 2H, central arene-*H*), 5.31 (br s, 1H, central arene-*H*), 2.14 (br m, 4H,  $\text{CH}(\text{CH}_3)_2$ ), 0.74-1.19 (br m, 24H,  $\text{CH}(\text{CH}_3)_2$ ).  $^{31}\text{P}\{^1\text{H}\}$  NMR (162 MHz,  $\text{THF-}d_8$ , 25 °C)  $\delta$ : 104.62 (s, Mo-P), 102.47 (br s, Mo-P), -0.03 (s), -2.66 (s). IR (powder sample, diamond ATR,  $\text{cm}^{-1}$ )  $\nu_{\text{CO}}$ : 1657, 1570. The broad NMR and IR spectra of **3** are attributed to fluxionality between oligomeric forms in solution. Anal. Calcd. for **3**  $\text{C}_{32}\text{H}_{40}\text{K}_2\text{MoO}_2\text{P}_2$  (%): C, 55.48; H, 5.82; N, 0.00. Found: C, 54.38; H, 6.03; N, <0.02. Duplicate samples analyzed at different laboratories failed to provide satisfactory combustion analysis results, likely due to the presence of trace oxygen ( $\geq 20$  ppm) in the gloveboxes at these facilities.

**3- $^{13}\text{C}$ O** was prepared analogously starting from **2- $^{13}\text{C}$ O**; the isotopically enhanced carbonyl carbons resonated as broad signals at 263.80 and 245.67 ppm and at 265.87, 260.90, 246.04, and 243.85 ppm in the 25 °C  $^{13}\text{C}\{^1\text{H}\}$  and -80 °C  $^{13}\text{C}\{^1\text{H}\}$  NMR spectra, respectively. IR (powder sample, diamond ATR,  $\text{cm}^{-1}$ )  $\nu_{^{13}\text{C}\text{O}}$ : 1621, 1534.

*Synthesis of 4*



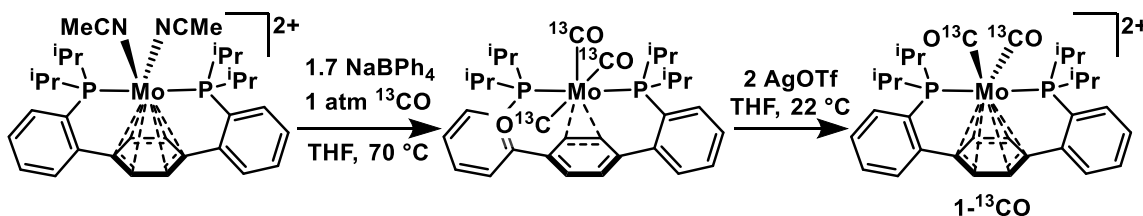
To a stirring red solution of **3** (107 mg, 0.117 mmol) in THF (6 mL),  $\text{KC}_8$  (48 mg, 0.351 mmol) was added as a solid in a single portion, resulting in an immediate color change to deep purple. Stirring continued for 30 minutes, at which time the mixture was filtered through a Celite plug. The filtrate was concentrated *in vacuo* to *ca.* 1 mL, layered with pentane (10 mL), and chilled ( $-35\text{ }^\circ\text{C}$ ) for 16 hours. Filtration, collection of the solids, and removal of residual volatiles under reduced pressure provided **4** as purple microcrystals (98 mg, 0.096 mmol, 82%). Single crystals of **4** suitable for X-ray diffraction were obtained via chilling a saturated THF/pentane (3:1) mixture ( $-35\text{ }^\circ\text{C}$ ).

Due to the extreme air and moisture sensitivity of **4**, its preparation is recommended in small batches. All samples of **4** were stored in the solid state at  $-35\text{ }^\circ\text{C}$ .

Anal. Calcd. for **4**  $\text{C}_{48}\text{H}_{71}\text{K}_3\text{MoO}_6\text{P}_2$  (%): C, 52.52; H, 5.51; N, 0.00. Found: C, 54.33; H, 6.24; N, <0.02. These CHN combustion analysis results are in agreement with those expected for  $\text{4}\cdot\text{THF}1.5$ : C, 54.40; H, 6.13; N, 0.00.

$\text{4-}^{13}\text{CO}$  was prepared analogously starting from  $\text{3-}^{13}\text{CO}$ .

*Synthesis of 1- $^{13}\text{C}$ O*



To a 500 mL Schlenk tube charged with a stir bar,  $\text{P}_2\text{Mo}(\text{MeCN})_2^{2\text{OTf}}$  (2.3 g, 2.45 mmol), and  $\text{NaBPh}_4$  (1.4 g, 4.09 mmol), THF (120 mL) was added via cannula. Stirring was

initiated, providing a purple/green heterogeneous mixture. The contents of the Schlenk were freeze-pump-thawed thrice, and  $^{13}\text{CO}$  (1 atm, *ca.* 14.3 mmol) was admitted to the reaction vessel. The Schlenk was sealed, heated to 70 °C, and stirred for 48 hours, resulting in the formation of a deep orange homogeneous solution. Volatiles were removed *in vacuo*, giving an orange residue. Addition of pentane (100 mL) via cannula, sonication, and filtration provided  $\text{P}_2\text{Mo}(^{13}\text{CO})_3$  as an orange powder (1.35 g, 2.1 mmol, 86 %). Spectral features of  $\text{P}_2\text{Mo}(^{13}\text{CO})_3$  match those reported for  $\text{P}_2\text{Mo}(\text{CO})_3$ ,<sup>43</sup> except the triplets in the  $^{13}\text{C}\{^1\text{H}\}$  NMR at 221.15 and 213.75 ppm are enhanced and the  $^{31}\text{P}\{^1\text{H}\}$  NMR resonance at 51.01 ppm is split into a quartet ( $J = 9.33$  Hz).

From  $\text{P}_2\text{Mo}(^{13}\text{CO})_3$ ,  $\mathbf{1}\text{-}^{13}\text{CO}$  can be prepared via the procedure reported for the  $^{12}\text{CO}$  isotopolog in comparable yield.<sup>43</sup> Spectral features of  $\mathbf{1}\text{-}^{13}\text{CO}$  match those of  $\mathbf{1}$ , except the  $^{13}\text{C}\{^1\text{H}\}$  resonance at 219.03 ppm is enhanced, the  $^{31}\text{P}\{^1\text{H}\}$  NMR resonance at 75.05 ppm is split into a triplet ( $J = 23.75$  Hz), and the IR stretches (powder sample, diamond ATR,  $\text{cm}^{-1}$ ) for the carbonyl ligands shift:  $\nu_{12\text{CO}}$ : 2044, 1989;  $\nu_{13\text{CO}}$ : 1999, 1946.

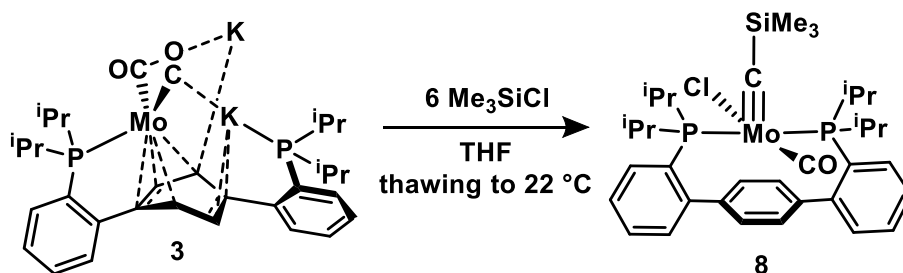
#### Synthesis of **6a**



**6a** was prepared via a modified literature procedure for the synthesis of trialkylsilyloxyethyne derivatives.<sup>69</sup> An oven-dried Schlenk flask, charged with a stir bar, was cooled to ambient temperature under vacuum. The flask was backfilled with argon and THF (50 mL) and freshly distilled diisopropyl amine (1.05 mL, 7.49 mmol) were added via cannula and syringe, respectively. The reaction vessel was cooled to 0 °C with stirring and  $n\text{BuLi}$  (3 mL, 2.5 M in hexanes, 7.50 mmol) was added via syringe. After stirring for 15 minutes, a solution of (*Z*)-(2-bromovinyl)triisopropylsilane (1.00 g, 3.58 mmol) in THF (10 mL) was added via cannula. Stirring at 0 °C continued for 75 minutes.

At this time, the flask was cooled to  $-78\text{ }^{\circ}\text{C}$  and  $\text{tPr}_3\text{SiCl}$  (1.5 mL, 7.01 mmol) was added via syringe. Stirring continued for 10 minutes at  $-78\text{ }^{\circ}\text{C}$  at which point the flask was removed from the bath and allowed to warm to room temperature. Volatiles were removed under reduced pressure, providing a mixture of off-white solids and a yellow oil. This mixture was separated via Kugelrohr distillation ( $85\text{ }^{\circ}\text{C}$ , 0.01 mm Hg), giving **6a** as a colorless oil (685 mg, 1.93 mmol, 54 %).  $^1\text{H}$  NMR (500 MHz,  $\text{CDCl}_3$ ,  $25\text{ }^{\circ}\text{C}$ )  $\delta$ : 1.30 (sext,  $J = 7.42\text{ Hz}$ , 1H,  $\text{CH}(\text{CH}_3)_3$ ), 1.14 (d,  $J = 7.42\text{ Hz}$ , 6H,  $\text{CH}(\text{CH}_3)_3$ ), 1.04 (d,  $J = 6.91\text{ Hz}$ , 6H,  $\text{CH}(\text{CH}_3)_3$ ), 0.98 (sext,  $J = 6.91\text{ Hz}$ , 1H,  $\text{CH}(\text{CH}_3)_3$ ).  $^{13}\text{C}\{^1\text{H}\}$  NMR (125 MHz,  $\text{C}_6\text{D}_6$ ,  $25\text{ }^{\circ}\text{C}$ )  $\delta$ : 108.27 (s, OCCSi), 25.18 (s, OCCSi), 18.86 (br s,  $\text{CH}(\text{CH}_3)_3$ ), 17.46 (br s,  $\text{CH}(\text{CH}_3)_3$ ), 12.02 (s,  $\text{CH}(\text{CH}_3)_3$ ), 11.92 (s,  $\text{CH}(\text{CH}_3)_3$ ).

#### Synthesis of **8**

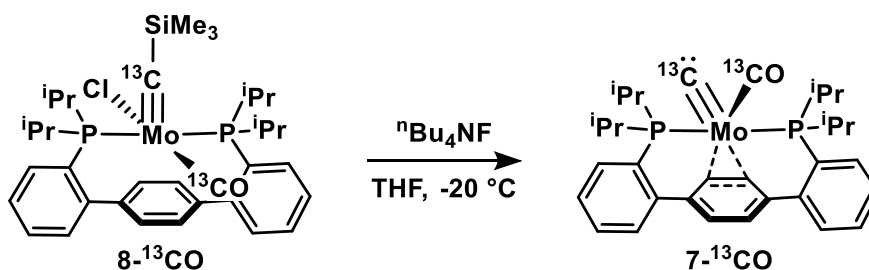


A 20 mL scintillation vial was charged with **3** (200 mg, 0.220 mmol), THF (7 mL), and a stir bar. The resulting deep red solution was frozen in a liquid nitrogen-cooled cold well. A second 20 mL scintillation vial was charged with a  $\text{Me}_3\text{SiCl}$  (188 mg, 1.73 mmol) solution in THF (3 mL) and likewise frozen. Immediately upon thawing, the  $\text{Me}_3\text{SiCl}$  solution was added dropwise to a thawing and stirring solution of **3**. Stirring at room temperature continued for 20 minutes, during which time the solution lightened to a red/orange. At this time, volatiles were removed *in vacuo*. The resulting red residue was triturated with 2 mL of hexanes and dried under reduced pressure, providing **8** as a deep red powder (121 mg, 0.172 mmol, 78 %). In all instances, **8** prepared this way contained *ca.* 5% **2** as observed by  $^1\text{H}$  and  $^{31}\text{P}\{^1\text{H}\}$  NMR. Separation was achieved by first washing with cold HMDSO (3 x 2 mL) and then washing with  $\text{C}_6\text{H}_6$  (1 mL). Dissolving the

remaining solids in  $C_6H_6$  (5 mL) and lyophilizing provided analytically pure **8** as a red powder (44 mg, 0.063 mmol, 29 %). X-ray quality crystals were obtained from vapor diffusion of pentane into a saturated  $C_6H_6$  solution of **8**.  $^1H$  NMR (400 MHz,  $C_6D_6$ , 25 °C)  $\delta$ : 7.48-7.51 (m, 2H, aryl-*H*), 7.45 (m, 2H, central arene-*H*), 7.32-7.34 (m, 2H, central arene-*H*), 7.28-7.31 (m, 2H, aryl-*H*), 7.16 (t,  $J = 7.90$  Hz, 2H, aryl-*H*), 7.12 (dt,  $J = 7.27$ , 1.71 Hz, 2H, aryl-*H*), 2.63-2.80 (m, 4H,  $CH(CH_3)_2$ ), 2.02-2.08 (m, 6H,  $CH(CH_3)_2$ ), 1.77-1.82 (m, 6H,  $CH(CH_3)_2$ ), 1.04-1.08 (m, 6H,  $CH(CH_3)_2$ ), 0.86-0.91 (m, 6 H,  $CH(CH_3)_2$ ), 0.11 (s, 9H,  $Si(CH_3)_3$ ).  $^{13}C\{^1H\}$  NMR (101 MHz,  $C_6D_6$ , 25 °C)  $\delta$ : 355.69-356.02 (m,  $CSiMe_3$ ), 247.27-247.56 (m, CO), 148.18 (vt,  $J = 6.85$  Hz, aryl-C), 140.32 (vt,  $J = 2.64$  Hz, aryl-C), 132.61 (s, aryl-C), 132.32 (vt,  $J = 9.96$  Hz, aryl-C), 130.17 (s, aryl-C), 129.59 (vt,  $J = 2.54$  Hz, aryl-C), 129.55 (s, aryl-C), 127.30 (vt,  $J = 2.50$  Hz, aryl-C), 125.07 (vt,  $J = 2.47$ , aryl-C), 36.92 (vt,  $J = 8.36$ ,  $CH(CH_3)_2$ ), 27.74 (vt,  $J = 27.74$ ,  $CH(CH_3)_2$ ), 20.19 (s,  $CH(CH_3)_2$ ), 19.82 (s,  $CH(CH_3)_2$ ), 19.77 (vt,  $J = 5.71$ ,  $CH(CH_3)_2$ ), 18.49 (vt,  $J = 3.49$ ,  $CH(CH_3)_2$ ), 0.11 (s,  $Si(CH_3)_3$ ).  $^{31}P\{^1H\}$  NMR (162 MHz,  $C_6D_6$ , 25 °C)  $\delta$ : 36.63 (s). IR (THF cast thin film,  $cm^{-1}$ )  $\nu_{CO}$ : 1873. Anal. Calcd. for **7**  $C_{35}H_{49}ClMoOP_2Si$  (%): C, 59.44; H, 6.98; N, 0.00 Found: C, 59.16; H, 6.77; N, <0.02.

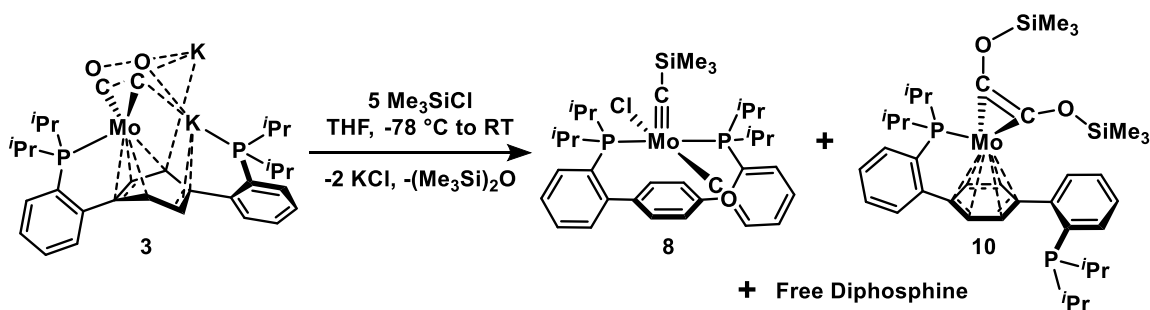
**8- $^{13}CO$**  was prepared analogously starting from **3- $^{13}CO$** ; the enhanced resonances in the  $^{13}C\{^1H\}$  NMR spectrum are the multiplets at 355.85 ppm ( $J_{PC} = 13.25$  Hz,  $J_{CC} = 8.9$  Hz) and 247.42 ( $J_{PC} = 11.35$  Hz,  $J_{CC} = 8.9$  Hz) ppm. The  $^{31}P\{^1H\}$  NMR signal at 36.63 ppm is split into a doublet of doublets ( $J = 13.25$ , 11.35 Hz).

#### Synthesis of **7- $^{13}CO$**



Due to thermal instability, **7-<sup>13</sup>CO** must be prepared *in situ*. In a typical procedure, a J. Young NMR tube was charged with **8-<sup>13</sup>CO** (20 mg, 0.028 mmol) and <sup>n</sup>Bu<sub>4</sub>NF (7.3 mg, 0.028 mmol). The headspace of the NMR tube was evacuated and THF-*d*<sub>8</sub> (0.4 mL) admitted at -196 °C via vacuum transfer. The contents of the J. Young tube were thawed to -80 °C and mixed. Warming to -20 °C in the NMR probe for 15 minutes showed complete conversion to **7-<sup>13</sup>CO** by <sup>13</sup>C{<sup>1</sup>H} and <sup>31</sup>P{<sup>1</sup>H} NMR spectroscopy and solutions prepared this way were re-cooled to -80 °C and used without further manipulation. THF solutions of **7-<sup>13</sup>CO** were stable at -80 °C, but demonstrated decomposition to intractable mixtures when allowed to warm to temperatures exceeding 0 °C. <sup>1</sup>H NMR (500 MHz, THF-*d*<sub>8</sub>, -20 °C) δ: 7.96 (br s, 2H, aryl-*H*), 7.57 (d, *J* = 3.57 Hz, 2H, aryl-*H*), 7.56 (d, *J* = 3.57 Hz, 2H, aryl-*H*), 7.43 (br s, 2H, aryl-*H*), 6.71 (s, 2H, central arene-*H*), 6.46 (br t, *J* = 2.20 Hz, 2H, central arene-*H*), 3.13-3.21 (m, 2H, CH(CH<sub>3</sub>)<sub>2</sub>), 2.45-2.53 (m, 2H, CH(CH<sub>3</sub>)<sub>2</sub>), 1.64-1.68 (m, 6H, CH(CH<sub>3</sub>)<sub>2</sub>), 1.55-1.59 (m, 2H, CH(CH<sub>3</sub>)<sub>2</sub>), 1.02-1.05 (m, 6H, CH(CH<sub>3</sub>)<sub>2</sub>), 0.21-0.26 (m, 6H, CH(CH<sub>3</sub>)<sub>2</sub>). <sup>13</sup>C{<sup>1</sup>H} NMR (125 MHz, THF-*d*<sub>8</sub>, -80 °C) δ: 546.20 (br s, C:), 233.16 (t, *J* = 12.25 Hz, CO), 150.72 (vt, *J* = 7.13 Hz, aryl-C), 139.73 (vt, *J* = 3.85 Hz, aryl-C), 132.69 (vt, *J* = 4.23 Hz, aryl-C), 130.98 (br s, aryl-C), 129.18 (br s, aryl-C), 128.49 (br s, aryl-C), 128.28 (br s, aryl-C), 124.00 (vt, *J* = 8.63 Hz, central arene-C), 86.17 (s, central arene-C), 29.97 (vt, *J* = 8.63 Hz, CH(CH<sub>3</sub>)<sub>2</sub>), 23.53 (br s, CH(CH<sub>3</sub>)<sub>2</sub>), 20.11 (br s, CH(CH<sub>3</sub>)<sub>2</sub>), 17.20 (br s, CH(CH<sub>3</sub>)<sub>2</sub>), 16.77 (br s, CH(CH<sub>3</sub>)<sub>2</sub>). <sup>31</sup>P{<sup>1</sup>H} NMR (202 MHz, THF-*d*<sub>8</sub>, -80 °C) δ: 51.66 (d, *J* = 12.55 Hz). Though decomposition occurred over the course of the experiment, NMR spectra collected at 25 °C demonstrated resolved C–C coupling, splitting the resonances as follows: <sup>13</sup>C{<sup>1</sup>H} NMR (125 MHz, THF-*d*<sub>8</sub>, 25 °C) δ: 546.20 (dd, *J* = 3.46, 3.26 Hz, C:), 233.16 (dd, *J* = 12.55, 3.46 Hz, CO). <sup>31</sup>P{<sup>1</sup>H} NMR (202 MHz, THF-*d*<sub>8</sub>, 25 °C) δ: 51.66 (dd, *J* = 12.55, 3.26 Hz).

*Synthesis of 10*



A Teflon stoppered Schlenk tube was charged with **3** (400 mg, 0.432 mmol), THF (20 mL), and a stir bar. The reaction vessel was placed in a dry ice/acetone bath and with a heavy dinitrogen counterflow, the stopper was replaced with a septum. With rapid stirring, Me<sub>3</sub>SiCl (0.25 mL, 1.970 mmol) was added dropwise via syringe. The flask was stoppered once more and the reaction was left to slowly warm to room temperature over 16 hours, with stirring. At this time, volatiles were removed *in vacuo*, providing a red/brown residue comprised primarily of **8**, **10** (major), and free ligand. This residue was extracted with (Me<sub>3</sub>Si)<sub>2</sub>O (2 mL x 2) to separate the desired product from **8**. The (Me<sub>3</sub>Si)<sub>2</sub>O extract was dried under reduced pressure and subsequently extracted with MeCN. The deep red MeCN solution was filtered through a Celite plug and chilled to -35 °C. Upon standing for 12 hours, a burgundy microcrystalline precipitate formed. These solids were collected via vacuum filtration as a 75:25 mixture of **10** and free diphosphine ligand (53 mg, *ca.* 0.077 mmol, 18%). <sup>1</sup>H NMR (400 MHz, C<sub>6</sub>D<sub>6</sub>, 23 °C) δ: 7.54 (s, 1H, aryl-*H*), 7.22 (v br, 3H, aryl-*H*), 6.96-7.08 (v br, 4H, aryl-*H*), 5.00 (v br, 4H, central arene-*H*), 2.37 (v br, 4H, CH(CH<sub>3</sub>)<sub>2</sub>), 1.14-1.19 (m, 12H, CH(CH<sub>3</sub>)<sub>2</sub>), 1.02-1.07 (m, 12H, CH(CH<sub>3</sub>)<sub>2</sub>), 0.22 (s, 18H, Si(CH<sub>3</sub>)<sub>3</sub>). <sup>13</sup>C{<sup>1</sup>H} NMR (101 MHz, THF, 23 °C) δ: 208.06 (t, *J* = 9.82 Hz, COSiMe<sub>3</sub>), 150.79 (d, *J* = 27.38 Hz, aryl-C), 149.62 (d, *J* = 26.28 Hz, aryl-C), 141.48 (d, *J* = 5.63 Hz, aryl-C), 135.22 (d, *J* = 24.16 Hz, aryl-C), 132.79 (d, *J* = 2.81 Hz, aryl-C), 131.03 (d, *J* = 5.00 Hz, aryl-C), 130.59 (d, *J* = 5.09 Hz, aryl-C), 128.70 (br s, aryl-C), 128.65 (br s, aryl-C), 128.59 (s, aryl-C), 128.46 (v br, aryl-C), 128.35 (br s, aryl-C),

126.77 (s, aryl-C), 126.09 (v br, aryl-C), 77.39 (v br, central arene-C), 74.44 (v br, central arene-C), 25.52 (v br, CH(CH<sub>3</sub>)<sub>2</sub>), 24.93 (d,  $J = 16.46$  Hz, CH(CH<sub>3</sub>)<sub>2</sub>), 20.48 (d,  $J = 20.12$  Hz, CH(CH<sub>3</sub>)<sub>2</sub>), 20.18 (v br, CH(CH<sub>3</sub>)<sub>2</sub>), 19.90 (d,  $J = 11.45$  Hz, CH(CH<sub>3</sub>)<sub>2</sub>), 19.40 (br s, CH(CH<sub>3</sub>)<sub>2</sub>), 0.78 (s, OSi(CH<sub>3</sub>)<sub>3</sub>). <sup>31</sup>P{<sup>1</sup>H} NMR (162 MHz, THF, 23 °C) δ: 84.26 (br s, Mo-P), -4.70 (s). Heating mixtures of **10** and free diphosphine to 70 °C provided <sup>1</sup>H and <sup>13</sup>C{<sup>1</sup>H} NMR spectra in which the broad resonances in the room temperature spectrum are better resolved. A full <sup>13</sup>C{<sup>1</sup>H} NMR spectrum could not be collected at this temperature as the sample began to decompose over the timescale of the experiment. <sup>1</sup>H NMR (400 MHz, C<sub>6</sub>D<sub>6</sub>, 70 °C) δ: 7.48 (br s, 1H, aryl-H), 7.27-7.30 (v br, 2H, aryl-H), 7.19-7.20 (v br, 1H, aryl-H), 7.00-7.06 (br m, 4H, aryl-H), 4.97 (v br, 4H, central arene-H), 2.39 (v br, 4H, CH(CH<sub>3</sub>)<sub>2</sub>), 1.15-1.20 (m, 12H, CH(CH<sub>3</sub>)<sub>2</sub>), 1.04-1.09 (m, 12H, CH(CH<sub>3</sub>)<sub>2</sub>), 0.21 (br s, 18H, Si(CH<sub>3</sub>)<sub>3</sub>). <sup>13</sup>C{<sup>1</sup>H} NMR (101 MHz, THF, 70 °C) δ: 77.04 (v br, central arene-C), 75.56 (v br, central arene-C).

Single crystals of **10** were isolated while attempting to crystallize **9**. The low-temperature crystallization procedure is described below:

A small swivel frit was assembled with a 50 mL round-bottom flask charged with **3** (60 mg, 0.066 mmol) and a small stir bar at one end and a 50 mL round-bottom flask charged with a stir bar at the other. The apparatus was sealed, and evacuated. THF was admitted to the flask containing **3** at -78 °C via vacuum transfer, resulting in a deep red solution. With a heavy argon counterflow, the Teflon pin in the side arm of the swivel frit was replaced with a rubber septum. The septum was pierced with a 12-gauge needle and an 8" section of Teflon cannula was carefully inserted. A Me<sub>3</sub>SiCl (14.3 mg, 0.132 mmol) solution in THF (1 mL) was introduced to the stirring reaction mixture via syringe through the short cannula. The solution lightened slightly upon addition and the Teflon pin was replaced, sealed, and the reaction was left to stir for 20 minutes. Volatiles were removed *in vacuo*, maintaining a temperature between -40 and -78 °C.



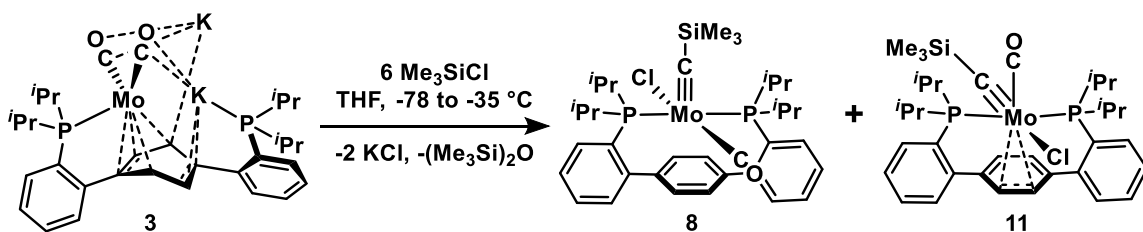
The residue remaining in the flask was dissolved in hexanes, introduced via vacuum transfer at  $-78\text{ }^{\circ}\text{C}$ . The top of the swivel frit (empty 50 mL flask) was pre-cooled with liquid nitrogen and the frit swiveled, utilizing a  $-78/-196\text{ }^{\circ}\text{C}$  temperature gradient to draw the red hexanes solution through the frit. The filtrate was dried under reduced pressure, again maintaining a temperature between  $-40$  and  $-78\text{ }^{\circ}\text{C}$ , providing a red/orange powder.

Butane (20 mL) was condensed into a trap at  $-78\text{ }^{\circ}\text{C}$  and freeze-pump-thawed three times to remove trace oxygen. It was then transferred from the trap ( $-78\text{ }^{\circ}\text{C}$ ) onto the powder ( $-196\text{ }^{\circ}\text{C}$ ), and stirring was initiated. Once the solids had dissolved, stirring was halted. The side-arm pin was once more replaced with a septum which was pierced with a 21-gauge needle. Solvent was evaporated at low temperature ( $-40$  to  $-78\text{ }^{\circ}\text{C}$ ) via evaporation with the aid of a slow argon flow, providing deep red single crystals of **10**.

**10- $^{13}\text{C}$**  can be prepared analogously, starting from **3- $^{13}\text{C}$** . It is also observed spectroscopically in reactions employing **9- $^{13}\text{C}$** ; the enhanced resonance is the acetylenic peak at 208.06 ppm. At room temperature,  $^{31}\text{P}/^{13}\text{C}$  scalar coupling is not resolved in the  $^{31}\text{P}\{\text{H}\}$  nor the  $^{13}\text{C}\{\text{H}\}$  NMR spectra; however, cooling samples containing **10- $^{13}\text{C}$**  to  $-40\text{ }^{\circ}\text{C}$  sharpened the resonances attributable to this species, resolving the  $^2J(\text{P,C}):^{13}\text{C}\{\text{H}\}$  NMR (126 MHz, THF,  $-40\text{ }^{\circ}\text{C}$ )  $\delta$ : 206.74 (d,  $J = 19.57\text{ Hz}$ ,  $\text{COSiMe}_3$ ).  $^{31}\text{P}\{\text{H}\}$  NMR (202 MHz, THF,  $-40\text{ }^{\circ}\text{C}$ )  $\delta$ : 86.21 (t,  $J = 19.57\text{ Hz}$ , Mo-P),  $-5.56$  (s).

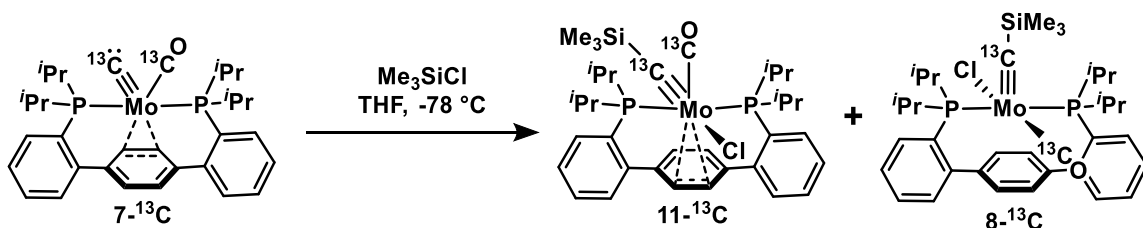
### Synthesis of **11**

Due to conversion to **8**, **11** must be prepared and handled at low temperature. The following two methods were employed:



Method A (from **3**):

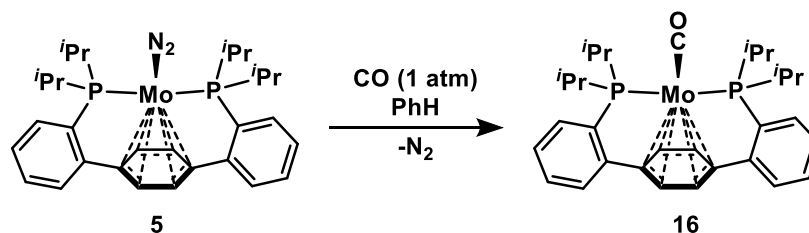
A 20 mL scintillation vial was charged with a deep red solution of **3** (80 mg, 0.088 mmol) in THF (2 mL) and a stir bar. The vial was capped and placed in a liquid nitrogen-cooled cold well. Once the solution had frozen, the vial was removed from the well. While thawing and stirring, Me<sub>3</sub>SiCl (67 μL, 0.528 mmol) was added dropwise via Hamilton syringe. The vial was returned to the cold well, immediately upon completion of the addition and the contents re-frozen. The vial was allowed to thaw with stirring, and this process of low-temperature mixing was repeated three times, at which time the THF solution was frozen a final time. Pre-chilled pentane (10 mL) was layered onto the frozen THF solution and the vial was sealed and placed in a -35 °C freezer. After four days, X-ray quality crystals of a roughly 60:40 mixture of **11** and **8** had formed. <sup>1</sup>H NMR (500 MHz, THF-*d*<sub>8</sub>, -80 °C) δ: 8.11 (br d, *J* = 4.89 Hz, 2H, aryl-*H*), 7.95 (v br, 2H, aryl-*H*), 7.72 (t, *J* = 7.34 Hz, 2H, aryl-*H*), 7.67 (d, *J* = 7.50 Hz, 2H, aryl-*H*), 7.64 (br s, 2H, aryl-*H*), 7.46 (s, 2H, central arene-*H*), 3.56 (v br, 2H, CH(CH<sub>3</sub>)<sub>2</sub>), 3.15 (v br, 2H, CH(CH<sub>3</sub>)<sub>2</sub>), 1.41 (m, 6H, CH(CH<sub>3</sub>)<sub>2</sub>), 1.25 (m, 12H, CH(CH<sub>3</sub>)<sub>2</sub>), -0.84 (s, 9H, Si(CH<sub>3</sub>)<sub>3</sub>). <sup>31</sup>P NMR (202 MHz, THF-*d*<sub>8</sub>, -80 °C) δ: 41.88 (br s).



Method B (from **7-<sup>13</sup>C**):

To a J. Young tube containing *in situ* prepared **7-<sup>13</sup>C** (*ca.* 0.024 mmol) in THF (500 μL) at -78 °C, Me<sub>3</sub>SiCl (14.5 μL, 0.114 mmol) was added via Hamilton syringe with a heavy counterflow of argon. The J. Young tube was sealed and shaken, providing a *ca.* 75:25 mixture of **11-<sup>13</sup>C** and **8-<sup>13</sup>C**. <sup>13</sup>C{<sup>1</sup>H} NMR (126 MHz, THF-*d*<sub>8</sub>, -80 °C) δ: 344.87 (br s, CSiMe<sub>3</sub>), 241.82 (br s, CO). <sup>31</sup>P{<sup>1</sup>H} NMR (202 MHz, THF-*d*<sub>8</sub>, -80 °C) δ: 41.86 (s).

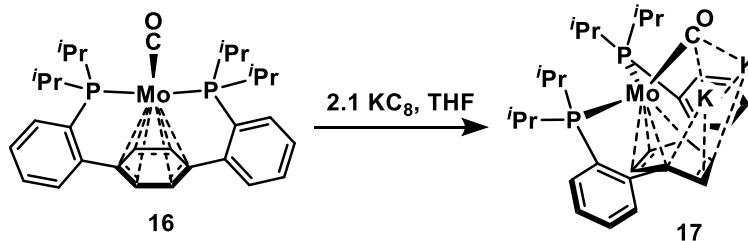
*Synthesis of 18*



A Teflon stoppered Schlenk tube was charged with **5** (200 mg, 0.340 mmol), PhH (10 mL), and a stir bar. The resulting red solution was degassed thoroughly via three freeze-pump-thaw cycles. Following the final thaw, CO (1 atm) was admitted to the headspace of the flask. The stopper was sealed and the reaction left to stir for 1 hr. At this time, the solvent was lyophilized, providing **18** as an orange powder (196 mg, 0.340 mmol, >99%). X-ray quality crystals of **18** were grown by cooling a saturated PhMe solution to -35 °C.  $^1\text{H}$  NMR (400 MHz,  $\text{C}_6\text{D}_6$ , 23 °C)  $\delta$ : 7.39-7.41 (m, 2H, aryl-*H*), 7.16 (br m, 2H, aryl-*H*), 7.00-7.04 (m, 4H, aryl-*H*), 4.60 (br s, 2H, central arene-*H*), 4.59 (br m, 2H, central arene-*H*), 2.40-2.49 (m, 2H,  $\text{CH}(\text{CH}_3)_2$ ), 2.11-2.20 (m, 2H,  $\text{CH}(\text{CH}_3)_2$ ), 1.35-1.41 (m, 6H,  $\text{CH}(\text{CH}_3)_2$ ), 1.07-1.13 (m, 6H,  $\text{CH}(\text{CH}_3)_2$ ), 0.97-1.05 (m, 12H,  $\text{CH}(\text{CH}_3)_2$ ).  $^{13}\text{C}\{^1\text{H}\}$  NMR (101 MHz,  $\text{C}_6\text{D}_6$ , 23 °C)  $\delta$ : 242.58 (t,  $J = 15.19$  Hz, CO), 152.32 (vt,  $J = 12.24$  Hz, aryl-C), 152.02 (vt,  $J = 11.99$  Hz, aryl-C), 130.18 (s, aryl-C), 128.59 (s, aryl-C), 126.70 (vt,  $J = 2.03$  Hz, aryl-C), 97.92 (t,  $J = 2.60$  Hz, central arene-C), 90.21 (s, central arene-C), 76.49 (t,  $J = 1.61$  Hz, central arene-C), 30.53 (vt,  $J = 5.16$  Hz,  $\text{CH}(\text{CH}_3)_2$ ), 29.62 (m,  $\text{CH}(\text{CH}_3)_2$ ), 21.17 (vt,  $J = 4.76$  Hz,  $\text{CH}(\text{CH}_3)_2$ ), 19.88 (vt,  $J = 4.25$  Hz,  $\text{CH}(\text{CH}_3)_2$ ), 19.50 (s,  $\text{CH}(\text{CH}_3)_2$ ), 18.92 (s,  $\text{CH}(\text{CH}_3)_2$ ).  $^{31}\text{P}\{^1\text{H}\}$  NMR (162 MHz,  $\text{C}_6\text{D}_6$ , 23 °C)  $\delta$ : 82.06 (s). IR (powder sample, diamond ATR,  $\text{cm}^{-1}$ )  $\nu_{\text{CO}} = 1798$ .

**18- $^{13}\text{C}$**  was prepared analogously, using  $^{13}\text{CO}$  in lieu of CO; the enhanced resonance in the  $^{13}\text{C}\{^1\text{H}\}$  NMR spectrum is the triplet at 242.60 ppm. The  $^{31}\text{P}\{^1\text{H}\}$  NMR signal at 82.06 ppm splits into a doublet ( $J = 15.91$  Hz). IR (powder sample, diamond ATR,  $\text{cm}^{-1}$ )  $\nu_{^{13}\text{CO}} = 1758$ .

Synthesis of **19**



To a stirring red/orange solution of **18** (250 mg, 0.426 mmol) in THF (10 mL),  $\text{KC}_8$  (121 mg, 0.895 mmol) was added as a solid in a single portion, resulting in an immediate color change to dark brown. Stirring continued for 30 minutes, at which time the mixture was filtered through a Celite plug. The dark red/brown filtrate was dried *in vacuo*, providing a tacky film. Trituration with hexanes (2 x 4 mL) provided a dark brown powder. This powder was suspended in benzene and the solids collected by vacuum filtration. Washing the filter cake with benzene until the rinses were colorless and collection of the solids provided **19** as a red/brown powder (258 mg, 0.281 mmol, 66%--NB: values were calculated using the molecular weight of **19**• $\text{THF}_{3.5}$ ,  $\text{C}_{45}\text{H}_{68}\text{K}_2\text{Mo}_1\text{O}_{4.5}\text{P}_2$ , 917.07 g/mol). X-ray quality crystals were grown via layering pentane onto a saturated THF solution of **19** at  $-35^\circ\text{C}$ .

Due to the extreme air and moisture sensitivity of **19**, its preparation is recommended in small batches. All samples of **19** were stored in the solid state at  $-35^\circ\text{C}$ .

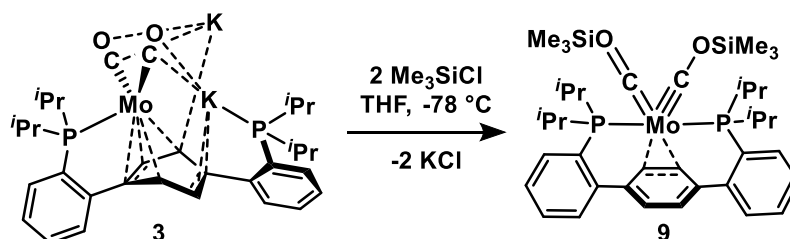
$^1\text{H}$  NMR (400 MHz,  $\text{C}_6\text{D}_6$ ,  $23^\circ\text{C}$ )  $\delta$ : 7.03 (br s, 2H, aryl-*H*), 6.68-6.72 (br m, 4H, aryl-*H*), 6.52 (br t,  $J = 6.49$  Hz, 2H, aryl-*H*), 5.70 (br s, 2H, central arene-*H*), 5.39 (br d,  $J = 10.38$  Hz, 2H, central arene *H*), 2.13-2.19 (m, 2H,  $\text{CH}(\text{CH}_3)_2$ ), 2.06-2.13 (m, 2H,  $\text{CH}(\text{CH}_3)_2$ ), 1.13-1.18 (m, 6H,  $\text{CH}(\text{CH}_3)_2$ ), 1.01-1.07 (br m, 12H,  $\text{CH}(\text{CH}_3)_2$ ), 0.68-0.73 (m,  $\text{CH}(\text{CH}_3)_2$ ).

$^{13}\text{C}$  { $^1\text{H}$ } NMR (101 MHz,  $\text{C}_6\text{D}_6$ ,  $23^\circ\text{C}$ )  $\delta$ : 258.49 (t,  $J = 7.58$  Hz, CO), 160.32 (d vt,  $J = 21.08$ , 1.84 Hz, aryl-C), 144.57 (d vt,  $J = 16.26$ , 1.41 Hz, aryl-C), 127.97 (s, aryl-C), 127.94 (s, aryl-C), 127.38 (br s, aryl-C), 125.77 (br s, aryl-C), 118.28 (br s, aryl-C), 117.3 (d,  $J = 6.54$  Hz, aryl-C), 99.85 (s, central arene-C), 70.94 (t,  $J = 7.40$ , central arene-C), 32.59 (v

br, CH(CH<sub>3</sub>)<sub>2</sub>), 32.41 (br s, CH(CH<sub>3</sub>)<sub>2</sub>), 21.64 (d,  $J = 2.96$  Hz, CH(CH<sub>3</sub>)<sub>2</sub>), 21.55 (s, CH(CH<sub>3</sub>)<sub>2</sub>), 21.46 (br s, CH(CH<sub>3</sub>)<sub>2</sub>), 19.90 (br d,  $J = 2.13$  Hz, CH(CH<sub>3</sub>)<sub>2</sub>). <sup>31</sup>P{<sup>1</sup>H} NMR (162 MHz, C<sub>6</sub>D<sub>6</sub>, 23 °C) δ: 114.09 (br s). IR (THF cast thin film, cm<sup>-1</sup>) ν<sub>CO</sub> = 1507.

**19-<sup>13</sup>C** can be prepared analogously starting from **18-<sup>13</sup>C**; the isotopically enhanced carbonyl carbon resonates as a triplet at 258.5 ppm (<sup>13</sup>C{<sup>1</sup>H} NMR, 101 MHz, THF-*d*<sub>8</sub>, 23 °C). No additional coupling is resolved in the <sup>31</sup>P{<sup>1</sup>H} NMR spectrum. IR (THF cast thin film, cm<sup>-1</sup>) ν<sub>13CO</sub> = 1461.

#### *In Situ* Preparation of **9-<sup>13</sup>C**



Due to thermal instability, **9-<sup>13</sup>C** must be prepared *in situ*. In a typical procedure, a J. Young NMR tube was charged with solid **3-<sup>13</sup>C** (25 mg, 0.027 mmol). The tube was evacuated, and THF-*d*<sub>8</sub> (ca. 300 μL) was admitted via vacuum transfer at -196 °C. The contents of the J. Young tube were warmed to room temperature and mixed thoroughly, providing a deep red solution. This solution was immersed in liquid nitrogen and THF-*d*<sub>8</sub> (ca. 100 μL) was again added to the reaction via vacuum transfer. Me<sub>3</sub>SiCl (33.4 mL at 3.1 cm Hg, 0.57 mmol) was then condensed into the reaction from a calibrated gas volume. The tube was sealed and carefully thawed to -78 °C, avoiding mixing of the layers as much as possible (the bottom of the tube must be kept coldest to prevent bumping). Upon thawing, the tube was shaken vigorously to mix and immediately refrozen. Samples prepared this way show 80-90% conversion to the desired product, but minor oxidation to **2-<sup>13</sup>C** typically occurs, as does some formation of bis(siloxy)acetylene **10-<sup>13</sup>C**. Solutions of **9-<sup>13</sup>C** were used for spectroscopic studies without further manipulation. At low temperatures, these samples are stable for hours, but show slow conversion to **10-<sup>13</sup>C**.

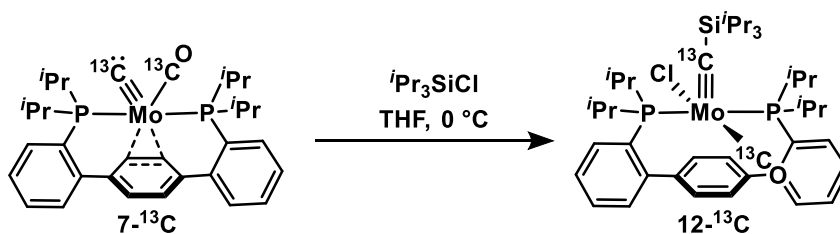
Upon warming, **9**-<sup>13</sup>C converts to a mixture of **2**-<sup>13</sup>C, **8**-<sup>13</sup>C, and **11**-<sup>13</sup>C as observed by multinuclear NMR. <sup>1</sup>H NMR (500 MHz, THF-*d*<sub>8</sub>, -80 °C) δ: 7.96 (br s, 2H, aryl-*H*), 7.67 (br s, 2H, aryl-*H*), 7.55 (br s, 2H, aryl-*H*), 7.50 (br s, 2H, aryl-*H*), 7.08 (br s, 2H, central arene-*H*), 6.24 (br s, 2H, central arene-*H*), 2.97 (br m, 2H, CH(CH<sub>3</sub>)<sub>2</sub>), 2.23 (br m, 2H, CH(CH<sub>3</sub>)<sub>2</sub>), 1.51 (br m, 6H, CH(CH<sub>3</sub>)<sub>2</sub>), 1.27-1.33 (br m, 12H, CH(CH<sub>3</sub>)<sub>2</sub>), 0.57 (br m, 6H, CH(CH<sub>3</sub>)<sub>2</sub>), 0.18 (br s, 9H, COSi(CH<sub>3</sub>)<sub>3</sub>), -0.43 (br s, 9H, COSi(CH<sub>3</sub>)<sub>3</sub>). <sup>13</sup>C{<sup>1</sup>H} NMR (126 MHz, THF-*d*<sub>8</sub>, -80 °C) δ: 284.27 (br s, Mo≡COSi), 274.35 (br s, Mo≡COSi), 149.59 (br s, aryl-*C*), 138.31 (br s, aryl-*C*), 133.27 (br s, aryl-*C*), 129.56 (br s, aryl-*C*), 128.84 (br s, aryl-*C*), 128.63 (v br, aryl-*C*), 127.40 (br s, aryl-*C*), 126.02 (v br, central arene-*C*), 90.15 (v br, central arene-*C*), 36.19 (v br, CH(CH<sub>3</sub>)<sub>2</sub>), 29.86 (v br, CH(CH<sub>3</sub>)<sub>2</sub>), 18.67 (v br, CH(CH<sub>3</sub>)<sub>2</sub>), 18.53 (v br, CH(CH<sub>3</sub>)<sub>2</sub>), -0.31 (v br, COSi(CH<sub>3</sub>)<sub>3</sub>), -0.47 (v br, COSi(CH<sub>3</sub>)<sub>3</sub>). <sup>31</sup>P{<sup>1</sup>H} NMR (202 MHz, THF-*d*<sub>8</sub>, -80 °C) δ: 66.48 (br t, *J* = 17.32 Hz).

Cooling the sample further resolves the <sup>2</sup>*J*(P,C) of the carbyne carbons: <sup>13</sup>C{<sup>1</sup>H} NMR (126 MHz, THF-*d*<sub>8</sub>, -100 °C) δ: 284.10 (br t, *J* = 14.26 Hz, Mo≡COSi), 273.84 (t, *J* = 23.05 Hz, Mo≡COSi).

Though **9**-<sup>13</sup>C began to react, the NMR spectra collected at -20 °C were consistent with two siloxycarbyne motifs in a fast exchange regime: <sup>1</sup>H NMR (500 MHz, THF-*d*<sub>8</sub>, -20 °C) δ: 7.90 (br s, 2H, aryl-*H*), 7.61 (br s, 2H, aryl-*H*), 7.49 (br s, 2H, aryl-*H*), 7.45 (br s, 2H, aryl-*H*), 6.71 (br s, 4H, central arene-*H*), 2.59 (v br, 4H, CH(CH<sub>3</sub>)<sub>2</sub>), 1.30 (v br, 12H, CH(CH<sub>3</sub>)<sub>2</sub>), 1.04 (v br, 12H, CH(CH<sub>3</sub>)<sub>2</sub>), -0.09 (br s, 18H, COSi(CH<sub>3</sub>)<sub>3</sub>). <sup>13</sup>C{<sup>1</sup>H} NMR (126 MHz, THF-*d*<sub>8</sub>, -20 °C) δ: 280.79 (br s, Mo≡COSi), 150.11 (br s, aryl-*C*), 138.67 (br s, aryl-*C*), 133.37 (br s, aryl-*C*), 130.74 (br s, aryl-*C*), 129.68 (br s, aryl-*C*), 129.08 (br s, aryl-*C*), 128.74 (v br, aryl-*C*), 127.54 (br s, aryl-*C*), 33.21 (v br, CH(CH<sub>3</sub>)<sub>2</sub>), 20.70 (br s, CH(CH<sub>3</sub>)<sub>2</sub>), 19.09 (br s, CH(CH<sub>3</sub>)<sub>2</sub>), 0.13 (br s, COSi(CH<sub>3</sub>)<sub>3</sub>). <sup>31</sup>P{<sup>1</sup>H} NMR (202 MHz, THF-*d*<sub>8</sub>, -20 °C) δ: 63.97 (t, *J* = 20.37 Hz).

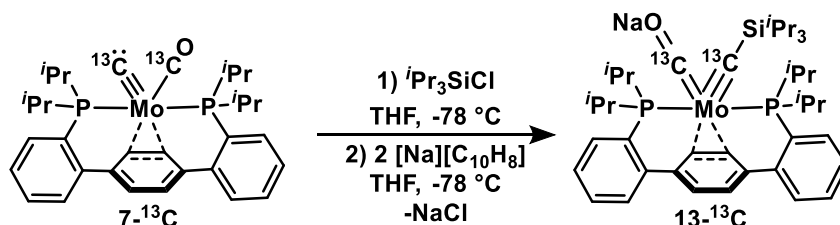
**9-<sup>13</sup>C-*d*<sub>18</sub>** was prepared analogously, substituting Me<sub>3</sub>SiCl-*d*<sub>9</sub> for Me<sub>3</sub>SiCl. These samples were prepared in proteo THF with a C<sub>6</sub>D<sub>6</sub> spike to facilitate study by <sup>2</sup>H NMR spectroscopy. <sup>2</sup>H NMR (76 MHz, THF/C<sub>6</sub>D<sub>6</sub>, -80 °C) δ: -0.1 (v br, COSi(CD<sub>3</sub>)<sub>3</sub>), -0.6 (v br, COSi(CD<sub>3</sub>)<sub>3</sub>).

*In Situ Preparation of 12-<sup>13</sup>C*



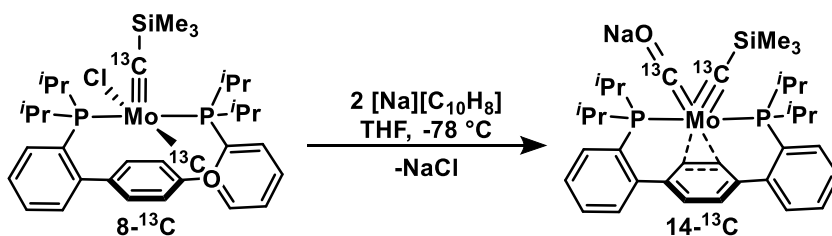
To a J. Young tube containing *in situ* prepared **7-<sup>13</sup>C** (ca. 0.024 mmol) in THF (400 μL) at -78 °C, a THF solution (100 μL) of *i*Pr<sub>3</sub>SiCl (4.6 mg, 0.024 mmol) was added via syringe with a heavy counterflow of argon. The tube was sealed and shaken thoroughly, ensuring the sample remained cold throughout. The J. Young tube was then transferred to an NMR spectrometer pre-cooled to -80 °C. The sample was warmed in the probe, in 10 °C increments. No conversion was observed up to 0 °C. At this temperature, new resonances attributable to **12-<sup>13</sup>C** (*vide infra*) were observed by <sup>13</sup>C{<sup>1</sup>H} and <sup>31</sup>P{<sup>1</sup>H} NMR spectroscopy. Warming was continued and complete consumption of the starting material was observed by 10 °C. <sup>13</sup>C{<sup>1</sup>H} NMR (126 MHz, THF, 0 °C) δ: 360.54 (br dt, CSiMe<sub>3</sub>), 250.55 (br dt, CO). <sup>31</sup>P{<sup>1</sup>H} NMR (202 MHz, THF, 0 °C) δ: 34.44 (s). <sup>13</sup>C{<sup>1</sup>H} NMR (126 MHz, THF, 25 °C) δ: 360.96 (dt, CSiMe<sub>3</sub>), 250.52 (dt, CO). <sup>31</sup>P{<sup>1</sup>H} NMR (202 MHz, THF, 25 °C) δ: 33.95 (s).

*In Situ Preparation of 13-<sup>13</sup>C*



To a J. Young tube containing *in situ* prepared **7-<sup>13</sup>C** (*ca.* 0.028 mmol) in THF (400  $\mu$ L) at -78  $^{\circ}$ C, a THF solution (100  $\mu$ L) of <sup>i</sup>Pr<sub>3</sub>SiCl (10.8 mg, 0.056 mmol) was added via syringe with heavy counterflow of argon. The tube was sealed and the contents mixed, resulting in no noticeable color change. Again, under a heavy counterflow of argon, a deep green THF solution (200  $\mu$ L) of [Na][C<sub>10</sub>H<sub>8</sub>] (0.056 mmol) was added via syringe. The tube was sealed and mixed, ensuring the sample remained cold throughout. The solution darkened to deep maroon. The J. Young tube was then transferred to an NMR spectrometer pre-cooled to -80  $^{\circ}$ C. Complete conversion of the starting material to **13-<sup>13</sup>C** was observed by multinuclear NMR spectroscopy. <sup>13</sup>C{<sup>1</sup>H} NMR (126 MHz, THF, -100  $^{\circ}$ C)  $\delta$ : 326.15 (v br, CSiMe<sub>3</sub> or CONa), 325.82 (v br, CSiMe<sub>3</sub> or CONa). <sup>31</sup>P{<sup>1</sup>H} NMR (202 MHz, THF, -100  $^{\circ}$ C)  $\delta$ : 60.59 (br s). <sup>13</sup>C{<sup>1</sup>H} NMR (126 MHz, THF, -60  $^{\circ}$ C)  $\delta$ : 326.02 (br t, *J* = 19.24 Hz, CSiMe<sub>3</sub> or CONa), 325.32 (br s, CSiMe<sub>3</sub> or CONa). <sup>31</sup>P{<sup>1</sup>H} NMR (202 MHz, THF, -60  $^{\circ}$ C)  $\delta$ : 59.58 (br s).

*In Situ Preparation of 14-<sup>13</sup>C*

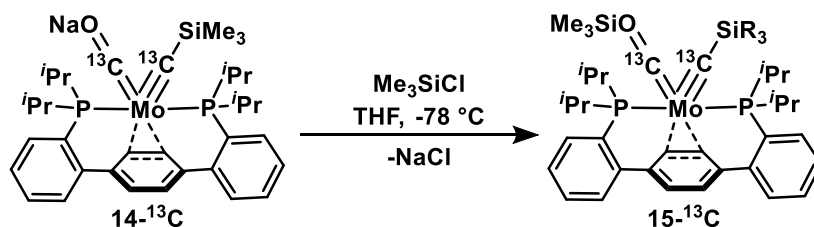


A J. Young tube was charged with homogenous red solution of **8-<sup>13</sup>C** (18 mg, 0.025 mmol) in THF (400  $\mu$ L). The tube was placed in a dry ice/acetone bath and the contents cooled to -78  $^{\circ}$ C; a deep green solution of [Na][C<sub>10</sub>H<sub>8</sub>] (0.059 mmol) in THF (200  $\mu$ L) was added via syringe with a heavy argon counterflow. The J. Young tube was sealed and mixed thoroughly, changing color to reddish purple. It was transferred to an NMR spectrometer pre-cooled to -80  $^{\circ}$ C. Complete conversion of the starting material to **14-<sup>13</sup>C** was observed by multinuclear NMR spectroscopy. <sup>13</sup>C{<sup>1</sup>H} NMR (126 MHz, THF, -100  $^{\circ}$ C)  $\delta$ : 329.20 (br t, *J* = 21.09 Hz, CSiMe<sub>3</sub> or CONa), 327.42 (br, CSiMe<sub>3</sub> or CONa). <sup>31</sup>P{<sup>1</sup>H} NMR (202



MHz, THF,  $-100\text{ }^{\circ}\text{C}$ )  $\delta$ : 57.81 (br s).  $^{13}\text{C}\{^1\text{H}\}$  NMR (126 MHz, THF,  $-80\text{ }^{\circ}\text{C}$ )  $\delta$ : 329.98 (br t,  $J = 19.16\text{ Hz}$ ,  $\text{CSiMe}_3$  and  $\text{CONa}$ ).  $^{31}\text{P}\{^1\text{H}\}$  NMR (202 MHz, THF,  $-80\text{ }^{\circ}\text{C}$ )  $\delta$ : 58.49 (br s).  $^{13}\text{C}\{^1\text{H}\}$  NMR (126 MHz, THF,  $-60\text{ }^{\circ}\text{C}$ )  $\delta$ : 331.81 (br s,  $\text{CSiMe}_3$  or  $\text{CONa}$ ), 330.50 (t,  $J = 20.39\text{ Hz}$ ,  $\text{CSiMe}_3$  or  $\text{CONa}$ ).  $^{31}\text{P}\{^1\text{H}\}$  NMR (202 MHz, THF,  $-60\text{ }^{\circ}\text{C}$ )  $\delta$ : 59.05 (br s).

#### *In Situ Preparation of 15- $^{13}\text{C}$*



A solution of  $14\text{-}^{13}\text{C}$  was prepared in a J. Young NMR tube, as described above, from the reduction of  $8\text{-}^{13}\text{C}$  (20 mg, 0.028 mmol) with  $[\text{Na}][\text{C}_{10}\text{H}_8]$  (0.062 mmol) in THF (600  $\mu\text{L}$ ). This solution was frozen in liquid nitrogen and the headspace of the tube evacuated.  $\text{Me}_3\text{SiCl}$  (33.4 mL at 1.7 cm Hg, 0.031 mmol) was then admitted via condensation from a calibrated gas volume. The J. Young tube was sealed and the contents carefully thawed to  $-78\text{ }^{\circ}\text{C}$ ; the reaction was mixed thoroughly, ensuring the sample remained cold. The tube was transferred to an NMR spectrometer pre-cooled to  $-40\text{ }^{\circ}\text{C}$ . Quantitative conversion to  $15\text{-}^{13}\text{C}$  was observed by multinuclear NMR.  $^{13}\text{C}\{^1\text{H}\}$  NMR (126 MHz, THF,  $-40\text{ }^{\circ}\text{C}$ )  $\delta$ : 379.45 (t,  $J = 19.92\text{ Hz}$ ,  $\text{CSiMe}_3$ ), 284.09 (t,  $J = 13.80\text{ Hz}$ ,  $\text{COSiMe}_3$ ).  $^{31}\text{P}\{^1\text{H}\}$  NMR (202 MHz, THF,  $-40\text{ }^{\circ}\text{C}$ )  $\delta$ : 57.41 (dd,  $J = 19.92, 13.80\text{ Hz}$ ).  $^{13}\text{C}\{^1\text{H}\}$  NMR (126 MHz, THF,  $0\text{ }^{\circ}\text{C}$ )  $\delta$ : 379.52 (t,  $J = 18.97\text{ Hz}$ ,  $\text{CSiMe}_3$ ), 284.81 (t,  $J = 14.47\text{ Hz}$ ,  $\text{COSiMe}_3$ ).  $^{31}\text{P}\{^1\text{H}\}$  NMR (202 MHz, THF,  $0\text{ }^{\circ}\text{C}$ )  $\delta$ : 57.95 (dd,  $J = 18.97, 14.47\text{ Hz}$ ).

#### **Stoichiometric Deoxygenative C–C Coupling**

In a representative reaction, a solution of  $4\text{-}^{13}\text{CO}$  (30 mg, 0.027 mmol) in THF (1.5 mL) in a 20 mL scintillation vial charged with a stir bar was frozen in a liquid nitrogen-cooled cold well. A second solution of  $^t\text{Pr}_3\text{SiCl}$  (20.8 mg, 0.108 mmol) in THF (0.5 mL) was likewise frozen. While thawing, the  $^t\text{Pr}_3\text{SiCl}$  solution was added to the stirring deep purple

solution of  $4\text{-}^{13}\text{CO}$ . As the reaction mixture continued to warm, the color changed to burgundy. An aliquot was removed and transferred to a J. Young NMR tube.  $\text{C}_6\text{D}_6$  (100  $\mu\text{L}$ ) was added via Hamilton syringe. The aliquot was then analyzed by  $^{13}\text{C}\{^1\text{H}\}$  and  $^{31}\text{P}\{^1\text{H}\}$  NMR.

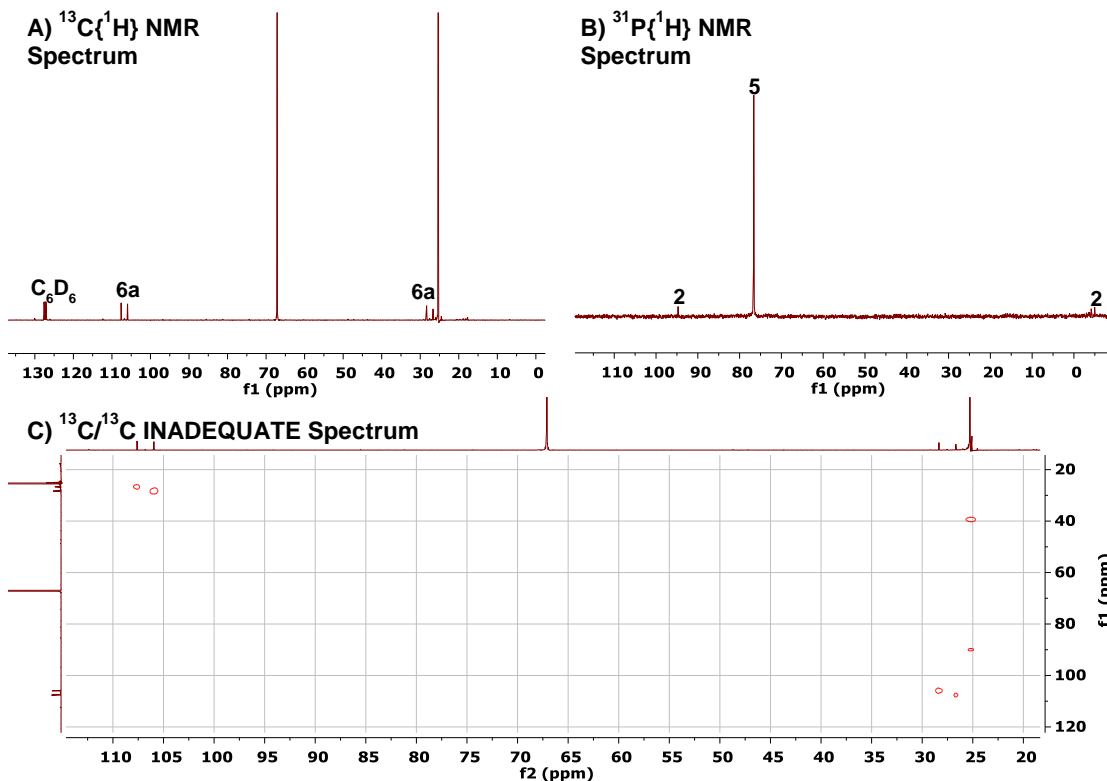


**Figure 3.10.** (A)  $^{13}\text{C}\{^1\text{H}\}$  NMR spectrum (101 MHz, THF/ $\text{C}_6\text{D}_6$ ,  $25^\circ\text{C}$ ) showing the formation of  $6a\text{-}^{13}\text{CO}$ , following treatment of  $4\text{-}^{13}\text{CO}$  with excess  $^i\text{Pr}_3\text{SiCl}$ . (B) The major metal containing product *ca.* 75% was identified as the dinitrogen complex **5**. (C) Strong C–C coupling ( $J_{\text{CC}} = 167.74$  Hz) consistent with  $6a\text{-}^{13}\text{CO}$  was verified via INADEQUATE NMR.

### Silyl Alkylidyne Reduction

A 20 mL scintillation vial was charged with a stir bar,  $7\text{-}^{13}\text{CO}$  (20 mg, 0.028 mmol), and  $\text{KC}_8$  (8 mg, 0.059 mmol). THF (1 mL) was added with stirring, resulting in the formation of a dark, heterogeneous mixture. The mixture was left to stir for 10 minutes, at which time it was filtered through a celite plug into an NMR tube.  $^{13}\text{C}\{^1\text{H}\}$  NMR demonstrated quantitative conversion of  $7\text{-}^{13}\text{CO}$  to **5** and silyl ethynolate **6b** (Figure 3.11., B).<sup>55</sup> Addition

of Me<sub>3</sub>SiCl (2 drops) to this NMR tube led to the formation of **6c** (major) and **6a**<sup>Me</sup> (minor) as evidenced by <sup>13</sup>C{<sup>1</sup>H} NMR spectroscopy (Figure 3.11., C).<sup>56</sup>

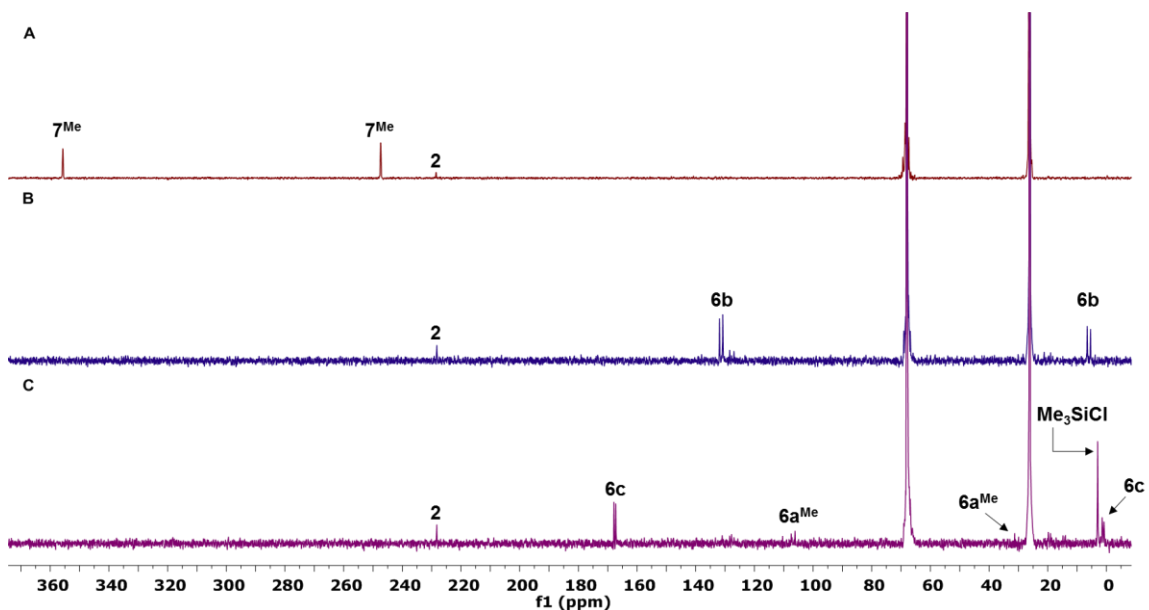


**Figure 3.11.** <sup>13</sup>C{<sup>1</sup>H} NMR spectrum (126 MHz, 25 °C, THF) of the stepwise reduction and silylation of **7**. <sup>13</sup>C{<sup>1</sup>H} NMR (A) shows the characteristic resonances at 355.8 and 247.5 attributable to the silyl alkylidyne and carbonyl carbons of **7**, respectively. Upon two electron reduction (B), formation of ethynolate **6b** (<sup>13</sup>C{<sup>1</sup>H} NMR (126 MHz, 25 °C, THF)  $\delta = 131.34, 5.94, ^1J_{CC} = 139.6$  Hz) is observed. Addition of Me<sub>3</sub>SiCl to this mixture (C) yields ketene **6c** (<sup>13</sup>C{<sup>1</sup>H} NMR (126 MHz, 25 °C, THF)  $\delta = 167.54, 1.13, ^1J_{CC} = 82.3$  Hz). Minimal formation of **6a**<sup>Me</sup> is observed (<sup>13</sup>C{<sup>1</sup>H} NMR (126 MHz, 25 °C, THF)  $\delta = 106.7, 30.6, ^1J_{CC} = 163.7$  Hz).

### Electrophilic Quenching of 3-<sup>13</sup>C with <sup>1</sup>Pr<sub>3</sub>SiCl

A J. Young NMR tube was charged with **3**-<sup>13</sup>C (20 mg, 0.021 mmol) and the headspace evacuated on the high vacuum line. THF-*d*<sub>8</sub> (ca. 400  $\mu$ L) was admitted via vacuum transfer at -196 °C. The tube was sealed, and the contents thawed and mixed thoroughly, providing a deep red solution. The J. Young tube was submerged in a -78 °C dry ice/acetone bath, and with a heavy counterflow of argon, <sup>1</sup>Pr<sub>3</sub>SiCl (16.6  $\mu$ L, 0.086 mmol) was admitted via microsyringe. The tube was again sealed and carefully transferred to the NMR probe (pre-chilled to -80 °C).

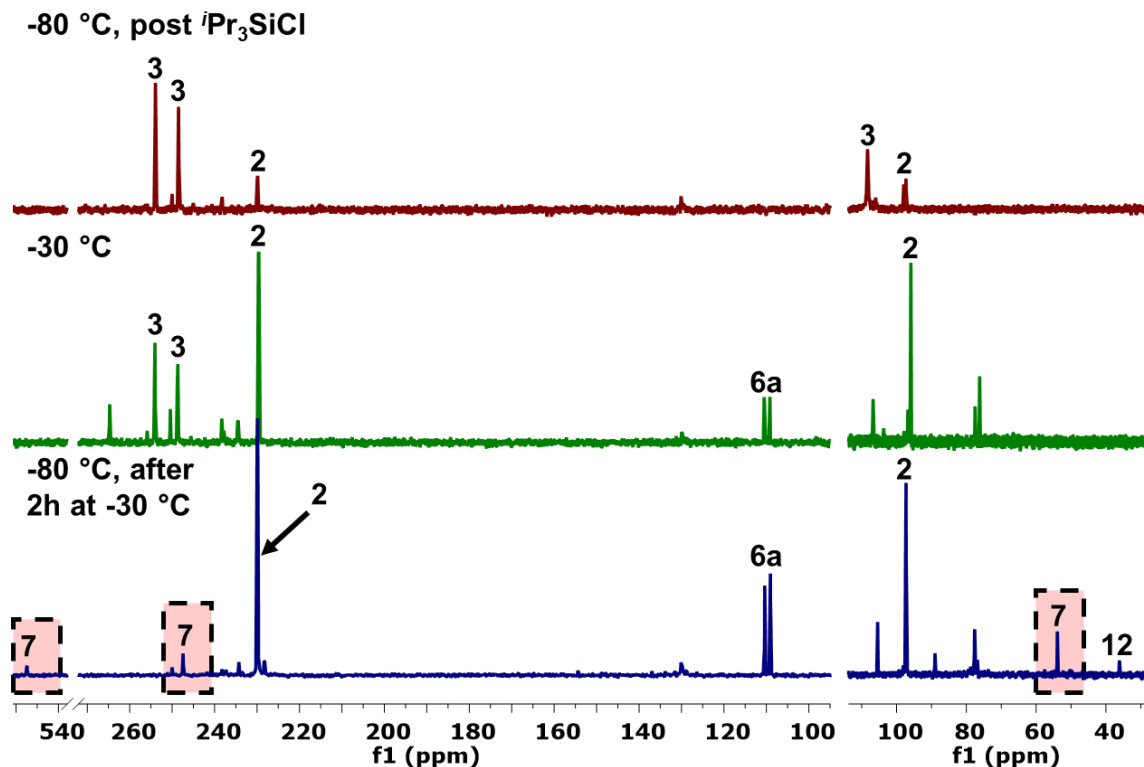


**Figure 3.12.** Stacked partial  $^{13}\text{C}\{^1\text{H}\}$  (126 MHz, left) and  $^{31}\text{P}\{^1\text{H}\}$  (202 MHz, right) NMR spectra (THF- $d_8$ ) of the low temperature addition of 4 equiv. of  $i\text{Pr}_3\text{SiCl}$  to  $3\text{-}^{13}\text{C}$ . Immediately after admitting  $i\text{Pr}_3\text{SiCl}$  to the reaction mixture, some oxidation to Mo(0) dicarbonyl  $2\text{-}^{13}\text{C}$  was observed (top). Warming the sample to  $-30\text{ }^\circ\text{C}$  in the NMR probe resulted in formation of metal-free  $\text{C}_2\text{O}_1$  fragment **6a** (middle). Maintaining this temperature (at which coupling occurs slowly) for two hours and then cooling the sample back to  $-80\text{ }^\circ\text{C}$  afforded spectra with features attributable to  $7\text{-}^{13}\text{C}$  consistent with the proposed intermediacy of this species in the coupling reaction. Note that with the chosen ratio of reagents, electrons are limiting (0.5 equiv.), and trace formation of silyl carbyne  $12\text{-}^{13}\text{C}$  is detected.

### Variable Temperature NMR of $9\text{-}^{13}\text{C}$

A J. Young NMR tube was charged with  $3\text{-}^{13}\text{C}$  (22 mg, 0.024 mmol) and THF- $d_8$  (400  $\mu\text{L}$ ) was added via vacuum transfer at  $-78\text{ }^\circ\text{C}$ . With an argon counterflow,  $\text{Me}_3\text{SiCl}$  (17  $\mu\text{L}$ , 0.132 mmol) was introduced to the NMR tube via Hamilton syringe. Mixing at low temperature provided a deep red solution of  $9\text{-}^{13}\text{C}$ , which was analyzed by multinuclear NMR at a series of temperatures. The experimental NMR spectra were fit using the dNMR module within the TopSpin Software Package.<sup>72</sup> Trace  $2\text{-}^{13}\text{C}$  formed following the addition of  $\text{Me}_3\text{SiCl}$  was likewise fit and used to determine the line broadening for the

simulation at -100 °C, as it is not involved in exchange processes. Simulations at higher temperatures were derived from the parameters of the -100 °C fit, via iterative variation of the exchange rate,  $k$ .

**Table 3.1.** Dynamic NMR fit parameters for carbyne exchange in  $9\text{-}^{13}\text{C}$ .

T [K]	$k$ [sec <sup>-1</sup> ]	1/T [K <sup>-1</sup> ]	Ln( $k$ )	Ln( $k/T$ )	$\Delta G^\ddagger$ (kcal/mol)
173.15	34.87	0.0058	3.55	-1.60	8.73
193.15	539.42	0.0052	6.29	1.03	8.73
213.15	1343.35	0.0047	7.20	1.84	9.28
233.15	7103.41	0.0043	8.86	3.42	9.42
243.15	12982.40	0.0041	9.47	3.98	9.56
253.15	28800.20	0.0040	10.27	4.73	9.57

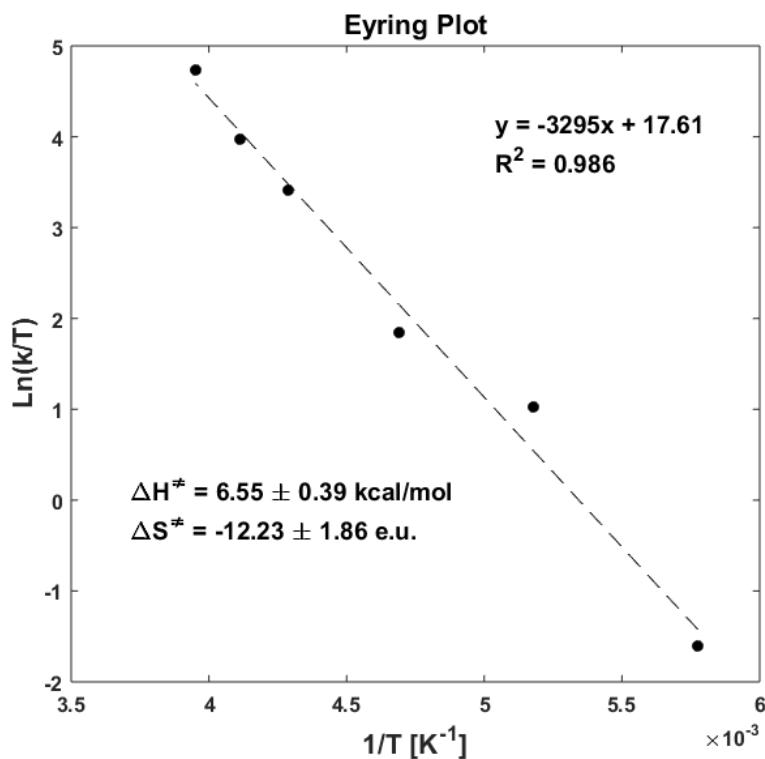


**Figure 3.13.** Eyring plot for dicarbyne exchange in  $9\text{-}^{13}\text{C}$  ( $^{13}\text{C}\{^1\text{H}\}$ , THF- $d_8$ , 126 MHz).

### ***In Situ* Reduction of 10**

A J. Young NMR tube was charged with a deep red solution of  $3\text{-}^{13}\text{C}$  (28 mg, 0.031 mmol) in THF (400  $\mu\text{L}$ ). The contents of the tube were frozen in liquid nitrogen and the headspace evacuated.  $\text{Me}_3\text{SiCl}$  (3.3 cm Hg in 33.4 mL, 0.060 mmol) was condensed into

the tube which was then sealed and warmed to  $-78\text{ }^{\circ}\text{C}$ . The reaction mixture was mixed and left at  $-78\text{ }^{\circ}\text{C}$ , in a dry ice/acetone slush bath, for 5 days.  $^{31}\text{P}\{^1\text{H}\}$  and  $^{13}\text{C}\{^1\text{H}\}$  NMR spectra collected at this point display significant conversion to bis(siloxy)acetylene  $10\text{-}^{13}\text{C}$  (Figure 3.14., A). With a heavy counterflow of argon, a THF solution of  $[\text{Na}][\text{C}_{10}\text{H}_8]$  (0.060 mmol in 200  $\mu\text{L}$ ) was added via syringe at  $-78\text{ }^{\circ}\text{C}$ . The tube was sealed, mixed, and the reduction reaction monitored by variable temperature NMR spectroscopy (Figure 3.14., B-C).

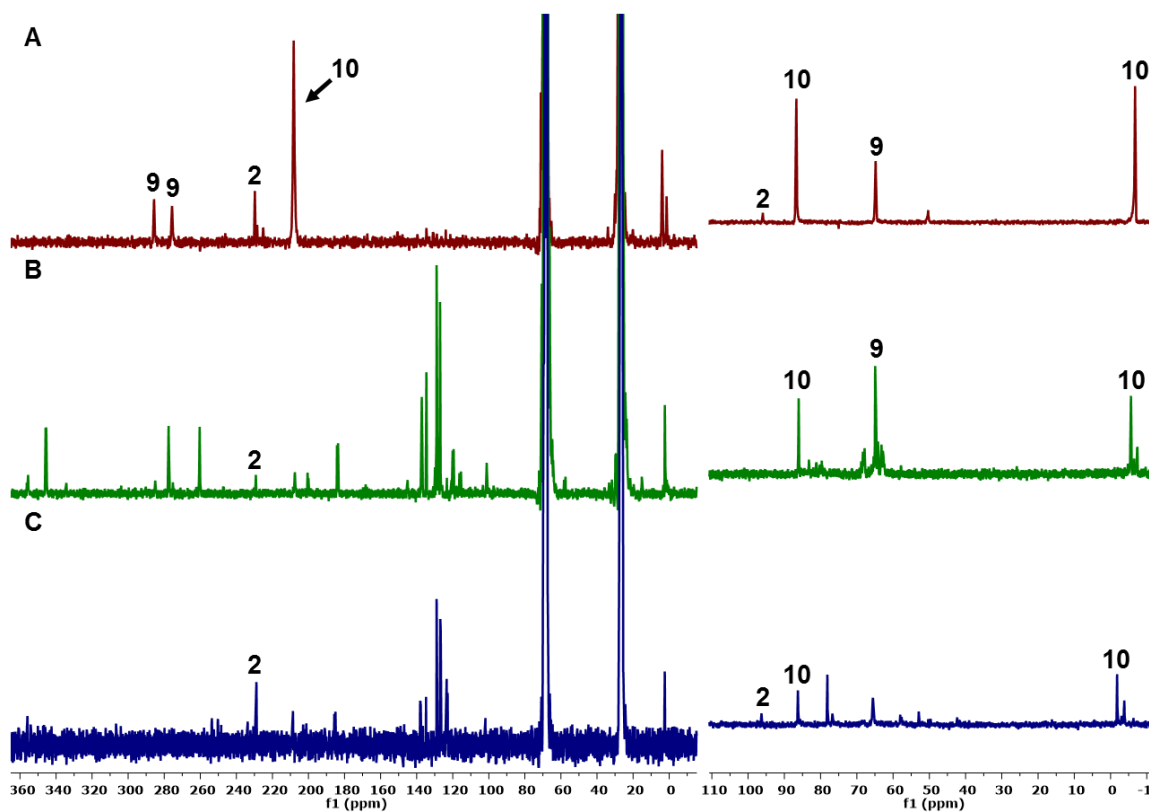


**Figure 3.14.** Stacked  $^{13}\text{C}\{^1\text{H}\}$  (left; 126 MHz, THF) and  $^{31}\text{P}\{^1\text{H}\}$  (right; 202 MHz, THF) following the two-electron reduction of  $10\text{-}^{13}\text{C}$ . From a reaction mixture comprised of a *ca.* 63:36:1 ratio of  $10\text{-}^{13}\text{C}$ ,  $9\text{-}^{13}\text{C}$ , and  $2\text{-}^{13}\text{C}$ , respectively, two-electron reduction at  $-78\text{ }^{\circ}\text{C}$  leads to an intractable mixture of species. Though downfield resonances at 345.5 and 355.7 ppm (Figure 3.14., B), attributable to  $11\text{-}^{13}\text{C}$  and  $8\text{-}^{13}\text{C}$ , respectively, are observed in the  $^{13}\text{C}\{^1\text{H}\}$  NMR spectrum, these are attributed to C–O cleavage chemistry from  $9\text{-}^{13}\text{C}$ . Warming the reaction mixture to room temperature (Figure 3.14., C) did not afford spectra consistent with C–O cleavage chemistry from  $10\text{-}^{13}\text{C}$ .

### Isomerization of **11** to **7**

A J. Young tube was charged with microcrystals from the preparation of **11** (method A, *vide supra*) and THF-*d*<sub>8</sub> (*ca.* 500 μL) was admitted at -78 °C via vacuum transfer. The contents of the tube were mixed at low temperature, providing a burgundy solution. <sup>1</sup>H and <sup>31</sup>P{<sup>1</sup>H} NMR spectroscopy at -80 °C showed a 57:43 mixture of **11** to **8**, respectively. The tube was warmed to room temperature for set time intervals before being returned to the probe for spectral analysis (Figure 3.15.).

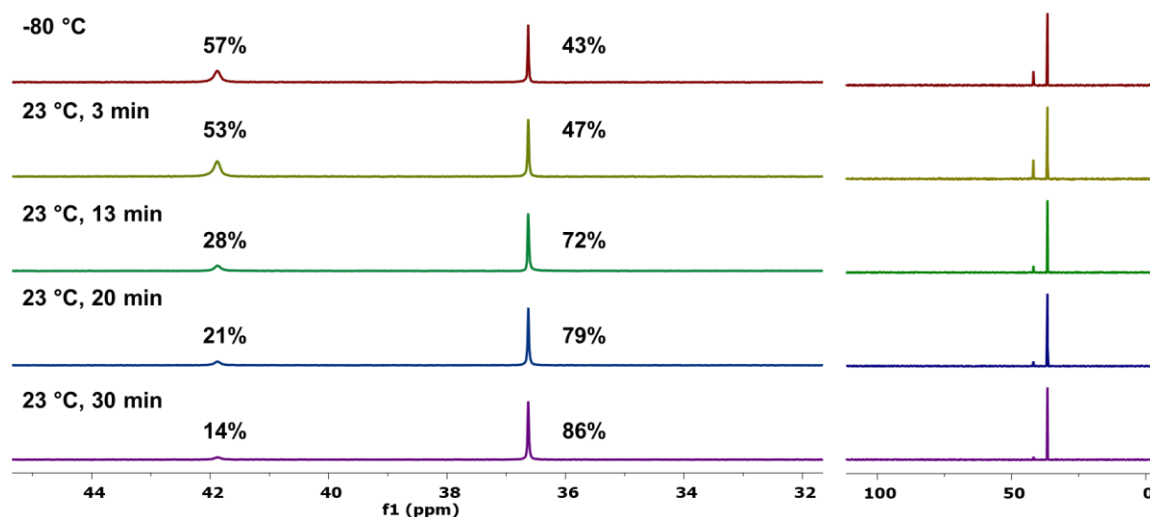


**Figure 3.15.** Stacked partial (left) and full (right) <sup>31</sup>P{<sup>1</sup>H} NMR spectra (202 MHz, THF-*d*<sub>8</sub>, -80°C) supporting the conversion of **11** to **8** after warming to room temperature. The resonances at 41.9 ppm and 36.6 ppm correspond to **11** and **8**, respectively.

### C–O Bond Cleavage Kinetics Experiments

In a representative reaction (5 equiv. of Me<sub>3</sub>SiCl), 0.5 mL of a deep red stock solution of **3**-<sup>13</sup>C (120 mg, 0.132 mmol) in THF (3 mL)/C<sub>6</sub>D<sub>6</sub> (12 drops) was added to a J. Young tube. THF (70 μL) was added via Hamilton syringe to ensure the desired 585 μL approximate sample volume (25 °C) following addition of silyl chloride. The tube was sealed and attached to the high vacuum line, where the contents were freeze-pump-thawed twice. Me<sub>3</sub>SiCl (33.4 mL at 2.0 cm Hg, 23 °C, 0.036 mmol) was admitted via condensation from a calibrated gas bulb. The contents of the J. Young were thawed, mixed quickly, and refrozen. Me<sub>3</sub>SiCl (33.4 mL at 4.0 cm Hg, 23 °C, 0.072 mmol) was

admitted as before. The tube was then sealed and placed in a liquid nitrogen cooled Dewar. Thawing occurred directly prior to placing the NMR tube in a 0 °C NMR probe.  $^{13}\text{C}\{^1\text{H}\}$  NMR spectra were recorded as an array utilizing the pre-acquisition delay mechanism in Agilent's VnmrJ software. Relative concentrations of species in the reaction mixture were determined via integration of their respective resonances against the  $\text{C}_6\text{D}_6$  triplet at 128.06.

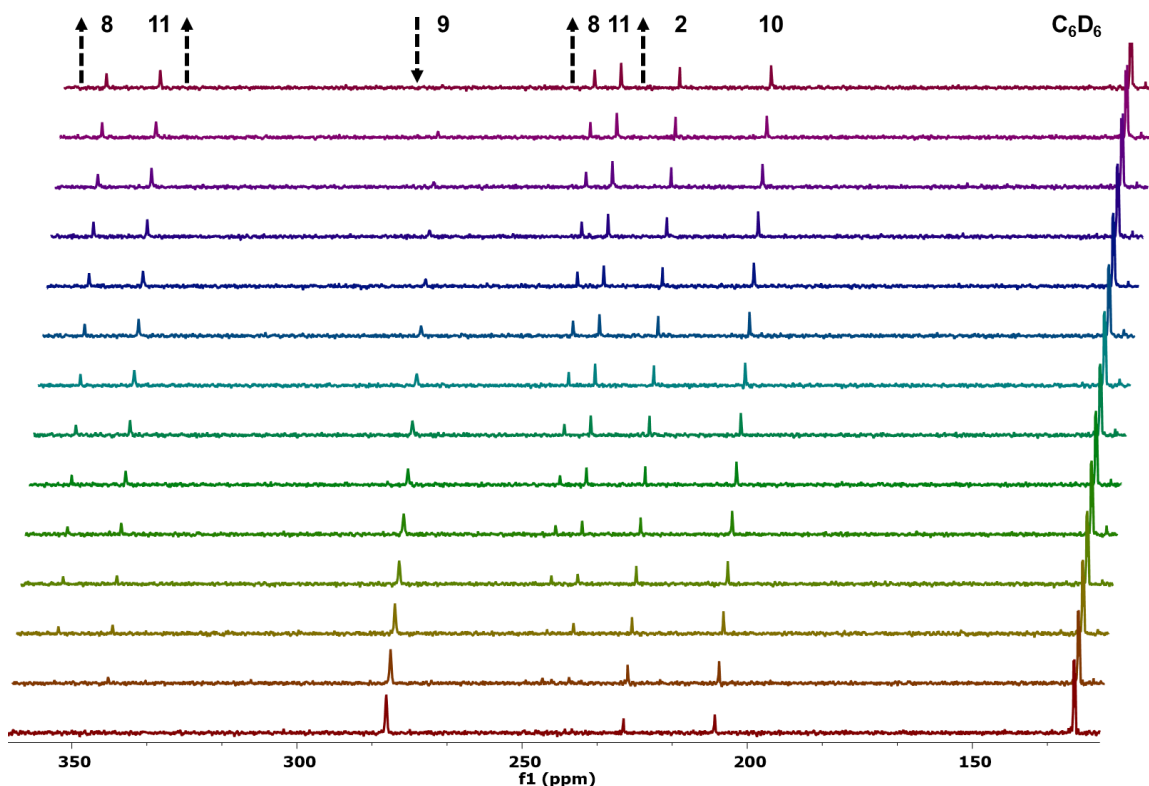


**Figure 3.16.** Representative  $^{13}\text{C}\{^1\text{H}\}$  NMR spectrum array (126 MHz, 0 °C, THF) for the conversion of  $9\text{-}^{13}\text{C}$  to  $11\text{-}^{13}\text{C}$  and  $8\text{-}^{13}\text{C}$ . For clarity, every third spectrum collected is displayed. Small amounts of  $2\text{-}^{13}\text{C}$  and  $10\text{-}^{13}\text{C}$  were formed upon electrophilic quenching, but their concentrations remain constant over the course of the kinetics experiment (Figure 3.17).



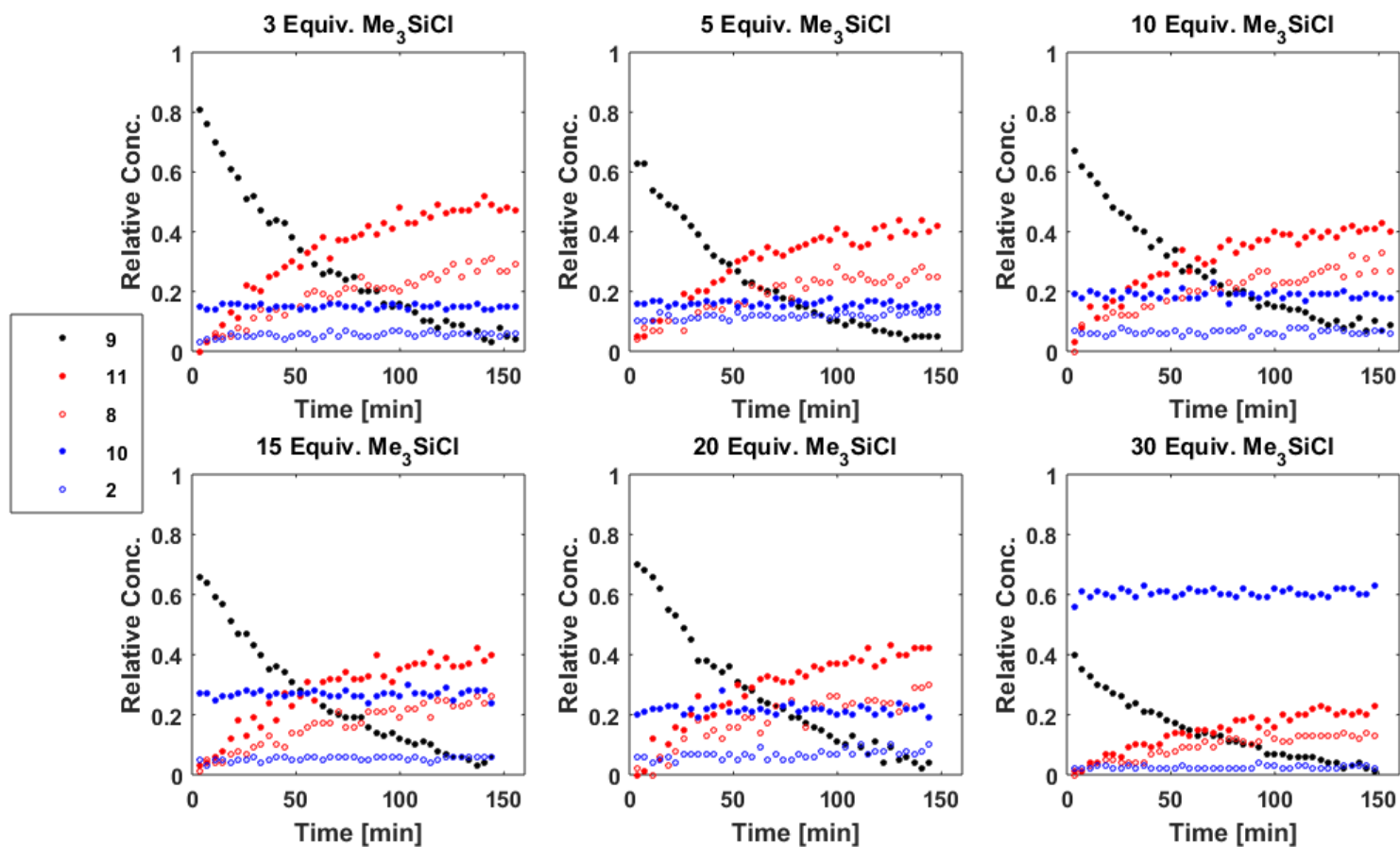


**Figure 3.17.** Relative concentration vs. time for species observed during C–O bond cleavage kinetics experiments. Variable amounts of  $2\text{-}^{13}\text{C}$  and  $10\text{-}^{13}\text{C}$  were formed in the initial addition of  $\text{Me}_3\text{SiCl}$ , but the concentrations of these complexes remain constant, within error, over the course of the reaction. Dicarbyne  $9\text{-}^{13}\text{C}$  is consumed and silyl carbynes  $11\text{-}^{13}\text{C}$  and  $8\text{-}^{13}\text{C}$  are concomitantly observed to grow in.

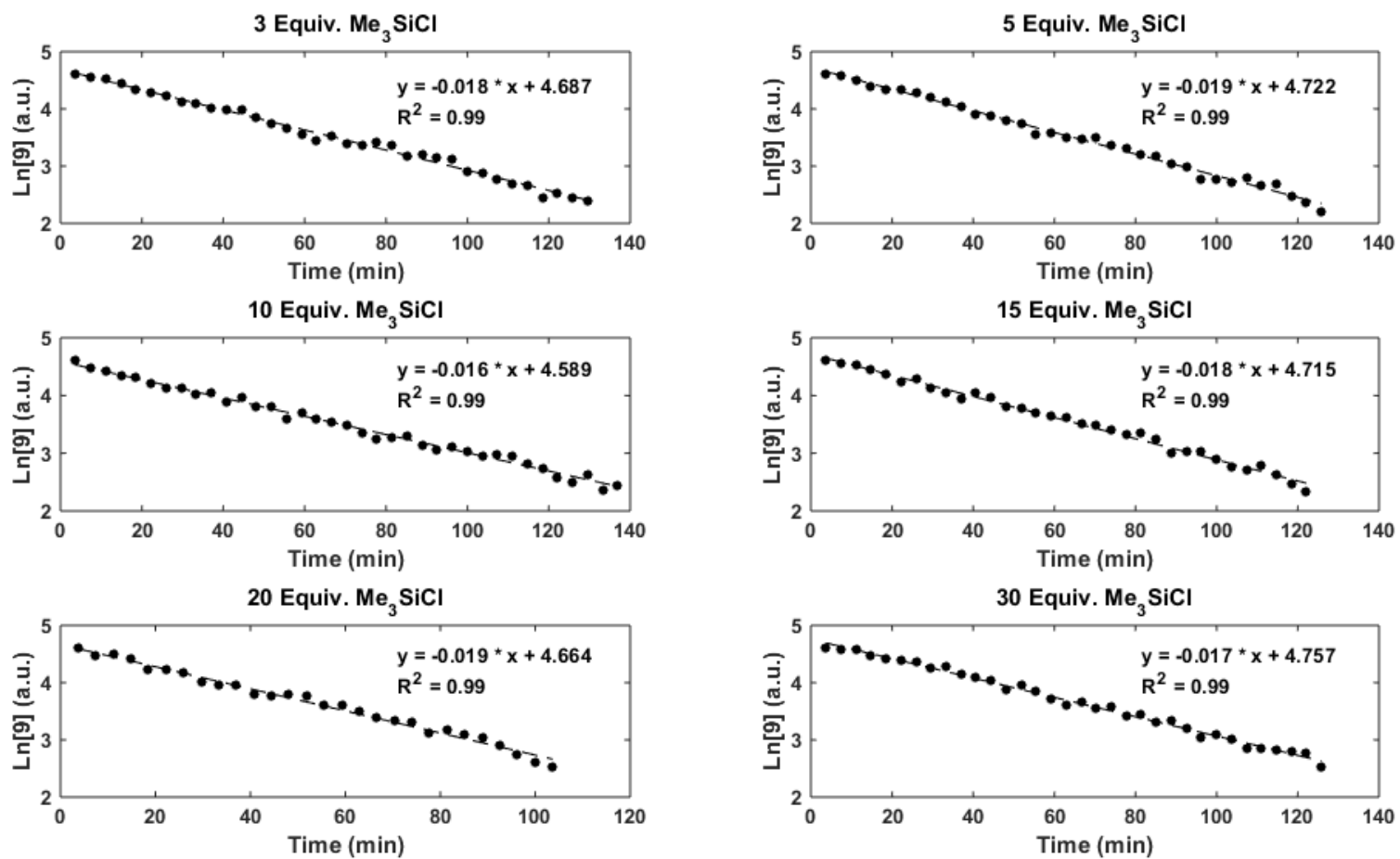
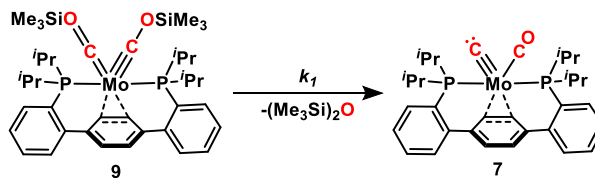


**Figure 3.18.** Log plots of  $[\text{9-}^{13}\text{C}]$  vs. time for variable silyl chloride concentrations as monitored by  $^{13}\text{C}\{^1\text{H}\}$  NMR spectroscopy at  $0^\circ\text{C}$ .

## Rate Equations for Elementary C–O Bond Cleavage Steps

### Case I: Irreversible Dicarbyne Formation

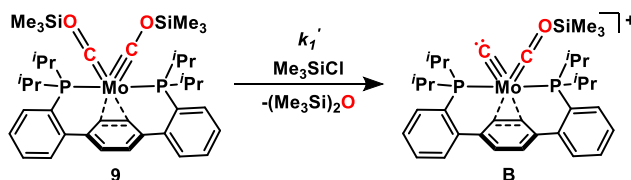
#### Path 1—Intramolecular HMDSO Formation from Dicarbyne 9



$$\text{Rate} = \frac{d[7]}{dt} = k_1[9] \quad (1)$$

Overall: Zeroth order in  $[\text{Me}_3\text{SiCl}]$

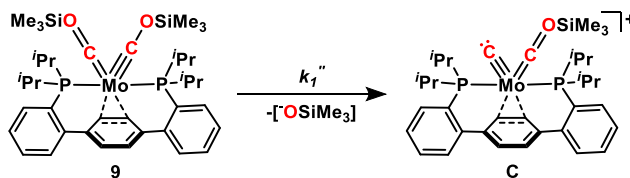
#### Path 2—External Silyl Electrophile Attack on Dicarbyne 9



$$\text{Rate} = \frac{d[7]}{dt} = k_1'[9][\text{Me}_3\text{SiCl}] \quad (2)$$

Overall: First order in  $[\text{Me}_3\text{SiCl}]$

#### Path 3—Siloxide Dissociation from Dicarbyne 9

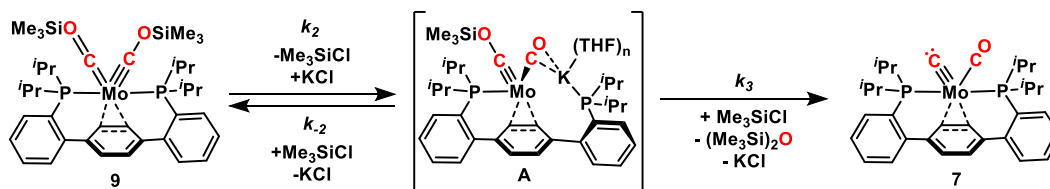


$$\text{Rate} = \frac{d[7]}{dt} = k_1''[9] \quad (3)$$

Overall: Zeroth order in  $[\text{Me}_3\text{SiCl}]$

### Case II: Reversible Dicarbyne Formation—Fast Pre-Equilibrium

#### Path 4—External Silyl Electrophile Attack on Carbyne Anion A



$$\text{Rate} = \frac{d[7]}{dt} = k_3[\mathbf{A}][\text{Me}_3\text{SiCl}]$$

Assuming a fast pre-equilibrium between **A** and **9**:

$$K_2 = \frac{k_2}{k_{-2}} = \frac{[\mathbf{A}][\text{Me}_3\text{SiCl}]}{[\mathbf{9}][\text{KCl}]}$$

$$[\mathbf{A}] = \frac{K_2[\mathbf{9}][\text{KCl}]}{[\text{Me}_3\text{SiCl}]} \quad \text{and let} \quad [\mathbf{9}] = [\text{Mo}]_0 - [\mathbf{A}]$$

$$\Rightarrow [\mathbf{A}] = \frac{K_2[\text{KCl}][\text{Mo}]_0 - K_2[\text{KCl}][\mathbf{A}]}{[\text{Me}_3\text{SiCl}]}$$

$$\Rightarrow [\mathbf{A}] + \frac{K_2[\text{KCl}][\mathbf{A}]}{[\text{Me}_3\text{SiCl}]} = \frac{K_2[\text{KCl}][\text{Mo}]_0}{[\text{Me}_3\text{SiCl}]}$$

$$\Rightarrow [\mathbf{A}] \left( 1 + \frac{K_2[\text{KCl}]}{[\text{Me}_3\text{SiCl}]} \right) = \frac{K_2[\text{KCl}][\text{Mo}]_0}{[\text{Me}_3\text{SiCl}]}$$

$$\Rightarrow [\mathbf{A}] = \frac{K_2[\text{KCl}][\text{Mo}]_0}{[\text{Me}_3\text{SiCl}] \left( 1 + \frac{K_2[\text{KCl}]}{[\text{Me}_3\text{SiCl}]} \right)} = \frac{K_2[\text{KCl}][\text{Mo}]_0}{[\text{Me}_3\text{SiCl}] + K_2[\text{KCl}]}$$

$$\therefore \frac{d[7]}{dt} = k_3[\mathbf{A}][\text{Me}_3\text{SiCl}] = \frac{k_3 K_2 [\text{KCl}] [\text{Me}_3\text{SiCl}] [\text{Mo}]_0}{[\text{Me}_3\text{SiCl}] + K_2 [\text{KCl}]} = \frac{\frac{k_2 k_3}{k_{-2}} [\text{KCl}] [\text{Me}_3\text{SiCl}] [\text{Mo}]_0}{[\text{Me}_3\text{SiCl}] + \frac{k_2}{k_{-2}} [\text{KCl}]}$$

$$\Rightarrow \frac{d[7]}{dt} = \frac{k_2 k_3 [\text{KCl}] [\text{Me}_3\text{SiCl}] [\text{Mo}]_0}{k_{-2} [\text{Me}_3\text{SiCl}] + k_2 [\text{KCl}]} \quad (4)$$

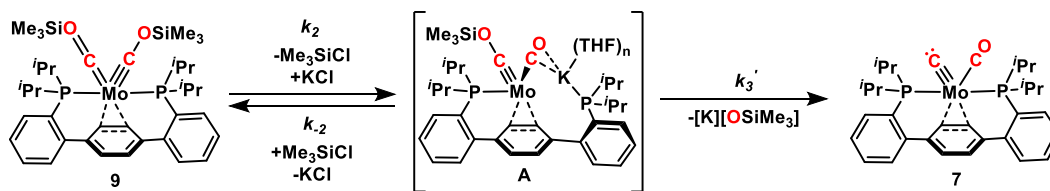
Overall: Complex positive rate dependence on  $[\text{Me}_3\text{SiCl}]$

Assuming  $k_{-2} \gg k_2$  (consistent with spectroscopic observation of **9** only):

$$\text{Then} \quad \frac{d[7]}{dt} = \frac{k_2 k_3 [\text{KCl}] [\text{Me}_3\text{SiCl}] [\text{Mo}]_0}{k_{-2} [\text{Me}_3\text{SiCl}]} = \frac{k_2 k_3}{k_{-2}} [\text{KCl}] [\text{Mo}]_0 \quad (4a)$$

Overall: Zeroth order in  $[\text{Me}_3\text{SiCl}]$

Path 5—Siloxide Dissociation from Carbyne Anion **A**



$$\text{Rate} = \frac{d[7]}{dt} = k_3'[\text{A}]$$

Assuming a fast pre-equilibrium between **A** and **9** (the pre-equilibrium expression is the same as in Path 4 above):

$$\Rightarrow [\text{A}] = \frac{K_2[\text{KCl}][\text{Mo}]_0}{[\text{Me}_3\text{SiCl}] + K_2[\text{KCl}]}$$

$$\therefore \frac{d[7]}{dt} = k_3'[\text{A}] = \frac{k_3'K_2[\text{KCl}][\text{Mo}]_0}{[\text{Me}_3\text{SiCl}] + K_2[\text{KCl}]} = \frac{\frac{k_2k_3'}{k_{-2}}[\text{KCl}][\text{Mo}]_0}{[\text{Me}_3\text{SiCl}] + \frac{k_2}{k_{-2}}[\text{KCl}]}$$

$$\Rightarrow \frac{d[7]}{dt} = \frac{k_2k_3'[\text{KCl}][\text{Mo}]_0}{k_{-2}[\text{Me}_3\text{SiCl}] + k_2[\text{KCl}]} \quad (5)$$

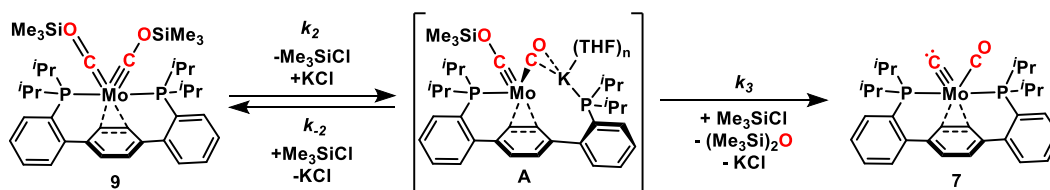
Assuming  $k_{-2} \gg k_2$  (consistent with spectroscopic observation of **9** only):

$$\text{Then} \quad \frac{d[7]}{dt} = \frac{k_2k_3'[\text{KCl}][\text{Mo}]_0}{k_{-2}[\text{Me}_3\text{SiCl}]} = \frac{k_2k_3'[\text{KCl}][\text{Mo}]_0}{k_{-2}[\text{Me}_3\text{SiCl}]} \quad (5a)$$

Overall: Inverse first order in  $[\text{Me}_3\text{SiCl}]$

Case II: Reversible Dicarbyne Formation—Rate Limiting Formation of **A**

Path 4—External Silyl Electrophile Attack on Carbyne Anion **A**



$$\text{Rate} = \frac{d[7]}{dt} = k_3[\text{A}][\text{Me}_3\text{SiCl}]$$

Applying the steady-state approximation:

$$\text{Assume} \quad \frac{d[\text{A}]}{dt} = 0 = k_2[\text{9}][\text{KCl}] - k_{-2}[\text{A}][\text{Me}_3\text{SiCl}] - k_3[\text{A}][\text{Me}_3\text{SiCl}]$$

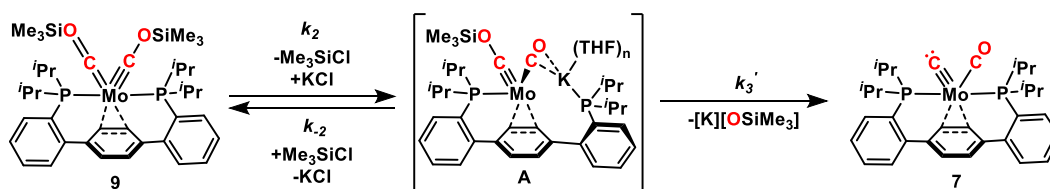
$$\Rightarrow k_2[\mathbf{9}][\text{KCl}] = [\mathbf{A}][\text{Me}_3\text{SiCl}](k_{-2} + k_3)$$

$$\Rightarrow [\mathbf{A}] = \frac{k_2[\mathbf{9}][\text{KCl}]}{[\text{Me}_3\text{SiCl}](k_{-2} + k_3)}$$

$$\therefore \frac{d[\mathbf{7}]}{dt} = \frac{k_2 k_3 [\mathbf{9}][\text{KCl}][\text{Me}_3\text{SiCl}]}{[\text{Me}_3\text{SiCl}](k_{-2} + k_3)} = \frac{k_2 k_3}{(k_{-2} + k_3)} [\mathbf{9}][\text{KCl}] \quad (6)$$

Overall: Zeroth order in  $[\text{Me}_3\text{SiCl}]$

Path 5—Siloxide Dissociation from Carbyne Anion A



$$\text{Rate} = \frac{d[\mathbf{7}]}{dt} = k_3'[\mathbf{A}]$$

Applying the steady-state approximation:

$$\text{Assume } \frac{d[\mathbf{A}]}{dt} = 0 = k_2[\mathbf{9}][\text{KCl}] - k_{-2}[\mathbf{A}][\text{Me}_3\text{SiCl}] - k_3'[\mathbf{A}]$$

$$\Rightarrow k_2[\mathbf{9}][\text{KCl}] = [\mathbf{A}](k_{-2}[\text{Me}_3\text{SiCl}] + k_3')$$

$$\Rightarrow [\mathbf{A}] = \frac{k_2[\mathbf{9}][\text{KCl}]}{k_{-2}[\text{Me}_3\text{SiCl}] + k_3'}$$

$$\therefore \frac{d[\mathbf{7}]}{dt} = \frac{k_2 k_3'}{k_{-2}[\text{Me}_3\text{SiCl}] + k_3'} [\mathbf{9}][\text{KCl}] \quad (7)$$

Overall: Complex inverse rate dependence on  $[\text{Me}_3\text{SiCl}]$

Assuming the rate of C–O bond cleavage is much faster than the rate of resilylation (*ie*:

$k_3' \gg k_{-2}[\text{Me}_3\text{SiCl}]$ ):

$$\frac{d[\mathbf{7}]}{dt} = \frac{k_2 k_3'}{k_3'} [\mathbf{9}] = k_2[\mathbf{9}] \quad (7a)$$

Overall: Zeroth order in  $[\text{Me}_3\text{SiCl}]$

### Isotopic Labeling Experiments Employing $(\text{CD}_3)_3\text{SiCl}$

*Reactivity of 9-<sup>13</sup>C with Excess  $(\text{CD}_3)_3\text{SiCl}$*

A J. Young NMR tube was charged with 600  $\mu\text{L}$  of a deep red solution of **3- $^{13}\text{C}$**  (20 mg, 0.022 mmol) in THF. One drop of  $\text{C}_6\text{D}_6$  was added as an internal standard for NMR spectroscopy. This tube was degassed thoroughly via three freeze-pump-thaw cycles. Following the third evacuation, the tube was left frozen in liquid nitrogen, and  $\text{Me}_3\text{SiCl}$  was admitted via condensation from a calibrated gas bulb (33.4 mL at 2.5 cm Hg, 0.045 mmol). The tube was sealed and thawed to  $-80\text{ }^\circ\text{C}$ , at which point it was mixed cold and refrozen.  $^{13}\text{C}\{^1\text{H}\}$  and  $^{31}\text{P}\{^1\text{H}\}$  NMR of this sample ( $-80\text{ }^\circ\text{C}$ ) showed conversion of the starting material to a mixture of **9- $^{13}\text{C}$**  (61%), **10- $^{13}\text{C}$**  (10%), **3- $^{13}\text{C}$**  (23%) and **2- $^{13}\text{C}$**  (6%) (Figure 3.19.). The tube was reattached to the vacuum line and the contents refrozen. To complete the conversion of **3- $^{13}\text{C}$**  to **9- $^{13}\text{C}$** , additional  $\text{Me}_3\text{SiCl}$  (33.4 mL at 0.6 cm Hg, 0.011 mmol) was condensed into the J. Young tube as before. The sample was thawed to  $-78\text{ }^\circ\text{C}$ , mixed vigorously, and refrozen.

$(\text{CD}_3)_3\text{SiCl}$  was admitted, in two portions, via condensation from a calibrated gas bulb (33.4 mL at 6.2 cm Hg per addition, 0.225 mmol total). The tube was thawed, mixed, and the reaction mixture was again analyzed by multinuclear NMR spectroscopy. allowed to warm to room temperature.

During this time, an oven-dried 100 mL Schlenk tube was charged with a stir bar, 4- $t\text{Bu-PhONa}$  (56.8 mg, 0.330 mmol), and THF (2 mL). The reaction mixture from the J. Young NMR tube was vacuum transferred into this collection flask. Following the transfer, the contents of the Schlenk tube were stirred at room temperature for 30 minutes and then vacuum transferred a second time into an empty Schlenk tube. Aliquots from this vessel were filtered through alumina and analyzed by GC/MS.

The terminal metal products of the reaction were analyzed via multinuclear NMR spectroscopy following addition of  $\text{C}_6\text{D}_6$  (*ca.* 400  $\mu\text{L}$ ) to the reaction J. Young NMR tube via vacuum transfer, indicating near exclusive deuteration at the silyl carbyne position (Figure 3.19.).

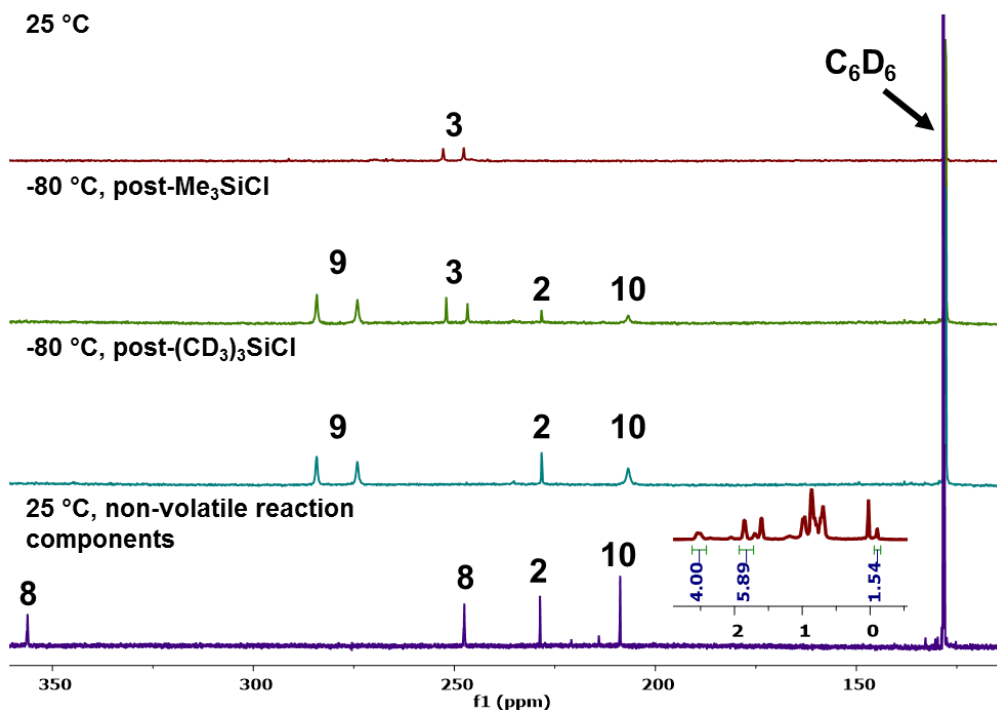


**Figure 3.19.**  $^{13}\text{C}\{^1\text{H}\}$  NMR spectra following the addition of proteo- and deuterio-silyl electrophiles to  $3\text{-}^{13}\text{C}$ . The inset shows the upfield region of the  $^1\text{H}$  NMR spectrum (500 MHz,  $\text{C}_6\text{D}_6$ , 25 °C) of the non-volatile reaction components.

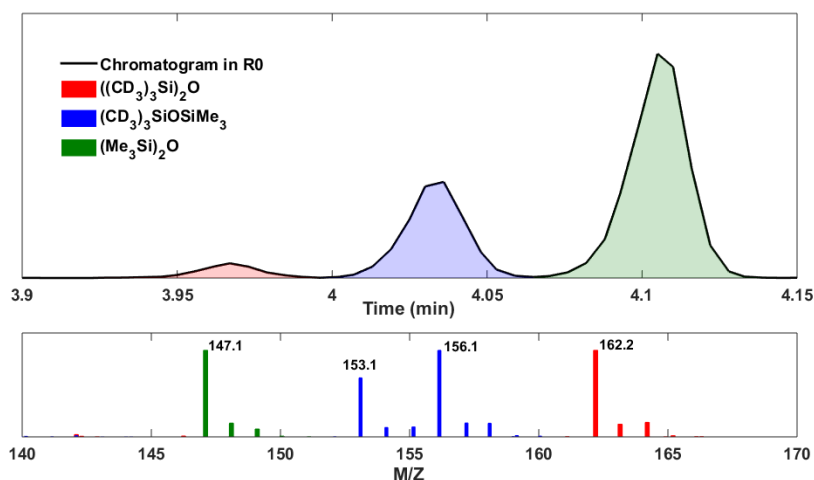


**Figure 3.20.** Partial gas chromatogram (top) and mass spectrum (bottom) of the HMDSO generated from warming  $9\text{-}^{13}\text{C}$  in the presence of excess  $(\text{CD}_3)_3\text{SiCl}$ . The isotopologs of HMDSO were resolved in the GC trace and the normalized mass spectra corresponding to each region are color coded.

#### *Reactivity of $9\text{-}^{13}\text{C}\text{-}d_{18}$ with Excess $\text{Me}_3\text{SiCl}$*

This reaction was conducted analogously to that described for the addition of excess  $(\text{CD}_3)_3\text{SiCl}$  to  $9\text{-}^{13}\text{C}$  except the deuterated silyl chloride was added first (2 equiv.) and the



proteo silyl electrophile was added second, in excess (10 equiv.). Following addition of  $(\text{CD}_3)_3\text{SiCl}$ , the reaction mixture was comprised of  $9\text{-}^{13}\text{C}\text{-}d_{18}$  (77%),  $10\text{-}^{13}\text{C}\text{-}d_{18}$  (14%), and  $2\text{-}^{13}\text{C}$  (9%). The terminal metal products of the reaction were analyzed as described above, and indicate near exclusive protonation at the silyl carbyne position (Figure 3.21).

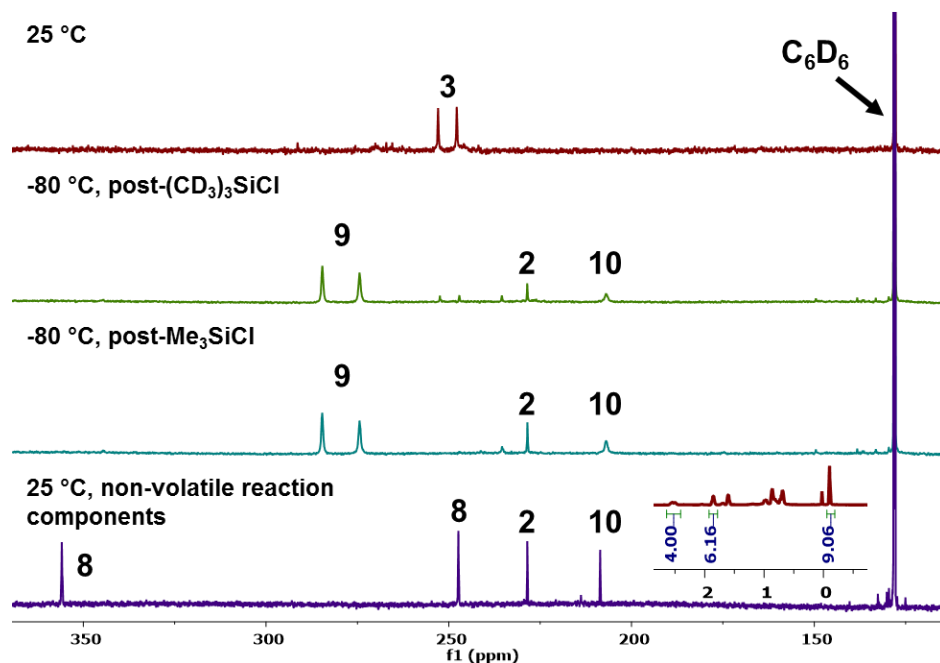


**Figure 3.21.**  $^{13}\text{C}\{^1\text{H}\}$  NMR spectra following the addition of deuterio- and proteo-silyl electrophiles to  $3\text{-}^{13}\text{C}$ . The inset shows the upfield region of the  $^1\text{H}$  NMR spectrum (500 MHz,  $\text{C}_6\text{D}_6$ , 25 °C) of the non-volatile reaction components.

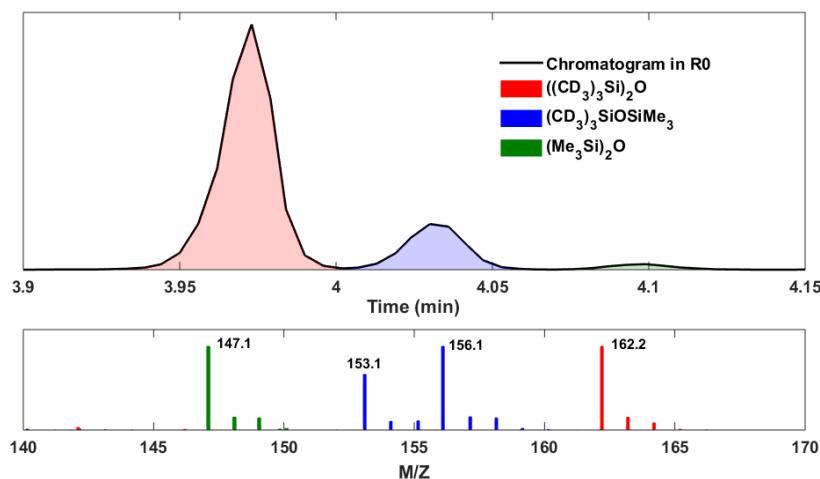


**Figure 3.22.** Partial gas chromatogram (top) and mass spectrum (bottom) of the HMDSO generated from warming  $9\text{-}^{13}\text{C}\text{-}d_{18}$  in the presence of excess  $\text{Me}_3\text{SiCl}$ . The isotopologs of HMDSO were resolved in the GC trace and the normalized mass spectra corresponding to each region are color coded.

$^2\text{H}$  NMR spectra of the reaction mixtures at different stages were collected to observe the fate of the deuterated trimethyl silyl fragment. These data are inconsistent with a fast exchange process scrambling the labeled electrophile onto (Figure 3.23., left) or off of (Figure 3.23., right) dicarbyne **9**. Though a small amount of free  $(\text{CD}_3)_3\text{SiCl}$  is observed upon warming the reaction mixture to  $0\text{ }^\circ\text{C}$  (Figure 3.23., panel 3, right), a temperature at which C–O cleavage is known to proceed, this is attributed to silyl dissociation from **9** (Scheme 3.6.) rather than an exchange process. In the latter case, a statistical distribution of silyl electrophiles would be expected (83% **9- $^{13}\text{C}$** , 17% **9- $^{13}\text{C-d}_{18}$** ). Moreover, the deuterated label is not observed to be incorporated into the metal complex in the complimentary experiment (Figure 3.23., left).

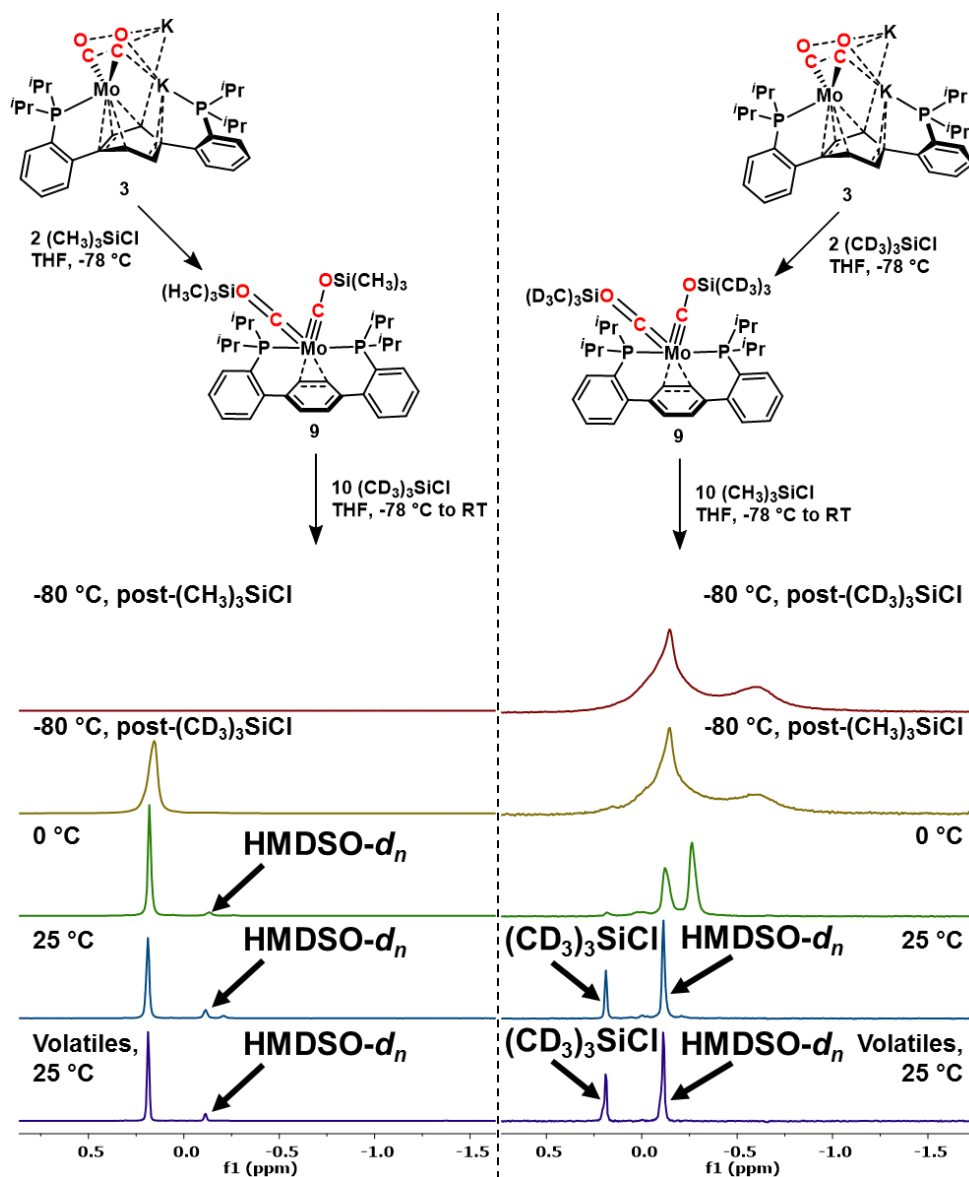


**Figure 3.23.** Partial  $^2\text{H}$  NMR spectra at various stages of the isotopic labeling experiments. A small amount of free  $(\text{CD}_3)_3\text{SiCl}$  is detected when  $9\text{-}^{13}\text{C}\text{-}d_{18}$  is warmed to  $0^\circ\text{C}$  in the presence of excess  $\text{Me}_3\text{SiCl}$  (right).

#### *Control Reaction for Sequestration of Excess Silyl Chloride*

A concern with HMDSO isotopolog end product analysis was siloxane formation from silyl chloride hydrolysis. To avoid this, the excess trimethylsilyl chloride remaining in the reaction mixture was sequestered with dry 4-*t*-Bu-PhONa (see experimental procedure description). To ensure that the phenoxide was not leading to silyl group redistribution, a control experiment was performed as follows. A J. Young NMR tube was charged with 4-*t*-Bu-PhONa (30 mg, 0.174 mmol) and THF (500  $\mu\text{L}$ ). The contents of the tube were

degassed via three freeze-pump-thaw cycles and  $\text{Me}_3\text{SiCl}$  (33.4 mL at 4 cm Hg, 0.072 mmol),  $(\text{CD}_3)_3\text{SiCl}$  (33.4 mL at 4 cm Hg, 0.072 mmol), and  $(\text{Me}_3\text{Si})_2\text{O}$  (33.4 mL at 4 cm Hg, 0.072 mmol) were sequentially condensed into the reaction vessel. The J. Young tube was sealed, the contents thawed, and the reaction mixed via inversion for 30 minutes. The reaction volatiles were vacuum transferred to a Schlenk tube and an aliquot was removed, filtered through alumina, and analyzed by GC/MS— $(\text{Me}_3\text{Si})_2\text{O}$ , 4- $t$ -Bu-PhOSiMe<sub>3</sub>, and 4- $t$ -Bu-PhOSi(CD<sub>3</sub>)<sub>3</sub> were observed (Figure 3.24.).

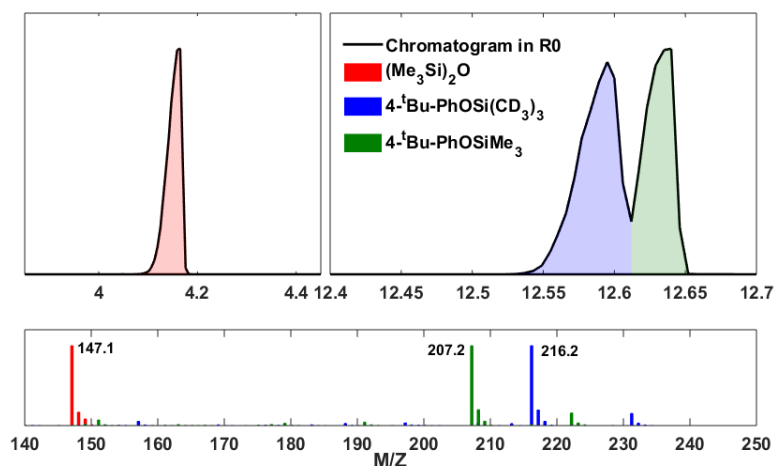


**Figure 3.24.** Partial gas chromatogram (top) and mass spectrum (bottom) of the control reaction for silyl chloride sequestration by 4- $t$ -Bu-PhONa.

#### *NaOSiMe<sub>3</sub> Mediated Silyl Scrambling*

The possibility of silyl group scrambling via siloxide initiated substitution chemistry was likewise explored. In an attempt to mimic reaction conditions, sodium trimethyl siloxide and HMDSO were present in a ten-fold excess with respect to silyl chloride.

A J. Young NMR tube was charged with 500  $\mu\text{L}$  of a THF solution of NaOSiMe<sub>3</sub> (5 mg, 0.045 mmol). The tube was degassed via three freeze-pump-thaw cycles. Following the third evacuation, the contents of the tube were left frozen and HMDSO (33.4 mL at 2.5 cm Hg, 0.045 mmol) was added via condensation from a calibrated gas bulb. Still without thawing,  $(\text{CD}_3)_3\text{SiCl}$  was admitted, in two portions, via condensation from a calibrated gas bulb (33.4 mL at 12.6 cm Hg twice, 0.450 mmol total). The tube was sealed and the contents thawed; the reaction was mixed vigorously immediately upon thawing.

The resulting clear reaction mixture was vacuum transferred into a dry Schlenk tube charged with 4-<sup>t</sup>Bu-PhONa (100 mg, 0.581 mmol) and a stir bar and mixed for 30 minutes. The volatiles were again vacuum transferred, this time to an empty Schlenk tube, and an aliquot was removed, filtered through alumina, and analyzed by GC/MS (Figure 3.25).

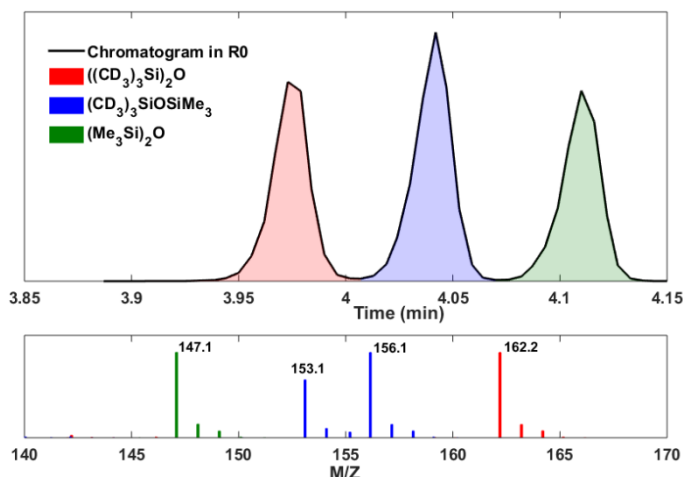


**Figure 3.25.** Partial gas chromatogram (top) and mass spectrum (bottom) supporting siloxide mediated silyl group scrambling.

*Addition of 1 Equiv. of Me<sub>3</sub>SiCl to Dianion 3-<sup>13</sup>C*

A J. Young NMR tube was charged with a deep red THF solution (600  $\mu$ L) of **3-<sup>13</sup>C** (20 mg, 0.022 mmol). The tube was degassed via three freeze-pump-thaw cycles. Following the third evacuation, the tube was left immersed in the liquid nitrogen cooling bath and Me<sub>3</sub>SiCl (33.4 mL at 1.24 cm Hg, 0.023 mmol) was condensed onto the frozen reaction mixture. The tube was thawed, mixed thoroughly whilst cold, and placed in a -78  $^{\circ}$ C dry ice/acetone cold bath. <sup>13</sup>C{<sup>1</sup>H} and <sup>31</sup>P{<sup>1</sup>H} NMR spectra were collected at -80  $^{\circ}$ C (Figure 3.26.), ensuring the sample remained cold. Resonances in the <sup>13</sup>C{<sup>1</sup>H} NMR spectrum at 263.6 and 232.7 ppm are within the range of Mo siloxycarbyne and Mo carbonyl carbons, respectively. This new species likewise shows <sup>31</sup>P{<sup>1</sup>H} resonances at 97.6 and -2.8 ppm, leading to assignment of this complex as carbyne anion **A**.

In this same sample, dianion **3-<sup>13</sup>C** and dicarbyne **9-<sup>13</sup>C** were present, presumably due to rapid disilylation of starting material, even at low temperature. The resonances for **3-**

$^{13}\text{C}$  in the  $^{13}\text{C}\{^1\text{H}\}$  NMR spectrum are in excellent agreement with an authentic sample; however, the  $^{31}\text{P}\{^1\text{H}\}$  resonances shift to 99.6 and -2.8 ppm for the bound and free phosphine arms, respectively. The upfield shifted phosphine signal is attributed to breaking of the dimeric structure of  $\mathbf{3}\text{-}^{13}\text{C}$  upon partial silylation. The free phosphine resonances for both  $\mathbf{3}$  and  $\mathbf{A}$  coincide at -80 °C but start to separate at -70 °C (Figure 3.26., inset); integration supports both species having a high-field phosphine resonance consistent with an arm-on/arm-off structure. We disfavor a silyl exchange process leading to the upfield shift observed for the Mo-bound phosphine for  $\mathbf{3}$  in these samples, as resonances at both 107.3 and 99.6 ppm are observed simultaneously in some samples (*cf.* Figure 3.27., panels 2 and 3).

Following NMR spectroscopy, the tube was refrozen and a second addition of  $\text{Me}_3\text{SiCl}$  (33.4 mL at 1.24 cm Hg, 0.023 mmol) was added. The tube was thawed, mixed thoroughly whilst cold, and placed in a -78 °C dry ice/acetone cold bath.  $^{13}\text{C}\{^1\text{H}\}$  and  $^{31}\text{P}\{^1\text{H}\}$  NMR spectra were collected at -80 °C (Figure 3.26.), and demonstrate conversion to  $\mathbf{9}\text{-}^{13}\text{C}$ . This reactivity is both consistent with the assignment of  $\mathbf{A}$  as a siloxycarbyne carbonyl anion as well as the assignment of the  $^{31}\text{P}\{^1\text{H}\}$  resonance at 99.7 ppm to dianion  $\mathbf{3}$ .

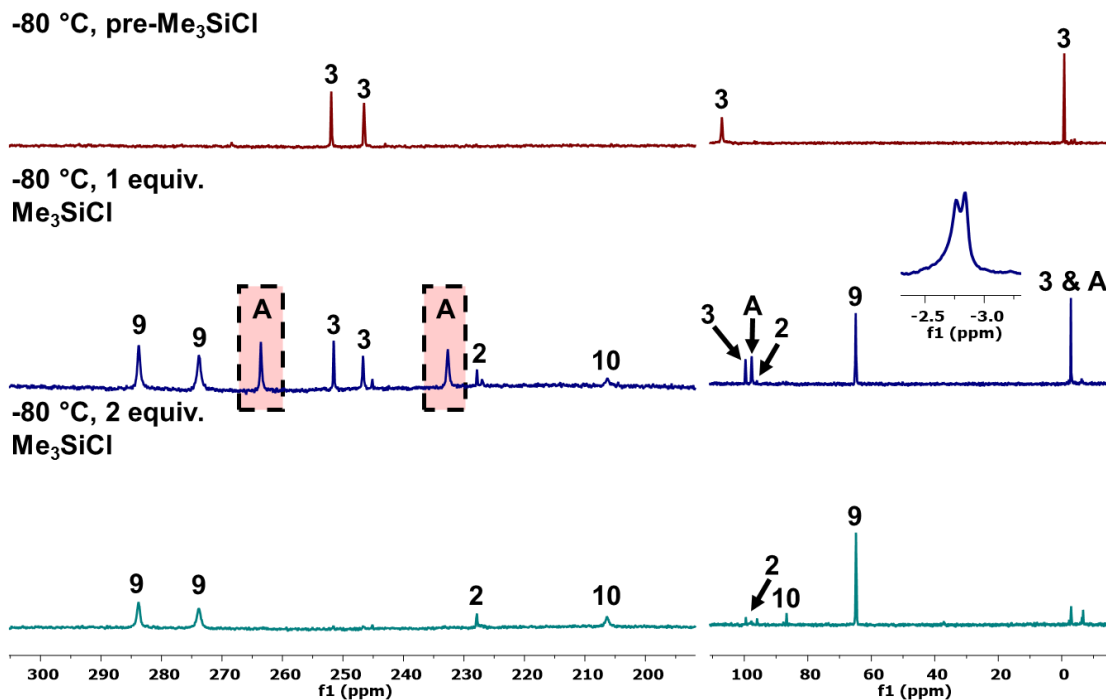


**Figure 3.26.** Stacked  $^{13}\text{C}\{^1\text{H}\}$  (left) and  $^{31}\text{P}\{^1\text{H}\}$  (right) spectra supporting the formation of an anionic siloxycarbyne complex, **A**. The downfield region of the  $^{13}\text{C}\{^1\text{H}\}$  NMR spectra show formation of an intermediate (denoted **A**, highlighted in red) upon treating dianion **3** with a single equiv. of  $\text{Me}_3\text{SiCl}$  at low temperature. Starting material (**3**) and the bis(siloxycarbyne) complex (**9**) are also observed in this reaction mixture. The inset shows the decoalescence of the resonances assigned to the free phosphine arms in **3** and **A** observed at  $-70\text{ }^\circ\text{C}$ . Following addition of a second equiv. of  $\text{Me}_3\text{SiCl}$ , **9** is formed as the major species.

#### *C–O Bond Cleavage from a Mixture of 3, 9, and A*

A J. Young NMR tube was charged with a deep red THF solution (600  $\mu\text{L}$ ) of **3**- $^{13}\text{C}$  (10 mg, 0.011 mmol). The tube was degassed via three freeze-pump-thaw cycles. Following the third evacuation, the tube was left immersed in the liquid nitrogen cooling bath and  $\text{Me}_3\text{SiCl}$  (2.8 mL at 2.4 cm Hg, 0.004 mmol) was condensed into the frozen reaction mixture. The tube was thawed, mixed thoroughly whilst cold, and refrozen. Two more  $\text{Me}_3\text{SiCl}$  additions (2.8 mL at 2.4 cm Hg, 0.004 mmol) were made in the same manner (0.012 mmol total), again mixing the contents of the tube between additions. The tube was submerged in liquid nitrogen to freeze the contents and thawed immediately before transfer to an NMR probe pre-cooled to  $-80\text{ }^\circ\text{C}$ , demonstrating a mixture of **3**- $^{13}\text{C}$ , **A**- $^{13}\text{C}$ ,

and **9-<sup>13</sup>C** by <sup>13</sup>C{<sup>1</sup>H} and <sup>31</sup>P{<sup>1</sup>H} NMR spectroscopy (Figure 3.27., top panel). This mixture was warmed in 10 °C increments in the NMR probe; <sup>13</sup>C{<sup>1</sup>H} and <sup>31</sup>P{<sup>1</sup>H} NMR spectra were collected at each temperature step (Figure 3.27.). Upon reaching -50 °C, complete consumption of putative carbyne anion **A** was observed.

The resulting mixture demonstrated several carbonyl resonances in the <sup>13</sup>C{<sup>1</sup>H} NMR spectrum from 225 to 235 ppm (Figure 3.27., panels 4 and 5). The <sup>31</sup>P{<sup>1</sup>H} NMR spectrum displayed new resonances upfield of 65 ppm, consistent with higher valent Mo species. However, these spectroscopic features did not match the expected product of C–O bond cleavage in the absence of excess silyl electrophile, carbide **7**. Hypothesizing that **7** may have been reduced *in situ* by remaining dianion **3**, the mixture was removed from the NMR probe and refrozen. Excess Me<sub>3</sub>SiCl (2.8 mL at 10.8 cm Hg, thrice, 0.066 mmol total) was condensed into the J. Young tube which was resealed, mixed at low temperature, and returned to the NMR probe. At both -80 °C and -20 °C, C–O cleavage products **8-<sup>13</sup>C**, **11-<sup>13</sup>C**, and **15-<sup>13</sup>C** were observed. Dicarbyne **9-<sup>13</sup>C**, oxidation byproduct **2-<sup>13</sup>C**, and bis(siloxy)acetylene adduct **10-<sup>13</sup>C** account for the balance of the Mo species in solution (Figure 3.27., bottom panel).

### Reactions from Carbide **7** and Mixed Dicarbynes

#### *Silylation Reactions: Me<sub>3</sub>SiCl*

A J. Young NMR tube was charged with **8-<sup>13</sup>C** (15 mg, 0.021 mmol) and <sup>n</sup>Bu<sub>4</sub>NF (7.3 mg, 0.028 mmol). The headspace of the NMR tube was evacuated and THF-*d*<sub>8</sub> (400 μL) admitted at -196 °C via vacuum transfer. The contents of the J. Young tube were thawed to -78 °C and mixed. Warming to -20 °C in the NMR probe for 15 minutes showed complete conversion to **7-<sup>13</sup>C** by <sup>13</sup>C{<sup>1</sup>H} and <sup>31</sup>P{<sup>1</sup>H} NMR spectroscopy (Figure 3.28., top).

The tube was returned to a -78 °C acetone/dry ice slush and a with a heavy argon counterflow, a THF (100 μL) solution of Me<sub>3</sub>SiCl was added via syringe. The J. Young tube was inverted quickly to mix and returned to the -80 °C NMR spectrometer, showing



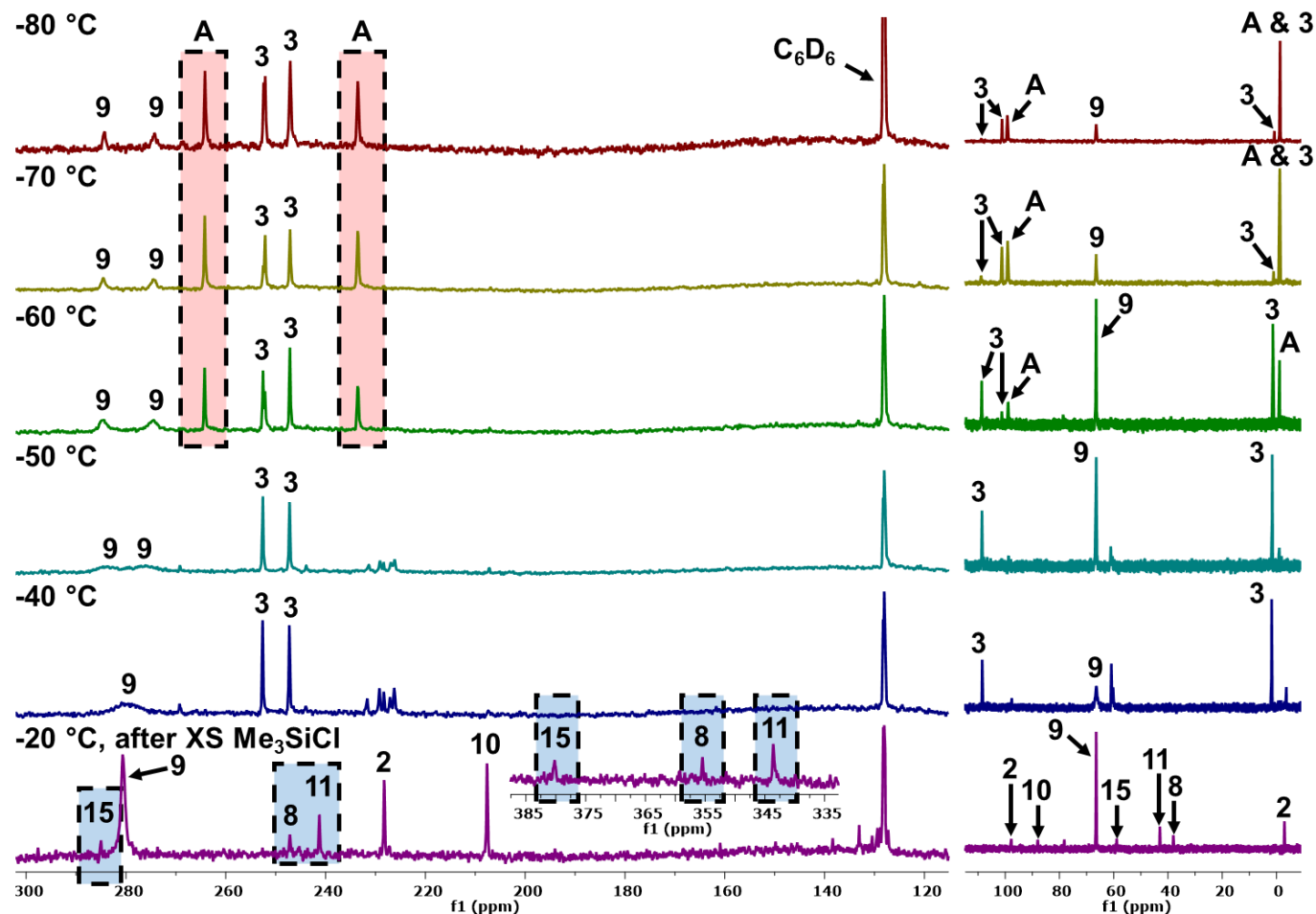


**Figure 3.27.** Partial  $^{13}\text{C}\{^1\text{H}\}$  and  $^{31}\text{P}\{^1\text{H}\}$  NMR spectra monitoring the formation and C–O bond cleavage reactivity of proposed siloxycarbyne anion **A**. Complete consumption of **A** is observed upon warming to  $-50\text{ }^\circ\text{C}$ . Though this provided an intractable mixture, low temperature silylation resulted in the formation of three C–O cleaved products—silyl carbynes **8** and **11** as well as mixed dicarbyne **15**.

complete conversion to **11**- $^{13}\text{C}$  (71%) and **8**- $^{13}\text{C}$  (29%) by  $^{13}\text{C}\{^1\text{H}\}$  and  $^{31}\text{P}\{^1\text{H}\}$  NMR spectroscopies (Figure 3.28., middle).

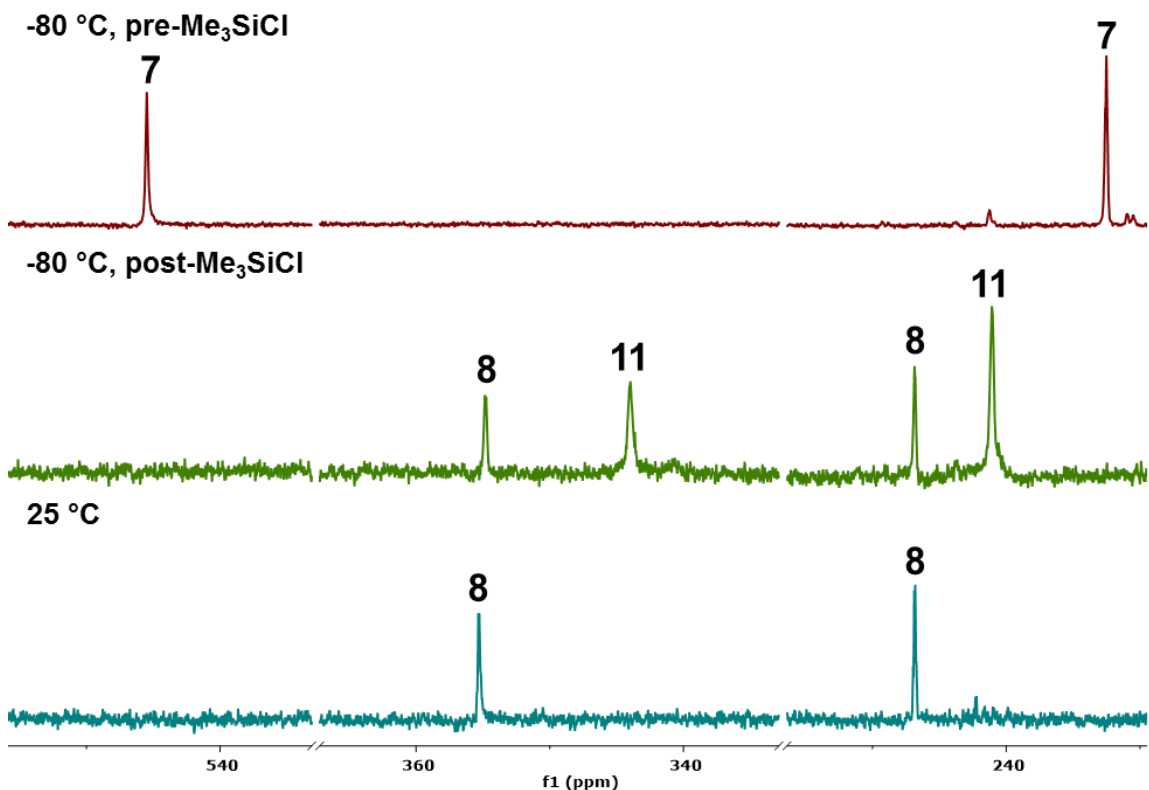


**Figure 3.28.** Partial  $^{13}\text{C}\{^1\text{H}\}$  NMR spectra of the *in situ* generation and silylation of **7**- $^{13}\text{C}$  with  $\text{Me}_3\text{SiCl}$ .

*Silylation Reactions:  $^i\text{Pr}_3\text{SiCl}$*

A J. Young NMR tube was charged with **8**- $^{13}\text{C}$  (17 mg, 0.024 mmol) and  $^n\text{Bu}_4\text{NF}$  (6.9 mg, 0.026 mmol). The headspace of the NMR tube was evacuated and  $\text{THF-}d_8$  (400  $\mu\text{L}$ ) admitted at  $-196\text{ }^\circ\text{C}$  via vacuum transfer. The contents of the J. Young tube were thawed to  $-78\text{ }^\circ\text{C}$  and mixed. Warming to  $-20\text{ }^\circ\text{C}$  in the NMR probe for 15 minutes showed complete conversion to **7**- $^{13}\text{C}$  by  $^{13}\text{C}\{^1\text{H}\}$  and  $^{31}\text{P}\{^1\text{H}\}$  NMR spectroscopy (Figure 3.29., top).

The tube was returned to a  $-78\text{ }^\circ\text{C}$  acetone/dry ice slush and a with a heavy argon counterflow, a  $\text{THF}$  (100  $\mu\text{L}$ ) solution of  $^i\text{Pr}_3\text{SiCl}$  (14.5  $\mu\text{L}$ , 0.114 mmol) was added via syringe. The J. Young tube was inverted quickly to mix and returned to the  $-80\text{ }^\circ\text{C}$  NMR

spectrometer.  $^{13}\text{C}\{^1\text{H}\}$  and  $^{31}\text{P}\{^1\text{H}\}$  NMR spectra were collected from  $-80\text{ }^\circ\text{C}$  to  $10\text{ }^\circ\text{C}$ , monitoring the conversion of  $7\text{-}^{13}\text{C}$  to  $12\text{-}^{13}\text{C}$ .

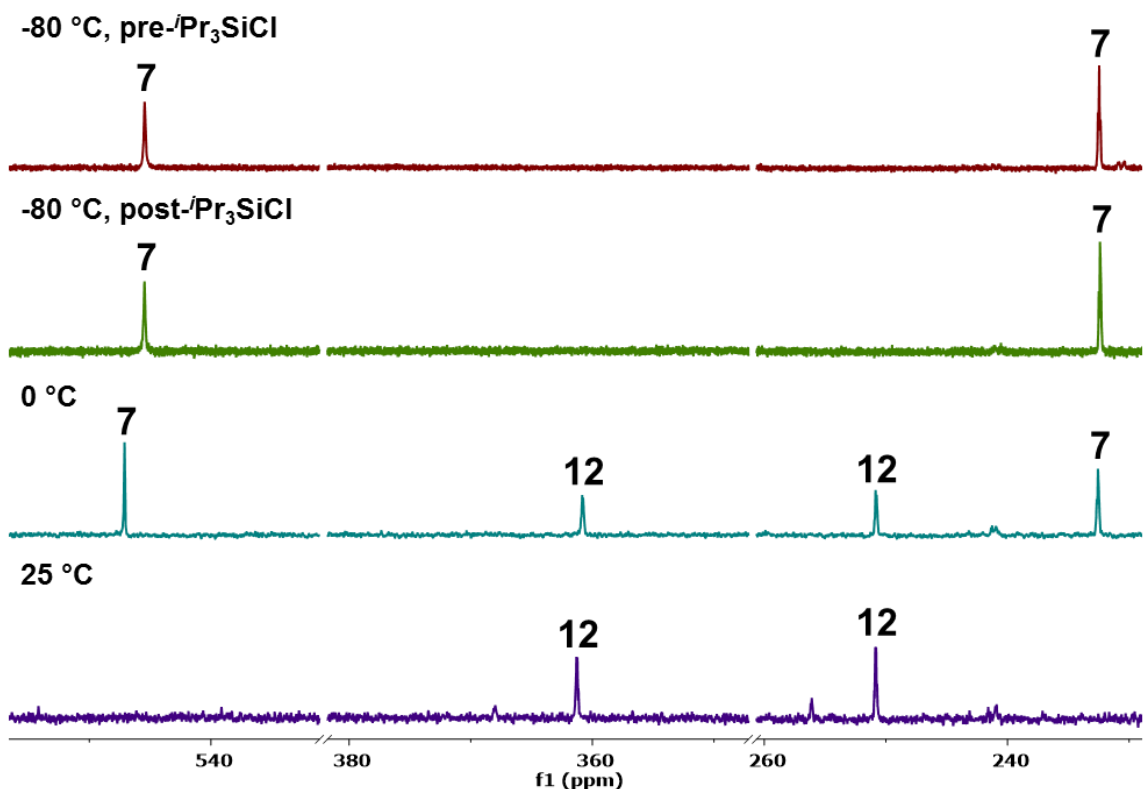


**Figure 3.29.** Partial  $^{13}\text{C}\{^1\text{H}\}$  NMR spectra of the *in situ* generation and silylation of  $7\text{-}^{13}\text{C}$  with  $t\text{-Pr}_3\text{SiCl}$ .

#### *Reduction Prior to Silylation*

Carbide  $7\text{-}^{13}\text{C}$  was prepared *in situ* from  $8\text{-}^{13}\text{C}$  (20 mg, 0.028 mmol) and  $^n\text{Bu}_4\text{NF}$  (8.1 mg, 0.031 mmol) as described above and characterized by  $^{13}\text{C}\{^1\text{H}\}$  and  $^{31}\text{P}\{^1\text{H}\}$  NMR spectroscopy at  $-20\text{ }^\circ\text{C}$  (Figure 3.30., A). The J. Young tube was cooled to  $-78\text{ }^\circ\text{C}$  and a solution of  $t\text{-Pr}_3\text{SiCl}$  (10.8 mg, 0.056 mmol) in THF (100  $\mu\text{L}$ ) was added via syringe with a heavy argon counterflow. The  $^{13}\text{C}\{^1\text{H}\}$  NMR spectrum at  $-80\text{ }^\circ\text{C}$  showed no change to the characteristic carbide resonance at 546.2 ppm (Figure 3.30., B). The tube was once again chilled to  $-78\text{ }^\circ\text{C}$  and a deep green solution of  $[\text{Na}][\text{C}_{10}\text{H}_8]$  (0.056 mmol) in THF (200  $\mu\text{L}$ ) was added via syringe with a heavy argon counterflow.  $^{13}\text{C}\{^1\text{H}\}$  NMR spectroscopy at  $-80\text{ }^\circ\text{C}$  showed quantitative conversion to a new species characterized by a broad resonance at 327.92 ppm (Figure 3.30., D). Cooling this solution to  $-100\text{ }^\circ\text{C}$  in

the NMR probe resulted in broadening of this signal and warming to  $-60\text{ }^{\circ}\text{C}$  resulted in decoalescence to two broad triplets (Figure 3.30. C and E, respectively). The chemical shifts of this species in both the  $^{13}\text{C}\{^1\text{H}\}$  and  $^{31}\text{P}\{^1\text{H}\}$  NMR spectra are consistent with an assignment as the silylcarbyne/oxycarbyne complex **13**- $^{13}\text{C}$ .

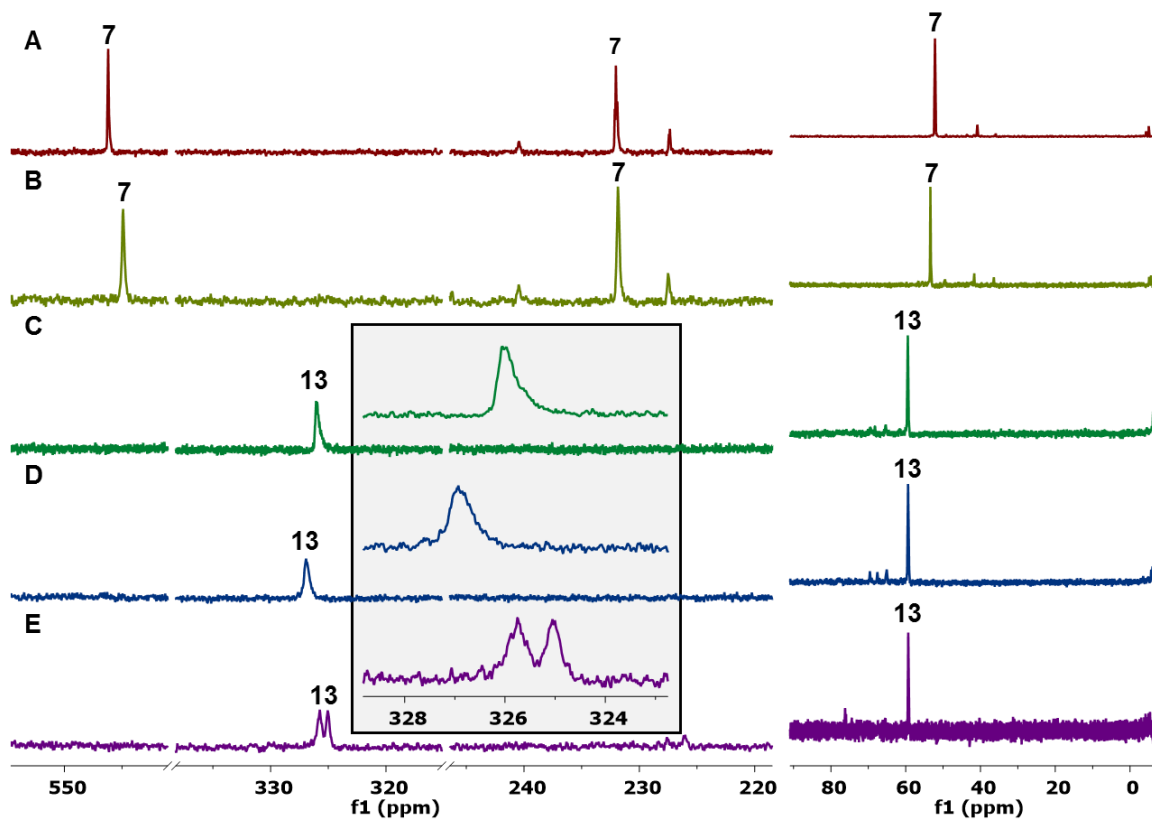


**Figure 3.30.** Partial  $^{13}\text{C}\{^1\text{H}\}$  (left) and full  $^{31}\text{P}\{^1\text{H}\}$  NMR spectra of the *in situ* generation of **7**- $^{13}\text{C}$  (A), addition of  $^t\text{Pr}_3\text{SiCl}$  (B), and subsequent reduction with  $[\text{Na}][\text{C}_{10}\text{H}_8]$  (C-E). The shaded inset shows an enlargement of the resonances attributed to the silylcarbyne and oxycarbyne carbons of **13**- $^{13}\text{C}$ —only at  $-60\text{ }^{\circ}\text{C}$  are the two carbon resonances resolved; warming the sample to higher temperatures resulted in reaction (*vide infra*).

#### *Independent Synthesis of a Silylcarbyne/Oxycarbyne Complex*

If the proposed assignment of **13** is indeed correct, it should be directly accessible via the two-electron reduction of **8**. To investigate this, a J. Young NMR tube was charged with a deep red THF (400  $\mu\text{L}$ ) solution of **8**- $^{13}\text{C}$  (20 mg, 0.028 mmol).  $^{13}\text{C}\{^1\text{H}\}$  NMR spectroscopy (Figure 3.31., A) showed the characteristic resonances at 355.8 and 247.5 attributable to the silyl alkylidyne and carbonyl carbons, respectively. The tube was chilled to  $-80\text{ }^{\circ}\text{C}$  and a deep green solution of  $[\text{Na}][\text{C}_{10}\text{H}_8]$  (0.059 mmol) in THF (200  $\mu\text{L}$ ) was

added via syringe with a heavy argon counterflow. The  $^{13}\text{C}\{^1\text{H}\}$  NMR spectrum ( $-80\text{ }^\circ\text{C}$ ) showed quantitative conversion of  $8\text{-}^{13}\text{C}$  to a new species characterized by a broad triplet at 338.7 ppm and a broad resonance at 58.49 ppm in the  $^{13}\text{C}\{^1\text{H}\}$  and  $^{31}\text{P}\{^1\text{H}\}$  NMR spectra, respectively (Figure 3.31., C). Cooling this mixture to  $-100\text{ }^\circ\text{C}$  showed decoalescence of the  $^{13}\text{C}\{^1\text{H}\}$  NMR resonance to two triplets (Figure S21, B). Warming the sample to  $-60\text{ }^\circ\text{C}$  likewise resulted in decoalescence, with the broader resonance now shifting downfield (Figure 3.31., D). These spectral features are consistent with those observed for **13**, leading to the assignment of this complex as the trimethylsilyl analog, **14**. Further warming resulted in C–C coupling chemistry and formation of dinitrogen complex **5** (*vide infra*).

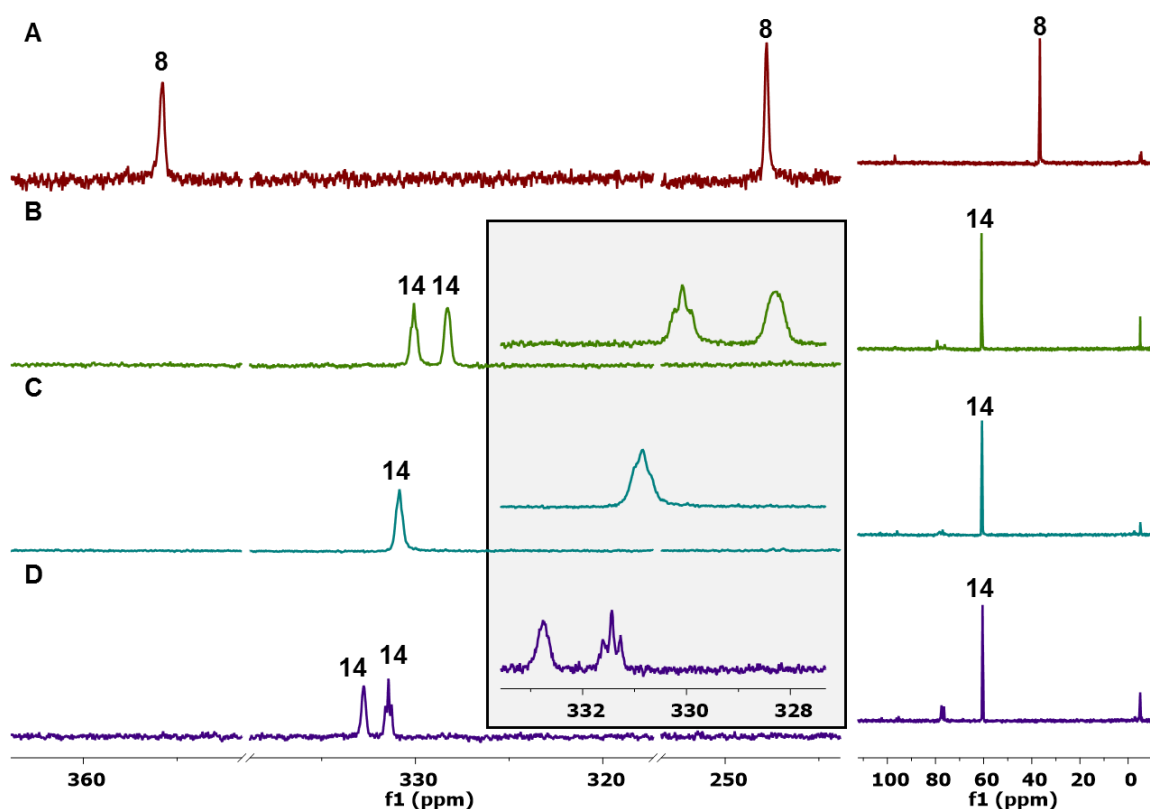


**Figure 3.31.** Partial  $^{13}\text{C}\{^1\text{H}\}$  (left) and full  $^{31}\text{P}\{^1\text{H}\}$  (right) NMR spectra of the reduction of  $8\text{-}^{13}\text{C}$ . The shaded inset shows an enlargement of the resonances attributed to the silylcarbyne and oxycarbyne carbons of  $14\text{-}^{13}\text{C}$  at  $-100\text{ }^\circ\text{C}$  (B),  $-80\text{ }^\circ\text{C}$  (C), and  $-60\text{ }^\circ\text{C}$  (D); warming the sample to higher temperatures resulted in reaction (*vide infra*).

*Demonstration of C–C Bond Formation and Organic Fragment Release from 14*

Warming either of the above samples of **13** or **14** to  $-60\text{ }^{\circ}\text{C}$  resulted in C–C coupling, release of the resulting silyl ethynolate, and adventitious binding of dinitrogen (Figure 3.32.). For **13**- $^{13}\text{C}$  doublets ( $\delta = 107.7, 23.98$ ,  $^1J(\text{C,C}) = 168.8\text{ Hz}$ ) characteristic of **6a** were observed in the  $^{13}\text{C}\{^1\text{H}\}$  NMR spectrum, with simultaneous observation of complex **5** in the  $^{31}\text{P}\{^1\text{H}\}$  NMR spectrum (Figure 3.32., A). The resonance for the second acetylenic carbon ( $\delta = 23.98\text{ ppm}$ ) is obscured, overlapping with the upfield side of the THF solvent residual.

Samples of **14**- $^{13}\text{C}$  showed two coupling doublets in the  $^{13}\text{C}\{^1\text{H}\}$  NMR spectrum—assigned as the silyl ethynolate **6b** based on chemical shift and  $^1J_{\text{CC}}$  coupling constant<sup>55</sup>—at  $-60\text{ }^{\circ}\text{C}$  (Figure 3.32., B); these resonances grow in as the sample is warmed to  $-30\text{ }^{\circ}\text{C}$  (Figure 3.32., B-E). Freezing the contents of the J. Young NMR tube, evacuating the headspace, and adding of one equiv. of  $\text{Me}_3\text{SiCl}$  (33.4 mL at 1.8 cm Hg, 0.030 mmol) via condensation at  $-196\text{ }^{\circ}\text{C}$  resulted in formation of disilyl ketene **6c** upon thawing to  $-78\text{ }^{\circ}\text{C}$  by  $^{13}\text{C}\{^1\text{H}\}$  NMR spectroscopy (Figure 3.32., F). This is the thermodynamically preferred isomer of oxyacetylenes bearing small silyl substituents.<sup>56</sup>

*Silylation of 14: Formation of Mixed Silyl/Siloxy Dicarbyne 15*

Complex **14**- $^{13}\text{C}$  was prepared *in situ*, as described above, from the reduction of **8**- $^{13}\text{C}$  (20 mg, 0.028 mmol) with  $[\text{Na}][\text{C}_{10}\text{H}_8]$  (0.028 mmol in 100  $\mu\text{L}$  of THF) in THF (500  $\mu\text{L}$ ) in a J. Young NMR tube (Figure 3.33., A). The contents of this tube were frozen by immersion in liquid nitrogen and  $\text{Me}_3\text{SiCl}$  (33.4 mL at 1.7 mL Hg, 0.031 mmol) was added via condensation from a calibrated bulb. The tube was sealed, the contents thawed and mixed, and placed in a  $-78\text{ }^{\circ}\text{C}$  dry ice/acetone slush bath. NMR spectroscopy studies at  $-80\text{ }^{\circ}\text{C}$  show new resonances in the  $^{13}\text{C}\{^1\text{H}\}$  ( $\delta = 378.9, 283.8\text{ ppm}$ ) and  $^{31}\text{P}\{^1\text{H}\}$  ( $\delta = 57.0\text{ ppm}$ ) spectra were assigned to the mixed dicarbyne **15** (Figures 3.33., B). Warming this sample to  $-40\text{ }^{\circ}\text{C}$  resolved the scalar coupling between the trans-spanning phosphines and carbyne carbons— $^{13}\text{C}\{^1\text{H}\}$   $\delta = 378.1\text{ ppm}$  (t,  $^2J(\text{P,C}) = 18.79\text{ Hz}$ ,  $\text{CSiMe}_3$ ), 301.3

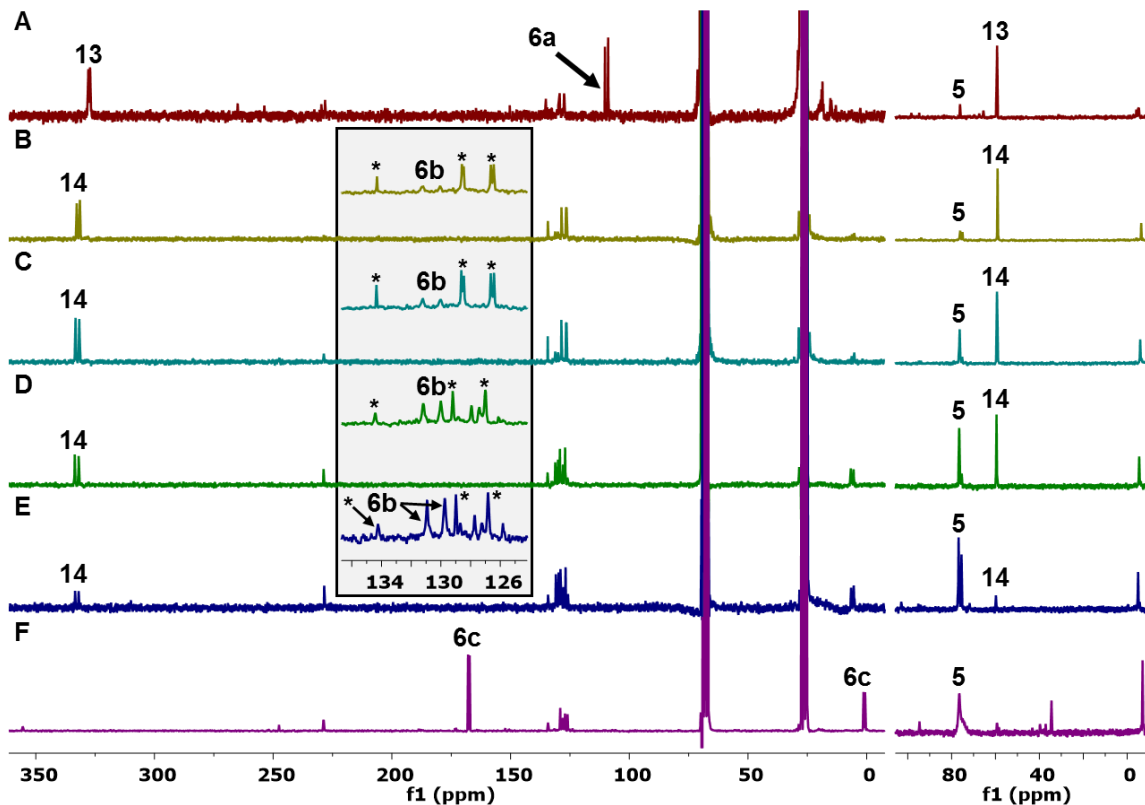


**Figure 3.32.**  $^{13}\text{C}\{^1\text{H}\}$  NMR spectra supporting the formation of silylated oxyacetylenes from mixed carbynes **13** and **14**. Warming **13**- $^{13}\text{C}$  (as prepared, a second equivalent of  $^i\text{Pr}_3\text{SiCl}$  is present in solution) affords **6a** ( $^{13}\text{C}\{^1\text{H}\}$  NMR (126 MHz,  $-60\text{ }^\circ\text{C}$ , THF)  $\delta = 107.72, 23.98, ^1J_{\text{CC}} = 168.83$  Hz) at  $-60\text{ }^\circ\text{C}$ . Warming **14**- $^{13}\text{C}$  likewise results in formation of the metal free organic, ethynolate **6b** ( $^{13}\text{C}\{^1\text{H}\}$  NMR (126 MHz,  $25\text{ }^\circ\text{C}$ , THF)  $\delta = 131.34, 5.94, ^1J_{\text{CC}} = 139.6$  Hz), as observed at  $-60\text{ }^\circ\text{C}$ ,  $-50\text{ }^\circ\text{C}$ ,  $-40\text{ }^\circ\text{C}$  and  $-30\text{ }^\circ\text{C}$  (B-E, respectively). Addition of  $\text{Me}_3\text{SiCl}$  to this mixture yields ketene **6c** ( $^{13}\text{C}\{^1\text{H}\}$  NMR (126 MHz,  $-80\text{ }^\circ\text{C}$ , THF)  $\delta = 167.54, 1.13, ^1J_{\text{CC}} = 82.3$  Hz). The shaded inset shows an enlargement of the 125-135 ppm region of the  $^{13}\text{C}\{^1\text{H}\}$  NMR spectrum; the starred resonances correspond to naphthalene.

ppm (t,  $^2J(\text{P,C}) = 13.55$  Hz,  $\text{COSiMe}_3$ );  $^{31}\text{P}\{^1\text{H}\}$   $\delta = 57.4$  ppm (dd,  $^2J(\text{P,C}) = 18.79, 13.55$  Hz). Further warming to  $0\text{ }^\circ\text{C}$  resulted in formation of disilylketene **6c** (Figure 3.33., B-D) and concomitant generation of **5**, as evidenced by  $^{31}\text{P}\{^1\text{H}\}$  NMR spectroscopy.

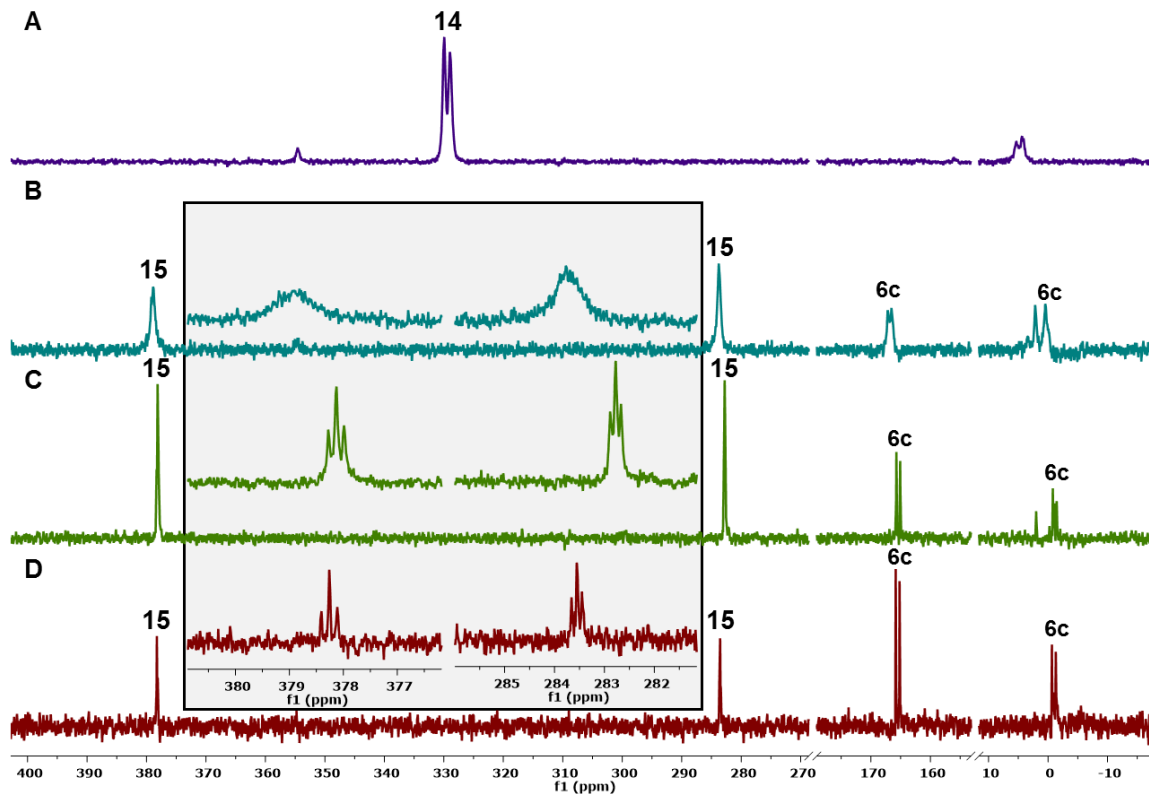


**Figure 3.33.** Partial  $^{13}\text{C}\{^1\text{H}\}$  NMR spectra following the formation of and C–C coupling from mixed dicarbyne  $15\text{-}^{13}\text{C}$ . The shaded inset shows an enlargement of the silyl- and siloxycarbyne resonances of  $15\text{-}^{13}\text{C}$ .

### Crossover Experiments

To rule out the possibility of a bimetallic pathway for C–C bond formation, crossover experiments were conducted. Both one-pot reduction and coupling from dicarbonyl dication precursors  $1/1\text{-}^{13}\text{C}$  as well as silyl ethynolate formation from  $8/8\text{-}^{13}\text{C}$  showed no evidence for label scrambling.

#### *One-Pot Reduction and Silylation*

A 20 mL scintillation vial was charged with **1** (52 mg, 0.057 mmol),  $1\text{-}^{13}\text{C}$  (70 mg, 0.077 mmol), THF (4 mL), and a stir bar. Stirring was initiated and  $\text{KC}_8$  (127 mg, 0.938 mmol) was added in a single portion to the yellow suspension. An immediate darkening of the mixture resulted; stirring continued for 30 minutes. At this time, the vial was placed in a liquid nitrogen cooled cold well and the dark purple mixture frozen solid. While thawing, a solution of  $^i\text{Pr}_3\text{SiCl}$  (103 mg, 0.536 mmol) in THF (1 mL) was added dropwise, with



stirring. Following the addition, the vial was allowed to warm to room temperature. An aliquot was removed, filtered through a Celite plug, and analyzed by  $^{13}\text{C}\{^1\text{H}\}$  and  $^{31}\text{P}\{^1\text{H}\}$  NMR spectroscopies, indicating no formation of monolabeled **6a** (Figure 3.34., top).

*Silyl Carbyne Reductive Coupling*

A 20 mL scintillation vial was charged with **8** (15 mg, 0.021 mmol), **8- $^{13}\text{C}$**  (17 mg, 0.024 mmol), THF (3 mL), and a stir bar. The deep burgundy solution was frozen in a liquid nitrogen cooled cold well and, while thawing,  $\text{KC}_8$  (20 mg, 0.148 mmol) was added in a single portion with stirring. An aliquot was removed, filtered through a Celite plug, and analyzed by  $^{13}\text{C}\{^1\text{H}\}$  and  $^{31}\text{P}\{^1\text{H}\}$  NMR spectroscopies, indicating no formation of monolabeled **6b** (Figure 3.34., bottom).

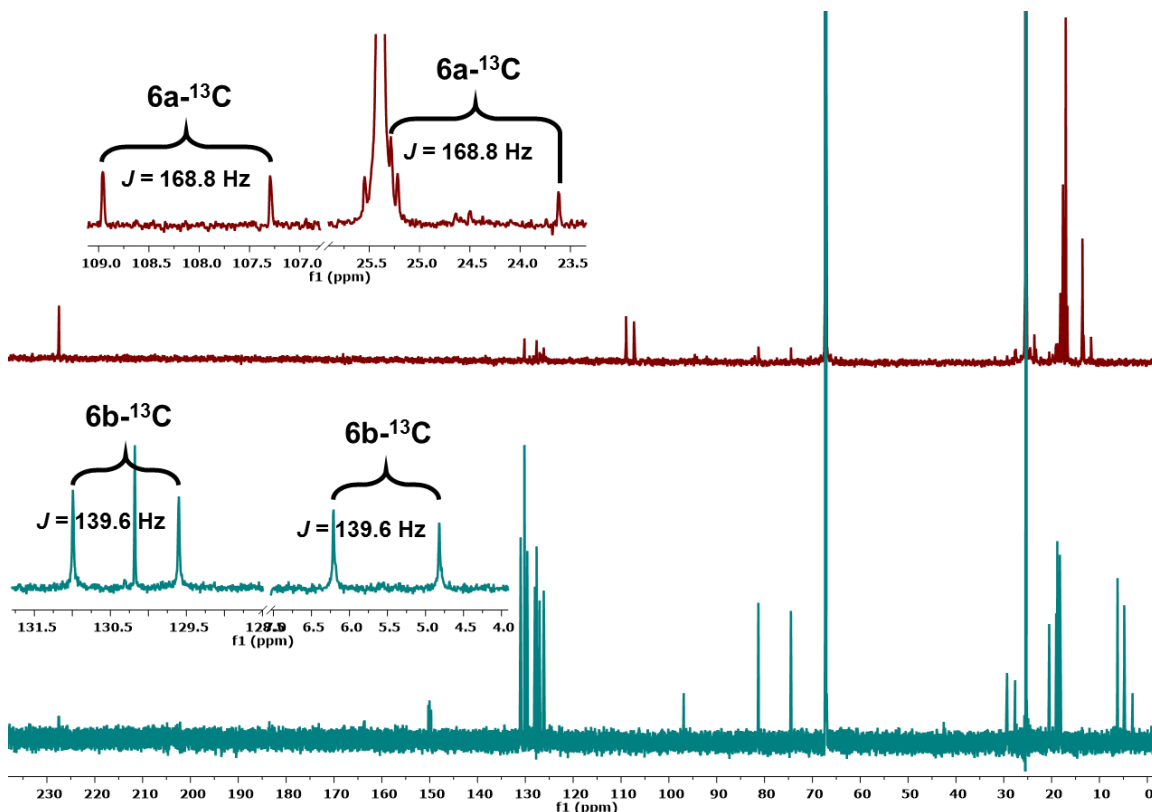


**Figure 3.34.**  $^{13}\text{C}\{^1\text{H}\}$  (126 MHz, THF, 23 °C) NMR spectra of aliquots of crossover experiment reaction mixtures. In both cases, no monolabeled C–C coupled products were observed; these would resonate as singlets midway between the doublets of the coupled products. The insets show enlargements of the  $\text{C}_2\text{O}_1$  organic product carbon resonances.

### Quantum Mechanics Data

**Computational Details:** All calculations were performed with DFT as implemented in Gaussian 09 Revision C.01.<sup>73</sup> Geometry optimizations and electronic structure calculations were performed with revised TPSS exchange and correlation functionals.<sup>59</sup> The LANL2DZ basis set<sup>60</sup> was used for all atoms. No solvent corrections were employed. All optimizations were performed ignoring molecular symmetry—crystallographic coordinates were used as a starting point when possible. Energetic minima were confirmed with subsequent frequency calculations which did not return imaginary frequencies. Structures optimized in this manner showed good agreement with bond lengths and angles determined via single crystal X-ray diffraction (Table 3.4.). To further validate the application of these calculations, <sup>13</sup>C NMR shifts were calculated using the GIAO method.<sup>61</sup> The trends observed in the calculated spectroscopic data (NMR and IR) are in good agreement with those established experimentally. In instances when the single-point energy was of interest, DF-TD3 single-point dispersion corrections<sup>74</sup> with BJ-damping<sup>75</sup> were conducted. All molecular orbital illustrations were generated using GaussView, the GUI component of the Gaussian software package, and depicted with a 0.04 e/ $\text{\AA}^3$  isosurface value.

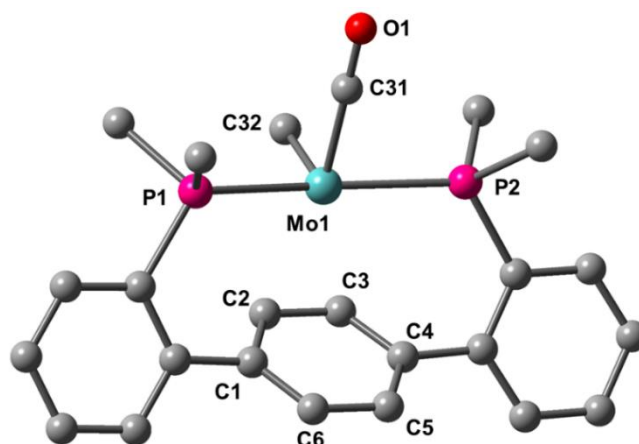


**Figure 3.35.** Geometry optimized structure of carbide 7 with atom radii scaled by 50%. Hydrogen atoms are omitted for clarity. Selected bond lengths [ $\text{\AA}$ ] and angles [ $^\circ$ ]: C1–C2 1.445, C2–C3 1.430, C3–C4 1.445, C4–C5 1.403, C5–C6 1.428, C6–C1 1.403, Mo1–C2 2.492, Mo1–C3 2.492, Mo1–C31 1.979, C31–O1 1.210, Mo1–C32 1.771, C31–Mo1–C32 89.09.

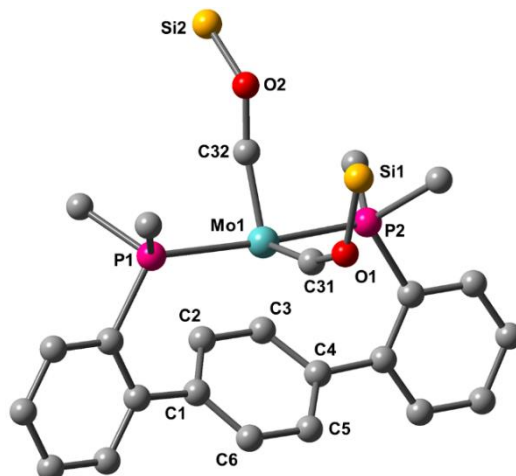


**Figure 3.36.** Geometry optimized structure of bis(siloxycarbyne) **9** with atom radii scaled by 50%. Hydrogen atoms are omitted for clarity. Selected bond lengths [ $\text{\AA}$ ] and angles [ $^\circ$ ]: C1–C2 1.437, C2–C3 1.425, C3–C4 1.437, C4–C5 1.411, C5–C6 1.415, C6–C1 1.411, Mo1–C2 2.593, Mo1–C3 2.593, Mo1–C31 1.850, C31–O1 1.360, Mo1–C32 1.850, C32–O2 1.381, C31–Mo1–C32 109.94, Mo1–C31–O1 160.57, Mo1–C32–O2 161.49.

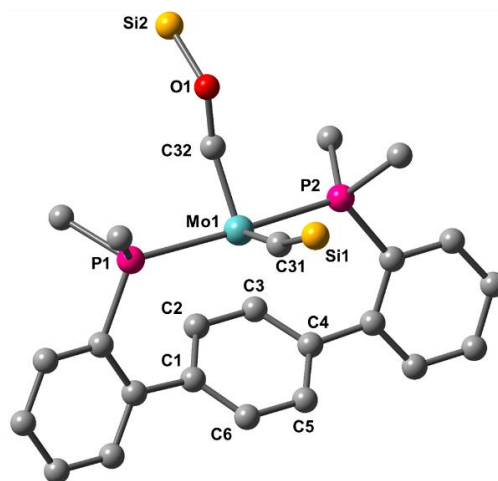


**Figure 3.37.** Geometry optimized structure of mixed dicarbyne **15** with atom radii scaled by 50%. Hydrogen atoms are omitted for clarity. Selected bond lengths [ $\text{\AA}$ ] and angles [ $^\circ$ ]: C1–C2 1.433, C2–C3 1.421, C3–C4 1.433, C4–C5 1.411, C5–C6 1.415, C6–C1 1.411, Mo1–C2 2.645, Mo1–C3 2.646, Mo1–C31 1.823, Mo1–C32 1.860, C32–O2 1.382, C31–Mo1–C32 109.27, Mo1–C32–O1 153.39.

Computation was employed to rationalize the thermodynamic preference for five-coordinate **8** over *pseudo*-octahedral **11**. Surprisingly, the absolute energy of silyl carbyne **8** was calculated to be 4.4 kcal/mol *higher* than that of silyl carbyne **11**. Optimizing both structures with a trimethylsilyl substituent on the alkylidyne ligand still predicted **11** to be more stable than **8**, but reduced the energetic difference to 2.9 kcal/mol. Changing the

phosphine substituents to isopropyl groups inverted the relative energies, favoring five-coordinate **8** by 2.3 kcal/mol in accord with experimental results (Table 3.2.). The calculated electronic structures of **8** and **11** are quite similar, both exhibiting complimentary  $\pi$ -acidic/ $\pi$ -basic interactions from the mixed ligand set. These data, in conjunction with the reluctance of bulkier  $\text{Pr}_3\text{SiCl}$  to silylate **7** at low temperatures support a steric, rather than electronic, preference for the five-coordinate silyl carbyne isomer.

**Table 3.2.** Optimized gas-phase single-point energies for variants of **8** and **11**.

	<b>SiH<sub>3</sub>, ArPMe<sub>2</sub></b>	<b>SiMe<sub>3</sub>, ArPMe<sub>2</sub></b>	<b>SiMe<sub>3</sub>, ArP<sup>t</sup>Pr<sub>2</sub></b>
<i>cis</i> arene/carbyne, <b>11</b>	-1105.54210326 a.u.	-1223.53528943 a.u.	-1538.01876179 a.u.
<i>trans</i> arene/carbyne, <b>8</b>	-1105.53681517 a.u.	-1223.53075602 a.u.	-1538.02236210 a.u.
$\Delta$ ( <b>8</b> – <b>11</b> )	3.32 kcal/mol	2.84 kcal/mol	-2.26 kcal/mol
$\Delta$ ( <b>8</b> – <b>11</b> ) <sup>‡</sup>	4.44 kcal/mol	2.85 kcal/mol	-2.26 kcal/mol

<sup>‡</sup>Energies include single-point dispersion correction terms.

**Table 3.3.** Comparison of experimental and calculated spectroscopic data for **2**, **7-11**, and **15**.

	<b>2</b>		<b>7</b>		<b>8</b>		<b>9</b>		<b>10</b>		<b>11</b>		<b>15</b>	
	Exp.	Calc.	Exp.	Calc.	Exp.	Calc.	Exp.	Calc.	Exp.	Calc.	Exp.	Calc.	Exp.	Calc.
$\delta_{\text{C31}}$ (ppm) <sup>‡</sup>	228.5	235.3	233.2	239.4	247.4	253.2	285.8	313.6	207.9	203.5	241.9	249.9	378.9	359.1
$\delta_{\text{C32}}$ (ppm) <sup>‡</sup>	228.5	234.7	546.2	567.7	355.9	323.7	279.8	286.2	207.9	205.7	344.9	297.2	283.7	311.5
$\nu_{\text{CO}}$ (cm <sup>-1</sup> )	1887	1805	N/A	1780	1873	1787	N/A	N/A	N/A	N/A	N/A	1817	N/A	N/A
$\nu_{\text{CO}}$ (cm <sup>-1</sup> )	1832	1764	N/A	N/A	N/A	N/A	N/A	N/A	N/A	N/A	N/A	N/A	N/A	N/A

<sup>‡</sup>Chemical shifts are referenced to the GIAO calculated <sup>13</sup>C NMR shift of Me<sub>4</sub>Si optimized using the same basis set (LANL2DZ) and functional (RTPSSTPSS) as the metal complexes.

Table 3.4. Comparison of experimental and calculated structural metrics for **2**, **8**, **10**, and **11**

	2		8			10		11		
	Exp.	Calc.	Exp.	Calc.	$\sqrt{\text{Pr}_2\text{-Me}_3\text{Si}}$ Calc.	Exp.	Calc.	Exp.	Calc.	$\sqrt{\text{Pr}_2\text{-Me}_3\text{Si}}$ Calc.
<b>C1-C2</b>	1.4183(8)	1.445	1.395(3)	1.423	1.423	1.424(2)	1.446	1.424(1)	1.407	1.409
<b>C2-C3</b>	1.4216(8)	1.442	1.392(3)	1.412	1.410	1.427(2)	1.450	1.395(1)	1.422	1.421
<b>C3-C4</b>	1.4210(8)	1.443	1.401(3)	1.423	1.423	1.430(2)	1.465	1.421(1)	1.407	1.406
<b>C4-C5</b>	1.4214(8)	1.444	1.390(3)	1.416	1.416	1.430(2)	1.450	1.382(1)	1.438	1.436
<b>C5-C6</b>	1.4254(8)	1.444	1.393(3)	1.412	1.413	1.426(2)	1.455	1.407(1)	1.422	1.420
<b>C6-C1</b>	1.4272(8)	1.443	1.395(3)	1.416	1.415	1.428(2)	1.451	1.383(1)	1.438	1.439
<b>Mo1-P1</b>	2.4191(2)	2.478	2.5869(6)	2.590	2.671	2.4712(4)	2.522	2.6027(2)	2.586	2.669
<b>Mo1-P2</b>	N/A	N/A	2.5562(6)	2.591	2.670	N/A	N/A	2.5972(2)	2.586	2.657
<b>Mo1-C31</b>	1.9675(7)	1.960	1.974(2)	1.968	1.958	2.054(1)	2.073	1.9758(9)	1.971	1.966
<b>Mo1-C32</b>	1.9710(6)	1.961	1.767(2)	1.793	1.797	2.032(1)	2.048	1.7691(8)	1.811	1.820
<b>Mo-C<sub>arene</sub> (ave.)</b>	2.3254(6)	2.373	2.82 (C2/C3 contact)	2.84 (C2/C3 contact)	2.85 (C2/C3 contact)	2.280(2)	2.314	2.5220(9)	2.541	2.534
<b>Mo-Cl</b>	N/A	N/A	2.5380(6)	2.570	2.590	N/A	N/A	2.5581(2)	2.620	2.645
<b>C31-O1</b>	1.1632(9)	1.210	1.138(3)	1.211	1.214	1.326(2)	1.384	1.158(1)	1.203	1.208
<b>C32-O2</b>	1.1645(8)	1.209	N/A	N/A	N/A	1.368(2)	1.397	N/A	N/A	N/A
<b>C32-Si1</b>	N/A	N/A	1.877(2)	1.878	1.902	N/A	N/A	1.8815(9)	1.884	1.912
<b>∠P1-Mo1-P2</b>	N/A	N/A	176.12(2)	171.87	172.06	N/A	N/A	171.00(1)	174.00	169.07
<b>∠C31-Mo1-C32</b>	85.01(3)	86.21	87.4(1)	86.15	87.99	38.02(6)	38.46	84.66(4)	89.27	88.11
<b>∠P1-Mo1-C31</b>	94.60(2)	92.03	89.46(7)	92.27	90.32	106.97(6)	113.15	94.48(3)	89.46	94.24
<b>∠P1-Mo1-C32</b>	91.38(2)	92.44	92.50(7)	93.49	93.93	82.70(4)	78.77	93.62(3)	92.93	94.85
<b>∠P2-Mo1-C31</b>	N/A	N/A	88.36(7)	92.28	90.03	N/A	N/A	87.06(3)	89.47	86.73
<b>∠P2-Mo1-C32</b>	N/A	N/A	90.61(7)	93.53	94.01	N/A	N/A	95.35(3)	92.95	96.07
<b>∠C31-Mo1-Cl</b>	N/A	N/A	170.88(7)	167.46	162.76	N/A	N/A	94.17(3)	88.03	91.62
<b>∠C32-Mo1-Cl</b>	N/A	N/A	101.62(7)	106.39	104.25	N/A	N/A	175.82(3)	177.30	176.55

### ***Crystallographic Information***

CCDC deposition numbers 1412062-1412064 and 1412066-1412067 contain the supplementary crystallographic data for this paper. These data can be obtained free of charge from The Cambridge Crystallographic Data Centre via [www.ccdc.cam.ac.uk/data\\_request/cif](http://www.ccdc.cam.ac.uk/data_request/cif).

**Refinement Details**—In each case, crystals were mounted on a glass fiber or MiTeGen loop using Paratone oil, then placed on the diffractometer under a nitrogen stream. Crystals for compounds **3** and **4** were manipulated under an Argon purge due to atmospheric sensitivity. Low temperature (100 K) X-ray data were obtained on a Bruker KAPPA APEXII CCD based diffractometer (Mo fine-focus sealed X-ray tube,  $K_{\alpha} = 0.71073 \text{ \AA}$ ) or a Bruker D8 VENTURE Kappa Duo PHOTON 100 CMOS based diffractometer (Mo  $I_{\mu}S$  HB micro-focus sealed X-ray tube,  $K_{\alpha} = 0.71073 \text{ \AA}$  OR Cu  $I_{\mu}S$  HB micro-focused X-ray tube,  $K_{\alpha} = 1.54178$ ). All diffractometer manipulations, including data collection, integration, and scaling were carried out using the Bruker APEXII software.<sup>76</sup> Absorption corrections were applied using SADABS.<sup>77</sup> Space groups were determined on the basis of systematic absences and intensity statistics and the structures were solved in the Olex 2 software interface<sup>78</sup> by intrinsic phasing using XT (incorporated into SHELXTL)<sup>79</sup> and refined by full-matrix least squares on  $F^2$ . All non-hydrogen atoms were refined using anisotropic displacement parameters. Hydrogen atoms were placed in the idealized positions and refined using a riding model. The structure was refined (weighed least squares refinement on  $F^2$ ) to convergence. Graphical representation of structures with 50% probability thermal ellipsoids were generated using Diamond 3 visualization software.<sup>80</sup>

**Table 3.5.** Crystal and refinement data for complexes **2-4** and **8**.

	<b>2</b>	<b>3</b>	<b>4</b>	<b>8</b>
CCDC Number <sup>81</sup>	1412068	1412062	1412063	1412064
Empirical formula	C <sub>38</sub> H <sub>46</sub> MoO <sub>2</sub> P <sub>2</sub>	C <sub>96</sub> H <sub>144</sub> K <sub>4</sub> Mo <sub>2</sub> O <sub>12</sub> P <sub>4</sub>	C <sub>178</sub> H <sub>264</sub> K <sub>12</sub> Mo <sub>4</sub> O <sub>18</sub> P <sub>8</sub>	C <sub>35</sub> H <sub>49</sub> ClMoOP <sub>2</sub> Si
Formula weight	692.63	1962.26	3792.60	707.16
T (K)	100	100	100	100
<i>a</i> , Å	17.1790(7)	13.2319(5)	24.1145(8)	9.1531(2)
<i>b</i> , Å	7.4663(3)	15.1410(6)	21.1590(7)	17.1136(4)
<i>c</i> , Å	27.0465(12)	25.4501(10)	38.2636(12)	21.8842(6)
$\alpha$ , °	90	101.2840(10)	90	90
$\beta$ , °	91.405(2)	100.0870(10)	94.002(2)	90
$\gamma$ , °	90	90.0560(10)	90	90
Volume, Å <sup>3</sup>	3468.0(3)	4919.6(3)	19476.0(11)	3428.00(14)
Z	4	2	4	4
Crystal system	Monoclinic	Triclinic	Monoclinic	Orthorhombic
Space group	<i>P</i> 2 <sub>1</sub> / <i>n</i>	$\bar{P}1$	<i>P</i> 2 <sub>1</sub> / <i>c</i>	<i>P</i> 2 <sub>1</sub> 2 <sub>1</sub>
<i>d</i> <sub>calc</sub> , g/cm <sup>3</sup>	1.327	1.325	1.293	1.370
$\theta$ range, °	1.389 to 45.898	2.203 to 37.810	2.315 to 75.840	2.209 to 37.904
$\mu$ , mm <sup>-1</sup>	0.502	0.546	5.420	0.615
Abs. Correction	Semi-empirical	Semi-empirical	Semi-empirical	Semi-empirical
GOF	1.032	1.080	1.012	1.086
R <sub>1</sub> , <sup>a</sup> wR <sub>2</sub> <sup>b</sup> [ <i>I</i> > 2 $\sigma$ ( <i>I</i> )]	0.0286, 0.0653	0.0748, 0.1285	0.0644, 0.1463	0.0395, 0.0742
Diffractometer	APEXII	PHOTON	PHOTON	PHOTON
Radiation Type	Mo K $\alpha$	Mo K $\alpha$	Cu K $\alpha$	Mo K $\alpha$

<sup>a</sup>  $R_1 = \sum ||F_o| - |F_c|| / \sum |F_o|$ . <sup>b</sup>  $wR_2 = [\sum [w(F_o^2 - F_c^2)^2] / \sum [w(F_o^2)^2]]^{1/2}$ .

**Table 3.6.** Crystal and refinement data for complexes **10**, **11**, **16**, and **17**.

	<b>10</b>	<b>11</b>	<b>16</b>	<b>17</b>
CCDC Number <sup>81</sup>				
Empirical formula	C <sub>42</sub> H <sub>68</sub> MoO <sub>2</sub> P <sub>2</sub> Si <sub>2</sub>	C <sub>35</sub> H <sub>49</sub> ClMoOP <sub>2</sub> Si	C <sub>38</sub> H <sub>48</sub> MoOP <sub>2</sub>	C <sub>90</sub> H <sub>136</sub> K <sub>4</sub> Mo <sub>2</sub> O <sub>9</sub> P <sub>4</sub>
Formula weight	819.02	707.16	678.64	1834.14
T (K)	100	100	100	100
<i>a</i> , Å	12.8387(8)	9.2760(3)	9.9837(4)	13.4834(7)
<i>b</i> , Å	13.2552(8)	11.7913(4)	33.2638(15)	25.6908(15)
<i>c</i> , Å	14.3715(8)	16.9954(6)	10.0569(4)	26.6360(14)
$\alpha$ , °	76.202(2)	108.1820(10)	90	90
$\beta$ , °	75.565(2)	100.2460(10)	92.5510(10)	100.108(2)
$\gamma$ , °	72.413(2)	98.8360(10)	90	90
Volume, Å <sup>3</sup>	2222.3(2)	1693.88(10)	3336.5(2)	9083.5(9)
Z	2	2	4	4
Crystal system	Triclinic	Triclinic	Monoclinic	Monoclinic
Space group	<i>P</i> $\bar{1}$	<i>P</i> $\bar{1}$	<i>P</i> <sub>2</sub> / <i>n</i>	<i>P</i> <sub>2</sub> / <i>n</i>
<i>d</i> <sub>calc</sub> , g/cm <sup>3</sup>	1.224	1.386	1.351	1.341
$\theta$ range, °	2.399 to 35.631	2.289 to 36.319	2.368 to 34.325	2.248 to 28.284
$\mu$ , mm <sup>-1</sup>	0.453	0.623	0.518	0.584
Abs. Correction	Semi-empirical	Semi-empirical	Semi-empirical	Semi-empirical
GOF	1.040	1.039	1.092	1.004
R <sub>1</sub> , <sup>a</sup> wR <sub>2</sub> <sup>b</sup> [I > 2 $\sigma$ (I)]	0.0447, 0.0721	0.0242, 0.0541	0.0419, 0.0844	0.0692, 0.0898
Diffractometer	PHOTON	PHOTON	PHOTON	PHOTON
Radiation Type	Mo K $\alpha$	Mo K $\alpha$	Mo K $\alpha$	Mo K $\alpha$

<sup>a</sup> R<sub>1</sub> =  $\sum ||F_o| - |F_c|| / \sum |F_o|$ . <sup>b</sup> wR<sub>2</sub> =  $[\sum [w(F_o^2 - F_c^2)^2] / \sum [w(F_o^2)^2]]^{1/2}$ .



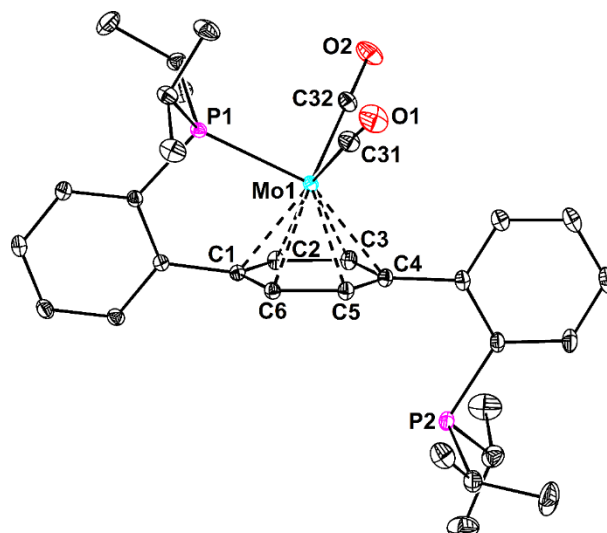


**Figure 3.38.** Structural drawing of **2** with 50% probability anisotropic displacement ellipsoids. Co-crystallized benzene and hydrogen atoms are omitted for clarity.

**Special Refinement Details for 2**—The co-crystallized benzene molecule was disordered over two positions and satisfactorily modeled in a 67:33 ratio. 1,2 and 1,3 distances of the minor component were restrained to be equivalent to those of the major component. Automatic bond generation was suppressed between the disordered groups.

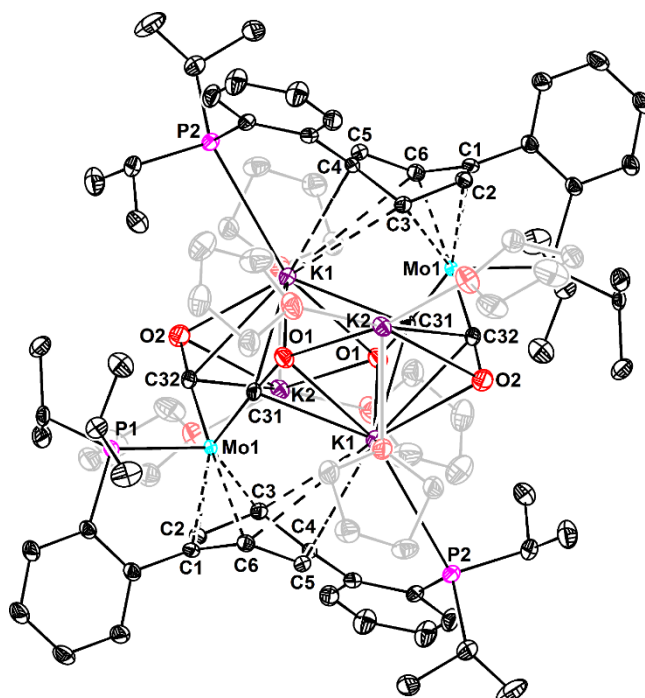


**Figure 3.39.** Structural drawing of **3** with 50% probability anisotropic displacement ellipsoids. K-bound THF molecules are represented in grey. Co-crystallized THF molecules and hydrogen atoms are omitted for clarity.

**Special Refinement Details for 3**—One of the ligand isopropyl groups, three of the K-bound THF molecules, and one of the co-crystallized THF molecules were positionally disordered. In each case, the disorder was modeled satisfactorily with populations as follow: C60 through C62 58%, C1A through C1C 42%; C78A 47%, C78B 53%; O9A and C82A through C84A 28%, O9B and C82B through C84B 72%; O10A and C86A 20 %, O10B and C86B 80%; and O12A through C96A 33%, O12B through C96B 67%. Automatic bond generation was suppressed between disordered groups.

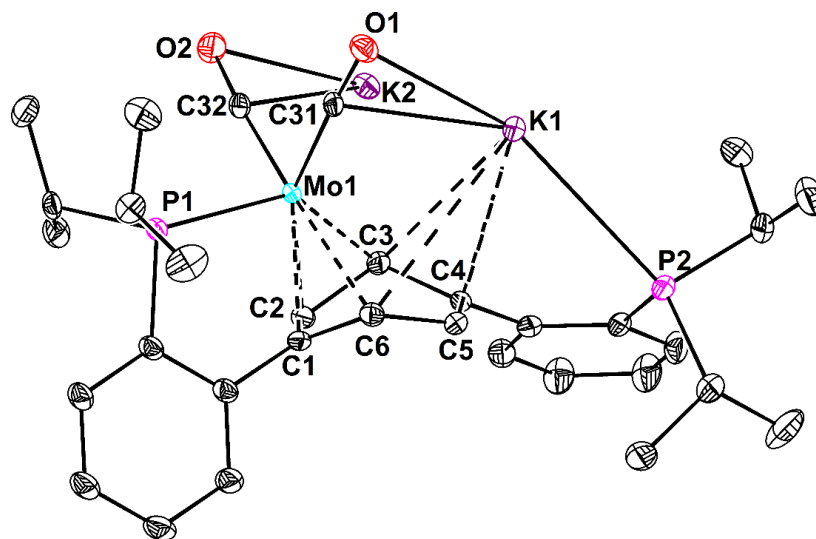


**Figure 3.40.** Structural drawing of the  $\text{PMo}(\text{CO})_2\text{KPK}$  core of **3** with 50% probability anisotropic displacement ellipsoids. Co-crystallized THF molecules, K-bound THF molecules, and hydrogen atoms are omitted for clarity.

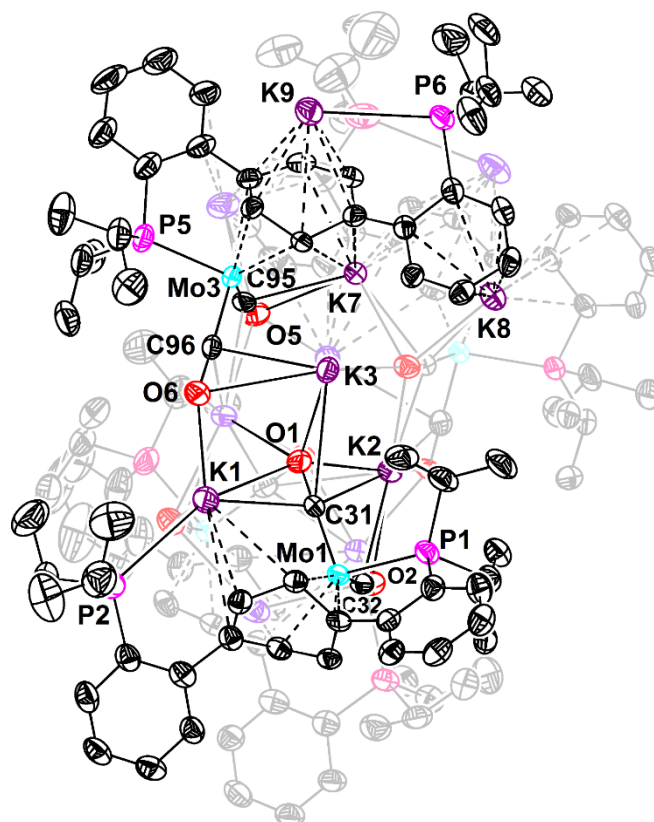


**Figure 3.41.** Structural drawing of **4** with 50% probability anisotropic displacement ellipsoids. The  $\eta^4$  (bottom) and  $\eta^3$  (top) subunits located in the back of the tetramer are represented in grey. K-bound THF molecules, co-crystallized pentane molecules, and hydrogen atoms are omitted for clarity.

**Special Refinement Details for 4**—There was significant positional disorder in all but two of the K-bound THF molecules in the structure. The disordered groups were satisfactorily modeled over two to four positions with populations as follows: O11 through C161 30%, O11A through C261 17%, O11B through C361 27%, O11C through C461 26%; O12 through C165 34%, O12A through C265 66%; O13 through C169 59%, O13A through C269 41%; O14 through C173 39%, O14A through C273 26%, O14B through C373 35%; O15 through C177 69%, O15A through C277 31%; O16 through C181 62%, O16A through C281 38%; O17 through C185 53%, O17A through C285 47%; and O18 through C189 52%, O18A through C289 48%. The 1,2 and 1,3 distances of these disordered THF groups were restrained to be equivalent to those of one of the single-site K-bound THF molecules (O9 through C153). In the case of the most heavily

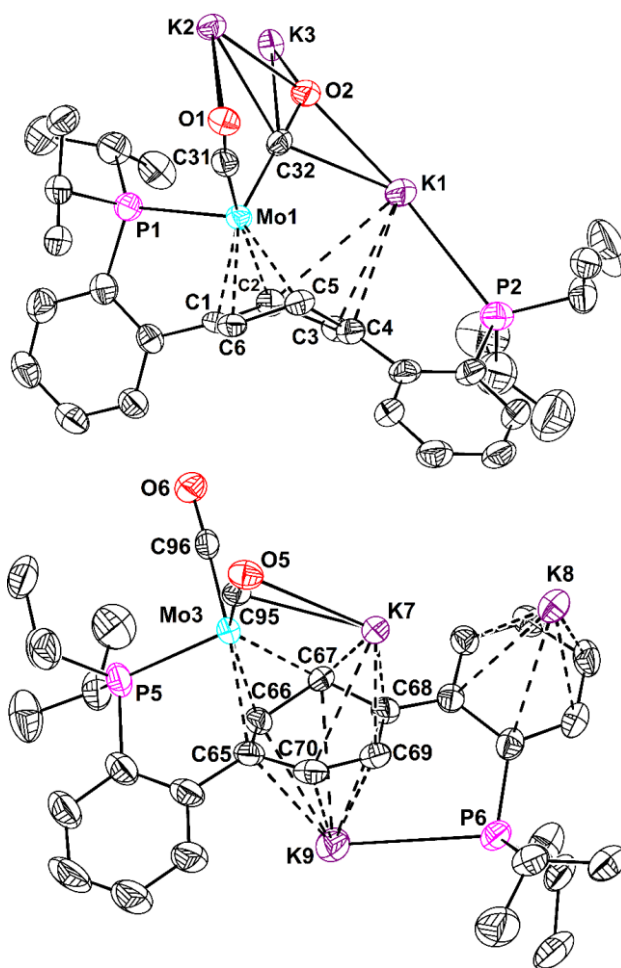


**Figure 3.42.** Structural drawing of the two distinct  $\text{PMo}(\text{CO})_2\text{KPK}_2$  cores of **4** with 50% probability anisotropic displacement ellipsoids. Co-crystallized THF and hydrogen atoms are omitted for clarity.

disordered THF molecule (O14 through C173, O14A through C273, O14B through C373), the K–O distances were restrained to be similar to those of a single-site THF molecule (O9 through C153). One of the co-crystallized pentane molecules was also disordered over two sites, complementary to one of the K-bound THF molecules (O17 through C185, O17A through C285). Both components were satisfactorily modeled, tied to the population of the corresponding THF fragment, and restrained to have 1,2 and 1,3 distances equivalent to the undisordered pentane solvate. Further, all disordered moieties were refined with similarity restraints on  $U_{ij}$  and rigid bond restraints. Automatic bond generation was suppressed between disordered groups. One of the ligand isopropyl

groups and one of the co-crystallized pentane molecules were disordered, but could not be satisfactorily modeled over two sites, even with restraints. Since the residual density for these groups was minor (*ca.* 8% of a carbon atom), they were left as single components.

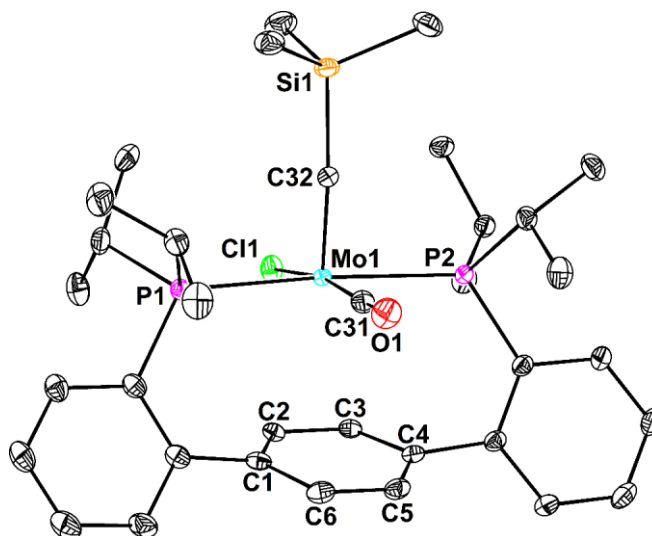


**Figure 4.43.** Structural drawing of **8** with 50% probability anisotropic displacement ellipsoids. Hydrogen atoms are omitted for clarity.

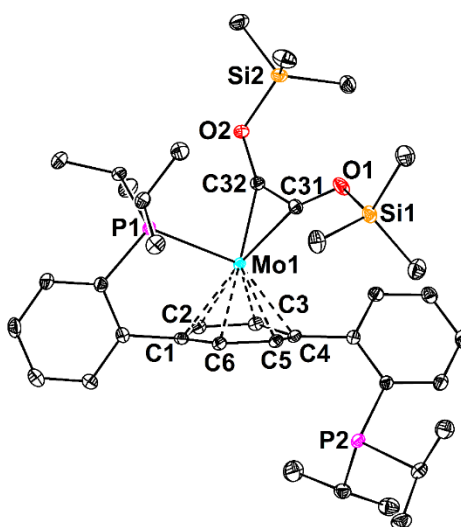


**Figure 3.44.** Structural drawing of **10** with 50% probability anisotropic displacement ellipsoids. Co-crystallized butane molecule and hydrogen atoms are omitted for clarity.

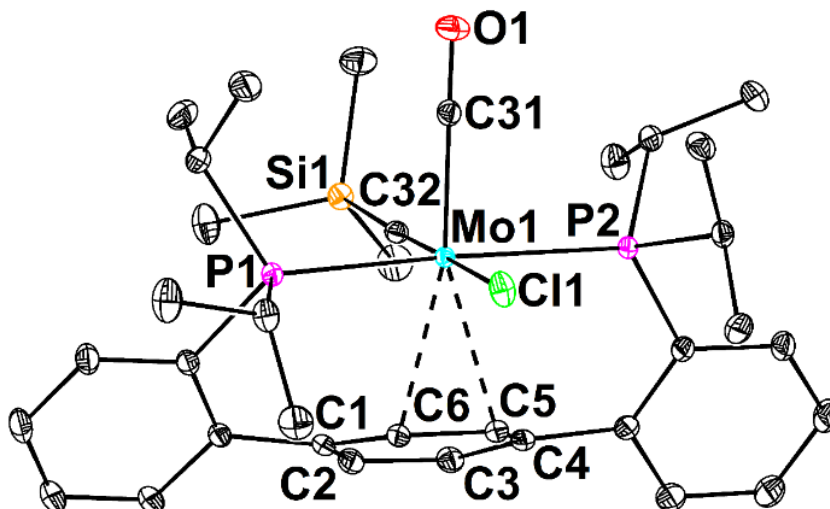


**Figure 3.45.** Structural drawing of **11** with 50% probability anisotropic displacement ellipsoids. Hydrogen atoms are omitted for clarity.

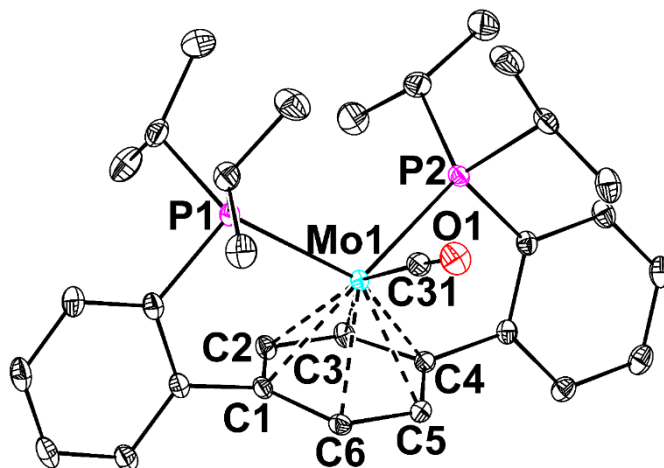


**Figure 3.46.** Structural drawing of **16** with 50% probability anisotropic displacement ellipsoids. Co-crystallized toluene molecule and hydrogen atoms are omitted for clarity.

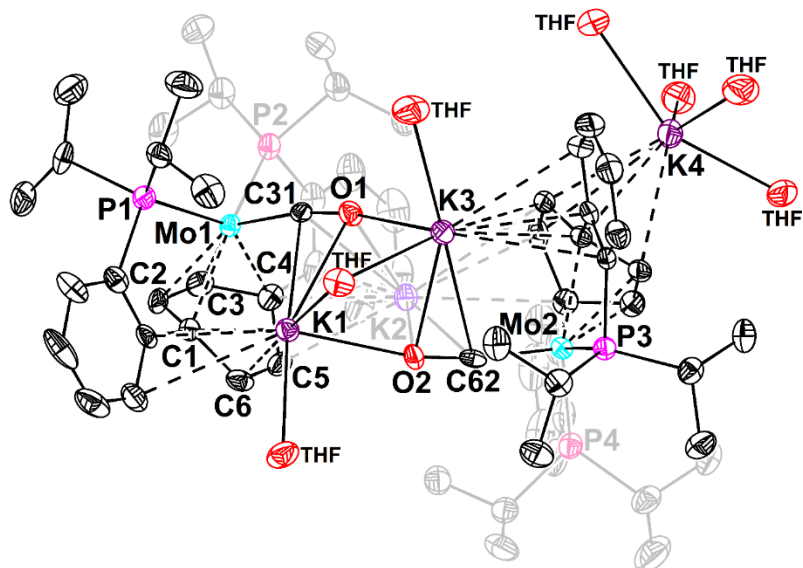


**Figure 3.47.** Full structural drawing of **17** with 50% probability anisotropic displacement ellipsoids. The carbon atoms of K-bound THF molecules and hydrogen atoms have been omitted for clarity.

**Special Refinement Details for 17**—There was significant positional disorder in all but two of the K-bound THF molecules in the structure. The disordered groups were satisfactorily modeled over two positions with populations as follows: O4A through C70A 90%; O4B through C70B 10%; O5A through C74A 63%; O5B through C74B 47%; O6A through C78A 46%; C6B through C78B 54%; O8A through C86A 79%; O8B through C86B 21%; O9A through C90A 58%; O9B through C90B 42%. The 1,2 and 2,3 distances of all of the K-bound THF molecules were restrained to be equivalent; the THF molecules were likewise restrained to be mirror equivalent. All disordered moieties were refined with similarity restraints on  $U_{ij}$  and rigid bond restraints.

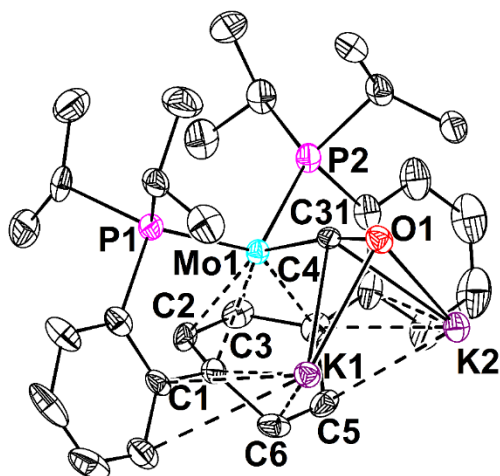


**Figure 3.48.** Structural drawing of the cofacial  $\text{Mo}(\text{CO})\text{K}_2$  core of **17** with 50% probability anisotropic displacement ellipsoids. Hydrogen atoms and K-bound THF molecules are omitted for clarity.

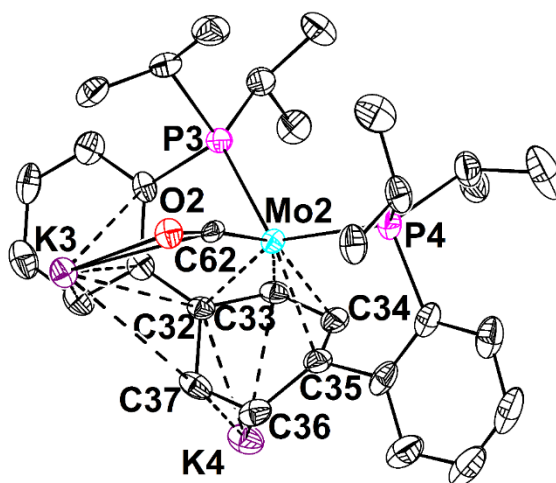


**Figure 3.49.** Structural drawing of the antifacial  $\text{Mo}(\text{CO})\text{K}_2$  core of **17** with 50% probability anisotropic displacement ellipsoids. Hydrogen atoms and K-bound THF molecules are omitted for clarity.



## REFERENCES

- (1) a) Appel, A. M.; Bercaw, J. E.; Bocarsly, A. B.; Dobbek, H.; DuBois, D. L.; Dupuis, M.; Ferry, J. G.; Fujita, E.; Hille, R.; Kenis, P. J. A.; Kerfeld, C. A.; Morris, R. H.; Peden, C. H. F.; Portis, A. R.; Ragsdale, S. W.; Rauchfuss, T. B.; Reek, J. N. H.; Seefeldt, L. C.; Thauer, R. K.; Waldrop, G. L. *Chem. Rev.* **2013**, *113*, 6621; b) Wayland, B.; Fu, X. F. *Science* **2006**, *311*, 790.
- (2) a) Costentin, C.; Robert, M.; Saveant, J.-M. *Chem. Soc. Rev.* **2013**, *42*, 2423; b) Benson, E. E.; Kubiak, C. P.; Sathrum, A. J.; Smieja, J. M. *Chem. Soc. Rev.* **2009**, *38*, 89.
- (3) Gattrell, M.; Gupta, N.; Co, A. J. *Electroanal. Chem.* **2006**, *594*, 1.
- (4) a) Lee, C. C.; Hu, Y. L.; Ribbe, M. W. *Science* **2010**, *329*, 642; b) Hu, Y. L.; Lee, C. C.; Ribbe, M. W. *Science* **2011**, *333*, 753.
- (5) a) Yang, Z. Y.; Dean, D. R.; Seefeldt, L. C. *J. Biol. Chem.* **2011**, *286*, 19417; b) Yan, L.; Dapper, C. H.; George, S. J.; Wang, H.; Mitra, D.; Dong, W.; Newton, W. E.; Cramer, S. P. *Eur. J. Inorg. Chem.* **2011**, *2011*, 2064.
- (6) a) Dance, I. *Dalton Trans.* **2011**, *40*, 5516; b) Dance, I. *Chem. Commun.* **2013**, *49*, 10893.
- (7) Spatzal, T.; Perez, K. A.; Einsle, O.; Howard, J. B.; Rees, D. C. *Science* **2014**, *345*, 1620.
- (8) Li, C. W.; Ciston, J.; Kanan, M. W. *Nature* **2014**, *508*, 504.
- (9) a) West, N. M.; Miller, A. J. M.; Labinger, J. A.; Bercaw, J. E. *Coord. Chem. Rev.* **2011**, *255*, 881; b) Maitlis, P. M.; Zanotti, V. *Chem. Commun.* **2009**, 1619; c) Rofer-DePoorter, C. K. *Chem. Rev.* **1981**, *81*, 447.
- (10) Liebig, J. *Annalen der Pharmacie* **1834**, *11*, 182.
- (11) a) Büchner, W. *Helv. Chim. Acta* **1965**, *48*, 1229; b) Buchner, W.; Lucken, E. A. C. *Helv. Chim. Acta* **1964**, *47*, 2113; c) Buchner, W.; Weiss, E. *Helv. Chim. Acta* **1964**, *47*, 1415.
- (12) Behrens, H.; Weber, R. Z. *Anorg. Allg. Chem.* **1957**, *291*, 122.
- (13) Ellis, J. E. *Organometallics* **2003**, *22*, 3322.
- (14) a) Ellis, J. E. *Inorg. Chem.* **2006**, *45*, 3167; b) Ellis, J. E.; Parnell, C. P.; Hagen, G. P. *J. Am. Chem. Soc.* **1978**, *100*, 3605.
- (15) Bennett, M. J.; Graham, W. A. G.; Smith, R. A.; Stewart, R. P. *J. Am. Chem. Soc.* **1973**, *95*, 1684.
- (16) a) Bianconi, P. A.; Williams, I. D.; Engeler, M. P.; Lippard, S. J. *J. Am. Chem. Soc.* **1986**, *108*, 311; b) Carnahan, E. M.; Protasiewicz, J. D.; Lippard, S. J. *Acc. Chem. Res.* **1993**, *26*, 90; c) Protasiewicz, J. D.; Bronk, B. S.; Masschelein, A.; Lippard, S. J. *Organometallics* **1994**, *13*, 1300; d) Protasiewicz, J. D.; Lippard, S. J. *J. Am. Chem. Soc.* **1991**, *113*, 6564; e) Protasiewicz, J. D.; Masschelein, A.; Lippard, S. J. *J. Am. Chem. Soc.* **1993**, *115*, 808; f) Vrtis, R. N.; Rao, C. P.; Bott, S. G.; Lippard, S. J. *J. Am. Chem. Soc.* **1988**, *110*, 7564; g) Bianconi, P. A.; Vrtis, R. N.; Rao, C. P.; Williams, I. D.; Engeler, M. P.; Lippard, S. J. *Organometallics* **1987**, *6*, 1968; h) Bronk, B. S.; Protasiewicz, J. D.; Lippard, S. J. *Organometallics* **1995**, *14*, 1385; i) Vrtis, R. N.; Bott, S. G.; Lippard, S. J. *Organometallics* **1992**, *11*, 270; j) Vrtis, R. N.; Liu, S.; Rao, C. P.; Bott, S. G.; Lippard, S. J. *Organometallics* **1991**, *10*, 275.
- (17) Suess, D. L. M.; Peters, J. C. *J. Am. Chem. Soc.* **2013**, *135*, 12580.
- (18) Sazama, G. T.; Betley, T. A. *Organometallics* **2011**, *30*, 4315.
- (19) Wayland, B. B.; Sherry, A. E.; Coffin, V. L. *J. Chem. Soc. Chem. Commun.* **1989**, 662.
- (20) Sherry, A. E.; Wayland, B. B. *J. Am. Chem. Soc.* **1989**, *111*, 5010.
- (21) Peters, J. C.; Odom, A. L.; Cummins, C. C. *Chem. Commun.* **1997**, 1995.
- (22) Miller, R. L.; Wolczanski, P. T.; Rheingold, A. L. *J. Am. Chem. Soc.* **1993**, *115*, 10422.
- (23) Gardner, B. M.; Stewart, J. C.; Davis, A. L.; McMaster, J.; Lewis, W.; Blake, A. J.; Liddle, S. T. *Proc. Natl. Acad. Sci. USA* **2012**, *109*, 9265.

- (24) Summerscales, O. T.; Cloke, F. G. N.; Hitchcock, P. B.; Green, J. C.; Hazari, N. *Science* **2006**, *311*, 829.
- (25) LaPointe, R. E.; Wolczanski, P. T.; Mitchell, J. F. *J. Am. Chem. Soc.* **1986**, *108*, 6382.
- (26) Matsuo, T.; Kawaguchi, H. *J. Am. Chem. Soc.* **2005**, *127*, 17198.
- (27) Shima, T.; Hou, Z. *J. Am. Chem. Soc.* **2006**, *128*, 8124.
- (28) a) Manriquez, J. M.; McAlister, D. R.; Sanner, R. D.; Bercaw, J. E. *J. Am. Chem. Soc.* **1976**, *98*, 6733; b) Wolczanski, P. T.; Bercaw, J. E. *Acc. Chem. Res.* **1980**, *13*, 121.
- (29) Neithamer, D. R.; LaPointe, R. E.; Wheeler, R. A.; Richeson, D. S.; Van Duyne, G. D.; Wolczanski, P. T. *J. Am. Chem. Soc.* **1989**, *111*, 9056.
- (30) a) Evans, W. J.; Grate, J. W.; Hughes, L. A.; Zhang, H.; Atwood, J. L. *J. Am. Chem. Soc.* **1985**, *107*, 3728; b) Evans, W. J.; Lee, D. S.; Ziller, J. W.; Kaltsoyannis, N. *J. Am. Chem. Soc.* **2006**, *128*, 14176.
- (31) a) Summerscales, O. T.; Cloke, F. G. N.; Hitchcock, P. B.; Green, J. C.; Hazari, N. *J. Am. Chem. Soc.* **2006**, *128*, 9602; b) Frey, A. S.; Cloke, F. G. N.; Hitchcock, P. B.; Day, I. J.; Green, J. C.; Aitken, G. *J. Am. Chem. Soc.* **2008**, *130*, 13816.
- (32) Frey, A. S. P.; Cloke, F. G. N.; Coles, M. P.; Maron, L.; Davin, T. *Angew. Chem. Int. Ed.* **2011**, *50*, 6881.
- (33) Belmonte, P. A.; Cloke, F. G. N.; Schrock, R. R. *J. Am. Chem. Soc.* **1983**, *105*, 2643.
- (34) Watanabe, T.; Ishida, Y.; Matsuo, T.; Kawaguchi, H. *J. Am. Chem. Soc.* **2009**, *131*, 3474.
- (35) Matsuo, T.; Kawaguchi, H. *J. Am. Chem. Soc.* **2005**, *127*, 17198.
- (36) Okazaki, M.; Ohtani, T.; Inomata, S.; Tagaki, N.; Ogino, H. *J. Am. Chem. Soc.* **1998**, *120*, 9135.
- (37) Gauntlett, J. T.; Taylor, B. F.; Winter, M. J. *J. Chem. Soc., Chem. Commun.* **1984**, 420.
- (38) Miller, A. J. M.; Labinger, J. A.; Bercaw, J. E. *J. Am. Chem. Soc.* **2008**, *130*, 11874.
- (39) a) Horwitz, C. P.; Shriver, D. F. *J. Am. Chem. Soc.* **1985**, *107*, 8147; b) Shriver, D. F.; Sailor, M. J. *Acc. Chem. Res.* **1988**, *21*, 374; c) Bradley, J. S. In *Adv. Organomet. Chem.*; Stone, F. G. A., Robert, W., Eds.; Academic Press: 1983; Vol. Volume 22, p 1.
- (40) a) Enriquez, A. E.; White, P. S.; Templeton, J. L. *J. Am. Chem. Soc.* **2001**, *123*, 4992; b) Buss, J. A.; Agapie, T. *Nature* **2016**, *529*, 72.
- (41) Shilov, A. E. *Russ. Chem. Bull.*, *52*, 2555.
- (42) a) Churchill, M. R.; Wasserman, H. J.; Holmes, S. J.; Schrock, R. R. *Organometallics* **1982**, *1*, 766; b) Kreissl, F. R.; Frank, A.; Schubert, U.; Lindner, T. L.; Huttner, G. *Angew. Chem. Int. Ed.* **1976**, *15*, 632; c) Fischer, E. O.; Friedrich, P. *Angew. Chem.* **1979**, *91*, 345; d) Mayr, A.; Hoffmeister, H. *Adv. Organomet. Chem.* **1991**, *32*, 227; e) Templeton, J. L. *Adv. Organomet. Chem.* **1989**, *29*, 1.
- (43) Buss, J. A.; Edouard, G. A.; Cheng, C.; Shi, J.; Agapie, T. *J. Am. Chem. Soc.* **2014**, *136*, 11272.
- (44) King, W. A.; DiBella, S.; Lanza, G.; Khan, K.; Duncalf, D. J.; Cloke, F. G. N.; Fragalà, I. L.; Marks, T. J. *J. Am. Chem. Soc.* **1996**, *118*, 627.
- (45) a) Cassani, M. C.; Gun'ko, Y. K.; Hitchcock, P. B.; Lappert, M. F.; Laschi, F. *Organometallics* **1999**, *18*, 5539; b) Sattler, A.; Parkin, G. *J. Am. Chem. Soc.* **2012**, *134*, 2355.
- (46) Dougherty, D. A. *Science* **1996**, *271*, 163.
- (47) Horak, K. T.; Velian, A.; Day, M. W.; Agapie, T. *Chem. Commun.* **2014**, *50*, 4427.
- (48) a) Todd, L. J.; Wilkinson, J. R.; Hickey, J. P.; Beach, D. L.; Barnett, K. W. *J. Organomet. Chem.* **1978**, *154*, 151; b) Gansow, O. A.; Schexnayder, D. A.; Kimura, B. Y. *J. Am. Chem. Soc.* **1972**, *94*, 3406.
- (49) a) Lee, Y.; Peters, J. C. *J. Am. Chem. Soc.* **2011**, *133*, 4438; b) Vrtis, R. N.; Rao, C. P.; Bott, S. G.; Lippard, S. J. *J. Am. Chem. Soc.* **1988**, *110*, 7564.

(50) We understand that d-block transition metals lack the requisite orbitals to form four independent p bonds; however, we maintain the oft used "bis-carbyne" nomenclature rather than "bis-carbene" or "carbene-carbyne" in accord with the monovalent substitution at carbon.

(51) a) Filippou, A. C.; Grünleitner, W.; Völkl, C.; Kiprof, P. *Angew. Chem. Int. Ed.* **1991**, *30*, 1167; b) Filippou, A. C.; Hofmann, P.; Kiprof, P.; Schmid, H. R.; Wagner, C. *J. Organomet. Chem.* **1993**, *459*, 233; c) Filippou, A. C.; Völkl, C.; Grünleitner, W.; Kiprof, P. *J. Organomet. Chem.* **1992**, *434*, 201; d) Wang, Y.; Da Silva, J. J. R. F.; Pombeiro, A. J. L.; Pellinghelli, M. A.; Tiripicchio, A.; Henderson, R. A.; Richards, R. L. *J. Chem. Soc., Dalton Trans.* **1995**, 1183.

(52) a) Ahmed, K. J.; Chisholm, M. H.; Huffman, J. C. *Organometallics* **1985**, *4*, 1168; b) Cordiner, R. L.; Hill, A. F.; Shang, R.; Willis, A. C. *Organometallics* **2011**, *30*, 139; c) Jamison, G. M.; Bruce, A. E.; White, P. S.; Templeton, J. L. *J. Am. Chem. Soc.* **1991**, *113*, 5057.

(53) a) Tsai, Y.-C.; Diaconescu, P. L.; Cummins, C. C. *Organometallics* **2000**, *19*, 5260; b) Cochran, F. V.; Schrock, R. R. *Organometallics* **2001**, *20*, 2127; c) Schrock, R. R.; Jamieson, J. Y.; Araujo, J. P.; Bonitatebus Jr, P. J.; Sinha, A.; Lopez, L. P. H. *J. Organomet. Chem.* **2003**, *684*, 56; d) Filippou, A. C.; Grünleitner, W.; Fischer, E. O.; Imhof, W.; Huttner, G. *J. Organomet. Chem.* **1991**, *413*, 165.

(54) a) Fay, R. C.; Lindmark, A. F. *J. Am. Chem. Soc.* **1983**, *105*, 2118; b) Marinescu, S. C.; Agapie, T.; Day, M. W.; Bercaw, J. E. *Organometallics* **2007**, *26*, 1178.

(55) Ito, M.; Shirakawa, E.; Takaya, H. *Synlett* **2002**, 1329.

(56) a) Groh, B. L.; Magrum, G. R.; Barton, T. J. *J. Am. Chem. Soc.* **1987**, *109*, 7568; b) Nikolaeva, S. N.; Ponomarev, S. V.; Petrosyan, V. S.; Lorberth, J. *J. Organomet. Chem.* **1997**, *535*, 213.

(57) Kreissl, F. R.; Sieber, W.; Wolfgruber, M. *Angew. Chem. Int. Ed.* **1983**, *22*, 493.

(58) Kreissl, F. R.; Uedelhoven, W.; Eberl, K. *Angew. Chem. Int. Ed.* **1978**, *17*, 859.

(59) a) Perdew, J. P.; Ruzsinszky, A.; Csonka, G. I.; Constantin, L. A.; Sun, J. *Phys. Rev. Lett.* **2009**, *103*, 026403; b) Perdew, J. P.; Ruzsinszky, A.; Csonka, G. I.; Constantin, L. A.; Sun, J. *Phys. Rev. Lett.* **2011**, *106*, 179902.

(60) a) Dunning, T. H.; Hay, P. J. In *Methods of Electronic Structure Theory*; Schaefer, H. F., Ed.; Springer US: Boston, MA, 1977, p 1; b) Hay, P. J.; Wadt, W. R. *J. Chem. Phys.* **1985**, *82*, 270; c) Wadt, W. R.; Hay, P. J. *J. Chem. Phys.* **1985**, *82*, 284; d) Hay, P. J.; Wadt, W. R. *J. Chem. Phys.* **1985**, *82*, 299.

(61) a) Wolinski, K.; Hinton, J. F.; Pulay, P. *J. Am. Chem. Soc.* **1990**, *112*, 8251; b) Cheeseman, J. R.; Trucks, G. W.; Keith, T. A.; Frisch, M. J. *J. Chem. Phys.* **1996**, *104*, 5497.

(62) a) Greco, J. B.; Peters, J. C.; Baker, T. A.; Davis, W. M.; Cummins, C. C.; Wu, G. *J. Am. Chem. Soc.* **2001**, *123*, 5003; b) Hejl, A.; Trnka, T. M.; Day, M. W.; Grubbs, R. H. *Chem. Commun.* **2002**, 2524; c) Carlson, R. G.; Gile, M. A.; Heppert, J. A.; Mason, M. H.; Powell, D. R.; Velde, D. V.; Vilain, J. M. *J. Am. Chem. Soc.* **2002**, *124*, 1580; d) Romero, P. E.; Piers, W. E.; McDonald, R. *Angew. Chem. Int. Ed.* **2004**, *43*, 6161; e) Morsing, T. J.; Reinholdt, A.; Sauer, S. P. A.; Bendix, J. *Organometallics* **2016**, *35*, 100; f) Stewart, M. H.; Johnson, M. J. A.; Kampf, J. W. *Organometallics* **2007**, *26*, 5102.

(63) a) Gary, J. B.; Buda, C.; Johnson, M. J. A.; Dunietz, B. D. *Organometallics* **2008**, *27*, 814; b) Krapp, A.; Pandey, K. K.; Frenking, G. *J. Am. Chem. Soc.* **2007**, *129*, 7596.

(64) a) Hoffmann, R.; Beier, B. F.; Muettterties, E. L.; Rossi, A. R. *Inorg. Chem.* **1977**, *16*, 511; b) Hoffmann, R.; Wilker, C. N.; Lippard, S. J.; Templeton, J. L.; Bower, D. C. *J. Am. Chem. Soc.* **1983**, *105*, 146; c) Wilker, C. N.; Hoffmann, R.; Eisenstein, O. **1983**.

(65) Brower, D. C.; Templeton, J. L.; Mingos, D. M. P. *J. Am. Chem. Soc.* **1987**, *109*, 5203.

(66) Lednor, P. W.; Versloot, P. C. *J. Chem. Soc., Chem. Commun.* **1983**, 284.

- (67) Pangborn, A. B.; Giardello, M. A.; Grubbs, R. H.; Rosen, R. K.; Timmers, F. J. *Organometallics* **1996**, *15*, 1518.
- (68) Weitz, I. S.; Rabinovitz, M. J. *Chem. Soc., Perkin Trans. 1* **1993**, 117.
- (69) Danheiser, R. L.; Nishida, A.; Savariar, S.; Trova, M. P. *Tetrahedron Lett.* **1988**, *29*, 4917.
- (70) Sun, H.; DiMugno, S. G. *J. Am. Chem. Soc.* **2005**, *127*, 2050.
- (71) Fulmer, G. R.; Miller, A. J. M.; Sherden, N. H.; Gottlieb, H. E.; Nudelman, A.; Stoltz, B. M.; Bercaw, J. E.; Goldberg, K. I. *Organometallics* **2010**, *29*, 2176.
- (72) Rohonczy, J. "TEDDY - Dynamic NMR Module (version 1.1.2)" Bruker Biospin, Rheinstetten, Germany.
- (73) Gaussian 09, Revision C.01, Frisch, M. J.; Trucks, G. W.; Schlegel, H. B.; Scuseria, G. E.; Robb, M. A.; Cheeseman, J. R.; Scalmani, G.; Barone, V.; Mennucci, B.; Petersson, G. A.; Nakatsuji, H.; Caricato, M.; Li, X.; Hratchian, H. P.; Izmaylov, A. F.; Bloino, J.; Zheng, G.; Sonnenberg, J. L.; Hada, M.; Ehara, M.; Toyota, K.; Fukuda, R.; Hasegawa, J.; Ishida, M.; Nakajima, T.; Honda, Y.; Kitao, O.; Nakai, H.; Vreven, T.; Montgomery, Jr., J. A.; Peralta, J. E.; Ogliaro, F.; Bearpark, M.; Heyd, J. J.; Brothers, E.; Kudin, K. N.; Staroverov, V. N.; Kobayashi, R.; Normand, J.; Raghavachari, K.; Rendell, A.; Burant, J. C.; Iyengar, S. S.; Tomasi, J.; Cossi, M.; Rega, N.; Millam, J. M.; Klene, M.; Knox, J. E.; Cross, J. B.; Bakken, V.; Adamo, C.; Jaramillo, J.; Gomperts, R.; Stratmann, R. E.; Yazyev, O.; Austin, A. J.; Cammi, R.; Pomelli, C.; Ochterski, J. W.; Martin, R. L.; Morokuma, K.; Zakrzewski, V. G.; Voth, G. A.; Salvador, P.; Dannenberg, J. J.; Dapprich, S.; Daniels, A. D.; Farkas, Ö.; Foresman, J. B.; Ortiz, J. V.; Cioslowski, J.; Fox, D. J. Gaussian, Inc., Wallingford CT, 2009.
- (74) Grimme, S.; Antony, J.; Ehrlich, S.; Krieg, H. *J. Chem. Phys.* **2010**, *132*, 154104.
- (75) Grimme, S.; Ehrlich, S.; Goerigk, L. *J. Comput. Chem.* **2011**, *32*, 1456.
- (76) APEX2, Version 2 User Manual, M86-E01078, Bruker Analytical X-ray Systems, Madison, WI, June 2006.
- (77) Sheldrick, G.M. "SADABS (version 2008/1): Program for Absorption Correction for Data from Area Detector Frames", University of Göttingen, 2008.
- (78) Dolomanov, O. V.; Bourhis, L. J.; Gildea, R. J.; Howard, J. A. K.; Puschmann, H. *J. Appl. Crystallogr.* **2009**, *42*, 339.
- (79) Sheldrick, G.M. (2008). *Acta Cryst. A* *64*, 112-122.
- (80) Brandenburg, K. (1999). DIAMOND. Crystal Impact GbR, Bonn, Germany.
- (81) Crystallographic data have been deposited at the CCDC, 12 Union Road, Cambridge CB2 1EZ, UK and copies can be obtained on request, free of charge, by quoting the publication citation and the respective deposition numbers.



**CHAPTER 4****Toward Molecular Fischer-Tropsch: The Role of Protons and Hydrides in Mo  
Mediated CO Catenation**

**ABSTRACT**

Efficient catenation of oxygenated C<sub>1</sub> feedstocks to reduced multi-carbon products represents a significant challenge in the context of energy conversion and fine chemical synthesis. Catalyses for these processes are mechanistically poorly understood, likely due to the lack of appropriate model systems, a manifestation of the difficulty of achieving this multi-electron multi-proton reactivity molecularly. As a continuation of our studies of Mo mediated CO reductive coupling, we describe here the transition away from silyl electrophiles, ultimately achieving formation of ethenone from the formal addition of H<sub>2</sub> and CO to a terminal Mo carbide.

## GENERAL INTRODUCTION

Mimicking photosynthetic carbon fixation, electrocatalytic reduction of  $\text{CO}_2$  to multicarbon products, using reducing equivalents generated from solar energy, has the potential to sustainably convert an inexpensive and abundant precursor into high energy density hydrocarbons.<sup>1</sup> A related approach involves the use of  $\text{H}_2$  as a reductant in Fisher-Tropsch (FT) CO coupling chemistry (Figure 4.1).<sup>2</sup> Employing photogenerated  $\text{H}_2$  and  $\text{CO}_2$  derived CO in this technology would facilitate the generation of sustainable liquid fuels.<sup>3</sup> The chemistry discussed here extends concepts developed in Chapter 3 of this dissertation, with the explicit goal of modeling CO reductive catenation catalyses with higher fidelity. In this sense, our goals were twofold i) enchainment of CO beyond  $\text{C}_2$ ; formation and release of  $\text{C}_{\geq 3}$  products and ii) construction of silicon-free multicarbon products.

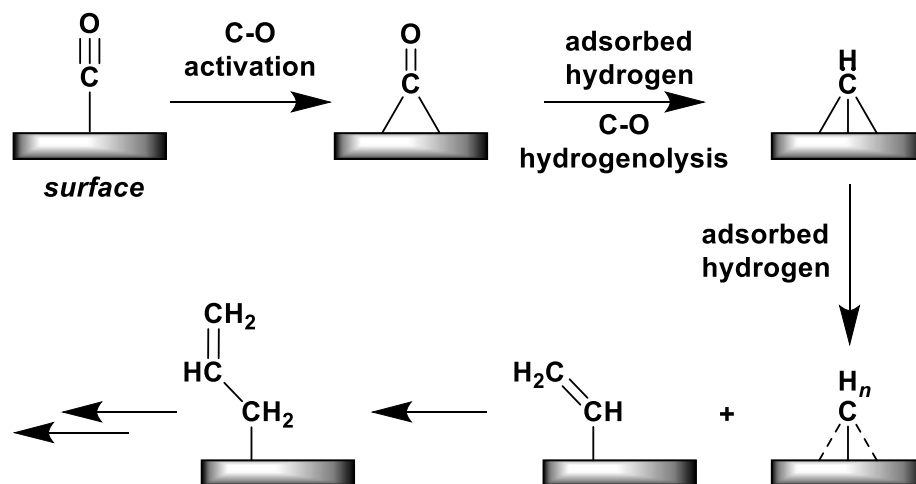


**Figure 4.1.** Schematic representation of a plausible mechanism for CO reduction and coupling in the industrial FT process.

### Goal (i):

Although the generation of  $\text{C}_2$  species is already in the range of liquid fuels, if oxygenated compounds such as ethanol are obtained as final products, higher homologs are more desirable as their properties better resemble fuels employed in the current energy infrastructure. Moreover, the FT process,<sup>2,4</sup> CO electroreduction on Cu electrodes,<sup>5</sup> and CO reduction by nitrogenases<sup>6</sup> all result in a distribution of products, including  $\text{C}_{>2}$ . Insight into the nature of



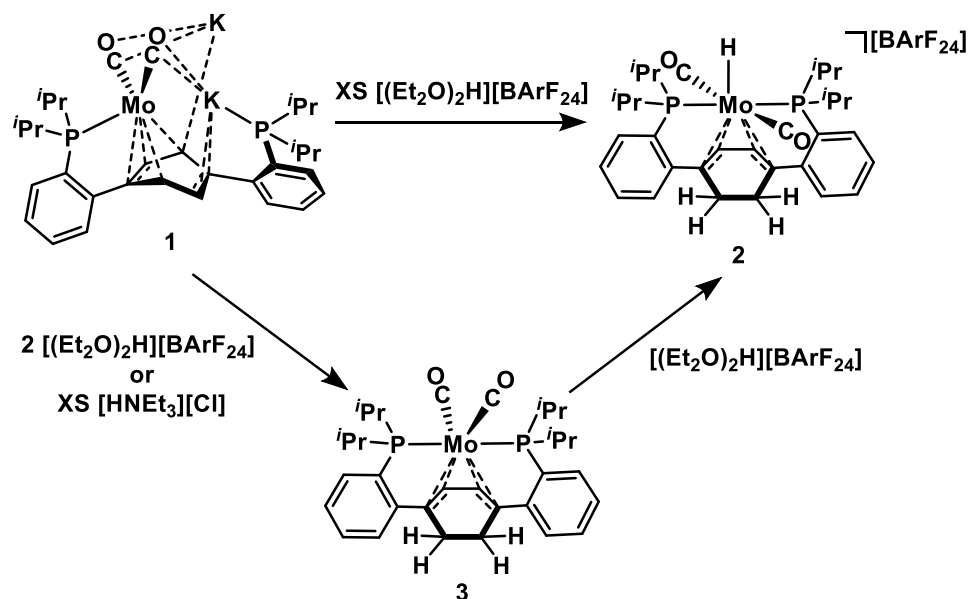
species capable of enchainment of more than two carbons is of interest for future catalyst design. Discussed herein are structure/function studies looking at the reactivity differences of Mo dicarbonyl compounds in reductive CO coupling chemistries. Work completed in collaboration with Dr. Siti Riduan, a postdoctoral scholar in the group, suggested that diphosphine binding is a necessary feature for C–O bond cleavage. Comparisons drawn below between Mo complexes with  $6e^-$  and  $4e^-$  basal  $\pi$ -systems show that two coordinating phosphines is not sufficient to engender this desirable reactivity. These complexes, though proving incompetent for C–O cleavage, do provide facile routes to Mo-bound  $C_3O_3$  linkages.

*Goal (ii):*

The CO reduction and coupling chemistry outlined thus far has enhanced our mechanistic understanding of CO enchainment chemistry; however, our preliminary results highlight significant limitations of these systems with respect to practical application: expensive silyl electrophiles and highly reducing reagents are used. Silyl electrophiles can be advantageous in CO reduction chemistry, favoring formation of strong Si–O bonds and blocking potential decomposition pathways (*e.g.* silyl groups cannot  $\beta$ -hydrogen eliminate). Biological and heterogeneous systems for CO conversion to  $C_{\geq 2}$  products use  $H^+$  and  $H_2$  as sources of hydrogen.<sup>2,5-7</sup> In Fischer-Tropsch chemistry,  $H_2$  is activated on the catalyst surface, providing adsorbed hydrides that reduce surface-bound carbon motifs (Figure 4.1).<sup>2a</sup> Herein, we discuss the addition of  $H^+$  and  $H^-$  to molecular mimics of proposed FT surface-bound intermediates.

## RESULTS AND DISCUSSION

Generation of metal-free organic fragments from CO was achieved via addition of silyl electrophiles to dianion **1**, but with respect to conversion of CO to hydrocarbons, protons are requisite electrophiles. To this end, the use of acid, rather than silyl chlorides, as a quenching reagent for **1** was explored (Scheme 4.1.). A thawing suspension of **1** in Et<sub>2</sub>O was combined with a thawing Et<sub>2</sub>O solution containing four equiv. of Brookhart's acid.<sup>8</sup> Upon warming, the deep red color lightened slightly. A single new resonance was observed in the <sup>31</sup>P{<sup>1</sup>H} NMR spectrum at 94.4 ppm, corresponding to the free phosphine arm in **1** reCOORDINATING the Mo center. The <sup>1</sup>H NMR of this species in CD<sub>3</sub>CN shows coupling multiplets at 2.5 and 3.1 ppm (confirmed by COSY NMR), each integrating to two protons, and a single central arene resonance at 5.1 ppm. These data suggest protonation not at the oxygen atoms of the bound COs, but rather at the central arene ring, giving a cyclohexadiene motif.<sup>9</sup> Additionally, a Mo–H resonance was observed as a triplet at -1.6 ppm, consistent with formation of diene dicarbonyl hydride **2**.



**Scheme 4.1.** Addition of protons to dianion **1**.

The assignment of **2** was confirmed by single crystal XRD (Figure 4.2.). Short C1–C2 and C3–C4 distances (1.394(6) and 1.398(6) Å, respectively), along with elongated C1–C6, C4–C5,

and C5–C6 distances (1.436(6), 1.520(6), and 1.542(5) Å, respectively) are consistent with formal hydrogenation of the arene to a cyclohexa-1,3-diene fragment. The disrupted aromaticity is further supported by deplanarization;<sup>10</sup> the angle between the C<sub>1</sub>–C<sub>2</sub>–C<sub>3</sub>–C<sub>4</sub> and C<sub>4</sub>–C<sub>5</sub>–C<sub>6</sub>–C<sub>1</sub> planes is 35.8°. The hydride was resolved from the Fourier map; the obtuse C<sub>31</sub>–Mo–C<sub>32</sub> angle (164.7°) in concert with the <sup>1</sup>H NMR spectroscopy data further corroborate this assignment.

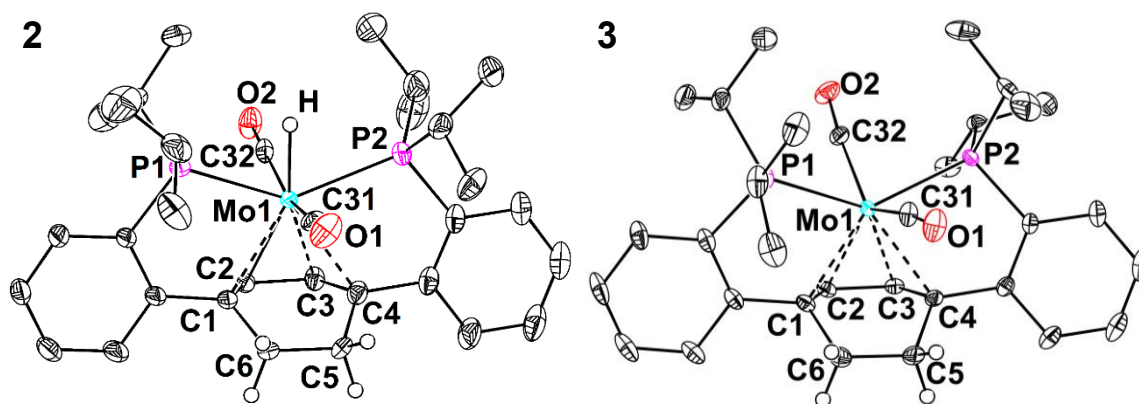
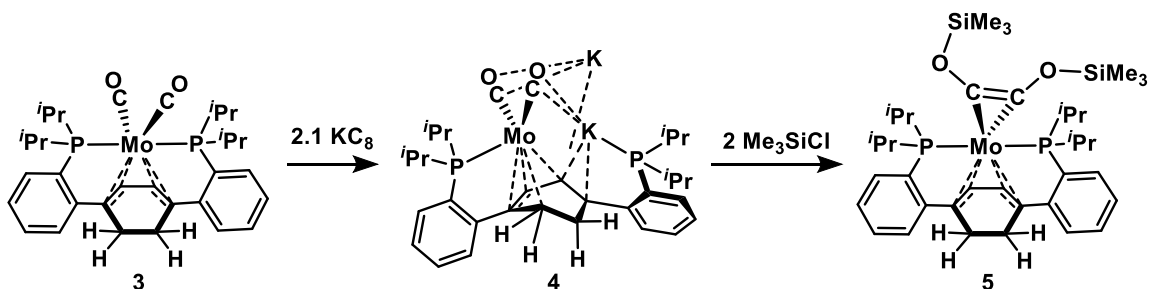


**Figure 4.2.** Solid-state structures of **2** and **3** with anisotropic displacement ellipsoids shown at the 50% probability level. Hydrogen atoms, except those of the 1,4-cyclohexadiene methylene groups and the hydride ligand of **2**, are omitted for clarity. Selected bond lengths [Å] and angles [°]: **2** Mo<sub>1</sub>–C<sub>diene</sub>(ave.) 2.337(5), Mo<sub>1</sub>–C<sub>31</sub> 2.036(6), Mo<sub>1</sub>–C<sub>32</sub> 2.040(6), C<sub>1</sub>–C<sub>2</sub> 1.394(6), C<sub>2</sub>–C<sub>3</sub> 1.436(6), C<sub>3</sub>–C<sub>4</sub> 1.398(6), C<sub>4</sub>–C<sub>5</sub> 1.520(6), C<sub>5</sub>–C<sub>6</sub> 1.536(7), C<sub>6</sub>–C<sub>1</sub> 1.542(5), C<sub>31</sub>–O<sub>1</sub> 1.148(7), C<sub>32</sub>–O<sub>2</sub> 1.141(7), ∠C<sub>31</sub>–Mo<sub>1</sub>–C<sub>32</sub> 164.7(3); **3** Mo<sub>1</sub>–C<sub>diene</sub>(ave.) 2.291(1), Mo<sub>1</sub>–C<sub>31</sub> 2.008(1), Mo<sub>1</sub>–C<sub>32</sub> 1.977(1), C<sub>1</sub>–C<sub>2</sub> 1.403(2), C<sub>2</sub>–C<sub>3</sub> 1.418(2), C<sub>3</sub>–C<sub>4</sub> 1.443(2), C<sub>4</sub>–C<sub>5</sub> 1.527(2), C<sub>5</sub>–C<sub>6</sub> 1.528(2), C<sub>6</sub>–C<sub>1</sub> 1.519(2), C<sub>31</sub>–O<sub>1</sub> 1.158(2), C<sub>32</sub>–O<sub>2</sub> 1.168(2), ∠C<sub>31</sub>–Mo<sub>1</sub>–C<sub>32</sub> 134.18(6).

Proton attack at the central arene supports significant delocalization of reducing equivalents into this ring, imparting cyclohexadienyl dianionic character (Chapter 2); however, reactivity at the carbonyl oxygen atoms is required for productive C–O cleavage or C–C coupling chemistry. With this in mind, a weaker acid with a coordinating counterion, [Et<sub>3</sub>NH][Cl], was used to quench dianion **1**. Addition of two equiv. or excess triethyl ammonium chloride to a thawing THF solution of **1** resulted in the formation of the same product which resonates as a singlet at 82.4 ppm in the <sup>31</sup>P{<sup>1</sup>H} NMR spectrum. The <sup>1</sup>H NMR spectrum of this product likewise showed coupling multiplets at 2.77 and 2.29 ppm, consistent with the cyclohexadiene methylene protons and formal arene hydrogenation to give **3**. Addition of [(Et<sub>2</sub>O)H][BAr<sup>F</sup><sub>24</sub>]

to complex **3** resulted in conversion to **2**, further corroborating its assignment. The structure of **3** was confirmed by single crystal XRD and displayed similar metrics to **2**, with the exception of the CO-Mo-CO angle which contracts to  $134.2(1)^\circ$  in the absence of the hydride ligand (Figure 4.2.). Unfortunately, varying the solvent conditions, reaction temperature, and proton source has thus far led strictly to arene hydrogenation or oxidation of the starting material.

As a Mo(0) dicarbonyl complex, **3** presents as a potential precursor for CO reductive coupling; it provides an opportunity to study how that nature of the basal  $\pi$ -system ( $6 \pi e^-$ , arene *vs.*  $4 \pi e^-$ , diene) effects CO functionalization chemistry. Though the diene in **3** was anticipated to be a poorer electron acceptor than the arene in the analogous terphenyl diphosphine Mo(0) dicarbonyl complex,<sup>11</sup> reduction was explored. Addition of 2 equiv. of  $\text{KC}_8$  to an orange solution of **3** resulted in a darkening to deep red concomitant with the appearance of two new resonances (94.51 and  $-2.47$  ppm) in the  $^{31}\text{P}\{^1\text{H}\}$  NMR spectrum (Scheme 4.2.). This spectroscopic signature is reminiscent of that of dianion **1**, suggesting dissociation of one of the *trans*-spanning phosphine donors upon successful reduction to **4**. Extremely reducing **4** was not characterized fully, but its assignment is supported by reactivity analogous to that seen for other dicarbonyl dianions (*vide infra*).



**Scheme 4.2.** Reduction and electrophilic quenching of diene dicarbonyl **3** to give bis(siloxy)acetylene adduct **5**.

Anticipating that further ring hydrogenation would be moderated by the lessened degree of electron delocalization into the basal  $\pi$ -system of **4**, dianion quenching with protons was explored. Addition of both strong ( $[(\text{Et}_2\text{O})_2\text{H}][\text{BAR}^{\text{F}}_{24}]$ ) and weak acids ( $[\text{Et}_3\text{NH}][\text{Cl}]$ )

afforded intractable mixtures that contained several Mo hydride species. Repeating these reactions from isotopically enriched  $4\text{-}^{13}\text{C}$  showed no significantly downfield shifted resonances in the  $^{13}\text{C}\{^1\text{H}\}$  NMR spectrum, suggesting that CO functionalization was not achieved. Instead, the data seems most consistent with the stepwise reduction and protonation resulting in net H-atom transfer to Mo.

Cleaner reactivity was afforded with silyl electrophiles. Addition of  $\text{Me}_3\text{SiCl}$  to a thawing THF solution of **4** provides a new species with a single broad signal in the  $^{31}\text{P}\{^1\text{H}\}$  NMR spectrum at 81.90 ppm ( $\Delta f_{\text{FWHM}} = 330$  Hz). The  $^1\text{H}$  NMR signature is consistent with a central diene motif—the diene  $\text{C}_{\text{sp}2}$  protons resonate as a singlet at 4.94 ppm, the methine protons as multiplets centered at 2.95 and 2.43 ppm—and addition of two chemically equivalent  $\text{Me}_3\text{Si}$  groups. The  $^{13}\text{C}\{^1\text{H}\}$  spectrum of a reaction from  $4\text{-}^{13}\text{C}$  has an enhanced resonance, a singlet at 217.64 ppm. These data are most consistent with silylation at oxygen, giving  $\eta^2$ -bis(siloxy)acetylene complex **5**. Single crystal XRD ratified this assignment, showing a  $C_1$  symmetric diphosphine complex (Figure 4.3.). The metrical parameters are similar to those observed for the analogous alkyne adduct **7**,<sup>11</sup> with the caveat that, in that species, a phosphine arm dissociates from Mo. The broad

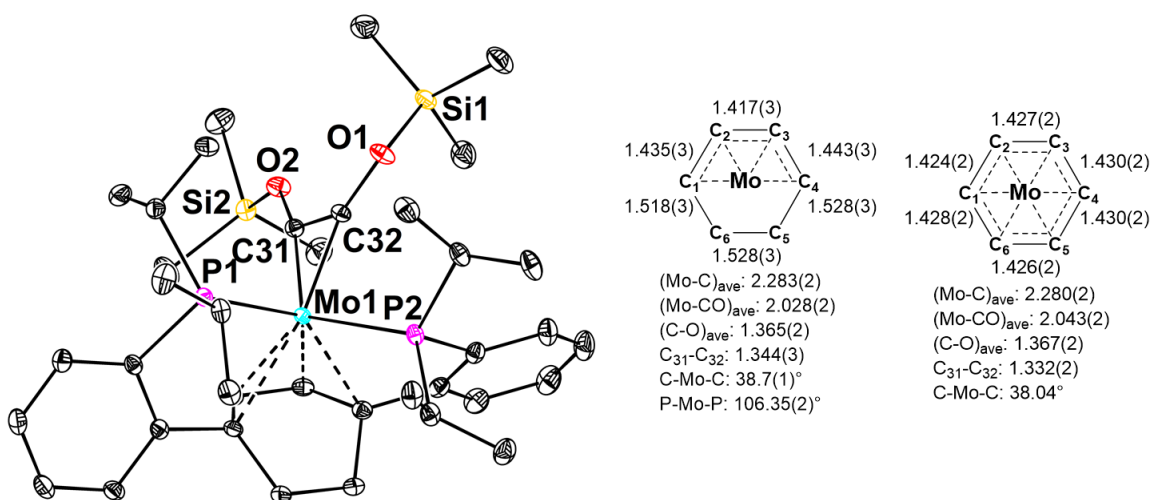
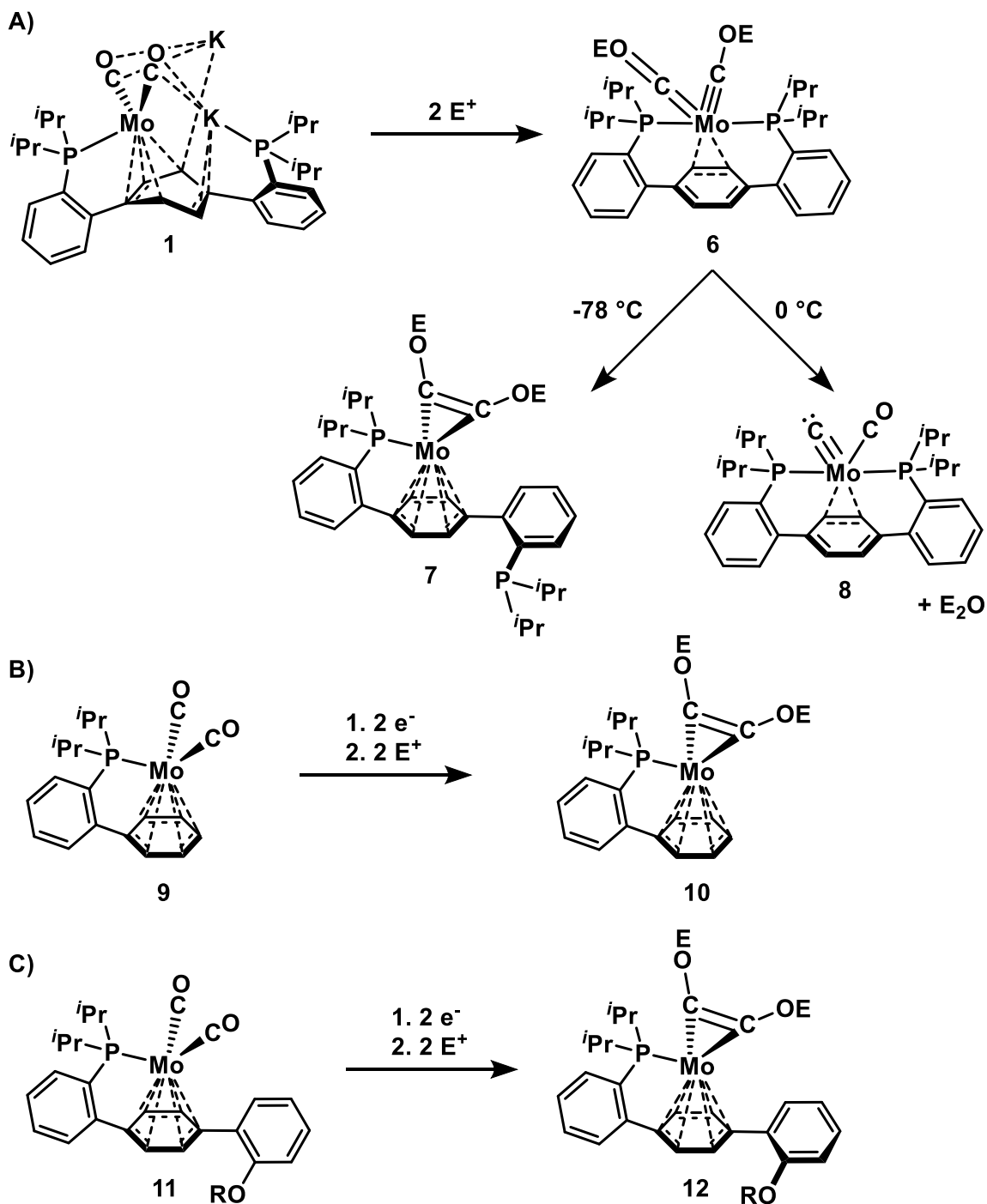


**Figure 4.3.** Solid-state structure of **5** with thermal anisotropic displacement ellipsoids shown at the 50% probability level. Hydrogen atoms are omitted for clarity. Relevant bond lengths ( $\text{\AA}$ ) and angles ( $^\circ$ ) for **5** and analogous **7** are provided.

spectroscopic features of **5** reflect a fluxional process, intermediate on the NMR timescale, that renders both the phosphine donors and acetylene carbons equivalent. Though aryl-aryl bond rotation can interconvert the phosphines, rotation of the sterically demanding alkyne seems unlikely. A hemilabile phosphine donor, affording a transient monophosphine complex (like that seen for the parent teraryl ancillary ligand), may facilitate the observed interchange.

Repeating electrophilic quenching with both large and small silyl electrophiles, in various stoichiometries, resulted in exclusive formation of the two  $e^-$  reduced, C–C coupled product. This result, in conjunction with studies on monophosphine systems, enables an important comparison of observed regioselectivities in electrophilic quenching reactions of dicarbonyl dianions (Scheme 4.3.). Mechanistic investigations of C–O bond cleavage from **1** (Chapter 3),<sup>11</sup> suggested that the operative pathway involves dicarbyne intermediate **6**. At low temperature, this complex undergoes C–C coupling; upon warming to 0 °C, C–O bond cleavage is observed. Monophosphines **9** and **11**, upon reduction and electrophile addition, show exclusive C–C coupling chemistry. These results, in conjunction with preliminary computation, suggest that diphosphine coordination stabilizes **6** to kinetically favorable C–C coupling. Once buttressed, **6** persists to sufficiently high temperatures to engage in C–O cleavage chemistry. The lack of this reactivity from **4** demonstrates that a diphosphine coordination environment is not sufficient to incite C–O cleavage. Altering the nature of the basal  $\pi$ -system may change the propensity of the phosphine donor(s) to dissociate, a process that could in turn lead to the exclusive C–C coupling observed.

Though the diene linker in **3** seems to prohibit C–O cleavage chemistry, acetylene adduct **5** looked a promising starting point for generating  $C_{\geq 3}$  CO catenation products. Precedent in our group had shown that CO addition to bis(siloxy)acetylene adduct **12** resulted in arene functionalization through a putative [2 + 2 + 1] Pauson Khand-type process.<sup>12</sup> CO insertion into the bound alkyne was proposed, giving a



**Scheme 4.3.** Regioselectivity comparison for electrophile-induced C–C coupling and C–O cleavage in a series of Mo dicarbonyl complexes.

metallacyclobutenone poised directly atop an unsaturated C–C bond of the central arene.<sup>13</sup> Subsequent cyclization afforded a dihydroxy-dihydro-indenone ligand motif (Figure 4.4., A). Hypothesizing that the additional phosphine donor in **5** may prohibit

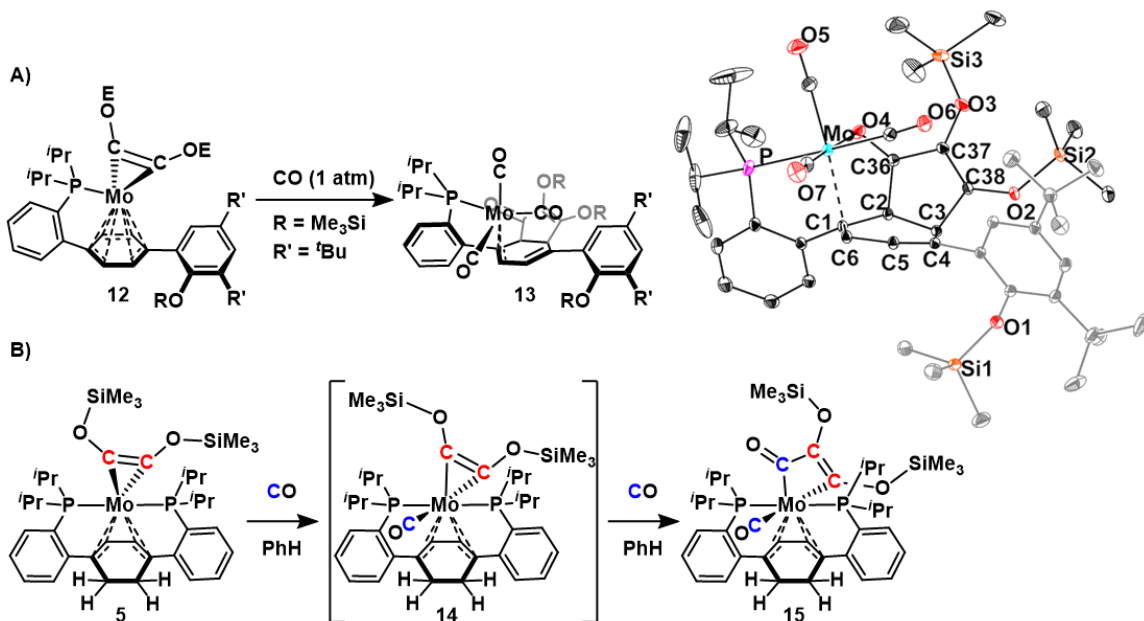


**Figure 4.4.** CO catenation from bis(siloxy)acetylene adducts **12** (A) and **5** (B). The solid-state structure of ligand-functionalized **13** is shown with anisotropic displacement ellipsoids shown at a 50% probability level. Hydrogen atoms are omitted for clarity.

an orientation favoring reactivity with the ligand  $\pi$ -system, it was treated with 1 atm. of  $^{13}\text{CO}$  gas (Figure 4.4., B). Two enhanced resonances were observed in the  $^{13}\text{C}\{^1\text{H}\}$  NMR spectrum, at 231.02 ( $^2J(\text{P},\text{C}) = 11.4$  Hz,  $^2J(\text{C},\text{C}) = 6.1$  Hz) and 190.66 ( $^2J(\text{P},\text{C}) = 12.9$  Hz,  $^2J(\text{C},\text{C}) = 6.1$  Hz) ppm, demonstrating incorporation of two isotopically enriched carbons into the reaction product. The chemical shift of the former is consistent with a CO ligand; the latter upfield shifted signal indicates CO insertion to form **15**. Repeating this reaction from **5**- $^{13}\text{C}$  corroborates this assignment. The  $^{13}\text{C}\{^1\text{H}\}$  NMR spectrum shows rich coupling information (Figure 4.5.), resulting from scalar coupling between the four  $S = \frac{1}{2}$   $^{13}\text{C}$  atoms derived from CO and the two  $S = \frac{1}{2}$  phosphine ligands. The solubility of **15** his prohibited growth of high quality crystals, but those suitable for collection of a preliminary structure were obtained via slow concentration of a pentane solution at  $-35$   $^{\circ}\text{C}$ . The solid-state structure corroborates the detailed spectroscopic data, substantiating metallacyclobutenone formation.



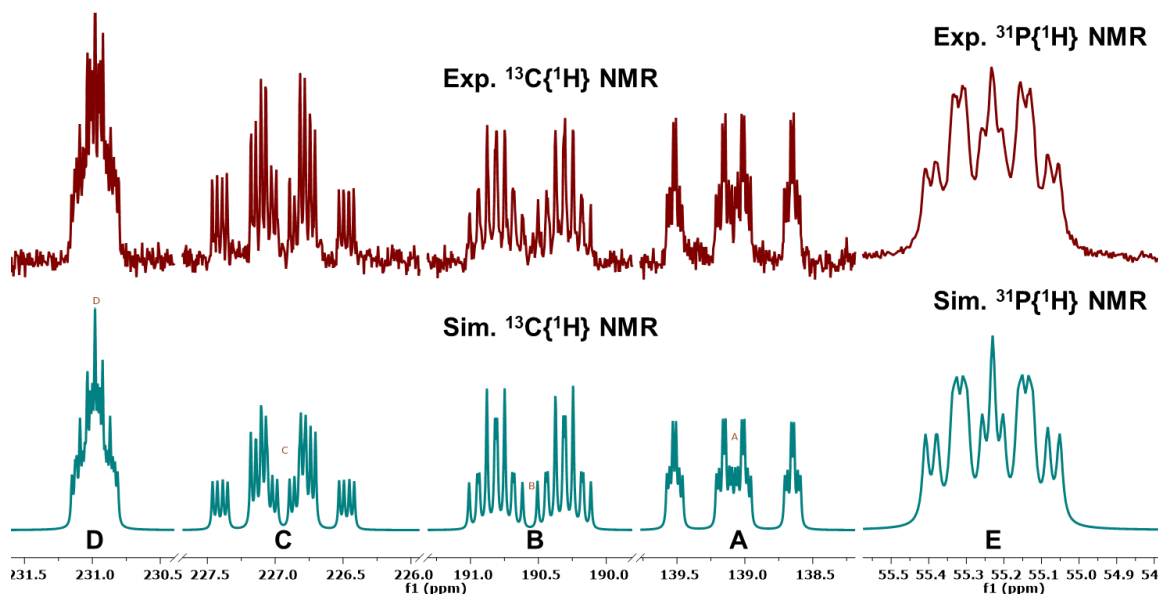


**Figure 4.5.** Experimental (top) and simulated (bottom) partial  $^{13}\text{C}\{^1\text{H}\}$  (126 MHz, 25 °C,  $\text{C}_6\text{D}_6$ ) and  $^{31}\text{P}\{^1\text{H}\}$  (202 MHz, 25 °C,  $\text{C}_6\text{D}_6$ ) NMR spectra of **15**.

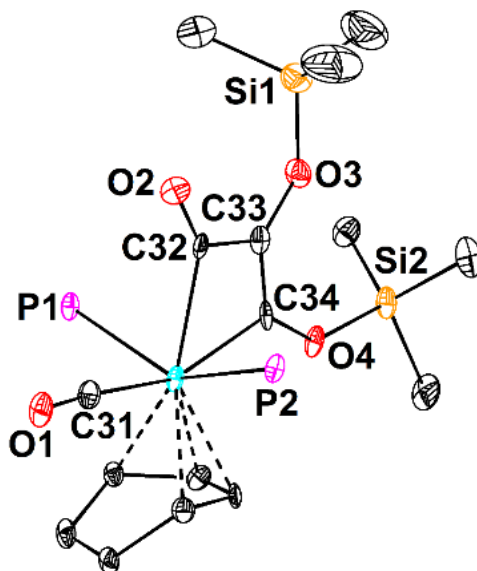
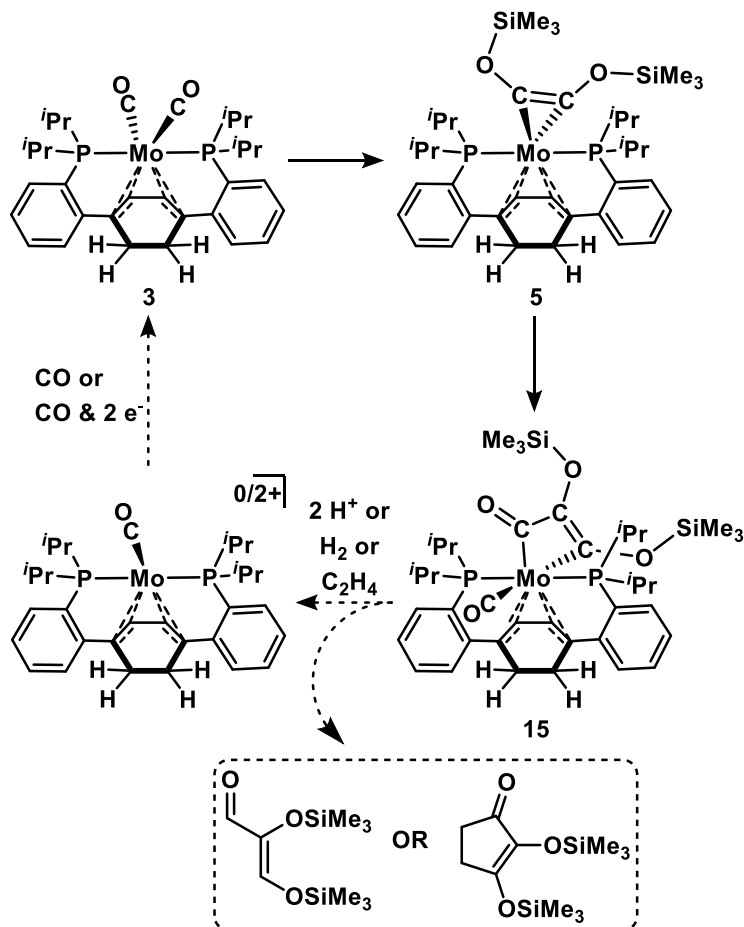


**Figure 4.6.** Truncated preliminary solid-state structure of **15**. Thermal anisotropic displacement ellipsoids are shown at the 50% probability level. Hydrogen atoms, phenylene linkers, and phosphine isopropyl groups are omitted for clarity.

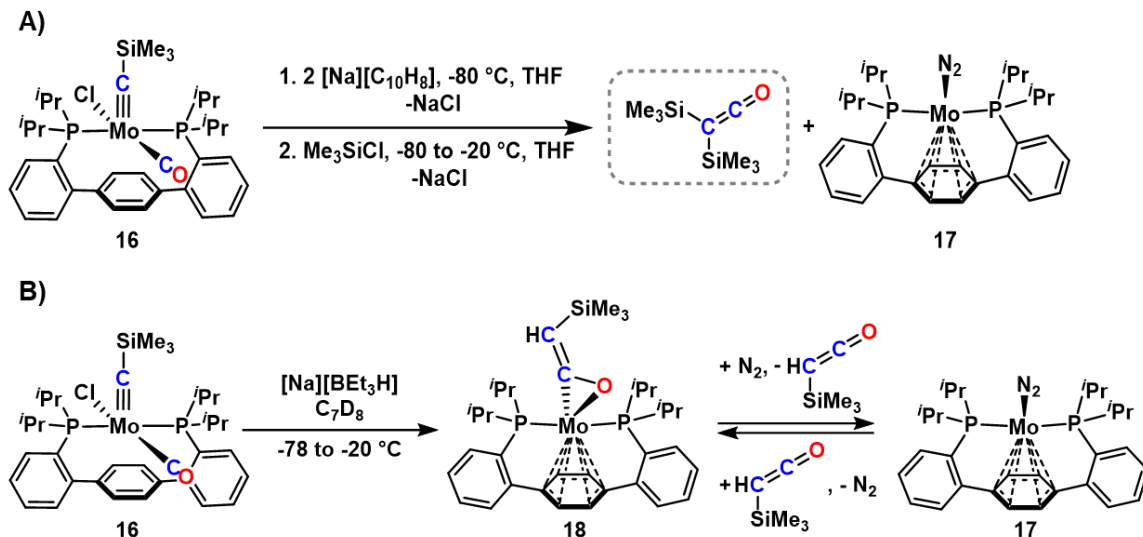
The CO-derived  $\text{C}_3$  fragment in **15** represents a functional-group rich building block. Efforts to liberate this organic motif, under mild conditions, as either a silyl-protected dihydroxy acrolein or dihydroxy cyclopentenone (Scheme 4.4.), are underway. Should this prove successful, a synthetic (or perhaps catalytic!) cycle for conversion of CO to reduced  $\text{C}_3$  motifs will be targeted (Scheme 4.4.).



**Scheme 4.4.** Envisioned synthetic cycle for formation of silylated dihydroxy acrolein or dihydroxy cyclopentenone from three molecules of CO.

As attempts to enact C–O bond cleavage, and access high-valent Mo–C multiply bonded species, have not proven fruitful, the reactivity of downstream FT-relevant intermediates with protons and hydrides was explored. In our studies of silyl electrophile promoted reductive cleaving, it was found that sequential addition of two electrons and one equiv. of electrophile to silyl carbyne **16** engendered C–C coupling and organic product release (Scheme 4.5., A). A hydride equivalent can be thought of as a single component source for two electrons and a proton. Naturally, we wondered: Can hydride addition instigate the same C–C coupling behavior?

Treating a C<sub>7</sub>D<sub>8</sub> solution of **16** with [Na][HBEt<sub>3</sub>] at -78 °C failed to stimulate a reaction; the <sup>31</sup>P{<sup>1</sup>H} chemical shift of the starting material, 36.63 ppm, remained unchanged.



**Scheme 4.5.** Sequential reduction and electrophile addition (A) and concerted hydride (B) addition prompting C–C bond formation from **16**.

Warming the sample in the NMR probe to -10 °C, resulted in formation of a Mo(0) N<sub>2</sub> adduct **17** (70%) and decomposition to free diphosphine (17%) as determined by <sup>31</sup>P{<sup>1</sup>H} and <sup>1</sup>H NMR spectroscopies. Encouraged by high conversion to the presumed product of coupling, compound **17**, the reaction was repeated, starting from isotopically labeled **16**-<sup>13</sup>C.

Silyl carbyne **16**-<sup>13</sup>C was observed to react with hydride at -30 °C, forming a mixture of species, as evidenced by multinuclear NMR spectroscopy. The primary reaction component, with a <sup>31</sup>P{<sup>1</sup>H} resonance at 48.53 ppm, had an unusual low field <sup>1</sup>H NMR signal—a doublet centered at 15.79 ppm (*J* = 121.7 Hz). The large scalar coupling and downfield chemical shift was suggestive of Mo formyl formation (B, Scheme 4.6).<sup>14</sup> Borane Lewis acids are known to stabilize metal formyls,<sup>4</sup> and hydride insertion in this fashion has been demonstrated.<sup>15</sup> 2-Dimensional NMR experiments, however, were inconsistent with this assignment (Figure 4.7.). The HSQC spectrum of this mixture showed a strong correlation between the proton resonance of interest and a carbon signal at 315.09 ppm. The HMBC spectrum showed a cross peak between this same carbon and the Me<sub>3</sub>Si protons at 0.18 ppm. These data indicate that hydride attack

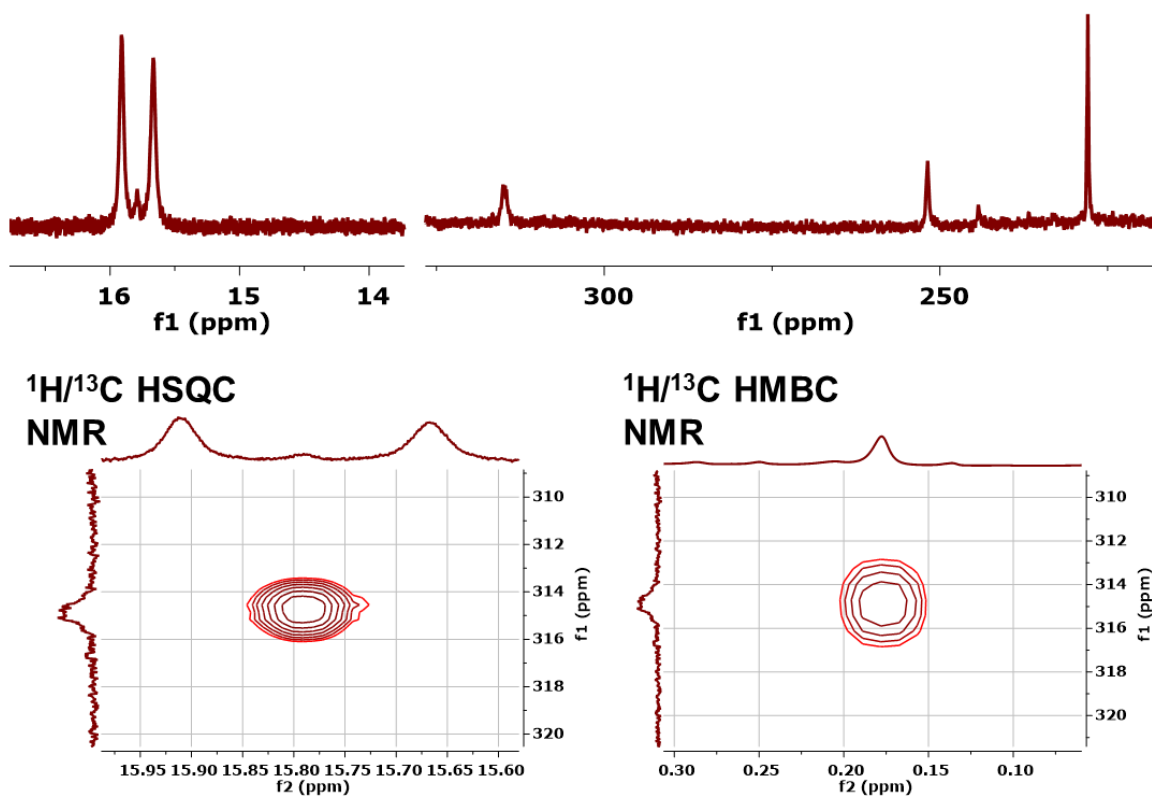
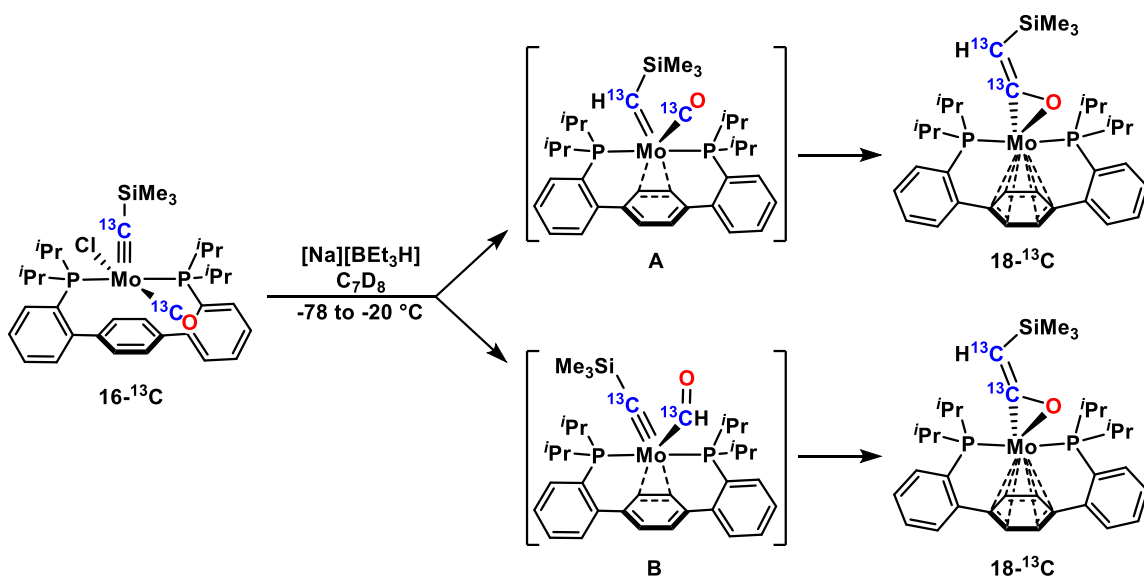


**Figure 4.7.** Proton (top) and 2D (bottom) NMR data for a reaction mixture comprised primarily of Mo carbene carbonyl complex **17-<sup>13</sup>C**.



**Scheme 4.6.** Possible mechanistic pathways for hydride addition to and C–C coupling from trimethylsilyl alkylidyne precursor **16-<sup>13</sup>C**.

affords a silyl carbene complex, **A**, rather than formyl species **B**. A strong  $^{13}\text{C}$  resonance at 251.83 ppm further supports the carbene/carbonyl assignment, attributable to an intact Mo-CO. Generation of a complex **A** is consistent with the proposed coupling reactivity, as carbene carbonylation to ketenes has precedent on Zr,<sup>16</sup> Mn,<sup>17</sup> Fe,<sup>18</sup> Ru,<sup>19</sup> and Os.<sup>20</sup>

During the course of these NMR experiments, two additional peaks of import were observed, a small singlet at 58.38 ppm and a strong signal at 76.24 ppm, in the  $^{31}\text{P}\{^1\text{H}\}$  NMR spectrum. The latter correlates to the  $\text{N}_2$  complex, **17**, demonstrating loss of the carbon-based ligands, presumably through C–C coupling, occurs at temperatures as low as  $-30\text{ }^\circ\text{C}$ . The former was observed in an orthogonal reaction, addition of independently synthesized TMS ketene<sup>21</sup> to **17**. TMS ketene was observed to bind **17**, providing ketene complex **18**, which was successfully crystallized at low temperature from liquid butane (Figure 4.8). Combined, the data are most congruent with this type of reactivity; however, no clear evidence corroborating the formation of free ketene has thus far been obtained. It is noteworthy that the precursors to C–C bond formation differ for a stepwise reduction/electrophile addition process and a concerted hydride

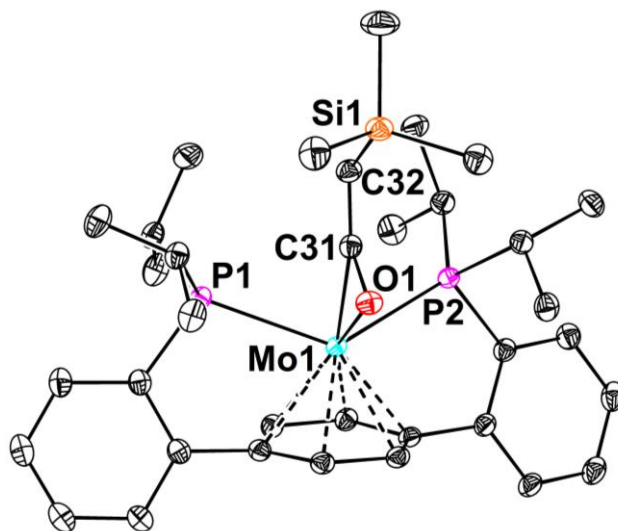
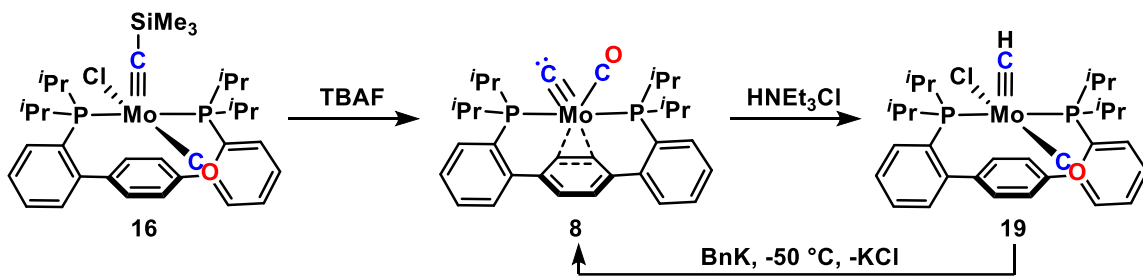


**Figure 4.8.** Solid-state structure of Mo(0) TMS ketene adduct **18**. Thermal anisotropic displacement ellipsoids are shown at the 50% probability level and hydrogen atoms are omitted for clarity.

addition process. The latter reactivity manifold, preceding through a carbene carbonyl rather than a dicarbene complex, is accessible under much milder conditions, and proves to be equally reactive.

The starting material for these reactions, carbyne **16**, still bears a silyl substituent. Toward generating silicon-free organic products from CO, we attempted the synthesis of a methylidyne from carbide **8** (Scheme 4.7). Both carbide protonation to methylidyne, and the reverse reaction, has literature precedent.<sup>22</sup> It was therefore not surprising that addition of the weak acid [HNEt<sub>3</sub>][Cl] to *in situ* generated **8** provided terminal methylidyne **19**. The <sup>1</sup>H NMR spectrum of **19** shows a single resonance between 3.5 and 6.5 ppm, a triplet ( $J = 3.1$  Hz) centered at 5.06 ppm, with a relative integration of one. This suggests both a terminal methylidyne and a five-coordinate *pseudo*-square pyramidal structure, analogous to **16**. Protonating **8**-<sup>13</sup>C instead, gives a doublet with a large scalar coupling of 147.8 Hz, centered at that same chemical shift, corroborating the assignment of the methylidyne proton. The methylidyne and carbonyl carbons resonate at 281.19 and 241.41 ppm, respectively.



**Scheme 4.7.** Terminal methylidyne synthesis from acid addition to terminal carbide **8**.

Gratifyingly, **19** is thermally stable, facilitating both its use for reaction chemistry and permitting facile growth of single crystals. A diffraction study of **19** corroborates the structure inferred from spectroscopy. The Mo center sits above the central arene ring at a distance of 2.749 Å, suggesting negligible metal arene interaction. The Mo≡CH distance is appropriately short, at 1.763(3) Å, and consistent with prior reports.<sup>22b,23</sup>

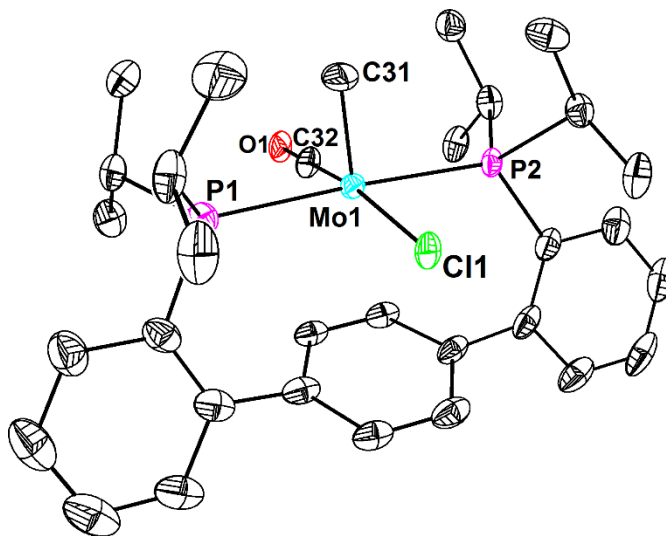
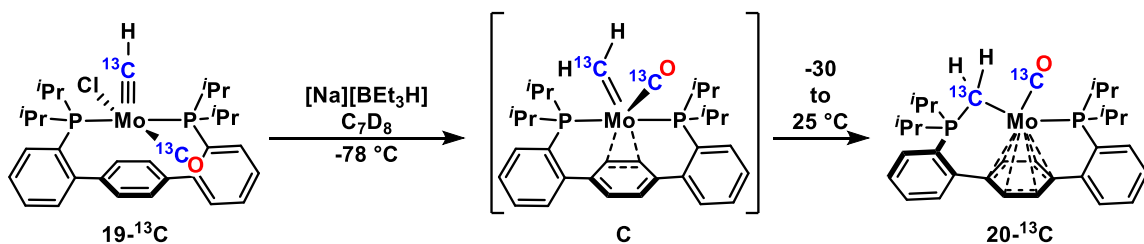


**Figure 4.9.** Solid-state structure of terminal methylidyne **19**. Thermal anisotropic displacement ellipsoids are shown at the 50% probability level and hydrogen atoms are omitted for clarity. The CO, CH, and Cl ligands demonstrated positional disorder, but were satisfactorily modeled over two positions, without restraints, in a 65:35 ratio. Only the major population is shown.

Mimicking the reaction chemistry developed for **16**, [Na][HBET<sub>3</sub>] was added to a C<sub>7</sub>D<sub>8</sub> solution of **19**-<sup>13</sup>C at -78 °C. Mixing the reagents immediately resulted in a color change to dark brown, and VT NMR spectroscopy showed signals in the <sup>31</sup>P{<sup>1</sup>H} NMR (s, 52.07 ppm), <sup>13</sup>C{<sup>1</sup>H} NMR (br s, 296.91 and br s, 237.52 ppm), and <sup>1</sup>H NMR (d, 15.03, *J* = 114.90 Hz and d, 13.27, *J* = 142.7 Hz) spectra, in line with formation of methylidene **C** (Scheme 4.8.). Warming the sample to 0 °C, in an attempt to observe C–C bonded products, showed quantitative conversion to a new asymmetric complex with triplets in the <sup>31</sup>P{<sup>1</sup>H} NMR spectrum at 88.91 (*J* = 15.66 Hz) and 52.07 (*J* = 19.5 Hz) ppm. The <sup>13</sup>C{<sup>1</sup>H} NMR spectrum likewise showed two signals, a broad doublet centered at 260.15 ppm (*J* = 13.80 Hz) and an extremely high-field doublet at -29.99 ppm (*J* = 21.86 Hz). These data are consistent with carbene insertion, but not into the CO ligand. Instead, P–C bond formation is suggested (Scheme 4.8.), giving rise to both the unusual negative chemical shift in the <sup>13</sup>C{<sup>1</sup>H} NMR spectrum and the C<sub>i</sub> symmetry.

In the course of studying *para*-terphenyl diphosphine complexes with multiply bonded carbon ligands, Mo(II) complexes with Mo–C double bonds have shown to be prone to

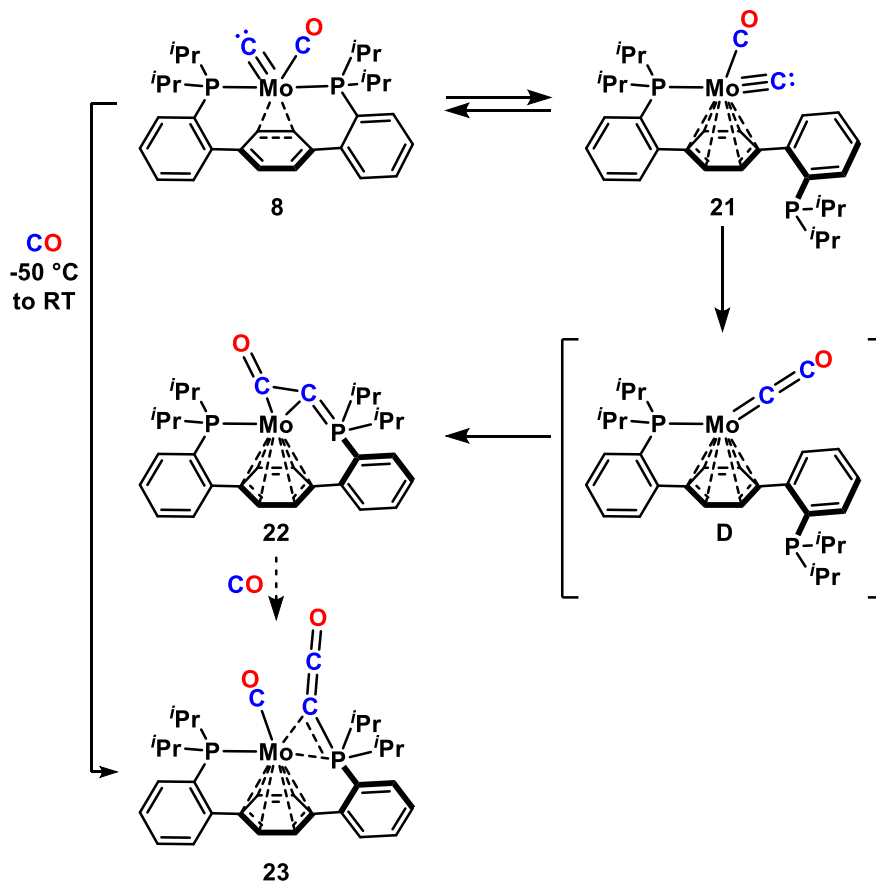


**Scheme 4.8.** Terminal methyldiene intermediate observed prior to P–C bond formation upon hydride addition to **19**.

unproductive P–C bond forming chemistry. One such example was discussed above. These asymmetric products have also been observed in reactions from terminal carbide **8**, and represent room temperature decomposition pathways for this molecule. From methylidyne **19**, deprotonation with  $BnK^{22b}$  affords carbide **8** at lower temperature ( $-50^\circ C$ ) and much more cleanly (PhMe and KCl are the only byproducts) than the prior *in situ* desilylation route. Notably, the spectroscopic signatures for the carbide synthesized each of these ways are identical, lending further credence to the proposed structure of **8** and affording evidence against a carbide chloride anion. Warming samples of **8** prepared by deprotonation show stability up to room temperature. With time, however, new resonances grow in and the reaction solution darkens from deep red to purple.

Concomitant with this color change, an even more downfield shifted carbide resonance is observed at 567.57 ppm. A corresponding carbonyl  $^{13}C$  shift is observed at 212.11 ppm, and two resonances are seen in the  $^{31}P\{^1H\}$  NMR spectrum, at 89.97 and  $-5.06$  ppm, consistent with arm-on arm-off carbide carbonyl complex **21** (Scheme 4.9.). Though persistent at room temperature for days, single crystals of **21** have not yet been obtained. Crystallization attempts have instead furnished single crystals of **22**, the first structurally characterized example of P–C insertion in this system. The  $^1H$  and  $^{31}P\{^1H\}$  NMR spectra of **22** are harmonious with a  $C_s$  symmetric solution structure, with two central arene resonances at 4.28 and 4.05 ppm, and two  $^{31}P$  signals at 82.53 and 15.17 ppm. The solid-state structure of **22** is unremarkable, the P–C, C–C, and C–O bonds that are all short—1.685, 1.348, and 1.231 Å, respectively—in line with a  $\eta^2$ -C:C phosphoranylidene ketene assignment.





**Scheme 4.9.** Sequential CO insertion and C–P bond formation leading to phosphoranylidene ketene complexes **22** and **23**.

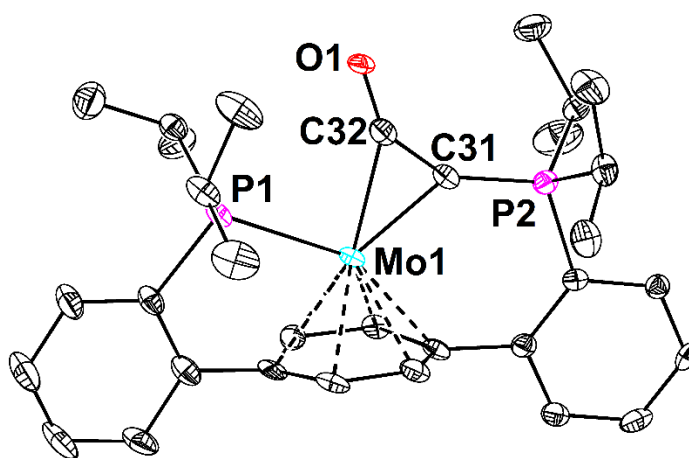
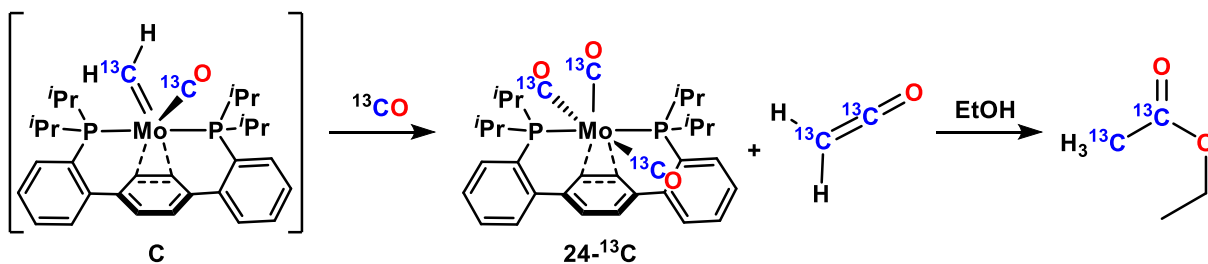


**Figure 4.10.** Solid-state structure of terminal phosphoranylidene ketene **22**. Thermal anisotropic displacement ellipsoids are shown at the 50% probability level and hydrogen atoms are omitted for quality.

Of more import is how **22** forms (Scheme 4.9.). A likely pathway involves CO insertion

from carbide **21** to give ketenylidene **D** (not observed). Phosphine attack at the highly electrophilic  $\alpha$ -carbon would afford **22**. Similar reactivity is proposed for Ta mediated CO cleavage, as a product of the reaction between Ta carbonyl complexes and a reactive Ta(III) silox, though carbide intermediacy, in this case, is not established.<sup>24</sup> Warming carbide **8** under a  $^{13}\text{CO}$  atmosphere accelerates phosphoranylidene ketene formation, leading to quantitative conversion to **23**, a species with three salient signals in the  $^{13}\text{C}\{^1\text{H}\}$  NMR spectrum at 241.52 (s, CO), 149.56 (dd,  $C_\beta$ ), and -33.11 (dd,  $C_\alpha$ ). The  $^{31}\text{P}\{^1\text{H}\}$  NMR spectrum of **23** shows peaks for the Mo-bound and  $C_\alpha$ -bound phosphorous nuclei at 82.77 and 38.81 ppm, respectively. A small scalar coupling (3.87 Hz) is observed between the  $^{31}\text{P}$  nuclei, suggesting some interaction of the phosphoranylidene with Mo (Scheme 4.9).

Extending the enhanced insertion reactivity observed for complex **8** under CO, we hypothesized that warming **C** under a CO atmosphere may alter the insertion selectivity, favoring productive C–C bond formation over undesired P–C coupling. Somewhat unexpectedly, no warming was needed. Placing a  $-78\text{ }^\circ\text{C}$  solution of in situ generated **C** under a  $^{13}\text{CO}$  atmosphere resulted in a gradual color change to bright orange, as the gas diffused down the sample (Scheme 4.10.). The  $^{13}\text{C}\{^1\text{H}\}$  NMR spectrum at  $-78\text{ }^\circ\text{C}$ , showed three resonances in addition to free  $^{13}\text{CO}$ , the CO signals of **24- $^{13}\text{C}$** , which are chemically equivalent at this temperature. No spectroscopic evidence for ethenone formation was obtained,<sup>25</sup> but it would be exceedingly dilute under the reaction conditions. Warming the sample showed



**Scheme 4.10.** Synthesis of carbonyl complex **24** from methylidene intermediate **C**. The proposed organic product, ketene, has yet to be detected, but should be trapped by alcohols.

persistence of **24- $^{13}\text{C}$** , but again ketene was not detected. Due to the instability of ketene at ambient temperature, chemical traps (such as ethanol addition) will be explored (Scheme

4.10).<sup>25</sup> But preliminary data, in addition to the chemistry of TMS analog **16**, suggest that sequential hydride and CO addition is resulting in C–H and C–C bond formation, providing a silicon-free multicarbon product, directly from CO.

## CONCLUSION

In summary, both metal-bound  $C_3$  organics and silicon-free organic products have been constructed via reductive catenation of CO. Though protons are not capable of CO functionalization from super reduced Mo CO complexes, they do afford access to a series of diene-linked compounds competent for CO reduction, coupling, and enchainment. Carbide protonation provides a thermally stable methylidyne complex and hydride addition induces C–C coupling. Reactions between the silyl alkylidyne congener and hydride suggest that this C–C bond formation differs from the mechanism established for stepwise reduction/electrophile addition, proceeding through carbene carbonyl intermediates rather than dicarbynes. Notably, this is the first demonstration of formal  $H_2$  addition (in the form of the heterolysis products:  $H^+$  and  $H^-$ ) to a terminal transition metal carbide, resulting in both C–H and C–C bond formation, in the presence of CO. These steps provide valuable precedent for the reactivity proposed for the heterogeneous FT process, mimicking the reactivity postulated following C–O scission (Figure 4.11.).

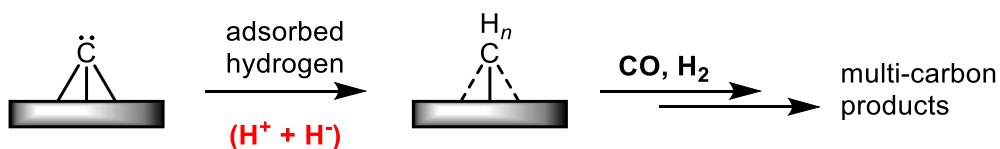


**Figure 4.11.** Schematic representation of carbide hydrogenation and subsequent C–C coupling in FT chemistry.

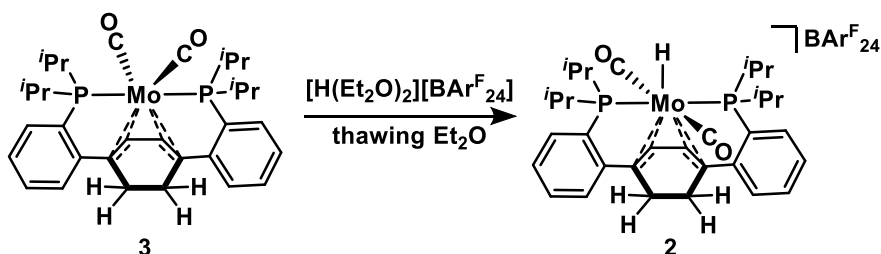
## EXPERIMENTAL SECTION

### *General Considerations*

Unless otherwise specified, all operations were carried out in an MBraun drybox under a nitrogen atmosphere or using standard Schlenk and vacuum line techniques. Pre-reduced Teflon-coated stir bars (prepared via stirring a Na[C<sub>10</sub>H<sub>8</sub>] solution overnight followed by rinsing three times with THF) were utilized in any stirred reaction in which KC<sub>8</sub> or **1** were employed as reagents or formed in the course of the reaction. Solvents for air- and moisture-sensitive reactions were dried over sodium benzophenone ketyl, calcium hydride, or by the method of Grubbs.<sup>26</sup> Deuterated solvents were purchased from Cambridge Isotope Laboratories and vacuum transferred from sodium benzophenone ketyl (C<sub>6</sub>D<sub>6</sub>) or CaH<sub>2</sub> (CD<sub>3</sub>CN). Solvents, once dried and degassed, were vacuum transferred directly prior to use or stored under inert atmosphere over 4 Å molecular sieves. Molybdenum complexes **1**, **8**, **16**,<sup>11</sup> and **17**<sup>27</sup> potassium graphite (KC<sub>8</sub>),<sup>28</sup> TMS ketene,<sup>21</sup> anhydrous TBAF in MeCN,<sup>29</sup> and Brookhart's acid ([H(Et<sub>2</sub>O)<sub>2</sub>][BAr<sup>F</sup><sub>24</sub>]),<sup>8</sup> were prepared and purified according to literature procedures. [Et<sub>3</sub>NH][Cl] was prepared by condensing HCl gas (freeze-pump-thawed three times and condensed from -78 to -196 °C) onto a frozen pentane solution of dry Et<sub>3</sub>N. The solids that formed were collected via vacuum filtration and used without further purification. Unless indicated otherwise, all other chemicals were utilized as received. Graphite (325 mesh), (Me<sub>3</sub>Si)<sub>2</sub>O (dried over sodium benzophenone ketyl and distilled prior to use), and trimethylsilyl chloride (dried over CaH<sub>2</sub> and distilled prior to use) were purchased from Alfa Aesar. Potassium metal (washed with hexanes), chloroacetaldehyde diethyl acetal, and CO gas were purchased from Sigma Aldrich. Et<sub>3</sub>N (dried over CaH<sub>2</sub> and distilled prior to use) was purchased from Oakwood Chemicals. 3,5-Bis(trifluoromethyl)bromobenzene, sodium tetrafluoroborate, and Mg<sup>0</sup> turnings (chemically activated with dilute HCl, mechanically activated by stirring under vacuum for 12h at 100 °C, and chemically activated once more with 1,2-dibromoethane immediately prior to use) were purchased from Fischer Scientific. <sup>13</sup>CO

gas was purchased from Monsanto Research; butane and  $\text{NH}_3$  gas were purchased from Matheson.  $^1\text{H}$ ,  $^{13}\text{C}\{^1\text{H}\}$ , and  $^{31}\text{P}\{^1\text{H}\}$  NMR spectra were recorded on Varian 400 MHz or Varian INOVA-500 spectrometers with shifts reported in parts per million (ppm).  $^1\text{H}$  and  $^{13}\text{C}\{^1\text{H}\}$  NMR spectra are referenced to residual solvent peaks.<sup>30</sup>  $^{31}\text{P}\{^1\text{H}\}$  chemical shifts are referenced to an external 85%  $\text{H}_3\text{PO}_4$  (0 ppm). Fourier transform infrared ATR spectra were collected from thin films or powders on a Thermo Scientific Nicolet iS5 Spectrometer with a diamond ATR crystal (utilized iD5 ATR insert).

### Synthesis of **2**

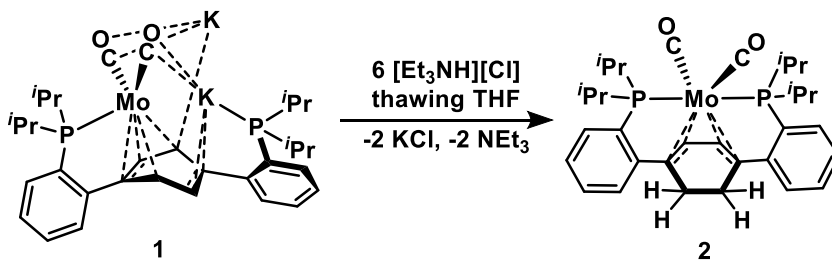


A 20 mL scintillation vial was charged with **3** (40 mg, 0.062 mmol),  $\text{Et}_2\text{O}$  (4 mL), and a stir bar. Following stirring for 15 min, the homogeneous orange solution was frozen in an  $\text{LN}_2$ -cooled cold well. A second 20 mL vial was charged with a solution of  $[(\text{Et}_2\text{O})_2\text{H}][\text{BAR}^{\text{F}}_{24}]$  (68.9 mg, 0.068 mmol) in  $\text{Et}_2\text{O}$  (2 mL) and likewise frozen. Immediately upon thawing, the acid solution was added to the vial containing **3**, with stirring. The reaction was left to warm to room temperature, during which time the color gradually lightened to golden yellow. Volatiles were removed *in vacuo*, providing a tan residue. Dissolution of this residue in minimal MeCN and chilling of the resulting solution to  $-35\text{ }^\circ\text{C}$  for 12 hr provided analytically pure microcrystals of **2** (81 mg, 0.054 mmol, 87%).  $^1\text{H}$  NMR (400 MHz,  $\text{C}_6\text{D}_6$ ,  $23\text{ }^\circ\text{C}$ )  $\delta$ : 7.72 (br t,  $J = 2.24\text{ Hz}$ , 8H, BARF aryl-H), 7.69 (br s, 4H, BARF aryl-H), 7.58-7.65 (m, 4H, aryl-H), 7.48-7.56 (m, 4H, aryl-H), 5.16 (s, 2H, diene-CH), 3.07-3.19 (m, 2H, diene- $\text{CH}_2$ ), 2.91-3.04 (m, 2H,  $\text{CH}(\text{CH}_3)_2$ ), 2.66-2.78 (m, 2H,  $\text{CH}(\text{CH}_3)_2$ ), 2.46-2.59 (m, 2H, diene- $\text{CH}_2$ ), 1.31-1.40 (m, 12H,  $\text{CH}(\text{CH}_3)_2$ ), 1.07-1.15

(m, 12H, CH(CH<sub>3</sub>)<sub>2</sub>), -1.56 (t, *J* = 51.60 Hz, 1H, Mo-*H*). <sup>13</sup>C{<sup>1</sup>H} NMR (101 MHz, C<sub>6</sub>D<sub>6</sub>, 23 °C) δ: 217.20 (t, *J* = 10.80 Hz, CO), 212.30 (t, *J* = 10.61 Hz, CO), 162.59 (q, *J* = 49.93 Hz, BArF aryl-C), 151.15 (d, *J* = 21.85 Hz, aryl-C), 136.08 (dd, *J* = 34.89, 1.53 Hz, aryl-C), 135.65 (br m, BArF aryl-C), 132.40 (m, aryl-C), 131.96 (s, aryl-C), 130.35 (d, *J* = 5.82 Hz, aryl-C), 129.92 (qq, *J* = 31.64, 2.97 Hz, BArF aryl-C), 128.44 (d, *J* = 13.09 Hz, aryl-C), 125.46 (q, *J* = 271.94 Hz, BArF CF<sub>3</sub>), 118.68 (br s, BArF aryl-C), 103.50 (t, *J* = 1.42 Hz, diene-C), 77.30 (d, *J* = 1.38 Hz, diene-CH), 32.68 (d, *J* = 29.04 Hz, CH(CH<sub>3</sub>)<sub>2</sub>), 30.52 (s, diene-CH<sub>2</sub>), 29.10 (d, *J* = 26.74 Hz, CH(CH<sub>3</sub>)<sub>2</sub>), 20.26 (br m, CH(CH<sub>3</sub>)<sub>2</sub>), 20.18 (s, CH(CH<sub>3</sub>)<sub>2</sub>), 20.08 (s, CH(CH<sub>3</sub>)<sub>2</sub>), 19.20 (s, CH(CH<sub>3</sub>)<sub>2</sub>). <sup>31</sup>P{<sup>1</sup>H} NMR (162 MHz, C<sub>6</sub>D<sub>6</sub>, 23 °C) δ: 85.05 (s). IR (powder sample, diamond ATR, cm<sup>-1</sup>) ν<sub>CO</sub> = 2037, 1973.

**2-<sup>13</sup>C** was prepared analogously starting from **3-<sup>13</sup>C**; the resonances in the <sup>13</sup>C{<sup>1</sup>H} NMR spectrum split to apparent quartets: 217.17 (q, *J* = 10.81 Hz) and 212.26 (q, *J* = 10.53 Hz). The <sup>31</sup>P{<sup>1</sup>H} NMR signal at 85.05 ppm splits into a triplet (*J* = 10.67 Hz). IR (powder sample, diamond ATR, cm<sup>-1</sup>) ν<sub>CO</sub> = 1992, 1932.

### Synthesis of **3**

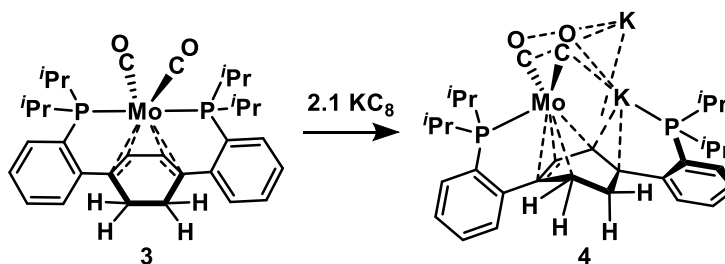


A deep burgundy THF (12 mL) solution of **1** (2 g, 2.2 mmol—NB: the molecular weight of **1** is ill-defined due to variable THF solvation but is assumed to be 909.1 g/mol, the formula weight of **1**•THF<sub>3</sub>) in a 20 mL scintillation vial charged with a stir bar was frozen solid in an LN<sub>2</sub> cooled cold well. The vial was removed from the well and immediately upon thawing, Et<sub>3</sub>NCl (1.8 g, 13.2 mmol) was added in a single portion as a solid. The vial was sealed and left to stir for 2 h, during which time the color lightened to a pale orange. Volatiles were removed *in vacuo* and the resulting tacky orange solid was triturated

with hexanes (2 x 10 mL). The resulting solids were washed with cold hexanes (3 mL) and then extracted with benzene until the washes were pale yellow/orange. The benzene extract was lyophilized, providing **2** as an orange powder (900 mg, 1.4 mmol, 64%). X-ray quality crystals of **2** were grown by cooling a saturated hexanes solution to  $-35\text{ }^{\circ}\text{C}$ .  $^1\text{H}$  NMR (400 MHz,  $\text{C}_6\text{D}_6$ ,  $23\text{ }^{\circ}\text{C}$ )  $\delta$ : 7.45 (dd,  $J = 7.68, 2.49\text{ Hz}$ , 2H, aryl- $H$ ), 7.14 (td,  $J = 7.45, 1.49\text{ Hz}$ , 2H, aryl- $H$ ), 7.00-7.06 (m, 4H, aryl- $H$ ), 4.78 (s, 2H, diene- $\text{CH}$ ), 2.75-2.80 (m, 2H, diene- $\text{CH}_2$ ), 2.62-2.71 (m, 2H,  $\text{CH}(\text{CH}_3)_2$ ), 2.46-2.55 (m, 2H,  $\text{CH}(\text{CH}_3)_2$ ), 2.27-2.32 (m, 2H, diene- $\text{CH}_2$ ), 1.26-1.35 (m, 12H,  $\text{CH}(\text{CH}_3)_2$ ), 1.07-1.15 (m, 12H,  $\text{CH}(\text{CH}_3)_2$ ).  $^{13}\text{C}\{^1\text{H}\}$  NMR (101 MHz,  $\text{C}_6\text{D}_6$ ,  $23\text{ }^{\circ}\text{C}$ )  $\delta$ : 260.51 (t,  $J = 27.13\text{ Hz}$ , CO), 243.58 (t,  $J = 18.62\text{ Hz}$ , CO), 157.23 (dd,  $J = 26.12, 1.34\text{ Hz}$ , aryl-C), 138.98 (dd,  $J = 32.29, 2.65\text{ Hz}$ , aryl-C), 129.98 (s, aryl-C), 129.63 (vt,  $J = 0.92\text{ Hz}$ , aryl-C), 127.32 (d,  $J = 12.99\text{ Hz}$ , aryl-C), 125.97 (m, aryl-C), 81.91 (m, diene-C), 79.21 (s, diene- $\text{CH}$ ), 33.57 (s, diene- $\text{CH}_2$ ), 30.97 (d,  $J = 22.56\text{ Hz}$ ,  $\text{CH}(\text{CH}_3)_2$ ), 27.83 (d,  $J = 22.79\text{ Hz}$ ,  $\text{CH}(\text{CH}_3)_2$ ), 19.68 (m,  $\text{CH}(\text{CH}_3)_2$ ), 19.60 (m,  $\text{CH}(\text{CH}_3)_2$ ), 18.62 (s,  $\text{CH}(\text{CH}_3)_2$ ).  $^{31}\text{P}\{^1\text{H}\}$  NMR (162 MHz,  $\text{C}_6\text{D}_6$ ,  $23\text{ }^{\circ}\text{C}$ )  $\delta$ : 82.39 (s). IR (powder sample, diamond ATR,  $\text{cm}^{-1}$ )  $\nu_{\text{CO}} = 1905, 1810$ .

**2- $^{13}\text{C}$**  was prepared analogously starting from **1- $^{13}\text{C}$** ; the enhanced resonances in the  $^{13}\text{C}\{^1\text{H}\}$  NMR spectrum are the triplets at 260.51 and 243.58 ppm. The  $^{31}\text{P}\{^1\text{H}\}$  NMR signal at 82.39 ppm splits into a doublet of doublets ( $J = 27.13, 18.62\text{ Hz}$ ). IR (powder sample, diamond ATR,  $\text{cm}^{-1}$ )  $\nu_{\text{CO}} = 1854, 1769$ .

#### *In Situ Preparation of 4*



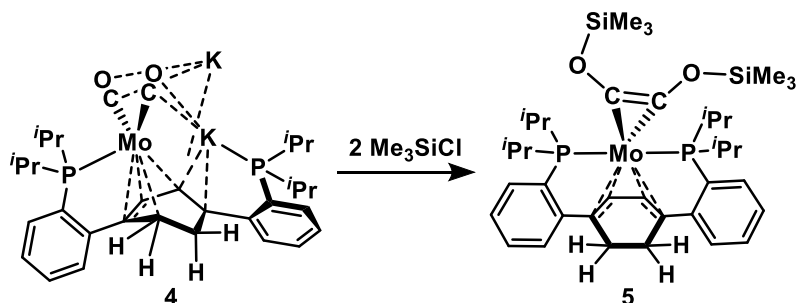
A 20 mL scintillation vial was charged with **3** (40 mg, 0.065 mmol), THF (4 mL), and a stir bar. Stirring was initiated and  $\text{KC}_8$  (18 mg, 0.083 mmol) was added, in a single portion,



resulting in an immediate darkening of the solution to dark red. After 30 min, the burgundy mixture was filtered through celite and the filtrate was dried *in vacuo*, affording a deep red residue. This residue was used without further purification.  $^{31}\text{P}\{^1\text{H}\}$  NMR (162 MHz, THF, 23 °C)  $\delta$ : 94.51 (br s, Mo-*P*), -2.47 (br s, free *P*).

$4\text{-}^{13}\text{C}$  was prepared analogously from  $3\text{-}^{13}\text{C}$ ; the enhanced resonances in the  $^{13}\text{C}\{^1\text{H}\}$  NMR spectrum (101 MHz, THF, 23 °C) resonate at 255.87 (br s) and 250.91 (br s) ppm.

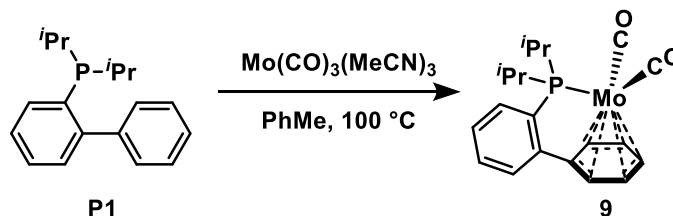
#### Synthesis of **5**



A THF solution of **4** (0.65 mmol in 4 mL) was prepared following the procedure described above; however, the reaction mixture was filtered into a 20 mL scintillation vial charged with a stir bar and the resulting homogeneous dark red solution frozen solid in an  $\text{LN}_2$  chilled cold well. Immediately upon thawing, a THF (1 mL) solution of  $\text{Me}_3\text{SiCl}$  (14 mg, 0.130 mmol) was added dropwise, with stirring. The vial was sealed and left to warm to room temperature with stirring, during this time, the solution color transitioned to deep green. The solvent was removed under reduced pressure, providing a green residue. These solids were triturated with hexanes (3 mL) and extracted with pentane (8 mL). Pumping down the pentane fraction provided **5** as a light green free-flowing powder. X-ray quality single crystals of **5** were grown via slow concentration of a concentrated pentane solution (vapor diffusion into HMDSO) at -35 °C.  $^1\text{H}$  NMR (400 MHz,  $\text{C}_6\text{D}_6$ , 23 °C)  $\delta$ : 7.26 (d,  $J$  = 8.3 Hz, 2H, aryl-*H*), 7.11 (t,  $J$  = 6.45 Hz, 2H, aryl-*H*), 7.02 (t,  $J$  = 7.4 Hz, 2H, aryl-*H*), 6.89 (t,  $J$  = 7.4 Hz, 2H, aryl-*H*), 4.99 (s, 2H, central diene-*H*), 2.97-3.01 (m, 2H, central-diene- $\text{CH}_2$ ), 2.67-2.77 (m, 2H,  $\text{CH}(\text{CH}_3)_2$ ), 2.49-2.57 (m, 2H,  $\text{CH}(\text{CH}_3)_2$ ), 2.46-2.49 (m,

2H, central diene-CH<sub>2</sub>), 1.39-1.46 (m, 6H, CH(CH<sub>3</sub>)<sub>2</sub>), 1.22-1.27 (m, 6H, CH(CH<sub>3</sub>)<sub>2</sub>), 0.95-1.00 (m, 6H, CH(CH<sub>3</sub>)<sub>2</sub>), 0.14 (s, 18H, Si(CH<sub>3</sub>)<sub>3</sub>). <sup>13</sup>C{<sup>1</sup>H} NMR (101 MHz, C<sub>6</sub>D<sub>6</sub>, 23 °C) δ: 219.46 (v br, Mo-(COSiMe<sub>3</sub>)<sub>2</sub>). <sup>31</sup>P{<sup>1</sup>H} NMR (162 MHz, C<sub>6</sub>D<sub>6</sub>, 23 °C) δ: 82.42 (v br).

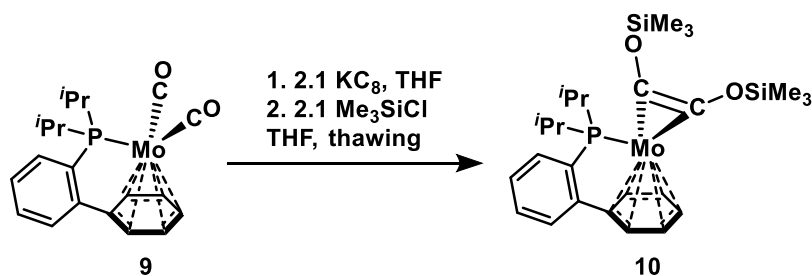
*Synthesis of 9*



A 100 mL Teflon stoppered Schlenk tube was charged with **P1** (1g, 3.70 mmol), Mo(CO)<sub>3</sub>(MeCN)<sub>3</sub> (1.23 g, 4.10 mmol), PhMe (40 mL), and a stir bar. The mixture was degassed via two freeze-pump-thaw cycles and then heated to 100 °C for 12 h, with stirring. The deep yellow/brown homogeneous solution was allowed to cool to room temperature, and was degassed as before. Heating and stirring continued for another 12 h. At this time, the reaction volatiles were concentrated under reduced pressure, until a fine yellow precipitate was observed (*ca.* 25 mL PhMe). The mixture was filtered and the filtrate left to stand in a -35 °C freezer for 72 h. Two morphologies of yellow crystals formed. These crystals were collected on a medium porosity fritted funnel, dissolved in minimal PhMe, and recrystallized twice more. At this point, the obtained crystals should be analytically pure **9** (196 mg, 0.464 mmol, 13%). If the tetracarbonyl metalation byproduct persists, additional crystallizations from PhMe may be required. <sup>1</sup>H NMR (400 MHz, C<sub>6</sub>D<sub>6</sub>, 23 °C) δ: 7.16 (br s, 1H, aryl-*H*), 7.01-7.05 (m, 1H, aryl-*H*), 6.92-6.94 (m, 2H, aryl-*H*), 4.83 (t, *J* = 5.9 Hz, 2H, central arene-*H*), 4.50 (t, *J* = 6.0 Hz, 1H, central arene-*H*), 4.31 (d, *J* = 5.41 Hz, 2H, central arene-*H*), 2.16-2.28 (m, 2H, CH(CH<sub>3</sub>)<sub>2</sub>), 1.11-1.17 (m, 6H, CH(CH<sub>3</sub>)<sub>2</sub>), 0.85-0.91 (m, 6H, CH(CH<sub>3</sub>)<sub>2</sub>). <sup>13</sup>C{<sup>1</sup>H} NMR (101 MHz, C<sub>6</sub>D<sub>6</sub>, 23 °C) δ: 228.67 (d, *J* = 11.4 Hz, Mo-CO), 146.40 (d, *J* = 22.81 Hz, aryl-C), 146.21 (s, aryl-C), 129.37 (d, *J* = 2.00 Hz, aryl-C), 129.32 (d, *J* = 0.73 Hz, aryl-C), 127.95 (d, *J* = 4.28 Hz, aryl-C), 127.05 (d, *J* = 10.79 Hz, aryl-C), 123.32 (d, *J* = 3.73 Hz, central arene-C), 86.77

(d,  $J = 1.45$  Hz, central arene-C), 83.77 (d,  $J = 2.03$  Hz, central arene-C), 81.66 (d,  $J = 3.56$  Hz, central arene-C), 28.48 (d,  $J = 21.7$  Hz,  $\text{CH}(\text{CH}_3)_2$ ), 18.92 (d,  $J = 6.3$  Hz,  $\text{CH}(\text{CH}_3)_2$ ), 18.82 (br s,  $\text{CH}(\text{CH}_3)_2$ ).  $^{31}\text{P}\{^1\text{H}\}$  NMR (162 MHz,  $\text{C}_6\text{D}_6$ , 23 °C)  $\delta$ : 93.05 (s).

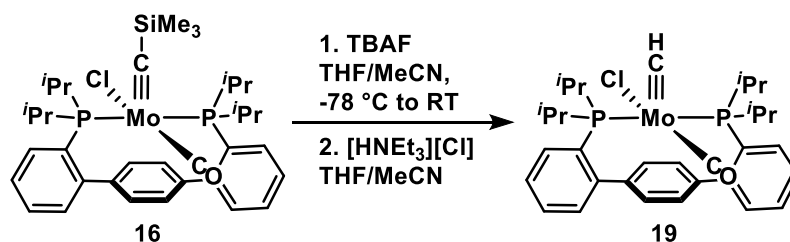
### Synthesis of **10**



A 100 mL RB flask was charged with **9** (400 mg, 0.950 mmol) and a stir bar. THF (50 mL) was added and stirring initiated, providing a deep yellow, homogenous solution.  $\text{KC}_8$  (310 mg, 2.27 mmol) was added to the flask in a single portion, resulting in an immediate darkening of the reaction mixture to dark red. The RB was placed in an  $\text{LN}_2$  cooled cold well and the contents frozen solid. Immediately upon thawing,  $\text{Me}_3\text{SiCl}$  (310 mg, 2.85 mmol) was added, resulting in a lightening of the mixture. Following the addition, stirring continued as the contents of the flask warmed to room temperature. At that time, the reaction mixture was filtered through a pad of celite and the filtrate was dried *in vacuo*, affording a red residue. The residue was triturated with hexanes (2 x 3 mL) and HMDSO (*ca.* 2 mL) was added. The vial was placed in a -35 °C freezer for 72 h; the dark red solids that had precipitated were collected (ensuring they remained cold) on a fine porosity fritted funnel, giving **10** as a sticky solid (174 mg, 0.306 mmol, 32%).  $^1\text{H}$  NMR (400 MHz,  $\text{C}_6\text{D}_6$ , 23 °C)  $\delta$ : 7.18-7.20 (m, 2H, aryl-*H*), 6.99 (t,  $J = 7.20$  Hz, 1H, aryl-*H*), 6.95 (t,  $J = 7.20$  Hz, 1H, aryl-*H*), 4.93 (t,  $J = 5.69$  Hz, 2H, central arene-*H*), 4.44 (t,  $J = 5.85$  Hz, 2H, central arene-*H*), 3.76 (t,  $J = 6.34$  Hz, 1H, central arene-*H*), 2.89-3.01 (m, 2H,  $\text{CH}(\text{CH}_3)_2$ ), 1.19-1.25 (m, 6H,  $\text{CH}(\text{CH}_3)_2$ ), 1.08-1.13 (m, 6H,  $\text{CH}(\text{CH}_3)_2$ ), 0.30 (s, 18H,  $\text{Si}(\text{CH}_3)_3$ ).  $^{13}\text{C}\{^1\text{H}\}$  NMR (101 MHz,  $\text{C}_6\text{D}_6$ , 23 °C)  $\delta$ : 190.48 (d,  $J = 22.5$  Hz,  $\text{Mo}-(\text{COSiMe}_3)_2$ ), 149.81

(d,  $J = 24.9$  Hz, aryl-C), 139.61 (d,  $J = 30.8$  Hz, aryl-C), 129.00 (d,  $J = 0.7$  Hz, aryl-C), 128.92 (d,  $J = 1.8$  Hz, aryl-C), 127.68 (s, aryl-C), 126.90 (d,  $J = 4.3$  Hz, aryl-C), 102.35 (d,  $J = 2.7$  Hz, central arene-C), 73.81 (d,  $J = 2.7$  Hz, central arene-C), 70.69 (s, central arene-C), 66.66 (d,  $J = 1.3$  Hz, central arene-C), 26.65 (d,  $J = 20.3$  Hz,  $\text{CH}(\text{CH}_3)_2$ ), 20.24 (d,  $J = 6.9$  Hz,  $\text{CH}(\text{CH}_3)_2$ ), 19.40 (s,  $\text{CH}(\text{CH}_3)_2$ ), 0.65 (s,  $\text{Si}(\text{CH}_3)_3$ ).  $^{31}\text{P}\{^1\text{H}\}$  NMR (162 MHz,  $\text{C}_6\text{D}_6$ , 23 °C)  $\delta$ : 82.96 (s).

### Synthesis of **19**



A 20 mL Teflon stoppered Schlenk tube was charged with **16** (400 mg, 0.565 mmol), THF (25 mL), and a stir bar. The flask was sealed, attached to a Schlenk line, and cooled to -78 °C via submersion in a dry ice/acetone slush bath. With a heavy  $\text{N}_2$  counterflow, the stopper was replaced with a septum. A dark red MeCN solution of anhydrous TBAF (0.791 mmol) was added dropwise via syringe. The reaction mixture was allowed to warm to room temperature, with stirring, over the course of 1 h. At this time, the flask was once again cooled to -78 °C and  $[\text{HNEt}_3][\text{Cl}]$  (235 mg, 1.695 mmol) was added, in a single portion, as a solid, with a heavy  $\text{N}_2$  counterflow. The vessel was sealed, shaken vigorously, and left to stir for 2 h. Volatile reaction components were removed under reduced pressure and the resulting residue was extracted with PhMe (3 x 7 mL) and filtered through a pad of celite. The orange/red homogeneous filtrate was dried *in vacuo*, affording a red/orange residue. This residue was suspended in minimal THF (2 mL), and cooled to -35 °C for 12 h. The ensuing mixture was filtered through celite and the filtrate set aside. The filter cake was washed with  $\text{C}_6\text{H}_6$  until the filtrate was colorless (*ca.* 8 mL). Lyophilization of the  $\text{C}_6\text{H}_6$  filtrate under reduced pressure afforded analytically pure **19**.

as an orange powder (251 mg, 0.387 mmol, 67%). The THF filtrates were observed to contain **19** by  $^{31}\text{P}\{^1\text{H}\}$  NMR spectroscopy and can be concentrated and cooled, leading to precipitation of **19** in additional crops.  $^1\text{H}$  NMR (300 MHz,  $\text{C}_6\text{D}_6$ , 23 °C)  $\delta$ : 7.51 (s, 2H, central arene-*H*), 7.43-7.48 (br m, 2H, aryl-*H*), 7.31-7.36 (br m, 2H, aryl-*H*), 7.25 (s, 2H, central arene-*H*), 5.08 (t,  $J = 3.44$  Hz, 1H,  $\text{Mo}\equiv\text{CH}$ ), 2.34-2.45 (m, 2H,  $\text{CH}(\text{CH}_3)_2$ ), 2.21-2.34 (m, 2H,  $\text{CH}(\text{CH}_3)_2$ ), 1.69-1.76 (m, 6H,  $\text{CH}(\text{CH}_3)_2$ ), 1.36-1.43 (m, 6H,  $\text{CH}(\text{CH}_3)_2$ ), 1.26-1.33 (m, 6H,  $\text{CH}(\text{CH}_3)_2$ ), 1.06-1.12 (m, 6H,  $\text{CH}(\text{CH}_3)_2$ ).  $^{31}\text{P}\{^1\text{H}\}$  NMR (121 MHz,  $\text{C}_6\text{D}_6$ , 23 °C)  $\delta$ : 40.21 (s).

**19- $^{13}\text{C}$**  can be prepared analogously, starting from **16- $^{13}\text{C}$** . The  $^1\text{H}$  NMR spectrum shows a 147.8 Hz  $^1J(\text{C},\text{H})$  scalar coupling for the methyldiyne proton, splitting it into a doublet of triplets. The enhanced resonances in the  $^{13}\text{C}\{^1\text{H}\}$  NMR spectrum are 281.19 (br,  $\text{Mo}\equiv\text{CH}$ ) and 241.41 (br,  $\text{Mo-CO}$ ).

### ***Crystallographic Information***

Refinement Details—In each case, crystals were mounted on a glass fiber or MiTeGen loop using Paratone oil, then placed on the diffractometer under a nitrogen stream. Crystals for compounds **3** and **4** were manipulated under an Argon purge due to atmospheric sensitivity. Low temperature (100 K) X-ray data were obtained on a Bruker KAPPA APEXII CCD based diffractometer (Mo fine-focus sealed X-ray tube,  $K_\alpha = 0.71073$  Å) or a Bruker D8 VENTURE Kappa Duo PHOTON 100 CMOS based diffractometer (Mo  $\text{I}_\mu\text{S}$  HB micro-focus sealed X-ray tube,  $K_\alpha = 0.71073$  Å OR Cu  $\text{I}_\mu\text{S}$  HB micro-focused X-ray tube,  $K_\alpha = 1.54178$ ). All diffractometer manipulations, including data collection, integration, and scaling were carried out using the Bruker APEXII or APEXIII software.<sup>31</sup> Absorption corrections were applied using SADABS.<sup>32</sup> Space groups were determined on the basis of systematic absences and intensity statistics and the structures were solved in the Olex 2 software interface<sup>33</sup> by intrinsic phasing using XT (incorporated into SHELXTL)<sup>34</sup> and refined by full-matrix least squares on  $F^2$ . All non-hydrogen atoms were refined using anisotropic displacement parameters. Hydrogen

atoms were placed in the idealized positions and refined using a riding model. The structure was refined (weighed least squares refinement on  $F^2$ ) to convergence. Graphical representation of structures with 50% probability thermal ellipsoids were generated using Diamond 3 visualization software.<sup>35</sup>

**Table 4.1.** Crystal and refinement data for complexes **2**, **3**, and **5**.

	<b>2</b>	<b>3</b>	<b>5</b>
CCDC # <sup>24</sup>			
Empirical formula	C <sub>64</sub> H <sub>55</sub> BF <sub>24</sub> MoO <sub>2</sub> P <sub>2</sub>	C <sub>32</sub> H <sub>42</sub> MoO <sub>2</sub> P <sub>2</sub>	C <sub>40</sub> H <sub>40</sub> MoO <sub>2</sub> P <sub>2</sub> Si <sub>2</sub>
Formula weight	1480.77	616.53	766.78
T (K)	100	100	100
<i>a</i> , Å	13.025(3)	9.3651(5)	21.8633(12)
<i>b</i> , Å	13.443(3)	20.8902(11)	10.9152(6)
<i>c</i> , Å	18.074(4)	14.9537(8)	35.7992(18)
$\alpha$ , °	90.751(9)	90	90
$\beta$ , °	96.679(9)	101.409(2)	103.067(3)
$\gamma$ , °	90.902(8)	90	90
Volume, Å <sup>3</sup>	3142.4(12)	2867.7(3)	8322.0(8)
Z	2	4	8
Crystal system	Triclinic	Monoclinic	Monoclinic
Space group	<i>P</i> $\bar{1}$	<i>P</i> 2 <sub>1</sub> / <i>n</i>	<i>C</i> 2 <sub>1</sub> / <i>c</i>
<i>d</i> <sub>calc</sub> , g/cm <sup>3</sup>	1.565	1.428	1.224
$\theta$ range, °	2.204 to 34.697	2.423 to 45.318	1.912 to 31.510
$\mu$ , mm <sup>-1</sup>	0.375	0.597	0.480
Abs. Correction	Semi-empirical	Semi-empirical	None
GOF	1.128	1.035	1.031
<i>R</i> <sub>1</sub> , <sup>a</sup> <i>wR</i> <sub>2</sub> <sup>b</sup>	0.0787, 0.1516	0.0538, 0.0892	0.0379, 0.0776
[I > 2 $\sigma$ (I)]			
Diffractometer	PHOTON	APEXII	APEXII
Radiation Type	Mo K $\alpha$	Mo K $\alpha$	Mo K $\alpha$

<sup>a</sup>  $R_1 = \sum ||F_o| - |F_c|| / \sum |F_o|$ . <sup>b</sup>  $wR_2 = [\sum [w(F_o^2 - F_c^2)^2] / \sum [w(F_o^2)^2]]^{1/2}$ .

**Table 4.2.** Crystal and refinement data for complexes **9**, **18**, **19**, and **22**.

	<b>9</b>	<b>18</b>	<b>19</b>	<b>22</b>
CCDC # <sup>24</sup>				
Empirical formula	C <sub>20</sub> H <sub>23</sub> MoO <sub>2</sub> P	C <sub>37</sub> H <sub>55</sub> MoOP <sub>2</sub> Si	C <sub>34.50</sub> H <sub>47.50</sub> ClMoOP <sub>2</sub>	C <sub>35.5</sub> H <sub>43</sub> MoOP <sub>2</sub>
Formula weight	422.29	701.78	671.55	710.60
T (K)	100	100	100	100
<i>a</i> , Å	8.3306(5)	11.6736(5)	13.1011(8)	17.5029(7)
<i>b</i> , Å	22.4172(12)	12.0522(5)	13.0037(8)	12.3149(5)
<i>c</i> , Å	9.7737(5)	14.3227(6)	19.0467(12)	16.5437(7)
$\alpha$ , °	90	94.987(2)	90	90
$\beta$ , °	96.433(3)	105.434(2)	95.462(4)	115.141(2)
$\gamma$ , °	90	110.315(2)	90	90
Volume, Å <sup>3</sup>	1813.73(17)	1785.40(13)	3230.1(3)	3228.1(2)
Z	4	2	4	4
Crystal system	Monoclinic	Triclinic	Monoclinic	Monoclinic
Space group	P 1 21/n 1	P-1	P 1 21/n 1	P 1 21/c 1
<i>d</i> <sub>calc</sub> , g/cm <sup>3</sup>	1.546	1.305	1.381	1.462
$\theta$ range, °	1.817 to 50.422	1.838 to 37.941	1.809 to 37.783	1.285 to 24.996
$\mu$ , mm <sup>-1</sup>	0.820	0.518	0.614	0.541
Abs. Correction	Semi-empirical	Semi-empirical	None	None
GOF	1.022	1.047	1.064	1.144
<i>R</i> <sub>1</sub> , <sup>a</sup> <i>wR</i> <sub>2</sub> <sup>b</sup>	0.0291, 0.0548	0.0292, 0.0693	0.0384, 0.0874	0.0456, 0.0999
[I>2 $\sigma$ (I)]				
Diffractometer	APEXII	APEXII	APEXII	APEXII
Radiation Type	Mo K $\alpha$	Mo K $\alpha$	Mo K $\alpha$	Mo K $\alpha$

$$^a R_1 = \sum ||F_o| - |F_c|| / \sum |F_o|. \quad ^b wR_2 = [\sum [w(F_o^2 - F_c^2)^2] / \sum [w(F_o^2)]^{1/2}.$$

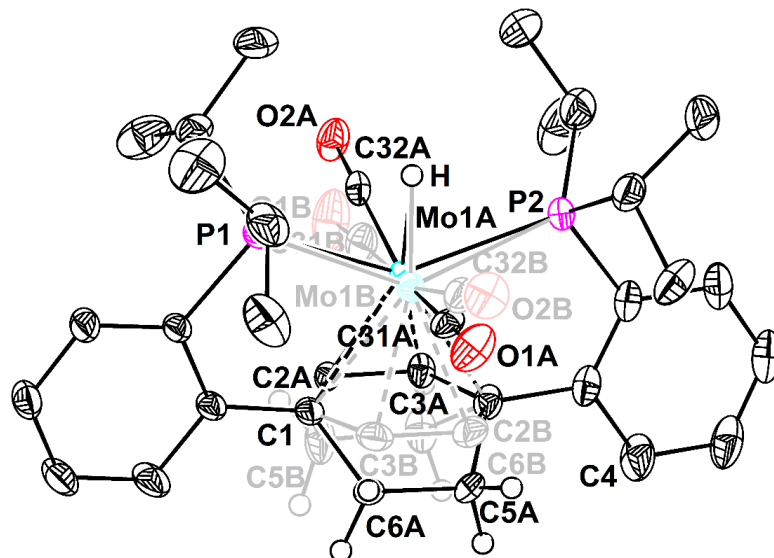


**Figure 4.12.** Structural drawing of both components of **2** with 50% probability anisotropic displacement ellipsoids. Hydrogen atoms, except for the hydride and those of the 1,4-cyclohexadiene methylene groups, and the outer-sphere  $\text{BAr}^{\text{F}}_{24}$  ion are omitted for clarity.

**Special Refinement Details for 16**—The solid-state structure of **2** showed whole molecule disorder over two positions related by a two-fold rotation. These components were satisfactorily modeled over two positions (in a 55:45 ratio) for the 1,4-cyclohexadiene motif, the Mo center, and the CO ligands; the disorder could not be resolved for the *trans*-spanning phosphines or the linking phenylenes, leading to uniform elongation of the ellipsoids for these atoms parallel to the Mo1A/Mo1B vector. The coordinates for the hydride ligand were located in the difference Fourier synthesis and refined isotropically.

In addition to the disorder in the metal complex, the  $\text{BAr}^{\text{F}}_{24}$  counterion showed significant positional and rotational disorder. The  $\text{CF}_3$  groups were rotationally disordered; the arene rings showed minor disorder due to rotation about the B–C bonds. Even though these disorders are over a continuous range of positions, the electron density in the Fourier map was satisfactorily modeled over two positions. Each disordered  $\text{CF}_3$  groups was refined with the help of similarity restraints on the 1,2- and 1,3-distances. The C–C distances of the disordered



arene rings were likewise restrained to be equivalent. All disordered groups were subjected to rigid bond restraints for anisotropic displacement parameters.

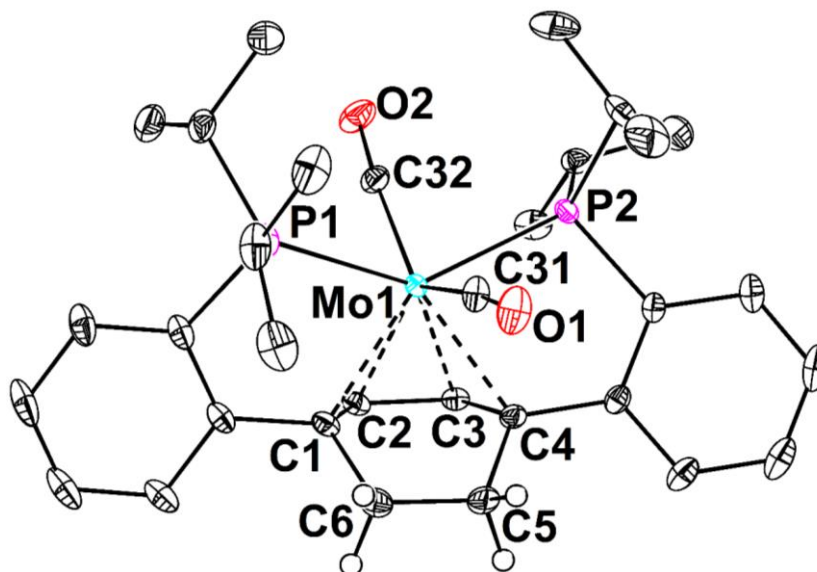


**Figure 4.13.** Structural drawing of 3 with 50% probability anisotropic displacement ellipsoids. Hydrogen atoms, except for those of the 1,4-cyclohexadiene methylene groups, are omitted for clarity.

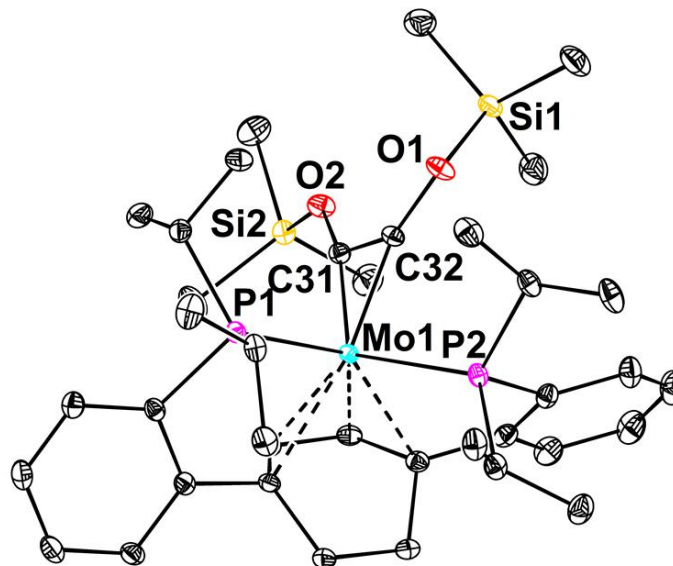


**Figure 4.14.** Structural drawing of 3 with 50% probability anisotropic displacement ellipsoids. Hydrogen atoms are omitted for clarity.

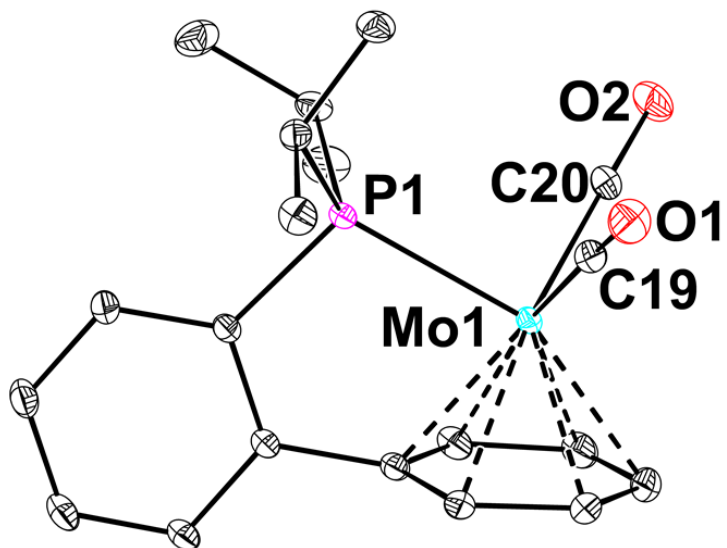


**Figure 4.15.** Structural drawing of **9** with 50% probability anisotropic displacement ellipsoids. Hydrogen atoms are omitted for clarity.

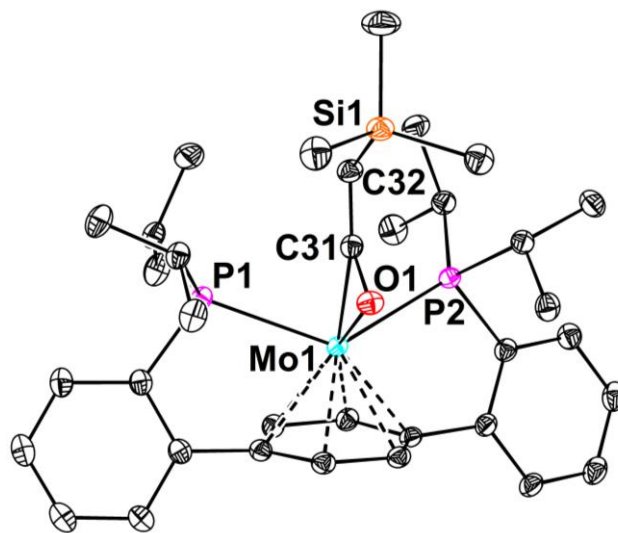


**Figure 4.16.** Structural drawing of **18** with 50% probability anisotropic displacement ellipsoids. Hydrogen atoms are omitted for clarity.

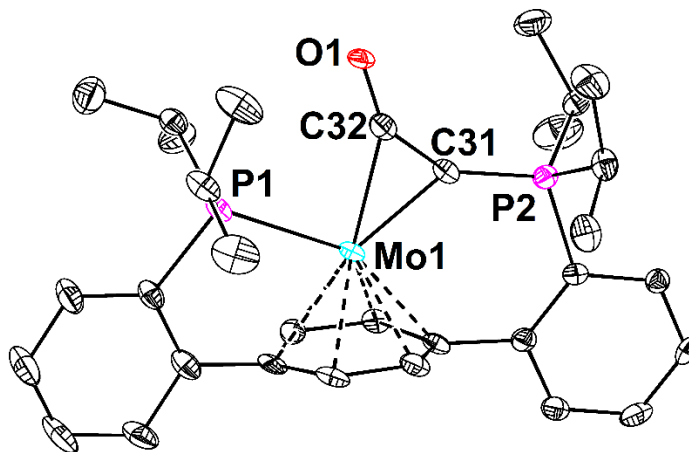


**Figure 4.17.** Structural drawing of **9** with 50% probability anisotropic displacement ellipsoids. Hydrogen atoms are omitted for clarity.

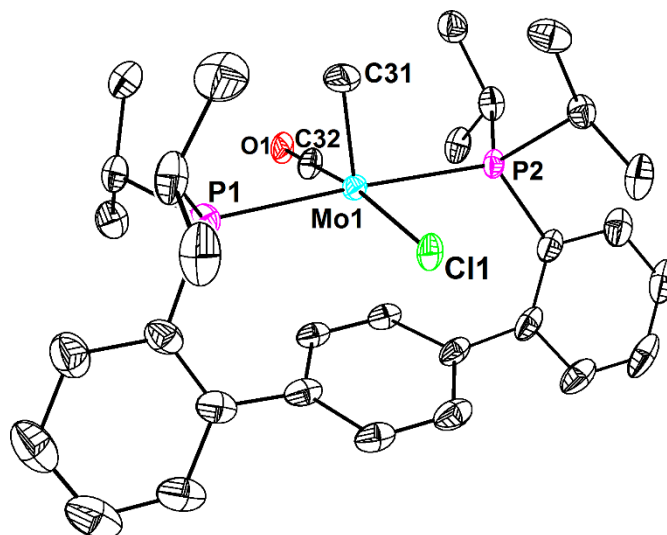


**Figure 4.18.** Structural drawing of **9** with 50% probability anisotropic displacement ellipsoids. Hydrogen atoms are omitted for clarity.

## REFERENCES

- (1) a) Costentin, C.; Robert, M.; Saveant, J.-M. *Chem. Soc. Rev.* **2013**, *42*, 2423; b) Benson, E. E.; Kubiak, C. P.; Sathrum, A. J.; Smieja, J. M. *Chem. Soc. Rev.* **2009**, *38*, 89.
- (2) a) Maitlis, P. M.; Zanotti, V. *Chem. Commun.* **2009**, 1619; b) Rofer-DePoorter, C. K. *Chem. Rev.* **1981**, *81*, 447.
- (3) Wang, W.-H.; Himeda, Y.; Muckerman, J. T.; Manbeck, G. F.; Fujita, E. *Chem. Rev.* **2015**, *115*, 12936.
- (4) West, N. M.; Miller, A. J. M.; Labinger, J. A.; Bercaw, J. E. *Coord. Chem. Rev.* **2011**, *255*, 881.
- (5) Li, C. W.; Ciston, J.; Kanan, M. W. *Nature* **2014**, *508*, 504.
- (6) a) Hu, Y. L.; Lee, C. C.; Ribbe, M. W. *Science* **2011**, *333*, 753; b) Lee, C. C.; Hu, Y. L.; Ribbe, M. W. *Science* **2010**, *329*, 642.
- (7) a) Dance, I. *Chem. Commun.* **2013**, *49*, 10893; b) Dance, I. *Dalton Trans.* **2011**, *40*, 5516.
- (8) Brookhart, M.; Grant, B.; Volpe, A. F. *Organometallics* **1992**, *11*, 3920.
- (9) a) Meiere, S. H.; Keane, J. M.; Gunnoe, T. B.; Sabat, M.; Harman, W. D. *J. Am. Chem. Soc.* **2003**, *125*, 2024; b) Brooks, B. C.; Brent Gunnoe, T.; Dean Harman, W. *Coord. Chem. Rev.* **2000**, *206-207*, 3.
- (10) a) Wang, T.-F.; Wen, Y.-S. *Acta Crystallographica Section C* **1996**, *52*, 525; b) Wang, T.-F.; Wen, Y.-S. *J. Organomet. Chem.* **1992**, *439*, 155; c) de Azevedo, C. G.; Calhorda, M. J.; de C.T. Carrondo, M. A. A. F.; Dias, A. R.; Duarte, M. T.; Galvão, A. M.; Gamelas, C. A.; Gonçalves, I. S.; da Piedade, F. M.; Romão, C. C. *J. Organomet. Chem.* **1997**, *544*, 257.
- (11) Buss, J. A.; Agapie, T. *Nature* **2016**, *529*, 72.
- (12) Magnus, P.; Principe, L. M. *Tetrahedron Lett.* **1985**, *26*, 4851.
- (13) Dr. Siti Riduan -- Unpublished Results.
- (14) Asdar, A.; Lapinte, C.; Toupet, L. *Organometallics* **1989**, *8*, 2708.
- (15) Miller, A. J. M.; Labinger, J. A.; Bercaw, J. E. *J. Am. Chem. Soc.* **2008**, *130*, 11874.
- (16) Barger, P. T.; Santarsiero, B. D.; Armantrout, J.; Bercaw, J. E. *J. Am. Chem. Soc.* **1984**, *106*, 5178.
- (17) Herrmann, W. A.; Plank, J. *Angew. Chem. Int. Ed.* **1978**, *17*, 525.
- (18) Bodnar, T. W.; Cutler, A. R. *J. Am. Chem. Soc.* **1983**, *105*, 5926.
- (19) Lin, Y. C.; Calabrese, J. C.; Wreford, S. S. *J. Am. Chem. Soc.* **1983**, *105*, 1679.
- (20) Morrison, E. D.; Steinmetz, G. R.; Geoffroy, G. L.; Fultz, W. C.; Rheingold, A. L. *J. Am. Chem. Soc.* **1984**, *106*, 4783.
- (21) Black, T. H.; Farrell, J. R.; Probst, D. A.; Zotz, M. C. *Synth. Commun.* **2002**, *32*, 2083.
- (22) a) Greco, J. B.; Peters, J. C.; Baker, T. A.; Davis, W. M.; Cummins, C. C.; Wu, G. *J. Am. Chem. Soc.* **2001**, *123*, 5003; b) Peters, J. C.; Odom, A. L.; Cummins, C. C. *Chem. Commun.* **1997**, 1995.
- (23) a) Hill, A. F.; Ward, J. S.; Xiong, Y. *Organometallics* **2015**, *34*, 5057; b) van der Eide, E. F.; Piers, W. E.; Parvez, M.; McDonald, R. *Inorg. Chem.* **2007**, *46*, 14.
- (24) Neithamer, D. R.; LaPointe, R. E.; Wheeler, R. A.; Richeson, D. S.; Van Duyne, G. D.; Wolczanski, P. T. *J. Am. Chem. Soc.* **1989**, *111*, 9056.
- (25) Hommeltoft, S. I.; Baird, M. C. *J. Am. Chem. Soc.* **1985**, *107*, 2548.
- (26) Pangborn, A. B.; Giardello, M. A.; Grubbs, R. H.; Rosen, R. K.; Timmers, F. J. *Organometallics* **1996**, *15*, 1518.
- (27) Buss, J. A.; Edouard, G. A.; Cheng, C.; Shi, J.; Agapie, T. *J. Am. Chem. Soc.* **2014**, *136*, 11272.
- (28) Weitz, I. S.; Rabinovitz, M. J. *Chem. Soc., Perkin Trans. 1* **1993**, 117.
- (29) Sun, H.; DiMagno, S. G. *J. Am. Chem. Soc.* **2005**, *127*, 2050.

- (30) Fulmer, G. R.; Miller, A. J. M.; Sherden, N. H.; Gottlieb, H. E.; Nudelman, A.; Stoltz, B. M.; Bercaw, J. E.; Goldberg, K. I. *Organometallics* **2010**, *29*, 2176.
- (31) a) Matsuo, T.; Kawaguchi, H. *J. Am. Chem. Soc.* **2005**, *127*, 17198; b) APEX3, Version 1 User Manual, M86-EXX229, Bruker Analytical X-ray Systems, Madison, WI, May 2016.
- (32) Shima, T.; Hou, Z. *J. Am. Chem. Soc.* **2006**, *128*, 8124.
- (33) Dolomanov, O. V.; Bourhis, L. J.; Gildea, R. J.; Howard, J. A. K.; Puschmann, H. *J. Appl. Crystallogr.* **2009**, *42*, 339.
- (34) Manriquez, J. M.; McAlister, D. R.; Sanner, R. D.; Bercaw, J. E. *J. Am. Chem. Soc.* **1976**, *98*, 6733.
- (35) Wolczanski, P. T.; Bercaw, J. E. *Acc. Chem. Res.* **1980**, *13*, 121.



## **CHAPTER 5**

### **A Low-Valent Anionic Molybdenum Nitride: Synthesis, Electronic Structure, and Group Transfer**

**ABSTRACT**

A series of terminal Mo(IV) nitride complexes were prepared within the context of exploring nitride/carbonyl coupling to cyanate. CO installation—giving a complex isoelectronic to alkylidyne carbonyl complexes known to undergo  $RC^-$  transfer—and subsequent reduction proved unfruitful. However, electron loading prior to the addition of CO affords the first Mo(II) nitrido complex, an early metal nitride with four valence d-electrons. The binding mode change of the *para*-terphenyl diphosphine ancillary ligand upon reduction acts not only to diminish the  $\sigma^*$  interactions of the now-occupied  $d_{(x^2-y^2)}$  orbital, but strong  $\delta$ -backbonding between Mo and the central arene ring stabilize both filled d orbitals. This electronic configuration facilitates a high electron count and a formal M–N bond order of three. Even with an intact  $Mo\equiv N$  bond, this low-valent nitrido complex proves to be highly reactive, readily undergoing complete N-atom transfer upon addition of CO.



## GENERAL INTRODUCTION

Transition metal nitrides have received significant attention in the context of  $N_2$  fixation and N-atom group transfer chemistries.<sup>1</sup>  $N_2$ -derived nitrides often result in thermodynamically stable M–N bonds, recompensing for the scission of  $N_2$ , and requiring forcing conditions to enact modest chemical changes.<sup>2</sup> A successful strategy for increasing the reactivity of metal nitrides is weakening the M–N bonds with a high metal d count.<sup>3</sup> Indeed, increasing the electron count at the metal can concomitantly facilitate metal-centered activation of small molecule coupling partners.<sup>3,4</sup> High electron count ( $d \geq 4$ ) nitrides are uncommon,<sup>3,5</sup> and unknown for early metals. They can display enhanced reactivity, including nitride hydrogenolysis<sup>3,5g</sup> and carbonylation.<sup>3</sup> Though alkylation, protonation, and silylation of terminal nitridos is well represented in the literature, redox-coupled transformations are uncommon, despite representing an efficient means using nitrides as N-atom building blocks.<sup>6</sup> Herein we report the reduction of a Mo(IV) terminal nitride, affording a Mo(II) nitride anion. This nucleophilic nitride, stabilized by metal-arene  $\delta$ -bonding, is competent for redox-coupled nitrogen atom transfer, affording cyanate upon low-temperature treatment with carbon monoxide (CO).

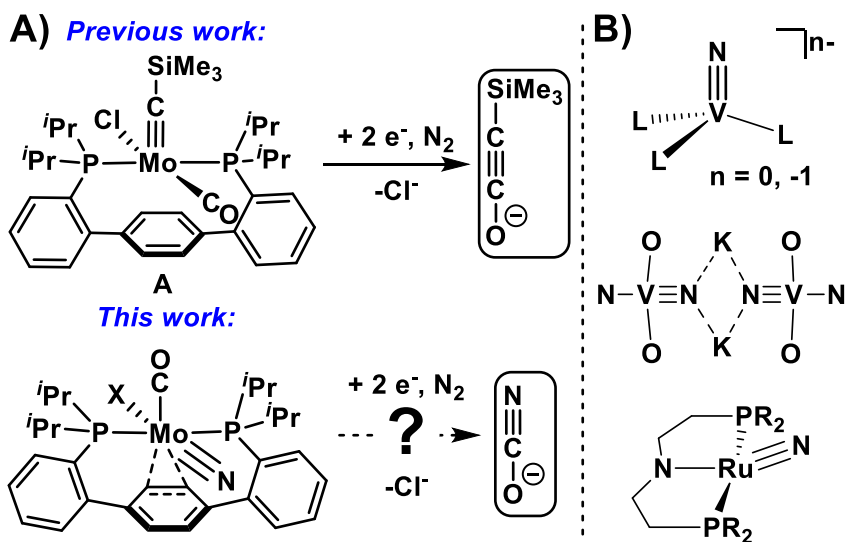
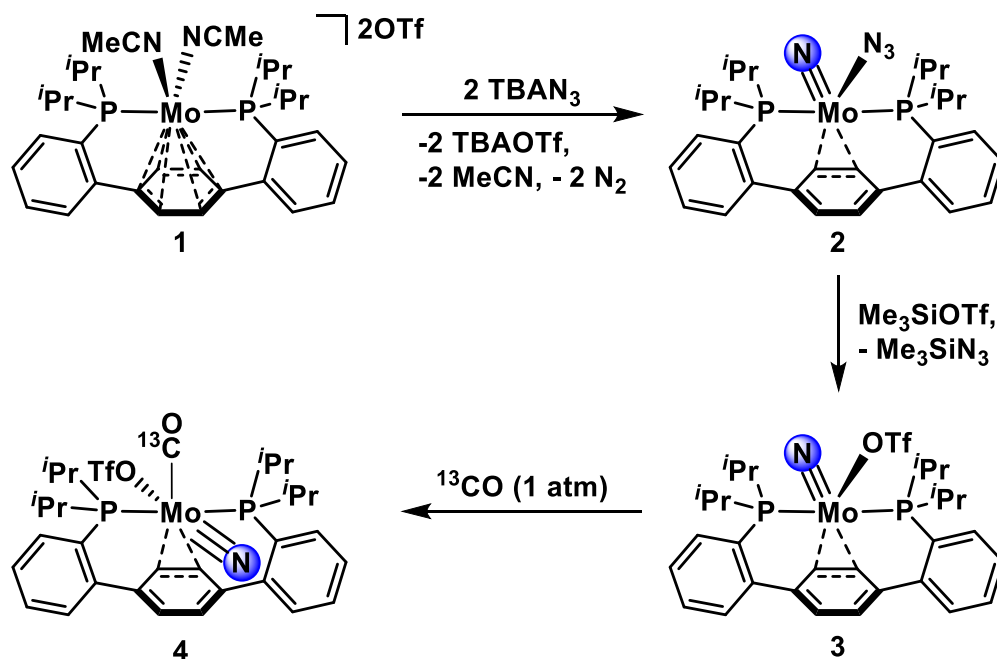


**Figure 5.1.** Envisioned extension of  $C \equiv C$  bond forming methodology to  $C \equiv N$  bond construction (A) based on prior reports of nitride/CO coupling (B).

Within the context of C<sub>1</sub> feedstock upgrading, our group has explored the reactivity of Mo(IV) alkylidyne carbonyl complexes.<sup>7</sup> Following two-electron reduction, these compounds forge a C≡C triple bond, ejecting the oxyacetylide anion and adventitiously binding N<sub>2</sub> (Figure 5.1., A). Intrigued by literature reports of nitride/CO coupling (Figure 5.1., B)<sup>3,8</sup> and realizing the isolobal relationship between cyanate and oxyacetylide, we sought to extend our C–C bond forming methodology to construct C–N bonds.

## RESULTS AND DISCUSSION

A terminal Mo nitride supported by the *para*-terphenyl diphosphine ancillary ligand is accessible via anionic azide thermolysis. Treating a deep purple MeCN solution of Mo(II) complex **1**<sup>9</sup> with two equiv. of TBAN<sub>3</sub> (TBA = *n*-tetrabutyl-ammonium) precipitates a burgundy powder, the <sup>31</sup>P{<sup>1</sup>H} NMR spectrum of which shows a single resonance upfield shifted to 35.01 ppm (C<sub>6</sub>D<sub>6</sub>). The <sup>1</sup>H NMR spectrum, consistent with a C<sub>s</sub> symmetric solution structure, displays two upfield shifted central arene resonances—5.93 and 4.43 ppm—suggestive of an η<sup>2</sup> metal-arene interaction. Using a <sup>15</sup>N enriched source of azide afforded a product with three resonances in the <sup>15</sup>N NMR spectrum at 833.09, 137.23, and 62.23 ppm, consistent with a terminal nitride motif<sup>10</sup> and a bound azide ligand,<sup>11</sup> respectively (**2**, Scheme 5.1).



**Scheme 5.1.** Synthesis of Mo(IV) terminal nitrido complexes.

The structure of Mo(IV) nitride **2** was confirmed by single crystal X-ray diffraction (XRD; Figure 5.2). The short Mo≡N distance of 1.641(2) Å agrees well with previously reported examples of Mo(IV) terminal nitride complexes,<sup>12</sup> and the close Mo–C2/C3 contacts and

elongated C2–C3 bond support the  $\eta^2$  arene binding mode inferred from solution spectroscopies.

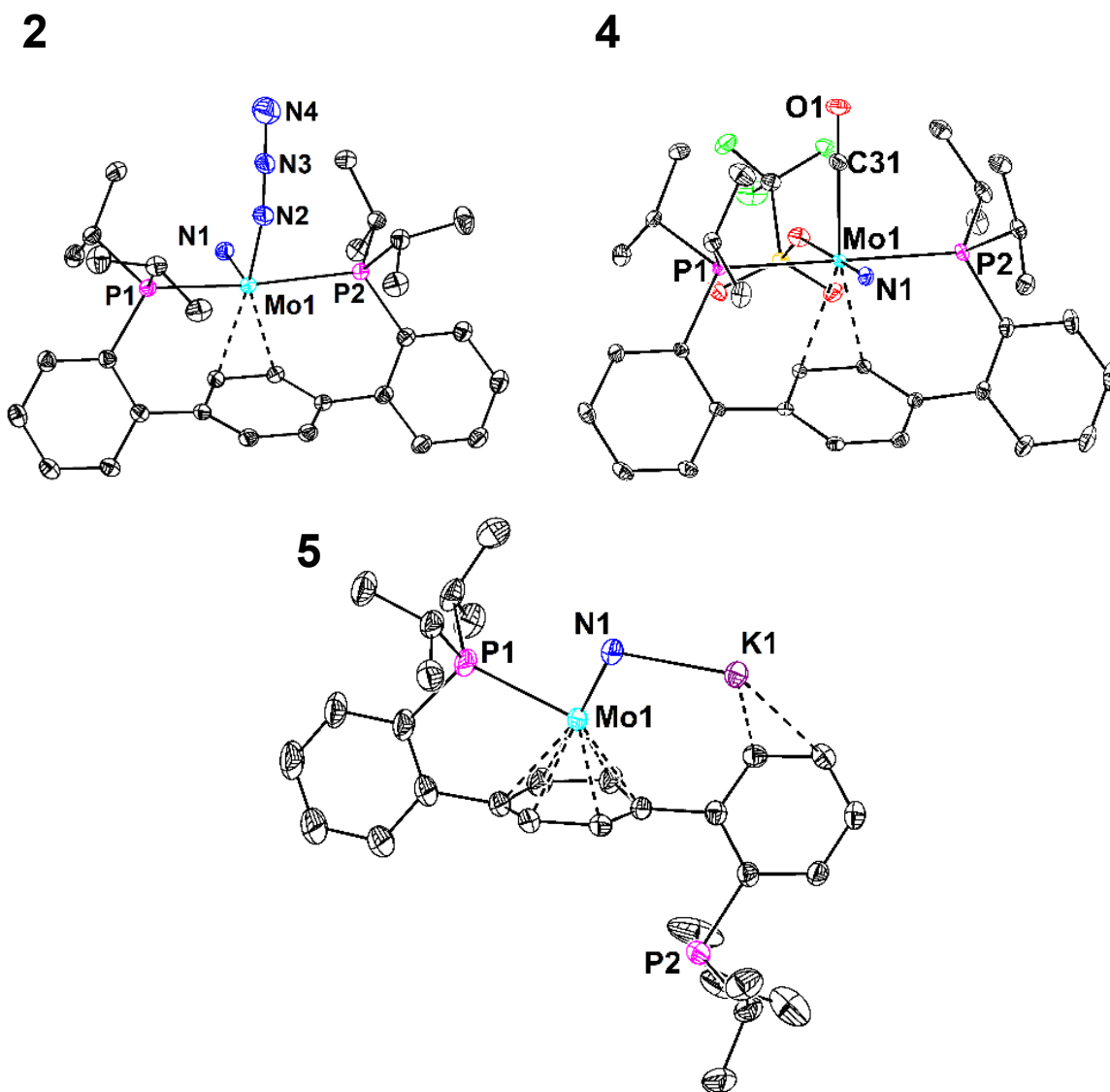


**Figure 5.2.** Solid state structures of **2**, **4**, and **5**. Anisotropic displacement ellipsoids are shown at the 50% probability level. Select bond distances [Å] and angles [°]: **2**: Mo1–N: 1.641(2), Mo1–N2: 2.140(2), Mo1–C<sub>arene</sub>(ave.): 2.264(2), ∠N1–Mo1–N2: 106.1(1); **4**: Mo1–N1: 1.663(1), Mo1–C31: 2.032(1), Mo–C<sub>arene</sub>(ave.): 2.496(1), Mo1–O2: 2.4822(1), ∠N1–Mo1–C31: 91.9(1); **5**: Mo1–N1: 1.728(3), Mo1–C<sub>arene</sub>(ave.): 2.304(3), N1–K1: 2.732(3), K1–C<sub>phenylene</sub>(ave.): 3.239(3), ∠Mo1–N2–K1: 115.0(1).

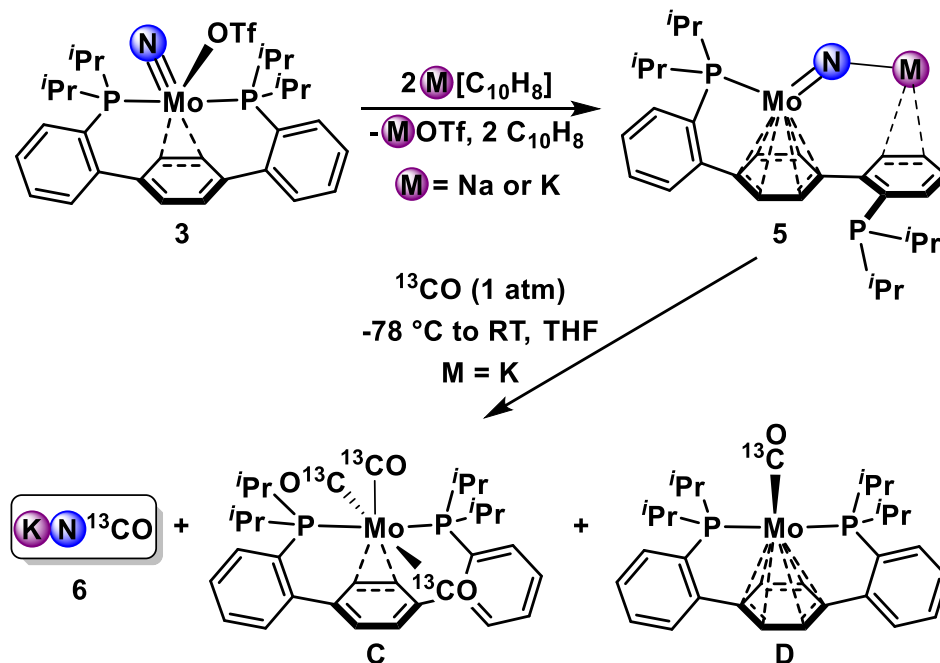
Concerned with undesired reactivity of the bound azide, complex **2** was treated with Me<sub>3</sub>SiOTf (OTf = trifluoromethanesulfonate) to enact ligand exchange. Addition of two equiv. of the silyl triflate cleanly formed a new species with a slightly downfield shifted <sup>31</sup>P{<sup>1</sup>H}

NMR resonance (36.42 ppm, C<sub>6</sub>D<sub>6</sub>) and a marginally downfield shifted <sup>15</sup>N NMR signal (842.22 ppm). A solid-state structure of nitride triflate **3** was not obtained, but the similarity of the spectroscopic signature with that of precursor **2**, and a single <sup>19</sup>F NMR resonance at -76.91 ppm support its assignment.

Gratifyingly, addition of an atmosphere of <sup>13</sup>CO to a magenta solution of **3** resulted in an immediate color change to orange and formation of an orange precipitate. The <sup>13</sup>C{<sup>1</sup>H} NMR spectrum of this mixture displays a broad resonance at 244.04 ppm, consistent with <sup>13</sup>CO binding and formation of six-coordinate nitride **4**. Both the <sup>1</sup>H and <sup>31</sup>P{<sup>1</sup>H} are likewise broad, suggesting a fluxional process that is intermediate on the NMR timescale. Multinuclear NMR spectroscopy evinces two distinct species at low temperature (-65 °C) and a single broad set of resonances upon warming (25 °C), attributed to interconversion of two isomers via slipping of the η<sup>2</sup> Mo-arene interaction across the face of the central ring.<sup>7a</sup> XRD ratified the structure of **4** (Figure 5.2), a nitride carbonyl complex with these moieties poised *cis* to one another. The Mo≡N bond in **4** remains short at 1.663(1) Å.

As an isoster of E≡E coupling precursor **A**, the reduction chemistry of **4** was explored. CO binding to **4** is weak and reversible, necessitating *in situ* preparation and reaction screening; addition of two equiv. of Na[C<sub>10</sub>H<sub>8</sub>], the same strong reductant used to enact C≡C coupling in **A**, led primarily to CO loss (**3**) and decomposition to free phosphine.

Stymied by the disparate reduction reactivity of **4** (when compared to **A**), reduction was explored prior to carbonylation. Treating a thawing THF solution of **3** with either Na or K[C<sub>10</sub>H<sub>8</sub>] results in an immediate darkening and concomitant formation of a C<sub>i</sub> symmetric species (Scheme 5.2). Resonances in the <sup>31</sup>P{<sup>1</sup>H} NMR spectrum at 53.73 and -2.04 ppm suggest dissociation of one of the phosphine arms of the terphenyl ligand, and four distinct signals at 5.85, 5.24, 5.04, and 5.00 ppm in the <sup>1</sup>H NMR spectrum point to an η<sup>6</sup> Mo-arene binding mode.



**Scheme 5.2.** Anionic nitride synthesis and  $\text{N}^-$  group transfer reactivity.

Complex **5-K** crystallizes from benzene as a tetrameric  $\text{N}_4\text{K}_4$  cubane (Figure 5.13.); each of the four equivalent units is comprised of an anionic nitride (Figure 5.2.). Species **5** represents the first example of a formally Mo(II) anionic nitride.<sup>13</sup> Consistent with the spectroscopic data, one phosphine arm dissociates upon reduction. The  $\text{Mo}\equiv\text{N}$  distance is considerably longer than in the Mo(IV) species, at 1.728(3) Å, one of the longer  $\text{Mo}\equiv\text{N}$  distances reported in the solid-state.<sup>12b,14</sup> The Mo atoms at the N-vertices of the cube are poised *ca.* 6.5 Å apart, clearly precluding Mo/Mo interactions. The potassium counterions are engaged in both a close contact with the nitride—2.733(3) Å—and display an interaction with the  $\pi$ -system of one of the phenylene linkers. Attempts to abstract the counterion and form an ate complex have thus far been unsuccessful, leading to decomposition to intractable mixtures comprised primarily of free phosphine.

Terminal nitrido complexes with high formal metal  $d$ -electron counts ( $d^n$ ,  $n \geq 4$ ), which help destabilize the often unreactive M–N bond, are to our knowledge, unknown for early transition metals. This motivated an investigation of the electronic structure of **5**. The bonding situation of square pyramidal precursor **3** is analogous to that of its Mo(IV) phosphide

congener.<sup>15</sup> The  $d$ -electrons occupy a Mo orbital of  $d_{xy}$  parentage that is strictly non-bonding with respect to the nitride, permitting the formal Mo $\equiv$ N triple bond. Upon two electron reduction, in this geometry, the  $d_{xz}$  and  $d_{yz}$  orbitals (Mo $\equiv$ N  $\pi^*$ ) would both become singly occupied, degrading the formal Mo–N bond order and likely making this complex unstable/unisolable.

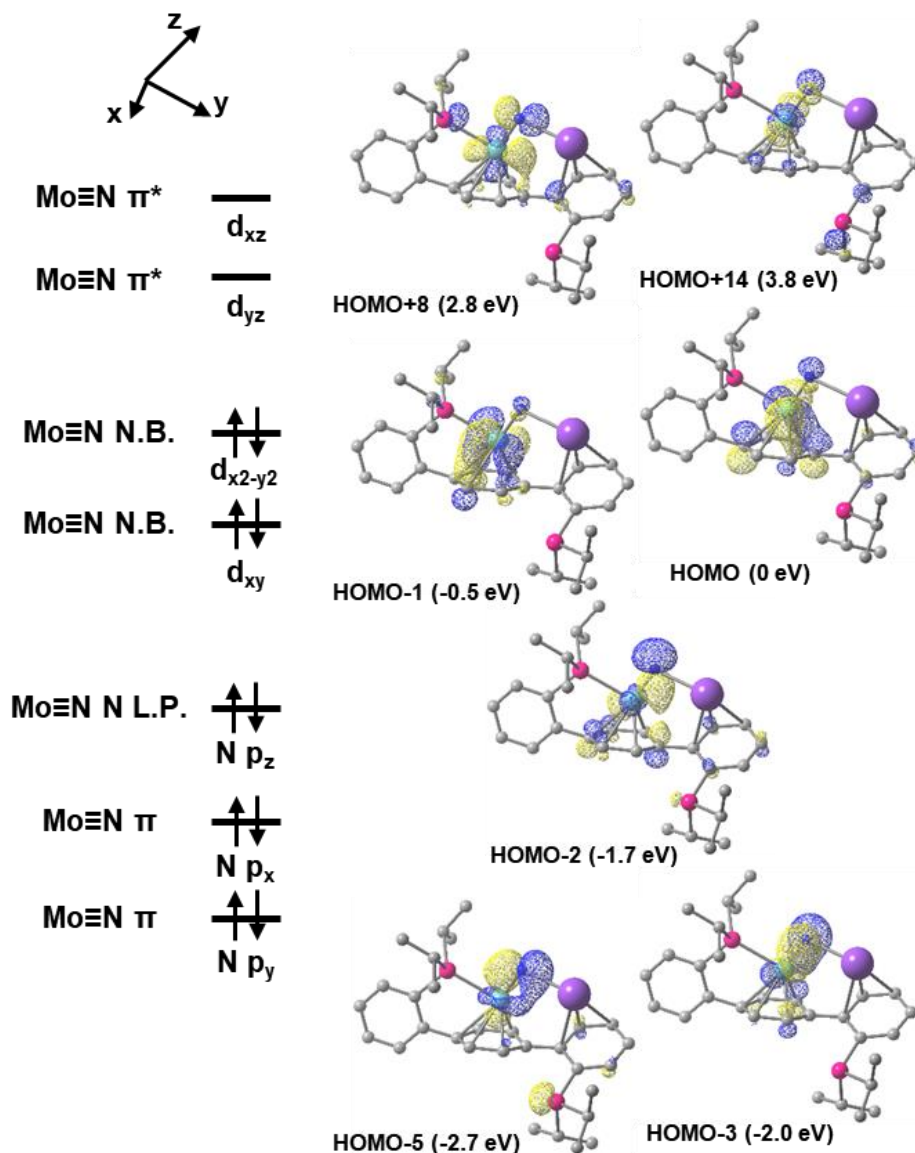


**Figure 5.3.** Qualitative MO diagram (left) and selected calculated valence MOs (right) depicting the Mo/nitride bonding in **5**. Isosurfaces are shown at the  $0.05 \text{ e}\cdot\text{\AA}^{-3}$  level and energies (relative to the HOMO) are provided.

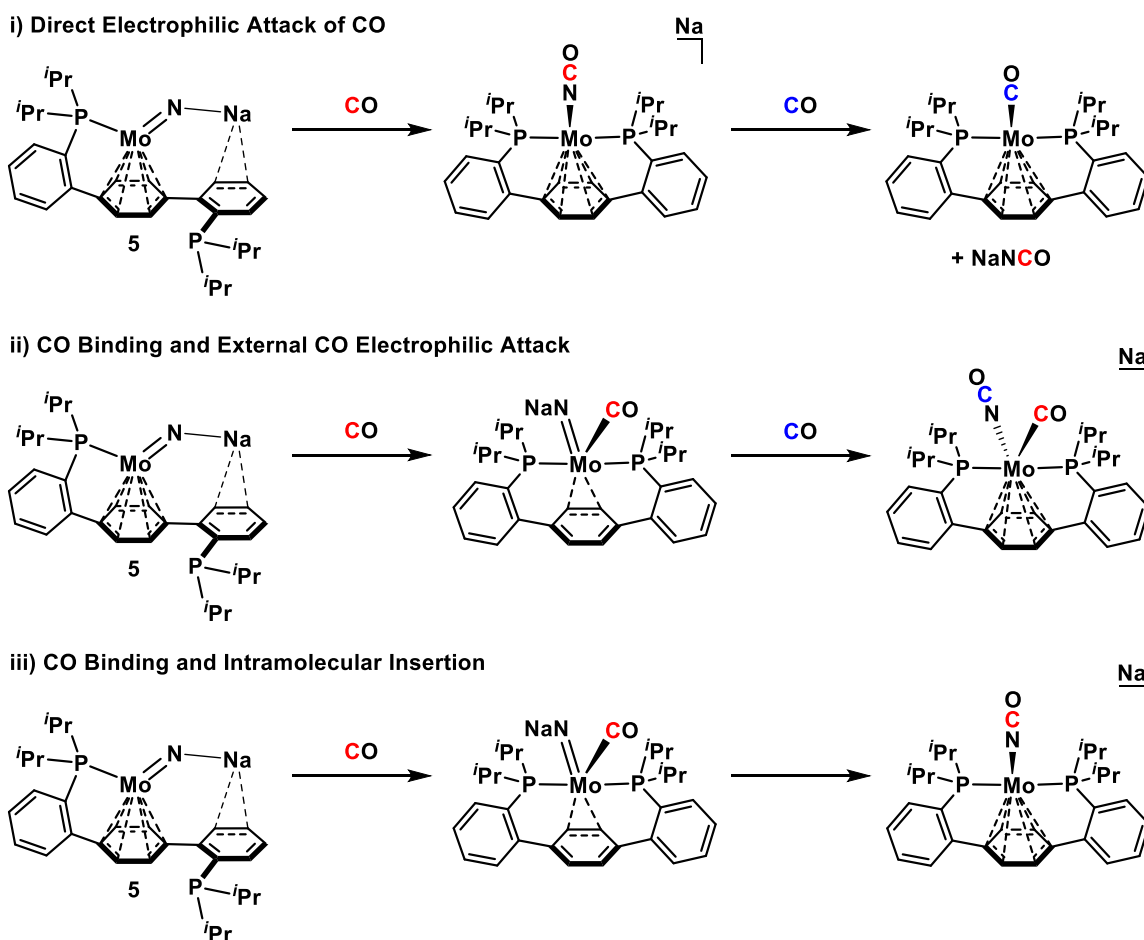
The structural flexibility of the terphenyl diphosphine ancillary ligand, however, obviates the need to diminish the Mo–N bonding. The electronic structure of **5** provides two low-energy *d* orbitals ( $d_{xy}$  and  $d_{(x^2-y^2)}$ , HOMO-1 and HOMO, Figure 5.3.) that are largely non-bonding with respect to the nitride ligand. These orbitals exhibit significant  $\delta$ -bonding character with the central arene, further lowering their overall energy. Phosphine arm dissociation is likely requisite to stabilize **5**, reducing the Mo–P  $\sigma^*$  character of the *d*-orbitals orthogonal to the Mo $\equiv$ N vector, and providing orbital(s) to accept the additional electrons. In this context, the electronic structure of **5** more closely matches that of axially distorted late metal nitrido complexes than that of high-valent terminal Mo nitrides in the trigonal or tetragonal ligand field;<sup>16</sup> however, the basal arene ligand, as a  $\delta$ -acid, acts to further stabilize the occupied *d*-orbitals.

Another salient feature of the electronic structure of **5** is the high energy N-based lone pair (HOMO-2, Figure 5.3.). Anticipating that this would render **5** highly nucleophilic, a THF solution of anion **5** was treated with 1 atm. of <sup>13</sup>CO at low temperature (Scheme 5.2.). Upon warming to room temperature, three signals were observed in the <sup>13</sup>C{<sup>1</sup>H} NMR spectrum at 242.6, 220.7, and 213.9 ppm (<sup>2</sup>J(P,C) = 14.6, 9.4, and 9.4 Hz, respectively). These resonances correlate to the known carbonyl complexes **C** and **D**, corroborated by observation of peaks in the <sup>31</sup>P{<sup>1</sup>H} NMR spectrum at 81.6 and 50.7 ppm, respectively.<sup>9</sup> Formation of **C/D** necessitates complete denitrogenation; removal of solvent and analysis of resulting residue in D<sub>2</sub>O demonstrated formation of cyanate anion as a triplet centered at 129.3 ppm in the <sup>13</sup>C{<sup>1</sup>H} NMR (Figure 5.7.).<sup>8a</sup> The N<sup>-</sup> abstraction observed upon treatment of **5** with CO supplements examples of Mo(II) imido complexes capable of isocyanate formation,<sup>17</sup> but represents the first instance of nitride transfer to CO on Mo. Similar to a tris(anilide) supported anionic V nitride,<sup>8a</sup> **5** releases the cyanate ion (likely due to the 2 e<sup>-</sup> reduction of Mo), albeit forming a mixture carbonyl complex as the terminal products. Curiously, addition of <sup>t</sup>BuNC did not lead to formation of a Mo(0) complex suggestive of group transfer, though



nucleophilic nitrides often react with isocyanides,<sup>8d,18</sup> and instead resulted in significant decomposition to free phosphine.

Reported examples of nitride/CO coupling favor a mechanism invoking electrophilic attack of the CO ligand at N.<sup>3,8a</sup> Though this is likely the case in  $d^0$  metal complexes, the low valency and coordinative unsaturation of **5** may prefer CO binding prior to coupling.<sup>8e</sup> Experiments detailing the elementary steps of C–C coupling in this system were consistent with reduction prior to electrophilic attack from a Mo(IV) carbide carbonyl complex.<sup>7a</sup> Analogously, CO binding and phosphine arm coordination from **5** would provide the nitride congener, which may likewise be prone to electrophilic attack at N (Scheme 5.3). However, the inability of **4**,



**Scheme 5.3.** Possible mechanisms for cyanate anion formation from **5-Na** and CO.

with a pre-installed CO ligand, to form significant of  $\text{NCO}^-$  upon reduction,<sup>19</sup> suggests otherwise. Both a mechanism that involves CO binding prior to CO electrophilic attack and one that invokes CO binding and intramolecular insertion, share a common intermediate that should be the direct product of the  $2 e^-$  reduction of **4**. Studies to elucidate the coupling mechanism and exploration of additional redox-coupled nitride group transfer reactions are ongoing.

## CONCLUSION

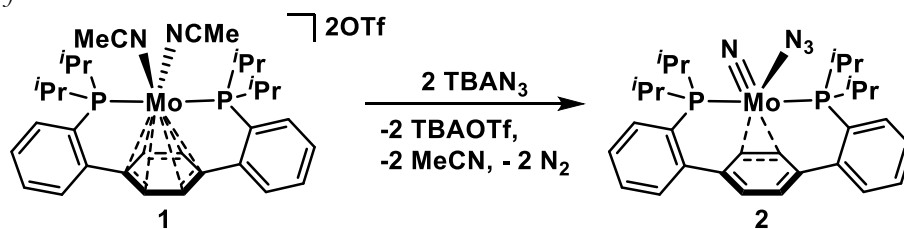
In summary, reactivity toward  $2 e^-$  coupling of a terminal Mo(IV) nitride and CO was induced by pre-reduction of the metal center. The resulting low-valent Mo(II) nitride is stabilized by significant changes in the ancillary ligand, supporting both four d-electrons and a formal Mo $\equiv$ N bond. This nucleophilic, anionic nitride complex reacts with CO at low temperature to afford a mixture of Mo carbonyl complexes and free cyanate anion. The presented strategy for engendering reactivity upon reduction may provide a means for accessing productive group transfer reactivity in stereotypically stable early transition metal nitrides.

## EXPERIMENTAL SECTION

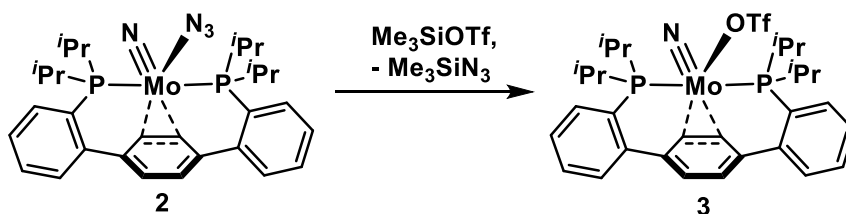
### *General Considerations*

Unless otherwise specified, all operations were carried out in an MBraun drybox under a nitrogen atmosphere or using standard Schlenk and vacuum line techniques. Solvents for air- and moisture-sensitive reactions were dried over sodium benzophenone ketyl, calcium hydride, or by the method of Grubbs.<sup>20</sup> Deuterated solvents were purchased from Cambridge Isotope Laboratories and vacuum transferred from sodium benzophenone ketyl (C<sub>6</sub>D<sub>6</sub>) or CaH<sub>2</sub> (CD<sub>3</sub>CN). D<sub>2</sub>O was used without further purification. Solvents, once dried and degassed, were vacuum transferred directly prior to use or stored under inert atmosphere over activated 4 Å molecular sieves. **1**<sup>9</sup> was prepared according to a literature procedure. Unless indicated otherwise, all chemicals were used as received. TBAN<sub>3</sub> (dried under vac. at 40 °C for 8 h), naphthalene (vacuum sublimed at 40 °C), <sup>13</sup>CO, Me<sub>3</sub>SiOTf, and <sup>t</sup>BuNC were purchased from Sigma Aldrich. Na<sup>0</sup> (washed with hexanes under N<sub>2</sub> to remove oil) and K<sup>0</sup> (washed with hexanes under N<sub>2</sub> to remove oil) were purchased from Alfa Aesar and Acros, respectively. <sup>1</sup>H, <sup>13</sup>C{<sup>1</sup>H}, and <sup>31</sup>P{<sup>1</sup>H} NMR spectra were recorded on a Varian 400 MHz or Varian INOVA-500 spectrometers with shifts reported in parts per million (ppm). <sup>1</sup>H and <sup>13</sup>C{<sup>1</sup>H} NMR spectra are referenced to residual solvent peaks.<sup>21</sup> <sup>31</sup>P{<sup>1</sup>H} chemical shifts are referenced to an external 85% H<sub>3</sub>PO<sub>4</sub> (0 ppm) standard. Multiplicities are abbreviated as follows: s = singlet, d = doublet, dd = doublet of doublets, t = triplet, vt = virtual triplet, q = quartet, app dq = apparent doublet of quartets, m = multiplet, br = broad, v br = very broad. Elemental analysis was performed at the Caltech XRCF using a PerkinElmer 2400 Series II CHN Elemental Analyzer.

### *Synthesis of 2*



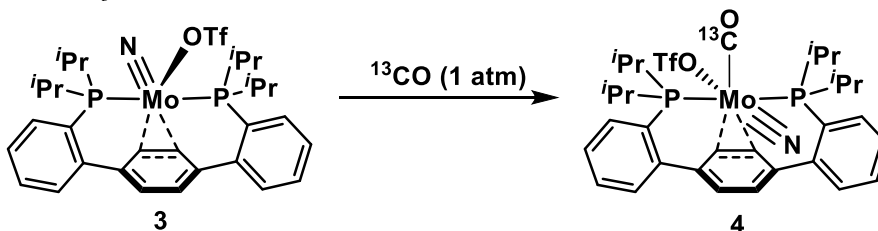
A 100 mL RB flask was charged with **1** (2 g, 2.13 mmol) and a stir bar. MeCN (40 mL) was added and stirring was initiated, affording a dark purple homogeneous solution. A solution of TBAN<sub>3</sub> (1.27 g, 4.47 mmol) in MeCN (10 mL) was added dropwise. The purple solution gradually turned deep maroon and gas evolution was evident. With prolonged stirring, formation of a brick red precipitate was observed. After 2.5 h, the solvent volume was concentrated to *ca.* 10 mL under reduced pressure. While still cold, the resulting suspension was filtered on a medium porosity sintered glass frit. The solids were washed with -35 °C MeCN (7 mL x 3), dried *in vacuo*, and collected, providing analytically pure **2** as a free-flowing red powder (1.1 g, 1.80 mmol, 84%). X-ray quality single crystals were grown via vapor diffusion of pentane into a concentrated toluene solution of **2**. <sup>1</sup>H NMR (400 MHz, C<sub>6</sub>D<sub>6</sub>, 23 °C) δ: 7.31 (app dq, *J* = 7.1 & 1.5 Hz, 2H, aryl-*H*), 7.22-7.25 (m, 2H, aryl-*H*), 7.13-7.16 (m, 2H, aryl-*H*), 7.07-7.11 (m, 2H, aryl-*H*), 5.93 (br s, 2H, central arene-*H*), 4.43 (t, *J* = 2.3 Hz, 2H, central arene-*H*), 3.01-3.12 (m, 2H, CH(CH<sub>3</sub>)<sub>2</sub>), 2.47-2.61 (m, 2H, CH(CH<sub>3</sub>)<sub>2</sub>), 1.94-2.00 (m, 6H, CH(CH<sub>3</sub>)<sub>2</sub>), 1.38-1.44 (m, 6H, CH(CH<sub>3</sub>)<sub>2</sub>), 0.72-0.76 (m, 6H, CH(CH<sub>3</sub>)<sub>2</sub>), 0.28-0.34 (m, 6H, CH(CH<sub>3</sub>)<sub>2</sub>). <sup>13</sup>C{<sup>1</sup>H} NMR (101 MHz, C<sub>6</sub>D<sub>6</sub>, 23 °C) δ: 150.88 (vt, *J* = 6.99, aryl-*C*), 140.99 (vt, *J* = 4.94 Hz, central arene-*C*), 132.07 (s, aryl-*C*), 130.79 (s, aryl-*C*), 127.64 (vt, *J* = 2.34 Hz, aryl-*C*), 127.35 (vt, *J* = 2.48 Hz, aryl-*C*), 122.58 (vt, *J* = 15.45 Hz, aryl-*C*), 121.95 (s, central arene-*C*), 62.13 (vt, *J* = 2.54 Hz, central arene-*C*), 23.19 (vt, *J* = 8.15 Hz, CH(CH<sub>3</sub>)<sub>2</sub>), 22.47 (vt, *J* = 8.73 Hz, CH(CH<sub>3</sub>)<sub>2</sub>), 18.60 (br s, CH(CH<sub>3</sub>)<sub>2</sub>), 17.31 (vt, *J* = 2.71 Hz, CH(CH<sub>3</sub>)<sub>2</sub>), 17.18 (vt, *J* = 4.59 Hz, CH(CH<sub>3</sub>)<sub>2</sub>), 15.59 (br s, CH(CH<sub>3</sub>)<sub>2</sub>). <sup>31</sup>P{<sup>1</sup>H} NMR (162 MHz, C<sub>6</sub>D<sub>6</sub>, 23 °C) δ: 35.01 (s). <sup>15</sup>N{<sup>1</sup>H} NMR (51 MHz, C<sub>6</sub>D<sub>6</sub>, 25 °C) δ: 833.09 (s, Mo≡*N*), 137.23 ppm (s, Mo-N<sub>3</sub>(*αN*)), 62.23 ppm (s, Mo-N<sub>3</sub>(*βN*)).

Synthesis of **3**

To a 20 mL scintillation vial charged with **2** (600 mg, 0.976 mmol) and a stir bar, C<sub>6</sub>H<sub>6</sub> (12 mL) was added. Stirring was initiated and Me<sub>3</sub>SiOTf (260 mg, 1.17 mmol) was added, resulting in a subtle lightening of the reaction mixture. Stirring continued for 1 h, at which time a *ca.* 0.5 mL aliquot was removed and analyzed by <sup>31</sup>P{<sup>1</sup>H} NMR spectroscopy. In some cases, residual **2** was observed spectroscopically, and additional Me<sub>3</sub>SiOTf (1.2 equiv. based off of relative integration of **2** to **3** in the <sup>31</sup>P{<sup>1</sup>H} NMR spectrum of the reaction aliquot) was added. Once complete conversion was observed, the vial was placed in the freezer (-35 °C) and the contents frozen solid. Lyophilization of the C<sub>6</sub>H<sub>6</sub> afforded a flocculent pink powder. This powder was triturated with (2 mL x 2) and then suspended in (*ca.* 4 mL) hexanes. The hexanes suspension as cooled to -35 °C and the solids were collected on a coarse frit. Removal of the volatiles under reduced pressure provided **3** as a reddish pink powder (493 mg, 0.685 mmol, 70%). <sup>1</sup>H NMR (400 MHz, C<sub>6</sub>D<sub>6</sub>, 23 °C) δ: 7.31 (br d, *J* = 6.69 Hz, 2H, aryl-*H*), 7.26 (br d, *J* = 6.92 Hz, 2H, aryl-*H*), 7.14-7.18 (m, 2H, aryl-*H*), 7.08-7.12 (m, 2H, aryl-*H*), 6.07 (s, 2H, central arene-*H*), 4.19 (br t, *J* = 2.04 Hz, 2H, central arene-*H*), 3.43-3.49 (m, 2H, CH(CH<sub>3</sub>)<sub>2</sub>), 2.56-2.66 (m, 2H, CH(CH<sub>3</sub>)<sub>2</sub>), 2.02-2.08 (m, 6H, CH(CH<sub>3</sub>)<sub>2</sub>), 1.29-1.35 (m, 6H, CH(CH<sub>3</sub>)<sub>2</sub>), 0.84-0.88 (m, 6H, CH(CH<sub>3</sub>)<sub>2</sub>), 0.26-0.32 (m, 6H, CH(CH<sub>3</sub>)<sub>2</sub>). <sup>13</sup>C{<sup>1</sup>H} NMR (101 MHz, C<sub>6</sub>D<sub>6</sub>, 23 °C) δ: 149.80 (vt, *J* = 6.46 Hz, aryl-*C*), 140.99 (vt, *J* = 4.77 Hz, aryl-*C*), 132.06 (s, aryl-*C*), 130.71 (s, aryl-*C*), 127.85 (aryl-*C*; coincides with C<sub>6</sub>D<sub>6</sub> residual but observed via 2D NMR spectroscopy), 127.11 (vt, *J* = 2.54 Hz, aryl-*C*), 123.10 (vt, *J* = 16.58 Hz, aryl-*C*), 122.53 (s, central arene-*C*), 120.36 (q, *J* = 318.47 Hz, CF<sub>3</sub>), 63.97 (s, central arene-*C*), 24.34 (t, *J* = 8.96 Hz, CH(CH<sub>3</sub>)<sub>2</sub>), 22.19 (m, CH(CH<sub>3</sub>)<sub>2</sub>), 18.62 (d, *J* = 40.92 Hz, CH(CH<sub>3</sub>)<sub>2</sub>), 17.91 (m, CH(CH<sub>3</sub>)<sub>2</sub>), 17.65 (m, CH(CH<sub>3</sub>)<sub>2</sub>), 15.78 (d, *J* = 13.14 Hz, CH(CH<sub>3</sub>)<sub>2</sub>). <sup>31</sup>P{<sup>1</sup>H} NMR (162

MHz, C<sub>6</sub>D<sub>6</sub>, 23 °C)  $\delta$ : 34.42 (s). <sup>19</sup>F NMR (376 MHz, C<sub>6</sub>D<sub>6</sub>, 23 °C): -76.91 (s). <sup>15</sup>N{<sup>1</sup>H} NMR (51 MHz, C<sub>6</sub>D<sub>6</sub>, 25 °C)  $\delta$ : 842.22 (s, Mo $\equiv$ N).

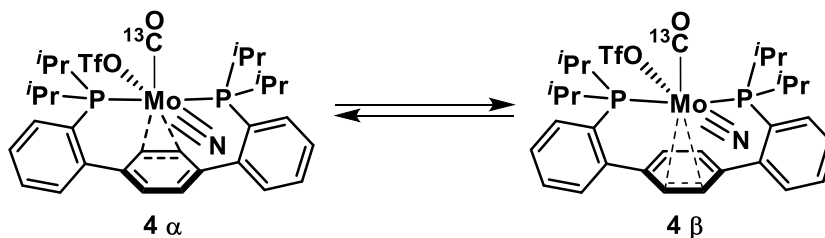
*In situ* Preparation of **4**



A J. Young style NMR tube was charged with a deep red C<sub>6</sub>D<sub>6</sub> (0.5 mL) solution of **3** (20 mg, 0.028 mmol). The tube was degassed via three freeze-pump-thaw cycles and the atmosphere was replaced with CO. Following mixing, the solution color changed from deep red to orange. Upon standing for 8 h, X-ray quality red/orange microcrystals of **4** formed. Further reactivity was probed using samples of **4** prepared in this fashion. The solubility of **4** in THF was not significantly improved; **4** was more soluble in CD<sub>2</sub>Cl<sub>2</sub>, but slowly decomposed to an intractable mixture in this solvent.

**4**-<sup>13</sup>C was prepared analogously using <sup>13</sup>CO in lieu of CO.

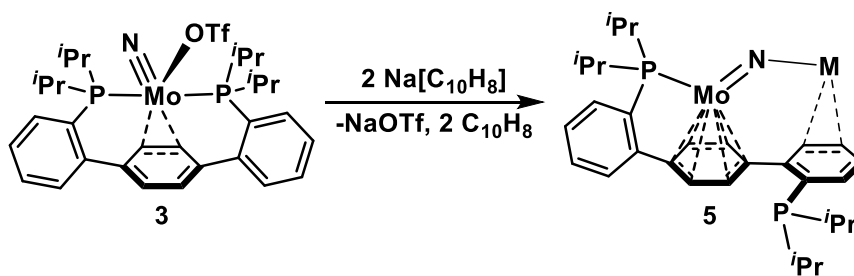
The room temperature spectra of **4**-<sup>13</sup>C are broad, suggesting an exchange process that is intermediate on the NMR timescale. <sup>1</sup>H NMR (400 MHz, CD<sub>2</sub>Cl<sub>2</sub>, 23 °C)  $\delta$ : 7.94 (br s, 2H, aryl-H), 7.69 (br s, 6H, aryl-H), 7.16 (br s, 2H, central arene-H), 6.93 (v br, 2H, central arene-H), 2.94 (v br, 2H, CH(CH<sub>3</sub>)<sub>2</sub>), 2.83 (v br, 2H, CH(CH<sub>3</sub>)<sub>2</sub>), 0.88-1.34 (br m, 24H, CH(CH<sub>3</sub>)<sub>2</sub>). <sup>13</sup>C{<sup>1</sup>H} NMR (101 MHz, C<sub>6</sub>D<sub>6</sub>, 23 °C)  $\delta$ : 238.43 (v br, Mo-CO). <sup>31</sup>P{<sup>1</sup>H} NMR (162 MHz, C<sub>6</sub>D<sub>6</sub>, 23 °C)  $\delta$ : 38.74 (br s). <sup>19</sup>F NMR (376 MHz, C<sub>6</sub>D<sub>6</sub>, 23 °C): -76.69 (s).



Spectra of the same sample collected at -80 °C show two distinct species, approaching the slow exchange limit. This process is attributed to the Mo center slipping across the

face of the arene, interconverting the coordination isomers ( $\alpha$  and  $\beta$ ) shown above.  $^1\text{H}$  NMR (500 MHz,  $\text{CD}_2\text{Cl}_2$ ,  $-65\text{ }^\circ\text{C}$ )  $\delta$ : 7.94 (br s, 2H, aryl-*H*), 7.89 (br s, 2H, aryl-*H*), 7.73 (br t,  $J = 6.6$  Hz, 4H, aryl-*H*), 7.65-7.66 (br m, 8H, aryl-*H*), 7.43 (s, 2H, central arene-*H*), 7.31 (s, 2H, central arene-*H*), 6.91 (br s, 2H, central arene-*H*), 6.37 (br t,  $J = 5.4$  Hz, 2H, central arene-*H*), 3.24 (br m, 2H,  $\text{CH}(\text{CH}_3)_2$ ), 3.11 (br m, 2H,  $\text{CH}(\text{CH}_3)_2$ ), 2.54 (br m, 4H,  $\text{CH}(\text{CH}_3)_2$ ), 1.50-1.56 (m, 12H,  $\text{CH}(\text{CH}_3)_2$ ), 1.43-1.48 (m, 6H,  $\text{CH}(\text{CH}_3)_2$ ), 1.37-1.41 (m, 6H,  $\text{CH}(\text{CH}_3)_2$ ), 1.40 (br m, 6H,  $\text{CH}(\text{CH}_3)_2$ ), 0.89 (br m, 6H,  $\text{CH}(\text{CH}_3)_2$ ), 0.77-0.78 (br m, 6H,  $\text{CH}(\text{CH}_3)_2$ ), 0.12-0.14 (br m, 6H,  $\text{CH}(\text{CH}_3)_2$ ).  $^{13}\text{C}\{^1\text{H}\}$  NMR (126 MHz,  $\text{C}_6\text{D}_6$ ,  $-65\text{ }^\circ\text{C}$ )  $\delta$ : 244.84 (br t,  $J = 10.1$  Hz, Mo-CO), 234.62 (br s, Mo-CO).  $^{31}\text{P}\{^1\text{H}\}$  NMR (202 MHz,  $\text{C}_6\text{D}_6$ ,  $-65\text{ }^\circ\text{C}$ )  $\delta$ : 39.02 (v br), 38.53 (v br).

#### Synthesis of **5**



A  $\text{Na}[\text{C}_{10}\text{H}_8]$  solution was prepared by stirring  $\text{C}_{10}\text{H}_8$  (196 mg, 1.53 mmol) in THF over a 20 mL scintillation vial charged with a  $\text{Na}^0$  mirror for 2 h.

During this time, a second scintillation vial was charged with **3** (500 mg, 0.695 mmol). THF (6 mL), and a stir bar. The vial was placed in an  $\text{LN}_2$  chilled cold well and the contents frozen solid. Immediately upon thawing, with stirring, the aforementioned  $\text{Na}[\text{C}_{10}\text{H}_8]$  solution was added dropwise. Following addition, the  $\text{Na}^0$  mirror was rinsed with THF (1 mL x 2) and these washes were likewise added to the reaction vial. Stirring continued for 20 minutes, affording a dark red, homogeneous solution. Volatiles were removed under reduced pressure, affording a tacky red/brown residue. This residue was triturated with hexanes (4 mL) and the resulting red/brown solids suspended in hexanes (5 mL). The mixture was filtered through a medium porosity fritted funnel and the filtrant was washed thoroughly with hexanes (3 x 7 mL) to remove residual  $\text{C}_{10}\text{H}_8$ . The solids



were collected and dried *in vacuo*, providing **5-Na** as a free-flowing deep red solid (320 mg, 0.535 mmol, 77%).  $^1\text{H}$  NMR (400 MHz,  $\text{C}_6\text{D}_6$ , 23 °C)  $\delta$ : 9.08 (t,  $J = 7.41$  Hz, 1H, aryl-*H*), 8.44 (dd,  $J = 7.04$  & 3.71 Hz, 1H, aryl-*H*), 7.41 (d,  $J = 7.62$  Hz, 1H, aryl-*H*), 7.35 (dd,  $J = 7.79$  & 2.85 Hz, 1H, aryl-*H*), 7.16-7.21 (2H, aryl-*H*; partially coincides with the  $\text{C}_6\text{D}_5\text{H}$  residual but observed via 2D NMR), 6.98 (t,  $J = 7.60$  Hz, 1H, aryl-*H*), 6.91 (t,  $J = 7.43$  Hz, 1H, aryl-*H*), 5.85 (d,  $J = 5.73$  Hz, 1H, central arene-*H*), 5.24 (d,  $J = 5.70$  Hz, 1H, central arene-*H*), 5.04 (t,  $J = 4.89$  Hz, 1H, central arene-*H*), 5.00 (t,  $J = 5.04$  Hz, 1H, central arene-*H*), 2.46-2.55 (m, 1H,  $\text{CH}(\text{CH}_3)_2$ ), 2.18-2.28 (m, 1H,  $\text{CH}(\text{CH}_3)_2$ ), 2.00-2.09 (m, 1H,  $\text{CH}(\text{CH}_3)_2$ ), 1.86-1.94 (m, 1H,  $\text{CH}(\text{CH}_3)_2$ ), 1.59-1.65 (m, 3H,  $\text{CH}(\text{CH}_3)_2$ ), 1.48-1.53 (m, 3H,  $\text{CH}(\text{CH}_3)_2$ ), 1.35-1.40 (m, 3H,  $\text{CH}(\text{CH}_3)_2$ ), 1.24-1.29 (m, 3H,  $\text{CH}(\text{CH}_3)_2$ ), 1.02-1.07 (m, 3H,  $\text{CH}(\text{CH}_3)_2$ ), 0.92-1.07 (m, 3H,  $\text{CH}(\text{CH}_3)_2$ ), 0.88-0.93 (m, 3H,  $\text{CH}(\text{CH}_3)_2$ ), 0.54-0.60 (m, 3H,  $\text{CH}(\text{CH}_3)_2$ ).  $^{13}\text{C}\{^1\text{H}\}$  NMR (101 MHz,  $\text{C}_6\text{D}_6$ , 23 °C)  $\delta$ : 152.05 (d,  $J = 24.05$  Hz, aryl-*C*), 150.80 (d,  $J = 24.54$  Hz, aryl-*C*), 138.14 (d,  $J = 25.96$  Hz, aryl-*C*), 137.52 (d,  $J = 38.91$  Hz, aryl-*C*), 132.91 (d,  $J = 2.29$  Hz, aryl-*C*), 131.56 (s, aryl-*C*), 130.67 (d,  $J = 4.05$  Hz, aryl-*C*), 126.52 (dd,  $J = 3.62$  & 1.56 Hz, aryl-*C*), 124.74 (s, aryl-*C*), 93.26 (d,  $J = 5.16$  Hz, central arene-*C*), 78.95 (d,  $J = 47.48$  Hz, central arene-*C*), 75.30 (d,  $J = 7.60$  Hz, central arene-*C*), 72.64 (s, central arene-*C*), 67.69 (d,  $J = 17.38$  Hz, central arene-*C*), 29.28 (d,  $J = 13.01$  Hz,  $\text{CH}(\text{CH}_3)_2$ ), 26.91 (d,  $J = 13.59$  Hz,  $\text{CH}(\text{CH}_3)_2$ ), 26.02 (d,  $J = 19.38$  Hz,  $\text{CH}(\text{CH}_3)_2$ ), 22.69 (d,  $J = 9.99$  Hz,  $\text{CH}(\text{CH}_3)_2$ ), 22.15 (d,  $J = 15.31$  Hz,  $\text{CH}(\text{CH}_3)_2$ ), 21.51 (d,  $J = 18.87$  Hz,  $\text{CH}(\text{CH}_3)_2$ ), 20.37 (d,  $J = 12.97$  Hz,  $\text{CH}(\text{CH}_3)_2$ ), 20.15 (d,  $J = 22.10$  Hz,  $\text{CH}(\text{CH}_3)_2$ ), 19.88 (d,  $J = 3.08$  Hz,  $\text{CH}(\text{CH}_3)_2$ ), 19.62 (s,  $\text{CH}(\text{CH}_3)_2$ ), 19.06 (d,  $J = 11.89$  Hz,  $\text{CH}(\text{CH}_3)_2$ ), 18.83 (d,  $J = 6.58$  Hz,  $\text{CH}(\text{CH}_3)_2$ ).  $^{31}\text{P}\{^1\text{H}\}$  NMR (162 MHz,  $\text{C}_6\text{D}_6$ , 23 °C)  $\delta$ : 53.73 (s, Mo-*P*), -2.04 (s, *P*).

**5-K** can be prepared analogously using  $\text{K}[\text{C}_{10}\text{H}_8]$  in lieu of  $\text{Na}[\text{C}_{10}\text{H}_8]$ . The spectroscopic features are identical to those of **5-Na**. Single crystals of **5-K** were grown via vapor diffusion of hexanes into a concentrated  $\text{C}_6\text{H}_6$  solution.

#### *Electrophile Addition Reactions*

*Addition of  $^{13}\text{C}$ CO to **5***

A 50 mL Teflon stoppered Schlenk tube was charged with **5-Na** (40 mg, 0.067 mmol), THF (5 mL), and a stir bar. The flask was sealed and attached to a 33.4 mL calibrated volume. The reaction mixture was thoroughly degassed via three freeze-pump-thaw cycles. Following thawing the final time, the Schlenk tube was submerged in a  $-78\text{ }^\circ\text{C}$  dry ice/acetone slush bath. Using a Hg manometer, 14.7 cm Hg of  $^{13}\text{C}$ CO was admitted to the calibrated volume (0.268 mmol). The  $^{13}\text{C}$ CO was then introduced to the reaction flask, which was allowed to warm to room temperature, with stirring, over the course of 12 h. At this time, volatiles were removed under reduced pressure, leaving red/orange solids. This residue was extracted with  $\text{C}_6\text{H}_6$  (2 mL) and then set aside. The  $\text{C}_6\text{H}_6$  fraction was pumped to dryness and analyzed by multinuclear NMR, evincing formation of Mo(0) carbonyl complexes in addition to free diphosphine. The insoluble material was taken up in  $\text{D}_2\text{O}$  (0.5 mL) and analyzed by  $^{13}\text{C}\{^1\text{H}\}$  NMR spectroscopy, demonstrating formation of  $\text{NaN}^{13}\text{CO}$ .

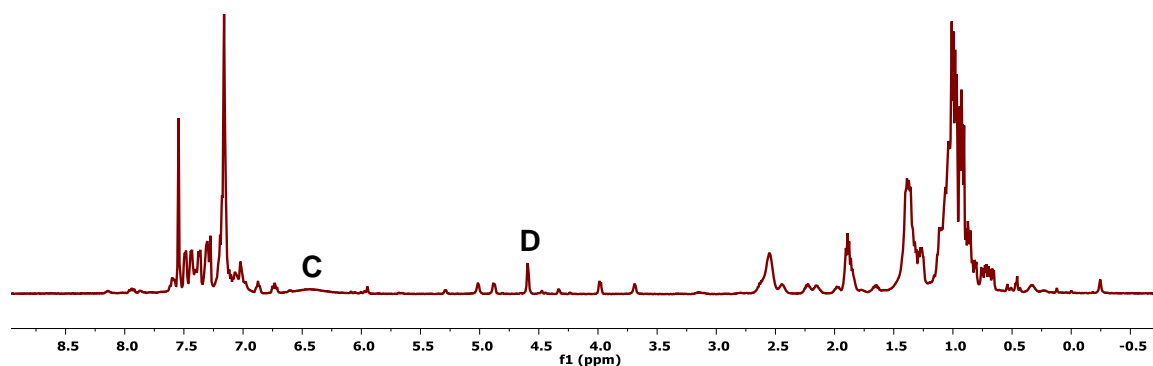


**Figure 5.4.**  $^1\text{H}$  NMR spectrum of the  $\text{C}_6\text{H}_6$  soluble reaction products following  $^{13}\text{C}$ CO addition to **5-Na**. The central arene resonances of carbonyl complexes  $\text{P2Mo}(^{13}\text{CO})_3$  [**C**] and  $\text{P2Mo}(^{13}\text{CO})$  [**D**] are labeled.

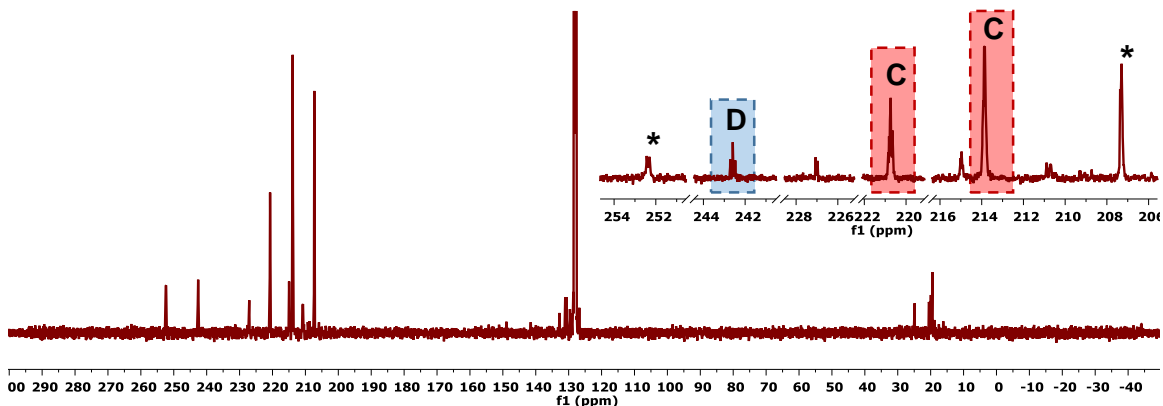


**Figure 5.5.**  $^{31}\text{P}\{^1\text{H}\}$  NMR spectrum of the  $\text{C}_6\text{H}_6$  soluble reaction products following  $^{13}\text{CO}$  addition to **5-Na**. The insets show enlargements of the resonances attributable to carbonyl complexes  $\text{P2Mo}(^{13}\text{CO})_3$  [**C**] and  $\text{P2Mo}(^{13}\text{CO})$  [**D**]. Significant decomposition to free diphosphine [**P2**] is observed.

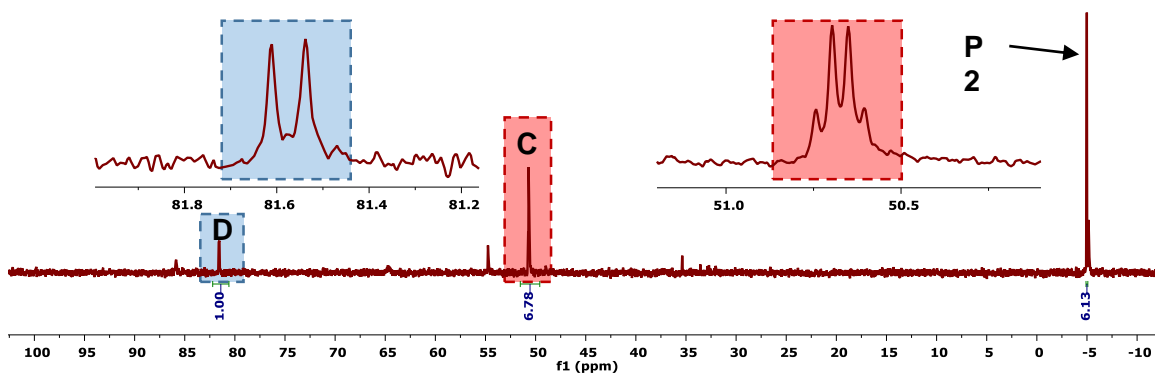


**Figure 5.6.**  $^{13}\text{C}\{^1\text{H}\}$  NMR spectrum of the  $\text{C}_6\text{H}_6$  soluble reaction products following  $^{13}\text{CO}$  addition to **5-Na**. The inset shows an enlargement of the resonances attributable to carbonyl complexes  $\text{P2Mo}(^{13}\text{CO})_3$  [**C**] and  $\text{P2Mo}(^{13}\text{CO})$  [**D**]. Unidentified  $^{13}\text{C}$  containing byproducts are designated with an asterisk (\*).

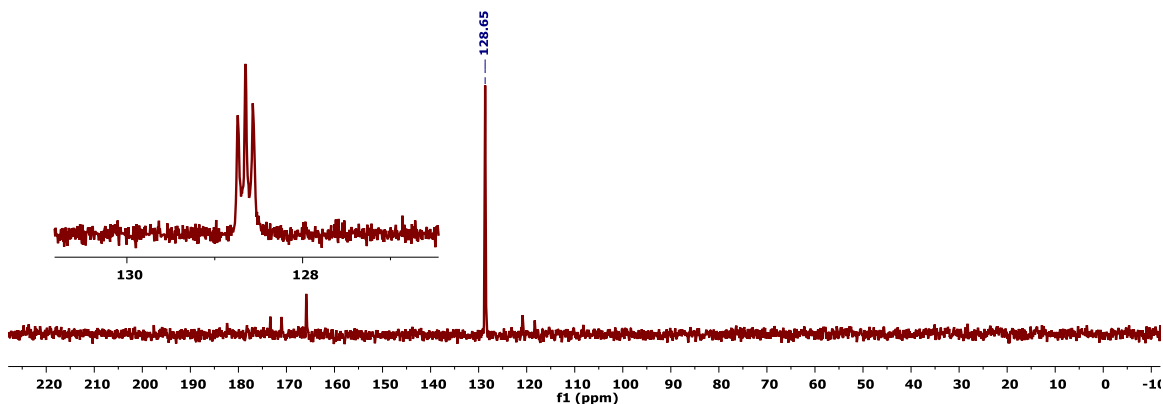


**Figure 5.7.**  $^{13}\text{C}\{^1\text{H}\}$  NMR spectrum of the  $\text{D}_2\text{O}$  soluble reaction products following  $^{13}\text{CO}$  addition to **5-Na**. The inset shows the triplet attributable to  $\text{NaN}^{13}\text{CO}$  ( $^1J(\text{N,C}) = 11.34$  Hz).

*Addition of <sup>t</sup>BuNC to 5-Na*

A 20 mL scintillation vial was charged with **5-Na** (40 mg, 0.067 mmol), THF (4 mL), and a stir bar. The vial was placed in an LN<sub>2</sub> chilled cold well and the contents frozen solid. Immediately upon thawing, <sup>t</sup>BuNC (16 μL, 0.134 mmol) was added via microsyringe, with stirring. The reaction was allowed to warm to room temperature. Volatiles were removed under reduced pressure and the resulting residue was extracted with C<sub>6</sub>D<sub>6</sub>. The extract was filtered through a glass microfilter into an NMR tube and analyzed by <sup>1</sup>H and <sup>31</sup>P{<sup>1</sup>H} NMR spectroscopy, indicating almost exclusive decomposition to free diphosphine.

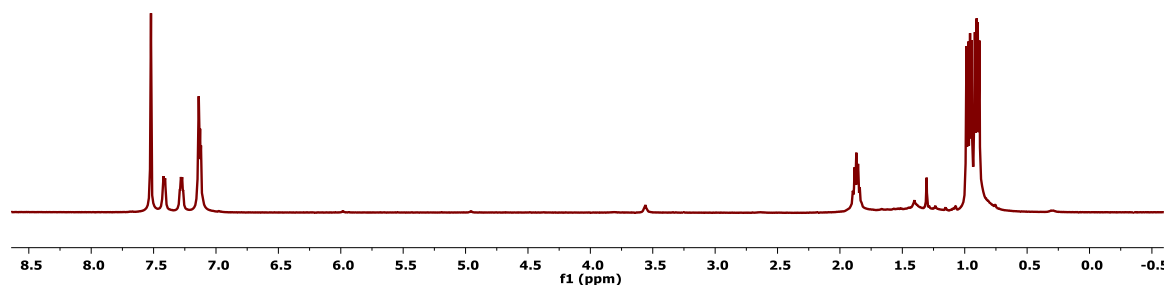


**Figure 5.8.** <sup>1</sup>H NMR spectrum of the C<sub>6</sub>D<sub>6</sub> soluble fraction following <sup>t</sup>BuNC addition to **5-Na**.

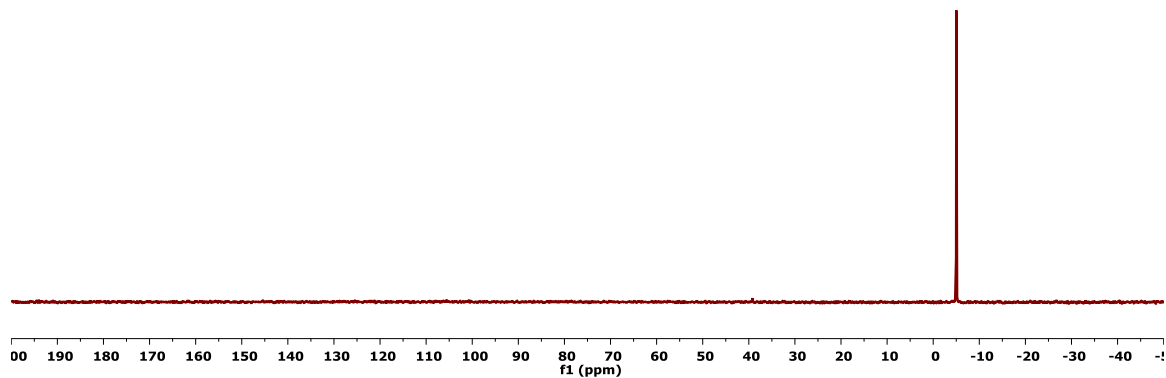


**Figure 5.9.** <sup>31</sup>P{<sup>1</sup>H} NMR spectrum of the C<sub>6</sub>D<sub>6</sub> soluble fraction following <sup>t</sup>BuNC addition to **5-Na**.

*Reduction Reactions from 4*

A J. Young NMR tube was charged with a deep red C<sub>6</sub>H<sub>6</sub> (0.4 mL) solution of **3** (20 mg, 0.028 mmol). The solution was degassed via three freeze-pump-thaw cycles and placed

under 1 atm of CO. The reaction mixture was mixed via inversion for 2 h, at which time the solution color had become bright orange and a significant amount of orange precipitate had formed;  $^{31}\text{P}\{^1\text{H}\}$  NMR spectroscopy showed near complete consumption of the starting material and conversion to **4** (>93%).

During *in situ* formation of **4**, a  $\text{Na}[\text{C}_{10}\text{H}_8]$  solution was prepared by stirring a THF (0.4 mL) solution of  $\text{C}_{10}\text{H}_8$  (7.5 mg, 0.059 mmol) over a  $\text{Na}^0$  mirror. With a strong Ar counterflow, the deep green  $\text{Na}[\text{C}_{10}\text{H}_8]$  solution was added to the J. Young tube. The tube was sealed, mixed vigorously, and the contents analyzed by  $^{31}\text{P}\{^1\text{H}\}$  NMR spectroscopy.

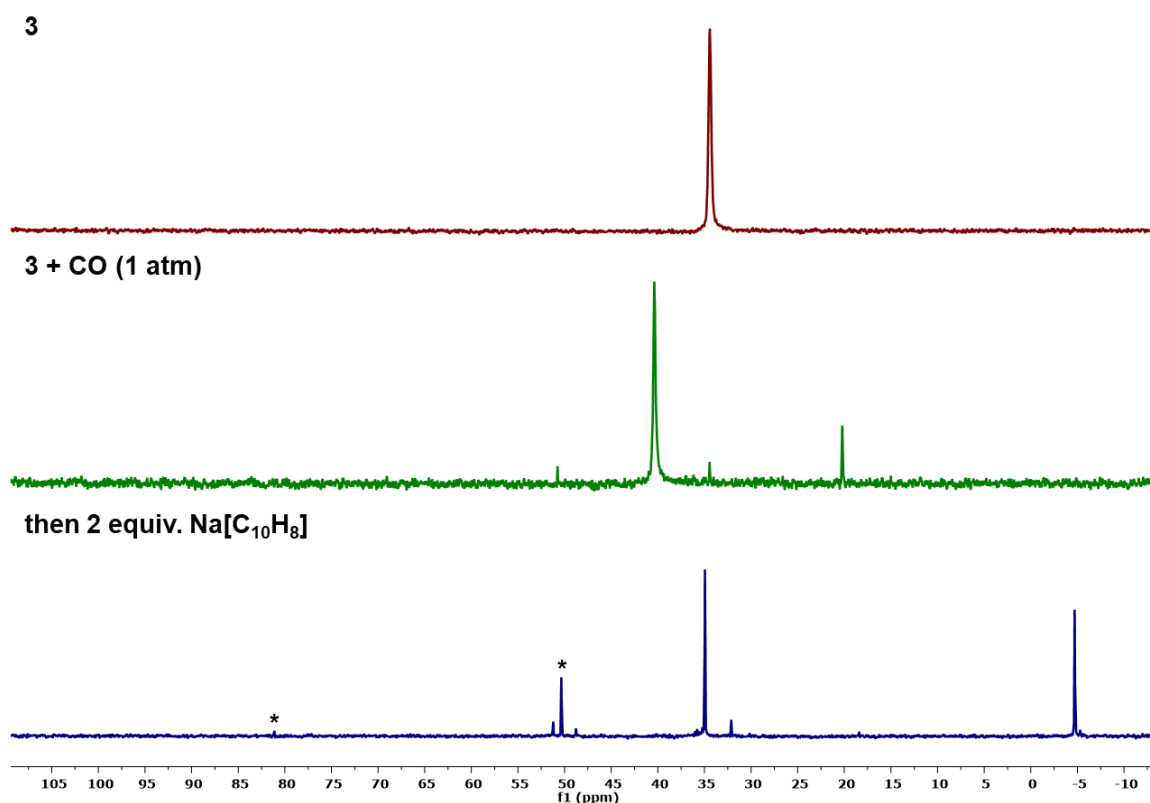


**Figure 5.10.** Sequential CO addition and reduction of nitride triflate complex **3**. Upon two-electron reduction, significant decomposition to free diphosphine is observed, in addition to significant reversion to CO-free starting material, **3**. Minor conversion to  $\text{N}^-$  group transfer products, **C** and **D** (denoted with asterisks), was observed.

*Computational Details*

All calculations were performed with DFT as implemented in Gaussian 09 Revision C.01.<sup>22</sup> Geometry optimizations and electronic structure calculations were performed with revised TPSS exchange and correlation functionals.<sup>23</sup> The LANL2DZ basis set was used for all atoms.<sup>24</sup> No solvent corrections were employed. All optimizations were performed ignoring molecular symmetry—crystallographic coordinates were used as a starting point—for complex **3**, the solid state structure of **2** was modified, replacing the N<sub>3</sub> ligand with a coordinated OTf. Energetic minima were confirmed with subsequent frequency calculations which did not return imaginary frequencies. Structures optimized in this manner showed good agreement with bond lengths and angles determined via single crystal X-ray diffraction (Table 5.1). Molecular orbital and spin density illustrations were generated using GaussView, the GUI component of the Gaussian software package, and depicted with 0.05 e/Å<sup>3</sup> or 0.001 e/Å<sup>3</sup> isosurface values, respectively.

**Table 5.1.** Comparison of Experimental and Calculated Structural Metrics and **5**.

	<b>5</b>		
	<b>Exp.</b>	<b>Calc.</b>	$\Delta$
<b>Mo1–N1</b>	1.728(2)	1.745	-0.02
<b>Mo1–P1</b>	2.518(1)	2.570	-0.05
<b>Mo1–C1</b>	2.432(3)	2.568	-0.14
<b>Mo1–C2</b>	2.284(3)	2.403	-0.12
<b>Mo1–C3</b>	2.230(3)	2.237	-0.01
<b>Mo1–C4</b>	2.266(3)	2.276	-0.01
<b>Mo1–C5</b>	2.245(3)	2.250	-0.01
<b>Mo1–C6</b>	2.370(3)	2.441	-0.07
<b>C1–C2</b>	1.422(5)	1.440	-0.02
<b>C2–C3</b>	1.433(4)	1.455	-0.02
<b>C3–C4</b>	1.419(5)	1.479	-0.06
<b>C4–C5</b>	1.446(5)	1.484	-0.04
<b>C5–C6</b>	1.427(5)	1.451	-0.02
<b>C6–C1</b>	1.394(5)	1.437	-0.04
<b>N1–K1</b>	2.733(3)	2.646	0.09

## ***Crystallographic Information***

### *Refinement Details*

In each case, crystals were mounted on a MiTeGen loop using Paratone oil, then placed on the diffractometer under a nitrogen stream. Low temperature (100 K) X-ray data were obtained on a Bruker D8 VENTURE Kappa Duo PHOTON 100 CMOS based diffractometer (Mo  $I_{\mu}S$  HB micro-focus sealed X-ray tube,  $K_{\alpha} = 0.71073 \text{ \AA}$ ). All diffractometer manipulations, including data collection, integration, and scaling were carried out using the Bruker APEXIII software.<sup>25</sup> Absorption corrections were applied using SADABS.<sup>26</sup> Space groups were determined on the basis of systematic absences and intensity statistics and the structures were solved in the Olex 2 software interface<sup>27</sup> by intrinsic phasing using XT (incorporated into SHELXTL)<sup>28</sup> and refined by full-matrix least squares on  $F^2$ . All non-hydrogen atoms were refined using anisotropic displacement parameters. Hydrogen atoms were placed in the idealized positions and refined using a riding model, unless noted otherwise. The structures were refined (weighed least squares refinement on  $F^2$ ) to convergence. Graphical representations of structures with 50% probability thermal ellipsoids were generated using the Diamond 3 visualization software.<sup>29</sup>

**Table 5.2.** Crystal and refinement data for complexes **2**, **4**, & **5**.

	<b>2</b>	<b>4</b>	<b>5</b>
CCDC Number <sup>30</sup>			
Empirical formula	C <sub>37</sub> H <sub>48</sub> MoN <sub>4</sub> P <sub>2</sub>	C <sub>128</sub> H <sub>160</sub> F <sub>12</sub> Mo <sub>4</sub> N <sub>4</sub> O <sub>16</sub> P <sub>8</sub> S <sub>4</sub>	C <sub>36</sub> H <sub>43</sub> K <sub>2</sub> MoNP <sub>2</sub>
Formula weight	706.67	2998.35	725.79
T (K)	100	100	100
<i>a</i> , Å	8.5855(3)	13.2537(4)	17.7222(6)
<i>b</i> , Å	27.9183(11)	12.0024(3)	35.4281(15)
<i>c</i> , Å	14.8982(6)	21.5922(6)	21.8598(9)
$\alpha$ , °	90	90	90
$\beta$ , °	99.244(2)	104.4520(10)	101.389(2)
$\gamma$ , °	90	90	90
Volume, Å <sup>3</sup>	3524.6(2)	3326.12(16)	13454.7(9)
Z	4	1	16
Crystal system	Monoclinic	Monoclinic	Monoclinic
Space group	P2 <sub>1</sub> /n	P2 <sub>1</sub> /c	P2 <sub>1</sub> /n
<i>d</i> <sub>calc</sub> , g/cm <sup>3</sup>	1.332	1.497	1.433
$\theta$ range, °	2.512 to 20.815	4.761 to 89.609	1.472 to 27.219
$\mu$ , mm <sup>-1</sup>	0.494	5.238	0.759
Abs. Correction	Semi-empirical	None	None
GOF	0.951	1.107	0.936
<i>R</i> <sub>1</sub> , <sup>a</sup> <i>wR</i> <sub>2</sub> <sup>b</sup> [I > 2 $\sigma$ (I)]	0.0189, 0.0614	0.0210, 0.0517	0.0821, 0.2053
Radiation Type	Mo K $\alpha$	Mo K $\alpha$	Mo K $\alpha$

$$^a R_1 = \sum ||F_o| - |F_c|| / \sum |F_o|. \quad ^b wR_2 = [\sum [w(F_o^2 - F_c^2)^2] / \sum [w(F_o^2)^2]]^{1/2}$$





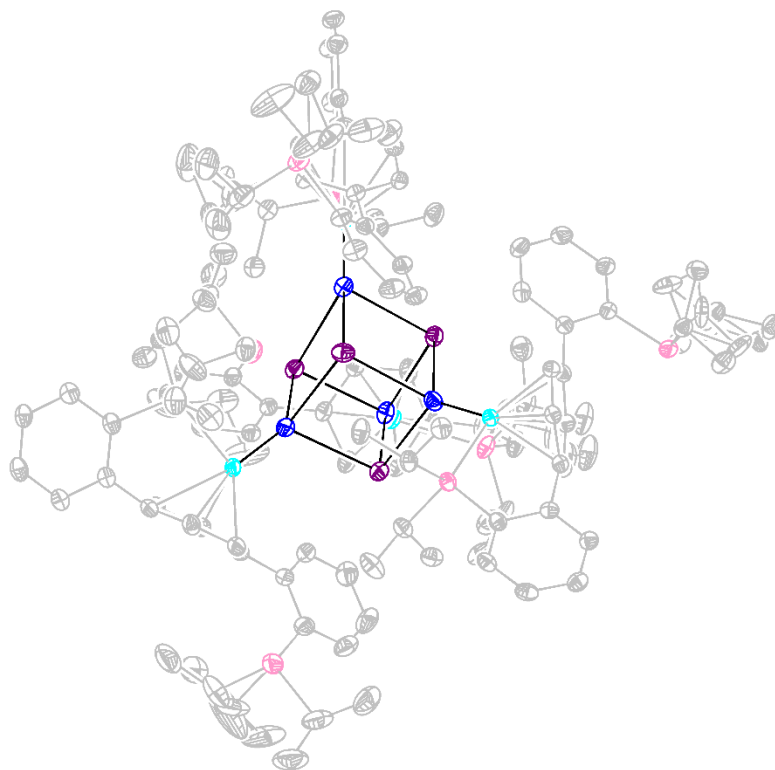


**Figure 5.13.** Structural drawing of **5** with 50% probability anisotropic displacement ellipsoids. H-atoms and benzene solvate molecules are omitted for clarity.

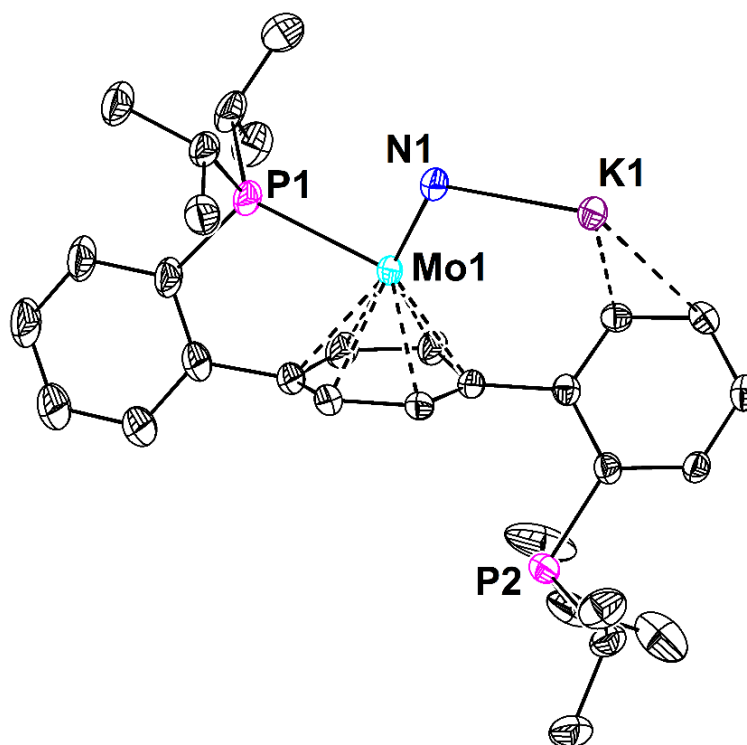


**Figure 5.14.** Structural drawing of a single P2MoNK unit of **5** with 50% probability anisotropic displacement ellipsoids. H-atoms and benzene solvate molecules are omitted for clarity.

**Special Refinement Details:**

Six of the phosphine isopropyl groups were positionally disordered. These disorders were satisfactorily modeled in two discreet positions with relative populations as follows: C55A/B through C57A/B (80/20), C58A/B through C60A/B (80/20), C80A/B and C81A/B (62/38), C88A/B through C90A/B (75/25), C115/215 through C117/217 (42/58), and C118/218 through C120/220 (56/44). Additionally, the two diisopropyl phosphine motifs (P6 and C85 through C90B, P8 and C115 through C220) were refined with similarity restraints on  $U_{ij}$  and rigid bond restraints.

## REFERENCES

- (1) a) Dehnicke, K.; Strähle, J. *Angew. Chem. Int. Ed.* **1992**, *31*, 955; b) Dehnicke, K.; Strähle, J. *Angew. Chem. Int. Ed.* **1981**, *20*, 413; c) Griffith, W. P. *Coord. Chem. Rev.* **1972**, *8*, 369; d) MacLeod, K. C.; Holland, P. L. *Nat. Chem.* **2013**, *5*, 559; e) Yi, X.-Y.; Liang, Y.; Li, C. *RSC Advances* **2013**, *3*, 3477.
- (2) Shaver, M. P.; Fryzuk, M. D. *Adv. Synth. Catal.* **2003**, *345*, 1061.
- (3) Askevold, B.; Nieto, J. T.; Tussupbayev, S.; Diefenbach, M.; Herdtweck, E.; Holthausen, M. C.; Schneider, S. *Nat. Chem.* **2011**, *3*, 532.
- (4) Caulton, K. G. *New J. Chem.* **1994**, *18*, 25.
- (5) a) Betley, T. A.; Peters, J. C. *J. Am. Chem. Soc.* **2004**, *126*, 6252; b) Scepaniak, J. J.; Young, J. A.; Bontchev, R. P.; Smith, J. M. *Angew. Chem. Int. Ed.* **2009**, *48*, 3158; c) Scepaniak, J. J.; Fulton, M. D.; Bontchev, R. P.; Duesler, E. N.; Kirk, M. L.; Smith, J. M. *J. Am. Chem. Soc.* **2008**, *130*, 10515; d) Walstrom, A.; Pink, M.; Yang, X.; Tomaszewski, J.; Baik, M.-H.; Caulton, K. G. *J. Am. Chem. Soc.* **2005**, *127*, 5330; e) Kropp, H.; King, A. E.; Khusniyarov, M. M.; Heinemann, F. W.; Lancaster, K. M.; DeBeer, S.; Bill, E.; Meyer, K. *J. Am. Chem. Soc.* **2012**, *134*, 15538; f) Vogel, C.; Heinemann, F. W.; Sutter, J.; Anthon, C.; Meyer, K. *Angew. Chem. Int. Ed.* **2008**, *47*, 2681; g) Schöffel, J.; Rogachev, A. Y.; DeBeer George, S.; Burger, P. *Angew. Chem. Int. Ed.* **2009**, *48*, 4734; h) Abbenseth, J.; Bete, S. C.; Finger, M.; Volkmann, C.; Würtele, C.; Schneider, S. *Organometallics* **2017**; i) Schendzielorz, F. S.; Finger, M.; Volkmann, C.; Würtele, C.; Schneider, S. *Angew. Chem. Int. Ed.* **2016**, *55*, 11417; j) Scheibel, M. G.; Abbenseth, J.; Kinauer, M.; Heinemann, F. W.; Würtele, C.; de Bruin, B.; Schneider, S. *Inorg. Chem.* **2015**, *54*, 9290; k) Maity, A. K.; Murillo, J.; Metta-Magaña, A. J.; Pinter, B.; Fortier, S. *J. Am. Chem. Soc.* **2017**, *139*, 15691; l) Thompson, N. B.; Green, M. T.; Peters, J. C. *J. Am. Chem. Soc.* **2017**, *139*, 15312.
- (6) Cozzolino, A. F.; Silvia, J. S.; Lopez, N.; Cummins, C. C. *Dalton Trans.* **2014**, *43*, 4639.
- (7) a) Buss, J. A.; Agapie, T. *J. Am. Chem. Soc.* **2016**, *138*, 16466; b) Buss, J. A.; Agapie, T. *Nature* **2015**, *529*, 72.
- (8) a) Silvia, J. S.; Cummins, C. C. *J. Am. Chem. Soc.* **2009**, *131*, 446; b) Tran, B. L.; Pink, M.; Gao, X.; Park, H.; Mindiola, D. J. *J. Am. Chem. Soc.* **2010**, *132*, 1458; c) Knobloch, D. J.; Lobkovsky, E.; Chirik, P. J. *Nat. Chem.* **2010**, *2*, 30; d) Ishida, Y.; Kawaguchi, H. *J. Am. Chem. Soc.* **2014**, *136*, 16990; e) Cleaves, P. A.; King, D. M.; Kefalidis, C. E.; Maron, L.; Tuna, F.; McInnes, E. J. L.; McMaster, J.; Lewis, W.; Blake, A. J.; Liddle, S. T. *Angew. Chem. Int. Ed.* **2014**, *53*, 10412; f) Brown, S. D.; Mehn, M. P.; Peters, J. C. *J. Am. Chem. Soc.* **2005**, *127*, 13146.
- (9) Buss, J. A.; Edouard, G. A.; Cheng, C.; Shi, J.; Agapie, T. *J. Am. Chem. Soc.* **2014**, *136*, 11272.
- (10) a) Nugent, W. A.; Mayer, J. M. *Metal-Ligand Multiple Bonds*; John Wiley & Sons: New York, 1988; b) Laplaza, C. E.; Cummins, C. C. *Science* **1995**, *268*, 861; c) O'Donoghue, M. B.; Davis, W. M.; Schrock, R. R. *Inorg. Chem.* **1998**, *37*, 5149.
- (11) Farrer, N. J.; Gierth, P.; Sadler, P. J. *Chem. Eur. J.* **2011**, *17*, 12059.
- (12) a) Watanabe, D.; Gondo, S.; Seino, H.; Mizobe, Y. *Organometallics* **2007**, *26*, 4909; b) Dilworth, J. R.; Dahlstrom, P. L.; Hyde, J. R.; Zubieta, J. *Inorg. Chim. Acta* **1983**, *71*, 21; c) Arashiba, K.; Kinoshita, E.; Kuriyama, S.; Eizawa, A.; Nakajima, K.; Tanaka, H.; Yoshizawa, K.; Nishibayashi, Y. *J. Am. Chem. Soc.* **2015**, *137*, 5666.
- (13) a) Sarkar, S.; Carlson, A. R.; Veige, M. K.; Falkowski, J. M.; Abboud, K. A.; Veige, A. S. *J. Am. Chem. Soc.* **2008**, *130*, 1116; b) Hebden, T. J.; Schrock, R. R.; Takase, M. K.; Muller, P. *Chem. Commun.* **2012**, *48*, 1851.
- (14) Tanaka, H.; Arashiba, K.; Kuriyama, S.; Sasada, A.; Nakajima, K.; Yoshizawa, K.; Nishibayashi, Y. *Nat. Commun.* **2014**, *5*, 3737.

- (15) Buss, J. A.; Oyala, P. H.; Agapie, T. *Angew. Chem. Int. Ed.* **2017**, *56*, 14502.
- (16) Smith, J. M.; Subedi, D. *Dalton Trans.* **2012**, *41*, 1423.
- (17) a) Keane, A. J.; Farrell, W. S.; Yonke, B. L.; Zavalij, P. Y.; Sita, L. R. *Angew. Chem. Int. Ed.* **2015**, *54*, 10220; b) Yonke, B. L.; Reeds, J. P.; Fontaine, P. P.; Zavalij, P. Y.; Sita, L. R. *Organometallics* **2014**, *33*, 3239.
- (18) Mindiola, D. J.; Hillhouse, G. L. *Chem. Commun.* **2002**, 1840.
- (19) CO binding to **4** is reversible and CO dissociation followed by reduction would provide anion **5** and one equiv. of CO.
- (20) Pangborn, A. B.; Giardello, M. A.; Grubbs, R. H.; Rosen, R. K.; Timmers, F. J. *Organometallics* **1996**, *15*, 1518.
- (21) Fulmer, G. R.; Miller, A. J. M.; Sherden, N. H.; Gottlieb, H. E.; Nudelman, A.; Stoltz, B. M.; Bercaw, J. E.; Goldberg, K. I. *Organometallics* **2010**, *29*, 2176.
- (22) Gaussian 09, Revision C.01, Frisch, M. J.; Trucks, G. W.; Schlegel, H. B.; Scuseria, G. E.; Robb, M. A.; Cheeseman, J. R.; Scalmani, G.; Barone, V.; Mennucci, B.; Petersson, G. A.; Nakatsuji, H.; Caricato, M.; Li, X.; Hratchian, H. P.; Izmaylov, A. F.; Bloino, J.; Zheng, G.; Sonnenberg, J. L.; Hada, M.; Ehara, M.; Toyota, K.; Fukuda, R.; Hasegawa, J.; Ishida, M.; Nakajima, T.; Honda, Y.; Kitao, O.; Nakai, H.; Vreven, T.; Montgomery, Jr., J. A.; Peralta, J. E.; Ogliaro, F.; Bearpark, M.; Heyd, J. J.; Brothers, E.; Kudin, K. N.; Staroverov, V. N.; Kobayashi, R.; Normand, J.; Raghavachari, K.; Rendell, A.; Burant, J. C.; Iyengar, S. S.; Tomasi, J.; Cossi, M.; Rega, N.; Millam, J. M.; Klene, M.; Knox, J. E.; Cross, J. B.; Bakken, V.; Adamo, C.; Jaramillo, J.; Gomperts, R.; Stratmann, R. E.; Yazyev, O.; Austin, A. J.; Cammi, R.; Pomelli, C.; Ochterski, J. W.; Martin, R. L.; Morokuma, K.; Zakrzewski, V. G.; Voth, G. A.; Salvador, P.; Dannenberg, J. J.; Dapprich, S.; Daniels, A. D.; Farkas, Ö.; Foresman, J. B.; Ortiz, J. V.; Cioslowski, J.; Fox, D. J. Gaussian, Inc., Wallingford CT, 2009.
- (23) a) Perdew, J. P.; Ruzsinszky, A.; Csonka, G. I.; Constantin, L. A.; Sun, J. *Phys. Rev. Lett.* **2011**, *106*, 179902; b) Perdew, J. P.; Ruzsinszky, A.; Csonka, G. I.; Constantin, L. A.; Sun, J. *Phys. Rev. Lett.* **2009**, *103*, 026403.
- (24) a) Wadt, W. R.; Hay, P. J. *J. Chem. Phys.* **1985**, *82*, 284; b) Hay, P. J.; Wadt, W. R. *J. Chem. Phys.* **1985**, *82*, 299; c) Hay, P. J.; Wadt, W. R. *J. Chem. Phys.* **1985**, *82*, 270; d) Dunning, T. H.; Hay, P. J. In *Methods of Electronic Structure Theory*; Schaefer, H. F., Ed.; Springer US: Boston, MA, 1977, p 1.
- (25) APEX3, Version 1 User Manual, M86-EXX229, Bruker Analytical X-ray Systems, Madison, WI, May 2016.
- (26) Sheldrick, G.M. "SADABS (version 2008/1): Program for Absorption Correction for Data from Area Detector Frames", University of Göttingen, 2008.
- (27) Dolomanov, O. V.; Bourhis, L. J.; Gildea, R. J.; Howard, J. A. K.; Puschmann, H. *J. Appl. Crystallogr.* **2009**, *42*, 339.
- (28) Sheldrick, G.M. *Acta Cryst.* **2008**, *A64*, 112.
- (29) Brandenburg, K. (1999). DIAMOND. Crystal Impact GbR, Bonn, Germany.
- (30) Crystallographic data have been deposited at the CCDC, 12 Union Road, Cambridge CB2 1EZ, UK and copies can be obtained on request, free of charge, by quoting the publication citation and the respective deposition numbers.

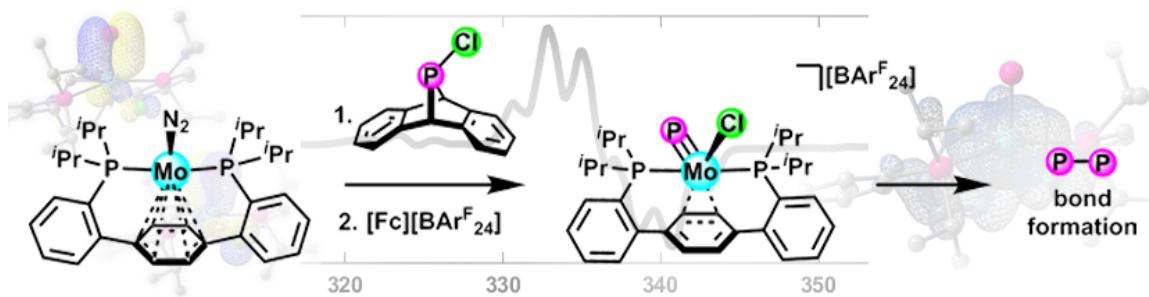


## CHAPTER 6

### Terminal Molybdenum Phosphides with d-Electrons and Structurally Related MoPR, MoPR<sub>2</sub>, and MoPMo Motifs

This work was published in part as:  
*Angew. Chem. Int. Ed.* **2017**, *56*, 14502.

## ABSTRACT



A terminal Mo phosphide was prepared via group transfer of both P- and Cl-atoms from chloro-substituted dibenzo-7λ<sup>3</sup>-phosphanorbornadiene. This compound represents the first structurally characterized terminal transition metal phosphide with valence d electrons. In the tetragonal ligand field, these electrons populate an orbital of d(xy) parentage, an electronic configuration that accommodates both metal d-electrons and a formal M–P triple bond. Single electron oxidation affords a transient open shell terminal phosphide cation with significant spin density on P, as corroborated by CW and pulsed EPR characterization. Facile P–P bond formation occurs from this species via intermolecular phosphide coupling. Using instead a dimethylamino-substituted dibenzo-7λ<sup>3</sup>-phosphanorbornadiene reagent affords a Mo phosphinidene, through a two-electron process. Protonation of the Mo-phosphinidene results in formation of a phosphide ([PH(NMe<sub>2</sub>)]) compound. Treatment of the terminal Mo-phosphide with a second equiv. of low-valent Mo provides access to both asymmetric and symmetric bridging phosphides, in unusually low oxidation states. Herein, we report a unique series of structurally related complexes displaying mononuclear MoP, MoPR, and MoPR<sub>2</sub> and dinuclear MoPMo motifs, accommodated by the coordinative hemilability of the supporting arene-diphosphine ligand, and explore their reactivity in the context of modeling heterogeneous metal phosphide proton reduction (HER) catalysts.



## GENERAL INTRODUCTION

Metal phosphides comprise an important and ubiquitous class of solid-state materials with applications as catalysts and semiconductors.<sup>1</sup> In contrast, discrete metal phosphide complexes are rare and their chemistry remains underexplored.<sup>2</sup> Owing to both end-on and side-on reactivity,<sup>2b</sup> rarer still are isolable terminal transition metal phosphides. Indeed, since the initial reports of a P<sub>1</sub> ligand bearing a M≡P triple bond two decades ago,<sup>3</sup> only a handful of examples of such a motif have been described (Figure 6.1).<sup>4</sup> These compounds all display d<sup>0</sup> group 5 and 6 metals in a trigonal coordination environment. Reported herein are the first examples of isolable transition metal complexes with both terminal phosphide ligands and d-electrons.

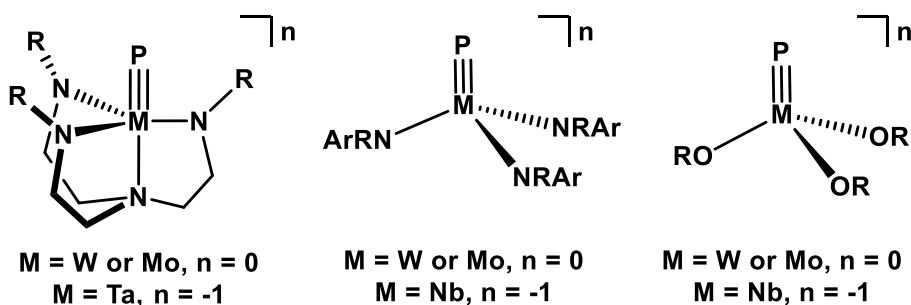
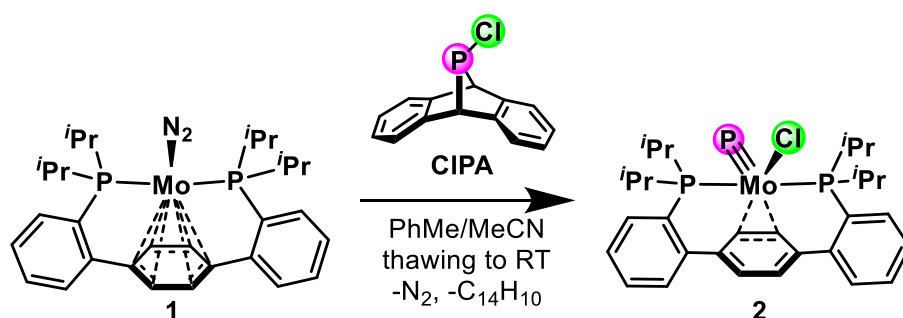


**Figure 6.1.** Classes of previously reported terminal phosphide complexes.

In a chapter 3 of this thesis, the ability of a *para*-terphenyl diphosphine supported molybdenum center to undergo a four-electron reductive coupling reaction from a Mo(IV) carbide to afford a Mo(0) dinitrogen adduct is described.<sup>5</sup> In an effort to access additional Mo≡E complexes, we targeted the reverse of this process—multi-electron oxidative group transfer.<sup>6</sup> Cummins and coworkers have reported a library of dibenzo-7λ<sup>3</sup>-phosphanorbornadiene derivatives that undergo anthracene elimination, releasing reactive phosphorous fragments, under mild conditions.<sup>6-7</sup> With precedent for arene elimination group transfer,<sup>6-7,8</sup> these bridgehead phosphinidenes represent promising reagents for the direct and mild installation of M–P multiple bonds.

## RESULTS AND DISCUSSION

Addition of **CIPA** to a thawing solution of molybdenum complex **1** resulted in a color change from red-orange to dark brown over the course of warming to room temperature (Scheme 6.1). The  $^{31}\text{P}\{^1\text{H}\}$  NMR spectrum of a reaction mixture aliquot showed complete consumption of **1** (76.4 ppm) and the generation of two new resonances—a broad triplet at 1300.7 ppm and a doublet at 41.3 ppm ( $^2J(\text{P,P}) = 11.1$  Hz). The upfield shift of the latter is consistent with a Mo(IV) center;<sup>9</sup> the highly deshielded chemical shift of the former supports the formation of a terminal phosphide.<sup>9</sup>



**Scheme 6.1.** Synthesis of terminal phosphide **2**.

The structure of **2** was determined by single-crystal X-ray diffraction (XRD), corroborating both the presence of a  $\text{P}_1$  ligand and the monomeric nature of the complex (Figure 6.2). The

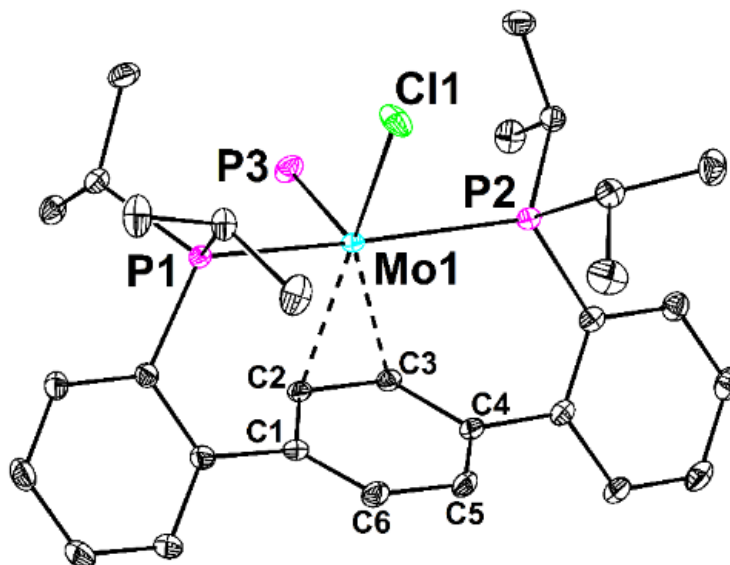


**Figure 6.2.** Solid-state structure of **2**. Protons are omitted for clarity. Anisotropic thermal displacement ellipsoids are shown at a 50% probability level.

Mo center adopts a *pseudo*-square pyramidal coordination geometry, with the phosphide in the axial position and the chloride ligand *trans* to an  $\eta^2$  interaction between Mo and the central arene of the *para*-**P2** ligand. Localization of single- and double-bond character in this arene, an average Mo–C contact of 2.258(1) Å (Table 6.1), and upfield shifted resonances for these aryl CH groups in both the  $^1\text{H}$  and  $^{13}\text{C}\{^1\text{H}\}$  NMR spectra are all consistent with the assigned metal-arene interaction. The short 2.1003(3) Å Mo–P bond distance is in excellent agreement with that of Mo(VI) phosphides,<sup>3-4,4c-e</sup> supporting a Mo–P triple bond.

**Table 6.1.** Selected bond metrics [Å] for phosphides **2** and **3**.

	Mo1–P3	Mo1–Cl1	Mo1–C2	Mo1–C3	C2–C3
<b>2</b>	2.1003(3)	2.4358(3)	2.261(1)	2.255(1)	1.433(2)
<b>3</b>	2.092(1)	2.3411(9)	2.465(3)	2.471(3)	1.402(4)

Elimination of arenes resulting in group transfer has been employed to deliver a variety of moieties, including  $\text{N}^-$ ,<sup>8c,8d,8h</sup>  $\text{NH}$ ,<sup>8b</sup>  $\text{CH}$ ,<sup>8f</sup>  $\text{NCN}$ ,<sup>8e,8g</sup>  $\text{O}$ ,<sup>8a</sup>  $\text{PCH}$ ,<sup>10</sup> and  $\text{P}_2$ .<sup>7a,7b</sup> Recently, **CIPA** was employed to transfer  $\text{P}^+$  to an anionic vanadium nitride to generate the pnictogen-pnictogen linkage in a transient P–N complex.<sup>6</sup> In line with this strategy, the formation of **2** demonstrates the successful transfer of both P- and Cl-atoms from CIPA, a four-electron process supported by a single metal center. Monometallic four-electron oxidative addition is known, but is limited to the insertion of metal fragments into unsaturated  $\text{C}=\text{O}$ ,<sup>11</sup>  $\text{C}=\text{S}$ ,<sup>11b</sup>  $\text{C}=\text{N}$ ,<sup>11</sup> and  $\text{N}=\text{N}$ <sup>12</sup> bonds. Group transfer by elimination of a single arene equivalent more typically results in two-electron processes,<sup>8a,8d,8e,8g,8h</sup> although four-electron reactivity has been demonstrated when employing two metal centers as group or atom acceptors.<sup>8f</sup> The hapticity change of the metal-arene interaction from  $\eta^6$  (**1**) to  $\eta^2$  (**2**) facilitates this multi-electron transformation; the d-orbitals engaging in Mo-arene  $\pi$ -bonding in the low-valent starting material are liberated to form the Mo–P bonds in the product.

The electronic structure of **2**, displaying a Mo(IV) center and two valence d electrons, is of

interest, contrasting previously reported  $C_{3v}$   $d^0$  terminal phosphides. Under threefold symmetry, the d orbital splitting varies depending upon both the P-M-L angle and the  $\pi$ -bonding character of the ancillary ligands, with some geometries resulting in orbitals of metal-P  $\pi$ -antibonding character being the lowest energy d-based orbitals.<sup>13</sup> Population of such orbitals would result in destabilization of the M-P interaction.<sup>13</sup> Quantum mechanics studies were employed to interrogate the Mo-P bonding in **2** (Figure 6.3). Qualitatively, the bonding in  $C_s$  symmetric **2** is similar to the vanadyl ion.<sup>14</sup> In *pseudo*-square pyramidal **2**, the HOMO

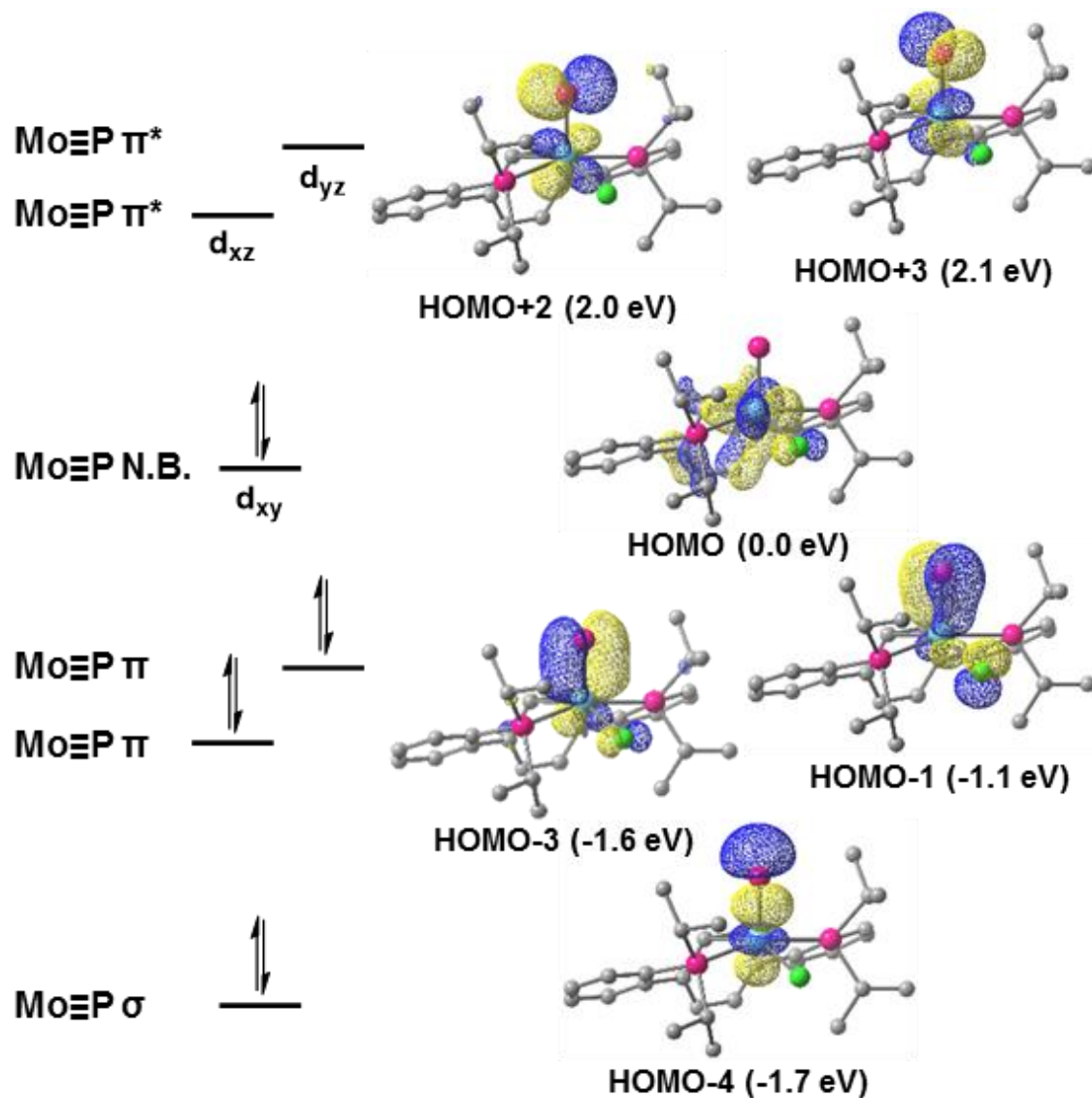


**Figure 6.3.** Qualitative MO energy diagram (left) and selected calculated valence MOs (right) depicting the Mo/phosphide bonding in **2**. Isosurfaces are shown at the  $0.05 \text{ e } \text{\AA}^3$  level and orbital energies (relative to the HOMO) are provided.

(Figure 6.3.) is of Mo d(xy) parentage and is strictly nonbonding (N.B.) with respect to the phosphide. This MO displays  $\pi$ -backbonding and  $\pi$ -antibonding character with respect to the M-arene and M-Cl interactions, respectively. The bonding between Mo and the phosphide ligand is consistent with a triple bond, involving a  $\sigma$ - (HOMO-4) and two  $\pi$ -bonding interactions (HOMO-1 and HOMO-3). The  $\pi$ -antibonding interactions, displaying Mo d(xz) and d(yz) parentage (HOMO+2 and HOMO+3), are unoccupied. The formal d<sup>2</sup> count is therefore not destabilizing; the valence electrons occupy a N.B. orbital, maintaining a formal M-P bond order of three.

As strictly non-bonding with respect to the phosphide ligand, we anticipated that a single electron oxidation of **2** might afford an open shell phosphide cation. The cyclic voltammogram of **2** in THF displays a one-electron oxidation event at -104 mV vs. Fc/Fc<sup>+</sup> (Figure 6.28.). Addition of [Fc][BAR<sup>F</sup><sub>24</sub>] (BAR<sup>F</sup><sub>24</sub> = B(3,5-(CF<sub>3</sub>)<sub>2</sub>C<sub>6</sub>H<sub>3</sub>)<sub>4</sub>) to a thawing 2-MeTHF solution of **2** results in a color change to deep purple upon mixing. The X-band CW EPR spectrum of a glass of this purple solution is consistent with generation of S=1/2 phosphide cation **3** (Scheme 6.2.). The EPR spectrum was satisfactorily fit using a slightly rhombic g tensor with g<sub>x</sub> = 2.0062, g<sub>y</sub> = 2.0037, and g<sub>z</sub> = 1.971 and with hyperfine couplings to <sup>95/97</sup>Mo ( $|A_{x,y,z}| = [94, 94, 198]$  MHz), two <sup>31</sup>P<sub>P2</sub> ( $|A_{x,y,z}| = [60, 72, 63]$  MHz) couplings from the phosphine ligands, and a single highly anisotropic <sup>31</sup>P coupling assigned to the phosphide <sup>31</sup>P<sub>Mo≡P</sub> ( $|A_{x,y,z}| = [15, 138, 15]$  MHz) (Figure 6.4.). These parameters were further corroborated by acquisition and analysis of pulse X-band Davies electron nuclear double resonance (ENDOR) spectra and pulse Q-band field swept EPR spectra (Figure 6.25.). Additional small hyperfine couplings were observed in the Davies ENDOR spectra (Figure 6.26.) to <sup>1</sup>H ( $|A_{x,y,z}| = [10, 18, 10]$  MHz), assigned to the two proximal protons from the arene ligand, and <sup>35/37</sup>Cl ( $|A_{x,y,z}| = [10.5, 10.5, 10.5]$  MHz). Computationally determined Mulliken spin densities and the large observed hyperfine coupling to <sup>95/97</sup>Mo agree well with primary localization of the unpaired spin on the Mo center.

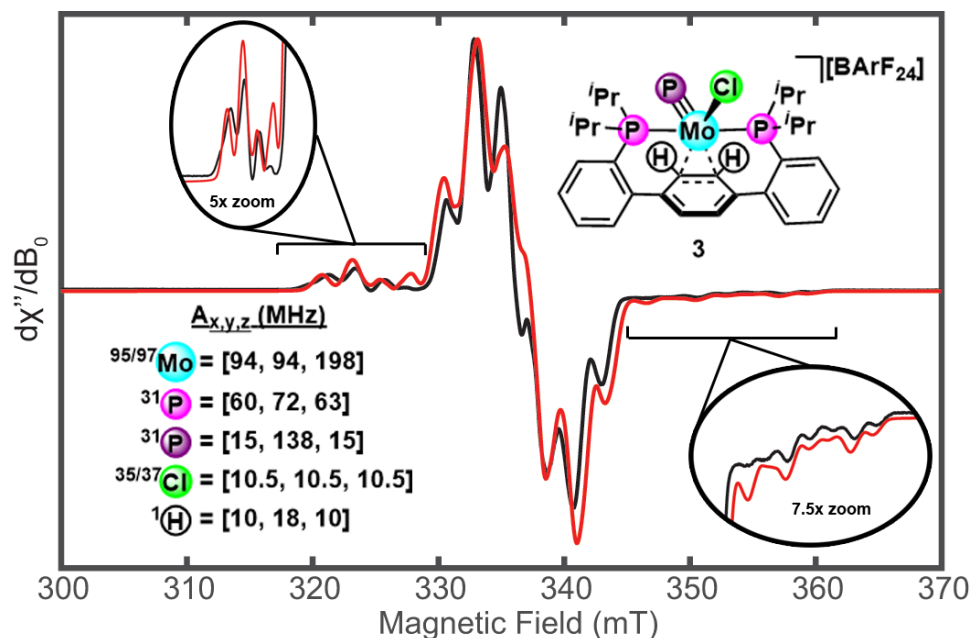
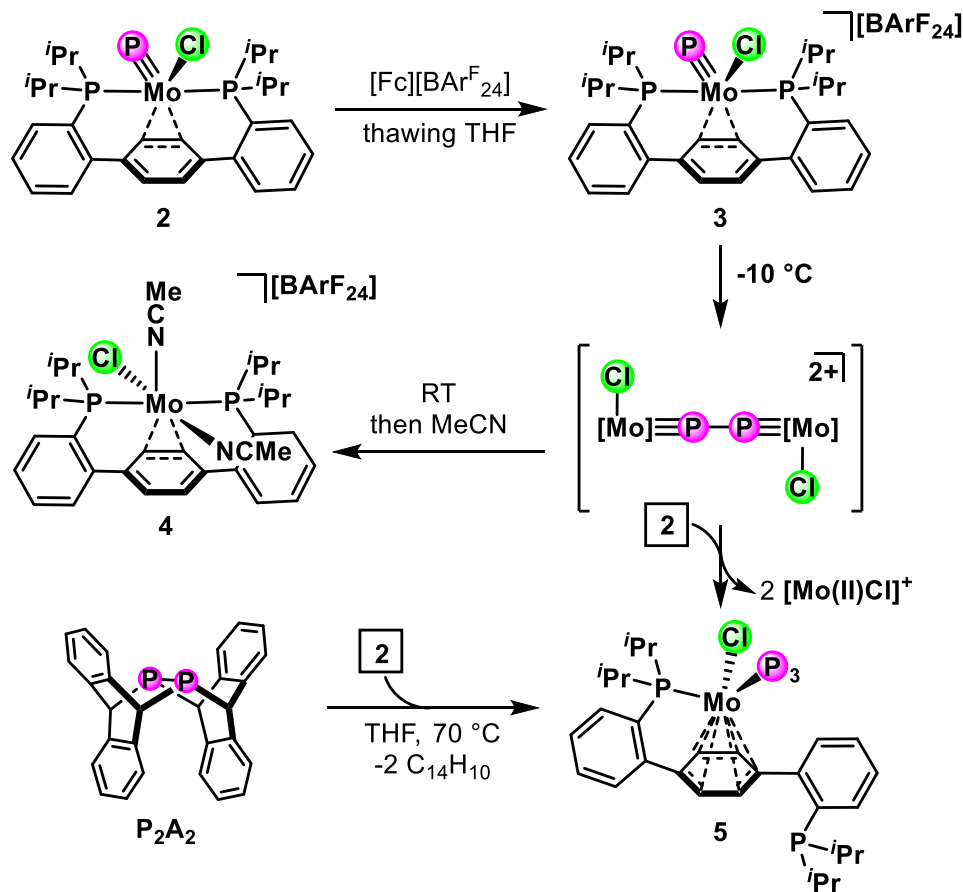


**Figure 6.4.** Experimental (black) and simulated (red) X-band CW EPR spectra of **3** (2Me-THF glass; 77 K).

Analysis of the anisotropic component of the phosphide  $^{31}\text{P}$  hyperfine coupling<sup>15</sup> indicates appreciable spin density of 0.1-0.14  $e^-$  in a single p-orbital at the terminal phosphide (*vide infra*).

Single crystal XRD confirmed the assignment of cation **3**. The structure of **3** is similar to **2**, with perturbations consistent with the bonding scheme shown in Figure 6.3. The Mo $\equiv$ P distance is only slightly contracted at 2.092(1) Å, likely due to the smaller radius for the higher oxidation state Mo(V) center (Table 6.1). The Mo–Cl and C2–C3 bonds both contract significantly (2.3411(9) and 1.402(4) Å, respectively, Table 6.1), consistent with a “push-pull” interaction<sup>16</sup> between the  $\pi$ -basic chloride and  $\pi$ -acidic  $\eta^2$  M-arene interaction. The Mo d(xy) orbital (HOMO of **2**, SOMO of **3**) is bonding with respect to the C2–C3  $\pi^*$ -bond, reflected in the elongation of the Mo–C2 and Mo–C3 distances from **2** to **3**, and consistent with reduction of the Mo-arene bond order upon oxidation.

Though stable in the solid state, warming solutions of **3** above  $-10^\circ\text{C}$  results in a color change to red-brown with the concomitant appearance of a singlet at 68 ppm in the  $^{31}\text{P}\{^1\text{H}\}$  NMR spectrum. The NMR data for this new species in  $\text{CD}_3\text{CN}$  is consistent with a C<sub>s</sub> symmetric acetonitrile adduct, confirmed by XRD as chloride cation **4** (Scheme 6.2). The net



**Scheme 6.2.** Oxidation-induced phosphide coupling.

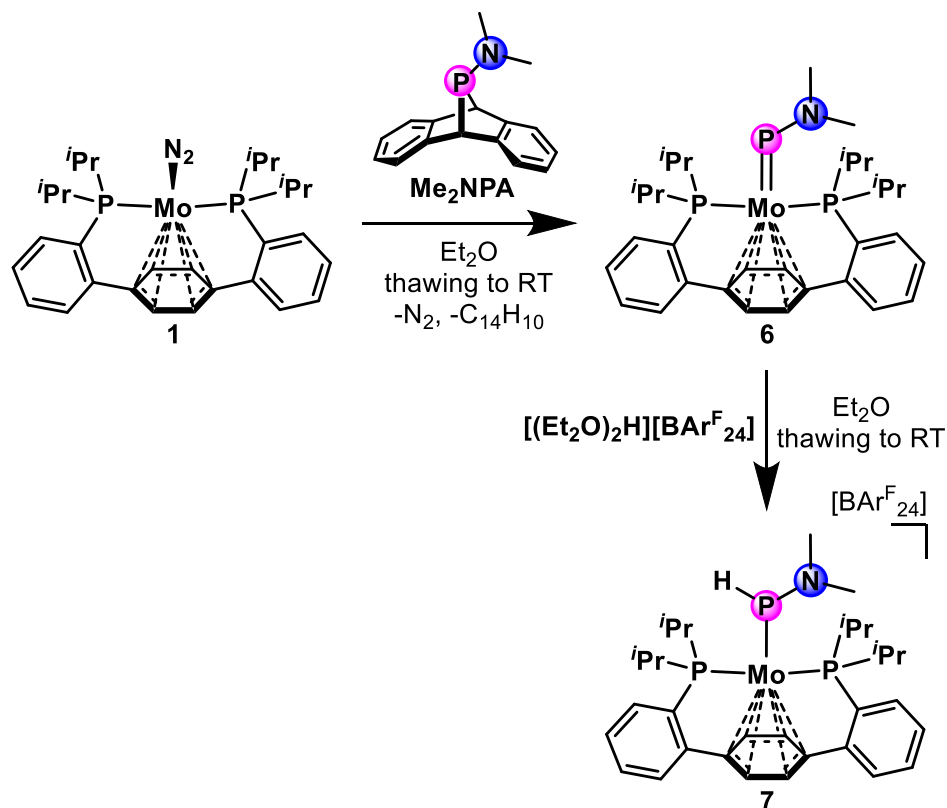
three electron reduction of the Mo center and the loss of the  $^{31}\text{P}$  signal corresponding to the terminal phosphide ligand is consistent with the formal loss of a P-atom, and suggests intermolecular phosphide coupling as a feasible reaction pathway to generate **4** from **3**; such coupling reactions of transition metal nitrides are known.<sup>8d,17</sup> Analogous to the formation of **4**, oxidatively induced bimetallic reactions resulting in the formation of new E–E bonds are invoked in both ammonia<sup>17g,17h</sup> and water<sup>13a</sup> oxidation chemistry.

Hypothesizing that the phosphide ligand converts to diphosphorous ( $\text{P}_2$ ) species, chemical traps were employed for its detection.<sup>7b,18</sup> Terminal phosphide complexes themselves have been reported to be efficient  $\text{P}_2$  traps, reacting in a one-to-one manner to generate cyclic  $\text{P}_3$  products.<sup>18a</sup> Warming THF solutions of **2** and **3** in a 1:2 ratio resulted in a complex  $^{31}\text{P}\{^1\text{H}\}$  NMR spectrum. Cation **4** was observed, in addition to a species (**5**) with three highly shielded

$^{31}\text{P}$  resonances: -155.2 (dd,  $J = 321.4$  and  $266.3$  Hz), -201.0 (app t,  $J = 266.1$  Hz) and -303.4 (ddd,  $J = 321.2$ ,  $266.6$ , and  $16.4$  Hz) ppm. The high field chemical shifts and large scalar coupling constants are consistent with a polyphosphorous ligand bearing at least three P–P bonds.<sup>19</sup> This new phosphorous rich complex could not be prepared in sufficient purity for further characterization. However, it can be prepared independently using an established  $\text{P}_2$  source,  $\text{P}_2\text{A}_2$ .<sup>7b</sup> Heating  $\text{P}_2\text{A}_2$  with complex **2** in THF results in the same high field  $^{31}\text{P}$  NMR signature. Establishing the mechanism of formation for **5** requires further experiments; generation of free  $\text{P}_2$ , direct reaction of **2** with a P–P bonded intermediate (Scheme 6.2., brackets), or P–P bond formation between **2** and **3** are all possible. Nevertheless, the NMR characteristics of species **5**, generated via any of these potential reactivity manifolds, establishes the ability of **3** to form new P–P bonds via coupling of a terminal phosphide with radical character.

Interested in exploring the scope of group transfer chemistry from dibenzo- $7\lambda^3$ -phosphanorbornadiene precursors to **1**, a  $\text{Me}_2\text{N}$ -substituted version (**Me<sub>2</sub>NPA**) was employed (Scheme 6.3.). Akin to **CIPA**, addition of **Me<sub>2</sub>NPA** to a thawing solution of **1** resulted in a darkening of the reaction mixture upon warming; the  $^{31}\text{P}\{^1\text{H}\}$  NMR spectrum of the reaction mixture shows two new resonances, a triplet at 1033.19 ppm and a doublet at 68.49 ppm ( $^2J(\text{P,P}) = 42.9$  Hz), consistent with successful “PNMe<sub>2</sub>” group transfer from **Me<sub>2</sub>NPA**. The  $^{31}\text{P}$  signal for the transferred P-atom in this new species, resonating *ca.* 300 ppm upfield of that in **2**, suggests formation of a phosphinidene<sup>20</sup> rather than a terminal phosphide. XRD analysis confirmed formation of the formally two-electron oxidized group transfer product, dimethylaminophosphinidene complex **6** (Figure 6.3.). The structural parameters—a Mo–P bond length of 2.3333(8) Å and a Mo–P–N angle of 120.4(1)°—are similar to reported aminophosphinidenes and, in conjunction with the down-field  $^{31}\text{P}\{^1\text{H}\}$  chemical shift observed for **6**, support the phosphinidene assignment.<sup>21</sup> Moreover, the Mo–P distance is between that of a phosphide (2.1003(3) Å) and a phosphine (*ca.* 2.49 Å), consistent with a Mo–P double bond. Due to the dimethylamido substituent’s lone pair, the PNR<sub>2</sub> ligand has





**Scheme 6.3.** Synthesis of Mo dimethylamino phosphinidene (**6**) and phosphide (**7**) complexes.

characteristics of a Fisher-type phosphinidene, making its assignment as a formally dianionic vs. neutral ligand ambiguous. Indeed, the nitrogen atom is planar ( $\sum \angle$  at N =  $359.9^\circ$ ), consistent with involvement of the lone pair in bonding with the P atom. The significant bending at P ( $\angle \text{Mo-P-N} = 120.4(1)$ ), a common feature of aminophosphinidenes, supports the presence of a lone pair not involved in bonding with Mo (nor N), in contrast to much more linear ( $\angle \text{M-P-E} > 150^\circ$ ) nucleophilic phosphinidenes which display higher order M–P  $\pi$  bonding.<sup>22</sup> The Mo–P and P–N ( $2.3333(8)$  and  $1.694(3)$  Å, respectively) bonds in **3** are contracted and elongated, respectively, when compared to known Mo(IV) electrophilic aminophosphinidenes.<sup>21a</sup> These metrics indicate diminished N- and increased Mo-to-P donation in more reduced **3**, which displays a Mo(II) center in this electron counting formalism.

Observation of both two- and four-electron group transfer products (**6** and **2**, respectively),

suggest a potential mechanism of formation of **2** involving coordination of **CIPA**, elimination of anthracene to form the chlorophosphinidene analogous to **6**, and  $\alpha$ -Cl abstraction. Alternatively, oxidation addition of the P–Cl moiety could occur first, followed by loss of anthracene; a path that cannot be ruled out at this time. In an attempt to explore stepwise conversion of **6** to **2**, on-metal protonolysis of the aminophosphinidene was targeted. Treating a thawing Et<sub>2</sub>O solution of **6** with [(Et<sub>2</sub>O)<sub>2</sub>H][BAR<sup>F</sup><sub>4</sub>] (BAR<sup>F</sup><sub>4</sub> = B(C<sub>6</sub>H<sub>3</sub>(CF<sub>3</sub>)<sub>2</sub>)<sub>4</sub>) cleanly affords a single diamagnetic product with a triplet and doublet in the <sup>31</sup>P{<sup>1</sup>H} NMR spectrum at 297.2 and 72.6 ppm (<sup>2</sup>J(P,P) = 47.9 Hz), respectively, consistent with maintenance of a pseudo-C<sub>3</sub> symmetric P<sub>3</sub> coordination environment around Mo. The <sup>1</sup>H NMR spectrum shows a distinct low-field doublet with a large coupling constant (10.14 ppm, <sup>1</sup>J(H,P) = 323.3 Hz), supporting protonation at P and formation of a Mo(II) phosphide cation, **7** (Scheme 6.3).<sup>3b</sup> This reactivity, which deviates from the general electrophilic behavior of Fischer-type phosphinidenes is likely a consequence of the electron rich metal center. The lower oxidation state of **6** may render the phosphinidene ligand more basic; indeed the electronic character of phosphinidene ligands is strongly coupled to that of the metal.<sup>23</sup>

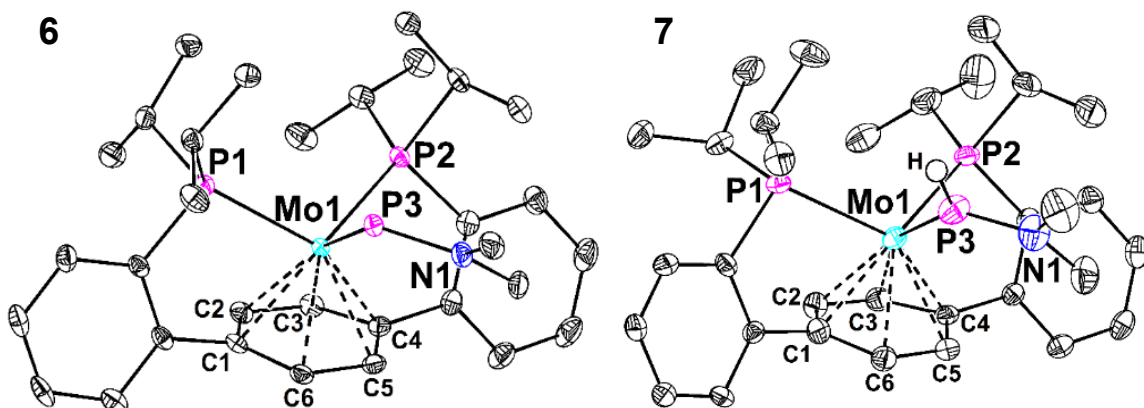


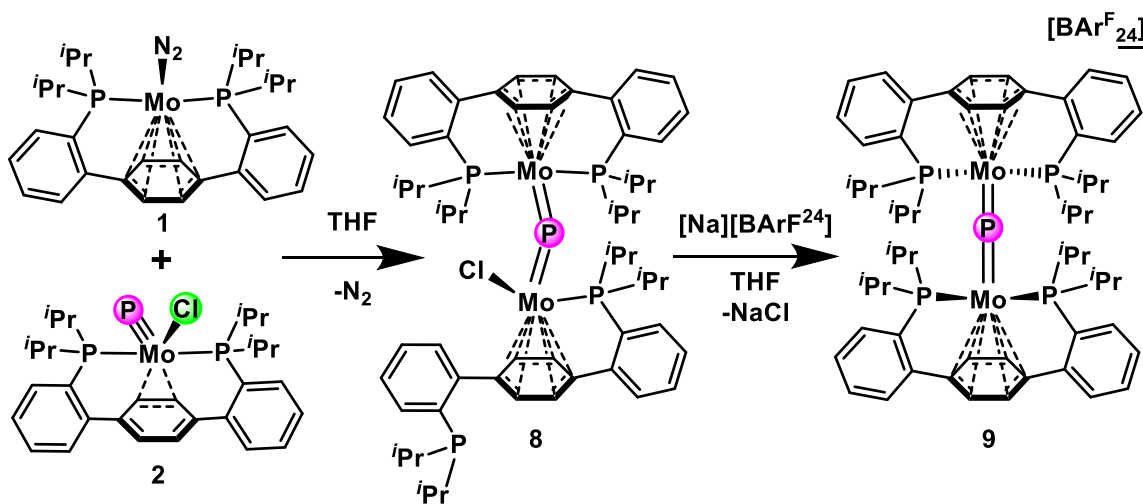
**Figure 6.5.** Solid-state structures of **6** and **7**. Select protons and counterions (**7**) are omitted for clarity. Anisotropic thermal displacement ellipsoids are shown at a 50% probability level. Select bond distances [Å] and angles **6** Mo1–P3 2.3333(8), P3–N1 1.694(3),  $\angle$ Mo1–P3–N1 120.4(1); **7** Mo1–P3 2.2248(9), P3–N1 1.659(3),  $\angle$ Mo1–P3–N1 132.9(1).

An XRD study confirmed this assignment (**7**, Figure 6.5). Amidophosphines are typically cleaved by Brønsted acids<sup>24</sup> making the isolation of **7** a unique example of structurally

characterized terminal phosphide with both amido- and H-substitution at P.<sup>25,26</sup> The Mo–P and P–N distances in **7** are similar to those in **6**. The Mo–P distance (2.2248(9) Å) remains in the range of a double bond. Moreover, both Mo–P and P–N distances are shorter than in **7** suggesting that, upon protonation, the P center becomes more electrophilic and interacts more strongly with electron rich Mo and N.

Heterogeneous metal phosphides are structurally diverse, with the stoichiometric or metal-rich phases display bridging phosphide building blocks.<sup>1a</sup> To compare Mo–P interactions supported by the same ligand framework, complexes with  $\mu$ -P motifs were targeted. Capping reactive terminal phosphides with transition metal-based Lewis acidic fragments has been employed to stabilize the  $M\equiv P$  moiety, resulting in asymmetric  $\mu$ -P complexes.<sup>4f,26-27</sup> The high valent metal maintains a short (*ca.* 2.15 Å) M–P distance, consistent with preservation of a formal triple bond.<sup>2b,4f</sup> Dinuclear symmetric bridging phosphides have been demonstrated as intermediates in intermetal P-atom transfer reactions<sup>4g</sup> and have been prepared by the activation of white phosphorous<sup>4e</sup> and phosphides.<sup>28</sup>

Addition of Mo(0) complex **1** to a solution of **2** affords a new species with five distinct <sup>31</sup>P{<sup>1</sup>H} NMR resonances, at 1161.0, 82.9, 73.7, 70.3, and -5.3 ppm. This spectral signature, consistent with a  $C_1$  symmetric Mo–P–Mo structure (**8**, Scheme 6.4.), was corroborated by the



**Scheme 6.4.** Synthesis of  $\mu$ -phosphide complexes **8** and **9**.

$^1\text{H}$  NMR spectrum, which showed eight discrete resonances for the central arene protons between 3.5 and 5.5 ppm. Though the low-field  $^{31}\text{P}$  signal in **8** resonates several hundred ppm downfield of diamagnetic symmetric or asymmetric bridging phosphide complexes,<sup>4e,4f</sup> the  $\mu$ -P assignment was conclusively established by XRD. The structure of **8** is dinuclear with a bridging phosphide ligand, one trans-spanning *para*-**P2** ligand, and one arm-on arm-off *para*-**P2** unit (Figure 6.6). The Mo–P3 distances are similar for both metal centers (2.2831(3) (Mo1) and 2.2409(3) Å (Mo2)), most consistent with double bonds between both Mo ions and the  $\mu$ -P.<sup>4g</sup> The chloride remains bound (2.5157(3) Å), prompting dissociation of one of the phosphine arms of the *para*-**P2** ligand. Both arenes bind in an  $\eta^6$  fashion with the Mo–C<sub>arene</sub> contacts averaging 2.281(1) and 2.309(1) Å for Mo1 and Mo2, respectively.

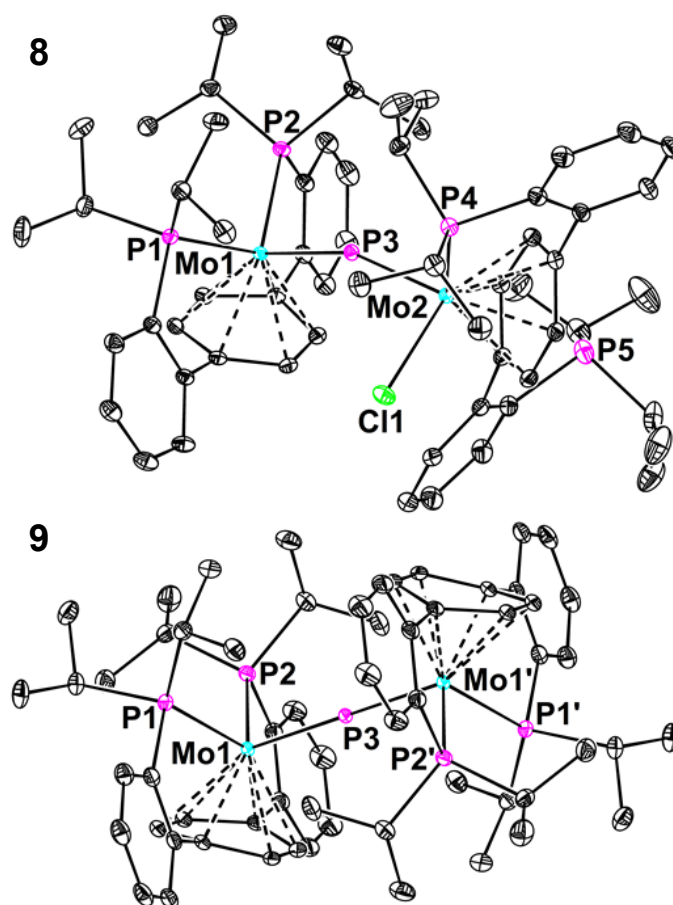


**Figure 6.6.** Solid-state structures of **8** and **9**. Protons and counterions (**9**) are omitted for clarity. Anisotropic thermal displacement ellipsoids are shown at a 50% probability level. Select bond distances [Å] and angles (°): **8** – Mo1–P3: 2.2831(3), Mo2–P3: 2.2409(3),  $\angle$  Mo1–P3–Mo2 154.23(1) **9** – Mo1–P3 2.2747(2).

A higher symmetry bridging phosphide was targeted via exchanging the chloride for a non-coordinating counterion (Scheme 6.4.). Halide abstraction from **8** with one equiv. of Na[BAr<sup>F</sup><sub>4</sub>] results in simpler NMR characteristics; the <sup>31</sup>P{<sup>1</sup>H} NMR spectrum shows only two resonances at 1123.3 and 68.6 ppm in a 1:4 ratio, in accord with formation of **9**. Complex **9** crystallizes with C<sub>2</sub> symmetry. The μ-P ligand lies on a crystallographic special position, imposing equivalent M–P distances of 2.2747(2) Å, which agree well with related symmetric μ-P complexes bearing metal phosphide double bonds.<sup>4e,4g</sup> The Mo-η<sup>6</sup>-arene contacts in **9** are slightly elongated (2.301(2) Å,) when compared to the analogous fragment in **8**, potentially a consequence of steric congestion resulting from phosphine arm recoordination.

Despite a litany of reports outlining the efficacy and stability heterogeneous metal phosphides for HER,<sup>1a,29</sup> their operative mechanism is not known. Computation suggests that both metal- and P-protonation could be viable pathways for generation of reactive intermediates that, upon application of a reducing potential, could release H<sub>2</sub>.<sup>30</sup> Symmetric **9**, an unusually electron rich μ-phosphido complex, seemed an appropriate homogeneous platform to probe the mechanism of HER. The cyclic voltammogram of **9** showed two reversible oxidation features (-0.52 V and 0.15 V) and one reversible reduction (-2.25 V), indicating strong electronic coupling through the bridging phosphide—K<sub>c</sub>(Mo<sup>II</sup>Mo<sup>III</sup>/Mo<sup>III</sup>Mo<sup>III</sup>) = 2.1 × 10<sup>11</sup> (Figure 6.7).<sup>31</sup> Initial electrolyses in the presence of [LutH][OTf], however, showed no evidence of HER activity on the timescale of the electrochemical experiment.

Stoichiometric reactions with a stronger acid, [(Et<sub>2</sub>O)<sub>2</sub>H][BAr<sup>F</sup><sub>4</sub>], resulted in formation of a new species. Four signals in the <sup>1</sup>H NMR spectrum—6.08, 5.75, 5.25, and 4.93 ppm—suggest a C<sub>s</sub> symmetric dinuclear zsolution structure. The <sup>31</sup>P{<sup>1</sup>H} chemical shift for the terphenyl phosphines corroborate this assignment, resonating at 90.81 and 79.08 ppm. The chemical shift of the μ-P, a broad peak (Δf<sub>FWHM</sub> = 112 Hz), moves upfield by 73 ppm relative the starting material. Addition of [(Et<sub>2</sub>O)<sub>2</sub>D][BAr<sup>F</sup><sub>4</sub>] to symmetric **9** formed a similar species with a slightly shifted (1051.05 ppm) and split (d, <sup>1</sup>J(P,D) = 155.0 Hz) μ-P resonance. To our knowledge,

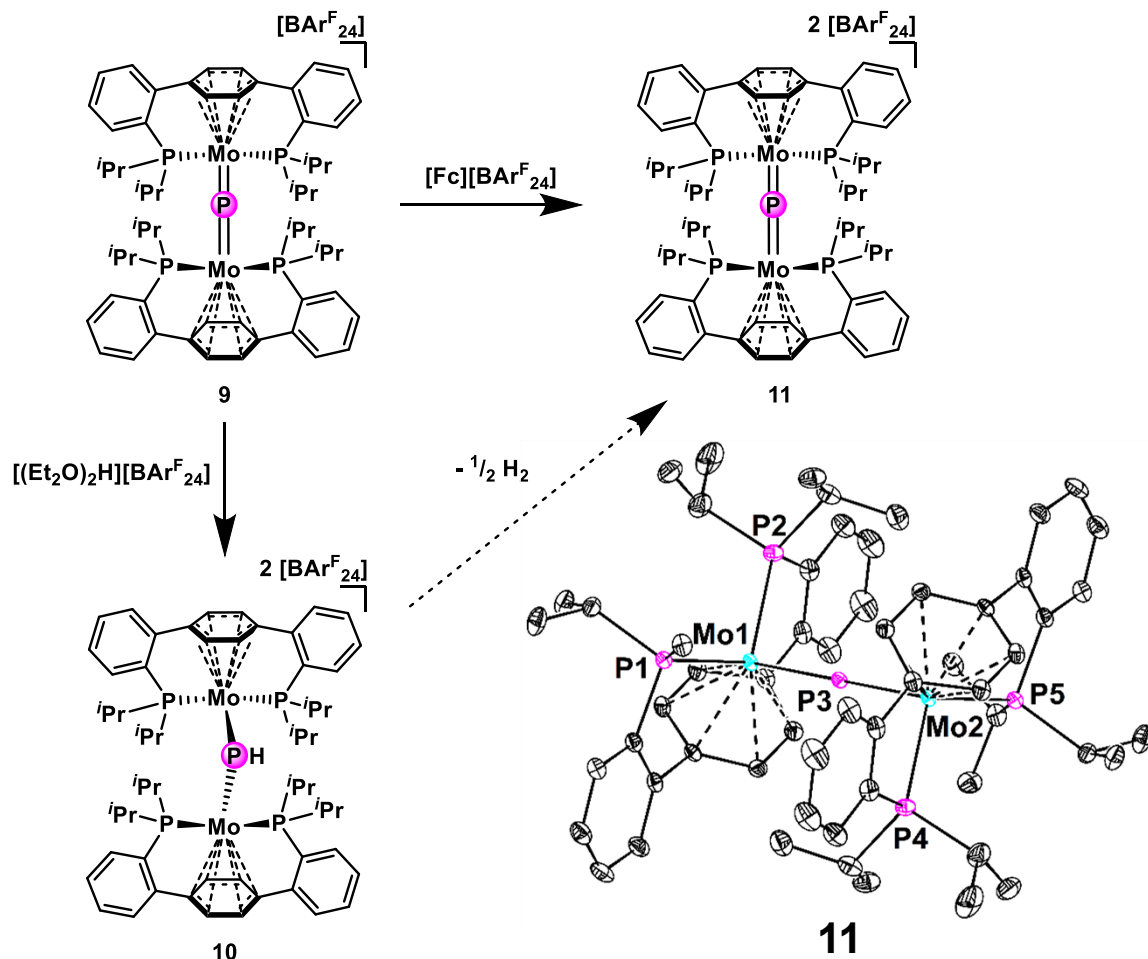


**Figure 6.7.** Synthesis of dinuclear Mo complexes bearing bridging phosphinidene and phosphido ligands. The solid state structure of  $\mu$ -P dication **11** is shown with anisotropic displacement ellipsoids shown at the 50% probability level. Counter anions and H-atoms are omitted for clarity.

diamagnetic bridging phosphinidene complexes have not been synthesized previously,<sup>4b,32</sup> however, terminal phosphinidenes supported by U and Zr and sterically protected by a bulky TREN variants were reported recently.<sup>33</sup> The chemical shifts for these PH moieties vary significantly, resonating at 2460 ppm for the U complex and at 247 ppm for the Zr compound. Despite this, the data, particularly the isotopic sensitivity of the  $\mu$ -P  $^{31}\text{P}\{^1\text{H}\}$  NMR resonance and the lack of a Mo hydride signal in the  $^1\text{H}$  NMR, seem consistent with protonation at the phosphide, giving  $\mu$ -phosphinidene **10** (Figure 6.7).

Efforts to crystallize **10** uniformly returned a complex missing a hydrogen atom—dinuclear Mo(II)- $\mu$ P-Mo(III), **11**. Dication **11** can be prepared independently by the one electron

oxidation of **10** with  $[\text{Fc}][\text{BAr}^{\text{F}}_{24}]$  (Figure 6.7.). The  $\mu$ -phosphide in the solid state structure of **11**, grown from a reaction of **9** with acid, lies on a symmetry special position, giving two equivalent Mo–P distances of 2.276(1) Å. The independently synthesized sample, crystallizes as an isoform of **11**; the unit cells differ but the Mo–P<sub>phosphide</sub> distances are consistent with those observed previously at 2.294 and 2.260 Å, in accord with the structure no longer bearing a hydrogen atom. These metrics are in close agreement with the Mo–P<sub>phosphide</sub> distances observed for **9**.

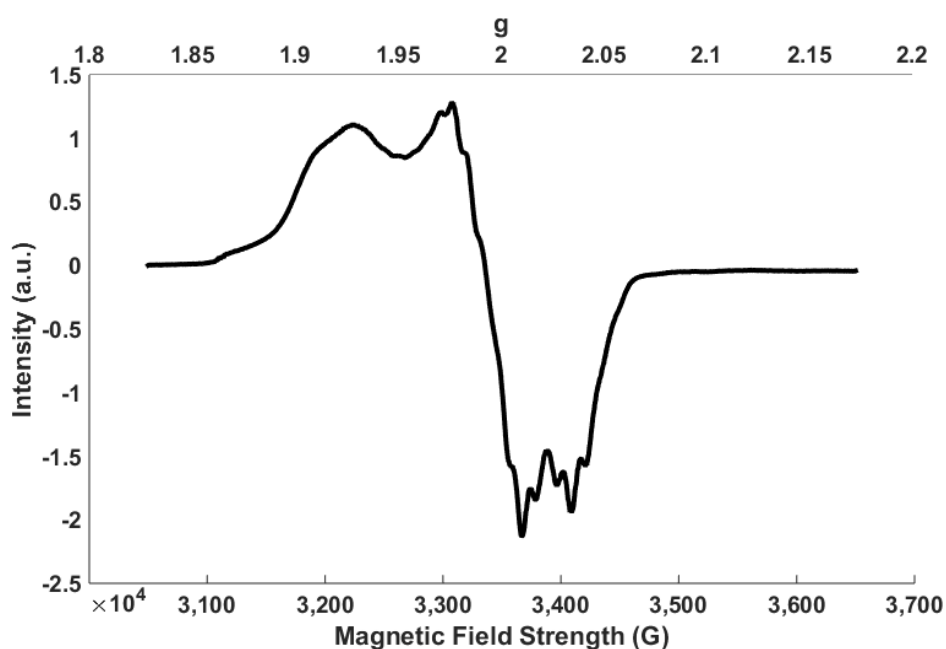
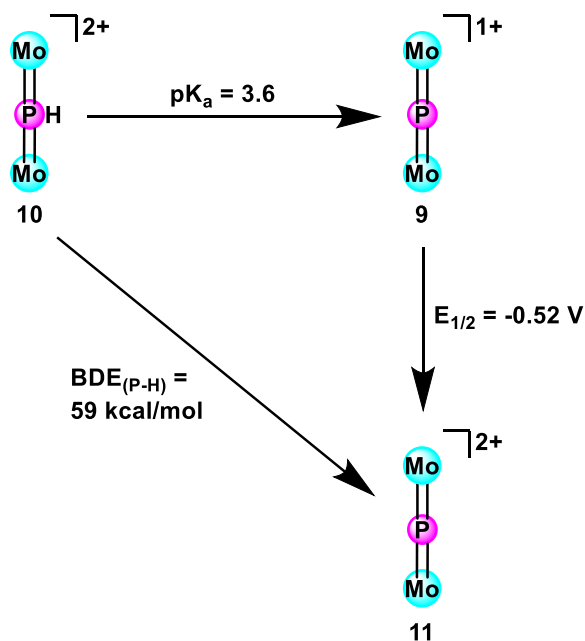


**Figure 6.8.** X-band CW EPR spectrum of a 2Me-THF glass (77 K) of **11**.

The X-band CW EPR spectrum of **11** shows a rhombic signal centered at  $g = 1.9921$  (Figure 6.8.), consistent with an  $S = 1/2$  species; broad but resolved hyperfine interactions with the spin-active  $^{31}\text{P}$  nuclei ( $I = 1/2$ ) are observed. The formation of **11** from protonation of **9** (via **10**) seemed suggestive of an intermolecular  $\text{H}_2$  evolution pathway. In an effort to access this reactivity rationally, a sample of **10** was heated to 50 °C in DME. After 4 h, less than 50 % of the  $^{31}\text{P}$  containing material remained diamagnetic, in line with possible generation of **11** and  $\text{H}_2$ .

Intermolecular H<sub>2</sub> evolution from **10** represents the formal loss of a hydrogen atom, a mechanism that may be relevant to HER catalysis.<sup>30b</sup> There is negligible data in the literature reporting P–H thermochemistry relevant to metal phosphide catalyzed HER, a shortcoming we sought to rectify. With the standard potential for oxidation of **9** in hand, a pK<sub>a</sub> for phosphide protonation was required to complete a square-scheme for HAT from **10** (Scheme 6.5). Titrating PyOTf into a THF solution of **9** showed partial protonation at higher equiv. of acid ( $\geq 3$ ), allowing for determination of the pK<sub>b</sub> of the  $\mu$ -phosphide via relative integration of the central arene resonances at 4.46 (**9**) and 6.17 (**10**) ppm. Calculating the BDE<sub>(P-H)</sub>,<sup>34</sup> including a THF solvent correction,<sup>35</sup> gives a value of 59 kcal/mol; this intermediate P–H bond strength is consistent with the relative stability of **10** to H<sub>2</sub> loss in solution at room temperature. Experiments examining both HAT from **10** (confirmation and quantification of H<sub>2</sub> formation) and to **11** (addition of strong H-atom donors) are ongoing.



**Scheme 6.5.** Thermochemical square scheme for HAT from  $\mu$ -phosphinidene **10**.

Encouraged by the reversible reduction observed in the CV of **9**, reduction with [Na][C<sub>10</sub>H<sub>8</sub>] was attempted. These reactions led to intractable mixtures, rather than the desired Mo(I)- $\mu$ P-Mo(II) species. Targeting more reduced species bearing H-atoms, asymmetric **8** was treated



with  $\text{LiEt}_3\text{BH}$  (Figure 6.9.). A new diamagnet with a triplet at -1.56 ppm ( $^2J(\text{P},\text{H}) = 17.0$  Hz) in the  $^1\text{H}$  NMR spectrum was observed, in line with generation of hydride  $\mu$ -phosphide. The  $^{31}\text{P}\{^1\text{H}\}$  NMR spectrum shows four resonances (1055.71, 102.19, 67.77, and -6.10 ppm), indicating maintenance of a  $C_1$  symmetric structure, consistent with that of **12**.

The solid-state structure of **12** corroborates the solution spectroscopy, demonstrating an assymmetric dinuclear complex in which one **P2** ligand is trans-spanning and the other adopts an arm-on arm-off binding motif (Figure 6.9., right). The  $\text{Mo}-\text{P}_{\text{phosphide}}$  distances remain relatively similar at 2.325 and 2.218 Å for the diphosphine and monophosphine coordinated Mo centers, respectively. These metrics suggest maintenance of the two  $\text{Mo}=\text{P}$  double bonds following hydride installation.<sup>48</sup> The preference for a Mo-bound H-atom in **12** versus a P-bound H-atom in **10** is notable. Indeed,  $\text{H}_2$  evolution from an acidic P-H motif and a hydridic Mo-H moiety would map nicely onto proposed HER mechanisms for metal phosphide materials,<sup>30</sup> providing valuable precedent for transformations of this type. Work investigating  $\text{H}_2$  evolution from mixtures of **10** and **12** and the interconversion of these remarkable coordination complexes is ongoing.

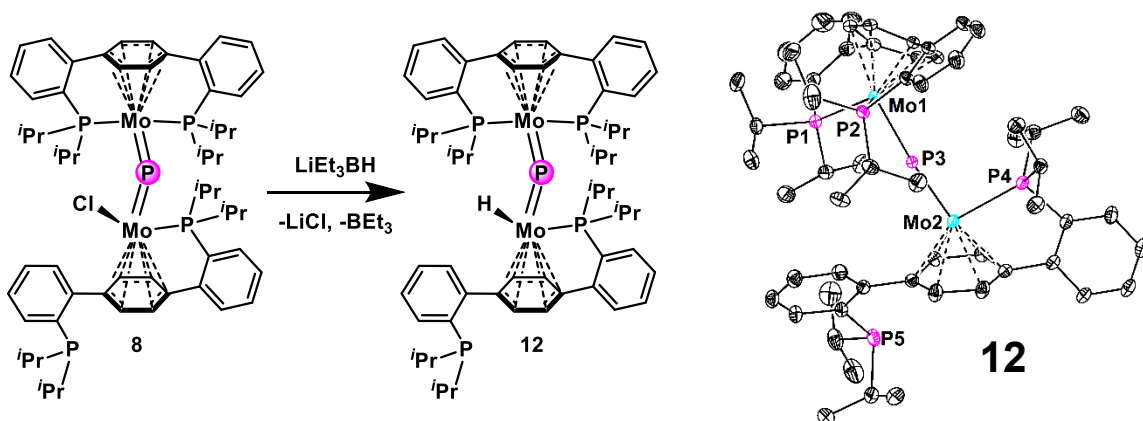


**Figure 6.9.** Synthesis and solid-state structure of phosphide hydride complex **12**. Thermal anisotropic displacement ellipsoids are shown at the 50% probability level and hydrogen atoms are omitted for clarity.

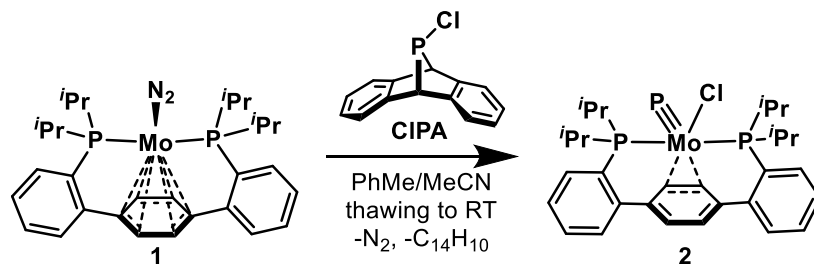
## CONCLUSION

In summary, **CIPA** affords facile transfer of both P- and Cl- atoms to Mo(0) to generate a terminal Mo phosphide. The tetragonal ligand field of the resulting Mo(IV) complex permits a  $d^2$  electron count at Mo and a formal Mo–P triple bond. Oxidation affords, at low temperatures, a paramagnetic Mo(V) phosphide cation with significant radical character on P. Upon warming, phosphide coupling occurs, demonstrating oxidatively induced E–E bond formation from a  $M\equiv E$  precursor. Dimethylamino-substituted **Me<sub>2</sub>NPA** affords two-electron group transfer, forming a phosphinidene complex. These precursors and their derivatives showcase monometallic species bearing MoP, MoPR, and MoPR<sub>2</sub> moieties. They also act as precursors to dinuclear complexes with a MoPMo moiety, still supported by the *para*-**P2** ligand framework. The coordinative flexibility of the ancillary ligand facilitates access to this diverse family of compounds with varying electronic requirements of the P-based donors. Such changes in the metal coordination sphere may be relevant to catalysis involving heterogeneous metal phosphides, the operative mechanisms of which remain largely unknown. Toward gaining insight into the mechanism of metal phosphide mediated HER catalysis, both  $\mu$ -PH and dinuclear phosphide hydride complexes have been prepared. Investigation of the electrochemical properties, thermochemistry, and reactivity of these molecular phosphide complexes is ongoing.

## EXPERIMENTAL SECTION

### *General Considerations*

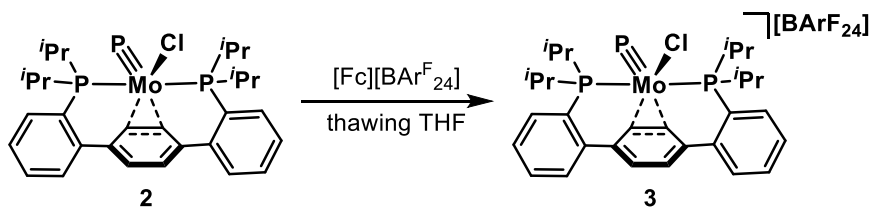
Unless otherwise specified, all operations were carried out in an MBraun drybox under a nitrogen atmosphere or using standard Schlenk and vacuum line techniques. Solvents for air- and moisture-sensitive reactions were dried over sodium benzophenone ketyl, calcium hydride, or by the method of Grubbs.<sup>36</sup> Deuterated solvents were purchased from Cambridge Isotope Laboratories and vacuum transferred from sodium benzophenone ketyl ( $C_6D_6$ ) or  $CaH_2$  ( $CD_3CN$ ). Solvents, once dried and degassed, were vacuum transferred directly prior to use or stored under inert atmosphere over activated 4 Å molecular sieves. **1**,<sup>37</sup>  $[P_2Mo(MeCN)_2][2OTf]$ ,<sup>37</sup> **CIPA**,<sup>7b</sup> **Me<sub>2</sub>NPA**,<sup>7b</sup> **P<sub>2</sub>A<sub>2</sub>**,<sup>7b</sup>  $Mg(THF)_3(C_{14}H_{10})$ ,<sup>38</sup>  $Me_2NPCl_2$ ,<sup>24</sup>  $Na[BAr^F_4]$ ,<sup>39</sup>  $[(Et_2O)_2H][BAr^F_4]$ ,<sup>40</sup>  $[Fc][BAr^F_{24}]$ ,<sup>41</sup> and  $[Fc][OTf]$ <sup>42</sup> were prepared according to literature procedures. Unless indicated otherwise, all chemicals were used as received.  $PCl_3$  (vacuum distilled from  $CaH_2$ ),  $HNMe_2$  (condensed trap-to-trap (0 °C to -78 °C)),  $HCl$  (4.0 M in dioxane or 2.0 M in diethyl ether), and  $PPH_4Cl$  (dried under vacuum at 40 °C, 12 h) were purchased from Sigma Aldrich.  $Mg^0$  (activated according to a literature report), 3,5-bis(trifluoromethyl)bromobenzene, and sodium tetrafluoroborate (dried under vacuum at 60 °C for 12 h) were obtained from Fischer Scientific. Anthracene was bought from Acros Organics.  $^1H$ ,  $^{13}C\{^1H\}$ , and  $^{31}P\{^1H\}$  NMR spectra were recorded on a Varian 400 MHz or Varian INOVA-500 spectrometers with shifts reported in parts per million (ppm).  $^1H$  and  $^{13}C\{^1H\}$  NMR spectra are referenced to residual solvent peaks.<sup>43</sup>  $^{31}P\{^1H\}$  chemical shifts are referenced to an external 85%  $H_3PO_4$  (0 ppm) standard. Multiplicities are abbreviated as follows: s = singlet, d = doublet, dd = doublet of doublets, ddd = doublet of doublet of doublets, t = triplet, vt = virtual triplet, app t = apparent triplet, dt = doublet of triplets, q = quartet, qq = quartet of quartets, m = multiplet, and br = broad. Elemental analysis was performed at the Caltech XRCF using a PerkinElmer 2400 Series II CHN Elemental Analyzer.

Synthesis of **2**

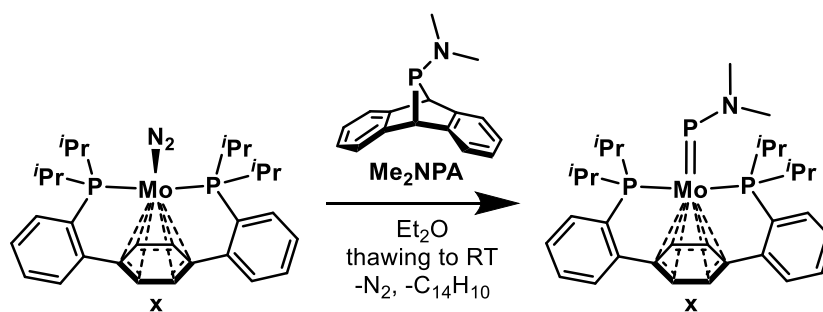
A 50 mL round bottom flask was charged with **1** (300 mg, 0.51 mmol), PhMe (5 mL), MeCN (2 mL), and a stir bar. After mixing for five minutes, the resulting red/brown solution was frozen in an LN<sub>2</sub> cooled cold well. A 20 mL scintillation vial was charged with a toluene solution of **CIPA** (137 mg, 0.56 mmol in 3 mL) and likewise frozen. The two solutions were combined, with stirring, immediately upon thawing. The round bottom was sealed and left to stir for one hour. At this time, the dark brown solution was dried *in vacuo*, providing a dark residue. Toluene was added to the residue which was transferred to a 20 mL scintillation vial and chilled to -35 °C for 8 hours. Collection of the resulting solids via vacuum filtration provided **2** as a black powder (212 mg, 0.34 mmol, 67% yield). Even after pumping on this powder for prolonged periods (>8 hours), a toluene solvent impurity persisted. Aside from this, the samples proved analytically pure. X-ray quality crystals of **2** could be grown by chilling a saturated toluene solution of **2** to -35 °C for two days or by slow diffusion of pentane into THF solutions of **2** at -35°C. <sup>1</sup>H (500 MHz, C<sub>6</sub>D<sub>6</sub>, 25 °C) δ: 7.33-7.36 (m, 4H, aryl-*H*), 7.15-7.19 (m, 4H, aryl-*H*), 5.86 (s, 2H, central arene-*H*), 5.46 (t, *J* = 2.8 Hz, 2H, central arene-*H*), 3.89-3.97 (m, 2H, CH(CH<sub>3</sub>)<sub>2</sub>), 2.69-2.77 (m, 2H, CH(CH<sub>3</sub>)<sub>2</sub>), 1.98-2.03 (m, 6H, CH(CH<sub>3</sub>)<sub>2</sub>), 1.51-1.55 (m, 6H, CH(CH<sub>3</sub>)<sub>2</sub>), 0.72-0.75 (m, 6H, CH(CH<sub>3</sub>)<sub>2</sub>), 0.16-0.20 (m, 6H, CH(CH<sub>3</sub>)<sub>2</sub>). <sup>13</sup>C{<sup>1</sup>H} (126 MHz, C<sub>6</sub>D<sub>6</sub>, 25 °C) δ: 151.14 (vt, *J* = 6.5 Hz, aryl-C), 142.07 (vt, *J* = 4.7 Hz, central arene-C), 132.06 (s, aryl-C), 130.30 (s, aryl-C), 127.42 (vt, *J* = 2.3 Hz, aryl-C), 127.16 (vt, *J* = 2.8 Hz, aryl-C), 123.45 (vt, *J* = 13.9 Hz, aryl-C), 123.19 (s, central arene-C), 59.73 (vt, *J* = 3.5 Hz, central arene-C), 22.03 (vt, *J* = 7.5 Hz, CH(CH<sub>3</sub>)<sub>2</sub>), 21.36 (vt, *J* = 9.1 Hz,

CH(CH<sub>3</sub>)<sub>2</sub>), 19.50 (br, CH(CH<sub>3</sub>)<sub>2</sub>), 17.71 (br, CH(CH<sub>3</sub>)<sub>2</sub>), 17.58 (br, CH(CH<sub>3</sub>)<sub>2</sub>), 15.81 (br, CH(CH<sub>3</sub>)<sub>2</sub>). <sup>31</sup>P{<sup>1</sup>H} (162 MHz, C<sub>6</sub>D<sub>6</sub>, 23 °C) δ: 1300.73 (br t, Mo≡P), 41.27 (d, J = 11.1 Hz, P<sub>2</sub>). Anal. Calcd. for **2**·<sup>1</sup>/<sub>2</sub>PhMe C<sub>33.5</sub>H<sub>44</sub>ClMoP<sub>3</sub> (%): C, 59.96; H, 6.61; N, 0.00 Found: C, 60.45, H, 6.29, N, <0.01.

### Synthesis of **3**



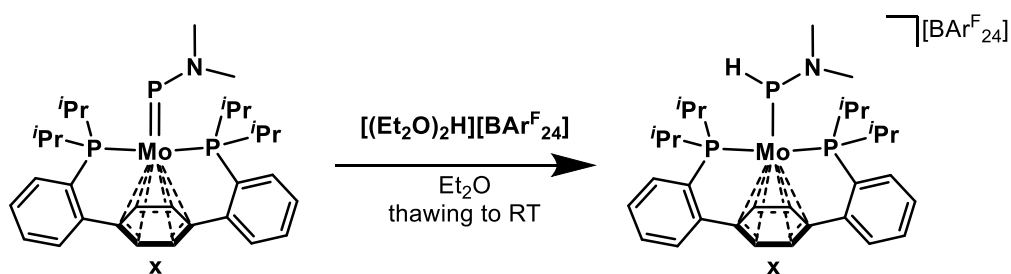
A 20 mL scintillation vial was charged with complex **2** (320 mg, 0.51 mmol) and a stir bar. THF (10 mL) was added and stirring was initiated, providing a red/brown solution. A second 20 mL scintillation vial was charged with a deep blue THF solution (10 mL) of [Fc][BARF<sub>24</sub>] (539 mg, 0.51 mmol). Both vials were placed in an LN<sub>2</sub> cooled cold well and the contents frozen. Upon thawing, the solution of [Fc][BARF<sub>24</sub>] was added dropwise to the solution of **2** with rapid stirring, resulting in an immediate color change to purple. Following the addition, the vial was returned to the cold well and to contents refrozen. The vial contents were allowed to thaw, mixed while cold, and then refrozen. This process was repeated four times, to facilitate complete oxidation of the starting material, and frozen a final time. A 125 mL Erlenmeyer flask charged with a stir bar, filled with pentane (100 mL), and placed in the cold well. Immediately upon thawing, the purple solution was added to the thawing pentane, with stirring, dropwise. A fine purple precipitate formed and the mixture was allowed to warm to room temperature. The solids were collected on a medium porosity frit, washed with hexanes (20 mL x 3), dried *in vacuo*, and collected as analytically pure **3** (710 mg, 0.48 mmol, 93%). X-ray quality crystals of **3** were obtained by vapor diffusion of pentane into a concentrated Et<sub>2</sub>O solution at -35 °C. The Et<sub>2</sub>O solution used for crystallization was prepared and filtered while cold to prevent further reactivity of complex **3**.

Synthesis of **3**

A 20 mL scintillation vial charged with a red/orange THF (3 mL) solution of **1** (300 mg, 0.51 mmol) and a stir bar was placed in a  $\text{LN}_2$  chilled cold well and the contents frozen. A solution of  $\text{Me}_2\text{NPA}$  (177 mg, 0.56 mmol) in  $\text{Et}_2\text{O}$  was likewise prepared and frozen. Immediately upon thawing, the ethereal suspension of  $\text{Me}_2\text{NPA}$  was added dropwise to the thawing solution of **1**. Stirring was initiated and the reaction was allowed to warm to room temperature, during which time it darkened significantly. After stirring at room temperature for 30 min., volatiles were removed *in vacuo*, affording a dark residue. This residue was triturated first with hexanes (2 mL) and then pentane (2 mL). Pentane (2 mL) was added to the vial which was sealed and placed in a  $-35\text{ }^\circ\text{C}$  freezer for 10 h. At this time, the contents of the vial were filtered through Celite. The filtrate was discarded and the filter cake was washed with room temperature pentane until the eluent was colorless (*ca.* 25 mL). This filtrate was concentrated to approximately 4 mL and chilled to  $-35\text{ }^\circ\text{C}$  for 2 h to precipitate a mixture of microcrystals of **3** and anthracene. The solids were collected by suction filtration on a fritted funnel and the filtrate was concentrated for a second precipitation. After two crops of solids, 230 mg of a mixture of **3** and anthracene was obtained (73% **3**: 27%  $\text{C}_{14}\text{H}_{10}$ , 0.27 mmol **3**, 52% yield) as dark red/brown microcrystalline solids. Efforts to further purify **3** away from anthracene were unsuccessful. Sublimation was attempted but resulted in decomposition of **3** to an intractable mixture of species upon even mild heating. Attempts to crystallize the metal complex away from the organic consistently provided mixtures of crystals. X-ray quality crystals of **3** were grown by chilling a saturated pentane solution to  $-35\text{ }^\circ\text{C}$  for 48 h, and were mechanically separated from co-crystallized anthracene immediately prior to diffraction.  $^1\text{H}$  (400 MHz,  $\text{C}_6\text{D}_6$ ,  $23\text{ }^\circ\text{C}$ )  $\delta$ : 7.49 (dt,  $J = 6.87$  &  $1.87$  Hz, 2H, aryl-*H*), 7.29-7.31 (m, 2H, aryl-*H*), 7.06 (t,  $J = 6.98$  Hz, 2H, aryl-*H*),

7.03 (t,  $J = 7.26$  Hz, 2H, aryl-*H*), 4.58 (s, 2H, central arene-*H*), 4.07 (t,  $J = 3.61$  Hz, 2H, central arene-*H*), 3.36 (br s, 3H, N(CH<sub>3</sub>)<sub>2</sub>), 3.24 (br s, 3H, N(CH<sub>3</sub>)<sub>2</sub>), 2.93-3.06 (m, 2H, CH(CH<sub>3</sub>)<sub>2</sub>), 2.17-2.29 (m, 2H, CH(CH<sub>3</sub>)<sub>2</sub>), 1.31-1.37 (m, 12H, CH(CH<sub>3</sub>)<sub>2</sub>), 1.07-1.15 (m, 12H, CH(CH<sub>3</sub>)<sub>2</sub>). <sup>13</sup>C{<sup>1</sup>H} (101 MHz, C<sub>6</sub>D<sub>6</sub>, 23 °C)  $\delta$ : 152.21 (d vt,  $J = 29.17$  & 14.07 Hz, aryl-C), 150.23 (d vt,  $J = 24.24$  & 13.56 Hz, aryl-C), 130.82 (s, aryl-C), 127.95 (vt,  $J = 3.95$  Hz, aryl-C; two aryl <sup>13</sup>C resonances coincide at this chemical shift as demonstrated by the <sup>1</sup>H/<sup>13</sup>C HSQC spectrum), 126.01 (vt,  $J = 1.89$  Hz, aryl-C), 97.86 (vt,  $J = 3.22$  Hz, central arene-C), 83.14 (s, central arene-C), 74.20 (s, central arene-C), 54.80 (br s, N(CH<sub>3</sub>)<sub>2</sub>), 47.47 (br s, N(CH<sub>3</sub>)<sub>2</sub>), 31.86 (vt,  $J = 4.88$  Hz, CH(CH<sub>3</sub>)<sub>2</sub>), 25.95 (vt,  $J = 6.07$  Hz, CH(CH<sub>3</sub>)<sub>2</sub>), 21.60 (br s, CH(CH<sub>3</sub>)<sub>2</sub>), 20.73 (br s, CH(CH<sub>3</sub>)<sub>2</sub>), 19.48 (br s, CH(CH<sub>3</sub>)<sub>2</sub>). <sup>31</sup>P{<sup>1</sup>H} (162 MHz, C<sub>6</sub>D<sub>6</sub>, 23 °C)  $\delta$ : 1027.89 (br t,  $J = 40.39$  Hz, PN(CH<sub>3</sub>)<sub>2</sub>), 63.27 (d,  $J = 40.69$  Hz, P2). Elemental analysis of complex **3** was forgone, as samples completely free of anthracene could not be prepared.

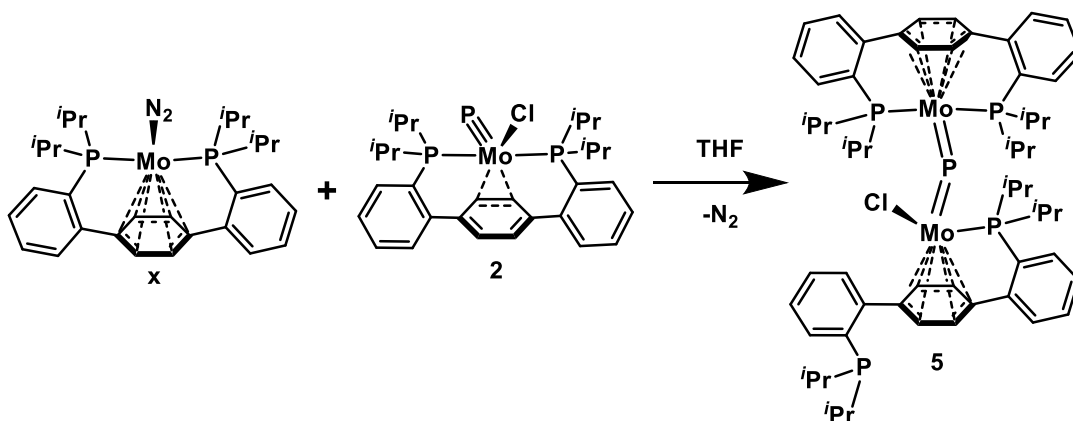
#### Synthesis of **4**



A 20 mL scintillation vial was charged with **3** (400 mg, 0.631 mmol), Et<sub>2</sub>O (5 mL), and a stir bar. It was placed in an LN<sub>2</sub> chilled cold well and the contents frozen. A second solution of [(Et<sub>2</sub>O)<sub>2</sub>H][BARF<sub>24</sub>] (638 mg, 0.631 mmol) in Et<sub>2</sub>O (5 mL) was similarly prepared in a vial and frozen. While thawing, the ethereal solution of acid was added to the solution of **3**, with stirring. After warming to room temperature, the volatiles were removed *in vacuo*. The resulting residue was triturated with pentane and then washed with hexanes (2 mL x 3). The residue was taken up in Et<sub>2</sub>O (*ca.* 2 mL), filtered into a 20 mL vial, layered with pentane (14 mL) and placed in a -35 °C freezer. After 12 h, compound **4** was collected on a medium porosity fritted funnel, via vacuum filtration, as greenish brown microcrystals (243 mg, 0.159 mmol, 25%

yield). X-ray quality crystals were obtained by vapor diffusion of pentane into a concentrated Et<sub>2</sub>O solution of **4** at -35 °C. Though stable as a solid stored at -35 °C, **4** decomposed within hours at room temperature as a solution in Et<sub>2</sub>O ( $t_{1/2} \approx 6$  h), THF ( $t_{1/2} \approx 1.5$  h), or MeCN ( $t_{1/2} < 1$  h). <sup>1</sup>H (500 MHz, THF-*d*8, -50 °C) δ: 10.09 (d,  $J = 323.17$  Hz, 1H, PH), 7.87 (br s, 8H, BAr<sup>F</sup><sub>24</sub> *ortho*-H), 7.68 (br s, 4H, BAr<sup>F</sup><sub>24</sub> *para*-H), 7.61-7.65 (m, 4H, aryl-H), 7.45-7.48 (m, 2H, aryl-H), 7.41-7.43 (m, 2H, aryl-H), 5.44 (br s, 2H, central arene-H), 5.37 (br, 2H, central arene-H), 3.15 (br s, 3H, N(CH<sub>3</sub>)<sub>2</sub>), 2.94 (br, 2H, CH(CH<sub>3</sub>)<sub>2</sub>), 2.73 (br s, 3H, N(CH<sub>3</sub>)<sub>2</sub>), 2.49 (br, 2H, CH(CH<sub>3</sub>)<sub>2</sub>), 1.27-1.30 (br m, 6H, CH(CH<sub>3</sub>)<sub>2</sub>), 1.16-1.21 (m, 6H, CH(CH<sub>3</sub>)<sub>2</sub>), 1.10 (br, 6H, CH(CH<sub>3</sub>)<sub>2</sub>), 1.01 (br, 6H, CH(CH<sub>3</sub>)<sub>2</sub>). <sup>13</sup>C{<sup>1</sup>H} (126 MHz, THF-*d*8, -50 °C) δ: 162.70 (q,  $J = 49.36$  Hz, BAr<sup>F</sup><sub>24</sub> aryl-C), 149.59 (d,  $J = 32.88$  Hz, aryl-C), 147.00 (d,  $J = 20.61$  Hz, aryl-C), 135.23 (br s, BAr<sup>F</sup><sub>24</sub> aryl-C), 132.99 (br s, aryl-C), 130.44 (s, aryl-C), 129.75 (qq,  $J = 31.38$  & 2.86 Hz, BAr<sup>F</sup><sub>24</sub> aryl-C), 128.24 (br, aryl-C), 128.15 (br, aryl-C), 125.24 (q,  $J = 272.35$  Hz, BAr<sup>F</sup><sub>24</sub> CF<sub>3</sub>), 118.15 (m, BAr<sup>F</sup><sub>24</sub> aryl-C), 102.86 (s, central arene-C), 97.17 (br, central arene-C), 83.69 (s, central arene-C), 48.02 (br s, N(CH<sub>3</sub>)<sub>2</sub>), 39.70 (br s, N(CH<sub>3</sub>)<sub>2</sub>), 31.79 (br, CH(CH<sub>3</sub>)<sub>2</sub>), 24.94 (CH(CH<sub>3</sub>)<sub>2</sub> coincides with the THF-*d*8 residual but is detected via <sup>1</sup>H/<sup>13</sup>C HSQC spectroscopy), 21.18 (br s, CH(CH<sub>3</sub>)<sub>2</sub>), 20.14 (br s, CH(CH<sub>3</sub>)<sub>2</sub>), 19.52 (s, CH(CH<sub>3</sub>)<sub>2</sub>), 18.23 (s, CH(CH<sub>3</sub>)<sub>2</sub>). <sup>31</sup>P{<sup>1</sup>H} (162 MHz, THF, 23 °C) δ: 296.04 (t,  $J = 48.87$  Hz, P(NMe<sub>2</sub>)(H)), 76.83 (d,  $J = 48.87$  Hz, P<sub>2</sub>). Anal. Calcd. for **4** C<sub>66</sub>H<sub>33</sub>BF<sub>24</sub>MoNP<sub>3</sub> (%): C, 51.95; H, 4.16; N, 0.92 Found: C, 51.64, H, 3.99, N, 0.72.

### Synthesis of **5**

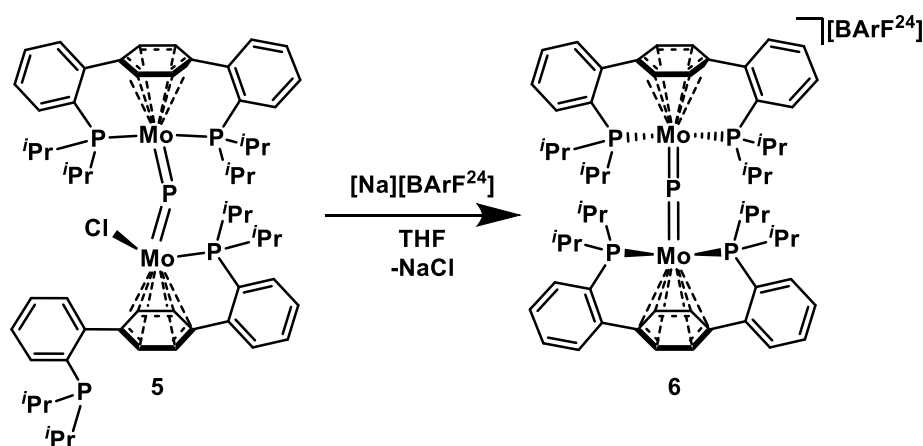




Complex **1** (38 mg, 0.064 mmol) was added to a 20 mL scintillation vial and dissolved in C<sub>6</sub>H<sub>6</sub> (2 mL) to afford a homogeneous red solution. A second scintillation vial was charged with a C<sub>6</sub>H<sub>6</sub> solution (3 mL) of **2** (40 mg, 0.064 mmol) and a stir bar. Stirring was initiated and the solution of **1** was added to the vial containing **2**, dropwise. The reaction was left to stir for 1 h, during which time it changed color from brown to deep red. The solvent was lyophilized and the resulting red powder was washed first with hexanes (1 mL x 3) and then Et<sub>2</sub>O (1 mL x 2). The residue was dried *in vacuo*, providing spectroscopically pure **5** as a dark red powder (66 mg, 0.056 mmol, 87% yield). X-ray quality crystals were obtained by diffusion of pentane into a PhMe solution of **5** at -35 °C or by layering hexanes onto a concentrated PhMe solution of **5**. <sup>1</sup>H (400 MHz, C<sub>6</sub>D<sub>6</sub>, 23 °C) δ: 9.00 (dd, *J* = 3.97 & 3.78 Hz, 1H, aryl-*H*), 7.46 (d, *J* = 7.25 Hz, 1H, aryl-*H*), 7.28-7.36 (m, 4H, aryl-*H*), 7.18-7.24 (m, 3H, aryl-*H*), 7.09-7.12 (m, 1H, aryl-*H*), 7.02-7.06 (m, 3H, aryl-*H*), 6.96-6.98 (m, 3H, aryl-*H*), 5.46 (d, *J* = 3.46 Hz, 1H, central arene-*H*), 5.29 (br s, 1H, central arene-*H*), 4.98 (d, *J* = 6.72 Hz, 1H, central arene-*H*), 4.95 (d, *J* = 4.35 Hz, 1H, central arene-*H*), 4.26 (d, *J* = 5.27 Hz, 1H, central arene-*H*), 4.03 (t, *J* = 5.07 Hz, 1H, central arene-*H*), 3.88 (t, *J* = 4.97 Hz, 1H, central arene-*H*), 3.62 (d, *J* = 6.76 Hz, 1H, central arene-*H*), 2.75-2.84 (m, 1H, CH(CH<sub>3</sub>)<sub>2</sub>), 2.64-2.72 (m, 2H, CH(CH<sub>3</sub>)<sub>2</sub>), 2.38-2.45 (m, 1H, CH(CH<sub>3</sub>)<sub>2</sub>), 2.17-2.27 (m, 2H, CH(CH<sub>3</sub>)<sub>2</sub>), 2.08 (m, 1H, CH(CH<sub>3</sub>)<sub>2</sub>), 1.79-1.88 (m, 1H, CH(CH<sub>3</sub>)<sub>2</sub>), 1.63-1.69 (m, 3H, CH(CH<sub>3</sub>)<sub>2</sub>), 1.45-1.50 (m, 3H, CH(CH<sub>3</sub>)<sub>2</sub>), 1.24-1.41 (m, 12H, CH(CH<sub>3</sub>)<sub>2</sub>), 1.15-1.20 (m, 9H, CH(CH<sub>3</sub>)<sub>2</sub>), 0.86-1.02 (m, 15H, CH(CH<sub>3</sub>)<sub>2</sub>), 0.78-0.84 (m, 3H, CH(CH<sub>3</sub>)<sub>2</sub>), 0.45-0.50 (m, 3H, CH(CH<sub>3</sub>)<sub>2</sub>). <sup>13</sup>C{<sup>1</sup>H} (126 MHz, C<sub>6</sub>D<sub>6</sub>, 23 °C) δ: 151.23 (d, *J* = 29.67 Hz, aryl-*C*), 150.93 (d, *J* = 29.15 Hz, aryl-*C*), 150.78 (d, *J* = 24.60 Hz, aryl-*C*), 149.84 (d, *J* = 23.19 Hz, aryl-*C*), 149.02 (d, *J* = 22.69 Hz, aryl-*C*), 147.64 (d, *J* = 22.28 Hz, aryl-*C*), 146.98 (d, *J* = 30.92 Hz, aryl-*C*), 134.09 (d, *J* = 23.08 Hz, aryl-*C*), 133.99 (d, *J* = 4.61 Hz, aryl-*C*), 131.57 (d, *J* = 4.44 Hz, aryl-*C*), 131.54 (d, *J* = 2.58 Hz, aryl-*C*), 130.86 (s, aryl-*C*), 129.24 (br s, aryl-*C*), 129.20 (d, *J* = 1.73 Hz, aryl-*C*), 129.00 (br s, aryl-*C*), 128.69 (br d, *J* = 1.46 Hz, aryl-*C*), 128.50 (br d, *J* = 2.52 Hz, aryl-*C*), 127.55 (br s, aryl-*C*; four overlapping <sup>13</sup>C resonances appear within a range of 0.18 ppm inhibiting multiplicity assignments—the signals are

unequivocally observed in the  $^1\text{H}/^{13}\text{C}$  HSQC spectrum), 127.47 (br, aryl-C), 127.41 (br, aryl-C), 127.37 (br, aryl-C), 181.11 (d,  $J = 4.18$  Hz, central arene-C), 116.34 (s, central arene-C), 103.56 (br, central arene-C), 101.61 (br d,  $J = 3.69$  Hz, central arene-C), 99.75 (br m, central arene-C), 88.75 (s, central arene-C), 86.68 (s, central arene-C), 84.26 (s, central arene-C), 83.52 (d,  $J = 17.50$  Hz, central arene-C), 79.26 (d,  $J = 3.58$  Hz, central arene-C), 78.86 (d,  $J = 3.35$  Hz, central arene-C), 76.21 (s, central arene-C), 33.38 (d,  $J = 18.04$  Hz,  $\text{CH}(\text{CH}_3)_2$ ), 31.39 (d,  $J = 15.52$  Hz,  $\text{CH}(\text{CH}_3)_2$ ), 31.33 (d,  $J = 13.37$  Hz,  $\text{CH}(\text{CH}_3)_2$ ), 30.25 (d,  $J = 9.55$  Hz,  $\text{CH}(\text{CH}_3)_2$ ), 29.79 (d,  $J = 9.59$  Hz,  $\text{CH}(\text{CH}_3)_2$ ), 26.24 (d,  $J = 16.30$  Hz,  $\text{CH}(\text{CH}_3)_2$ ), 26.09 (d,  $J = 12.25$  Hz,  $\text{CH}(\text{CH}_3)_2$ ), 22.76 (s,  $\text{CH}(\text{CH}_3)_2$ ), 21.86 (d,  $J = 18.32$  Hz,  $\text{CH}(\text{CH}_3)_2$ ), 21.71 (d,  $J = 6.82$  Hz,  $\text{CH}(\text{CH}_3)_2$ ), 21.56 (d,  $J = 7.72$  Hz,  $\text{CH}(\text{CH}_3)_2$ ), 21.08 (d,  $J = 3.40$  Hz,  $\text{CH}(\text{CH}_3)_2$ ), 20.90 (br s,  $\text{CH}(\text{CH}_3)_2$ ), 20.79 (d,  $J = 11.24$  Hz,  $\text{CH}(\text{CH}_3)_2$ ), 20.66 (d,  $J = 1.96$  Hz,  $\text{CH}(\text{CH}_3)_2$ ), 20.44 (s,  $\text{CH}(\text{CH}_3)_2$ ), 20.15 (d,  $J = 3.45$  Hz,  $\text{CH}(\text{CH}_3)_2$ ), 20.11 (d,  $J = 20.85$  Hz,  $\text{CH}(\text{CH}_3)_2$ ), 19.92 (s,  $\text{CH}(\text{CH}_3)_2$ ), 19.78 (d,  $J = 3.54$  Hz,  $\text{CH}(\text{CH}_3)_2$ ), 18.79 (d,  $J = 5.56$  Hz,  $\text{CH}(\text{CH}_3)_2$ ), 18.65 (d,  $J = 7.50$  Hz,  $\text{CH}(\text{CH}_3)_2$ ), 18.39 (d,  $J = 5.14$  Hz,  $\text{CH}(\text{CH}_3)_2$ ), 17.85 (d,  $J = 6.46$  Hz,  $\text{CH}(\text{CH}_3)_2$ ).  $^{31}\text{P}\{^1\text{H}\}$  (162 MHz,  $\text{C}_6\text{D}_6$ , 23 °C)  $\delta$ : 1161.00 (br s,  $\mu\text{-P}$ ), 82.89 (d,  $J = 13.21$  Hz, Mo-P), 73.74 (app t,  $J = 19.59$ , Mo-P), 70.34 (app t,  $J = 18.47$  Hz, Mo-P), -5.27 (s).

### Synthesis of 6

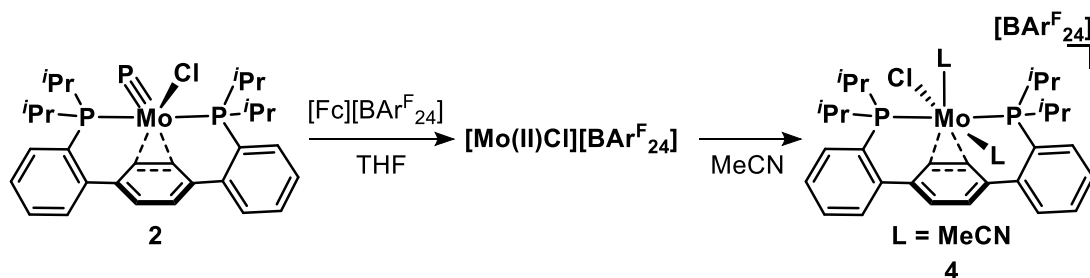


A solution of  $\text{Na}[\text{BArF}_{24}]$  (33 mg, 0.037 mmol) in  $\text{Et}_2\text{O}$  (2 mL) was added to a 20 mL scintillation vial charged with a  $\text{C}_6\text{H}_6$  (3 mL) solution of **5** (40 mg, 0.034 mmol) and a stir bar.

The vial was capped and left to stir for 12 h; during this time, a significant amount of precipitate formed. The suspension was filtered through Celite, and the filter cake washed with Et<sub>2</sub>O (1 mL x 3) and then C<sub>6</sub>H<sub>6</sub> (1 mL x 3). The residue was then extracted with THF until the filtrate was colorless. The deep red THF solution was concentrated under reduced pressure (to a volume of *ca.* 1 mL) and layered with pentane (10 mL). After 12 h, complex **6** was collected as analytically pure dark red microcrystals (43 mg, 0.024 mmol, 72% yield). X-ray quality single crystals of **6** were grown from the diffusion of pentane into a THF solution of the complex. <sup>1</sup>H (500 MHz, THF-*d*8, 25 °C) δ: 7.80 (br s, 8H, BAr<sup>F</sup><sub>24</sub> *ortho*-H), 7.58 (s, 4H, BAr<sup>F</sup><sub>24</sub> *para*-H), 7.50 (d, *J* = 7.69 Hz, 4H, aryl-H), 7.42 (br d, *J* = 7.32 Hz, 4H, aryl-H), 7.37 (app t, *J* = 6.96 Hz, 4H, aryl-H), 7.26 (app t, *J* = 7.57 Hz, 4H, aryl-H), 5.41 (s, 4H, central arene-H), 4.51 (s, 4H, central arene-H), 2.63-2.70 (m, 4H, CH(CH<sub>3</sub>)<sub>2</sub>), 2.18-2.23 (m, 4H, CH(CH<sub>3</sub>)<sub>2</sub>), 1.18-1.23 (m, 24H, CH(CH<sub>3</sub>)<sub>2</sub>), 0.94-0.98 (m, 12H, CH(CH<sub>3</sub>)<sub>2</sub>), 0.74-0.79 (m, 12H, CH(CH<sub>3</sub>)<sub>2</sub>). <sup>13</sup>C{<sup>1</sup>H} (126 MHz, THF-*d*8, 25 °C) δ: 161.82 (q, *J* = 49.83 Hz, BAr<sup>F</sup><sub>24</sub> aryl-C), 149.33 (d, *J* = 31.81 Hz, aryl-C), 147.61 (vt, *J* = 11.13 Hz, aryl-C), 134.60 (br s, BAr<sup>F</sup><sub>24</sub> aryl-C), 133.19 (s, BAr<sup>F</sup><sub>24</sub> aryl-C), 129.19 (s, aryl-C), 129.03 (qq, *J* = 31.49 & 2.86 Hz, BAr<sup>F</sup><sub>24</sub> aryl-C), 127.21 (vt, *J* = 3.80 Hz, aryl-C), 126.81 (br s, aryl-C), 124.52 (q, *J* = 272.37 Hz, BAr<sup>F</sup><sub>24</sub> CF<sub>3</sub>), 117.17 (m, BAr<sup>F</sup><sub>24</sub> aryl-C), 101.66 (t, *J* = 2.62 Hz, central arene-C), 93.62 (s, central arene-C), 81.93 (br s, central arene-C), 32.27 (br s, CH(CH<sub>3</sub>)<sub>2</sub>), 28.74 (br s, CH(CH<sub>3</sub>)<sub>2</sub>), 21.17 (s, CH(CH<sub>3</sub>)<sub>2</sub>), 19.85 (br s, CH(CH<sub>3</sub>)<sub>2</sub>), 19.61 (s, CH(CH<sub>3</sub>)<sub>2</sub>). <sup>31</sup>P{<sup>1</sup>H} (162 MHz, THF, 23 °C) δ: 1123.27 (br s, Mo=P), 68.62 (br s, P2). Anal. Calcd. for **6**•THF C<sub>96</sub>H<sub>100</sub>BF<sub>24</sub>Mo<sub>2</sub>OP<sub>5</sub> (%): C, 55.34; H, 4.84; N, 0.00 Found: C, 55.38, H, 5.21, N, 0.04.

## Phosphide Oxidation Reactions

### Formation of **4**



In a typical reaction, a 20 mL scintillation vial was charged with a THF (10 mL) solution of **2** (239 mg, 0.38 mmol) and a stir bar. The vial was placed in an LN<sub>2</sub> chilled cold well and the contents frozen. While thawing, a thawing solution of [Fc][BARF<sub>24</sub>] (400 mg, 0.38 mmol) in THF (6 mL) was added dropwise, with stirring. This addition resulted in an immediate color change to deep purple. Upon warming to room temperature, the color changed to a red/brown. An aliquot of the reaction mixture at this juncture showed clean conversion to a single diamagnetic <sup>31</sup>P{<sup>1</sup>H} NMR resonance at 76.3 ppm. The THF was removed under reduced pressure and the resulting residue triturated with hexanes (3 mL), providing a brown foamy solid. These solids were suspended in hexanes (6 mL) and filtered through celite. The filter cake was washed with a 3:1 mixture of hexanes and benzene (*ca.* 8 mL x 3) until the washes were colorless. The filter cake was extracted with Et<sub>2</sub>O (10 mL) and solvent was removed *in vacuo*, affording a tacky brown residue. The <sup>1</sup>H and <sup>31</sup>P{<sup>1</sup>H} NMR spectra of this material in CD<sub>3</sub>CN are consistent with a single diamagnetic metal complex, **4**. The BARF<sub>24</sub> salt of **4** eluded crystallization, but repeating the above procedure with [Fc][OTf] in lieu of [Fc][BARF<sub>24</sub>] and extracting the filter cake with MeCN (5 mL) rather than Et<sub>2</sub>O afforded the OTf salt of **4**. Single crystals of this complex were obtained from slow diffusion of Et<sub>2</sub>O into a concentrated MeCN solution of **4** at -35 °C. <sup>1</sup>H (400 MHz, CD<sub>3</sub>CN, 21 °C) δ: 7.73 (br, 8H, BARF<sub>24</sub> *ortho*-H), 7.69 (br, 4H, BARF<sub>24</sub> *para*-H), 7.56-7.61 (m, 4H, aryl-H), 7.51-7.54 (m, 2H, aryl-H), 7.39-7.41 (m,

2H, aryl-*H*), 5.20 (t,  $J = 3.81$  Hz, 4H, central arene-*H*), 3.24 (br m, 4H,  $\text{CH}(\text{CH}_3)_2$ ), 1.22-1.29 (m, 24H,  $\text{CH}(\text{CH}_3)_2$ ).  $^{31}\text{P}$  (162 MHz,  $\text{CD}_3\text{CN}$ , 21 °C)  $\delta$ : 69.26 (s).

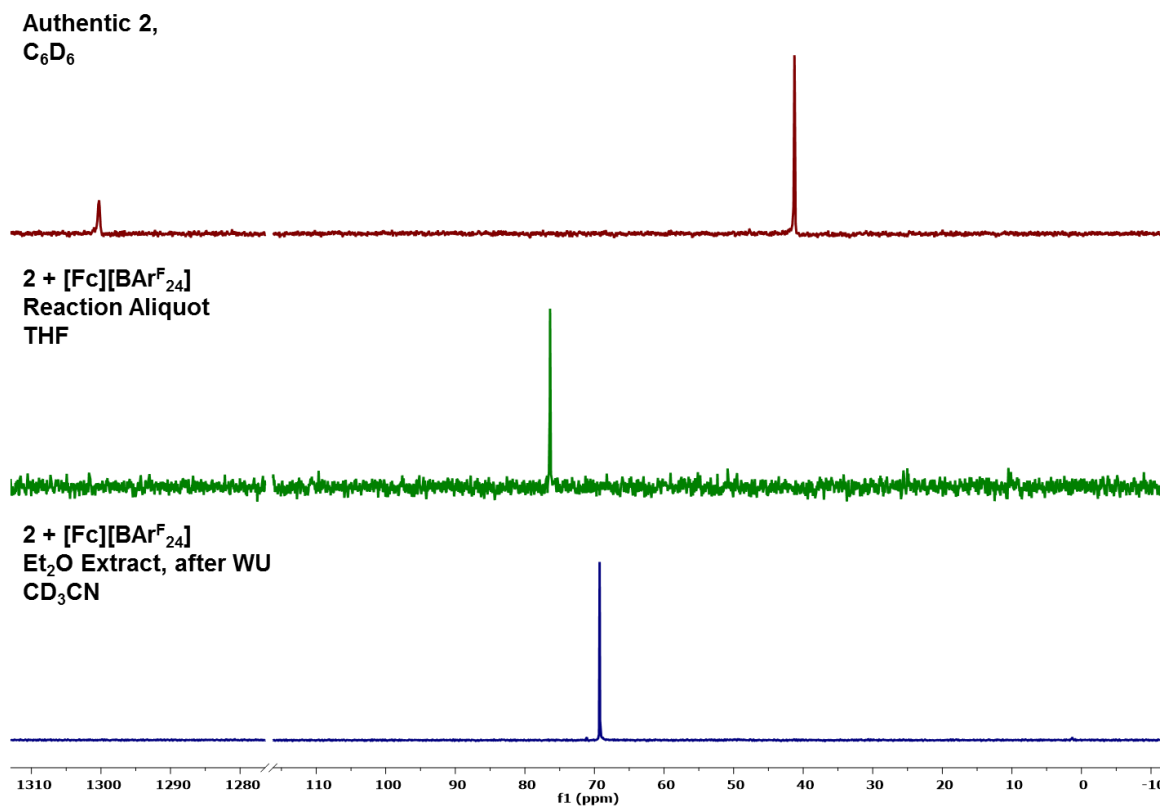


**Figure 6.10.** Partial  $^{31}\text{P}\{^1\text{H}\}$  NMR spectra tracking the one electron oxidation of **2**. A single resonance at 76.3 ppm is observed upon oxidation in THF (assigned to  $[\text{Mo}(\text{II})\text{Cl}][\text{BAR}^{\text{F}}_{24}]$ , Figure 6.10, middle) which shifts upfield to 69.3 ppm upon addition of MeCN. This species has been confirmed by single crystal XRD and independent synthesis as the bis(acetonitrile) chloride cation, **4**.

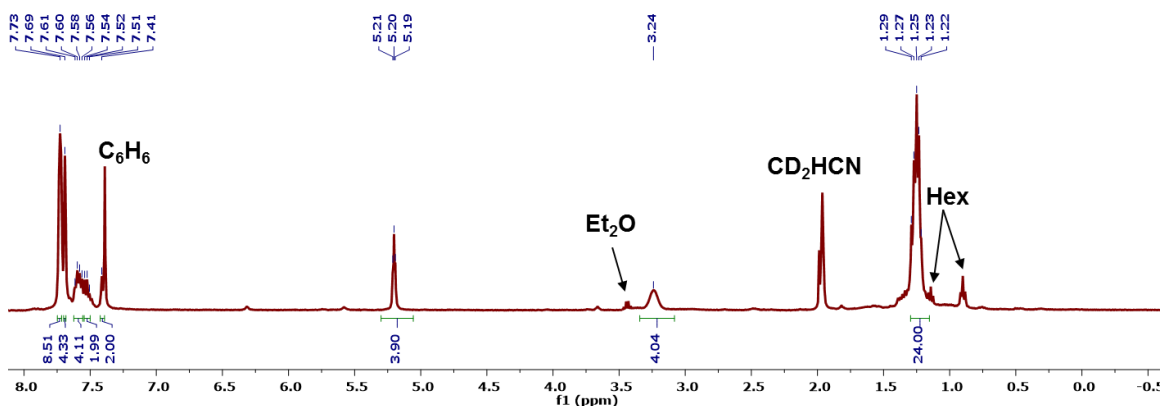


**Figure 6.11.**  $^1\text{H}$  NMR Spectrum (400 MHz,  $\text{CD}_3\text{CN}$ , 21°C) of **4**.

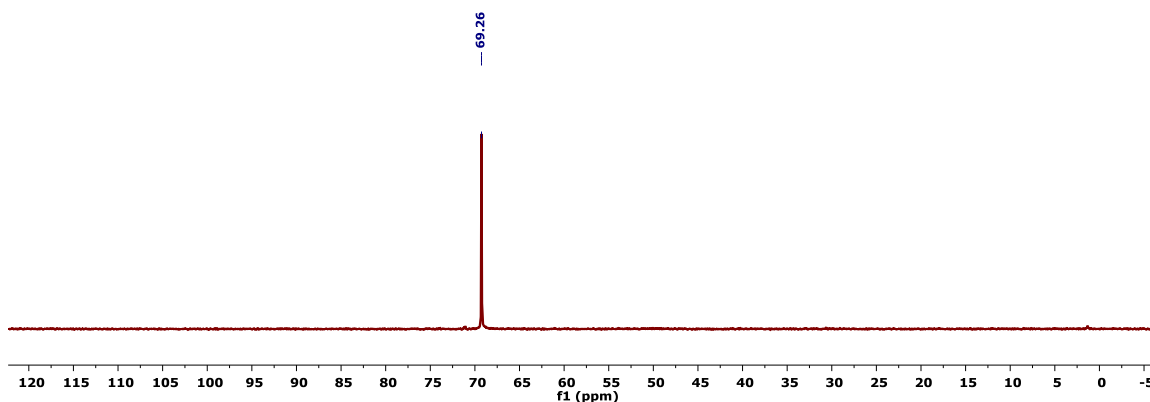
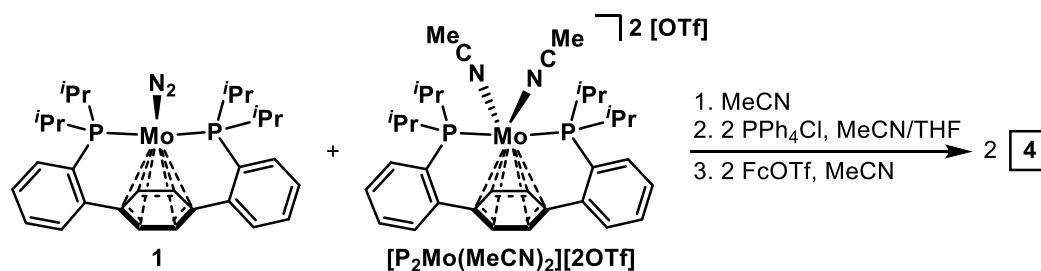


**Figure 6.12.**  $^{31}\text{P}\{^1\text{H}\}$  NMR Spectrum (126 MHz,  $\text{CD}_3\text{CN}$ ,  $21^\circ\text{C}$ ) of **4**.

*Independent Preparation of 4*



To confirm the identity of complex **4**, an independent preparation was performed according to the scheme above. A 20 mL scintillation vial was charged with **1** (200 mg, 0.34 mmol) and a stir bar. MeCN (5 mL) was added, resulting in a dark brown heterogeneous mixture. A MeCN (5 mL) solution of  $[\text{P}_2\text{Mo}(\text{MeCN})_2][2\text{OTf}]$  (320 mg, 0.33 mmol) was added dropwise, resulting in a color change to deep green. Solvent was removed *in vacuo* and the resulting green solids were suspended in  $\text{Et}_2\text{O}$  and filtered, washing away unreacted **1**. The filter cake was extracted with MeCN and volatiles were removed under reduced pressure. The resulting green residue was triturated with  $\text{Et}_2\text{O}$ , providing a pale green powder that was used without further purification or characterization.

To a THF (4 mL) solution of the green residue in a 20 mL scintillation vial charged with a stir bar, a MeCN (3 mL) solution of  $\text{PPh}_4\text{Cl}$  (25 mg, 0.067 mmol) was added with stirring. An immediate color change to red/orange was observed and the reaction was left to stir for 3 h. At this time, volatiles were removed *in vacuo* and the resulting solids triturated

with hexanes, providing an orange powder. Benzene was added and the resulting mixture filtered through celite. The filtrate was lyophilized, affording an orange powder that was used without further purification or characterization.

A J. Young NMR tube was charged with the aforementioned orange powder (20 mg, 0.034 mmol), [Fc][OTf] (11 mg, 0.034 mmol), and CD<sub>3</sub>CN (0.6 mL). Upon dissolution of the starting materials, the color darkened to red/brown. <sup>1</sup>H and <sup>31</sup>P{<sup>1</sup>H} NMR spectroscopy of the reaction mixture was consistent with formation of chloride cation **4**.

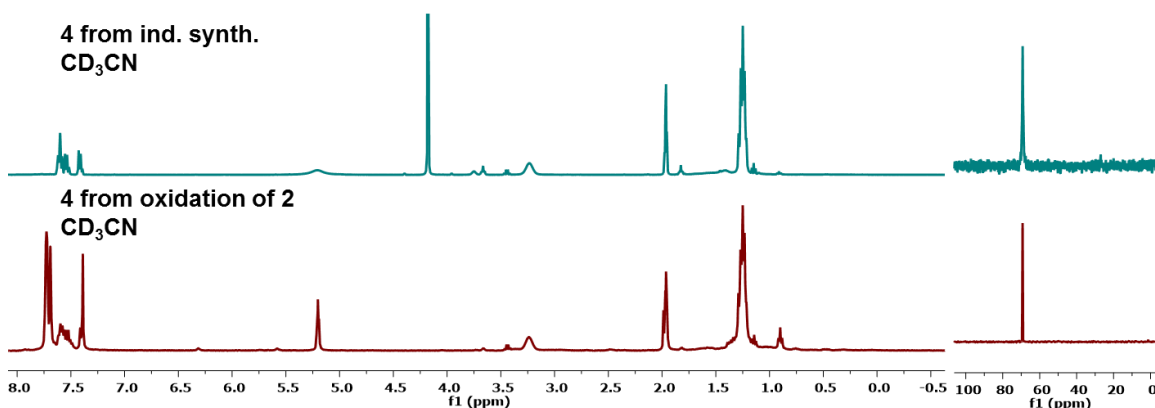
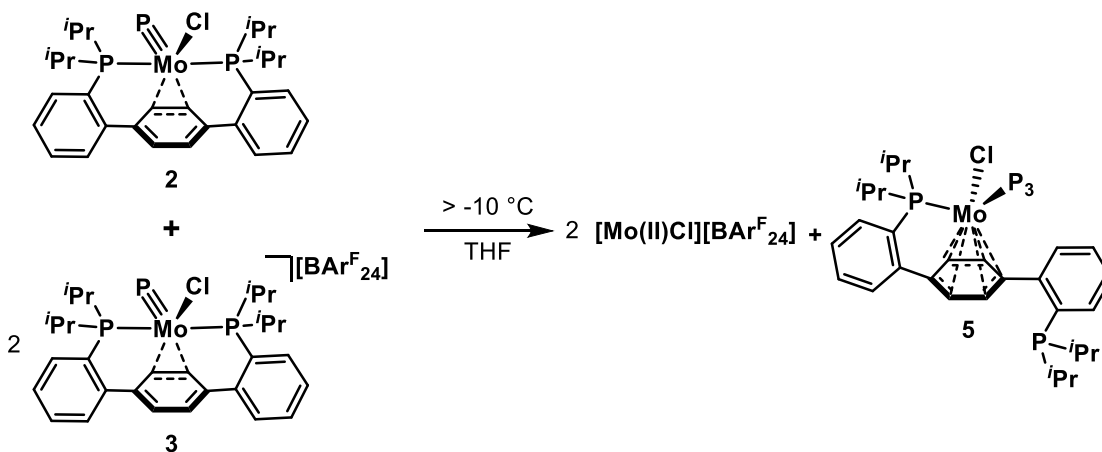


**Figure 6.13.** <sup>1</sup>H NMR Spectra (400 MHz, CD<sub>3</sub>CN, 21 °C—left) and <sup>31</sup>P{<sup>1</sup>H} NMR spectra (126 MHz, CD<sub>3</sub>CN, 21 °C—right) of complex **4** prepared via sequential conproportionation, chlorination, and oxidation (top) and phosphide oxidation (bottom).

#### Formation of **5**

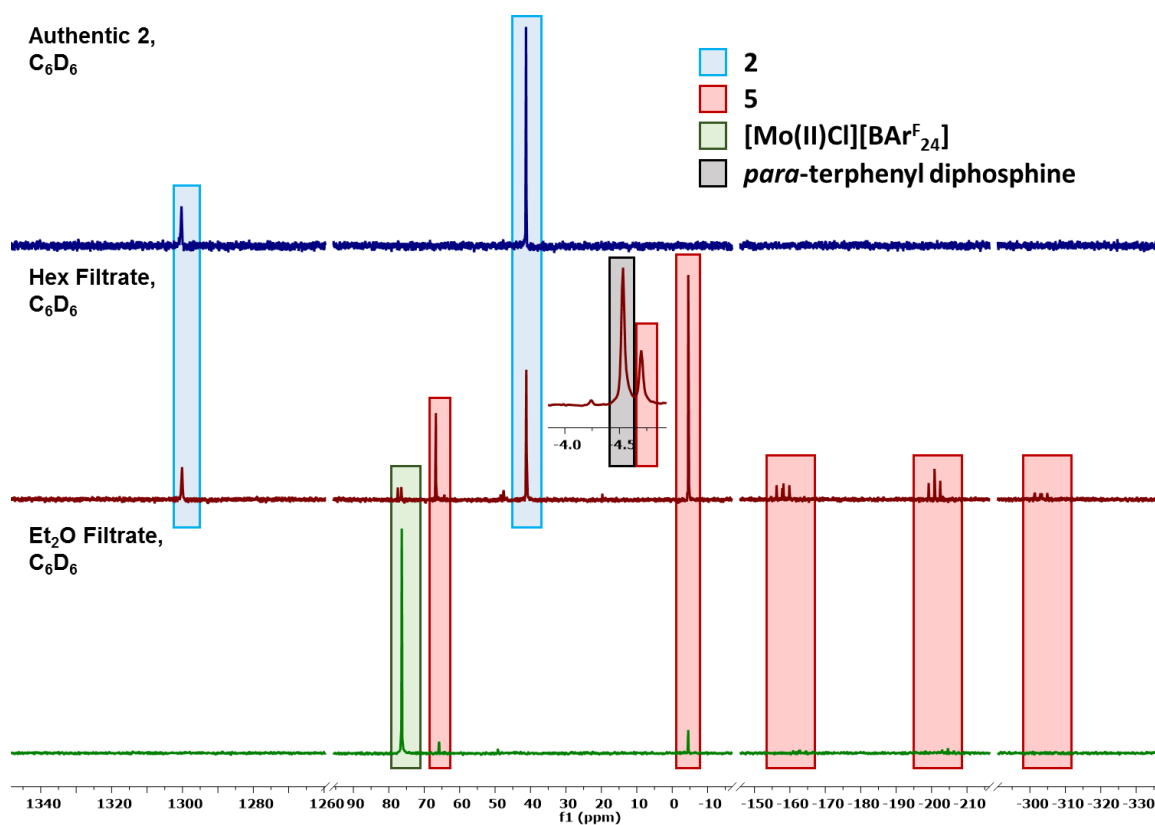


A 20 mL scintillation vial was charged with **3** (120 mg, 0.081 mmol) and a stir bar. The vial was placed in a LN<sub>2</sub> cooled cold well and the solids were cooled for 5 min. At this time, thawing THF (5 mL) was added, providing a deep purple solution. The vial was

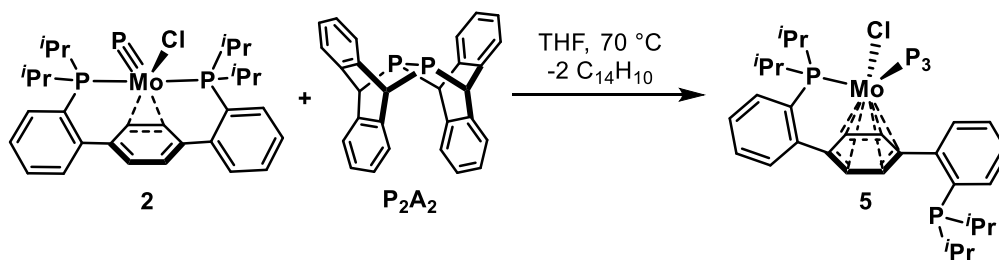
returned to the cold well and the solution frozen. Complex **2** (26 mg, 0.041 mmol) was added as a solid and the reaction mixture left to thaw, with stirring. After stirring at room temperature for 30 min, the volatiles were removed under reduced pressure, providing a brown residue. This residue was suspended in hexanes (5 mL) and filtered through Celite. The filter cake was extracted with hexanes (5 mL x 3) and these washes were combined. The remaining solids were washed with Et<sub>2</sub>O until the filtrate was colorless. Both filtrate solutions were dried *in vacuo*, providing mixtures primarily comprised of free *para*-terphenyl diphosphine, **2**, and **5** (hexane wash, Figure 6.14., middle), a Mo(II) chloride cation (which upon MeCN addition forms **4**), and a paramagnetic impurity (Et<sub>2</sub>O wash, Figure 6.14., bottom). <sup>1</sup>H (500 MHz, C<sub>6</sub>D<sub>6</sub>, 25 °C) δ: 8.08-8.09 (br m, 1H, aryl-*H*), 7.49 (br d, *J* = 6.04 Hz, 1H, aryl-*H*), 7.20-2.21 (m, 1H, aryl-*H*; overlaps with residual C<sub>6</sub>D<sub>5</sub>H but corroborated by 2D NMR), 7.11 (br dd, *J* = 7.83 Hz, 1H, aryl-*H*; overlaps with residual C<sub>6</sub>D<sub>5</sub>H but corroborated by 2D NMR), 7.01 (br dd, *J* = 6.71 Hz, 1H, aryl-*H*), 6.89 (br m, 2H, aryl-*H*), 6.77 (br m, 1H, aryl-*H*), 5.34 (br s, 1H, central arene-*H*), 5.25 (br d, *J* = 6.53 Hz, 1H, central arene-*H*), 4.58 (br d, *J* = 3.73 Hz, 1H, central arene-*H*), 4.20 (br s, 1H, central arene-*H*), 3.70-3.76 (m, 1H, CH(CH<sub>3</sub>)<sub>2</sub>), 3.03-3.09 (m, 1H, CH(CH<sub>3</sub>)<sub>2</sub>), 2.82-2.89 (m, 1H, CH(CH<sub>3</sub>)<sub>2</sub>), 2.40-2.49 (m, 1H, CH(CH<sub>3</sub>)<sub>2</sub>), 1.98-2.03 (m, 1H, CH(CH<sub>3</sub>)<sub>2</sub>), 1.69-1.74 (m, 1H, CH(CH<sub>3</sub>)<sub>2</sub>), 1.38-1.43 (m, 1H, CH(CH<sub>3</sub>)<sub>2</sub>; overlaps with residual THF but corroborated by 2D NMR), 1.03-1.09 (m, 1H, CH(CH<sub>3</sub>)<sub>2</sub>), 0.85-0.88 (m, 1H, CH(CH<sub>3</sub>)<sub>2</sub>; overlaps with *para*-terphenyl diphosphine impurity but corroborated by 2D NMR), 0.47-0.52 (m, 1H, CH(CH<sub>3</sub>)<sub>2</sub>), 0.28-0.32 (m, 1H, CH(CH<sub>3</sub>)<sub>2</sub>). <sup>13</sup>C {<sup>1</sup>H} (126 MHz, C<sub>6</sub>D<sub>6</sub>, 25 °C) δ: 148.78-148.89 (m, aryl-C), 145.95 (d, *J* = 8.08 Hz, aryl-C), 133.78 (s, aryl-C), 132.63 (s, aryl-C), 131.61 (d, *J* = 2.63 Hz, aryl-C), 131.03 (d, *J* = 4.93 Hz, aryl-C), 130.25 (s, aryl-C), 129.90 (s, aryl-C), 129.73 (s, aryl-C), 128.85 (s, aryl-C; overlaps with residual C<sub>6</sub>D<sub>6</sub> but corroborated by 2D NMR), 126.20 (d, *J* = 9.53 Hz, aryl-C), 123.08 (s, central arene-C), 106.46 (s, central arene-C), 94.11 (d, *J* = 16.59 Hz, central arene-C), 90.85 (d, *J* = 3.48 Hz, central arene-C), 85.95 (d, *J* = 2.06 Hz, central arene-C), 29.17 (d,



$J = 19.47$  Hz,  $\text{CH}(\text{CH}_3)_2$ , 27.68 (m,  $\text{CH}(\text{CH}_3)_2$ ), 25.09 (m,  $\text{CH}(\text{CH}_3)_2$ ), 23.26 (br s,  $\text{CH}(\text{CH}_3)_2$ ), 20.36 (s,  $\text{CH}(\text{CH}_3)_2$ ), 20.23 (s,  $\text{CH}(\text{CH}_3)_2$ ), 19.31 (d,  $J = 9.60$  Hz,  $\text{CH}(\text{CH}_3)_2$ ), 18.33 (s,  $\text{CH}(\text{CH}_3)_2$ ), 18.16 (s,  $\text{CH}(\text{CH}_3)_2$ ), 18.08 (d,  $J = 2.67$  Hz,  $\text{CH}(\text{CH}_3)_2$ ), 17.73 (s,  $\text{CH}(\text{CH}_3)_2$ ), 17.58 (d,  $J = 6.55$  Hz,  $\text{CH}(\text{CH}_3)_2$ ), 16.99 (m,  $\text{CH}(\text{CH}_3)_2$ ).  $^{31}\text{P}\{^1\text{H}\}$  (162 MHz,  $\text{C}_6\text{D}_6$ , 23 °C)  $\delta$ : 65.75 (d,  $J = 17.04$  Hz, Mo- $P_{\text{diphosphine}}$ ), -4.62 (s,  $P_{\text{diphosphine}}$ ), -162.35 (dd,  $J = 314.71$  and 264.90 Hz,  $P_3$ ), -204.70 (t,  $J = 264.90$  Hz,  $P_3$ ), -306.93 (ddd,  $J = 314.71$ , 264.90, and 17.04 Hz,  $P_3$ ).



**Figure 6.14.** Partial  $^{31}\text{P}\{^1\text{H}\}$  NMR spectra (126 MHz,  $\text{C}_6\text{D}_6$ , 25 °C) of an authentic sample of **2** (top), the hexane extract of a reaction between **2** and **3** (middle), and the diethyl ether extract of the same reaction (bottom).

Independent Synthesis of **5**

A J. Young NMR tube was charged with **2** (24 mg, 0.039 mmol), **P<sub>2</sub>A<sub>2</sub>** (17 mg, 0.039 mmol), and THF (600  $\mu$ L). A  $^{31}\text{P}\{^1\text{H}\}$  NMR spectrum of the resulting red/brown solution was recorded (Figure 6.15., top). The J. Young tube was placed in an oil bath pre-heated to 70  $^\circ\text{C}$  for 3 h. A second  $^{31}\text{P}\{^1\text{H}\}$  NMR spectrum was collected at this time, demonstrating consumption of **P<sub>2</sub>A<sub>2</sub>**, as well as a mixture of **2**, **5**, **P<sub>4</sub>**, and free *para*-terphenyl diphosphine (Figure 6.15., bottom).

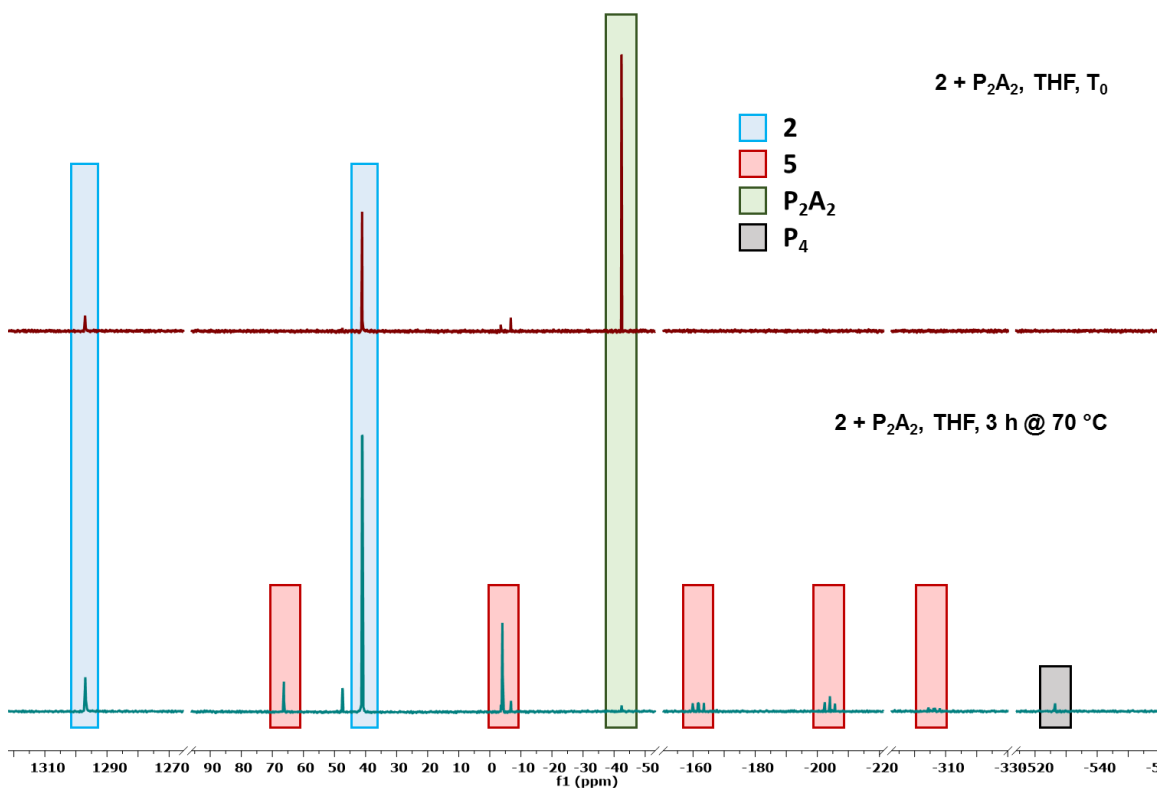


**Figure 6.15.** Partial  $^{31}\text{P}\{^1\text{H}\}$  NMR spectra (126 MHz, THF, 25  $^\circ\text{C}$ ) of a 1:1 mixture of **2** and **P<sub>2</sub>A<sub>2</sub>** prior to (top) and following (bottom) heating to 70  $^\circ\text{C}$ .

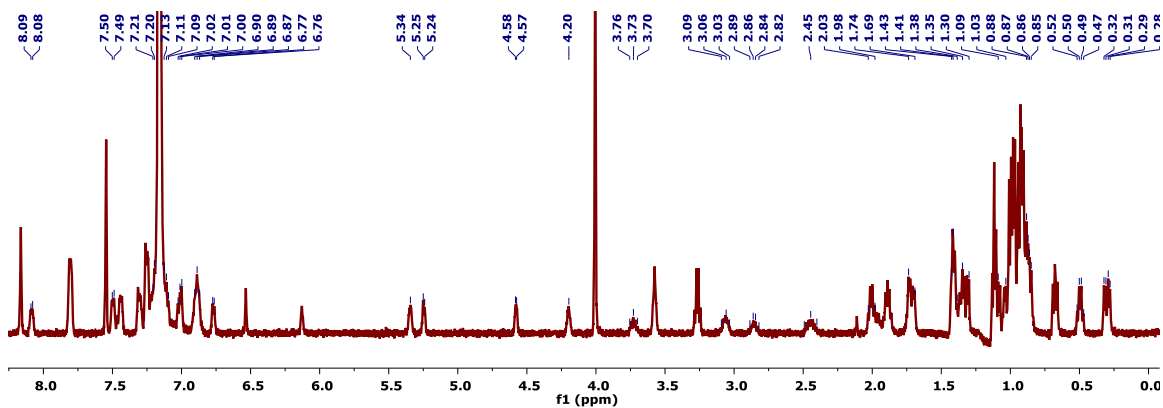


**Figure 6.16.**  $^1\text{H}$  NMR Spectrum (400 MHz,  $\text{C}_6\text{D}_6$ ,  $25^\circ\text{C}$ ) of a mixture containing **5** as the major component. Only the resonances corresponding to **5** are labeled.

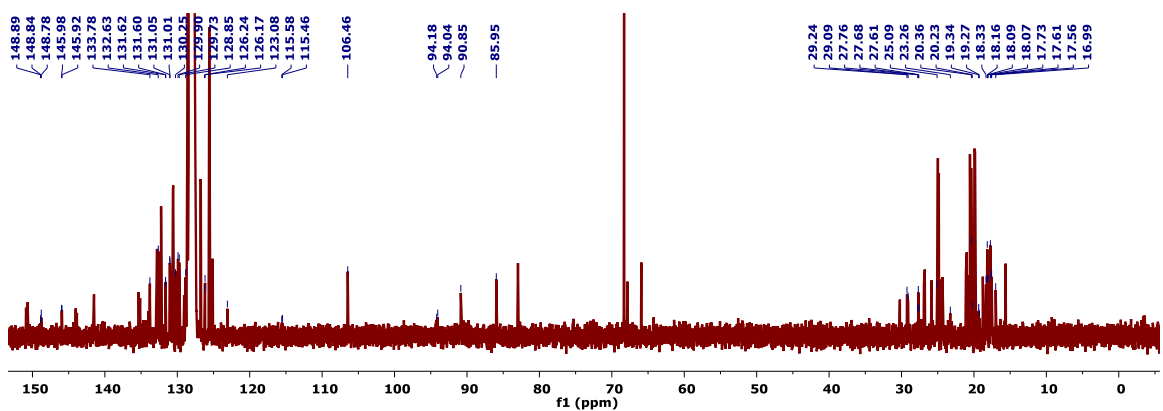


**Figure 6.17.**  $^{13}\text{C}\{^1\text{H}\}$  NMR Spectrum (126 MHz,  $\text{C}_6\text{D}_6$ ,  $25^\circ\text{C}$ ) of a mixture containing **5** as the major component. Only the resonances corresponding to **5** are labeled.

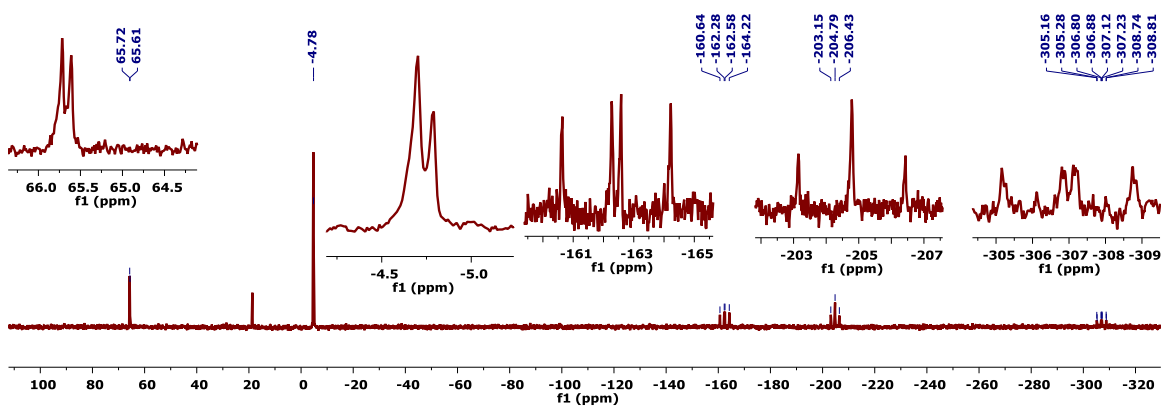
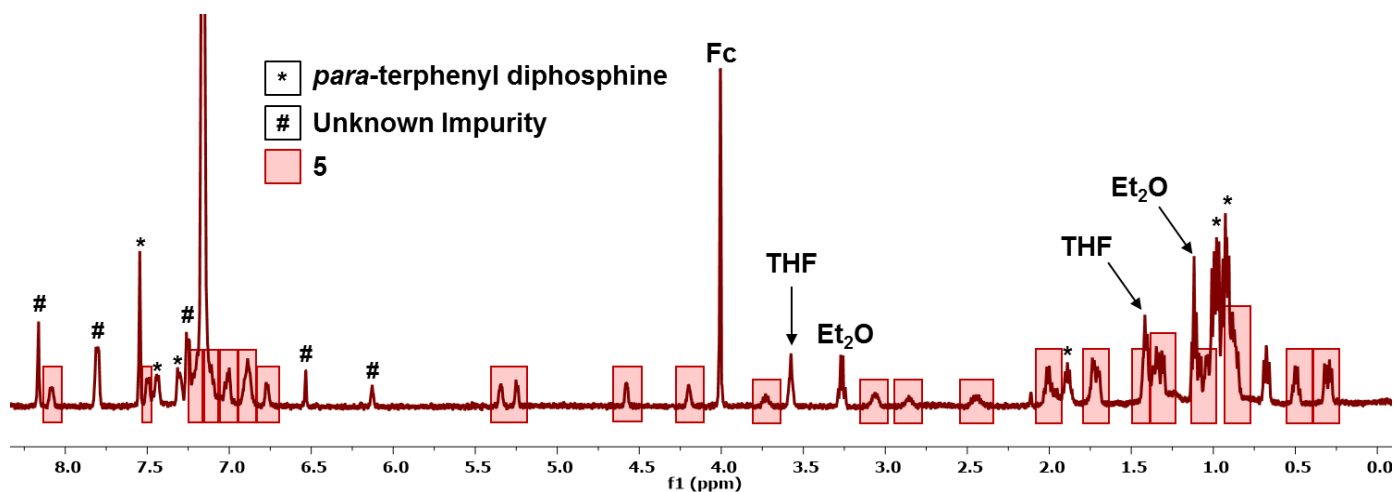


**Figure 6.18.**  $^{31}\text{P}\{^1\text{H}\}$  NMR Spectrum (162 MHz,  $\text{C}_6\text{D}_6$ ,  $23^\circ\text{C}$ ) of a mixture containing **5** as the major component. Only the resonances corresponding to **5** are labeled.



**Figures 6.19.**  $^1\text{H}$  NMR Spectrum (500 MHz,  $\text{C}_6\text{D}_6$ ,  $25^\circ\text{C}$ ) of a mixture containing **5** as the major component. All resonances have been assigned, with those corresponding to complex **5** emphasized in red.

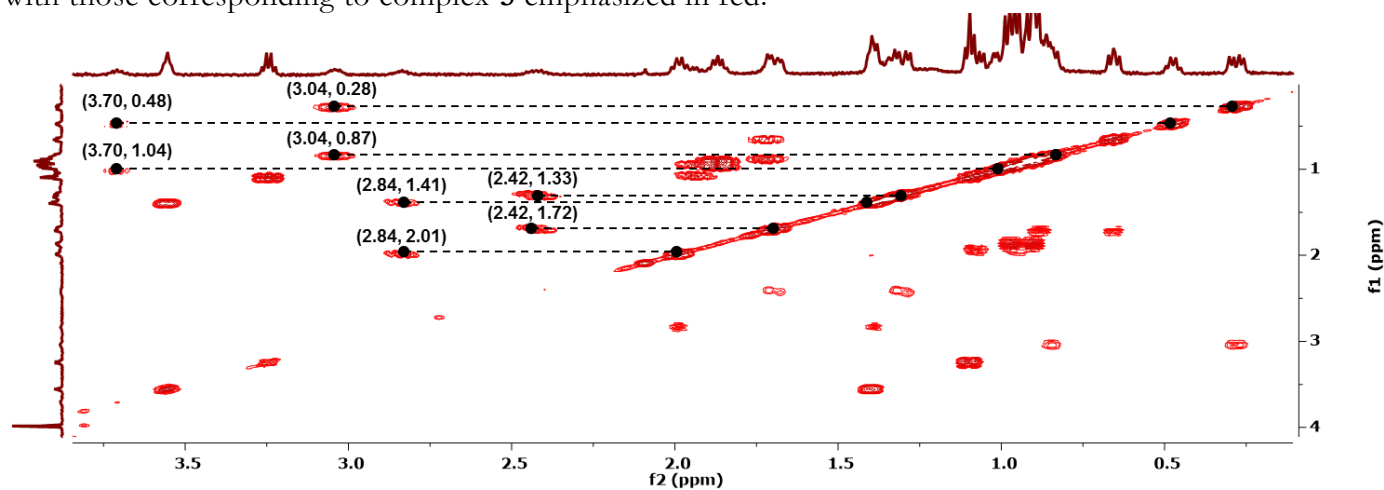


**Figure 6.20.** Partial  $^1\text{H}/^1\text{H}$  COSY NMR Spectrum (500 MHz,  $\text{C}_6\text{D}_6$ ,  $25^\circ\text{C}$ ) of mixture containing **5** as the major component. The scalar coupling correlations between the isopropyl methine and isopropyl methyl resonances are labeled.

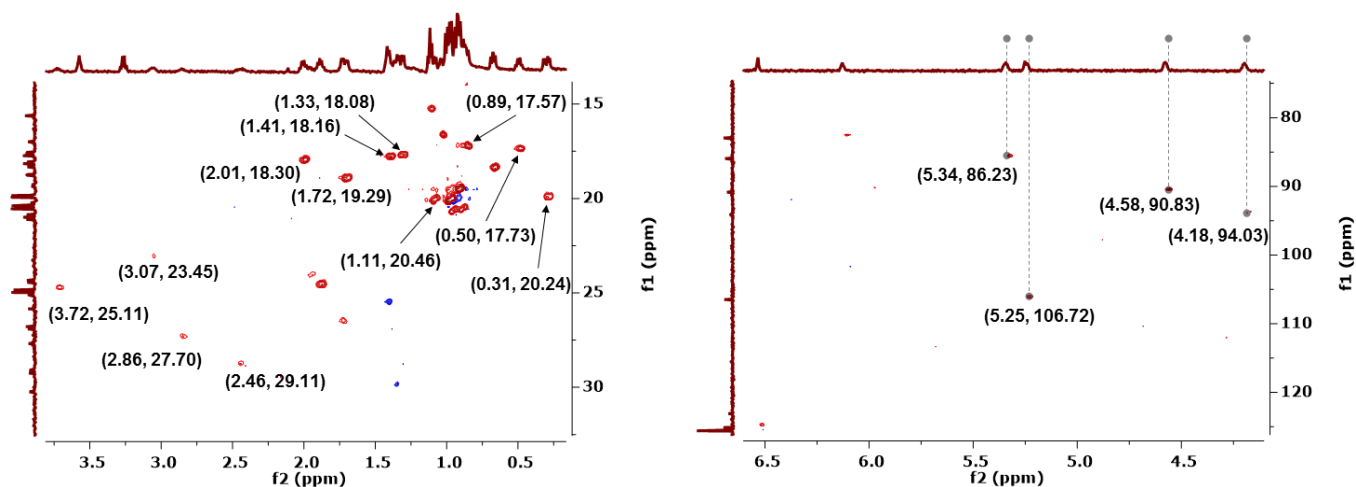


**Figure 6.21.** Partial  $^1\text{H}/^{13}\text{C}$  HSQC NMR Spectra (500/126 MHz,  $\text{C}_6\text{D}_6$ ,  $25^\circ\text{C}$ ) of mixture containing **5** as the major component. Cross peaks corresponding to the aliphatic (left) and central arene (center)  $^1J(\text{C},\text{H})$  correlations are labeled.

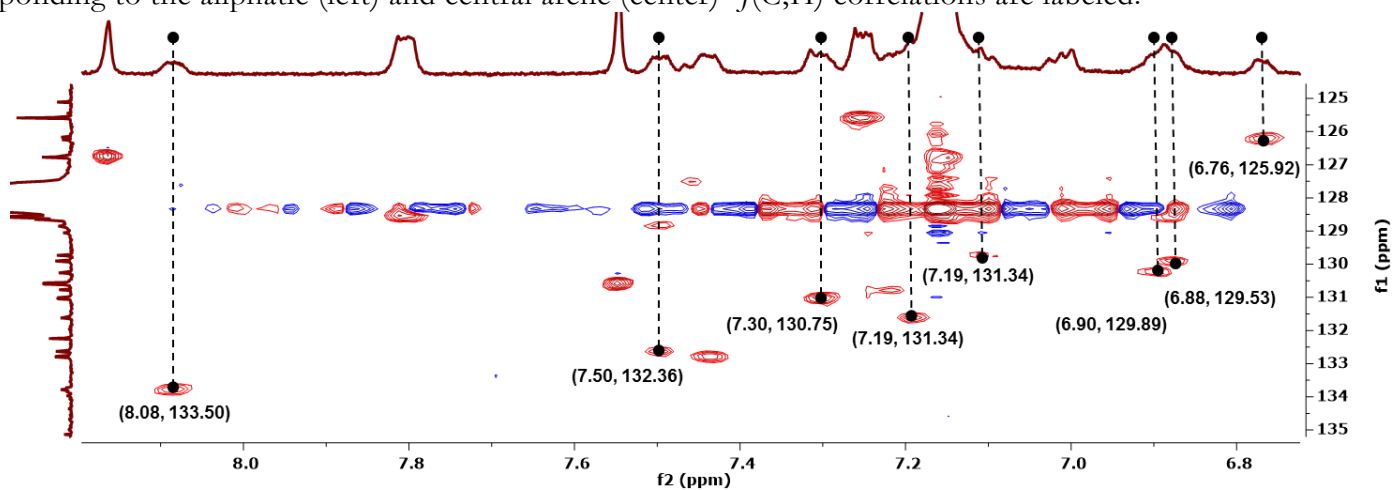


**Figure 6.22.** Partial  $^1\text{H}/^{13}\text{C}$  HSQC NMR Spectrum (500/126 MHz,  $\text{C}_6\text{D}_6$ ,  $25^\circ\text{C}$ ) of a mixture containing **5** as the major component.

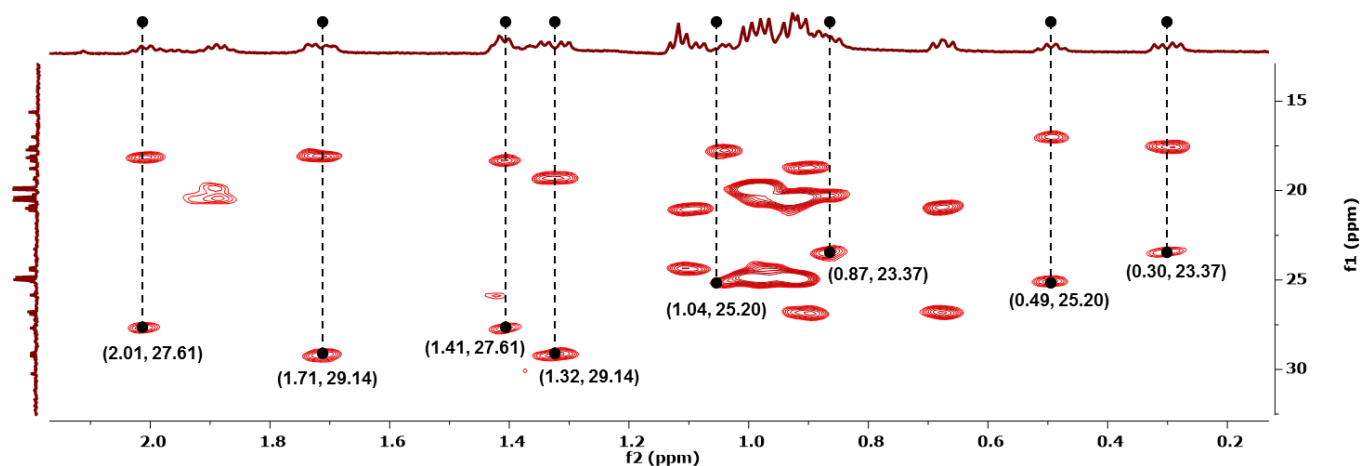


**Figure 6.23.** Partial  $^1\text{H}/^{13}\text{C}$  HMBC NMR Spectrum (500/126 MHz,  $\text{C}_6\text{D}_6$ ,  $25^\circ\text{C}$ ) of a mixture containing **5** as the major component.

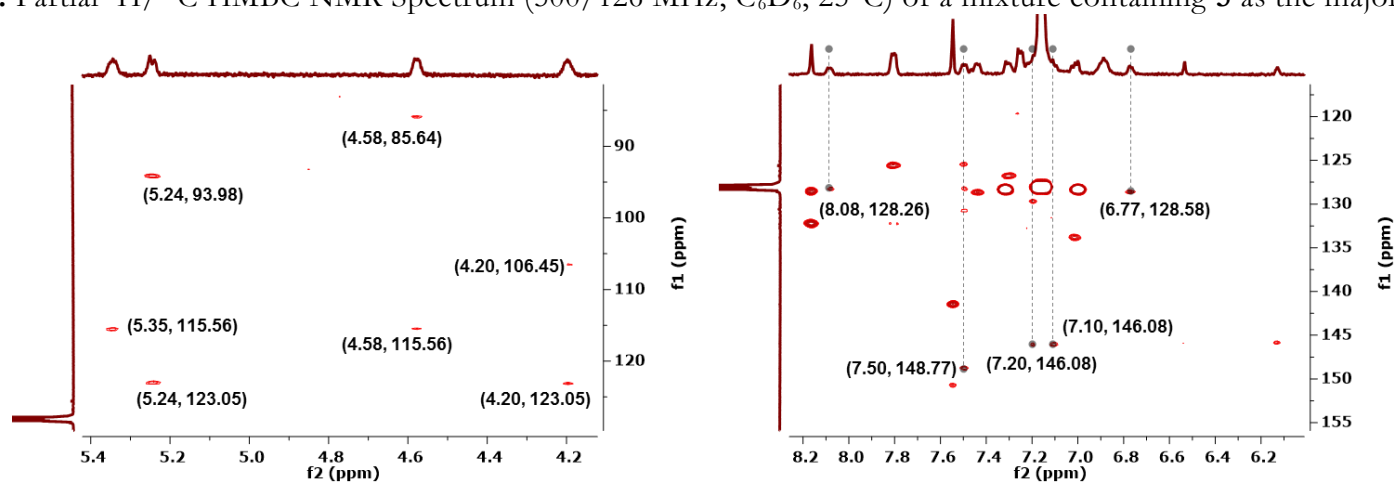


**Figure 6.24.** Partial  $^1\text{H}/^{13}\text{C}$  HMBC NMR Spectrum (500/126 MHz,  $\text{C}_6\text{D}_6$ ,  $25^\circ\text{C}$ ) of a mixture containing **5** as the major component. The central arene (left) and phenylene (right)  $^{2/3}J(\text{C},\text{H})$  scalar coupling correlations are labeled.

## ***EPR Spectroscopy***

### *Experimental Details*

#### *CW EPR Spectroscopy*

X-band CW EPR spectra were obtained on a Bruker EMX spectrometer at 77 K in a liquid nitrogen immersion dewar using Bruker Win-EPR software (ver. 3.0). Samples were prepared as solutions (2 mM) in 2-methyltetrahydrofuran (2Me-THF) and rapidly cooled in liquid nitrogen to form a frozen glass. Spectra were simulated using the EasySpin<sup>44</sup> simulation toolbox (release 5.1.8) with Matlab 2016b.

#### *Pulse EPR Spectroscopy*

All pulse EPR and electron nuclear double resonance (ENDOR) experiments were acquired using a Bruker (Billerica, MA) ELEXSYS E580 pulse EPR spectrometer using a Bruker MD4 pulse ENDOR resonator for all X-band experiments and a Bruker D2 pulse ENDOR resonator for all Q-band ( $\approx 33.7$  GHz) experiments. Temperature control was achieved using an ER 4118HV-CF5-L Flexline Cryogen-Free VT cryostat manufactured by ColdEdge (Allentown, PA) equipped with an Oxford Instruments Mercury ITC.

Pulse Q-band electron spin-echo detected EPR (ESE-EPR) field-swept spectra were acquired using the 2-pulse “Hahn-echo” sequence ( $\pi/2 - \tau - \pi - \text{echo}$ ) and subsequently, each field swept echo-detected EPR absorption spectrum was modified using a pseudo-modulation function<sup>45</sup> (modulation amplitude = 1 mT) to approximate the effect of field modulation and produce the CW-like 1<sup>st</sup> derivative spectrum.

Pulse X-band ENDOR was acquired using the Davies pulse sequence ( $\pi - T_{RF} - \pi_{RF} - T_{RF} - \pi/2 - \tau - \pi - \text{echo}$ ), where  $T_{RF}$  is the delay between mw pulses and RF pulses,  $\pi_{RF}$  is the length of the RF pulse and the RF frequency is randomly sampled during each pulse sequence.

In general, the ENDOR spectrum for a given nucleus with spin  $I = 1/2$  ( $^1\text{H}$ ,  $^{31}\text{P}$ ) or  $I = 3/2$  ( $^{95/97}\text{Mo}$  and  $^{35/37}\text{Cl}$ ) coupled to the  $S = 1/2$  electron spin exhibits a doublet at frequencies

$$\nu_{\pm} = \left| \frac{A}{2} \pm \nu_N \right| \quad \text{S1}$$

Where  $\nu_N$  is the nuclear Larmor frequency and  $A$  is the hyperfine coupling. For nuclei with  $I \geq 1$  ( $^{95/97}\text{Mo}$ ,  $^{35/37}\text{Cl}$ ), an additional splitting of the  $\nu_{\pm}$  manifolds is produced by the nuclear quadrupole interaction (P)

$$\nu_{\pm, m_I} = \left| \nu_N \pm \frac{3P(2m_I - 1)}{2} \right| \quad \text{S2}$$

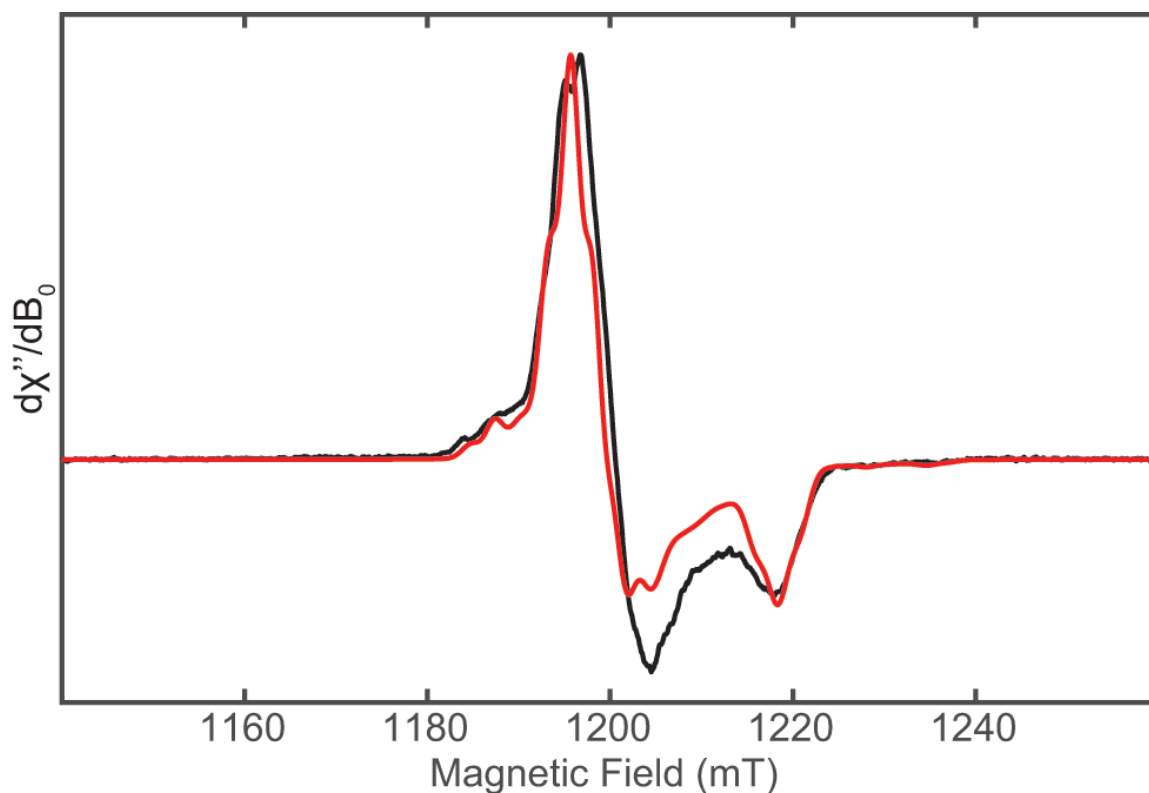
In the current study, these quadrupole transitions are not clearly resolved in any of the ENDOR spectra for either  $^{95/97}\text{Mo}$  or  $^{35/37}\text{Cl}$ . Particularly for  $^{95/97}\text{Mo}$ , these terms are likely vanishingly small in comparison to the strong hyperfine coupling, and thus are neglected in the spectral simulations.

Simulations of all EPR data were achieved using the EasySpin simulation toolbox (release 5.1.8) with Matlab 2016 using the following Hamiltonian:

$$\hat{H} = \mu_B \vec{B}_0 g \hat{S} + \mu_N g_N \vec{B}_0 \hat{I} + h \hat{S} \cdot \mathbf{A} \cdot \hat{I} \quad \text{S3}$$

In this expression, the first term corresponds to the electron Zeeman interaction term where  $\mu_B$  is the Bohr magneton,  $g$  is the electron spin  $g$ -value matrix with principle components  $g = [g_{xx} \ g_{yy} \ g_{zz}]$ , and  $\hat{S}$  is the electron spin operator; the second term corresponds to the nuclear Zeeman interaction term where  $\mu_N$  is the nuclear magneton,  $g_N$  is the characteristic nuclear  $g$ -value for each nucleus (e.g.  $^1\text{H}$ ,  $^{31}\text{P}$ ) and  $\hat{I}$  is the nuclear spin operator; the third term corresponds to the electron-nuclear hyperfine term, where  $\mathbf{A}$  is the hyperfine coupling tensor with principle components  $\mathbf{A} = [A_{xx} \ A_{yy} \ A_{zz}]$ .



*EPR Spectra*

**Figure 6.25.** Q-band Pseudomodulated Electron Spin-Echo (ESE) detected EPR spectrum (black) of **3** in 2Me-THF with simulated CW EPR spectrum (red) using the same simulation parameters as for the X-band CW and ENDOR spectra. Pseudomodulation function amplitude = 1 mT. Experimental conditions: microwave frequency = 33.609 GHz;  $\pi$  pulse length = 160 ns; interpulse delay  $\tau$  = 300ns; shot repetition time (srt) = 5 ms; temperature = 20 K.

**Table 6.2.** Absolute values of hyperfine coupling parameters for **3**, all units are in MHz.

Nucleus	x	y	z
<sup>95/97</sup> Mo	94	94	178
Phosphine <sup>31</sup> P	62	72	63
Phosphide <sup>31</sup> P	15	138	15
Arene <sup>1</sup> H	10	18	10
<sup>35/37</sup> Cl	10.5	10.5	10.5

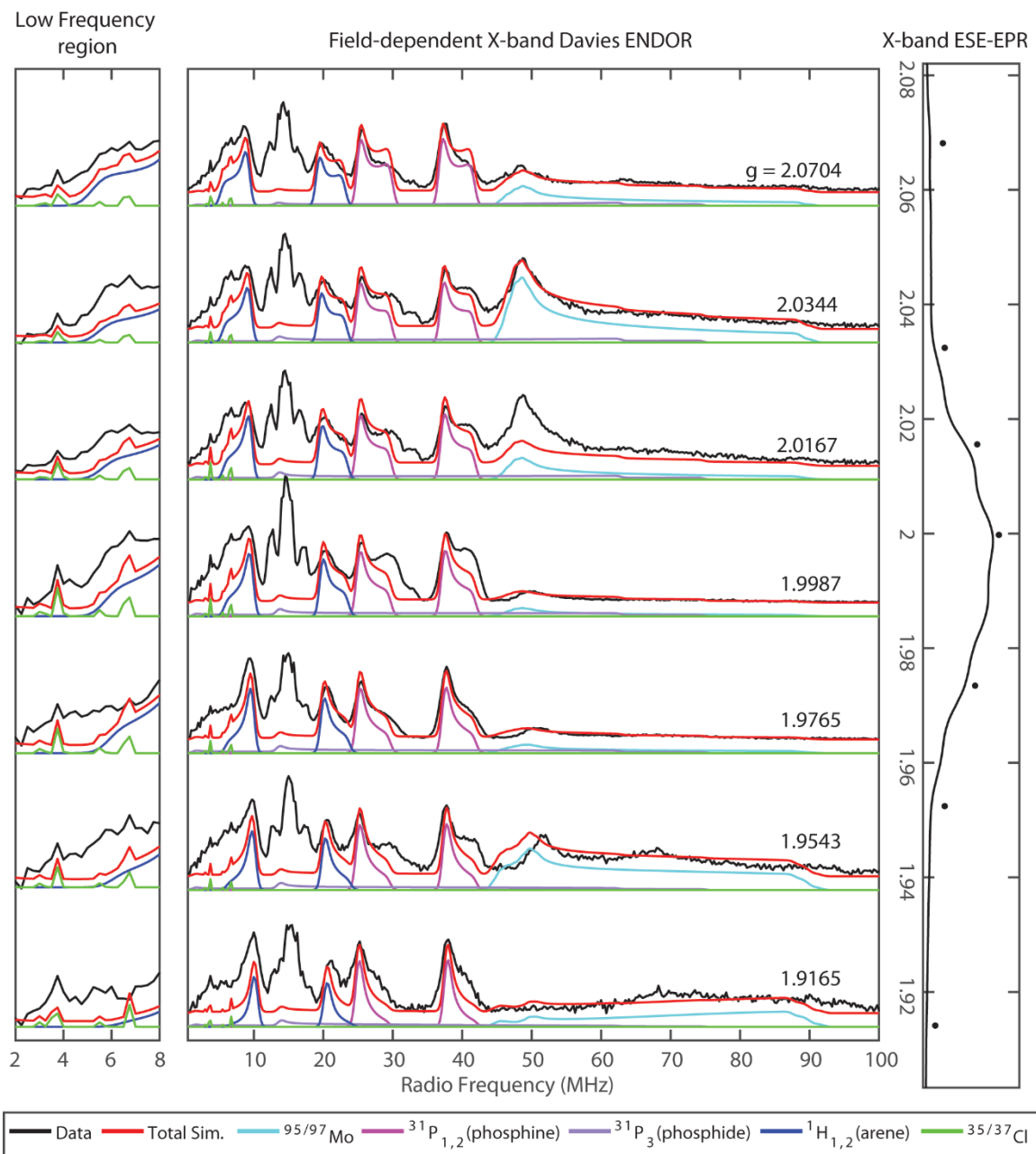


**Figure 6.26.** Field-dependent X-band Davies ENDOR spectra (black) of **3** in 2Me-THF and simulated ENDOR spectra of each hyperfine coupled nucleus (colored traces) using the same simulation parameters as for the X-band CW and ENDOR spectra. An enlargement of the low frequency region is offset to the left. Experimental conditions: microwave frequency = 9.724 GHz; MW  $\pi$  pulse length = 80 ns; RF  $\pi$  pulse length = 15  $\mu\text{s}$ ; interpulse delay  $\tau = 240\text{ns}$ ;  $T_{\text{RF}}$  delay = 2  $\mu\text{s}$ ; shot repetition time (srt) = 5 ms; temperature = 20.

*Estimation of spin density from hyperfine coupling parameters for 3*

Each hyperfine coupling tensor can be considered as the sum of an isotropic term,  $a_{iso}$ , which is the average value of the three principle components of the hyperfine tensor, and an anisotropic term dipolar term  $T_{obs}$ . These hyperfine values can be compared to calculated hyperfine values for a unit of spin in the appropriate orbital in order to obtain an estimate of the spin density at the nucleus in question.

*Decomposition of  $^{95/97}\text{Mo}$  Hyperfine and estimation of spin density*

The observed  $^{95/97}\text{Mo}$  Hyperfine coupling tensor is the sum of the isotropic term,  $a_{iso}$ , and an anisotropic term  $a_{aniso}$ . Here we will consider only the more abundant  $^{95}\text{Mo}$  nucleus (15.92 %), though the analagous analysis could be approached by simply scaling the  $^{95}\text{Mo}$  hyperfine by the ratio of the gyromagnetic ratios of  $^{95}\text{Mo}$  and  $^{97}\text{Mo}$ .

$$\begin{aligned} A(^{95}\text{Mo}) &= [94, 94, 178] \text{ MHz} \\ &= a_{iso} + \mathbf{A}_{aniso} \quad \text{S4} \\ &= 122 + [-28 \ -28 \ 56] \text{ MHz} \end{aligned}$$

Taking  $|a_{iso}^0(^{95}\text{Mo})| = 1984 \text{ MHz}$  for a single electron in a 5s orbital of Mo,<sup>15b</sup> the isotropic hyperfine coupling  $a_{iso}(^{95}\text{Mo}) = 122 \text{ MHz}$  corresponds to a small 5s orbital density on Mo of  $\rho_s \approx 0.06 e^-$ . This is unsurprising considering the majority of unpaired spin resides within a valence d-orbital of xy parentage which gives rise to the sizable dipolar component. Taking a unit of unpaired spin in a  $d_{xy}$  orbital of Mo  $\mathbf{A}_{d_{xy}}^0 = [-43.1 \ -43.1 \ 86.2]$ ,<sup>15b</sup> the anisotropic term  $\mathbf{A}_{aniso}(^{95}\text{Mo}) = [-28 \ -28 \ 56] \text{ MHz}$  corresponds to a  $5d_{xy}$  orbital spin density of  $\rho_{d_{xy}} \approx 0.65 e^-$ . Between these two contributions, the total spin density at Mo is estimated to be  $\rho_{Mo} \approx 0.71 e^-$ , in reasonable agreement with the DFT-predicted Mulliken spin density of  $0.774 e^-$ .

*Decomposition of terminal phosphide  $^{31}\text{P}$  hyperfine and estimation of spin density for 3*

Following the procedures of Hoffman and coworkers for analysis of the  $^{15}\text{N}$  hyperfine coupling in an Fe(V) nitride,<sup>15a</sup> the highly anisotropic  $^{31}\text{P}$  hyperfine coupling tensor measured for the terminal phosphide can also be decomposed to its constituent s- and p-orbital origins.

In the case of this  $^{31}\text{P}$  coupling, the relative signs of the individual principle components are not explicitly known, thus two cases must be considered,

$$\begin{aligned} A(^{31}\text{P}) &= [15, 138, 15] \text{ or } [-15, 138, -15] \text{ MHz} \\ &= \mathbf{a}_{iso} + \mathbf{T}_{obs} \\ &= 56 + [-41, 82, -41] \text{ MHz or } 36 + [-51, 102, -51] \text{ MHz} \end{aligned}$$

Taking  $\mathbf{a}_{iso}^0(^{31}\text{P}) = 13308$  MHz for a single electron in a  $3s$  orbital, the isotropic hyperfine  $\mathbf{a}_{iso}(^{31}\text{P}) = 56$  or  $36$  MHz corresponds to a small  $3s$  orbital density on the phosphide P of  $\rho_s \approx 0.004 e^-$  or  $\rho_s \approx 0.003 e^-$ , respectively, either case indicating that the terminal phosphide can be treated as having a filled  $3s$  orbital with little hybridization with p-orbitals containing unpaired spin density.

In the case of the phosphide, the dipolar term  $\mathbf{T}_{obs}$  can be decomposed into two separate axial contributions: one local contribution,  $\mathbf{T}^{x,y}_{loc}$ , from spin density at P with its unique axis along an axis (x or y) orthogonal to the Mo-P bond vector, and a second component,  $\mathbf{T}^z_{obs}$ , with its unique axis parallel to the Mo-P bond vector. In turn,  $\mathbf{T}^z_{obs}$  is a composite of the nonlocal contribution ( $\mathbf{T}^z_{nloc}$ ) due to the through-space dipolar interaction between the  $^{31}\text{P}$  nucleus and unpaired spin density at the Mo nucleus, and a local contribution ( $\mathbf{T}^z_{loc}$ ) from spin density at P in a p-orbital with its unique axis parallel to the Mo-P bond vector. The nonlocal contribution  $\mathbf{T}^z_{nloc}$  can be estimated using the point-dipole approximation:

$$\mathbf{T}^z_{nloc} = [-a, -a, 2a]; a = \frac{\rho_{Mo} g_e \mu_B g_n \mu_n}{r^3} \quad \text{S5}$$

Using the crystallographically determined Mo-P distance ( $r = 2.092(1) \text{ \AA}$ ) and  $\rho_{Mo} \approx 0.71$ , the spin density at Mo determined in the previous section, results in an estimation of  $\mathbf{T}^z_{nloc} = [-2.5, -2.5, 5.0]$  MHz. Subtraction of this nonlocal contribution  $\mathbf{T}^z_{nloc}$  from  $\mathbf{T}_{obs}$  yields the sum of the local contributions:

$$\begin{aligned} \mathbf{T}_{loc} &= \mathbf{T}_{obs} - \mathbf{T}^z_{nloc} \\ &= [-38.5, 84.5, -46.0] \text{ or } [-48.5, 104.5, -46.0] \end{aligned}$$

$$= \mathbf{T}^{x,y}_{loc} + \mathbf{T}^z_{loc}$$

For both cases considered for  $\mathbf{T}_{obs}$ ,  $\mathbf{T}_{loc}$  can be uniquely decomposed into  $\mathbf{T}^{x,y}_{loc} + \mathbf{T}^z_{loc}$  components with  $\mathbf{T}^z_{loc} = [2.5, 2.5, -5.0]$  for both and  $\mathbf{T}^{x,y}_{loc} = [-41, 82, -41]$  or  $[-51, 102, -51]$ , respectively. Though a definitive assignment of the orientation of these hyperfine tensors relative to the molecular frame cannot be made from the current data, the uniaxial symmetry of both of these two  $\mathbf{T}^{x,y}_{loc}$  tensors implies that in either case that only one p-orbital is contributing, with either  $\rho_{p_x}$  or  $\rho_{p_y} \approx 0$ . In the simulations presented, hyperfine and g-tensor principle coordinates are co-linear, and the most likely orientation of the g-tensor coordinate frame is with  $g_z$  parallel to the Mo-phosphide bond vector, while  $g_y$  is roughly aligned with the phosphine-Mo-phosphine vector. Taking a unit of unpaired spin in a  $p_y$  orbital of P  $\mathbf{A}^o_{p_{x,y}} = [-366.8 \ 733.6 \ -366.8]$  MHz,<sup>15b</sup> these two cases of  $\mathbf{T}^{x,y}_{loc}$  correspond to a p-orbital spin density of  $\rho_{p_y} \approx 0.11$  or  $0.14 e^-$ , respectively. This significant unpaired spin in the  $p_y$  orbital of the terminal phosphide arises either from electron donation from filled orbitals on P to the partially filled  $d_{xy}$  orbital of Mo, or through spin polarization of the filled  $3p$  orbitals on P by the same partially filled Mo  $d_{xy}$  orbital.

### Absorbance Spectra

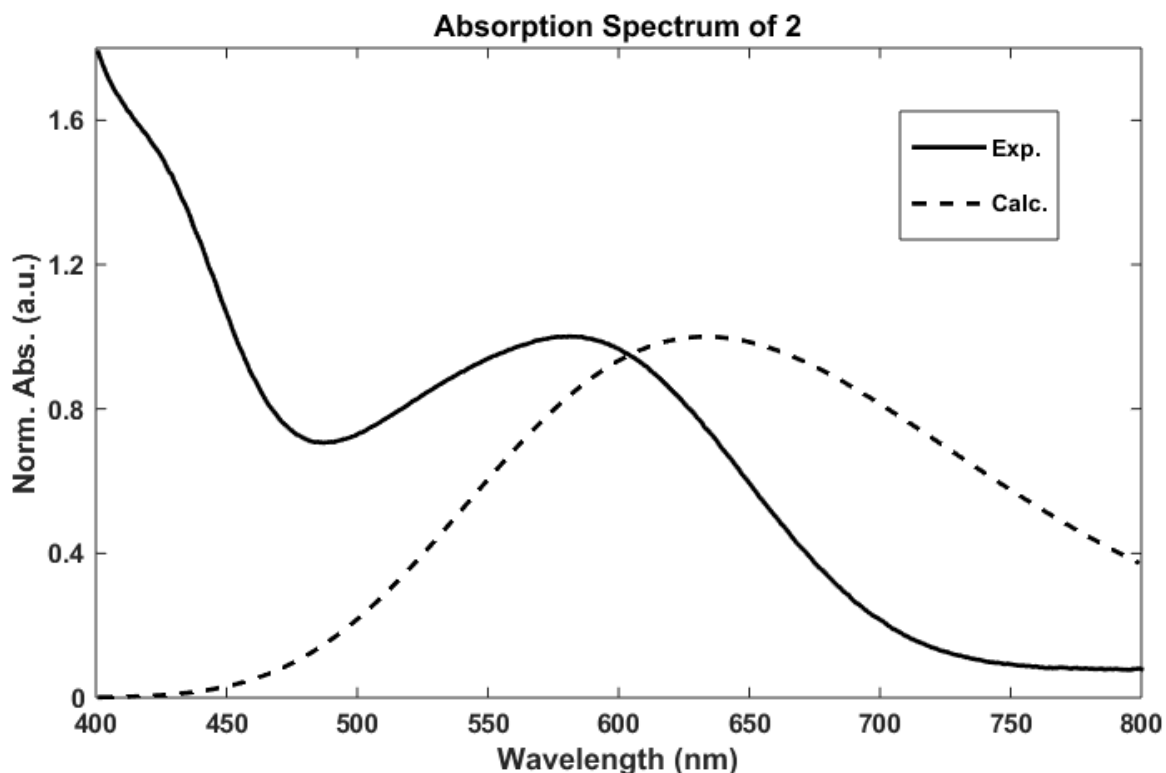


**Figure 6.27.** Experimental (solid) and TD-DFT calculated (dashed) UV-Vis spectra for terminal phosphide **2**. The data demonstrate reasonable agreement for the absorption maximum ( $\Delta \approx 50$  nm)—with calculated  $2a' \rightarrow 3a''$  and  $2a' \rightarrow 4a''$  ( $\text{Mo}\equiv\text{P N.B. to } \pi^*$ ) transitions at 613 and 561 nm, respectively.

### Electrochemical Measurements

#### General Considerations

Electrochemical measurements were recorded with a Pine Instrument Company AFCBP1 bipotentiostat using the AfterMath software package. Cyclic Voltammograms (CVs) were recorded on a *ca.* 3 mmol solution of **2** in a 0.1 M [ $n\text{Bu}_4\text{N}$ ][ $\text{PF}_6$ ] electrolyte solution in THF. A two-compartment cell was employed; a Ag wire pseudo-reference electrode was separated from a Pt wire counter and 3.0 mm glassy carbon disk working electrode by a fine porosity sintered glass frit. Reported potentials were referenced internally to cobaltacene/cobaltacenium and are reported versus ferrocene/ferrocenium ( $\text{Fc}/\text{Fc}^+$ ). For low temperature measurements, the two compartment cell was cooled in a low form

Dewar flask containing acetone. Dry ice was added as needed to maintain a temperature of  $-20 \pm 3$  °C, as measured with a  $-100$  to  $50$  °C alcohol thermometer (VWR).

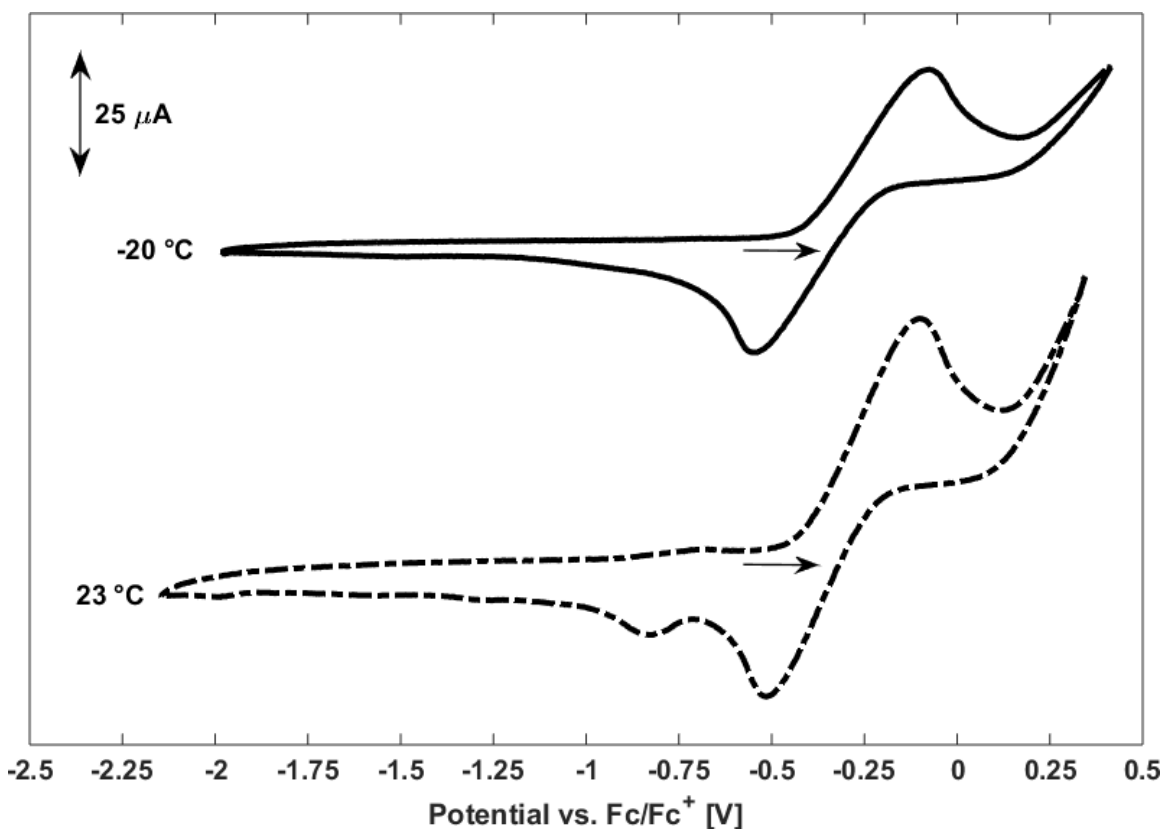


**Figure 6.28.** CVs of **2** in 0.1 M [ $n$ BuN][PF<sub>6</sub>] in THF recorded with a scan rate of 100 mV/s at  $-20$  °C (solid) and  $23$  °C (dashed). Potentials are referenced to Fc/Fc<sup>+</sup>. The open circuit potential and scan direction are designated by the arrows under each voltammogram.

Though chemically reversible at  $-20$  °C (*vide infra*), the Mo(IV)/Mo(V) redox couple of **2** demonstrates chemical irreversibility at room temperature. Upon scanning anodically, the low temperature CV shows a single return wave, corresponding to the reduction of *in situ* generated **3**. The room temperature CV has two cathodic features; one corresponding to reduction of **3**, and a second feature at  $-841$  mV vs. Fc/Fc<sup>+</sup>. Despite being run under significantly more dilute conditions (*ca.* 20 fold more dilute), these data are consistent with the reactivity observed from **3** upon chemical oxidation of **2** (a process proposed to be second order in [Mo]).

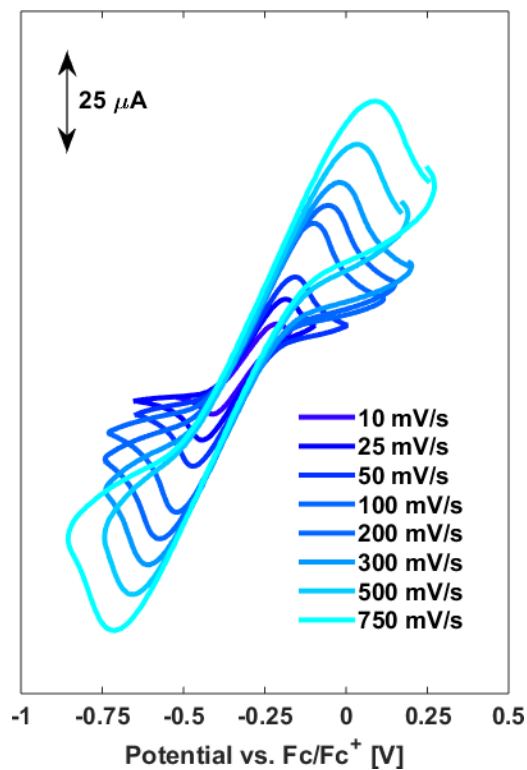


**Figure 6.29.** CVs corresponding to the Mo(IV)/Mo(V) redox couple of **2** in 0.1 M [tBuN][PF<sub>6</sub>] in THF recorded with variable scan rates at -20 °C.

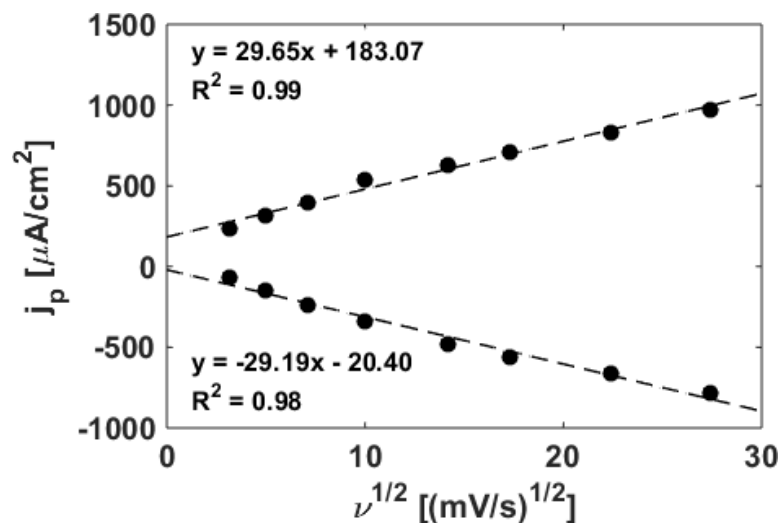


**Figure 6.30.** Current density dependence on the square root of the scan rate for the Mo(IV)/Mo(V) redox couple of **2** measured at -20 °C.



### *Computational Details*

All calculations were performed with DFT as implemented in Gaussian 09 Revision C.01.<sup>46</sup> Geometry optimizations and electronic structure calculations were performed with revised TPSS exchange and correlation functionals.<sup>47</sup> The LANL2DZ basis set was used for all atoms.<sup>48</sup> No solvent corrections were employed. All optimizations were performed ignoring molecular symmetry—crystallographic coordinates were used as a starting point. Energetic minima were confirmed with subsequent frequency calculations which did not return imaginary frequencies. Structures optimized in this manner showed good agreement with bond lengths and angles determined via single crystal X-ray diffraction (Table 6.3). The TD-DFT calculated absorption spectrum of **2** demonstrated reasonable agreement with the experimentally determined UV-Vis spectrum (Figure 6.27). Molecular orbital and spin density illustrations were generated using GaussView, the GUI component of the Gaussian software package, and depicted with 0.05 e/Å<sup>3</sup> or 0.001 e/Å<sup>3</sup> isosurface values, respectively.

**Table 6.3.** Comparison of experimental and calculated structural metrics for **2** and **3**.

	<b>2</b>			<b>3</b>		
	<b>Exp.</b>	<b>Calc.</b>	$\Delta$	<b>Exp.</b>	<b>Calc.</b>	$\Delta$
<b>Mo1–P1</b>	2.5959(3)	2.644	-0.05	2.6092(8)	2.667	-0.06
<b>Mo1–P2</b>	2.5922(3)	2.644	-0.05	2.6226(8)	2.667	-0.04
<b>Mo1–P3</b>	2.1003(3)	2.150	-0.05	2.092(1)	2.141	-0.05
<b>Mo1–Cl1</b>	2.4358(3)	2.508	-0.07	2.3411(9)	2.425	-0.08
<b>Mo1–C2</b>	2.261(1)	2.277	-0.02	2.465(3)	2.476	-0.01
<b>Mo1–C3</b>	2.255(1)	2.277	-0.02	2.471(3)	2.476	-0.01
<b>C1–C2</b>	1.453(2)	1.467	-0.01	1.413(4)	1.438	-0.03
<b>C2–C3</b>	1.433(2)	1.462	-0.03	1.402(4)	1.428	-0.03
<b>C3–C4</b>	1.453(2)	1.467	-0.01	1.414(4)	1.438	-0.02
<b>C4–C5</b>	1.361(2)	1.389	-0.03	1.387(5)	1.411	-0.02
<b>C5–C6</b>	1.435(2)	1.446	-0.01	1.401(5)	1.420	-0.02
<b>C6–C1</b>	1.359(2)	1.389	-0.03	1.388(5)	1.411	-0.02
$\angle$ <b>P1–Mo1–P2</b>	162.3(1)	160.8	1.5	161.8(1)	161.3	0.5
$\angle$ <b>P1–Mo1–P3</b>	97.5(1)	97.4	0.1	96.8(1)	98.1	-1.3
$\angle$ <b>P2–Mo1–P3</b>	96.2(1)	97.4	-1.2	98.2(1)	98.1	0.1
$\angle$ <b>P1–Mo1–Cl1</b>	82.0(1)	82.2	-0.2	82.9(1)	83.6	-0.7
$\angle$ <b>P2–Mo1–Cl1</b>	83.5(1)	82.2	1.3	83.6(1)	83.6	0
$\angle$ <b>P3–Mo1–Cl1</b>	105.7(1)	105.5	0.2	103.0(1)	103.0	0

**Table 6.4.** Computed Mulliken spin densities and experimental isotropic hyperfine coupling constants for **3**.

	<b>Calculated Mulliken Spin Density (<math>e^-</math>)</b>	<b><math>A_{\text{iso}}</math> (MHz)</b>
<b>Mo1</b>	0.774	122.0
<b>Cl1</b>	0.067	10.5
<b>H2</b>	0.018	12.7
<b>H3</b>	0.018	12.7

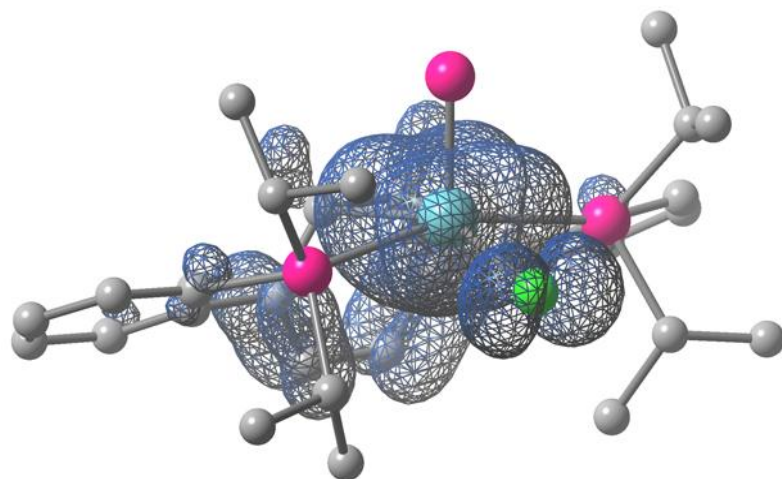


**Figure 6.31.** Spin density plot ( $0.001 \text{ e}/\text{\AA}^3$  isocontours) of phosphide cation **3**.

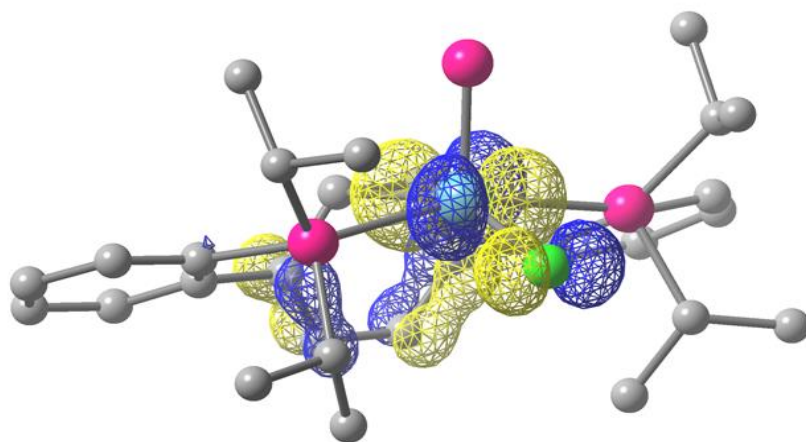


**Figure 6.32.** Calculated SOMO ( $0.05 \text{ e}/\text{\AA}^3$  isocontours) for phosphide cation **3**.

### ***Crystallographic Information***

CCDC deposition numbers 1571924-1571926 contain the supplementary crystallographic data for this paper. These data can be obtained free of charge from The Cambridge Crystallographic Data Centre via [www.ccdc.cam.ac.uk/data\\_request/cif](http://www.ccdc.cam.ac.uk/data_request/cif).

### ***Refinement Details***

In each case, crystals were mounted on a MiTeGen loop using Paratone oil, then placed on the diffractometer under a nitrogen stream. Low temperature (100 K) X-ray data were obtained on a Bruker D8 VENTURE Kappa Duo PHOTON 100 CMOS based diffractometer (Mo I<sub>μ</sub>S HB micro-focus sealed X-ray tube,  $K_{\alpha} = 0.71073 \text{ \AA}$ ). All diffractometer manipulations, including data collection, integration, and scaling were carried out using the Bruker APEXIII software.<sup>49</sup> Absorption corrections were applied using SADABS.<sup>50</sup> Space groups were determined on the basis of systematic absences and intensity statistics and the structures were solved in the Olex 2 software interface<sup>51</sup> by intrinsic phasing using XT (incorporated into SHELXTL)<sup>52</sup> and refined by full-matrix least squares on  $F^2$ . All non-hydrogen atoms were refined using anisotropic displacement parameters. Hydrogen atoms were placed in the idealized positions and refined using a riding model, unless noted otherwise. The structures were refined (weighed least squares refinement on  $F^2$ ) to convergence. Graphical representations of structures with 50% probability thermal ellipsoids were generated using the Diamond 3 visualization software.<sup>53</sup>

**Table 6.5.** Crystal and refinement data for complexes **2 – 4** and **6 – 9**.

	<b>2</b>	<b>3</b>	<b>4</b>	<b>6</b>	<b>7</b>	<b>8</b>	<b>9</b>
CCDC Number <sup>30b</sup>	1571924	1571925	1571926				
Empirical formula	C <sub>30</sub> H <sub>40</sub> Cl MoP <sub>3</sub>	C <sub>71.08</sub> H <sub>74.70</sub> BClF <sub>24</sub> MoO <sub>2.27</sub> P <sub>3</sub>	C <sub>35</sub> H <sub>46</sub> ClF <sub>3</sub> MoN <sub>2</sub> O <sub>3</sub> P <sub>2</sub> S	C <sub>32</sub> H <sub>46</sub> MoNP <sub>3</sub>	C <sub>64</sub> H <sub>59</sub> BF <sub>24</sub> MoNP <sub>3</sub>	C <sub>60</sub> H <sub>80</sub> Cl Mo <sub>2</sub> P <sub>5</sub>	C <sub>104</sub> H <sub>116</sub> BF <sub>24</sub> Mo <sub>2</sub> O <sub>3</sub> P <sub>5</sub>
Formula weight	624.92	1656.39	825.13	633.55	1497.78	1183.42	2227.50
T (K)	100	100	100	100	100	100	100
<i>a</i> , Å	9.3388(5)	12.6893(4)	8.4978(5)	8.3733(5)	13.3132(10)	11.8746(9)	12.2440(4)
<i>b</i> , Å	15.0643(8)	16.9145(5)	13.3117(9)	9.2800(6)	13.7005(10)	14.7473(11)	16.2106(5)
<i>c</i> , Å	21.1092(11)	19.5016(6)	16.8759(11)	38.903(2)	18.0167(14)	17.0077(13)	26.1554(9)
$\alpha$ , °	90	108.333(2)	75.595(2)	90	78.710(2)	105.040(2)	102.6320(10)
$\beta$ , °	98.942(2)	100.223(2)	85.718(2)	90	81.561(2)	91.616(2)	100.3340(10)
$\gamma$ , °	90	101.417(2)	76.193(2)	90	87.579(2)	97.773(2)	97.7210(10)
Volume, Å <sup>3</sup>	2933.6(3)	3763.1(2)	1795.3(2)	3022.9(3)	3187.4(4)	2843.7(4)	4901.4(3)
<i>Z</i>	4	2	2	4	2	2	2
Crystal system	Monoclinic	Triclinic	Triclinic	Orthorhombic	Triclinic	Triclinic	Triclinic
Space group	P2 <sub>1</sub> / <i>n</i>	P $\bar{1}$	P $\bar{1}$	P2 <sub>1</sub> 2 <sub>1</sub> 2 <sub>1</sub>	P $\bar{1}$	P $\bar{1}$	P $\bar{1}$
<i>d</i> <sub>calc</sub> , g/cm <sup>3</sup>	1.415	1.462	1.526	1.392	1.561	1.382	1.509
$\theta$ range, °	2.589 to 33.145	2.470 to 79.676	2.269 to 39.789	2.256 to 33.454	2.190 to 30.242	2.479 to 35.999	2.101 to 35.019
$\mu$ , mm <sup>-1</sup>	0.720	3.274	0.641	0.615	0.393	0.666	0.435
Abs. Correction	Semi-empirical	Semi-empirical	Semi-empirical	Semi-empirical	Semi-empirical	Semi-empirical	Semi-empirical
GOF	1.029	1.059	0.800	1.098	1.042	1.051	1.015
R <sub>1</sub> , <sup>a</sup> wR <sub>2</sub> <sup>b</sup> [I > 2 $\sigma$ (I)]	0.0243, 0.0528	0.0562, 0.1390	0.0564, 0.1271	0.0412, 0.0673	0.0577, 0.1428	0.0254, 0.0572	0.0544, 0.0969
Radiation Type	Mo K $\alpha$	Cu K $\alpha$	Mo K $\alpha$	Mo K $\alpha$	Mo K $\alpha$	Mo K $\alpha$	Mo K $\alpha$

<sup>a</sup> R<sub>1</sub> =  $\sum ||F_o| - |F_c|| / \sum |F_o|$ . <sup>b</sup> wR<sub>2</sub> =  $[\sum [w(F_o^2 - F_c^2)^2] / \sum [w(F_o^2)^2]]^{1/2}$ .

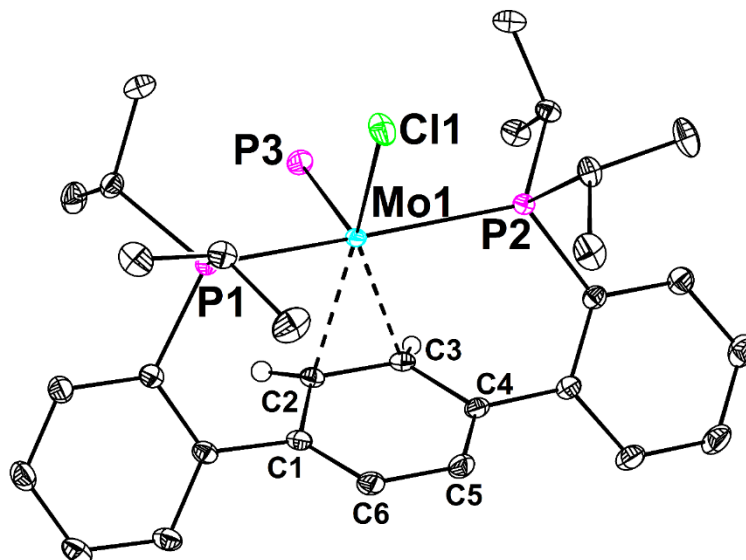


**Figure 6.33.** Structural drawing of **2** with 50% probability anisotropic displacement ellipsoids. Selected H-atoms are omitted for clarity.

#### Special Refinement Details:

The structure was of sufficient quality that the coordinates of the hydrogen atoms attached to both C2 and C3 were found in the difference map and refined freely. The  $\eta^2$  metal-arene interaction results in a significant displacement of these H-atoms from their idealized positions.

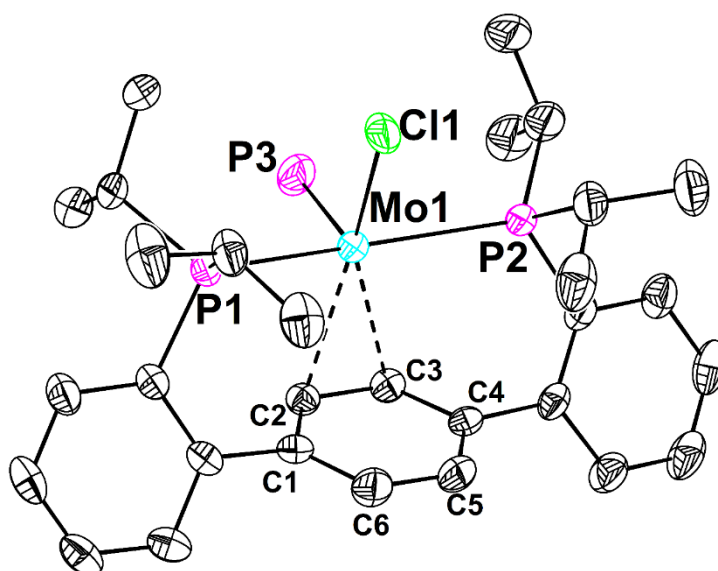


**Figure 6.34.** Structural drawing of **3** with 50% probability anisotropic displacement ellipsoids. H-atoms, the outer sphere  $\text{BAr}^{\text{F}}_{24}$  anion, and  $\text{Et}_2\text{O}$  solvate molecules are omitted for clarity.

### Special Refinement Details:

One of the phosphine isopropyl groups (C28 through C30) was positionally disordered but was satisfactorily modeled over two positions in a 64:36 ratio. The 1,2 and 1,3 distances of the disordered group were restrained to be equivalent and enhanced rigid bond restraints were applied. Several of the CF<sub>3</sub> groups of the BAr<sup>F</sup><sub>24</sub> counterion likewise displayed positional disorder. These groups were satisfactorily modeled over two (F4 through F6 [57:43], F7 through F9 [63:37], F10 through F12 [54:46], F13 through F15 [27:73], and F19 through F22 [49:51]) or three (F22 through F24 [20:33:47]) positions and refined with enhanced rigid bond restraints. Additionally, the most rotationally disordered CF<sub>3</sub> group (F13 through F15) was refined with the 1,2 and 1,3 distances to be equivalent; similarity restraints on U<sub>ij</sub> and rigid bond restraints were likewise applied.

Highly disordered Et<sub>2</sub>O solvent molecules were present in the crystal packing voids. Rather than employing a SQUEEZE operation, the density attributed to these solvate molecules was modeled discretely with 1,2 and 1,3 distance and enhanced rigid bond restraints. A total of 2.3 Et<sub>2</sub>O molecules were modeled, giving rise to the non-integer unit cell contents.

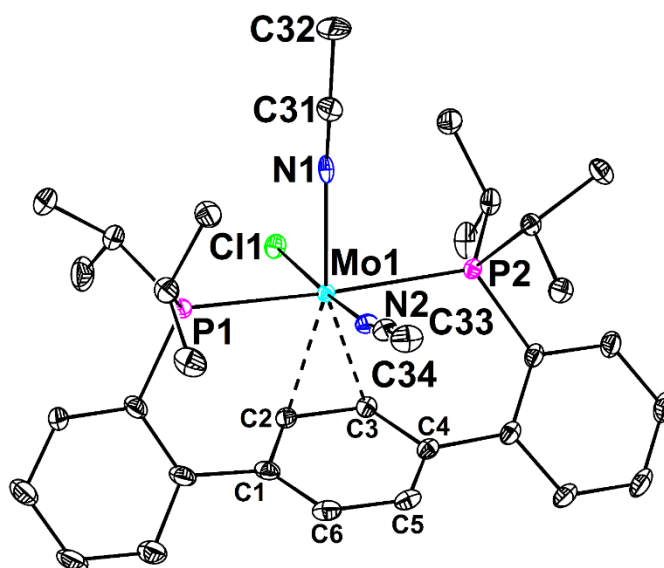


**Figure 6.35.** Structural drawing of **4** with 50% probability anisotropic displacement ellipsoids. H-atoms and the outer sphere triflate counterion are omitted for clarity.

### Special Refinement Details:

One of the phenylene linkers (C9 through C12) demonstrated positional disorder but was satisfactorily modeled over two positions and refined without restraints. The triflate counterion (C35, F1 through F3, S1, and O1 through O3) was likewise positionally disordered. This anion was satisfactorily modeled over three positions in a 22:34:44 ratio and refined with 1,2 and 1,3 distance and enhanced rigid bond restraints.

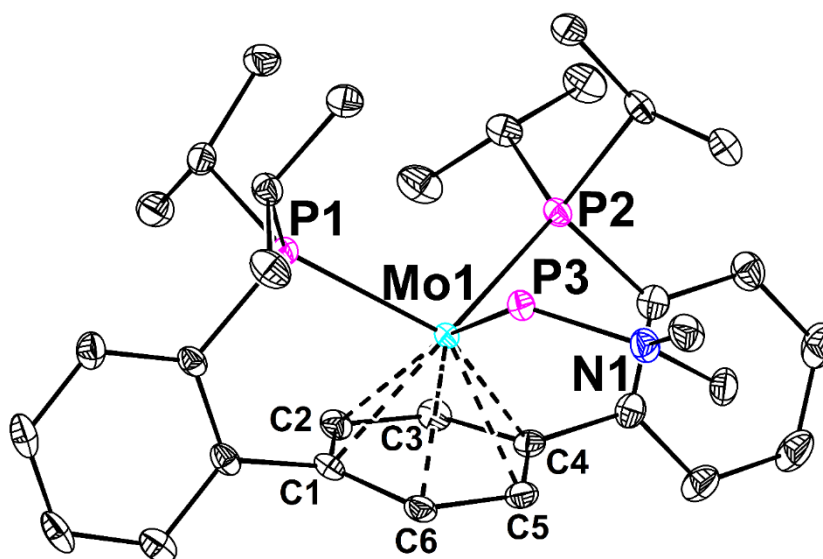


**Figure 6.36.** Structural drawing of **6** with 50% probability anisotropic displacement ellipsoids. H-atoms are omitted for clarity.

**Special Refinement Details:** The crystal was merohedrally twinned. The twinning was modeled satisfactorily as two-components related by inversion. The twin law  $[-1.0, 0.0, 0.0, 0.0, -1.0, 0.0, 0.0, 0.0, -1.0]$  was determined using the Twinning option in Olex2 and the twin ratio refined to 0.84:0.16.



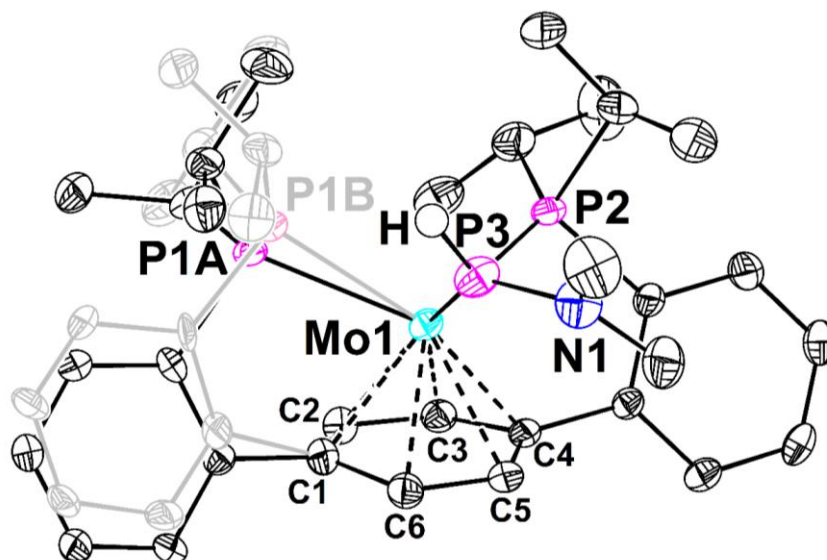


**Figure 6.37.** Structural drawing of **7** with 50% probability anisotropic displacement ellipsoids. Selected H-atoms are omitted for clarity. The minor component of the positional disorder exhibited by the left half of the molecule is shown in grey.

**Special Refinement Details:**

One of the phenylene linkers (C7 through C12) and diisopropylphosphine (P1 and C19 through C24) motifs of **7** were disordered and satisfactorily modeled over two positions in a 74:26 ratio. The major component was refined without restraints. The minor component was refined with  $U_{ij}$  and rigid bond restraints. The H-atom attached to the phosphide (P3) was found in the low-angle Fourier map (data truncated at 50 degrees in two-theta) and once assigned, refined freely with the complete dataset.

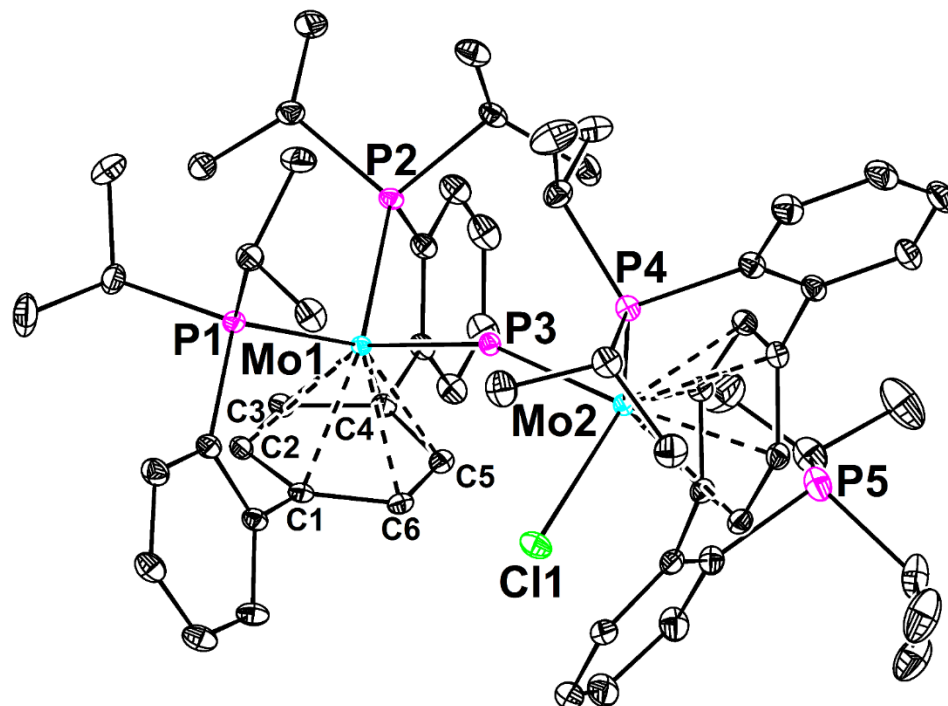


**Figure 6.38.** Structural drawing of **8** with 50% probability anisotropic displacement ellipsoids. H-atoms are omitted for clarity.

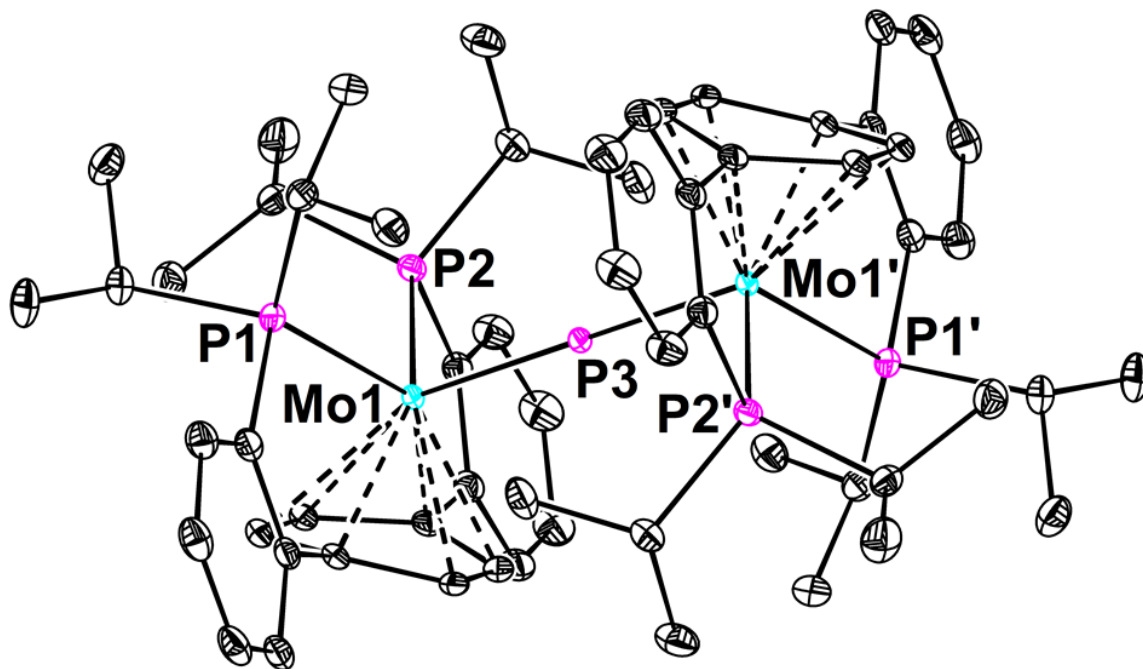


**Figure 6.39.** Structural drawing of **9** with 50% probability anisotropic displacement ellipsoids. H-atoms, outer sphere anions, and THF solvate molecules are omitted for clarity.

**Note:**

There are two distinct *para*-**P2** Mo units in the asymmetric unit. The Mo– $\mu$ -P distances in these molecules are 2.2769(2) and 2.2725(2) Å, for Mo1 and Mo2 respectively. Likewise, the average Mo–C<sub>arene</sub> distances are 2.302(2) and 2.299(2) for Mo1 and Mo2, respectively. The averages of these values are reported in the Results and Discussion section of this chapter.

**Special Refinement Details:**

One of the isopropyl methine and methyl groups (C55 and C56) is positionally disordered, but was satisfactorily modeled over two positions in a 58:42 ratio and refined without restraints. Additionally, one of the CF<sub>3</sub> groups of the BAr<sup>F</sup><sub>24</sub> counterion (C92 and F22A through F24B) shows positional disorder. This motif was satisfactorily modeled over two positions, in an 89:11 ratio. The 1,2 and 1,3 distances of these disordered CF<sub>3</sub> groups were restrained to be equivalent and enhanced rigid bond restraints were applied.

## REFERENCES

- (1) a) Callejas, J. F.; Read, C. G.; Roske, C. W.; Lewis, N. S.; Schaak, R. E. *Chem. Mater.* **2016**, *28*, 6017; b) Carencu, S.; Portehault, D.; Boissière, C.; Mézailles, N.; Sanchez, C. *Chem. Rev.* **2013**, *113*, 7981; c) Alexander, A.-M.; Hargreaves, J. S. J. *Chem. Soc. Rev.* **2010**, *39*, 4388; d) Oyama, S. T.; Gott, T.; Zhao, H.; Lee, Y.-K. *Catal. Today* **2009**, *143*, 94; e) Oyama, S. T. *J. Catal.* **2003**, *216*, 343.
- (2) a) Cossairt, B. M.; Piro, N. A.; Cummins, C. C. *Chem. Rev.* **2010**, *110*, 4164; b) Balázs, G.; Gregoriades, L. J.; Scheer, M. *Organometallics* **2007**, *26*, 3058; c) Johnson, B. P.; Balázs, G.; Scheer, M. *Coord. Chem. Rev.* **2006**, *250*, 1178.
- (3) a) Laplaza, C. E.; Davis, W. M.; Cummins, C. C. *Angew. Chem. Int. Ed.* **1995**, *34*, 2042; b) Zanetti, N. C.; Schrock, R. R.; Davis, W. M. *Angew. Chem. Int. Ed.* **1995**, *34*, 2044.
- (4) a) Fox, A. R.; Clough, C. R.; Piro, N. A.; Cummins, C. C. *Angew. Chem. Int. Ed.* **2007**, *46*, 973; b) Hirsekorn, K. F.; Veige, A. S.; Wolczanski, P. T. *J. Am. Chem. Soc.* **2006**, *128*, 2192; c) Figueroa, J. S.; Cummins, C. C. *Angew. Chem. Int. Ed.* **2004**, *43*, 984; d) Stephens, F. H.; Figueroa, J. S.; Diaconescu, P. L.; Cummins, C. C. *J. Am. Chem. Soc.* **2003**, *125*, 9264; e) Cherry, J.-P. F.; Johnson, A. R.; Baraldo, L. M.; Tsai, Y.-C.; Cummins, C. C.; Kryatov, S. V.; Rybak-Akimova, E. V.; Capps, K. B.; Hoff, C. D.; Haar, C. M.; Nolan, S. P. *J. Am. Chem. Soc.* **2001**, *123*, 7271; f) Scheer, M.; Kramkowski, P.; Schuster, K. *Organometallics* **1999**, *18*, 2874; g) Johnson, M. J. A.; Lee, P. M.; Odom, A. L.; Davis, W. M.; Cummins, C. C. *Angew. Chem. Int. Ed.* **1997**, *36*, 87; h) Freundlich, J. S.; Schrock, R. R.; Davis, W. M. *J. Am. Chem. Soc.* **1996**, *118*, 3643.
- (5) Buss, J. A.; Agapie, T. *J. Am. Chem. Soc.* **2016**, *138*, 16466.
- (6) Courtemanche, M.-A.; Transue, W. J.; Cummins, C. C. *J. Am. Chem. Soc.* **2016**.
- (7) a) Velian, A.; Cummins, C. C. *Science* **2015**, *348*, 1001; b) Velian, A.; Nava, M.; Temprado, M.; Zhou, Y.; Field, R. W.; Cummins, C. C. *J. Am. Chem. Soc.* **2014**, *136*, 13586; c) Velian, A.; Cummins, C. C. *J. Am. Chem. Soc.* **2012**, *134*, 13978.
- (8) a) Palluccio, T. D.; Rybak-Akimova, E. V.; Majumdar, S.; Cai, X.; Chui, M.; Temprado, M.; Silvia, J. S.; Cozzolino, A. F.; Tofan, D.; Velian, A.; Cummins, C. C.; Captain, B.; Hoff, C. D. *J. Am. Chem. Soc.* **2013**, *135*, 11357; b) Bowman, A. C.; Bart, S. C.; Heinemann, F. W.; Meyer, K.; Chirik, P. J. *Inorg. Chem.* **2009**, *48*, 5587; c) Adhikari, D.; Basuli, F.; Fan, H.; Huffman, J. C.; Pink, M.; Mindiola, D. J. *Inorg. Chem.* **2008**, *47*, 4439; d) Betley, T. A.; Peters, J. C. *J. Am. Chem. Soc.* **2004**, *126*, 6252; e) Soo, H. S.; Figueroa, J. S.; Cummins, C. C. *J. Am. Chem. Soc.* **2004**, *126*, 11370; f) Agapie, T.; Diaconescu, P. L.; Cummins, C. C. *J. Am. Chem. Soc.* **2002**, *124*, 2412; g) Mindiola, D. J.; Tsai, Y.-C.; Hara, R.; Chen, Q.; Meyer, K.; Cummins, C. C. *Chem. Commun.* **2001**, 125; h) Mindiola, D. J.; Cummins, C. C. *Angew. Chem. Int. Ed.* **1998**, *37*, 945; i) Henry N. C. Wong, T.-K. N., and Tai-Yuen Wong *Heterocycles* **1983**, *20*, 1815.
- (9) Wu, G.; Rovnyak, D.; Johnson, M. J. A.; Zanetti, N. C.; Musaev, D. G.; Morokuma, K.; Schrock, R. R.; Griffin, R. G.; Cummins, C. C. *J. Am. Chem. Soc.* **1996**, *118*, 10654.
- (10) Transue, W. J.; Velian, A.; Nava, M.; Martin-Drumel, M.-A.; Womack, C. C.; Jiang, J.; Hou, G.-L.; Wang, X.-B.; McCarthy, M. C.; Field, R. W.; Cummins, C. C. *J. Am. Chem. Soc.* **2016**, *138*, 6731.
- (11) a) Bryan, J. C.; Mayer, J. M. *J. Am. Chem. Soc.* **1990**, *112*, 2298; b) Bryan, J. C.; Geib, S. J.; Rheingold, A. L.; Mayer, J. M. *J. Am. Chem. Soc.* **1987**, *109*, 2826.
- (12) a) Warner, B. P.; Scott, B. L.; Burns, C. J. *Angew. Chem. Int. Ed.* **1998**, *37*, 959; b) Lockwood, M. A.; Fanwick, P. E.; Eisenstein, O.; Rothwell, I. P. *J. Am. Chem. Soc.* **1996**, *118*, 2762.

- (13) a) Betley, T. A.; Wu, Q.; Van Voorhis, T.; Nocera, D. G. *Inorg. Chem.* **2008**, *47*, 1849; b) Nugent, W. A.; Mayer, J. M. *Metal-Ligand Multiple Bonds*; John Wiley & Sons: New York, 1988; c) Mayer, J. M.; Thorn, D. L.; Tulip, T. H. *J. Am. Chem. Soc.* **1985**, *107*, 7454.
- (14) Ballhausen, C. J.; Gray, H. B. *Inorg. Chem.* **1962**, *1*, 111.
- (15) a) Cutsail III, G. E.; Stein, B. W.; Subedi, D.; Smith, J. M.; Kirk, M. L.; Hoffman, B. M. *J. Am. Chem. Soc.* **2014**, *136*, 12323; b) Morton, J. R.; Preston, K. F. *J. Mag. Res.* **1978**, *30*, 577.
- (16) Caulton, K. G. *New J. Chem.* **1994**, *18*, 25.
- (17) a) Scheibel, M. G.; Abbenseth, J.; Kinauer, M.; Heinemann, F. W.; Würtele, C.; de Bruin, B.; Schneider, S. *Inorg. Chem.* **2015**, *54*, 9290; b) MacLeod, K. C.; Vinyard, D. J.; Holland, P. L. *J. Am. Chem. Soc.* **2014**, *136*, 10226; c) Miyazaki, T.; Tanaka, H.; Tanabe, Y.; Yuki, M.; Nakajima, K.; Yoshizawa, K.; Nishibayashi, Y. *Angew. Chem. Int. Ed.* **2014**, *53*, 11488; d) Gloaguen, Y.; Rebreyend, C.; Lutz, M.; Kumar, P.; Huber, M.; van der Vlugt, J. I.; Schneider, S.; de Bruin, B. *Angew. Chem. Int. Ed.* **2014**, *53*, 6814; e) Scheibel, M. G.; Wu, Y.; Stückl, A. C.; Krause, L.; Carl, E.; Stalke, D.; de Bruin, B.; Schneider, S. *J. Am. Chem. Soc.* **2013**, *135*, 17719; f) Scheibel, M. G.; Askevold, B.; Heinemann, F. W.; Reijerse, E. J.; de Bruin, B.; Schneider, S. *Nat Chem* **2012**, *4*, 552; g) Seymore, S. B.; Brown, S. N. *Inorg. Chem.* **2002**, *41*, 462; h) Ware, D. C.; Taube, H. *Inorg. Chem.* **1991**, *30*, 4605.
- (18) a) Piro, N. A.; Cummins, C. C. *J. Am. Chem. Soc.* **2008**, *130*, 9524; b) Piro, N. A.; Figueroa, J. S.; McKellar, J. T.; Cummins, C. C. *Science* **2006**, *313*, 1276.
- (19) a) Cossairt, B. M.; Cummins, C. C. *Inorg. Chem.* **2008**, *47*, 9363; b) Masuda, J. D.; Schoeller, W. W.; Donnadiou, B.; Bertrand, G. *Angew. Chem. Int. Ed.* **2007**, *46*, 7052; c) Fox, A. R.; Wright, R. J.; Rivard, E.; Power, P. P. *Angew. Chem. Int. Ed.* **2005**, *44*, 7729; d) Gröer, T.; Baum, G.; Scheer, M. *Organometallics* **1998**, *17*, 5916.
- (20) Hitchcock, P. B.; Lappert, M. F.; Leung, W.-P. *J. Chem. Soc., Chem. Commun.* **1987**, 1282.
- (21) a) Sterenberg, B. T.; Senturk, O. S.; Udachin, K. A.; Carty, A. J. *Organometallics* **2007**, *26*, 925; b) Sterenberg, B. T.; Udachin, K. A.; Carty, A. J. *Organometallics* **2001**, *20*, 2657; c) Niecke, E.; Hein, J.; Nieger, M. *Organometallics* **1989**, *8*, 2290.
- (22) a) Cowley, A. H.; Pellerin, B.; Atwood, J. L.; Bott, S. G. *J. Am. Chem. Soc.* **1990**, *112*, 6734; b) Cummins, C. C.; Schrock, R. R.; Davis, W. M. *Angew. Chem. Int. Ed.* **1993**, *32*, 756; c) Zhao, G.; Basuli, F.; Kilgore, U. J.; Fan, H.; Aneetha, H.; Huffman, J. C.; Wu, G.; Mindiola, D. J. *J. Am. Chem. Soc.* **2006**, *128*, 13575; d) Basuli, F.; Bailey, B. C.; Huffman, J. C.; Baik, M.-H.; Mindiola, D. J. *J. Am. Chem. Soc.* **2004**, *126*, 1924.
- (23) Ehlers, A. W.; Baerends, E. J.; Lammertsma, K. *J. Am. Chem. Soc.* **2002**, *124*, 2831.
- (24) Burg, A. B.; Slota, P. J. *J. Am. Chem. Soc.* **1958**, *80*, 1107.
- (25) A handful of examples of structurally characterized bimetallic bridging dialkylamino phosphides are known: a) Vaheesar, K.; Bolton, T. M.; East, A. L. L.; Sterenberg, B. T. *Organometallics*, **2010**, *29*, 484; b) Kumar, V.; Lee, D. W.; Newton, M. G.; King, R. B. *J. Organomet. Chem.* **1996**, *512*, 1; c) King, R. B.; Fu, W. -K.; Holt, E. M. *Inorg. Chem.* **1986**, *25*, 2394; d) King, R. B.; Fu, W. -K.; Holt, E. M. *Inorg. Chem.* **1985**, *24*, 3094. .
- (26) Kramkowski, P.; Baum, G.; Radius, U.; Kaupp, M.; Scheer, M. *Chem. Eur. J.* **1999**, *5*, 2890.
- (27) a) Scheer, M.; Müller, J.; Häser, M. *Angew. Chem. Int. Ed.* **1996**, *35*, 2492; b) García, M. E.; Riera, V.; Ruiz, M. A.; Sáez, D.; Hamidov, H.; Jeffery, J. C.; Rüs-Johannessen, T. *J. Am. Chem. Soc.* **2003**, *125*, 13044.
- (28) a) Fermin, M. C.; Ho, J.; Stephan, D. W. *J. Am. Chem. Soc.* **1994**, *116*, 6033; b) Scheer, M.; Müller, J.; Schiffer, M.; Baum, G.; Winter, R. *Chem. Eur. J.* **2000**, *6*, 1252.
- (29) a) McEnaney, J. M.; Crompton, J. C.; Callejas, J. F.; Popczun, E. J.; Biacchi, A. J.; Lewis, N. S.; Schaak, R. E. *Chem. Mater.* **2014**, *26*, 4826; b) Popczun, E. J.; Read, C. G.; Roske, C. W.; Lewis, N. S.; Schaak, R. E. *Angew. Chem. Int. Ed.* **2014**, *53*, 5427; c) Popczun, E. J.; McKone, J.

- R.; Read, C. G.; Biacchi, A. J.; Wiltrout, A. M.; Lewis, N. S.; Schaak, R. E. *J. Am. Chem. Soc.* **2013**, *135*, 9267.
- (30) a) Hansen, M. H.; Stern, L.-A.; Feng, L.; Rossmesl, J.; Hu, X. *PCCP* **2015**, *17*, 10823; b) Liu, P.; Rodriguez, J. A. *J. Am. Chem. Soc.* **2005**, *127*, 14871.
- (31) a) Cotton, F. A.; Liu, C. Y.; Murillo, C. A.; Villagrán, D.; Wang, X. *J. Am. Chem. Soc.* **2004**, *126*, 14822; b) Richardson, D. E.; Taube, H. *Inorg. Chem.* **1981**, *20*, 1278; c) Creutz, C. In *Prog. Inorg. Chem.*; John Wiley & Sons, Inc.: 2007, p 1.
- (32) Sekar, P.; Scheer, M.; Voigt, A.; Kirmse, R. *Organometallics* **1999**, *18*, 2833.
- (33) a) Stafford, H.; Rookes, T. M.; Wildman, E. P.; Balázs, G.; Wooles, A. J.; Scheer, M.; Liddle, S. T. *Angew. Chem. Int. Ed.* **2017**, *56*, 7669; b) Gardner, B. M.; Balázs, G.; Scheer, M.; Tuna, F.; McInnes, E. J. L.; McMaster, J.; Lewis, W.; Blake, A. J.; Liddle, S. T. *Angew. Chem. Int. Ed.* **2014**, *53*, 4484.
- (34) Warren, J. J.; Tronic, T. A.; Mayer, J. M. *Chem. Rev.* **2010**, *110*, 6961.
- (35) Cappellani, E. P.; Drouin, S. D.; Jia, G.; Maltby, P. A.; Morris, R. H.; Schweitzer, C. T. *J. Am. Chem. Soc.* **1994**, *116*, 3375.
- (36) Pangborn, A. B.; Giardello, M. A.; Grubbs, R. H.; Rosen, R. K.; Timmers, F. J. *Organometallics* **1996**, *15*, 1518.
- (37) Buss, J. A.; Edouard, G. A.; Cheng, C.; Shi, J.; Agapie, T. *J. Am. Chem. Soc.* **2014**, *136*, 11272.
- (38) Freeman, P. K.; Hutchinson, L. L. *J. Org. Chem.* **1983**, *48*, 879.
- (39) Lesley, M. J. G.; Norman, N. C.; Rice, C. R.; Reger, D. L.; Little, C. A.; Lamba, J. J. S.; Brown, K. J.; Peters, J. C.; Thomas, J. C.; Sahasrabudhe, S.; Yearwood, B. C.; Atwood, D. A.; Hill, R. F.; Wood, G. L.; Danzer, R.; Paine, R. T.; Wagner, N. L.; Murphy, K. L.; Haworth, D. T.; Bennett, D. W.; Byers, P. K.; Canty, A. J.; Honeyman, R. T.; Arnáiz, F. J.; Miranda, M. J.; Bohle, D. S.; Sagan, E. S.; Chivers, T.; Sandblom, N.; Schatte, G. In *Inorg. Synth.*; John Wiley & Sons, Inc.: 2004, p 1.
- (40) Brookhart, M.; Grant, B.; Volpe, A. F. *Organometallics* **1992**, *11*, 3920.
- (41) Heinekey, D. M.; Radzewich, C. E. *Organometallics* **1998**, *17*, 51.
- (42) Adhikari, D.; Mossin, S.; Basuli, F.; Huffman, J. C.; Szilagyi, R. K.; Meyer, K.; Mindiola, D. J. *J. Am. Chem. Soc.* **2008**, *130*, 3676.
- (43) Fulmer, G. R.; Miller, A. J. M.; Sherden, N. H.; Gottlieb, H. E.; Nudelman, A.; Stoltz, B. M.; Bercaw, J. E.; Goldberg, K. I. *Organometallics* **2010**, *29*, 2176.
- (44) Stoll, S.; Schweiger, A. *J. Mag. Res.* **2006**, *178*, 42.
- (45) Hyde, J. S.; Pasenkiewicz-Gierula, M.; Jesmanowicz, A.; Antholine, W. E. *Appl. Magn. Reson.* **1990**, *1*, 483.
- (46) Gaussian 09, Revision C.01, Frisch, M. J.; Trucks, G. W.; Schlegel, H. B.; Scuseria, G. E.; Robb, M. A.; Cheeseman, J. R.; Scalmani, G.; Barone, V.; Mennucci, B.; Petersson, G. A.; Nakatsuji, H.; Caricato, M.; Li, X.; Hratchian, H. P.; Izmaylov, A. F.; Bloino, J.; Zheng, G.; Sonnenberg, J. L.; Hada, M.; Ehara, M.; Toyota, K.; Fukuda, R.; Hasegawa, J.; Ishida, M.; Nakajima, T.; Honda, Y.; Kitao, O.; Nakai, H.; Vreven, T.; Montgomery, Jr., J. A.; Peralta, J. E.; Ogliaro, F.; Bearpark, M.; Heyd, J. J.; Brothers, E.; Kudin, K. N.; Staroverov, V. N.; Kobayashi, R.; Normand, J.; Raghavachari, K.; Rendell, A.; Burant, J. C.; Iyengar, S. S.; Tomasi, J.; Cossi, M.; Rega, N.; Millam, J. M.; Klene, M.; Knox, J. E.; Cross, J. B.; Bakken, V.; Adamo, C.; Jaramillo, J.; Gomperts, R.; Stratmann, R. E.; Yazyev, O.; Austin, A. J.; Cammi, R.; Pomelli, C.; Ochterski, J. W.; Martin, R. L.; Morokuma, K.; Zakrzewski, V. G.; Voth, G. A.; Salvador, P.; Dannenberg, J. J.; Dapprich, S.; Daniels, A. D.; Farkas, Ö.; Foresman, J. B.; Ortiz, J. V.; Cioslowski, J.; Fox, D. J. Gaussian, Inc., Wallingford CT, 2009.

- (47) a) Perdew, J. P.; Ruzsinszky, A.; Csonka, G. I.; Constantin, L. A.; Sun, J. *Phys. Rev. Lett.* **2011**, *106*, 179902; b) Perdew, J. P.; Ruzsinszky, A.; Csonka, G. I.; Constantin, L. A.; Sun, J. *Phys. Rev. Lett.* **2009**, *103*, 026403.
- (48) a) Wadt, W. R.; Hay, P. J. *J. Chem. Phys.* **1985**, *82*, 284; b) Hay, P. J.; Wadt, W. R. *J. Chem. Phys.* **1985**, *82*, 299; c) Hay, P. J.; Wadt, W. R. *J. Chem. Phys.* **1985**, *82*, 270; d) Dunning, T. H.; Hay, P. J. In *Methods of Electronic Structure Theory*; Schaefer, H. F., Ed.; Springer US: Boston, MA, 1977, p 1.
- (49) APEX2, Version 2 User Manual, M86-E01078, Bruker Analytical X-ray Systems, Madison, WI, June 2006.
- (50) Sheldrick, G.M. "SADABS (version 2008/1): Program for Absorption Correction for Data from Area Detector Frames", University of Göttingen, 2008.
- (51) Dolomanov, O. V.; Bourhis, L. J.; Gildea, R. J.; Howard, J. A. K.; Puschmann, H. *J. Appl. Crystallogr.* **2009**, *42*, 339.
- (52) Sheldrick, G.M. *Acta Cryst.* **2008**, *A64*, 112.
- (53) Brandenburg, K. (1999). DIAMOND. Crystal Impact GbR, Bonn, Germany.





**CHAPTER 7****Tying Down Metal-Bound Small Molecules: Proton Induced C–O Bond Cleavage of  
CO<sub>2</sub> Facilitated by Lewis Acid Coordination**

**ABSTRACT**

Though Lewis acids (LAs) have been shown to have profound effects on carbon dioxide (CO<sub>2</sub>) reduction catalyses, understanding of the cause of the reactivity enhancement remains limited. Herein, we report a well-defined molecular system for probing the role of LA additives in the reduction of CO<sub>2</sub> to carbon monoxide (CO) and water. A Mo(0) CO<sub>2</sub> complex (**2**) forms adducts with a series of LAs, demonstrating activation of the metal-bound small molecule that trends well with the strength of the LA. Proton induced C–O cleavage, a transformation that does not proceed in the absence of LA; however, demonstrates both thermodynamic and kinetic sensitivity, suggesting that the residence time of the bound small molecule is equally important to the degree of thermodynamic activation in achieving productive CO<sub>2</sub> reduction chemistry.

## GENERAL INTRODUCTION

As the terminal product of fossil fuel combustion, the conversion of carbon dioxide (CO<sub>2</sub>) to energy-dense, liquid fuels is a necessary step in closing an anthropogenic carbon cycle.<sup>1</sup> Technologies for the capture,<sup>2</sup> copolymerization,<sup>3</sup> and hydrogenation<sup>4</sup> of CO<sub>2</sub> have recently emerged, and their study and design is topical. However, the controlled reduction of CO<sub>2</sub> with protons and electrons is most relevant to artificial photosynthesis and couples most directly to the storage of renewable energies in the form of chemical bonds.<sup>1a,5</sup> Due to the kinetic stability of CO<sub>2</sub>,<sup>6</sup> the range of products formed in a narrow potential window, and competing reduction reactions,<sup>5a,7</sup> efficient and robust catalysts capable of the selective reduction of CO<sub>2</sub> remain a subject of intense interest.<sup>6a</sup>

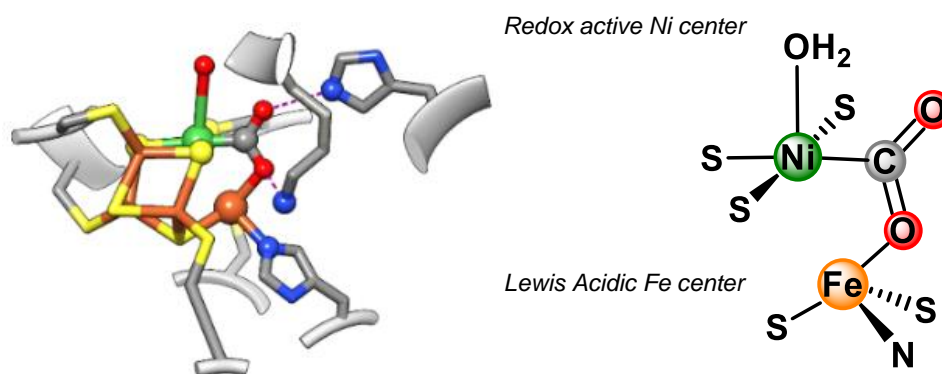
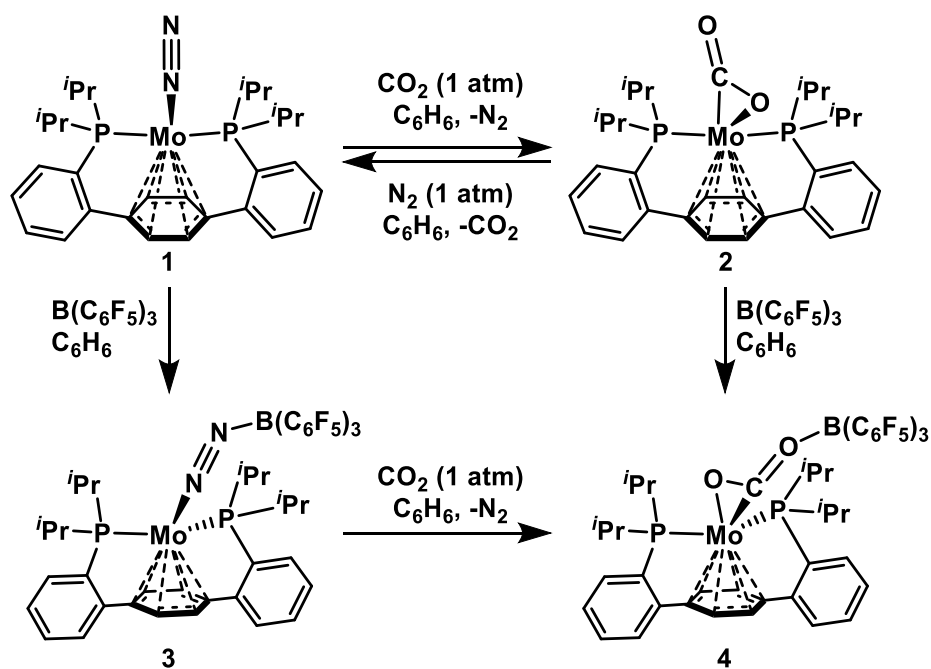


**Figure 7.1.** Solid-state structure (left, PDB: 4UDX)<sup>8</sup> and schematic representation (right) of the CO<sub>2</sub>-bound NiFe-CODH active site.

In Nature, the two-electron two-proton reduction of CO<sub>2</sub> is executed reversibly by NiFe CO-Dehydrogenase (CODH, Figure 7.1).<sup>9</sup> The enzyme active site features a redox active Ni center and an Fe(III) ion that coordinate CO<sub>2</sub> in a  $\mu$ - $\eta$ C: $\eta$ O binding motif.<sup>9b</sup> Lewis acids (LAs) also initiate remarkable rate enhancements in electrocatalytic CO<sub>2</sub> reduction.<sup>10</sup> This strategy of cooperative CO<sub>2</sub> activation has inspired molecular mimics both in the form of ligand scaffolds that feature LAs in the coordination sphere<sup>11</sup> and exogenous LA addition to CO<sub>2</sub> bound metal complexes.<sup>12</sup> Though LAs are capable of promoting CO<sub>2</sub> binding<sup>13</sup> and increasing the degree of CO<sub>2</sub> activation,<sup>12b</sup> their effect on reactivity of the bound CO<sub>2</sub> unit remains underexplored. Herein, we describe a fundamental study correlating Lewis acidity and the

degree of CO<sub>2</sub> activation in a low-valent Mo complex. Moreover, we demonstrate that LA addition facilitates C–O bond cleavage, chemistry that does not proceed from the parent CO<sub>2</sub> complex, via *both* kinetic stabilization and increased small molecule activation.

## RESULTS AND DISCUSSION



**Scheme 7.1.** CO<sub>2</sub> binding and LA adduct formation at low-valent Mo.

Compound **1** reversibly binds CO<sub>2</sub>, interconverting between an η<sup>2</sup>-CO<sub>2</sub> complex, **2**, and an N<sub>2</sub> adduct (Scheme 7.1). Under an atmosphere of <sup>13</sup>CO<sub>2</sub>, the <sup>31</sup>P{<sup>1</sup>H} and <sup>13</sup>C{<sup>1</sup>H} NMR spectra display a coupling doublet and triplet at 62.8 and 192.4 ppm (<sup>2</sup>J(C,P) = 29.3 Hz), respectively, spectral features consistent with binding of <sup>13</sup>CO<sub>2</sub>.<sup>14</sup> The IR spectrum of **2** (solid state, ATR) demonstrates stretches at 1716 and 1198 cm<sup>-1</sup>, sensitive to <sup>13</sup>CO<sub>2</sub> enrichment (Figure 7.4.), again supporting a bound CO<sub>2</sub> motif.<sup>14-15</sup> Solid-state analysis of single crystals of **2** grown under a CO<sub>2</sub> atmosphere confirm the η<sup>2</sup> binding mode (Figure 7.2.), but demonstrate positional disorder of the CO<sub>2</sub> unit, prohibiting detailed analysis of the metrical parameters.

Interested in the thermodynamics of this reversible small molecule binding, longitudinal relaxation (T<sub>1</sub>) times were measured for the relevant <sup>13</sup>C and <sup>15</sup>N resonances of an equilibrium mixture of **1**-<sup>15</sup>N and **2**-<sup>13</sup>C (*vide infra*). Uncharacteristically short T<sub>1</sub> times were observed for **1**-<sup>15</sup>N, free <sup>15</sup>N<sub>2</sub>, **2**-<sup>13</sup>C, and free <sup>13</sup>CO<sub>2</sub>—5.1(4), 4.9(3), 12.5(4), and 16.8(7) s, respectively.<sup>16</sup> These short and near equivalent T<sub>1</sub> times suggest a chemical exchange process that enables new relaxation pathways unavailable to the free small molecules. This exchange, in the case of

CO<sub>2</sub>, was confirmed by magnetization transfer (Figure 7.11.).

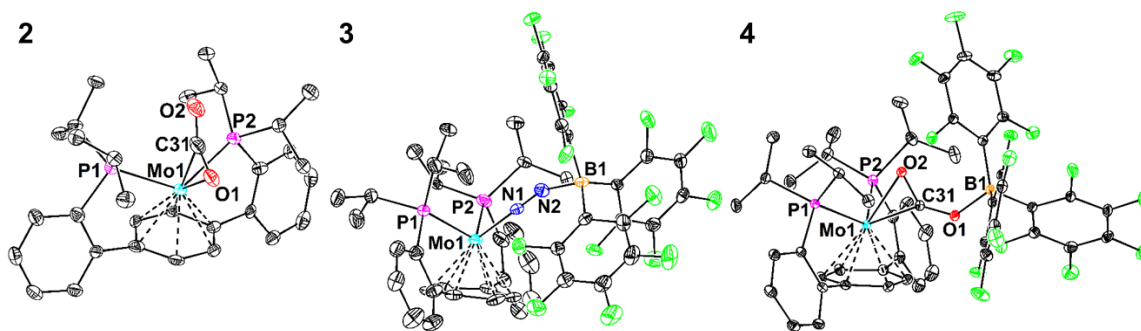


**Figure 7.2.** Solid-state structures of Mo(0) complexes **2**, **3**, and **4**. Thermal anisotropic displacement ellipsoids are shown at the 50% probability level. Hydrogen atoms are omitted for clarity. Selected bond distances [Å] and angles [°]—**3**: Mo1–N1 1.913(2), N1–N2 1.163(3), N2–B1 1.585(37),  $\angle$ Mo1–N1–N2 179.1(3),  $\angle$ N1–N2–B1 158.2(1.2); **4**: Mo1–O2 2.2535(6), Mo1–C31 2.0574(8), O2–C31 1.246(1), C31–O1 1.275(1), O1–B1 1.554(1),  $\angle$ O2–C31–O1 130.93(8),  $\angle$ C31–O1–B1 132.13(7).

The lability of the CO<sub>2</sub> ligand was reflected in the reactivity of **2**. Attempts to protonate the bound CO<sub>2</sub> molecule resulted in CO<sub>2</sub> dissociation and formation of a Mo(II) hydride cation (**5**).<sup>17</sup> Despite its implication as a critical step in CO<sub>2</sub> reduction catalysis,<sup>18</sup> there is a paucity of reports of the protonation of well-defined CO<sub>2</sub> adducts of transition metals.<sup>12a,19</sup> Indeed, protolytic dissociation and subsequent gas analysis was a common characterization technique for metal CO<sub>2</sub> complexes.<sup>20</sup>

Borane LAs have been successfully employed to activate metal coordinated small molecules.<sup>12,21</sup> Addition of the strong LA tris(pentafluorophenyl)borane (B(C<sub>6</sub>F<sub>5</sub>)<sub>3</sub>) to complex **1** affords the Lewis acid/base adduct **3** (Scheme 7.1.), as confirmed by single crystal XRD (Figure 7.2.). The bond metrics of complex **3** are consistent with significant activation of the N<sub>2</sub> unit; the N1–N2 distance elongates by 0.06 Å. The N2–B distance, at 1.586(5) Å, is similar to that of a reported borane N<sub>2</sub> adduct.<sup>21b</sup> The solid-state IR spectrum corroborates this weakening of the N–N bond, with the stretch red shifting by 134 cm<sup>-1</sup>. NMR spectroscopy is consistent with a strong borane/nitrogen interaction in solution. Upon borane coordination, the <sup>31</sup>P{<sup>1</sup>H} NMR resonance shifts upfield to 68.0 ppm and both the <sup>19</sup>F (-135.0, -157.9, and -166.8 ppm)<sup>22</sup> and <sup>11</sup>B (-14.4 ppm)<sup>23</sup> NMR spectra are consistent with a four coordinate boron.

Treating either adduct **3** with CO<sub>2</sub>, or complex **2** with B(C<sub>6</sub>F<sub>5</sub>)<sub>3</sub>, results in the formation of

a new LA adduct, **4**, quantitatively. Contrasting the equilibrium between complexes **1** and **2**, which slightly favors N<sub>2</sub> binding ( $K_{\text{eq}} = 0.48$ ), addition of B(C<sub>6</sub>F<sub>5</sub>)<sub>3</sub> renders CO<sub>2</sub> binding

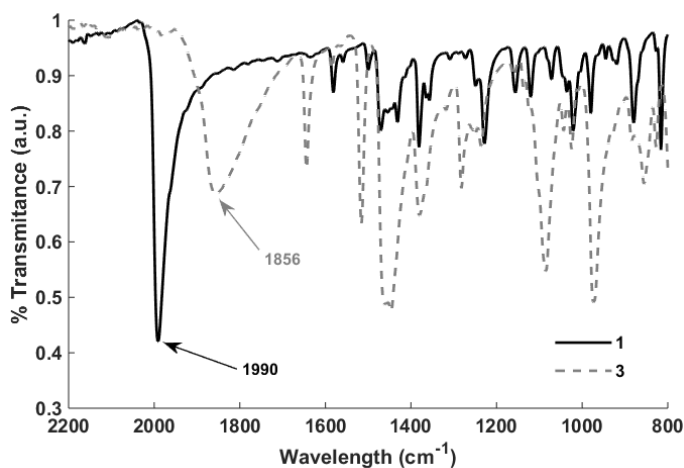


**Figure 7.3.** ATR IR Spectra of Mo(0) N<sub>2</sub> complex, **1**, and its B(C<sub>6</sub>F<sub>5</sub>)<sub>3</sub> adduct, **3**.

irreversible (Scheme 7.1.), likely a consequence of the strong B–O interaction; the Lewis acid/base pair **4** is stable under N<sub>2</sub> in both the solid-state and solution. Adduct **4** exhibits a broad <sup>31</sup>P{<sup>1</sup>H} resonance at 62.6 ppm, upfield shifted from that of **2**. The triplet for the <sup>13</sup>CO<sub>2</sub> unit of isotopically labeled **4**-<sup>13</sup>C moves downfield relative to **2** (218.9 ppm, C<sub>6</sub>D<sub>6</sub>) and exhibits smaller <sup>2</sup>J(C,P) scalar coupling (11.47 Hz). Akin to **3**, the <sup>11</sup>B and <sup>19</sup>F NMR data are consistent with a four coordinate boron.

The solid-state structure of **4** exhibits a μ-η<sup>2</sup>C,O:ηO bridging CO<sub>2</sub> unit between Mo and B (Figure 7.2.). Borane binding to metal-coordinated CO<sub>2</sub> is rare,<sup>12b</sup> but **4** displays similar bond metrics to such complexes, with a C31–O1 distance of 1.275(1) Å and a O1–B1 distance of 1.554(1) Å. The Mo1–O2 (2.2535(6) Å), Mo1–C31 (2.0574(8) Å), and C31–O1 bonds are all consistent with significant CO<sub>2</sub> activation, a phenomenon also borne out in the IR spectrum. The stretches for the CO<sub>2</sub> unit shift to 1602 cm<sup>-1</sup> and 1218 cm<sup>-1</sup>, as confirmed by isotopic labeling (Figure 7.4.).

When stabilized with a LA additive, the reactivity of the Mo CO<sub>2</sub> complexes is decidedly different. The low temperature reaction of **4**-<sup>13</sup>C with [H(Et<sub>2</sub>O)<sub>2</sub>][BAr<sup>F</sup><sub>24</sub>] (BAr<sup>F</sup><sub>24</sub> = tetrakis[3,5-bis(trifluoromethyl)phenyl]borate) resulted in the formation of a single

diamagnetic Mo complex (Scheme 7.2). The  $^{31}\text{P}\{^1\text{H}\}$  and  $^{13}\text{C}\{^1\text{H}\}$  NMR spectra display a doublet (92.64 ppm) and triplet (220.08 ppm), respectively ( $^2J(\text{P,C}) = 14.6$  Hz), consistent

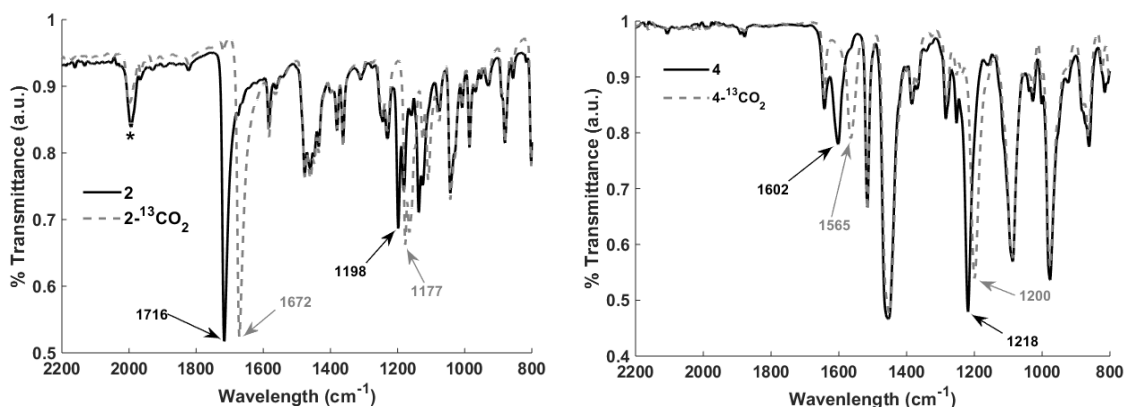
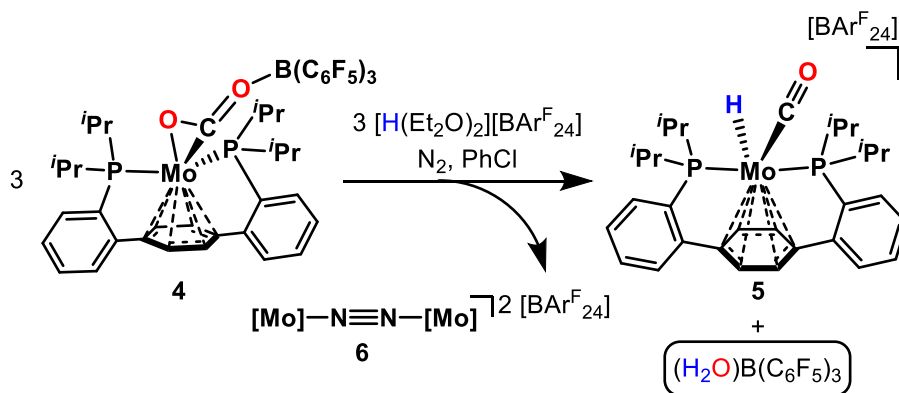


**Figure 7.4.** ATR IR Spectra of isotopologs **2**/ $2\text{-}^{13}\text{C}$  and **4**/ $4\text{-}^{13}\text{C}$ . The signals sensitive to  $\text{CO}_2$  isotope enrichment are demarcated with arrows.

with  $\text{CO}_2$  cleavage to a metal-bound carbonyl. The identity of this product was confirmed as carbonyl hydride cation,  $6\text{-}^{13}\text{C}$ , via XRD and independent synthesis. Cation **6** is accessible via addition of  $[\text{H}(\text{Et}_2\text{O})_2][\text{BAr}^{\text{F}}_{24}]$  to Mo(0) monocarbonyl complex **P2Mo(CO)** (Chapter 3).



**Scheme 7.2.** Acid-induced C–O bond cleavage of Mo-bound LA-adducted  $\text{CO}_2$ .

A balanced reaction for the formation of **6** requires a reductant. When run under  $\text{N}_2$ , the obligatory electrons are provided by **1**. Concomitantly with generation of **6**, a paramagnetic Mo(I)– $\text{N}_2$ –Mo(I) dinuclear complex, **7**, is formed (Figure 7.19), as confirmed by XRD. Quantifying conversion to **6** shows *ca.* 33% C–O cleavage, consistent with a mechanism involving **1** acting as a single electron reductant; one electron oxidation of **1** with  $[\text{Fc}][\text{BAr}^{\text{F}}_{24}]$  likewise provides **7**. Borane speciation in the protonation reactions was tracked by  $^{19}\text{F}$  NMR



spectroscopy (Figure 7.14.), evincing initial formation of a bis(borane) hydroxide<sup>24</sup> and subsequent protonation to a borane aquo adduct.<sup>25</sup> Via independent synthesis and spectroscopic studies, a plausible mechanism balancing the protonation reaction has been developed (Scheme 7.3.).

Protic cleavage of a C–O bond would provide Mo(II) carbonyl cation, **A**, and a highly nucleophilic borane hydroxide anion (Eq. 1), which would subsequently coordinate a second equiv. of B(C<sub>6</sub>F<sub>5</sub>)<sub>3</sub> (Eq. 2). Stripped of LA, and under an N<sub>2</sub> atmosphere, naked CO<sub>2</sub> adduct **2** would form **1**, a reasonable reductant for carbonyl adduct **A** (Eq. 3 and 4). This sequence of reactions forms the dinuclear μ-N<sub>2</sub> dication and a Mo(0) CO adduct. Protonation of the latter gives the terminal diamagnetic product, **6** (Eq. 5), and protonation of HO(B(C<sub>6</sub>F<sub>5</sub>)<sub>3</sub>)<sub>2</sub> affords the borane aquo adduct (Eq. 6). Equations 3, 5, and 6 have been demonstrated independently, as has the synthesis of dinuclear **7** via chemical oxidation at a moderate potential. Equation 2 seems reasonable considering the projected nucleophilicity of “HO(B(C<sub>6</sub>F<sub>5</sub>)<sub>3</sub>)<sub>2</sub>”, and HO(B(C<sub>6</sub>F<sub>5</sub>)<sub>3</sub>)<sub>2</sub> is observed directly in reactions employing stoichiometric acid (Figure 7.14.) Though this reaction sequence is complex, it confirms that LA coordination “turns-on” C–O cleavage chemistry, affording CO and H<sub>2</sub>O from CO<sub>2</sub> and acid.

Interested in the generality of the activation and stabilization observed upon LA coordination to **2**, a series of alkali metal (Na(BAr<sup>F</sup><sub>24</sub>) and Cs(BAr<sup>F</sup><sub>24</sub>)) and borane (B(C<sub>6</sub>H<sub>2</sub>F<sub>3</sub>)<sub>3</sub>, B(C<sub>6</sub>F<sub>5</sub>)<sub>3</sub>, and B(C<sub>6</sub>H<sub>3</sub>(CF<sub>3</sub>)<sub>2</sub>)<sub>3</sub>) LAs were added to solutions of **2**-<sup>13</sup>C. In each case, the orange color of **2** darkened to a deep red, consistent with formation of a discreet LA adduct. <sup>13</sup>C{<sup>1</sup>H} and <sup>31</sup>P{<sup>1</sup>H} NMR spectroscopies supported adduct formation, demonstrating resonances shifted downfield and upfield, respectively, from those of **2** (Tables 7.1. and 7.3.). The degree of CO<sub>2</sub> activation, as reported by the <sup>13</sup>C chemical shift, trends linearly with the strength of the LA, as quantified by the acceptor number (AN, Figure 7.5.)).<sup>26</sup>

Revisiting protonation with these new LA adducts,<sup>27</sup> we were gratified to see that Na<sup>+</sup>, a LA relevant to electrocatalysis, induced *ca.* 35% C–O bond cleavage. Increasing the [Na<sup>+</sup>], though it has a negligible effect on the degree of activation of bound CO<sub>2</sub>,

increased the selectivity for CO formation to *ca.* 40% (Table 7.1.). Similar trends were observed for borane LAs. Changing the solvent from neat PhCl to a PhCl/Et<sub>2</sub>O mixture results in a significant decrease in B(C<sub>6</sub>F<sub>5</sub>)<sub>3</sub> induced cleavage chemistry, 44% and 20%, respectively, despite revealing no change on the <sup>13</sup>C chemical shift.

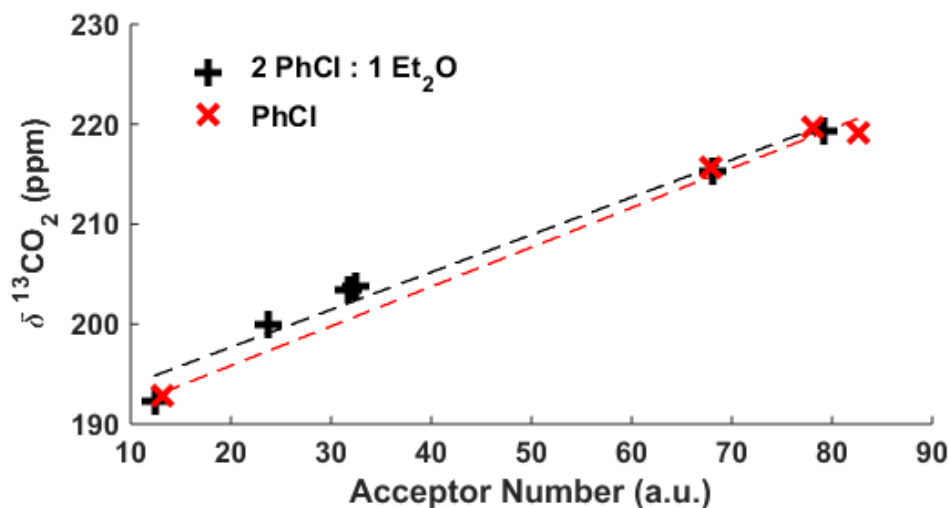
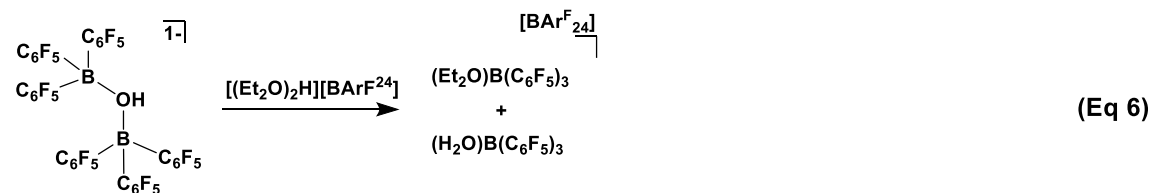
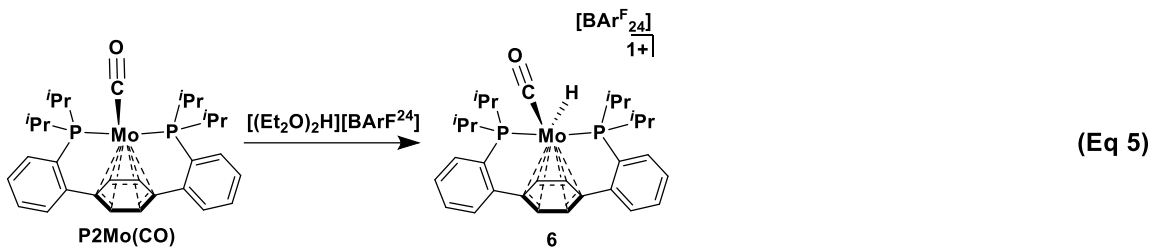
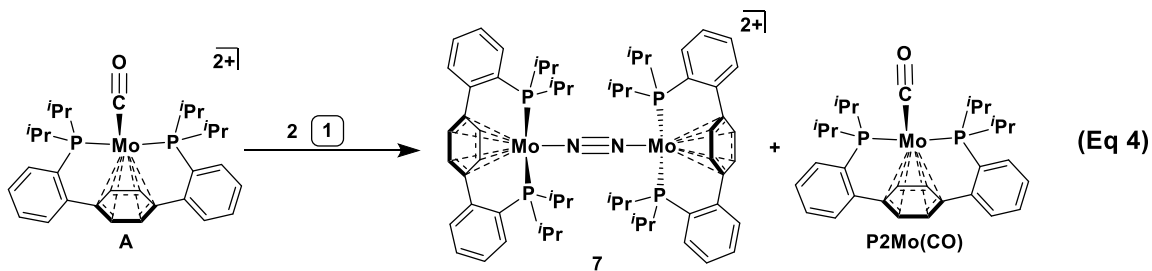
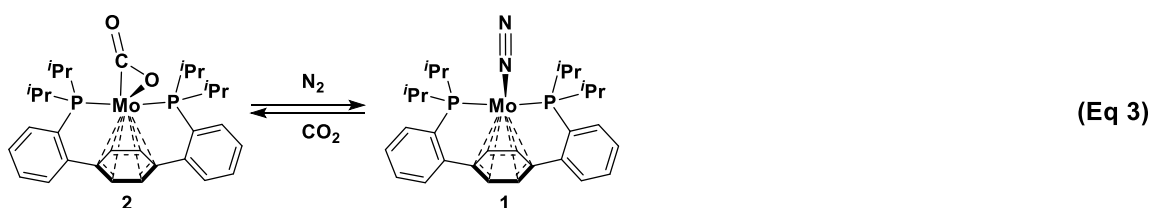
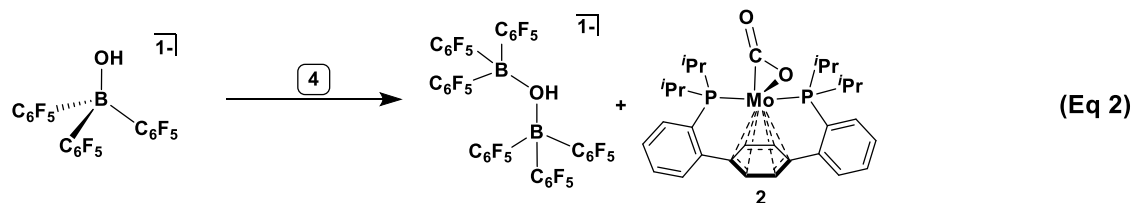
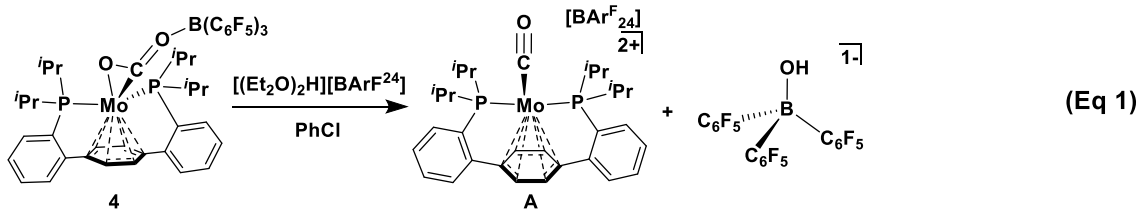


**Figure 7.5.** CO<sub>2</sub> Activation as a function of Lewis acidity.

**Table 7.1.** CO<sub>2</sub> adduct activation, exchange rates, and C–O bond cleavage selectivities as a function of LA.

	LA	AN	δ <sup>13</sup> C (ppm)	Exchange Rate (s <sup>-1</sup> )	% C–O Cleavage
2 PhCl : 1 Et <sub>2</sub> O	None	12.4	192.3	> 7 x 10 <sup>-5</sup>	0
	Cs(BAr <sup>F</sup> <sub>24</sub> )	23.7	199.9	2 x 10 <sup>-5</sup>	--
	Na(BAr <sup>F</sup> <sub>24</sub> )	31.8	203.5	6 x 10 <sup>-6</sup>	37
	Na(BAr <sup>F</sup> <sub>24</sub> ) <sup>‡</sup>	32.4	203.7	1 x 10 <sup>-6</sup>	42
	B(C <sub>6</sub> H <sub>2</sub> F <sub>3</sub> ) <sub>3</sub>	68.1	215.3	3 x 10 <sup>-6</sup>	29
	B(C <sub>6</sub> F <sub>5</sub> ) <sub>3</sub>	79.2	219.3	9 x 10 <sup>-7</sup>	25
PhCl	None	13.2	192.9	> 7 x 10 <sup>-5</sup>	0
	B(C <sub>6</sub> H <sub>2</sub> F <sub>3</sub> ) <sub>3</sub>	67.9	215.7	1 x 10 <sup>-6</sup>	--
	B(C <sub>6</sub> F <sub>5</sub> ) <sub>3</sub>	78.1	219.6	3 x 10 <sup>-6</sup>	44
	B(C <sub>6</sub> H <sub>3</sub> (CF <sub>3</sub> ) <sub>2</sub> ) <sub>3</sub>	82.7	219.1	9 x 10 <sup>-7</sup>	--

<sup>‡</sup>The [Na(BAr<sup>F</sup><sub>24</sub>)] was doubled.



**Scheme 7.3.** Proposed mechanism for proton-induced CO<sub>2</sub> cleavage from 4.

Observing that C–O cleavage did not track with the level of thermodynamic *activation*, the extent of kinetic *stabilization* was interrogated. Exposing solutions of 2-<sup>13</sup>C and a LA additive to an excess of <sup>12</sup>CO<sub>2</sub> at 0 °C, resulted in decay of the resonance associated with bound CO<sub>2</sub>

in the  $^{13}\text{C}\{^1\text{H}\}$  NMR spectrum, providing a handle for kinetic analysis (Figure 7.12. and 7.13.). The LA-free exchange rate is approximately two orders of magnitude faster than those of the LA adducts, which fail to track with the strength of the added LA (Table 7.1.). Increasing the concentration of the LA additive further impedes the exchange, implicating a dissociative mechanism. Borane LA adducts exchange faster in the presence of  $\text{Et}_2\text{O}$ , a competing Lewis base that may sequester dissociated LA, again supporting LA dissociation as a rate effecting chemical step.

The rates of exchange are similar for most of the LAs, irrespective of their AN or the  $^{13}\text{C}$  chemical shift of the adduct they form. This is consistent with the C–O cleavage selectivity;  $\text{Na}^+$ , with a modest AN, half that of  $\text{B}(\text{C}_6\text{F}_5)_3$ , still affords *ca.* 40% C–O cleavage. These data are consistent with the ‘residence time’ of the  $\text{CO}_2$  adduct, the propensity of the substrate to be coordinated to the metal center, not the degree of  $\text{CO}_2$  activation, being a determining factor for C–O cleavage.

## CONCLUSION

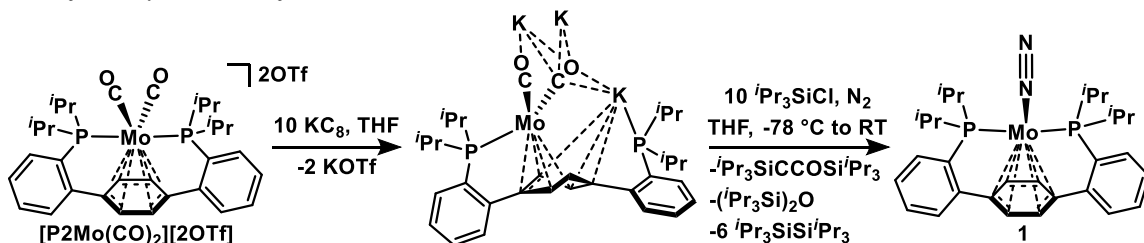
In summary, a labile Mo(0) CO<sub>2</sub> adduct has been prepared and characterized. This complex interacts with a variety of LAs, which increase both the degree of activation and the stability of bound CO<sub>2</sub>. LA addition facilitates proton-induced cleavage to CO and H<sub>2</sub>O, chemistry that correlates with the kinetics of CO<sub>2</sub> exchange. This work establishes that the residence time of a small molecule substrate bound to a metal center, and not just the degree of activation, is a critical factor in engendering desirable transformation chemistries. Studies exploring the kinetic stability of additional small molecule LA adducts, and the effect it has on their reduction chemistry, is ongoing.

## EXPERIMENTAL SECTION

### *General Considerations*

Unless otherwise specified, all operations were carried out in an MBraun drybox under a nitrogen atmosphere or using standard Schlenk and vacuum line techniques. Solvents for air- and moisture-sensitive reactions were dried over sodium benzophenone ketyl, calcium hydride, or by the method of Grubbs.<sup>28</sup> Deuterated solvents were purchased from Cambridge Isotope Laboratories and vacuum transferred from sodium benzophenone ketyl ( $C_6D_6$ ) or  $CaH_2$  ( $CD_3CN$ ). Solvents, once dried and degassed, were vacuum transferred directly prior to use or stored under inert atmosphere over activated 4 Å molecular sieves.  $[P_2Mo(CO)_2][2OTf]$ <sup>17</sup> and potassium graphite ( $KC_8$ ),<sup>3</sup>  $CsBAr^F_{24}$ ,<sup>29</sup>  $NaBAr^F_{24}$ ,<sup>30</sup>  $B(C_6H_2F_3)_3$ ,<sup>31</sup>  $B(C_6F_5)_3$ ,<sup>32</sup>  $B(C_6H_3(CF_3)_2)_3$ ,<sup>33</sup> and Brookhart's acid ( $[H(Et_2O)_2][BAr^F_{24}]$ ),<sup>34</sup> were prepared according to literature procedures. Commercial reagents were purchased from standard vendors and used without further purification unless noted otherwise.  $^1H$ ,  $^{13}C\{^1H\}$ , and  $^{31}P\{^1H\}$  NMR spectra were recorded on a Varian 400 MHz or Varian INOVA-500 spectrometers with shifts reported in parts per million (ppm).  $^1H$  and  $^{13}C\{^1H\}$  NMR spectra are referenced to residual solvent peaks.<sup>35</sup>  $^{31}P\{^1H\}$  chemical shifts are referenced to an external 85%  $H_3PO_4$  (0 ppm) standard. Fourier transform infrared ATR spectra were collected from thin films or powders on a Thermo Scientific Nicolet iS5 Spectrometer with a diamond ATR crystal (utilized iD5 ATR insert). Elemental analysis was performed at the Caltech XRCF using a PerkinElmer 2400 Series II CHN Elemental Analyzer.

### *Modified Synthesis of 1*

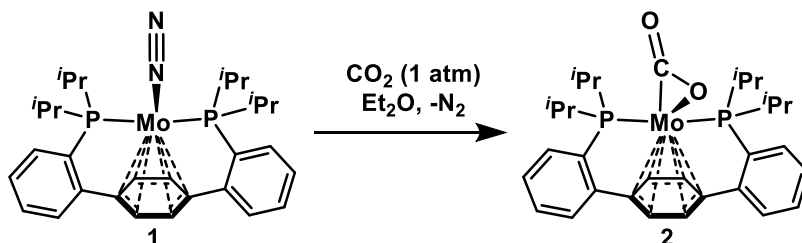


A 500 mL Teflon stoppered Schlenk tube was charged with  $[P_2Mo(CO)_2][2OTf]$  (10.0 g, 10.96 mmol),  $KC_8$  (14.8 g, 109.47 mmol), and a large stir bar. THF (100 mL) was added slowly with swirling, resulting in the formation of a dark purple slurry (Note: this process is quite exothermic and THF condensing on the walls of the flask is normal). Stirring was initiated and additional THF (300 mL) was added, giving a dark purple mixture. With a heavy  $N_2$  counterflow, the Teflon stopper of the flask was exchanged with a septum. The flask was then cooled to  $-78\text{ }^\circ\text{C}$  in a dry ice/acetone bath and  $Pr_3SiCl$  (23.5 mL, 109.82 mmol) was added dropwise via syringe. Following this addition, the flask was re-stoppered and sealed. It was left to warm to room temperature, with stirring, during which time the color of the solution changed from deep purple to burgundy. The volatiles were removed *in vacuo*, providing a dark black/brown residue.

Hexanes (500 mL) was added via cannula and the flask contents shaken vigorously, giving a suspension of graphite in a dark red/brown solution. This mixture was subjected to filtration through a thick pad of celite. The reaction residue and the filter cake were extracted with hexanes until the washes were near colorless (*ca.* 1 L of solvent on this scale, 1.5 L of hexanes in total) and the combined filtrate was concentrated under reduced pressure to a volume of *ca.* 70 mL, precipitating microcrystals of **1**. These microcrystals were collected on a medium porosity fritted funnel, washed with cold ( $-78\text{ }^\circ\text{C}$ ) hexanes (*ca.* 20 mL), and dried *in vacuo*. The resulting red solids were collected as analytically pure **1** (4.1 g, 6.99 mmol, 64 % yield).

The spectroscopic data for **1** prepared in this way match prior literature. Additionally,  $^1\text{H}$  and  $^{31}\text{P}\{^1\text{H}\}$  NMR of the described solids are presented in Appendix C.

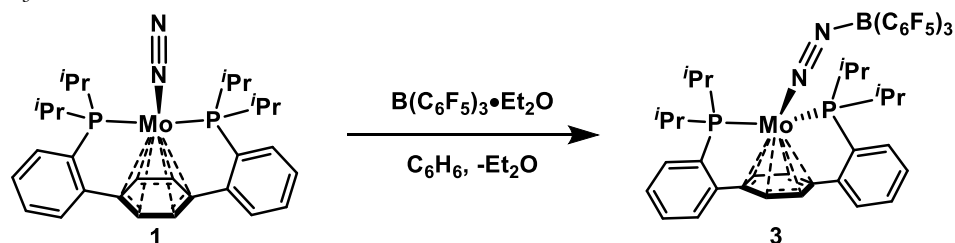
### Synthesis of **2**



A 100 mL round bottom flask was charged with **1** (1.15 g, 1.96 mmol) and a stir bar. The flask was attached to a swivel frit apparatus and connected to a high vacuum line. Et<sub>2</sub>O (70 mL) was admitted via vacuum transfer at -78 °C and stirring was initiated. The flask was allowed to warm to room temperature, providing a red orange homogeneous solution. A partial atmosphere of CO<sub>2</sub> (*ca.* 600 Torr) was admitted to the flask. After stirring for 30 sec., flocculent light orange solids precipitated from solution. Stirring continued for 5 min. The reaction vessel was partially degassed and the CO<sub>2</sub> atmosphere (*ca.* 600 Torr) was refreshed. This process was repeated thrice, with 5 min intervals of stirring in between each atmosphere exchange. The apparatus was subjected to vacuum and the total volume concentrated to *ca.* 50 mL. The suspension was filtered and the solids were washed twice via condensation of the filtrate solvent. All volatiles were removed *in vacuo*, giving **2** as an analytically pure pale orange powder (1.10 g, 1.82 mmol, 93%). Complex **2** is stable under a N<sub>2</sub> atmosphere in the solid state, but reverts to **1** in solution in the presence of N<sub>2</sub>. <sup>1</sup>H NMR (400 MHz, C<sub>6</sub>D<sub>6</sub>, 23 °C) δ: 7.36 (d, *J* = 6.8 Hz, 2H, aryl-*H*), 7.11 (d, *J* = 5.2 Hz, 2H, aryl-*H*), 7.03 (t, *J* = 7.39 Hz, 2H, aryl-*H*), 6.97 (t, *J* = 6.10 Hz, 2H, aryl-*H*), 4.98 (s, 2H, central arene-*H*), 3.54-3.56 (m, 2H, central arene-*H*), 2.85-2.92 (m, 2H, CH(CH<sub>3</sub>)<sub>2</sub>), 2.45-2.57 (m, 2H, CH(CH<sub>3</sub>)<sub>2</sub>), 1.70-1.76 (m, 6H, CH(CH<sub>3</sub>)<sub>2</sub>), 1.04-1.10 (m, 6H, CH(CH<sub>3</sub>)<sub>2</sub>), 0.92-0.96 (m, 6H, CH(CH<sub>3</sub>)<sub>2</sub>), 0.57-0.63 (m, 6H, CH(CH<sub>3</sub>)<sub>2</sub>). <sup>31</sup>P{<sup>1</sup>H} NMR (162 MHz, C<sub>6</sub>D<sub>6</sub>, 23 °C) δ: 62.67 (br s). IR (powder ATR, cm<sup>-1</sup>): 1716, 1198.

**2**-<sup>13</sup>C can be prepared analogously using <sup>13</sup>CO<sub>2</sub> in lieu of CO<sub>2</sub>. The enhanced <sup>13</sup>C{<sup>1</sup>H} NMR (101 MHz, C<sub>6</sub>D<sub>6</sub>, 23 °C) resonance is observed at 191.89 (t, *J* = 29.9 Hz) ppm. The IR bands redshift to 1672 and 1177 cm<sup>-1</sup>.

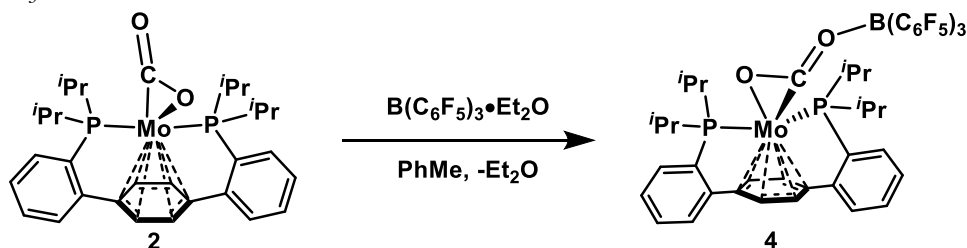
### Synthesis of **3**





A 100 mL RB flask was charged with **1** (300 mg, 0.511 mmol),  $B(C_6F_5)_3 \cdot Et_2O$  (300 mg, 0.511 mmol), and a stir bar. PhMe (25 mL) was added, resulting in dissolution of the reagents and formation of a dark red/brown homogeneous solution. Stirring continued to 15 min. At this time, solvent was removed *in vacuo*, giving a dark residue. This residue was triturated with hexanes (4 mL) and dried under reduced pressure, affording crude **3**. Prepared this way, samples of **3** contain *ca.* 20% of an unidentified asymmetric impurity and 7% free diphosphine ligand. Attempts to separate the two species have thus far been unsuccessful. This mixture of products can be crystallized from cold PhMe ( $-35\text{ }^\circ\text{C}$ ), but NMR spectra of the crystals show both **3** and the impurity. Mechanical separation of the crystals under a microscope (in an effort to obtain a solids state structure of the impurity) proved futile.  $^1\text{H}$  NMR (400 MHz,  $C_6D_6$ ,  $23\text{ }^\circ\text{C}$ )  $\delta$ : 7.22 (d,  $J = 7.32\text{ Hz}$ , 2H, aryl-*H*), 6.92-7.04 (m, 6H, aryl-*H*), 4.62 (s, 2H, central arene-*H*), 3.99 (s, 2H, central arene-*H*), 2.23-2.32 (m, 2H,  $CH(CH_3)_2$ ), 2.00-2.09 (m, 2H,  $CH(CH_3)_2$ ), 0.90-0.95 (m, 6H,  $CH(CH_3)_2$ ), 0.75-0.85 (m, 18H,  $CH(CH_3)_2$ ).  $^{31}\text{P}\{^1\text{H}\}$  NMR (162 MHz,  $C_6D_6$ ,  $23\text{ }^\circ\text{C}$ )  $\delta$ : 68.71 (s).  $^{11}\text{B}\{^1\text{H}\}$  NMR (128 MHz,  $C_6D_6$ ,  $23\text{ }^\circ\text{C}$ )  $\delta$ : -14.47 (s).  $^{19}\text{F}$  NMR (376 MHz,  $C_6D_6$ ,  $23\text{ }^\circ\text{C}$ )  $\delta$ : -131.53 (br s), -158.24 (v br s), -164.51 (br s).

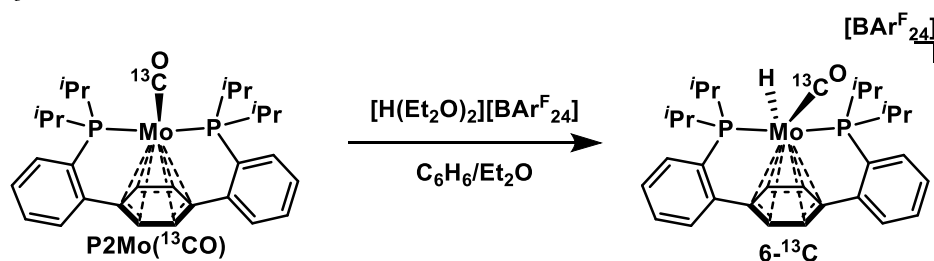
#### Synthesis of **4**



A 100 mL Teflon stoppered Schlenk tube was charged with **2** (300 mg, 0.498 mmol),  $B(C_6F_5)_3 \cdot Et_2O$  (291 mg, 0.498 mmol) and a stir bar. The flask was attached to a high vacuum line and evacuated. Toluene (25 mL) was condensed into the reaction vessel at  $-78\text{ }^\circ\text{C}$ , and stirring was initiated. While warming to room temperature, orange **2** dissolved to give a deep red homogenous solution. The volume was reduced to *ca.* 5 mL under reduced pressure and transferred, in a glovebox, to a 20 mL scintillation vial. Upon

standing for 12 hours at  $-35\text{ }^{\circ}\text{C}$ , the precipitated maroon solids were collected on a medium porosity fritted funnel. Washing with cold hexanes (2 x 2 mL) afforded analytically pure **3** as the persisting solid material (462 mg, 0.415 mmol, 83 %). Complex **4** is stable in the presence of  $\text{N}_2$  both in solution and as a solid, but is reactive toward coordinating solvents such as THF or MeCN.  $^1\text{H}$  (500 MHz,  $\text{C}_6\text{D}_6$ ,  $25\text{ }^{\circ}\text{C}$ )  $\delta$ : 7.19 (s, 2H, aryl-*H*), 7.01 (t,  $J = 7.08\text{ Hz}$ , 2H, aryl-*H*), 6.94 (t,  $J = 7.44\text{ Hz}$ , 2H, aryl-*H*), 6.85-6.87 (m, 2H, aryl-*H*), 5.36 (br d,  $J = 2.34\text{ Hz}$ , 2H, central arene-*H*), 3.94 (s, 2H, central arene-*H*), 1.93-2.00 (m, 2H,  $\text{CH}(\text{CH}_3)_2$ ), 1.78-1.86 (m, 2H,  $\text{CH}(\text{CH}_3)_2$ ), 0.85-0.90 (m, 6H,  $\text{CH}(\text{CH}_3)_2$ ), 0.78-0.81 (m, 6H,  $\text{CH}(\text{CH}_3)_2$ ), 0.63-0.67 (m, 6H,  $\text{CH}(\text{CH}_3)_2$ ), 0.38-0.43 (m, 6H,  $\text{CH}(\text{CH}_3)_2$ ).  $^{13}\text{C}\{^1\text{H}\}$  (126 MHz,  $\text{C}_6\text{D}_6$ ,  $25\text{ }^{\circ}\text{C}$ )  $\delta$ : 218.94 (t,  $J = 11.47\text{ Hz}$ , Mo- $\text{CO}_2$ ), 148.93 (app dt,  $J = 241.92\text{ \& } 8.68\text{ Hz}$ ,  $\text{B}(\text{C}_6\text{F}_5)_3$ ), 146.47 (m, aryl-C), 146.27 (m, aryl-C), 140.08 (app dt,  $J = 248.72\text{ \& } 14.84\text{ Hz}$ ,  $\text{B}(\text{C}_6\text{F}_5)_3$ ), 137.48 (ddd,  $J = 246.57, 19.91, \text{ \& } 9.95\text{ Hz}$ ,  $\text{B}(\text{C}_6\text{F}_5)_3$ ), 132.25 (s, aryl-C), 130.09 (s, aryl-C), 127.80 (s, aryl-C; coincides with residual  $\text{C}_6\text{D}_6$  but corroborated by HMBC), 127.46 (s, aryl-C; coincides with residual  $\text{C}_6\text{D}_6$  but corroborated by HMBC), 104.21 (t,  $J = 3.81\text{ Hz}$ , central arene-C), 85.40 (s, central arene-C), 82.66 (s, central arene-C), 27.87 (br d,  $J = 7.32\text{ Hz}$ ,  $\text{CH}(\text{CH}_3)_2$ ), 24.40 (br d,  $J = 7.30\text{ Hz}$ ,  $\text{CH}(\text{CH}_3)_2$ ), 20.72 (m,  $\text{CH}(\text{CH}_3)_2$ ), 19.54 (s,  $\text{CH}(\text{CH}_3)_2$ ), 18.01 (m,  $\text{CH}(\text{CH}_3)_2$ ), 17.81 (m,  $\text{CH}(\text{CH}_3)_2$ ).  $^{31}\text{P}\{^1\text{H}\}$  (202 MHz,  $\text{C}_6\text{D}_6$ ,  $25\text{ }^{\circ}\text{C}$ )  $\delta$ : 50.47 (s,  $P_2$ ).  $^{19}\text{F}$  (470 MHz,  $\text{C}_6\text{D}_6$ ,  $25\text{ }^{\circ}\text{C}$ )  $\delta$ : -131.13 (d,  $J = 19.36\text{ Hz}$ ,  $\text{B}(\text{C}_6\text{F}_5)_3$ ), -159.58 (t,  $J = 20.87\text{ Hz}$ ,  $\text{B}(\text{C}_6\text{F}_5)_3$ ), -165.24 (m,  $\text{B}(\text{C}_6\text{F}_5)_3$ ). IR (solid ATR,  $\text{cm}^{-1}$ ): 1602, 1218.

**4- $^{13}\text{C}$**  can be prepared analogously starting from **2- $^{13}\text{C}$** . The enhanced resonance in the  $^{13}\text{C}$  NMR spectrum is the triplet at 219.94 ppm. No  $^2J(\text{P,C})$  scalar coupling is resolved in the  $^{31}\text{P}\{^1\text{H}\}$  NMR spectrum. The IR bands (solid ATR) shift to 1565 and  $1200\text{ cm}^{-1}$ .

Synthesis of **5**

A 20 mL scintillation vial was charged with a deep orange solution of **P2Mo**(<sup>13</sup>C<sub>O</sub>) (200 mg, 0.340 mmol) in C<sub>6</sub>H<sub>6</sub> (10 mL). With stirring, an ethereal solution of [H(Et<sub>2</sub>O)<sub>2</sub>][BARF<sub>24</sub>] (345 mg, 0.340 mmol, in 5 mL) was added dropwise. The reaction mixture was dried *in vacuo* and the resulting residue triturated with hexanes (5 mL) and dried under reduced pressure, affording **6-<sup>13</sup>C** as a yellow/orange powder (468 mg, 0.323 mmol, 95 %). X-ray quality crystals were grown via vapor diffusion of pentane into an MeCN/Et<sub>2</sub>O solution of **6-<sup>13</sup>C**. <sup>1</sup>H (500 MHz, CD<sub>3</sub>CN, 25 °C) δ: 7.71 (br s, 8H, BARF<sub>24</sub> *ortho*-H), 7.67 (br s, 4H, BARF<sub>24</sub> *para*-H), 7.57-7.62 (m, 6H, aryl-H), 7.52-7.55 (m, 2H, aryl-H), 6.29 (br s, 2H, central arene-H), 5.92 (br d, *J* = 1.05 Hz, 2H, central arene-H), 2.82-2.93 (m, 2H, CH(CH<sub>3</sub>)<sub>2</sub>), 2.62-2.71 (m, 2H, CH(CH<sub>3</sub>)<sub>2</sub>), 1.28-1.32 (m, 6H, CH(CH<sub>3</sub>)<sub>2</sub>), 1.19-1.21 (m, 6H, CH(CH<sub>3</sub>)<sub>2</sub>), 1.16-1.18 (m, 6H, CH(CH<sub>3</sub>)<sub>2</sub>), 0.90-0.94 (m, 6H, CH(CH<sub>3</sub>)<sub>2</sub>), -3.02 (td, *J* = 65.37 & 4.02 Hz, 1H, Mo-H). <sup>13</sup>C{<sup>1</sup>H} (126 MHz, CD<sub>3</sub>CN, 25 °C) δ: 221.81 (t, *J* = 13.82 Hz, Mo-CO), 162.62 (q, *J* = 49.28 Hz, BARF<sub>24</sub> aryl-C), 145.16 (d, *J* = 20.71 Hz, aryl-C), 142.82 (dd, *J* = 28.66 & 1.83 Hz, aryl-C), 135.67 (br d, *J* = 20.15 Hz, BARF<sub>24</sub> aryl-C), 132.36 (vt, *J* = 8.55 Hz, aryl-C), 132.03 (vt, *J* = 7.36 Hz, aryl-C), 130.06 (m, aryl-C), 129.95 (qq, *J* = 32.02 & 2.83 Hz, BARF<sub>24</sub> aryl-C), 128.15 (dvt, *J* = 11.93 & 9.54 Hz, aryl-C), 125.48 (q, *J* = 271.73 Hz, BARF<sub>24</sub> CF<sub>3</sub>), 118.93 (d, *J* = 4.24 Hz, central arene-C), 118.68 (br d, *J* = 15.72 Hz, BARF<sub>24</sub> aryl-C), 98.86 (t, *J* = 2.03 Hz, central arene-C), 90.69 (s, central arene-C), 33.26 (d, *J* = 31.94 Hz, CH(CH<sub>3</sub>)<sub>2</sub>), 29.33 (d, *J* = 29.93 Hz, CH(CH<sub>3</sub>)<sub>2</sub>), 20.31 (d, *J* = 1.82 Hz, CH(CH<sub>3</sub>)<sub>2</sub>), 19.59 (d, *J* = 1.69 Hz, CH(CH<sub>3</sub>)<sub>2</sub>), 19.14 (d, *J* = 3.07 Hz, CH(CH<sub>3</sub>)<sub>2</sub>), 18.40 (s, CH(CH<sub>3</sub>)<sub>2</sub>). <sup>31</sup>P{<sup>1</sup>H} (202 MHz, CD<sub>3</sub>CN, 25 °C) δ: 93.01 (dd, *J* = 13.68 & 9.92 Hz, P2).

*In Situ Preparation of Lewis Acid Adducts of 3*

To ensure strict exclusion of N<sub>2</sub>, solvents used for the preparation of LA adducts of **3** were thoroughly degassed via three freeze-pump-thaw cycles and vacuum transferred prior to use. The 2 PhCl : Et<sub>2</sub>O stock solutions used for generation of LA adducts and kinetics experiments were prepared in 12 mL batches by sequentially vacuum transferring PhCl (8 mL) and Et<sub>2</sub>O (4 mL) into a calibrated volume and then a storage flask sealed with a Teflon stopper. Solvents prepared this way were stored and manipulated under Ar.

*Representative Procedure for LA AN Determination*

In a N<sub>2</sub> filled glovebox, a J. Young NMR tube was charged with Et<sub>3</sub>PO (4.5 mg, 0.033 mmol), 1,3,5-trimethoxybenzene (10 mg, 0.059 mmol), and LA (0.033 mmol). The tube was sealed and attached to a high vacuum line. Following thorough evacuation of the headspace, the J. Young tube was backfilled with Ar gas. Under a heavy Ar counterflow, solvent (0.5 mL) was added via syringe. The tube was sealed and the contents mixed, affording a colorless homogeneous solution. The tube was introduced to an NMR probe, pre-cooled to 0 °C. After allowing 10 min for temperature equilibration, <sup>31</sup>P{<sup>1</sup>H} NMR spectra were collected.

The AN was calculated using the following equation: AN = 2.21 × (δ <sup>31</sup>P - 41.0)

**Table 7.2.** Lewis Acid acceptor number determination.

Solvent	2 PhCl : Et <sub>2</sub> O		PhCl		
	LA	δ <sup>31</sup> P (ppm)	AN	δ <sup>31</sup> P (ppm)	AN
None		46.63	12.4	46.98	13.2
Cs(BAr <sup>F</sup> <sub>24</sub> )		51.70	23.6	--	--
Na(BAr <sup>F</sup> <sub>24</sub> )		55.39	31.8	--	--
Na(BAr <sup>F</sup> <sub>24</sub> )		55.65	32.4	--	--
B(C <sub>6</sub> H <sub>2</sub> F <sub>3</sub> ) <sub>3</sub>		71.82	68.1	71.70	67.8
B(C <sub>6</sub> F <sub>5</sub> ) <sub>3</sub>		76.82	79.2	76.34	78.1
B(C <sub>6</sub> H <sub>3</sub> (CF <sub>3</sub> ) <sub>2</sub> ) <sub>3</sub>		--	--	78.43	82.7

*Representative Procedure for LA Adduct Preparation*

In a representative procedure, a J. Young NMR tube was charged with 2- $^{13}\text{C}$  (20 mg, 0.033 mmol), 1,3,5-trimethoxybenzene (10 mg, 0.059 mmol), and LA (0.033 mmol). The tube was sealed and attached to a high vacuum line. Following thorough evacuation of the headspace, the J. Young tube was backfilled with Ar gas. Under a heavy Ar counterflow, solvent (0.5 mL) was added via syringe. The tube was sealed and the contents mixed, affording a colorless homogeneous solution. Samples prepared this way were used for kinetics studies (*vide infra*) as well as adduct characterization.

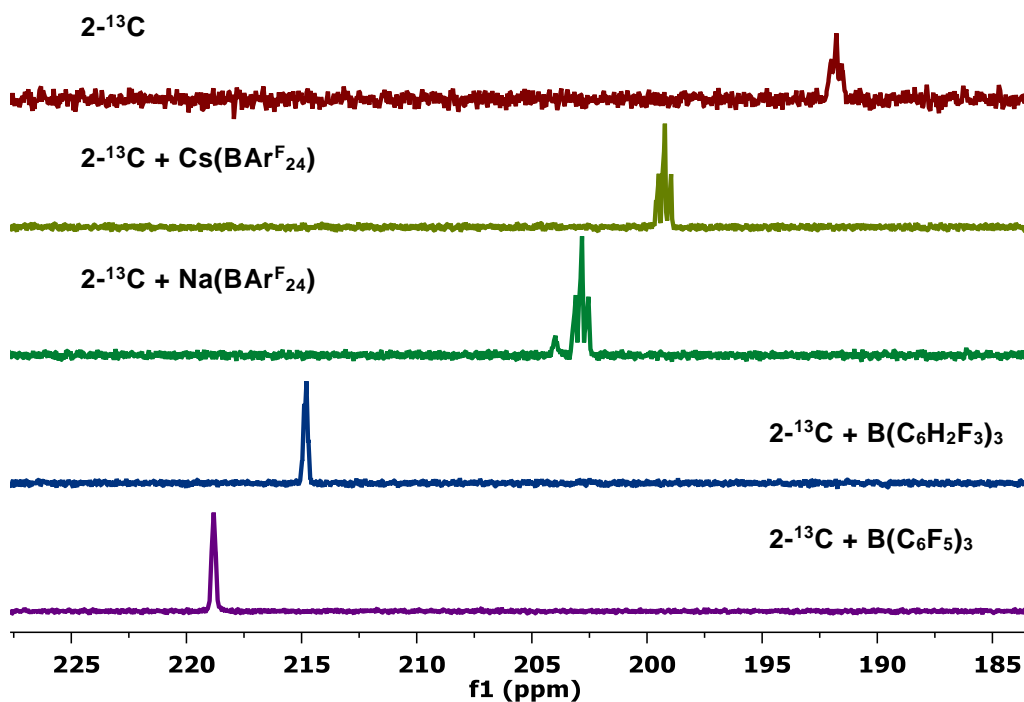


**Figure 7.6.** Stacked Partial  $^{13}\text{C}\{^1\text{H}\}$  NMR spectra (2 PhCl : Et $_2$ O, 0°C, 126 MHz) of *in situ* generated Lewis acid adducts of 2- $^{13}\text{C}$ . The identity of the LA is indicated on each trace.

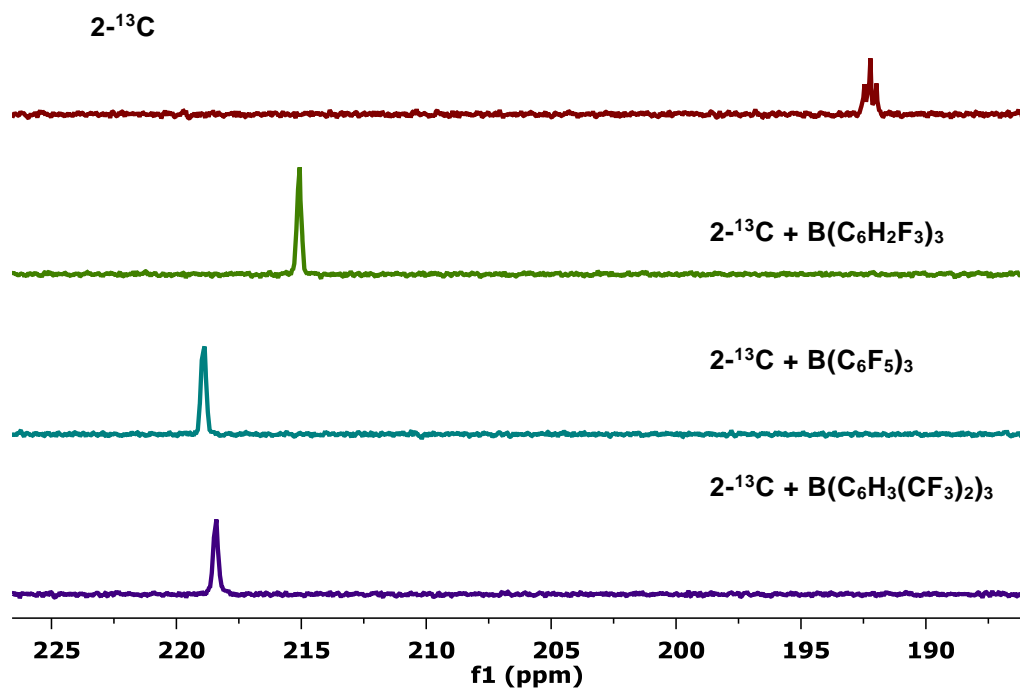


**Figure 7.7.** Stacked Partial  $^{13}\text{C}\{^1\text{H}\}$  NMR Spectra ( $\text{PhCl}$ ,  $0^\circ\text{C}$ , 126 MHz) of *in situ* Generated Lewis Acid Adducts of  $2\text{-}^{13}\text{C}$ . The identity of the LA is indicated on each trace.

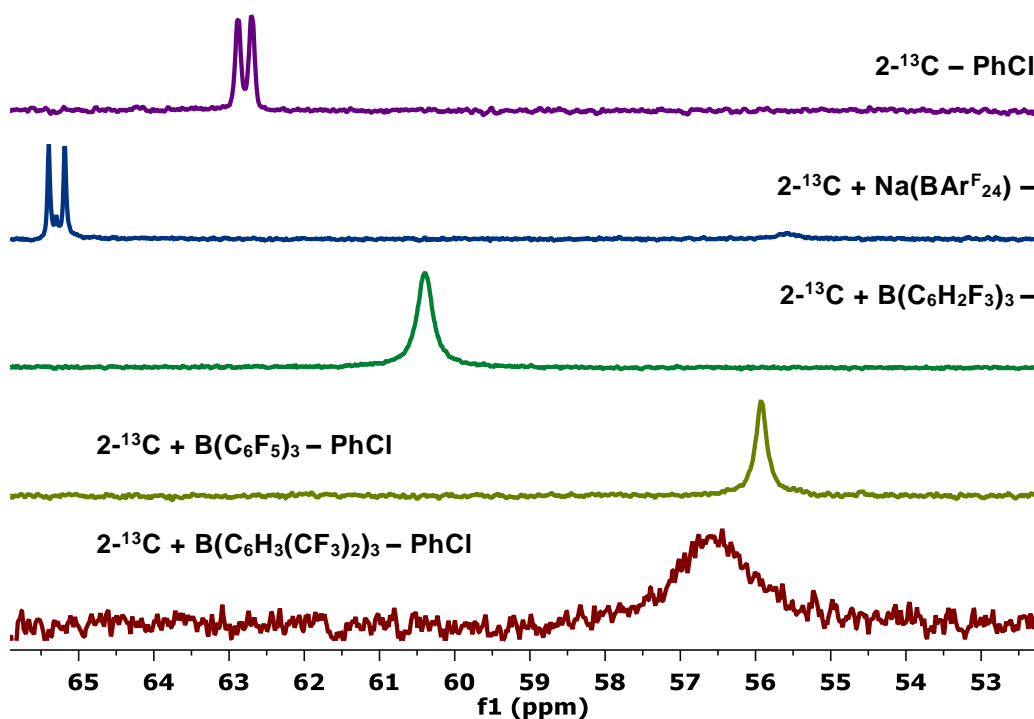


**Figure 7.8.** Stacked partial  $^{31}\text{P}\{^1\text{H}\}$  NMR spectra of *in situ* generated Lewis acid adducts of  $2\text{-}^{13}\text{C}$ . The identity of the LA and the solvent used are indicated on each trace.

**Table 7.3.** Compiled NMR data for Lewis acid adducts of **3**.

LA	AN	$\delta^{13}\text{CO}_2$ (ppm)	$^2J_{\text{(P,C)}}$ (Hz)	$\delta^{31}\text{P}$ (ppm)
None	12.4	192.3	28.4	62.8
<b>Cs(BAr<sup>F</sup><sub>24</sub>)</b>	23.6	199.9	34.0	--
<b>Na(BAr<sup>F</sup><sub>24</sub>)</b>	31.8	203.5	34.1	65.3
<b>B(C<sub>6</sub>H<sub>2</sub>F<sub>3</sub>)<sub>3</sub></b>	68.1	215.7	8.21	60.4
<b>B(C<sub>6</sub>F<sub>5</sub>)<sub>3</sub></b>	79.2	219.6	NR <sup>‡</sup>	55.9
<b>B(C<sub>6</sub>H<sub>3</sub>(CF<sub>3</sub>)<sub>2</sub>)<sub>3</sub></b>	82.7	219.1	10.0	56.6

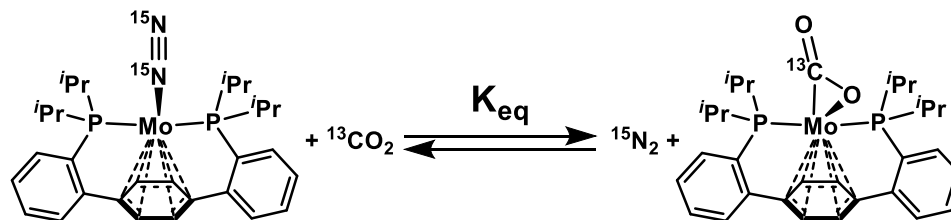
<sup>‡</sup>The  $^2J_{\text{(P,C)}}$  is not resolved in either the  $^{31}\text{P}\{^1\text{H}\}$  or  $^{13}\text{C}\{^1\text{H}\}$  NMR spectra.

#### *Small Molecule Exchange Rate Measurements*

To determine the equilibrium constant for the interconversion of **1** and **2**, a mixture was prepared as follows. A J. Young NMR tube was charged with a deep red C<sub>6</sub>D<sub>6</sub> (0.6 mL) solution of **1** (20 mg, 0.034 mmol). The tube was sealed and attached to a high vacuum line. The contents of the tube were degassed via three freeze-pump-thaw cycles.  $^{13}\text{CO}_2$  (ca. 500 Torr) was admitted to the tube, which was subsequently sealed a mixed. The solution lightened slightly, and an orange precipitate formed. The tube was submerged in LN<sub>2</sub> and the N<sub>2</sub> liberated upon  $^{13}\text{CO}_2$  binding was removed *in vacuo*. This process was repeated twice more, thawing and mixing the reaction between degassing.  $^1\text{H}$  and  $^{31}\text{P}\{^1\text{H}\}$  NMR spectroscopy evidenced complete conversion of **1** to **2**- $^{13}\text{C}$ . The tube was carefully opened to vacuum, removing any free  $^{13}\text{CO}_2$ , as confirmed by  $^{13}\text{C}\{^1\text{H}\}$  NMR spectroscopy. Finally, the tube was submerged in LN<sub>2</sub>, the headspace evacuated, and  $^{15}\text{N}_2$  (ca. 300 Torr) was admitted to the tube. The J. Young tube was sealed, removed from the LN<sub>2</sub>, and carefully thawed. A mixture of **1**- $^{15}\text{N}$  and **2**- $^{13}\text{C}$  was observed by  $^{31}\text{P}\{^1\text{H}\}$  NMR spectroscopy. After 12 h, the same ratio of **1**- $^{15}\text{N}$  to **2**- $^{13}\text{C}$  was observed, suggesting equilibrium had been reached.

To obtain accurate integral values for the relative concentrations of **1**- $^{15}\text{N}$ , free  $^{15}\text{N}_2$ , **2**- $^{13}\text{C}$ , and free  $^{13}\text{CO}_2$ , T<sub>1</sub> scalar relaxation times were measured for representative

resonances of each species (Figure 7.9. and Table 7.4.).  $^{15}\text{N}$  and  $^{13}\text{C}\{^1\text{H}\}$  spectra were then collected with  $d_1$  times of 25 s and 100 s, respectively ( $5 \times T_1$ ). The equilibrium constant can be determined by the ratio of these integrals (Figure 7.10.):



$$K_{\text{eq}} = \frac{[^{15}\text{N}_2][2]}{[1][^{13}\text{CO}_2]} = \frac{[^{15}\text{N}_2]}{[1]} \frac{[2]}{[^{13}\text{CO}_2]} = \frac{(0.37)}{(0.94)} \frac{(1.00)}{(0.87)} = 0.45$$

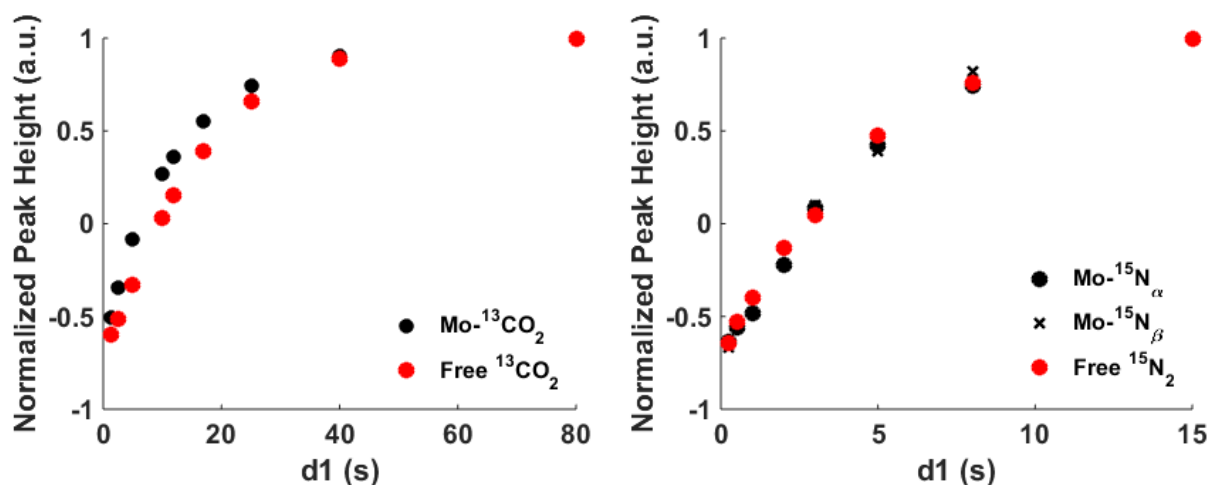


**Figure 7.9.** Peak intensities from  $^{13}\text{C}$  (left) and  $^{15}\text{N}$  (right) NMR inversion recovery experiments for an equilibrium mixture of  $1\text{-}^{15}\text{N}$  and  $2\text{-}^{13}\text{C}$ . The peak intensities for the free small molecule resonances are shown.

**Table 7.4.** Inversion Recovery Experiments for and Equilibrium Mixture of  $1\text{-}^{15}\text{N}/2\text{-}^{13}\text{C}$ .

	$\text{Mo-}^{13}\text{CO}_2$	$\text{Free } ^{13}\text{CO}_2$	$\text{Mo-}^{15}\text{N}_\alpha$	$\text{Mo-}^{15}\text{N}_\beta$	$\text{Free } ^{15}\text{N}_2$
$T_1$	12.5(4)	16.8(7)	5.2(4)	4.9(3)	4.9(3)
<b>Average</b>	--	--	5.1(4)		--



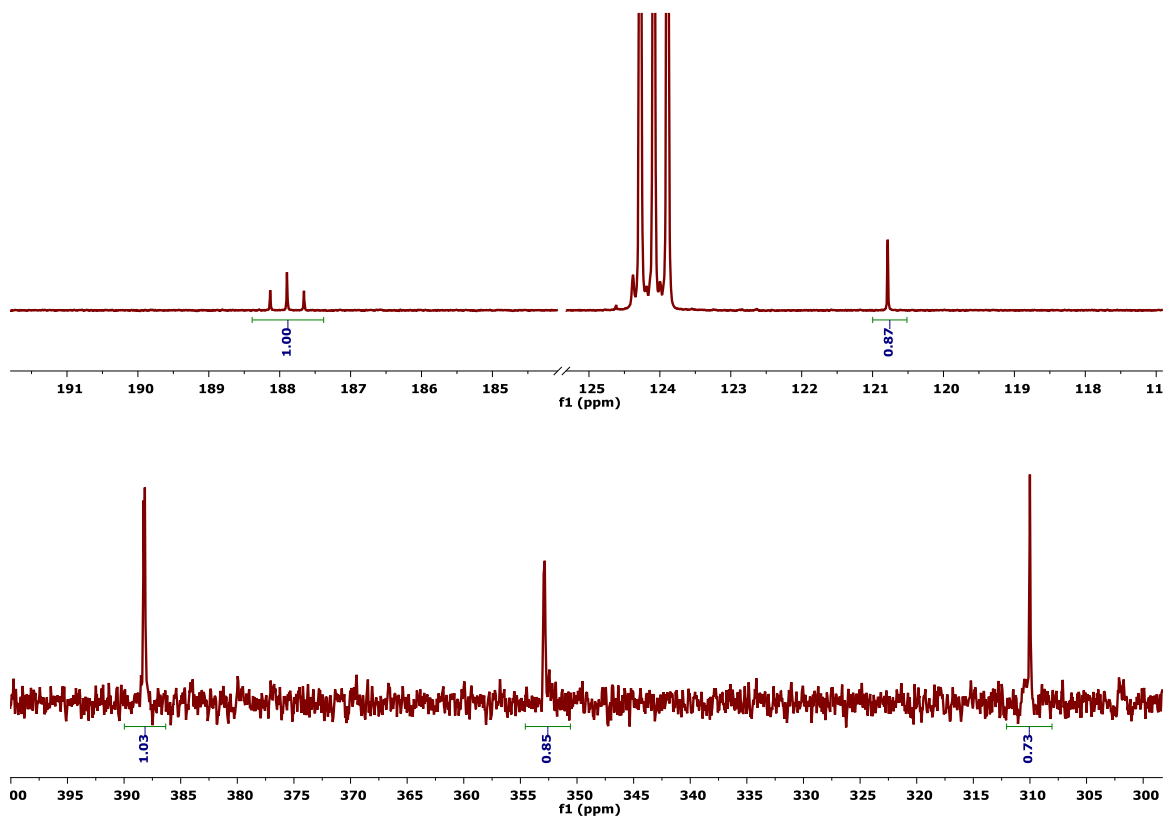


**Figure 7.10.**  $^{13}\text{C}\{^1\text{H}\}$  (126 MHz,  $\text{C}_6\text{D}_6$ , 25 °C, d1 = 100 s) and  $^{15}\text{N}\{^1\text{H}\}$  (51 MHz,  $\text{C}_6\text{D}_6$ , 25 °C, d1 = 25 s) NMR spectra of an equilibrium mixture of  $1\text{-}^{15}\text{N}$  and  $2\text{-}^{13}\text{C}$ .

To verify that the short and near-average  $T_1$  times observed above were a manifestation of chemical exchange, a magnetization transfer experiment was conducted. Using the PRESAT pulse sequence in VnmrJ, a saturation pulse centered at free  $\text{CO}_2$  (124.76 ppm) with a power of

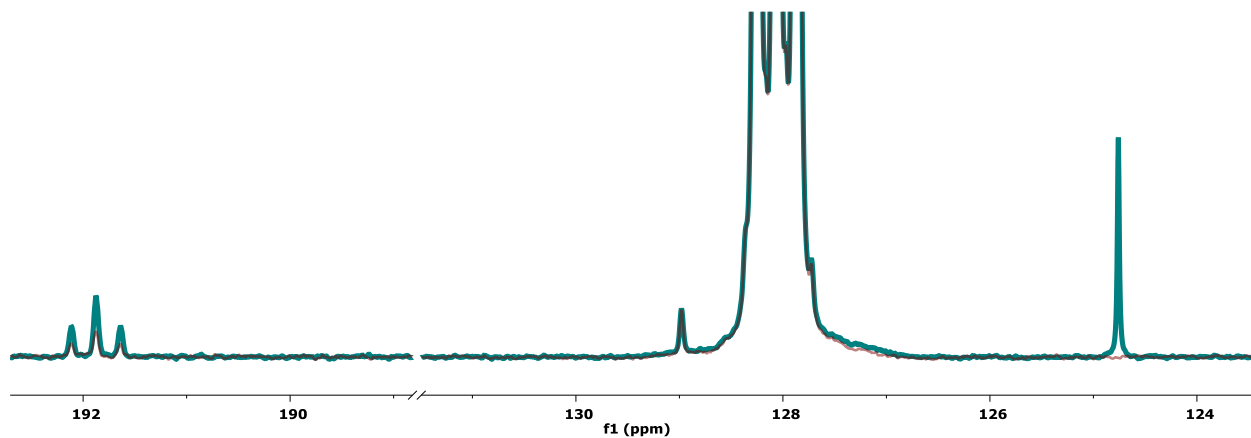


**Figure 7.11.** PRESAT  $^{13}\text{C}\{^1\text{H}\}$  NMR spectrum (126 MHz,  $\text{C}_6\text{D}_6$ , 25 °C) demonstrating saturation transfer from free  $\text{CO}_2$  (124.8 ppm) to bound  $\text{CO}_2$  (191.9 ppm).

4 dB was applied for 100 s. A second spectrum was collected with an off resonance saturation pulse (100.0 ppm), as a control. The intensity of the bound  $^{13}\text{CO}_2$  resonance is dampened in the former case, demonstrating exchange (Figure 7.11.).

#### CO<sub>2</sub> Exchange Kinetics

In a N<sub>2</sub> filled glovebox, a J. Young NMR tube was charged with 2- $^{13}\text{C}$  (20 mg, 0.033 mmol), 1,3,5-trimethoxybenzene (10 mg, 0.059 mmol), and LA (0.033 mmol). The tube was sealed and attached to a high vacuum line. Following thorough evacuation of the headspace, the J. Young tube was backfilled with Ar gas. Under a heavy Ar counterflow, solvent (0.5 mL) was added via syringe. The tube was sealed and the contents mixed, affording a colorless homogeneous solution.  $^{13}\text{C}\{^1\text{H}\}$  and  $^{31}\text{P}\{^1\text{H}\}$  NMR spectra were collected at this point to confirm sample integrity and act as a T<sub>0</sub>. The tube was attached to the vacuum line below a 33.4 mL calibrated volume and the contents frozen via submersion in LN<sub>2</sub>. Following evacuation of the headspace,  $^{12}\text{CO}_2$  (14.5 cm Hg in 33.4 mL, 0.265 mmol) was condensed into the tube. The tube contents were thawed, shaken once, and immediately introduced to an NMR probe pre-cooled to 0 °C for kinetic analysis.

Following collection of an array of  $^{13}\text{C}\{^1\text{H}\}$  NMR spectra, a 20<sup>th</sup> order polynomial baseline correction and automatic phase correction was applied to all data. Max peak vs. time data was extracted for the isotopically enriched  $^{13}\text{C}$  resonance corresponding to the Mo- $^{13}\text{CO}_2$  complexes. These data were normalized to the 1,3,5-trimethoxybenzene resonance at 93.0 ppm.

All data were fit, using the cftool feature of MatLab, according to a three-parameter exponential function:

$$y = a \times e^{(-b \times x)} + c$$

and the rate of exchange was determined according to the following equation:

$$\text{rate} = \frac{[\text{Mo}] \times [\text{CO}_2] \times b}{[\text{Mo}] + [\text{CO}_2]}$$

The fraction of soluble  $^{12/13}\text{CO}_2$  in each sample was estimated assuming rapid diffusion on the exchange timescale, equivalent solubility for  $^{12}\text{CO}_2$  and  $^{13}\text{CO}_2$ , and approximating that all  $^{13}\text{CO}_2$  originated from  $2\text{-}^{13}\text{C}$ . Under these conditions, the percent soluble  $\text{CO}_2$  could be determined for each time point (t) as follows:

$$\text{frac sol. CO}_2 = \frac{1}{\frac{([\text{MO}]_0 - [\text{MO}]_t)}{[\text{CO}_2]_t}}$$

Averaging these values across all timepoints for a given sample, and across all samples, afforded average  $\text{CO}_2$  solubilities of approximately 40% at the given temperature (0 °C) and pressure (*ca.* 2.4 atm).

**Table 7.5.**  $\text{CO}_2$  Exchange rate as a function of LA identity.

<b>2 PhCl : Et<sub>2</sub>O</b>					
	<b>Cs (BAr<sup>F</sup><sub>24</sub>)</b>	<b>Na (BAr<sup>F</sup><sub>24</sub>)</b>	<b>Na (BAr<sup>F</sup><sub>24</sub>)<sup>‡</sup></b>	<b>B(C<sub>6</sub>H<sub>2</sub>F<sub>3</sub>)<sub>3</sub></b>	<b>B(C<sub>6</sub>F<sub>5</sub>)<sub>3</sub></b>
a	0.88	0.90	0.97	0.95	0.74
b	0.00083	0.00024	0.000058	0.00010	0.000038
c	0.086	0.10	0.00	0.03	0.13
R <sup>2</sup>	0.99	0.99	0.99	0.99	0.97
rate	2 x 10 <sup>-5</sup>	6 x 10 <sup>-6</sup>	1 x 10 <sup>-6</sup>	3 x 10 <sup>-6</sup>	1 x 10 <sup>-6</sup>
<b>PhCl</b>					
	<b>NONE</b>	<b>B(C<sub>6</sub>H<sub>2</sub>F<sub>3</sub>)<sub>3</sub></b>	<b>B(C<sub>6</sub>F<sub>5</sub>)<sub>3</sub></b>	<b>B(C<sub>6</sub>H<sub>3</sub>(CF<sub>3</sub>)<sub>2</sub>)<sub>3</sub></b>	
a	0.80	0.98	0.70	0.74	
b	0.0031	0.000047	0.00012	0.000037	
c	0.80	0.0016	0.30	0.13	
R <sup>2</sup>		0.99	0.98	0.97	
rate	8 x 10 <sup>-5</sup>	1 x 10 <sup>-6</sup>	3 x 10 <sup>-6</sup>	9 x 10 <sup>-7</sup>	

<sup>‡</sup>The [Na(BAr<sup>F</sup><sub>24</sub>)] was doubled.

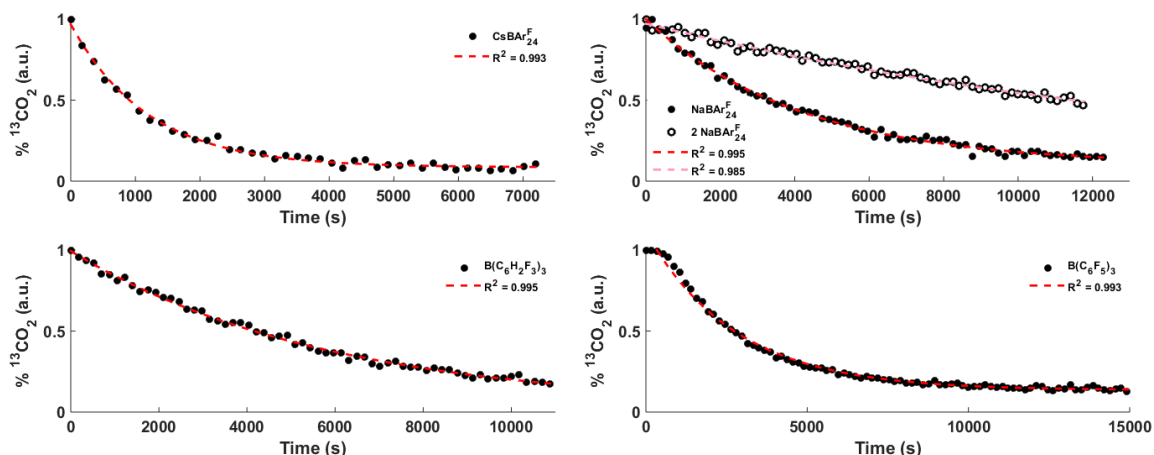


Figure 7.12. Representative  $^{12/13}\text{CO}_2$  exchange in 2 PhCl : Et<sub>2</sub>O at 0 °C.

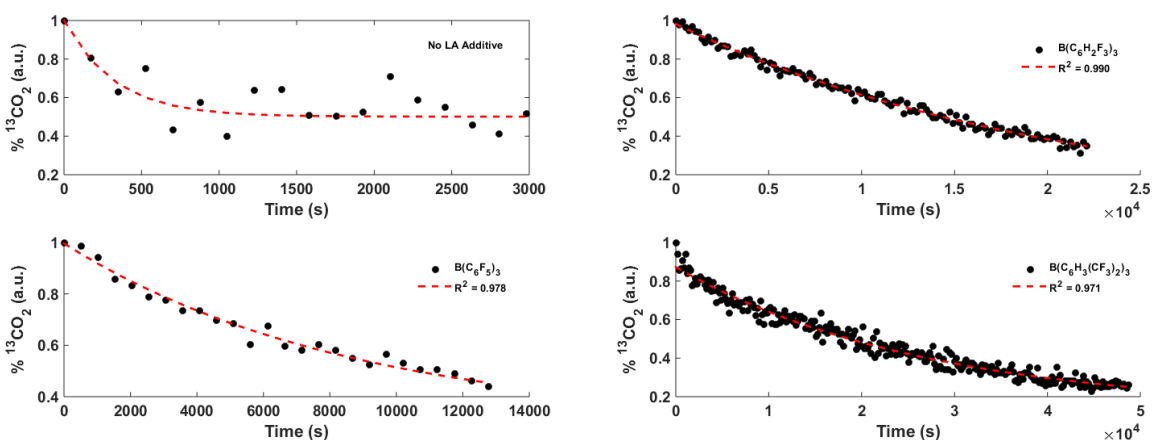


Figure 7.13. Representative  $^{12/13}\text{CO}_2$  exchange in PhCl at 0 °C.

### *CO<sub>2</sub> Protonation Reactions*

Under N<sub>2</sub>:

In a typical reaction, a 20 mL scintillation vial was charged with 4-<sup>13</sup>C (40 mg, 0.036 mmol) and a stir bar. PhCl (1.5 mL) was added, providing a deep red solution. In a second vial, [(Et<sub>2</sub>O)<sub>2</sub>H][BAR<sup>F</sup><sub>24</sub>] (36 mg, 0.036 mmol) was dissolved in PhCl (1.5 mL), affording a colorless solution. With stirring, the acid solution was added to the solution of 4-<sup>13</sup>C, dropwise, resulting in a color change to yellow/green. <sup>31</sup>P{<sup>1</sup>H}, <sup>13</sup>C{<sup>1</sup>H}, and <sup>19</sup>F NMR spectroscopy evidence formation of 6-<sup>13</sup>C, B(C<sub>6</sub>F<sub>5</sub>)<sub>3</sub>•Et<sub>2</sub>O, B(C<sub>6</sub>F<sub>5</sub>)<sub>3</sub>•H<sub>2</sub>O, and a small amount of [(B(C<sub>6</sub>F<sub>5</sub>)<sub>3</sub>)<sub>2</sub>OH]<sup>-</sup> (Figure 7.14). Upon standing for 12 h, green X-ray quality crystals form, the identity of which was confirmed as 7.

Reactions run analogously, but with 2 equiv. of [(Et<sub>2</sub>O)<sub>2</sub>H][BAr<sup>F</sup><sub>24</sub>] showed no remaining [(B(C<sub>6</sub>F<sub>5</sub>)<sub>3</sub>)<sub>2</sub>OH]<sup>-</sup> by <sup>19</sup>F NMR spectroscopy. Based on the borane speciation (confirmed by comparison to independently synthesized authentic samples, Figure 7.14.) and the Mo complexes formed in the course of the reaction (deduced from independent reactivity, spectroscopy, and XRD), a plausible mechanism for the cleavage of CO<sub>2</sub> to CO and H<sub>2</sub>O is outlined in Scheme 7.3.. Such a mechanism accounts for the overall conversion to **6**—33%, <sup>31</sup>P NMR spectroscopy—observed experimentally.

Under Ar:

In a typical reaction, a 25 mL Teflon stoppered Schlenk tube was charged with **2**-<sup>13</sup>C (30 mg, 0.050 mmol), LA (0.050 mmol), and a stir bar. The reaction vessel was attached to a high vacuum line and the headspace replaced with Ar. With a heavy Ar counterflow, the Teflon stopper was exchanged for a rubber septum. Solvent (3 mL, PhCl or 2 PhCl : Et<sub>2</sub>O, *vide supra*) was added via syringe and the stopper replaced. Stirring was initiated, affording a deep red homogeneous solution. The reaction was cooled to -78 °C with a dry ice/acetone slush bath, and with a heavy Ar counterflow, solid [(Et<sub>2</sub>O)<sub>2</sub>H][BAr<sup>F</sup><sub>24</sub>] was added. The flask was quickly sealed, removed from the line, and shaken. After warming to RT, volatiles were removed under reduced pressure, giving a dark residue. This residue was dissolved in a THF solution of PPh<sub>3</sub> (6 mg, 0.023 mmol in 1 mL). A 0.5 mL aliquot of the resulting solution was transferred to an NMR tube and analyzed by <sup>31</sup>P{<sup>1</sup>H} and <sup>13</sup>C{<sup>1</sup>H} NMR spectroscopy. The extent of C–O cleavage was determined by integration of the carbonyl doublet against the PPh<sub>3</sub> standard.

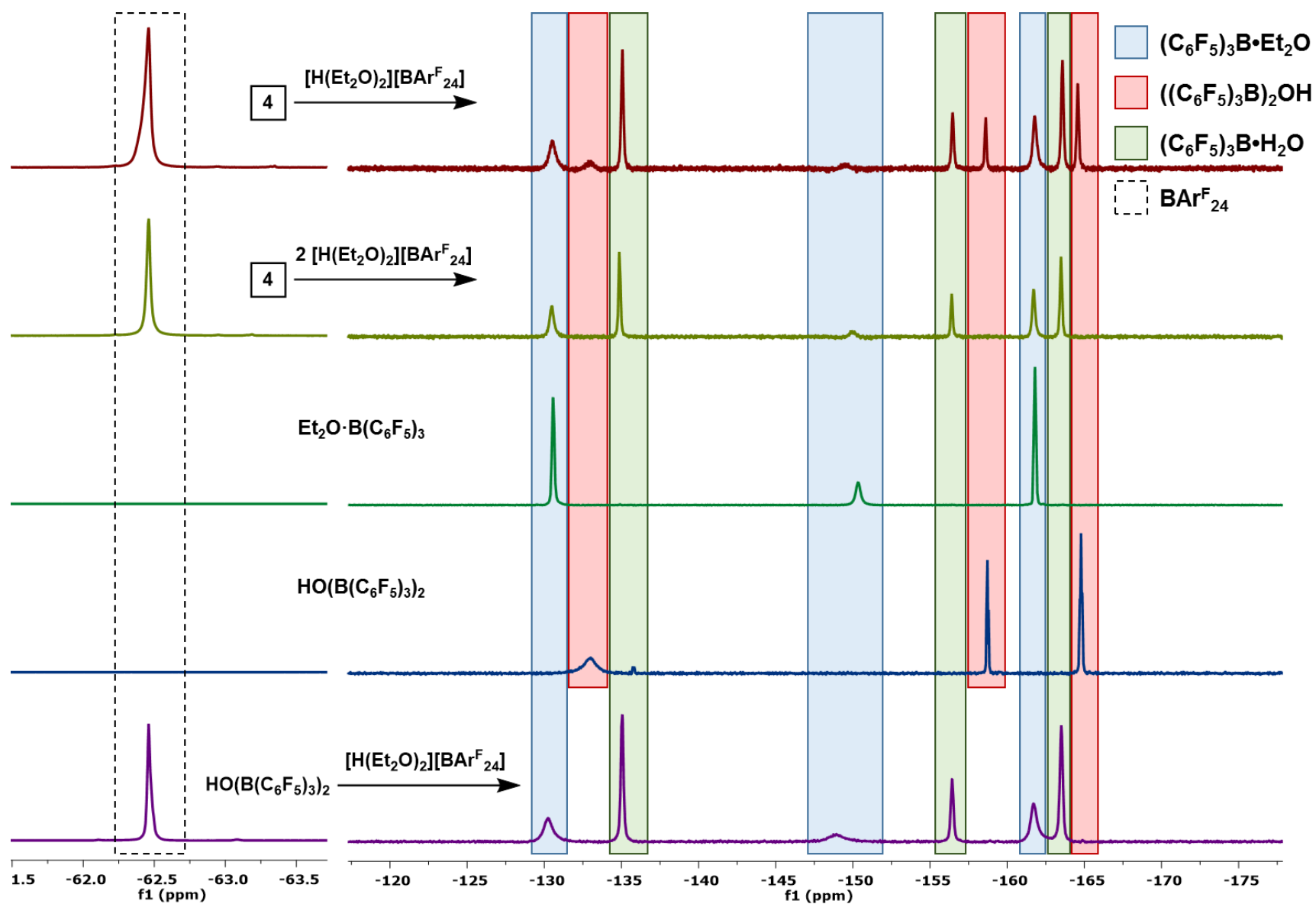


**Figure 7.14.**  $\text{B}(\text{C}_6\text{F}_5)_3$  speciation following  $\text{CO}_2$  protonation reactions as reported by  $^{19}\text{F}$  NMR spectroscopy (376 MHz,  $\text{PhCl}$ ,  $23^\circ\text{C}$ ). Spectra of authentic samples are provided for reference.

## ***Crystallographic Information***

### *Refinement Details*

In each case, crystals were mounted on a MiTeGen loop using Paratone oil, then placed on the diffractometer under a nitrogen stream. Low temperature (100 K) X-ray data were obtained on a Bruker D8 VENTURE Kappa Duo PHOTON 100 CMOS based diffractometer (Mo I<sub>μ</sub>S HB micro-focus sealed X-ray tube,  $K_{\alpha} = 0.71073 \text{ \AA}$ ). All diffractometer manipulations, including data collection, integration, and scaling were carried out using the Bruker APEXIII software.<sup>4a</sup> Absorption corrections were applied using SADABS.<sup>4b</sup> Space groups were determined on the basis of systematic absences and intensity statistics and the structures were solved in the Olex 2 software interface<sup>36</sup> by intrinsic phasing using XT (incorporated into SHELXTL)<sup>5a</sup> and refined by full-matrix least squares on  $F^2$ . All non-hydrogen atoms were refined using anisotropic displacement parameters. Hydrogen atoms were placed in the idealized positions and refined using a riding model, unless noted otherwise. The structures were refined (weighed least squares refinement on  $F^2$ ) to convergence. Graphical representations of structures with 50% probability thermal ellipsoids were generated using the Diamond 3 visualization software.<sup>5b</sup>

**Table 7.6.** Crystal and refinement data for complexes **2** - **4**, **6**, & **7**.

	<b>2</b>	<b>3</b>	<b>4</b>	<b>6</b>	<b>7</b>
CCDC Number <sup>5c</sup>					
Empirical formula	C <sub>37</sub> H <sub>46</sub> MoO <sub>2</sub> P <sub>2</sub>	C <sub>48</sub> H <sub>40</sub> BF <sub>15</sub> MoN <sub>2</sub> P <sub>2</sub>	C <sub>49</sub> H <sub>40</sub> BF <sub>15</sub> MoO <sub>2</sub> P <sub>2</sub>		
Formula weight	680.62	1098.51	1114.50		
T (K)	100	100	100		
<i>a</i> , Å	8.773(3)	23.5019(11)	9.4051(4)		
<i>b</i> , Å	11.504(3)	9.3504(5)	11.3058(5)		
<i>c</i> , Å	16.681(5)	20.5286(9)	22.0674(10)		
$\alpha$ , °	93.575(10)	90	103.065(2)		
$\beta$ , °	98.963(9)	90	94.669(2)		
$\gamma$ , °	103.528(10)	90	96.976(2)		
Volume, Å <sup>3</sup>	1608.3(8)	4511.2(4)	2254.39(17)		
Z	2	4	2		
Crystal system	Triclinic	Orthorhombic	Triclinic		
Space group	<i>P</i> 1	<i>Pca</i> 2 <sub>1</sub>	<i>P</i> 1		
<i>d</i> <sub>calc</sub> , g/cm <sup>3</sup>	1.405	1.617	1.642		
$\theta$ range, °	1.830 to 28.726	1.984 to 31.511	0.953 to 36.319		
$\mu$ , mm <sup>-1</sup>	0.540	0.462	0.466		
Abs. Correction	Semi-empirical	Semi-empirical	Semi-empirical		
GOF	1.044	1.008	0.988		
<i>R</i> <sub>1</sub> , <sup>a</sup> <i>wR</i> <sub>2</sub> <sup>b</sup> [I>2 $\sigma$ (I)]	0.0719, 0.1592	0.0371, 0.0668	0.0268, 0.0647		
Radiation Type	Mo K $\alpha$	Mo K $\alpha$	Mo K $\alpha$		

<sup>a</sup>  $R_1 = \sum ||F_o| - |F_c|| / \sum |F_o|$ . <sup>b</sup>  $wR_2 = [\sum [w(F_o^2 - F_c^2)^2] / \sum [w(F_o^2)^2]]^{1/2}$ .



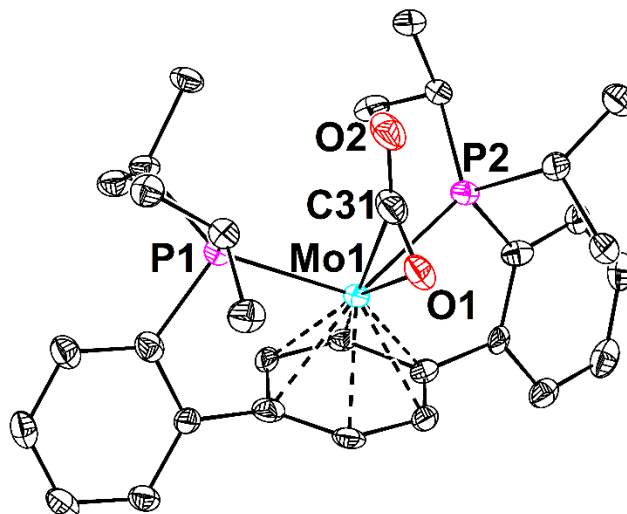


**Figure 7.15.** Structural drawing of **2** with 50% probability anisotropic displacement ellipsoids. H-atoms are omitted for clarity.

**Special Refinement Details:** The CO<sub>2</sub> ligand (C31, O1, and O2) in **2** was positionally disordered but satisfactorily modeled over two positions. To prevent the minor component (40%) from refining as non-positive definite, similarity restraints on U<sub>ij</sub> and rigid bond restraints were applied to the disordered unit.

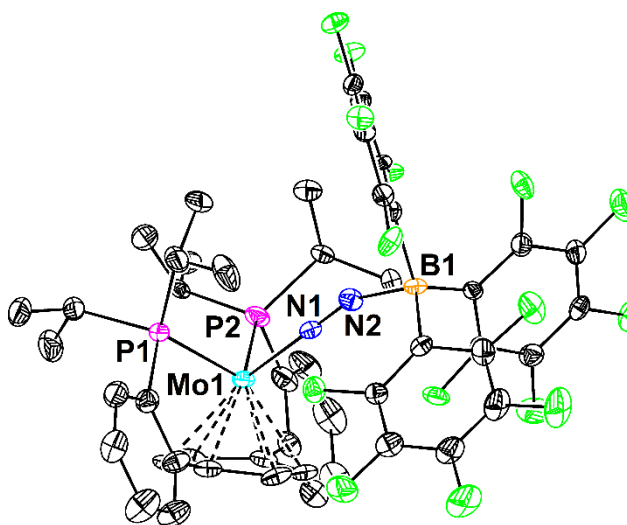


**Figure 7.16.** Structural drawing of **3** with 50% probability anisotropic displacement ellipsoids. H-atoms are omitted for clarity.

**Special Refinement Details:** The B(C<sub>6</sub>F<sub>5</sub>)<sub>3</sub> motif in **3** was positionally disordered, but satisfactorily modeled over two positions. Similarity restraints on U<sub>ij</sub> and rigid bond restraints were applied to the entire perfluoroaryl borane (B1 and C31 through F15).

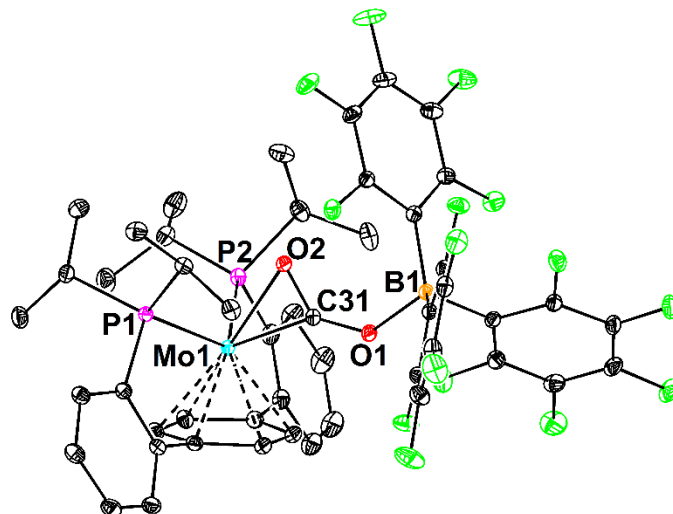


**Figure 7.17.** Structural drawing of **4** with 50% probability anisotropic displacement ellipsoids. H-atoms are omitted for clarity.

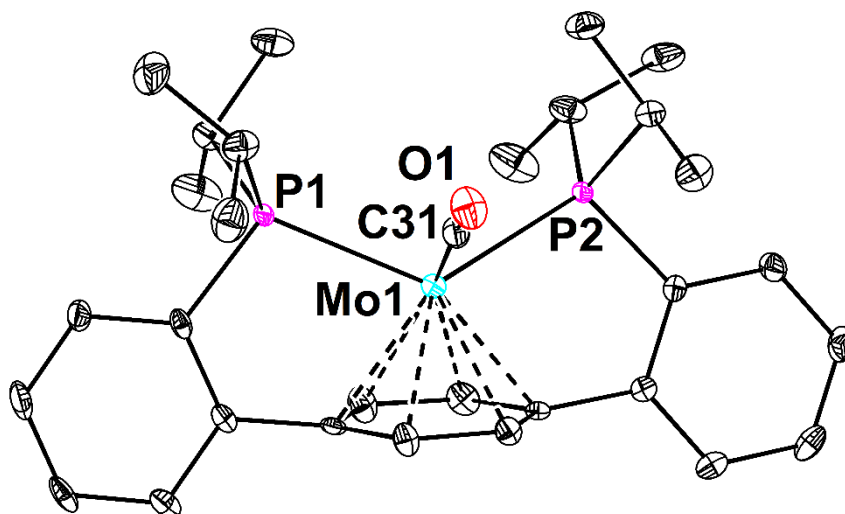


**Figure 7.18.** Structural drawing of **6** with 50% probability anisotropic displacement ellipsoids. H-atoms and the  $\text{BAR}^{\text{F}}_{24}$  counterion are omitted for clarity.

**Special Refinement Details:** The solid-state structure of **6** demonstrated whole molecule disorder in two independently grown crystals. Modeling this in a 90 : 10 ratio provide a satisfactory but preliminary solution.

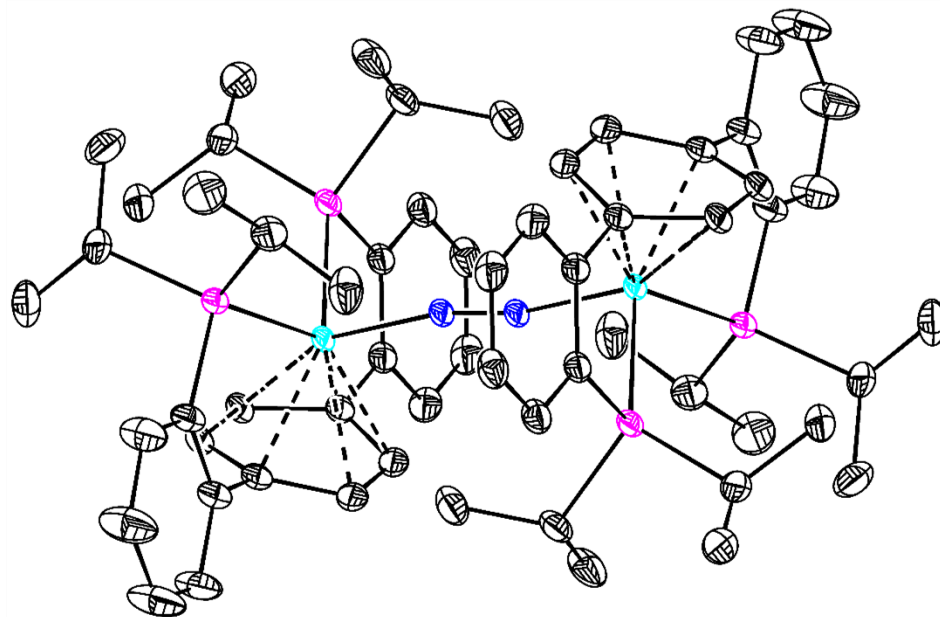


**Figure 7.19.** Structural drawing of **7** with 50% probability anisotropic displacement ellipsoids. H-atoms and two  $\text{BAr}^{\text{F}}_{24}$  counterions are omitted for clarity.

**Special Refinement Details:** Several of the  $\text{CF}_3$  groups on the  $\text{BAr}^{\text{F}}_{24}$  counterions are positionally disordered due to rotation around the C–C bond. Modeling of these disorders is ongoing and the reported structures is merely a satisfactory preliminary solution.

## REFERENCES

- (1) a) Olah, G. A.; Prakash, G. K. S.; Goepfert, A. *J. Am. Chem. Soc.* **2011**, *133*, 12881; b) Liu, Q.; Wu, L.; Jackstell, R.; Beller, M. **2015**, *6*, 5933; c) Aresta, M.; Dibenedetto, A. *Dalton Trans.* **2007**, 2975; d) Aresta, M.; Dibenedetto, A.; Angelini, A. *Chem. Rev.* **2014**, *114*, 1709.
- (2) a) Belmabkhout, Y.; Guillerm, V.; Eddaoudi, M. *Chem. Eng. J.* **2016**, *296*, 386; b) Leung, D. Y. C.; Caramanna, G.; Maroto-Valer, M. M. *Renewable and Sustainable Energy Reviews* **2014**, *39*, 426; c) Schoedel, A.; Ji, Z.; Yaghi, O. M. *Nature Energy* **2016**, *1*, 16034.
- (3) a) Sakakura, T.; Choi, J.-C.; Yasuda, H. *Chem. Rev.* **2007**, *107*, 2365; b) Zhang, X.; Fevre, M.; Jones, G. O.; Waymouth, R. M. *Chem. Rev.* **2018**, *118*, 839; c) Coates, G. W.; Moore, D. R. *Angew. Chem. Int. Ed.* **2004**, *43*, 6618.
- (4) a) Mellmann, D.; Sponholz, P.; Junge, H.; Beller, M. *Chem. Soc. Rev.* **2016**, *45*, 3954; b) Bernskoetter, W. H.; Hazari, N. *Acc. Chem. Res.* **2017**, *50*, 1049; c) Sordakis, K.; Tang, C.; Vogt, L. K.; Junge, H.; Dyson, P. J.; Beller, M.; Laurenczy, G. *Chem. Rev.* **2018**, *118*, 372.
- (5) a) Benson, E. E.; Kubiak, C. P.; Sathrum, A. J.; Smieja, J. M. *Chem. Soc. Rev.* **2009**, *38*, 89; b) Costentin, C.; Robert, M.; Saveant, J.-M. *Chem. Soc. Rev.* **2013**, *42*, 2423; c) Rakowski Dubois, M.; Dubois, D. L. *Acc. Chem. Res.* **2009**, *42*, 1974.
- (6) a) Grice, K. A. *Coord. Chem. Rev.* **2017**, *336*, 78; b) Paparo, A.; Okuda, J. *Coord. Chem. Rev.* **2017**, *334*, 136.
- (7) Qiao, J.; Liu, Y.; Hong, F.; Zhang, J. *Chem. Soc. Rev.* **2014**, *43*, 631.
- (8) Fessler, J.; Jeoung, J.-H.; Dobbek, H. *Angew. Chem. Int. Ed.* **2015**, *54*, 8560.
- (9) a) Can, M.; Armstrong, F. A.; Ragsdale, S. W. *Chem. Rev.* **2014**, *114*, 4149; b) Jeoung, J.-H.; Dobbek, H. *Science* **2007**, *318*, 1461.
- (10) a) Sampson, M. D.; Kubiak, C. P. *J. Am. Chem. Soc.* **2016**, *138*, 1386; b) Hammouche, M.; Lexa, D.; Momenteau, M.; Saveant, J. M. *J. Am. Chem. Soc.* **1991**, *113*, 8455; c) Bhugun, I.; Lexa, D.; Savéant, J.-M. *The Journal of Physical Chemistry* **1996**, *100*, 19981.
- (11) a) Takaya, J.; Iwasawa, N. *J. Am. Chem. Soc.* **2017**, *139*, 6074; b) Devillard, M.; Declercq, R.; Nicolas, E.; Ehlers, A. W.; Backs, J.; Saffon-Merceron, N.; Bouhadir, G.; Sloopweg, J. C.; Uhl, W.; Bourissou, D. *J. Am. Chem. Soc.* **2016**, *138*, 4917.
- (12) a) Yoo, C.; Lee, Y. *Chem. Sci.* **2017**, *8*, 600; b) Kim, Y.-E.; Kim, J.; Lee, Y. *Chem. Commun.* **2014**, *50*, 11458.
- (13) Forrest, S. J. K.; Clifton, J.; Fey, N.; Pringle, P. G.; Sparkes, H. A.; Wass, D. F. *Angew. Chem. Int. Ed.* **2015**, *54*, 2223.
- (14) a) Alvarez, R.; Carmona, E.; Marin, J. M.; Poveda, M. L.; Gutierrez-Puebla, E.; Monge, A. *J. Am. Chem. Soc.* **1986**, *108*, 2286; b) Carden, R. G.; Ohane, J. J.; Pike, R. D.; Graham, P. M. *Organometallics* **2013**, *32*, 2505; c) Contreras, L.; Paneque, M.; Sellin, M.; Carmona, E.; Perez, P. J.; Gutierrez-Puebla, E.; Monge, A.; Ruiz, C. *New J. Chem.* **2005**, *29*, 109; d) Bernskoetter, W. H.; Tyler, B. T. *Organometallics* **2011**, *30*, 520.
- (15) Gambarotta, S.; Floriani, C.; Chiesi-Villa, A.; Guastini, C. *J. Am. Chem. Soc.* **1985**, *107*, 2985.
- (16) a) Sheldrick, G.M. "SADABS (version 2008/1): Program for Absorption Correction for Data from Area Detector Frames", University of Göttingen, 2008; b) Seravalli, J.; Ragsdale, S. W. *Biochemistry* **2008**, *47*, 6770.
- (17) Buss, J. A.; Edouard, G. A.; Cheng, C.; Shi, J.; Agapie, T. *J. Am. Chem. Soc.* **2014**, *136*, 11272.
- (18) a) Ishida, H.; Tanaka, K.; Tanaka, T. *Organometallics* **1987**, *6*, 181; b) DuBois, D. L.; Miedaner, A.; Haltiwanger, R. C. *J. Am. Chem. Soc.* **1991**, *113*, 8753; c) Sampson, M. D.; Nguyen, A. D.; Grice, K. A.; Moore, C. E.; Rheingold, A. L.; Kubiak, C. P. *J. Am. Chem. Soc.* **2014**, *136*,

- 5460; d) Chapovetsky, A.; Do, T. H.; Haiges, R.; Takase, M. K.; Marinescu, S. C. *J. Am. Chem. Soc.* **2016**, *138*, 5765; e) Bhugun, I.; Lexa, D.; Savéant, J.-M. *J. Am. Chem. Soc.* **1996**, *118*, 1769.
- (19) a) Tsai, J. C.; Khan, M.; Nicholas, K. M. *Organometallics* **1989**, *8*, 2967; b) Sahoo, D.; Yoo, C.; Lee, Y. *J. Am. Chem. Soc.* **2018**, *140*, 2179.
- (20) Vol'pin, M. E. K., I.S. *Pure Appl. Chem.* **1973**, *33*, 567.
- (21) a) Simonneau, A.; Turrel, R.; Vendier, L.; Etienne, M. *Angew. Chem. Int. Ed.* **2017**, *56*, 12268; b) Geri, J. B.; Shanahan, J. P.; Szymczak, N. K. *J. Am. Chem. Soc.* **2017**, *139*, 5952.
- (22) a) Horton, A. D.; de With, J. *Organometallics* **1997**, *16*, 5424; b) Parks, D. J.; Piers, W. E.; Yap, G. P. A. *Organometallics* **1998**, *17*, 5492.
- (23) Lewiński, J.; Kubicki, D. In *Encyclopedia of Spectroscopy and Spectrometry (Third Edition)*; Tranter, G. E., Koppenaal, D. W., Eds.; Academic Press: Oxford, 2017, p 318.
- (24) Xu, T.; Chen, E. Y. X. *J. Am. Chem. Soc.* **2014**, *136*, 1774.
- (25) Bergquist, C.; Bridgewater, B. M.; Harlan, C. J.; Norton, J. R.; Friesner, R. A.; Parkin, G. *J. Am. Chem. Soc.* **2000**, *122*, 10581.
- (26) Beckett, M. A.; Strickland, G. C.; Holland, J. R.; Sukumar Varma, K. *Polymer* **1996**, *37*, 4629.
- (27) These reactions were run with strict exclusion of N<sub>2</sub> to avoid potential exchange prior to protonation.
- (28) Pangborn, A. B.; Giardello, M. A.; Grubbs, R. H.; Rosen, R. K.; Timmers, F. J. *Organometallics* **1996**, *15*, 1518.
- (29) Mon, I.; Jose, D. A.; Vidal-Ferran, A. *Chem. Eur. J.* **2013**, *19*, 2720.
- (30) Lesley, M. J. G.; Norman, N. C.; Rice, C. R.; Reger, D. L.; Little, C. A.; Lamba, J. J. S.; Brown, K. J.; Peters, J. C.; Thomas, J. C.; Sahasrabudhe, S.; Yearwood, B. C.; Atwood, D. A.; Hill, R. F.; Wood, G. L.; Danzer, R.; Paine, R. T.; Wagner, N. L.; Murphy, K. L.; Haworth, D. T.; Bennett, D. W.; Byers, P. K.; Canty, A. J.; Honeyman, R. T.; Arnáiz, F. J.; Miranda, M. J.; Bohle, D. S.; Sagan, E. S.; Chivers, T.; Sandblom, N.; Schatte, G. In *Inorg. Synth.*; John Wiley & Sons, Inc.: 2004, p 1.
- (31) Nicasio, J. A.; Steinberg, S.; Inés, B.; Alcarazo, M. *Chem. Eur. J.* **2013**, *19*, 11016.
- (32) Soltani, Y.; Wilkins, L. C.; Melen, R. L. *Angew. Chem. Int. Ed.* **2017**, *56*, 11995.
- (33) Herrington, T. J.; Thom, A. J. W.; White, A. J. P.; Ashley, A. E. *Dalton Trans.* **2012**, *41*, 9019.
- (34) Brookhart, M.; Grant, B.; Volpe, A. F. *Organometallics* **1992**, *11*, 3920.
- (35) Fulmer, G. R.; Miller, A. J. M.; Sherden, N. H.; Gottlieb, H. E.; Nudelman, A.; Stoltz, B. M.; Bercaw, J. E.; Goldberg, K. I. *Organometallics* **2010**, *29*, 2176.
- (36) Dolomanov, O. V.; Bourhis, L. J.; Gildea, R. J.; Howard, J. A. K.; Puschmann, H. *J. Appl. Crystallogr.* **2009**, *42*, 339.



## CHAPTER 8

### Bimodal CO<sub>2</sub> Reduction at Low-Valent Mo Terphenyl Diphosphine Complexes

**ABSTRACT**

CO<sub>2</sub> reduction, whether it be to liquid fuels, for reversible H<sub>2</sub> storage, or for fine chemical synthesis, represents an unsolved challenge in sustainable chemistry. Herein, we report a low-valent Mo complex capable of stoichiometric and catalytic CO<sub>2</sub> reduction. In the former case, a unique mechanism for silanol formation from CO<sub>2</sub> is presented. In the latter, *para*-terphenyl diphosphine supported Mo hydride complexes—P<sub>2</sub>Mo(H)(OOCH) and P<sub>2</sub>Mo(H)<sup>+</sup>—are invoked as reactive intermediates in both CO<sub>2</sub> hydrogenation and formic acid dehydrogenation catalyses. Preliminary results show turn over numbers in the hundreds for each of these processes, starting from the same precatalyst.



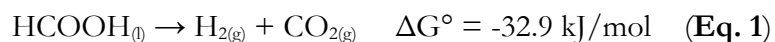
## GENERAL INTRODUCTION

Chapter 7 of this thesis reports a fundamental study exploring proton-induced CO<sub>2</sub> reduction chemistry. In these reactions, CO<sub>2</sub> is converted to CO and H<sub>2</sub>O, with the aid of a Lewis acid. The requisite electrons for this process are provided by the Mo(0) starting material. Toward accessing catalytic CO<sub>2</sub> reduction chemistries, hydrogenation and hydrosilylation, processes that are redox neutral with respect to the transition metal catalyst, were explored.

With increasing atmospheric CO<sub>2</sub> levels, the implementation of this abundant resource in the synthesis of value-added organic chemicals is becoming ever more attractive.<sup>1</sup> A major impediment to this goal is the kinetic and thermodynamic stability of CO<sub>2</sub>.<sup>2</sup> Direct CO<sub>2</sub> hydrogenation is often challenging,<sup>3</sup> hydrosilylation is a related approach that offers several advantages.<sup>4</sup> Thermodynamically, Si–H bond addition to CO<sub>2</sub> is more favorable than that of H<sub>2</sub>.<sup>4</sup> Hydrosilylation of CO<sub>2</sub> can also proceed in a well-defined, stepwise manner, furnishing a series of products and detailed mechanistic insight.<sup>5</sup> Current hydrosilylation chemistry invokes CO<sub>2</sub> insertion into a M–H bond and subsequent silyl formate formation in the initial catalytic steps. Silyl formate serves as a potential synthon for the preparation of a variety of valuable chemicals,<sup>6</sup> and additional silane driven reductions can form disilyl acetals, methoxy silanes, and methane.<sup>7</sup> Herein, we describe a different pathway for CO<sub>2</sub> reduction with silanes. The reduction chemistry is driven by low-valent Mo, an earth-abundant metal, with silane acting as a terminal oxygen atom acceptor.

In conjunction with exploring CO<sub>2</sub> hydrosilylation chemistry, hydrogenation chemistry was targeted. Though H<sub>2</sub> is an ideal clean fuel that can be efficiently sourced from water and sunlight using inexpensive and robust catalysts (see Chapter 6),<sup>8</sup> its low energy density makes storage and transportation problematic.<sup>9</sup> Chapter 2 of this thesis focused on ammonia borane (AB) as a H<sub>2</sub> carrier; however, though AB provides unparalleled gravimetric H<sub>2</sub> content, its dehydrogenation proves too thermodynamically favorable to be practical in a reversible H<sub>2</sub> storage scheme. Looking at thermodynamic data for hydrogenation/dehydrogenation, CO<sub>2</sub> poses as a viable carrier for solar-generated H<sub>2</sub> (Eq. 1 & 2).<sup>9</sup> Both the hydrogenation of CO<sub>2</sub>

to formate (Eq. 1) and the dehydrogenation of formic acid (HCOOH, FA, Eq. 2) are topical subfields in green-energy research.

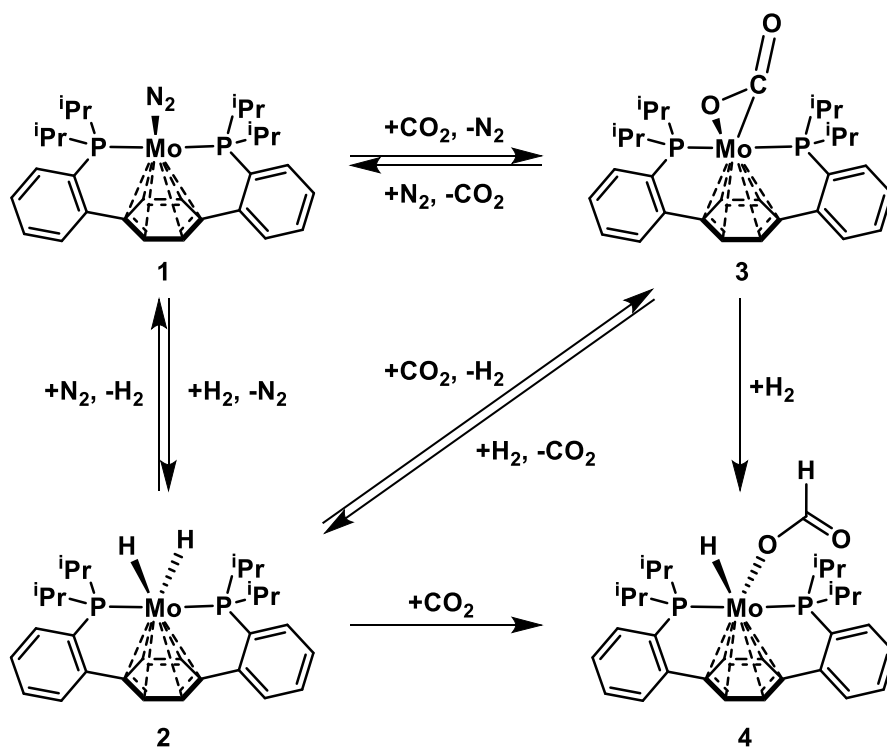


Many effective catalysts for FA dehydrogenation are known, with turn over numbers (TONs) exceeding the millions.<sup>10</sup> Several of these catalysts utilize precious metals, but robust examples with earth-abundant metals are also known.<sup>10c,11</sup> Less common are examples of catalysts capable of both FA dehydrogenation and the reverse, CO<sub>2</sub> hydrogenation.<sup>12</sup> The latter reaction has less precedent and remains a challenge, often requiring high pressures of both CO<sub>2</sub> and H<sub>2</sub> to achieve high TON.<sup>9</sup> Herein, we describe a Mo formate hydride complex that forms, at ambient temperature and atmospheric pressure, from CO<sub>2</sub> and H<sub>2</sub>. This complex is demonstrated to be a precatalyst for both FA dehydrogenation and CO<sub>2</sub> hydrogenation. Stoichiometric studies inform reasonable operative mechanisms for each process, which seem to share a monohydride cation intermediate. Catalyst optimization is ongoing, but current TONs of >100 for each process have been achieved.

## RESULTS AND DISCUSSION

### Coordination Chemistry

Small molecule binding equilibria at zero-valent Mo were established for  $\text{N}_2/\text{H}_2$  and  $\text{N}_2/\text{CO}_2$  in Chapters 2 and 7 of this dissertation, respectively. This suggested the potential for an additional equilibrium between  $\text{H}_2$  and  $\text{CO}_2$  binding in this system. Placing dihydride complex **2** under an atmosphere of  $\text{CO}_2$  afforded a mixture of **2** and **3** (Scheme 8.1). With time, a new resonance was observed in the  $^{31}\text{P}\{^1\text{H}\}$  NMR spectrum at 89.82 ppm. Addition of 1 atm. of  $\text{CO}_2$  and 4 atm. of  $\text{H}_2$  to **1** led to quantitative conversion to this new complex, as determined by  $^{31}\text{P}\{^1\text{H}\}$  NMR spectroscopy. The  $^1\text{H}$  NMR spectrum displayed an edifying low-field resonance at 8.9 ppm, consistent with formation of formate hydride **4**. Unexpectedly, there were no  $^1\text{H}$  signals downfield of 0 ppm; a triplet ( $J = 86.3$  Hz) was observed at 1.85 ppm. This large scalar coupling and a COSY NMR correlation to the central arene signal at 6.20 ppm (Figure 8.4.), both support the assignment of this spectral feature to a hydride.



**Scheme 8.1.** Small-molecule binding equilibria and stoichiometric  $\text{CO}_2$  hydrogenation at low-valent Mo.

Crystallization of **4** has proven elusive, but a related complex, carboxylate hydride **6**, can be prepared and structurally characterized. Treating Mo N<sub>2</sub> adduct **1** with one equiv. of <sup>t</sup>BuCOOH in C<sub>6</sub>H<sub>6</sub> confers quantitative conversion to the protonation product, **6** (Figure 8.1.). The spectroscopic signature of **6** closely matches that of **5**, with a hydride resonance at 2.11 ppm showing a <sup>2</sup>J(P,H) coupling of 90.73 Hz. The metrical data for **6** is in accord with the structure inferred from solution spectroscopy; an η<sup>6</sup> Mo-arene interaction is observed with *trans*-spanning diphosphines and a κ<sup>1</sup> carboxylate (Figure 8.1.).

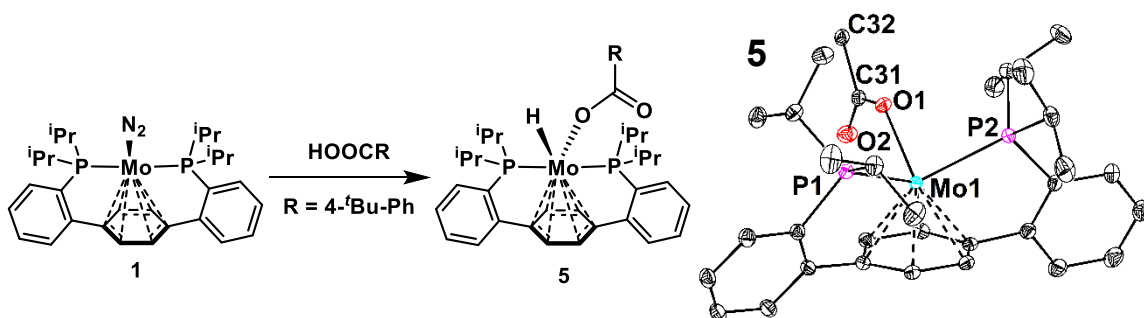
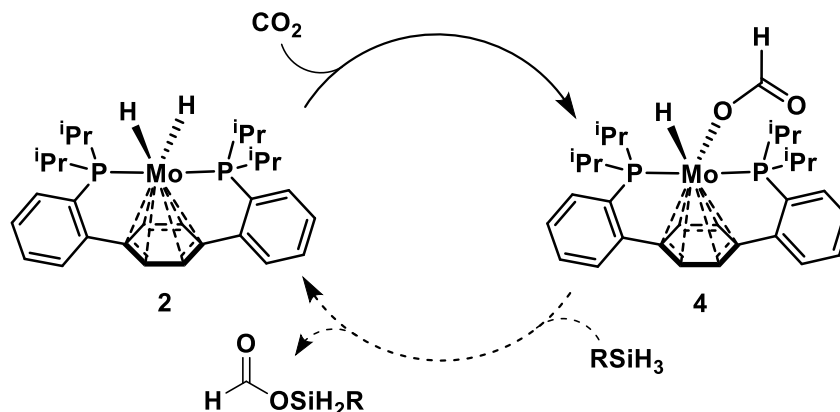


**Figure 8.1.** Synthesis and solid-state structure of carboxylate hydride complex **5**. Thermal anisotropic displacement ellipsoids are shown at a 50% probability level. Hydrogen atoms and all but the ipso carbon of the <sup>t</sup>Bu phenyl motif are omitted for clarity. Selected bond distances [Å]: Mo1-C<sub>arene</sub>(ave.): 2.266(2), Mo1-O1: 2.196(1), O1-C31: 1.284(2), C31-O2: 1.237(2).

### Hydrosilylation Chemistry

Formation of formate hydride **4** prompted evaluation of *para*-terphenyl diphosphine Mo complexes as precatalysts for CO<sub>2</sub> hydrosilylation catalysis. CO<sub>2</sub> reduction in this manner often proceeds via insertion into a M–H bond and trapping of the resultant formate fragment via formation of a strong Si–O bond (Scheme 8.2.).<sup>4</sup> In the envisioned system, reaction of thus formed **2** with CO<sub>2</sub> would close a catalytic cycle.

Addition of silanes to electron-rich Mo complexes has been shown to result in E–H bond activation chemistry,<sup>13</sup> a reactivity trend that holds true for **1** (Figure 8.2.). Treating a solution of **1** with PhSiH<sub>3</sub> leads to a lightening of the reaction and effervescence consistent with N<sub>2</sub> loss. The <sup>1</sup>H NMR spectrum shows both a highly shielded triplet (*J* = 43.6 Hz) at -3.13 ppm and a singlet at 5.51 ppm with clear <sup>29</sup>Si satellites (*J* = 166.34 Hz, <sup>29</sup>Si: *I* = 1/2, 5%). The <sup>31</sup>P{<sup>1</sup>H} NMR spectrum shows a single peak at 70.82 ppm. Combined, these



**Scheme 8.2.** Proposed catalytic cycle for CO<sub>2</sub> hydrosilylation from precatalyst **2**.

spectroscopic features are consistent with Si–H oxidative addition, yielding phenylsilyl hydride **6<sup>PhH</sup>** (Figure 8.2). N<sub>2</sub> adduct **1** also reacts readily with the smaller silane, SiH<sub>4</sub>, to give a similar silyl hydride product, **6<sup>HH</sup>**. The <sup>1</sup>H NMR spectrum of this molecule is analogous to that of **6<sup>PhH</sup>**, but with upfield shifted Si–H (4.52 ppm, <sup>1</sup>J(Si,H) = 81.35 Hz) and Mo–H (–3.26 ppm, t, J = 45.93 Hz). Single crystals of **6<sup>PhH</sup>** were obtained by cooling a concentrated hexanes solution to –35 °C, validating the proposed structure (Figure 8.2).

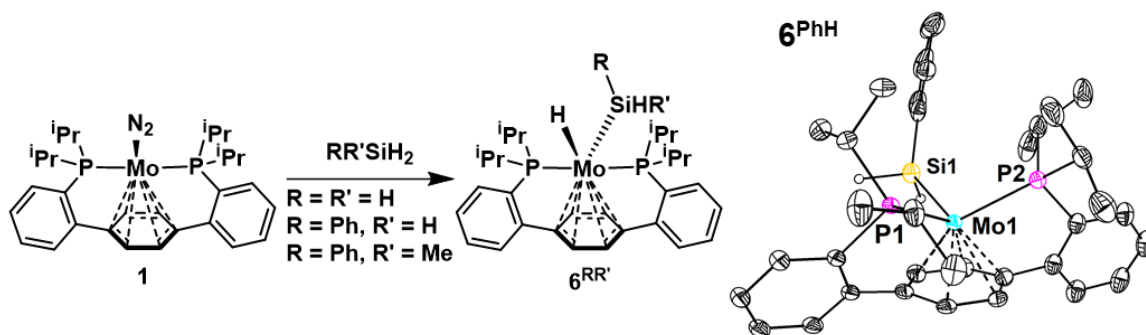
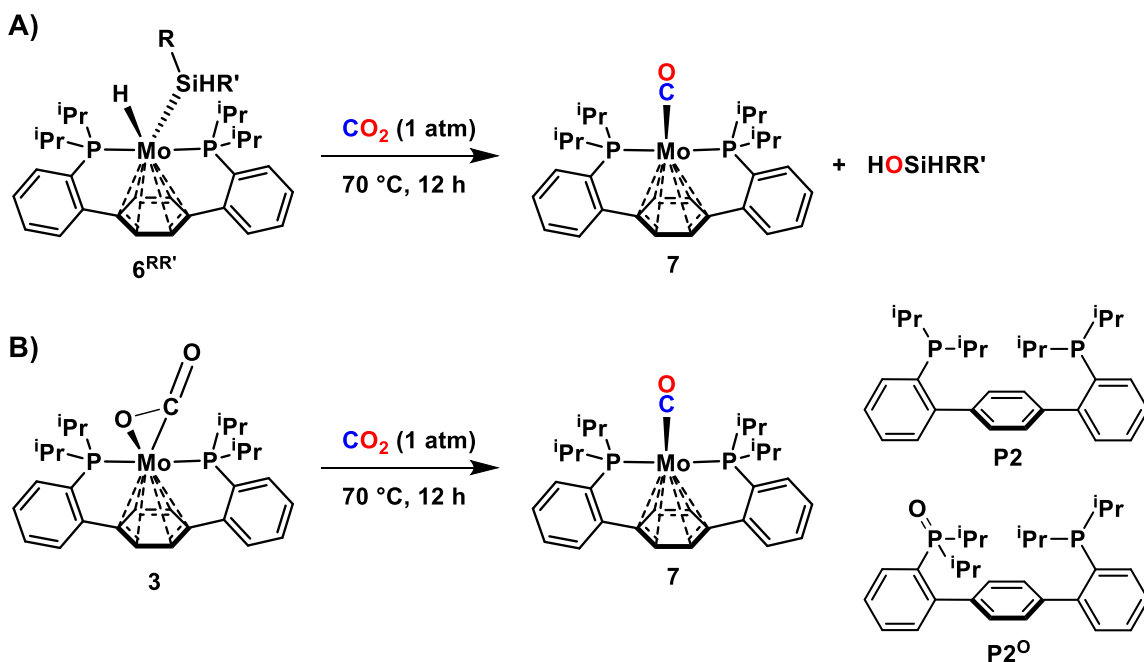


**Figure 8.2.** Synthesis and solid-state structure of carboxylate hydride complex **5**. Thermal anisotropic displacement ellipsoids are shown at a 50% probability level. Select hydrogen atoms and all but the ipso carbon of the <sup>t</sup>Bu phenyl motif are omitted for clarity. Selected bond distances [Å]: Mo1–C<sub>arene</sub>(ave.): 2.268(1), Mo1–Si1: 2.5313(4).

Reactions with secondary silanes showed oxidative addition chemistry sensitive to the steric environment at Si. PhMeSiH<sub>2</sub> (1 equiv.) afforded 40% conversion (<sup>31</sup>P{<sup>1</sup>H} NMR integration) to **6<sup>PhMe</sup>**; adding 25 equiv. increased conversion to the silyl hydride to 97%, which was made quantitative by degassing the reaction via a single freeze-pump-thaw cycle (Figure 8.5).

Notably, the hydride resonance for  $6^{\text{PhMe}}$  shows a larger  $^2J(\text{P,H})$  scalar coupling constant (51.48 Hz), a spectroscopic manifestation attributed to a more crowded coordination sphere and a contracted  $\angle\text{P1-Mo1-P2}$ . The tertiary silane,  $\text{Et}_3\text{SiH}$ , showed no reactivity with **1**.

With precedent for  $\text{CO}_2$  insertion into both  $\text{M-Si}$  and  $\text{M-H}$  bonds, complexes **6** were treated with 1 atm. of  $\text{CO}_2$ . Disappointingly, no reaction was observed, regardless of the substitution on silicon. Under more forcing conditions—heating to  $70^\circ\text{C}$  for 12 h—formation of  $\text{Mo(0)}$  CO complex, **7** (Chapter 3), was observed, as well as minor decomposition to free diphosphine (*ca.* 5%) (Scheme 8.3., A). Kinetic analysis of this C–O cleavage reaction showed complicated dependence on silane concentration; from 1 to 25 equiv., added silane increased the rate of reaction (Figure 8.7.). However, higher silane concentration actually impeded the reaction, providing the first clue suggesting an abnormal  $\text{CO}_2$  reduction mechanism (*vide infra*). Additionally, increased steric bulk at Si resulted in faster reactivity, with  $6^{\text{PhH}}$  forming **7** more slowly than  $6^{\text{PhMe}}$ .



**Scheme 8.3.**  $\text{CO}_2$  cleavage in the presence (A) and absence (B) of silane.

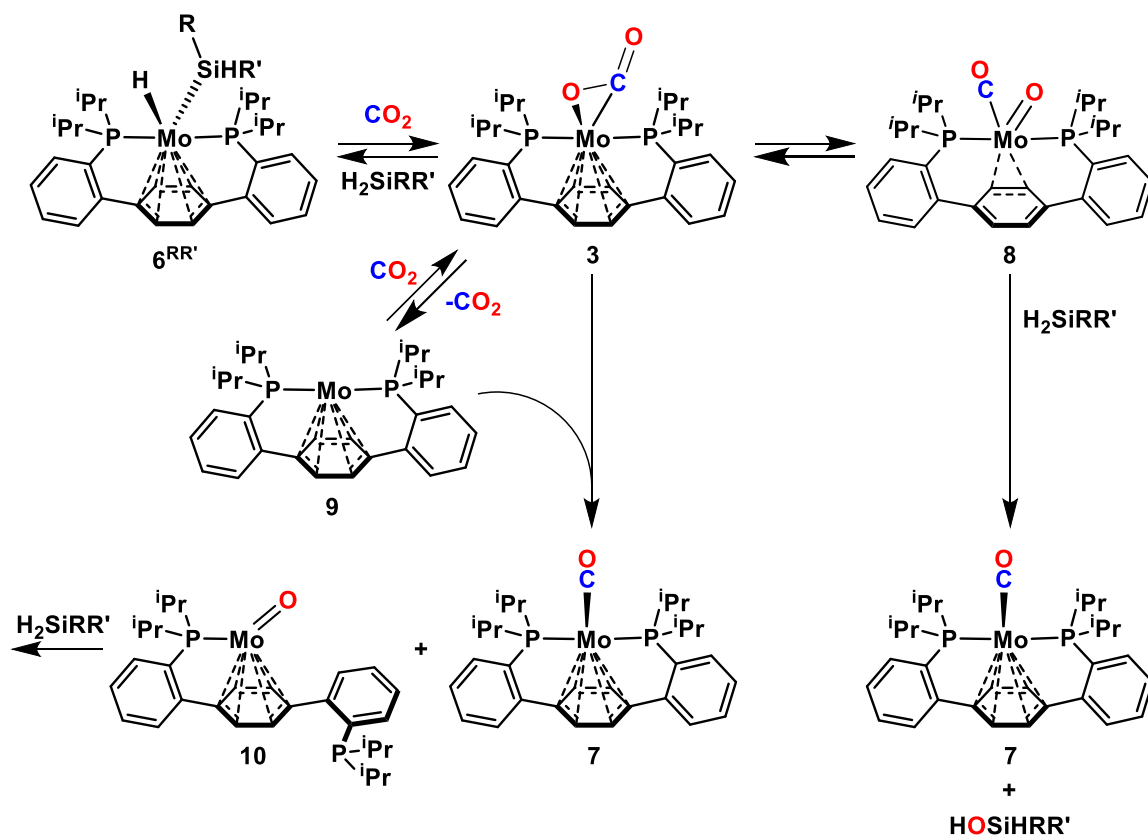
A control reaction demonstrated that silane was superfluous to C–O cleavage chemistry. Heating a  $\text{C}_6\text{D}_6$  solution of **3** afforded a mixture of **7** (56%),  $\text{P}_2^{\text{O}}$  (17%), and free diphosphine

(**P2**, 27%), as determined by relative integration of the  $^{31}\text{P}\{^1\text{H}\}$  NMR spectrum ( $\text{PPh}_3$  capillary standard). Heating isotopically labeled **3**- $^{13}\text{C}$  provided **7**- $^{13}\text{C}$ , as evidenced by  $^{31}\text{P}\{^1\text{H}\}$  and  $^{13}\text{C}\{^1\text{H}\}$  NMR spectroscopies, confirming the source of the CO unit. Though Mo  $\text{CO}_2$  complexes are known to undergo redistribution reactions, providing carbonyl carbonate complexes,<sup>14</sup> the observation of both >50% conversion to **7** and phosphine oxide, **P2**<sup>o</sup>, contradict this pathway. Phosphine-supported Ni  $\text{CO}_2$  adducts have been demonstrated to cleave  $\text{CO}_2$  to a Ni carbonyl complex and phosphine oxide,<sup>15</sup> a reactivity manifold that is congruent with the experimental data.

But what is the fate of the cleaved O-atom in the silane reactions? Oxygen atom transfer to silane seemed most likely, as no phosphine oxide was observed and conversion to **7** was effectively quantitative. GC/MS analysis of the reaction mixture following heating **6**<sup>PhMe</sup> under  $\text{CO}_2$  for 12 h demonstrated formation of both phenyl methyl silanol as well as polysiloxanes, both of which were absent in the control (Figure 8.8.).

At this juncture, two mechanisms seemed plausible, both involving Mo-mediated C–O cleavage to a Mo(II) oxo complex that is subsequently reduced by silane (Scheme 8.4.). A pre-equilibrium between silyl hydride and  $\text{CO}_2$  is consistent with the reaction kinetics. Bulky silanes favor persistence of **2**, the species proposed to undergo C–O scission; while less sterically imposing silanes (and high silane concentrations), sequester Mo as unreactive **6**. Relatively low  $\text{PhMeSiH}_2$  concentrations increase the rate of formation of **7**, consistent with a silane dependent rate effecting step. Presumably, the rate determining step for the intermolecular pathway (Scheme 8.4., left) would be O-atom abstraction, which should be zeroth order in silane and second order in Mo. Intramolecular C–O scission (Scheme 8.4., right), in contrast, may be reversible and would therefore show silane dependence. The initial equilibrium between silane oxidative addition and  $\text{CO}_2$  binding (inverse order in  $[\text{Si}]$ ), in conjunction with silane capture of carbonyl oxo **8** (first order in  $[\text{Si}]$ ), is consistent with the complex silane dependence observed in the kinetics.

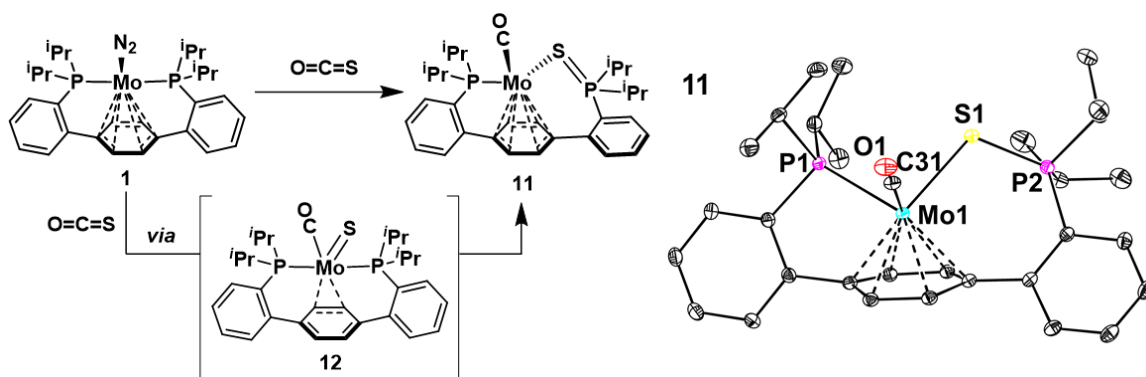
Additional evidence supporting an intramolecular pathway was provided by reactions with



**Scheme 8.4.** Plausible mechanisms for the formation of **7** from **6** and CO<sub>2</sub>.

carbonyl sulfide. Placing a C<sub>6</sub>D<sub>6</sub> solution of **1** under an atmosphere of OCS resulted in immediate formation of an asymmetric complex, as demonstrated by two coupling doublets (83.41 and 54.34 ppm,  $J = 17.8$  Hz) in the <sup>31</sup>P{<sup>1</sup>H} NMR spectrum. Upon standing, X-ray quality single crystals were obtained, evincing formation of carbonyl phosphine sulfide complex **11** (Figure 8.3.). Asymmetric **11** likely forms via initial cleavage of the more reactive C–S bond of OCS, giving a transient Mo carbonyl sulfide complex, **12**. Oxidative cleavage of C=E multiple bonds has been demonstrated on W;<sup>16</sup> a similar process is likely operative here. Analogously to the P–C bond forming Mo(II) methyldiene complex discussed in Chapter 4, the Mo(II) sulfide afforded by C–S cleavage inserts into the Mo–P bond, giving the observed phosphine sulfide. Under the CO<sub>2</sub> reduction conditions, the oxo congener of sulfide **12** is proposed to oxidize silanes faster than the phosphine ligand, but in the absence of silanes, the oxygen congener of **11** is likely formed, leading ultimately to the observed decomposition to

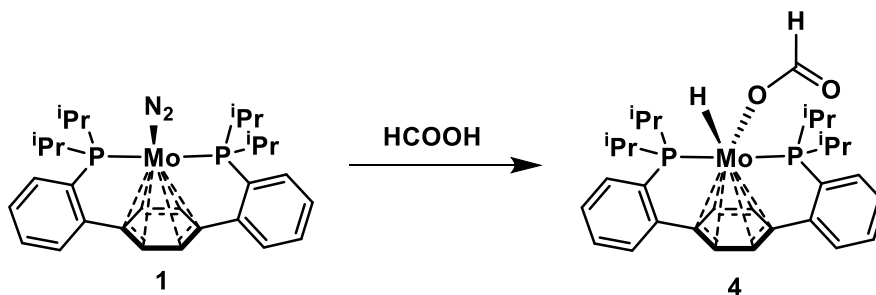


P2<sup>o</sup>.

**Figure 8.3.** Synthesis and solid-state structure of **11**. Thermal anisotropic displacement ellipsoids are shown at a 50% probability level. Hydrogen atoms are omitted for clarity. Selected bond distances [Å]: Mo1–S1: 2.5016(3), S1–P2: 2.0053(4).

#### *CO<sub>2</sub> Hydrogenation/Dehydrogenation*

In preliminary studies of formate hydride complex **4**, we recognized that it should be accessible, in a similar way to carboxylate hydride **5**, from protonation of Mo N<sub>2</sub> adduct **1** with FA (Scheme 8.5). Not only was this confirmed, but catalytic FA dehydrogenation was demonstrated; addition of 5 equiv. FA to **1** resulted in conversion to **4** at room temperature, with subsequent heating (70 °C) resulting in complete consumption of the FA (Figure 8.9). Building off of this preliminary result, a collaborative project with a postdoctoral scholar in the group, Dr. Naoki Shida, has developed both catalytic FA dehydrogenation and CO<sub>2</sub> hydrogenation chemistries.

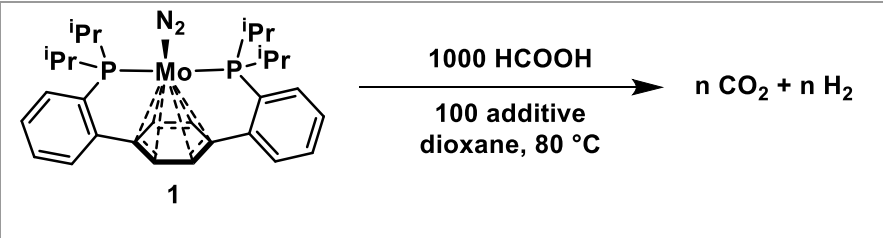


**Scheme 8.5.** Formic acid protonation of N<sub>2</sub> adduct **1**.

Heating a C<sub>6</sub>D<sub>6</sub> solution of formate hydride **4** to 70 °C for one hour, under N<sub>2</sub>, afforded 85% conversion of the starting material to a mixture of N<sub>2</sub> adduct **1** (42%), CO<sub>2</sub> adduct **3**

(25%), and H<sub>2</sub> complex **2** (18%). Though insertion is favored at room temperature, at higher temperature, formate dissociation is entropically preferred, leading to reversion to the gaseous small molecules (Figure 8.10.). We anticipated that simply heating a solution of **1** in the presence of FA (which has been shown to form **4**), would therefore lead to dehydrogenation catalysis. However, with 0.001 mol% **1** in dioxane at 80 °C, super stoichiometric reactivity was observed; only 1.5 turnovers for FA dehydrogenation were achieved, as determined by eudiometry (Table 8.1.).

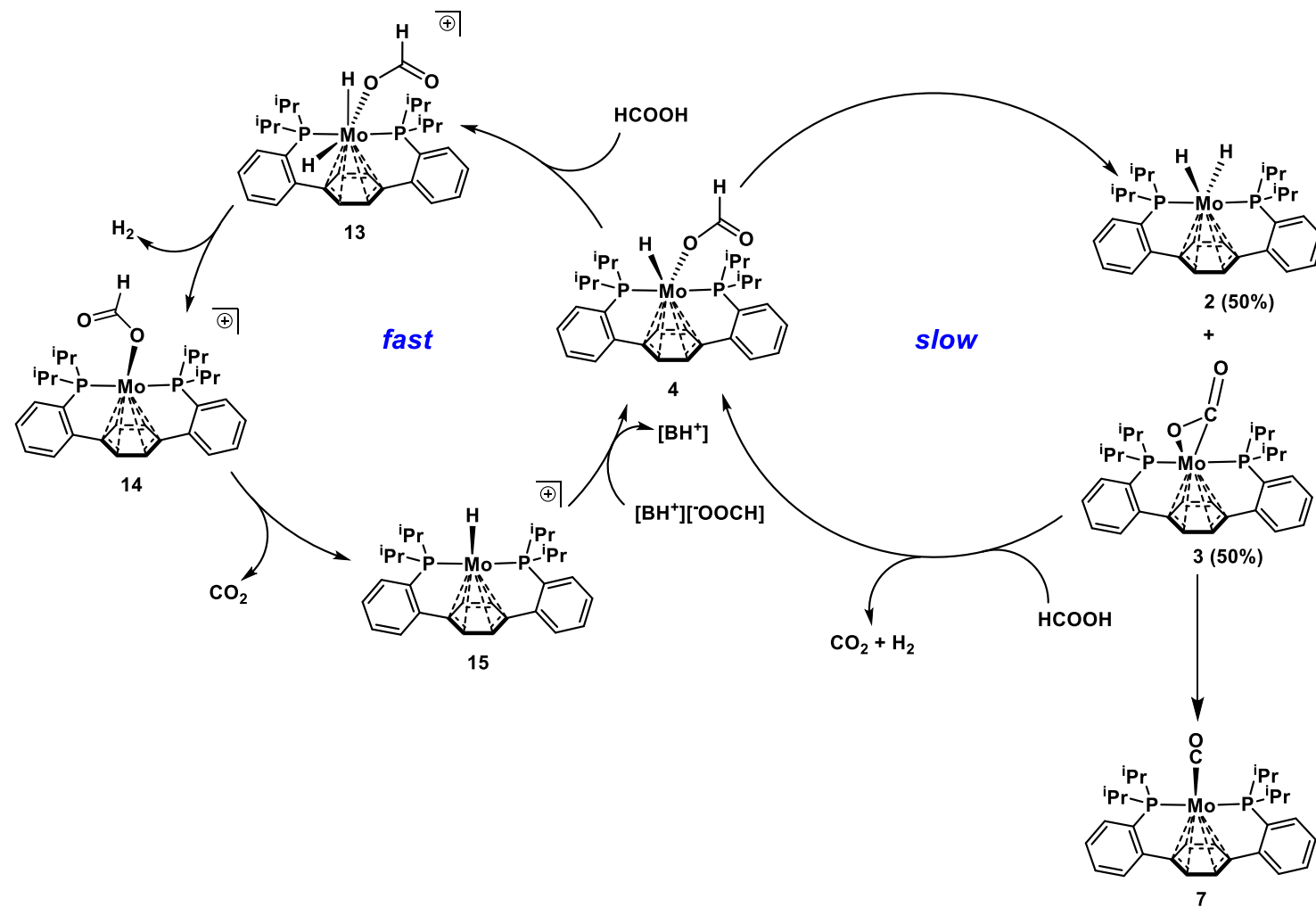
**Table 8.1.** Preliminary catalytic screening for FA dehydrogenation.

			
Entry	Additive	time	TON
1	-	1	1.5
2	LiCl	1	3
3	B(C <sub>6</sub> F <sub>5</sub> ) <sub>3</sub>	1	3
4	NaBAR <sup>F</sup> <sub>24</sub>	1	3
5	NaBF <sub>4</sub>	1	0
6	HCOONa	5	298
7 <sup>‡</sup>	DMAP	3	196
8	NaOMe	4	0
9	DBU	3.3	615

BAR<sup>F</sup><sub>24</sub> = tetrakis(3,5-bis(trifluoromethyl)phenyl)borate, DMAP = N,N-dimethyl-4-aminopyridine, DBU = 1,8-diazabicyclo[5.4.0]undec-7-ene

<sup>‡</sup>0.05 mL (500 eq) of FA was used

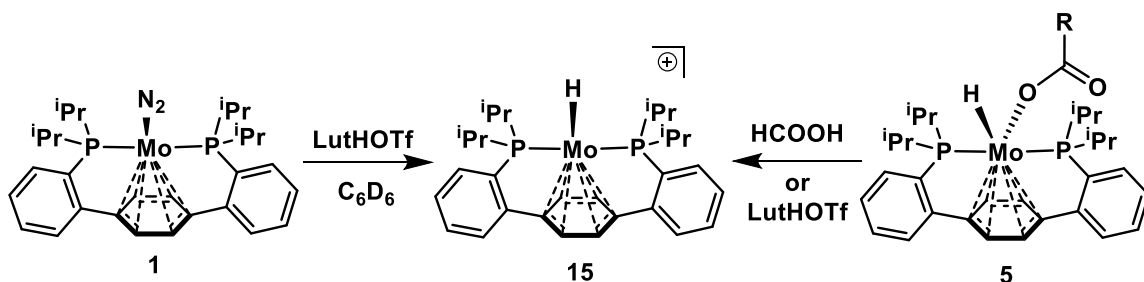
Literature reports have demonstrated that addition of Lewis acid additives can have profound effects on the efficacy of FA dehydrogenation catalysts.<sup>10c</sup> The proposed mechanism for reactivity enhancement invokes a LA-assisted formate decarboxylation step; LA acids were screened as additives in reactions from **1** (Table 8.1., Entry 2-5), with no success. Surprisingly, addition of base was found to drastically increase the turnover number (TON), with the best activity being observed with DBU (1,8-diazabicyclo[5.4.0]undec-7-ene, Entry 9), providing *ca.* 600 turnovers in one hour.



**Scheme 8.6.** Plausible mechanisms for FA dehydrogenation from **4**.

Mechanistic studies are ongoing, but current data supports two distinct pathways for FA dehydrogenation (Scheme 8.6.). An inefficient, but demonstrated, cycle involves thermal decarboxylation of **4** to a mixture of **2** and **3** (Scheme 8.6., right). As reported above, a decomposition pathway from CO<sub>2</sub> adduct **3** is thermally induced C–O cleavage to monocarbonyl **7**. If the rate of this process is comparable to that of deinsertion, it may explain the low TON observed in the absence of additives (*vide supra*); all of the Mo would be appropriated as inactive **7**. In a productive sense, the mixture of **2** and **3** could react with FA to return complex **4**, closing the cycle.

The alternative pathway, which is postulated to be responsible for the high turnovers observed in the presence of bases, involves protonation of **4** to a dihydride formate cation. This reaction step is supported by independent reactions between **5**, a surrogate for **4**, and FA. In that reaction, a new hydridic resonance is observed in the <sup>1</sup>H NMR spectrum at -4.99 ppm (t, *J* = 35.31 Hz) corresponding to a complex with a central arene resonance at 5.39 ppm (s). This same spectroscopic signature is observed when **4** is treated with LutHOTf, and when N<sub>2</sub> adduct **1** is protonated with LutHOTf in C<sub>6</sub>D<sub>6</sub>, consistent with the assignment of this resonance to hydride cation **15** (Figure 8.11.). This complex is similar to the hydride acetonitrile cation shown to be competent for AB dehydrogenation (Chapter 2), but the MeCN adduct was not a competent precatalyst for FA dehydrogenation.

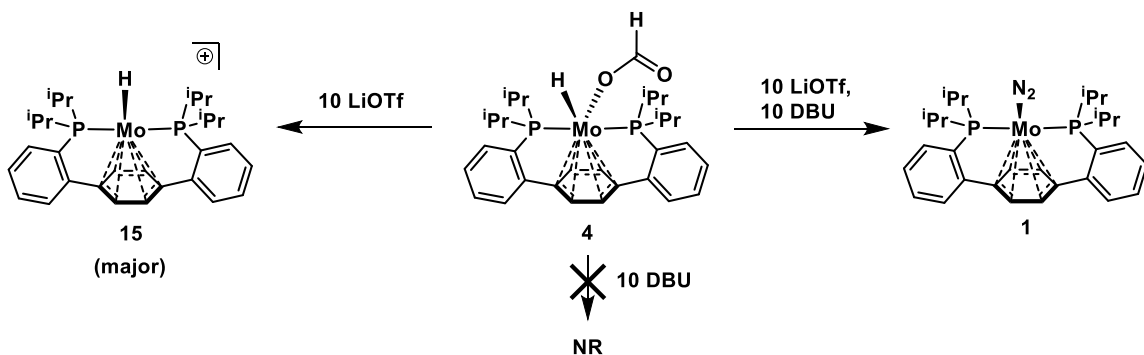


**Scheme 8.7.** Independent synthetic routes to hydride cation **15**.

A reasonable pathway for the formation of hydride cation **15** involves initial protonation of **4** to dihydride formate cation **13**. An isoelectronic Mo(IV) trihydride is accessible on the *para*-terphenyl diphosphine ligand scaffold (Chapter 2) and readily loses H<sub>2</sub>. Analogously, H<sub>2</sub>

elimination from **13** yields formate cation **14**, which could undergo decarboxylation to **15**. Formate coordination would regenerate **4**, closing the catalytic cycle. The role of the basic additives is not immediately obvious, but all of the bases used are sufficiently strong to deprotonate FA. This would increase the solution concentration of formate anion, which may in turn aid turnover (**15**  $\rightarrow$  **4**), if formate coordination is rate limiting. Alternatively, the amine bases may act to provide a soluble source of formate, both keeping Mo intermediates from precipitating over the course of the reaction and aiding in regeneration of **4**. Further studies are ongoing, including independent synthesis and competency studies from hydride cation **15**.

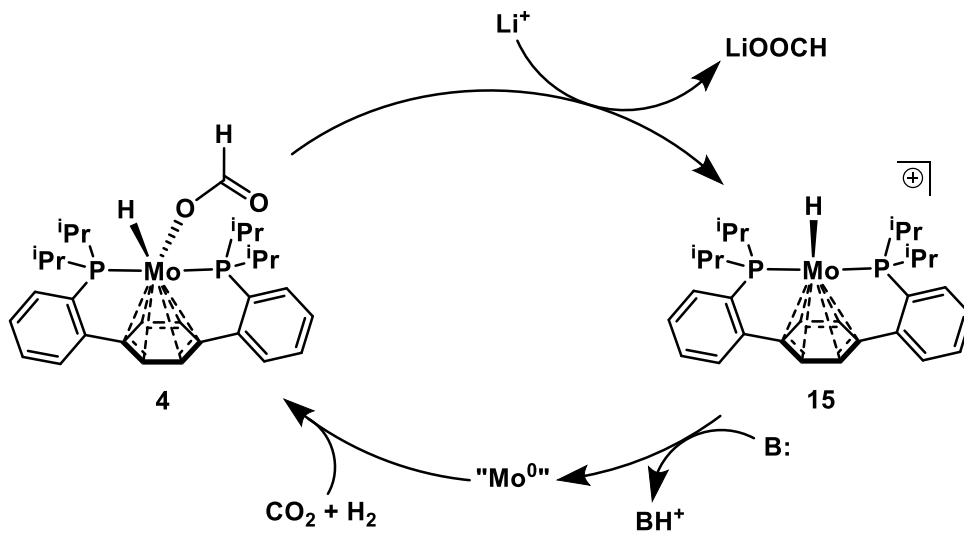
In concert with the development of FA dehydrogenation catalysis, the reverse reaction, CO<sub>2</sub> hydrogenation, was targeted. As a base is required to make CO<sub>2</sub> hydrogenation exergonic, complex **4** was treated with 10 equiv. of DBU under N<sub>2</sub> (Figure 8.12.). No reaction was observed, even over the course of 24 h. Again, recalling that LAs can assist in formate dissociation,<sup>12a</sup> soluble alkali metal salts were screened as reaction additives. Addition of 10 equiv. of LiOTf to **4** in C<sub>6</sub>D<sub>6</sub> resulted in moderate conversion to a mixture of species, including **1**, **15**, and **3** (Figure 8.12.). Monitoring this reaction over 12 h showed less than 50% total conversion of the starting material. Treating a C<sub>6</sub>D<sub>6</sub> solution of **4** with 10 equiv. of both base (DBU) and LA (LiOTf) resulted in quantitative conversion to **1** (86%) and **3** (14%) in just 30 min (Figure 8.12.).



**Scheme 8.8.** Stoichiometric reactions of **4** with LA (left), base (down), and both (right).

These stoichiometric reactions map out a catalytic cycle for CO<sub>2</sub> hydrogenation to formate (Scheme 8.9.). As a first step, LA-assisted formate dissociation gives Mo hydride cation **15**; **15**

is observed in the stoichiometric reaction of **4** with LiOTf. Deprotonation of **15** affords a Mo(0) species, consistent with conversion to N<sub>2</sub> adduct **1** in the presence of both LiOTf and DBU. CO<sub>2</sub>/H<sub>2</sub> addition and insertion closes the cycle.



**Scheme 8.9.** Plausible catalytic cycle for CO<sub>2</sub> hydrogenation from **4**.

Applying this mechanistic understanding to catalysis has proven successful, affording up to 100 turnovers for formate under very low pressures of CO<sub>2</sub> and H<sub>2</sub> (Table 8.2).<sup>9</sup> Lithium bases have proven the most effective in these reactions, likely reflecting improved formate abstraction by the stronger alkali metal LA. Further work to optimize these catalytic conditions and look at reactions under higher CO<sub>2</sub> and H<sub>2</sub> pressures is currently underway.

**Table 8.2.** Catalytic data for formic acid dehydrogenation.

Entry	Base/additive	P <sub>CO<sub>2</sub></sub> :P <sub>H<sub>2</sub></sub> (atm)	Solvent	Time	Temp (°C)	TON
<b>1*</b>	DBU/NaOTf	1:1	THF	20	70	6
<b>2*</b>	LiHMDS	1:1	THF	20	70	106
<b>3*</b>	LiO <sup>t</sup> Bu	1:1	THF	20	70	55
<b>4**</b>	LiO <sup>t</sup> Bu	2:1	THF	12	75	33
<b>5**</b>	DBU	2:1	Toluene	12	75	20
<b>6**</b>	LiHMDS	2:1	Toluene	12	75	0
<b>7**</b>	LiO <sup>t</sup> Bu	2:1	Toluene	12	75	33

\* 0.005 mmol of molybdenum complex, 100 eq. of base, 1 mL of solvent

\*\* 0.015 mmol of molybdenum complex, 100 eq. of base, 3 mL of solvent

## CONCLUSION

Two modes of CO<sub>2</sub> reduction have been presented. Stoichiometric reactions with silanes afford CO and silanol from CO<sub>2</sub> via a mechanism involving intramolecular C–O bond cleavage and O-atom transfer to silane. Catalytic CO<sub>2</sub> hydrogenation proceeds in the presence of both LA and base, affording respectable turn over numbers under very mild reaction conditions. The same species demonstrated to be catalytically competent for formate formation catalyze the reverse reaction, formic acid dehydrogenation, the mechanism of which is explored in detail.

## EXPERIMENTAL SECTION

Unless otherwise specified, all operations were carried out in an MBraun drybox under a nitrogen atmosphere or using standard Schlenk and vacuum line techniques. Solvents for air- and moisture-sensitive reactions were dried over sodium benzophenone ketyl, calcium hydride, or by the method of Grubbs.<sup>17</sup> Deuterated solvents were purchased from Cambridge Isotope Laboratories and vacuum transferred from sodium benzophenone ketyl. Solvents, once dried and degassed, were vacuum transferred directly prior to use or stored under inert atmosphere over 4 Å molecular sieves. Molybdenum complexes **1**, **2**,<sup>18</sup> and **3** (Chapter 7) were prepared and purified according to reported procedures. Unless indicated otherwise, all chemicals obtained from standard vendors and utilized as received. <sup>1</sup>H, <sup>13</sup>C{<sup>1</sup>H}, and <sup>31</sup>P{<sup>1</sup>H} NMR spectra were recorded on Varian 400 MHz or Varian INOVA-500 spectrometers with shifts reported in parts per million (ppm). <sup>1</sup>H and <sup>13</sup>C{<sup>1</sup>H} NMR spectra are referenced to residual solvent peaks.<sup>19</sup> <sup>31</sup>P{<sup>1</sup>H} chemical shifts are referenced to an external 85% H<sub>3</sub>PO<sub>4</sub> (0 ppm).

### *Synthesis of 4*

A brown/red solution of **1** (49.9 mg, 0.085 mmol) in C<sub>6</sub>H<sub>6</sub> (3 mL) was transferred to a Schlenk tube charged with a stir bar. The solution was degassed via three freeze-pump-thaw cycles. The headspace was backfilled with 1 atm of CO<sub>2</sub> gas, enacting slight reddening of the solution. The schlenk tube was sealed and then submerged in LN<sub>2</sub>, freezing the contents and condensing the CO<sub>2</sub>. It was then opened to 1 atm of H<sub>2</sub> gas, maintaining the -196 °C temperature. The flask was resealed and the contents were allowed to warm to ambient temperature with stirring for 2 h. The now red solution was lyophilized *in vacuo*, giving **4** as a reddish powder. <sup>1</sup>H NMR (400 MHz, C<sub>6</sub>D<sub>6</sub>, 23 °C) δ: 8.90 (s, 1H, OCHO), 7.24 (d, J = 7.07 Hz, 2H, aryl-H), 7.05-7.08 (br m, 2H, aryl-H), 6.99 (t, J = 7.46 Hz, 2H, aryl-H), 6.94 (t, J = 7.17 Hz, 2H, aryl-H), 6.21 (s, 2H, central arene-H), 3.59-3.62 (m, 2H, central arene-H), 2.46-2.57 (m, 2H, CH(CH<sub>3</sub>)<sub>2</sub>), 2.35-2.46 (m, 2H, CH(CH<sub>3</sub>)<sub>2</sub>), 1.81 (t, 1H, J = 86.41 Hz, Mo-H), 1.21-1.27 (m, 6H, CH(CH<sub>3</sub>)<sub>2</sub>), 0.94-1.05



(m, 12H, CH(CH<sub>3</sub>)<sub>2</sub>), 0.80-0.85 (m, 6H, CH(CH<sub>3</sub>)<sub>2</sub>). <sup>31</sup>P{<sup>1</sup>H} NMR (162 MHz, C<sub>6</sub>D<sub>6</sub>, 23 °C) δ: 89.82.

#### *Synthesis of 5*

A 20 mL scintillation vial was charged with **1** (200 mg, 0.340 mmol), C<sub>6</sub>H<sub>6</sub> (5 mL), and 4-Bu-PhCOOH (73 mg, 0.408 mmol). The red solution was allowed to stir for 8 h, at which time the vial contents were frozen solid in a -35 °C freeze and the C<sub>6</sub>H<sub>6</sub> lyophilized under reduced pressure, giving **5** as a red powder. X-ray quality single crystals were grown via diffusion of pentane into a concentrated C<sub>6</sub>H<sub>6</sub> solution of **5**. <sup>1</sup>H NMR (400 MHz, C<sub>6</sub>D<sub>6</sub>, 23 °C) δ: 8.31 (d, *J* = 8.2 Hz, 2H, aryl-*H*), 7.28 (t, *J* = 7.0 Hz, 2H, aryl-*H*), 7.03-7.05 (m, 2H, aryl-*H*), 6.97 (t, *J* = 7.3 Hz, 2H, aryl-*H*), 6.89 (t, *J* = 7.4 Hz, 2H, aryl-*H*), 6.46 (v br, 2H, central arene-*H*), 3.61-3.64 (m, 2H, central arene-*H*), 2.60-2.64 (m, 2H, CH(CH<sub>3</sub>)<sub>2</sub>), 2.44-53 (m, 2H, CH(CH<sub>3</sub>)<sub>2</sub>), 2.10 (t, *J* = 84.93 Hz, Mo-*H*), 1.34-1.39 (m, 6H, CH(CH<sub>3</sub>)<sub>2</sub>), 0.96-1.01 (m, 6H, CH(CH<sub>3</sub>)<sub>2</sub>), 0.75-0.80 (m, 12H, CH(CH<sub>3</sub>)<sub>2</sub>). <sup>31</sup>P{<sup>1</sup>H} NMR (162 MHz, C<sub>6</sub>D<sub>6</sub>, 23 °C) δ: 89.61 (s).

#### *Synthesis of 6*

A brown/red solution of **1** (61 mg, 0.103 mmol) in benzene (4 mL) was transferred to a 20 mL scintillation vial, charged with a stir bar. With stirring, PhSiH<sub>3</sub> (12.8 μL, 0.104 mmol) was added via microsyringe, causing a lightening of the solution. Stirring continued for 30 min. At that time, the solution was lyophilized under reduced pressure, providing **6<sup>PhH</sup>** as a yellow/orange powder (58.4 mg, 0.088 mmol, 85 %). X-ray quality crystals were grown by chilling a saturated hexanes solution of **6<sup>PhH</sup>** (-35 °C). <sup>1</sup>H NMR (400 MHz, C<sub>6</sub>D<sub>6</sub>, 23 °C) δ: 7.67-7.69 (m, 2H, aryl-*H*), 7.33 (d, *J* = 7.3 Hz, 2H, aryl-*H*), 7.06-7.07 (m, 3H, aryl-*H*), 6.97-7.00 (m, 2H, aryl-*H*), 6.88-6.94 (m, 4H, aryl-*H*), 5.51 (s, 2H, Si-*H*), 4.59-4.62 (m, 2H, central arene-*H*), 4.46 (s, 2H, central arene-*H*), 2.13-2.23 (m, 2H, CH(CH<sub>3</sub>)<sub>2</sub>), 2.04-2.13 (m, 2H, CH(CH<sub>3</sub>)<sub>2</sub>) 1.13-1.18 (m, 6H, CH(CH<sub>3</sub>)<sub>2</sub>), 0.92-1.08 (m, 18H, CH(CH<sub>3</sub>)<sub>2</sub>), -3.13 (t, *J* = 43.41 Hz, 1H, Mo-*H*). <sup>31</sup>P{<sup>1</sup>H} NMR (162 MHz, C<sub>6</sub>D<sub>6</sub>, 23 °C) δ: 70.79 (d, *J* = 8.22 Hz).

**6<sup>HH</sup>** can be synthesized by condensing SiH<sub>4</sub> (0.043 mmol) from a calibrated volume into a J. Young style NMR tube charged with a C<sub>6</sub>D<sub>6</sub> solution (0.5 mL) of **1** (25 mg, 0.043 mmol). <sup>1</sup>H NMR (400 MHz, C<sub>6</sub>D<sub>6</sub>, 23 °C) δ: 7.35 (d, *J* = 6.03 Hz, 2H, aryl-*H*), 6.90-6.96 (m, 6H, aryl-*H*), 4.61-4.64 (m, 2H, central arene-*H*), 4.52 (s, 3H, Si-*H*), 4.36 (s, 2H, central arene-*H*), 2.20-2.34 (m, 2H, CH(CH<sub>3</sub>)<sub>2</sub>), 1.94-2.03 (m, 2H, CH(CH<sub>3</sub>)<sub>2</sub>), 1.26-1.32 (m, 6H, CH(CH<sub>3</sub>)<sub>2</sub>), 1.01-1.07 (m, 6H, CH(CH<sub>3</sub>)<sub>2</sub>), 0.86-0.95 (m, 12H, CH(CH<sub>3</sub>)<sub>2</sub>), -3.26 (t, *J* = 45.69 Hz, 1H, Mo-*H*). <sup>31</sup>P{<sup>1</sup>H} NMR (162 MHz, C<sub>6</sub>D<sub>6</sub>, 23 °C) δ: 75.45 (s).

#### *Preparation of 11*

A J. Young style NMR tube was charged with a deep red solution of **1** (25 mg, 0.043 mmol) in C<sub>6</sub>D<sub>6</sub> (0.5 mL). The reaction was degassed via three freeze-pump-thaw cycles and then backfilled with OCS (1 atm.). The contents of the tube were mixed by inversion for 15 min, forming **11**. **11** was never isolated, but X-ray quality single crystals were obtained by allowing the tube to stand, unperturbed, for 12 h. <sup>1</sup>H NMR (400 MHz, C<sub>6</sub>D<sub>6</sub>, 23 °C) δ: 7.52-7.56 (m, 1H, aryl-*H*), 7.46-7.49 (m, 1H, aryl-*H*), 7.19-7.23 (m, 1H, aryl-*H*), 6.98-7.04 (m, 3H, aryl-*H*), 6.86 (br t, *J* = 6.6 Hz, 1H, aryl-*H*), 6.75 (t, *J* = 8.5 Hz, 1H, aryl-*H*), 4.79 (d, *J* = 4.6 Hz, 1H, central arene-*H*), 4.71 (d, *J* = 6.5 Hz, 1H, central arene-*H*), 4.03 (d, *J* = 6.6 Hz, 1H, central arene-*H*), 3.83 (d, *J* = 4.7 Hz, 1H, central arene-*H*), 3.45-2.60 (m, 2H, CH(CH<sub>3</sub>)<sub>2</sub>), 2.23-2.35 (m, 1H, CH(CH<sub>3</sub>)<sub>2</sub>), 1.80-1.91 (m, 1H, CH(CH<sub>3</sub>)<sub>2</sub>), 1.37-1.42 (m, 3H, CH(CH<sub>3</sub>)<sub>2</sub>), 1.18-1.27 (m, 6H, CH(CH<sub>3</sub>)<sub>2</sub>), 1.00-1.12 (m, 6H, CH(CH<sub>3</sub>)<sub>2</sub>), 0.77-0.95 (m, 9H, CH(CH<sub>3</sub>)<sub>2</sub>). <sup>31</sup>P{<sup>1</sup>H} NMR (162 MHz, C<sub>6</sub>D<sub>6</sub>, 23 °C) δ: 88.64 (d, *J* = 17.7 Hz, Mo-*P*), 59.57 (d, *J* = 17.8 Hz, P=*S*).

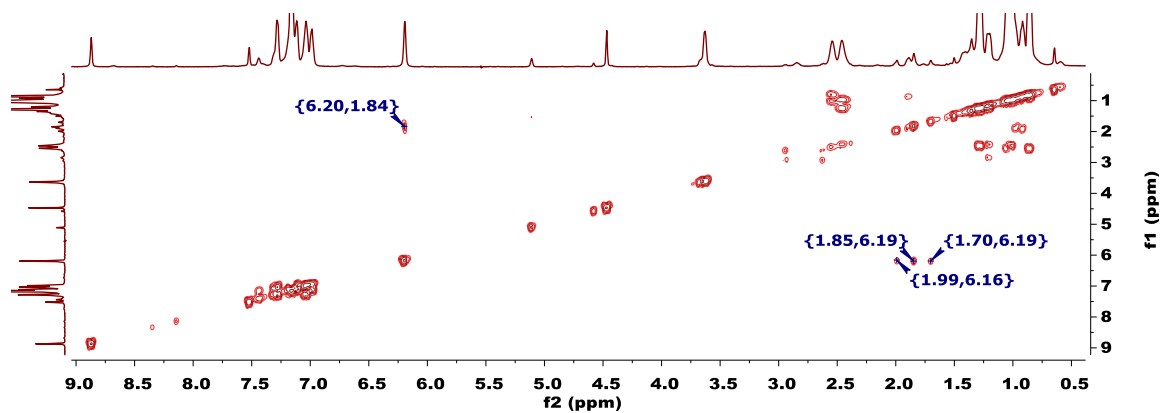


**Figure 8.4.**  $^1\text{H}/^1\text{H}$  COSY NMR spectrum (600 MHz,  $\text{C}_6\text{D}_6$ , 25 °C) of complex 4. The correlation between the hydride resonance at 1.85 ppm and that of the central arene proton at 6.20 ppm is highlighted.

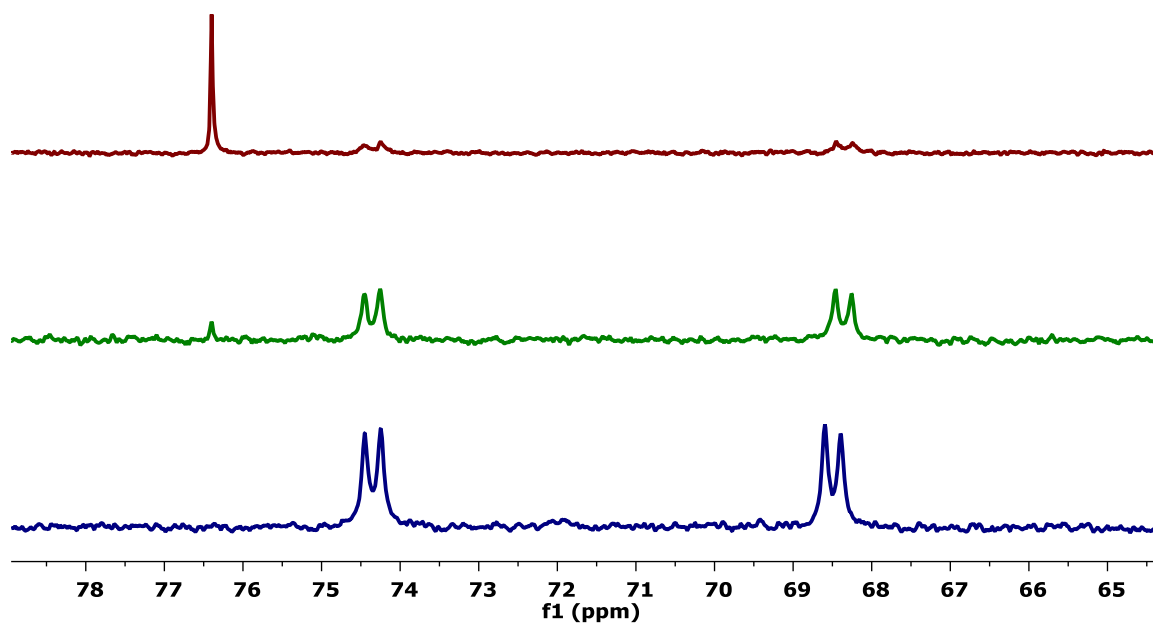


**Figure 8.5.** Stacked  $^{31}\text{P}\{^1\text{H}\}$  NMR spectra (162 MHz,  $\text{C}_6\text{D}_6$ , 23 °C) of addition of  $\text{PhMeSiH}_2$  to  $\text{N}_2$  adduct 1. Top: 1 equiv.  $\text{PhMeSiH}_2$ ; Middle: 100 equiv.  $\text{PhMeSiH}_2$ ; Bottom: 100 equiv.  $\text{PhMeSiH}_2$  and one freeze-pump-thaw.

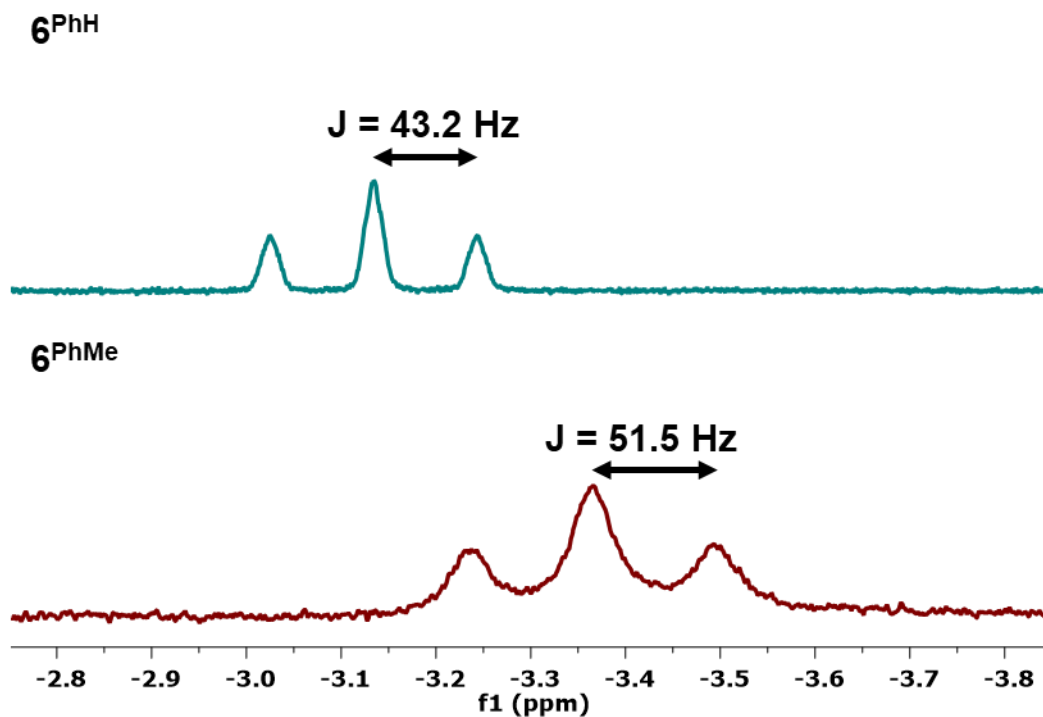


Figure 8.6. Partial  $^1\text{H}$  NMR spectra of the hydridic resonance for  $6^{\text{PhH}}$  (top) and  $6^{\text{PhMe}}$  (bottom).

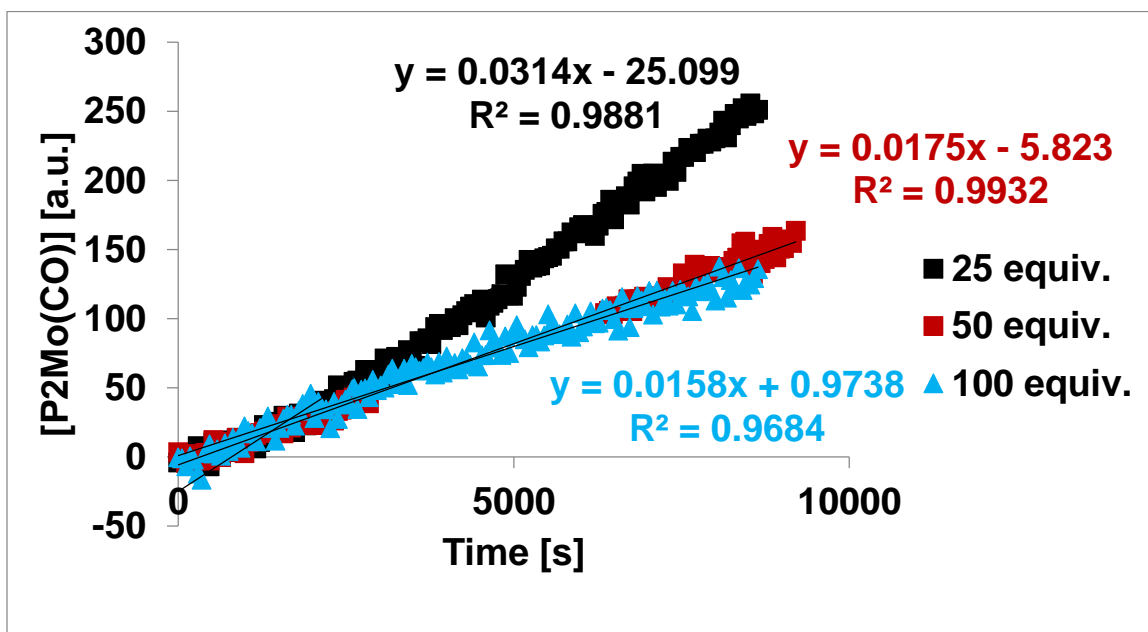
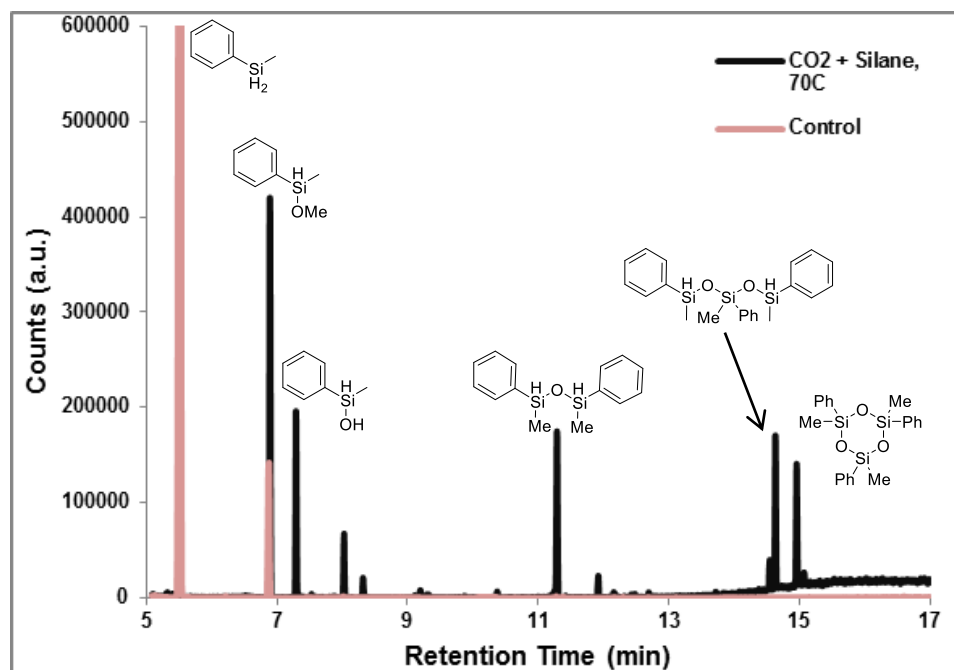
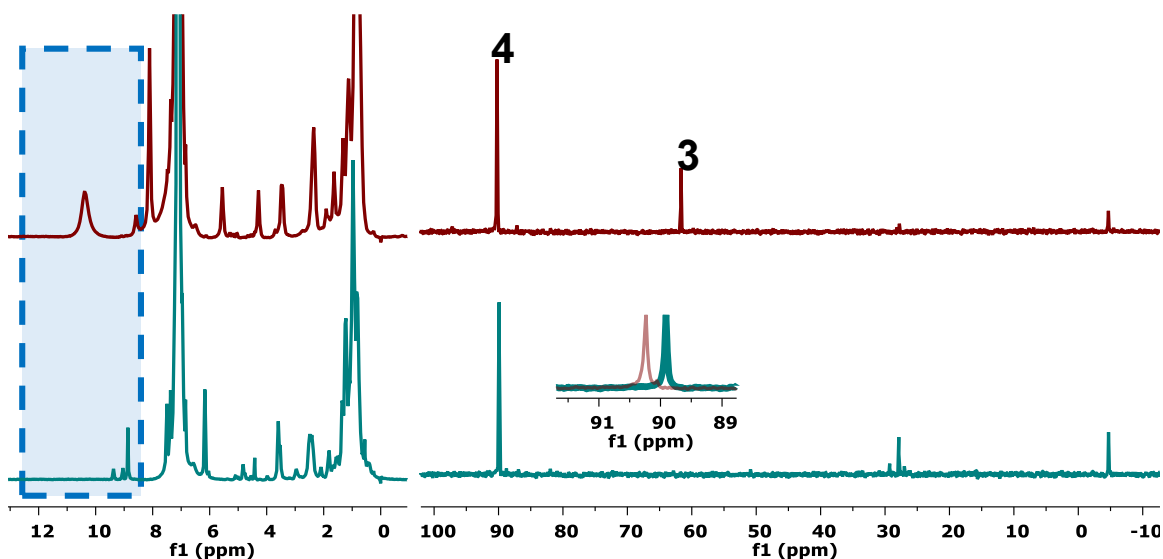


Figure 8.7. Concentration vs. Time plot for the conversion of **2** to **7** in the presence of variable  $\text{PhMeSiH}_2$  equivalents.



**Figure 8.8.** GC trace from a CO<sub>2</sub> cleavage reaction mixture demonstrating the formation of silanol, silyl ethers, and polysiloxane (black). The GC trace of a control reaction run in the absence of **2** is included for reference (red).



**Figure 8.9.** Stacked partial <sup>1</sup>H (left, 300 MHz, C<sub>6</sub>D<sub>6</sub>, 23 °C) and <sup>31</sup>P{<sup>1</sup>H} (right, 121 MHz, C<sub>6</sub>D<sub>6</sub>, 23 °C) NMR spectra monitoring addition of 5 equiv. of FA to N<sub>2</sub> adduct **1**. Top: After addition, RT; Bottom: After 3 h, 50 °C.

*Standard procedure for FA dehydrogenation catalysis:*

In the glove box, **1** (0.0155 mg, 0.000265 mmol) in dioxane (5 mL), prepared as a stock solution and kept frozen when not in use, and additive were loaded into 25 mL Schlenk flask charged with a stir bar. After sealing, the Schlenk flask was brought out of the glove

box and connected to Eudrometry setup filled with nitrogen atmosphere. The Schlenk flask was submerged in an oil bath pre-heated to 80 °C and stirred for 15 min to reach thermal equilibrium. Formic acid (0.1 mL) was added quickly via syringe.

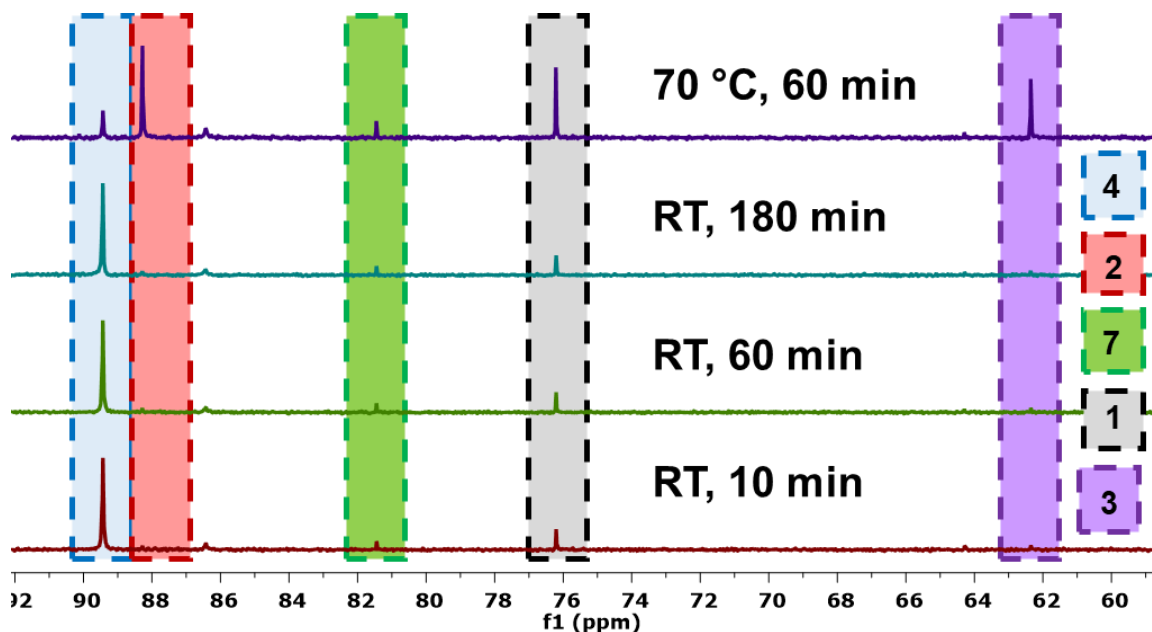


**Figure 8.10.** Stacked  $^{31}\text{P}\{^1\text{H}\}$  NMR spectra (121 MHz,  $\text{C}_6\text{D}_6$ , 23 °C) monitoring decomposition of formate hydride complex **4** at both room temperature and 70 °C.

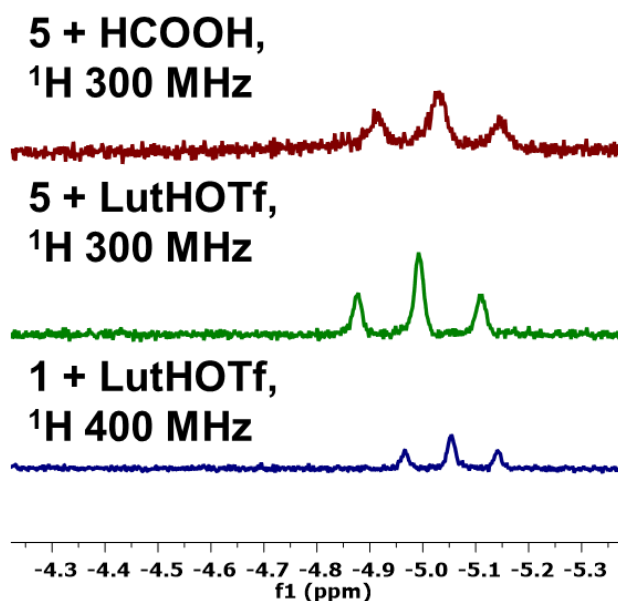


**Figure 8.11.** Stacked  $^1\text{H}$  NMR spectra (300/400 MHz,  $\text{C}_6\text{D}_6$ , 23 °C) comparing the hydride resonances observed for different independent syntheses of hydride cation **15**.

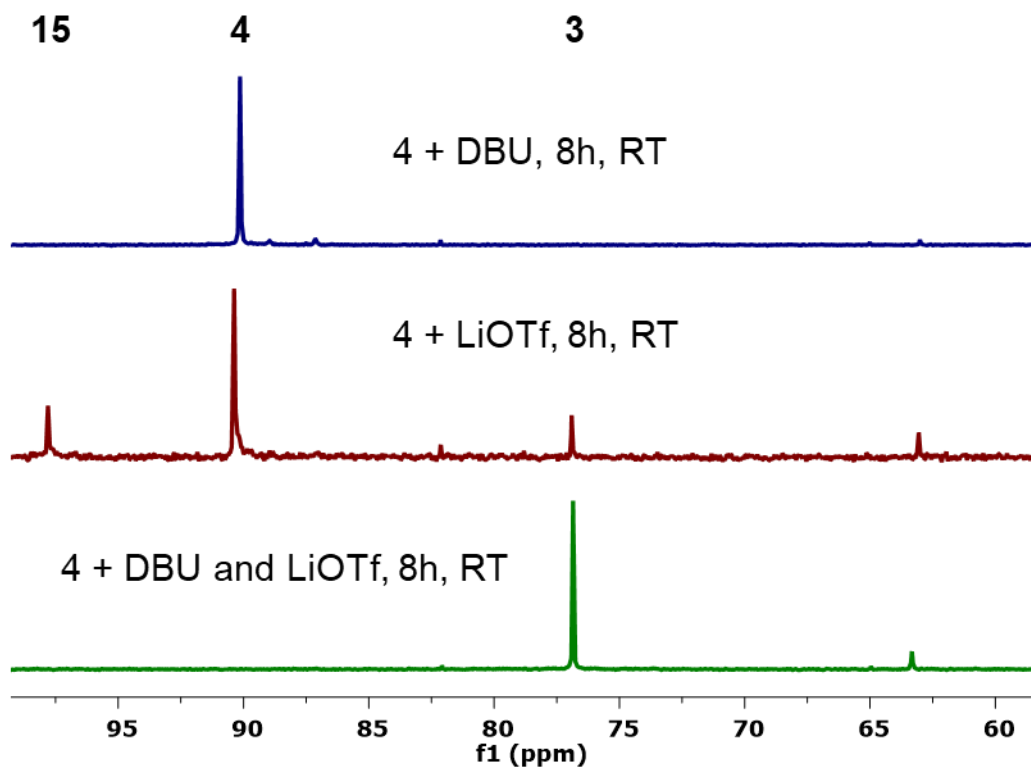


**Figure 8.12.** Stacked  $^{31}\text{P}\{^1\text{H}\}$  NMR spectra (121 MHz,  $\text{C}_6\text{D}_6$ , 23 °C) monitoring super stoichiometric addition of LA and base to formate hydride **4**.

*Standard procedure for  $\text{CO}_2$  hydrogenation catalysis:*

In the glove box, **1**, base, solvent and additive were loaded into a Schlenk tube charged with a stir bar. After sealing, the vessel was brought out of the glove box, connected to a Schlenk line, and the reaction solution was degassed via three freeze-pump-thaw cycles. The flask was backfilled with  $\text{CO}_2$  (1 atm) and then submerged in  $\text{LN}_2$ , freezing the reaction solution and condensing the  $\text{CO}_2$ .  $\text{H}_2$  (1 atm) was then admitted. After the gas addition, the reaction vessel was submerged in an oil bath pre-heated to the desired temperature. Following completion, the reaction was quenched by opening the vessel to the air. The solution was pumped down under reduced pressure, then deuterium oxide (*ca.* 3 mL) was added to solubilize any formate salt. The insolubles were removed by filtration over glass fiber. To the filtrate, DMF was added as an internal standard and the formate salt formed was quantified by  $^1\text{H}$  NMR spectroscopy.

## ***Crystallographic Information***

### *Refinement Details*

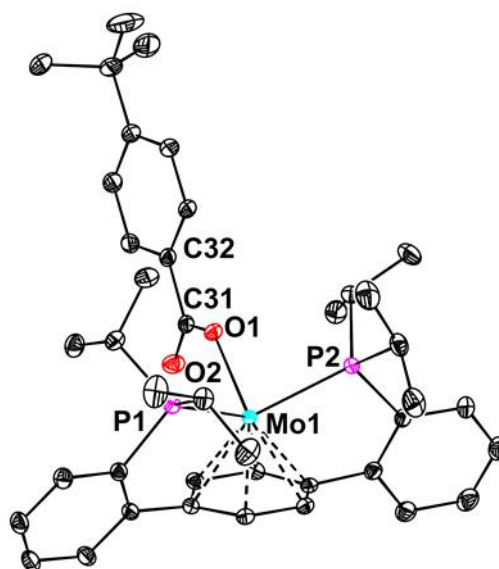
In each case, crystals were mounted on a MiTeGen loop using Paratone oil, then placed on the diffractometer under a nitrogen stream. Low temperature (100 K) X-ray data were obtained on a Bruker D8 VENTURE Kappa Duo PHOTON 100 CMOS based diffractometer (Mo  $I_{\mu}S$  HB micro-focus sealed X-ray tube,  $K_{\alpha} = 0.71073 \text{ \AA}$ ). All diffractometer manipulations, including data collection, integration, and scaling were carried out using the Bruker APEXIII software.<sup>20</sup> Absorption corrections were applied using SADABS.<sup>21</sup> Space groups were determined on the basis of systematic absences and intensity statistics and the structures were solved in the Olex 2 software interface<sup>22</sup> by intrinsic phasing using XT (incorporated into SHELXTL)<sup>23</sup> and refined by full-matrix least squares on  $F^2$ . All non-hydrogen atoms were refined using anisotropic displacement parameters. Hydrogen atoms were placed in the idealized positions and refined using a riding model, unless noted otherwise. The structures were refined (weighed least squares refinement on  $F^2$ ) to convergence. Graphical representations of structures with 50% probability thermal ellipsoids were generated using the Diamond 3 visualization software.<sup>24</sup>



**Table 8.3.** Crystal and refinement data for complexes **5**, **6<sup>PhH</sup>**, and **11**.

	<b>5</b>	<b>6<sup>PhH</sup></b>	<b>11</b>
CCDC Number <sup>25</sup>			
Empirical formula	C <sub>41</sub> H <sub>53</sub> MoO <sub>2</sub> P <sub>2</sub>	C <sub>36</sub> H <sub>44</sub> MoP <sub>2</sub> Si	C <sub>43</sub> H <sub>52</sub> MoOP <sub>2</sub> S
Formula weight	735.71	662.68	774.78
T (K)	100	100	100
<i>a</i> , Å	14.939(4)	9.8613(4)	13.2942(13)
<i>b</i> , Å	14.781(2)	19.1509(8)	12.9633(13)
<i>c</i> , Å	17.032(4)	18.1822(8)	22.396(2)
$\alpha$ , °	90	90	90
$\beta$ , °	97.488(10)	105.215(2)	99.288(5)
$\gamma$ , °	90	90	90
Volume, Å <sup>3</sup>	3728.9(14)	3313.4(2)	3809.1(7)
Z	4	4	4
Crystal system	Monoclinic	Monoclinic	Monoclinic
Space group	P2 <sub>1</sub> /n	P2 <sub>1</sub> /n	P2 <sub>1</sub> /c
<i>d</i> <sub>calc</sub> , g/cm <sup>3</sup>	1.310	1.328	1.351
$\theta$ range, °	2.750 to 38.610	2.127 to 46.189	1.552 to 42.221
$\mu$ , mm <sup>-1</sup>	0.471	0.552	0.516
Abs. Correction	Semi-empirical	Semi-empirical	Semi-empirical
GOF	1.228	1.023	1.055
<i>R</i> <sub>1</sub> , <sup>a</sup> <i>wR</i> <sub>2</sub> <sup>b</sup> [I > 2 $\sigma$ (I)]	0.0514, 0.1026	0.0523, 0.1220	0.0364, 0.0745
Radiation Type	Mo K $\alpha$	Mo K $\alpha$	Mo K $\alpha$

<sup>a</sup>  $R_1 = \sum ||F_o| - |F_c|| / \sum |F_o|$ . <sup>b</sup>  $wR_2 = [\sum [w(F_o^2 - F_c^2)^2] / \sum [w(F_o^2)^2]]^{1/2}$ .

**Figure 8.13.** Solid-state structure of **5** with thermal anisotropic displacement ellipsoids shown at the 50% probability level. Hydrogen atoms have been omitted for clarity.

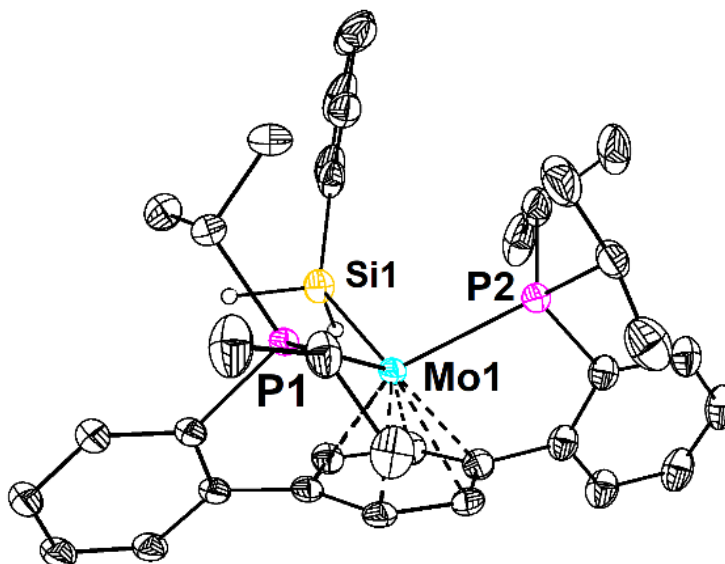


**Figure 8.14.** Solid-state structure of  $6^{\text{PhH}}$  with thermal anisotropic displacement ellipsoids shown at the 50% probability level. Hydrogen atoms, except for those bound to Si, have been omitted for clarity.

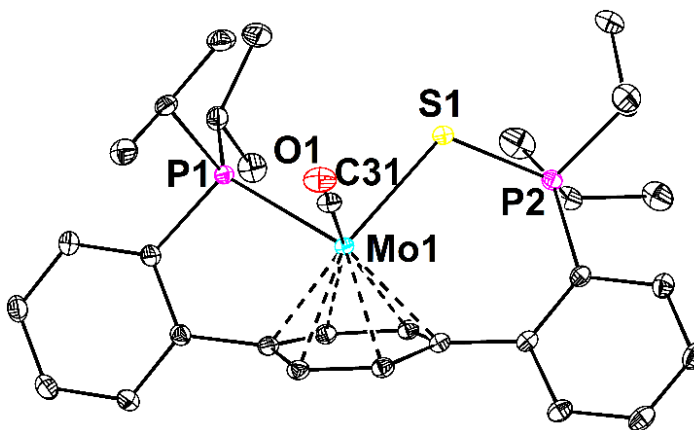


**Figure 8.15.** Solid-state structure of **11** with thermal anisotropic displacement ellipsoids shown at the 50% probability level. Hydrogen atoms have been omitted for clarity.

## REFERENCES

- (1) a) Aresta, M.; Dibenedetto, A.; Angelini, A. *Chem. Rev.* **2014**, *114*, 1709; b) Olah, G. A.; Prakash, G. K. S.; Goepfert, A. *J. Am. Chem. Soc.* **2011**, *133*, 12881; c) Liu, Q.; Wu, L.; Jackstell, R.; Beller, M. *Nat. Commun.* **2015**, *6*, 5933; d) Yang, H.; Zhang, C.; Gao, P.; Wang, H.; Li, X.; Zhong, L.; Wei, W.; Sun, Y. *Cat. Sci. Technol.* **2017**, *7*, 4580; e) Mikkelsen, M.; Jorgensen, M.; Krebs, F. C. *Energy Environ. Sci.* **2010**, *3*, 43.
- (2) a) Paparo, A.; Okuda, J. *Coord. Chem. Rev.* **2017**, *334*, 136; b) Grice, K. A. *Coord. Chem. Rev.* **2017**, *336*, 78.
- (3) Álvarez, A.; Bansode, A.; Urakawa, A.; Bavykina, A. V.; Wezendonk, T. A.; Makkee, M.; Gascon, J.; Kapteijn, F. *Chem. Rev.* **2017**, *117*, 9804.
- (4) Fernandez-Alvarez, F. J.; Aitani, A. M.; Oro, L. A. *Cat. Sci. Technol.* **2014**, *4*, 611.
- (5) a) Park, S.; Bézier, D.; Brookhart, M. *J. Am. Chem. Soc.* **2012**, *134*, 11404; b) Mitton, S. J.; Turculet, L. *Chem. Eur. J.* **2012**, *18*, 15258; c) Matsuo, T.; Kawaguchi, H. *J. Am. Chem. Soc.* **2006**, *128*, 12362; d) Berkefeld, A.; Piers, W. E.; Parvez, M.; Castro, L.; Maron, L.; Eisenstein, O. *Chem. Sci.* **2013**, *4*, 2152; e) Scheuermann, M. L.; Semproni, S. P.; Pappas, I.; Chirik, P. J. *Inorg. Chem.* **2014**, *53*, 9463.
- (6) Riduan, S. N.; Zhang, Y. *Dalton Trans.* **2010**, *39*, 3347.
- (7) Fernández-Alvarez, F. J.; Iglesias, M.; Oro, L. A.; Polo, V. *ChemCatChem* **2013**, *5*, 3481.
- (8) Callejas, J. F.; Read, C. G.; Roske, C. W.; Lewis, N. S.; Schaak, R. E. *Chem. Mater.* **2016**, *28*, 6017.
- (9) Sordakis, K.; Tang, C.; Vogt, L. K.; Junge, H.; Dyson, P. J.; Beller, M.; Laurenczy, G. *Chem. Rev.* **2018**, *118*, 372.
- (10) a) Boddien, A.; Loges, B.; Junge, H.; Beller, M. *ChemSusChem* **2008**, *1*, 751; b) Celaje, J. J. A.; Lu, Z.; Kedzie, E. A.; Terrile, N. J.; Lo, J. N.; Williams, T. J. *Nat. Commun.* **2016**, *7*, 11308; c) Bielinski, E. A.; Lagaditis, P. O.; Zhang, Y.; Mercado, B. Q.; Würtele, C.; Bernskoetter, W. H.; Hazari, N.; Schneider, S. J. *J. Am. Chem. Soc.* **2014**, *136*, 10234.
- (11) a) Boddien, A.; Mellmann, D.; Gärtner, F.; Jackstell, R.; Junge, H.; Dyson, P. J.; Laurenczy, G.; Ludwig, R.; Beller, M. *Science* **2011**, *333*, 1733; b) Zell, T.; Butschke, B.; Ben-David, Y.; Milstein, D. *Chem. Eur. J.* **2013**, *19*, 8068; c) Myers, T. W.; Berben, L. A. *Chem. Sci.* **2014**, *5*, 2771; d) Neary, M. C.; Parkin, G. *Chem. Sci.* **2015**, *6*, 1859.
- (12) a) Bernskoetter, W. H.; Hazari, N. *Acc. Chem. Res.* **2017**, *50*, 1049; b) Tanaka, R.; Yamashita, M.; Nozaki, K. *J. Am. Chem. Soc.* **2009**, *131*, 14168; c) Hull, J. F.; Himeda, Y.; Wang, W.-H.; Hashiguchi, B.; Periana, R.; Szalda, D. J.; Muckerman, J. T.; Fujita, E. *Nat. Chem.* **2012**, *4*, 383.
- (13) Zuzek, A. A.; Parkin, G. *J. Am. Chem. Soc.* **2014**, *136*, 8177.
- (14) Alvarez, R.; Atwood, J. L.; Carmona, E.; Perez, P. J.; Poveda, M. L.; Rogers, R. D. *Inorg. Chem.* **1991**, *30*, 1493.
- (15) Anderson, J. S.; Iluc, V. M.; Hillhouse, G. L. *Inorg. Chem.* **2010**, *49*, 10203.
- (16) a) Bryan, J. C.; Mayer, J. M. *J. Am. Chem. Soc.* **1990**, *112*, 2298; b) Bryan, J. C.; Geib, S. J.; Rheingold, A. L.; Mayer, J. M. *J. Am. Chem. Soc.* **1987**, *109*, 2826.
- (17) Pangborn, A. B.; Giardello, M. A.; Grubbs, R. H.; Rosen, R. K.; Timmers, F. J. *Organometallics* **1996**, *15*, 1518.
- (18) Buss, J. A.; Edouard, G. A.; Cheng, C.; Shi, J.; Agapie, T. *J. Am. Chem. Soc.* **2014**, *136*, 11272.
- (19) Fulmer, G. R.; Miller, A. J. M.; Sherden, N. H.; Gottlieb, H. E.; Nudelman, A.; Stoltz, B. M.; Bercaw, J. E.; Goldberg, K. I. *Organometallics* **2010**, *29*, 2176.

- (20) APEX3, Version 1 User Manual, M86-EXX229, Bruker Analytical X-ray Systems, Madison, WI, May 2016.
- (21) Sheldrick, G.M. "SADABS (version 2008/1): Program for Absorption Correction for Data from Area Detector Frames", University of Göttingen, 2008.
- (22) Dolomanov, O. V.; Bourhis, L. J.; Gildea, R. J.; Howard, J. A. K.; Puschmann, H. *J. Appl. Crystallogr.* **2009**, *42*, 339.
- (23) Sheldrick, G.M. *Acta Cryst.* **2008**, *A64*, 112.
- (24) Brandenburg, K. (1999). DIAMOND. Crystal Impact GbR, Bonn, Germany.
- (25) Crystallographic data have been deposited at the CCDC, 12 Union Road, Cambridge CB2 1EZ, UK and copies can be obtained on request, free of charge, by quoting the publication citation and the respective deposition numbers.



## Appendix A

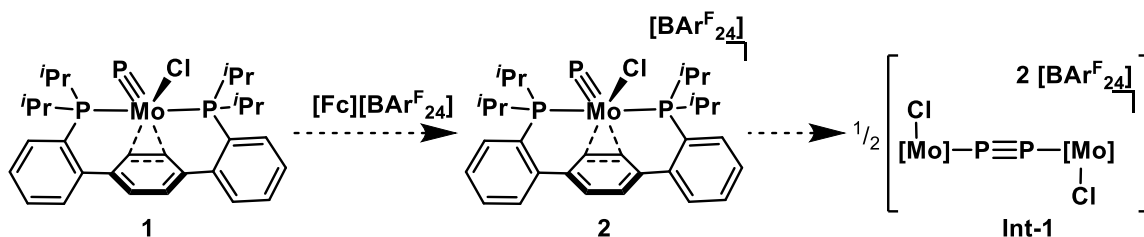
### Open-Shell Mo(V) Nitrides and Alkylidynes: Does Radical Character Dictate Coupling Chemistry?

**ABSTRACT**

Reported in this brief abstract is the synthesis of a series of open-shell  $d^1$  Mo(V) complexes bearing Mo $\equiv$ E triple bonds. CW and pulse EPR techniques, in combination with isotopic enrichment, has facilitated a detailed spectroscopic study of these complexes. Building off of precedent reported for the phosphide congener (Chapter 6), the ability of these radical complexes to undergo E–E bond formation is interrogated. Computational methods compliment spectroscopy in the determination of spin leakage in these complexes, as a function of the identity of the multiply bonded element, E.

## GENERAL INTRODUCTION

Chapter 6 of this dissertation reports the first terminal transition metal phosphides with  $d$ -electrons. The Mo(V) complex proved unstable in solution at temperatures about  $-10\text{ }^{\circ}\text{C}$ . Employing a terminal phosphide as a chemical trap for diphosphorous ( $\text{P}_2$ ) showed evidence for a reactivity pathway that involved P–P bond formation (Scheme A.1). With synthetic access to isoelectronic Mo nitride (Chapter 5), alkylidyne (Chapter 3), and carbide complexes (Chapters 3 and 4), we sought to develop a structure/function relationship, correlating the identity of the multiply-bonded element, the degree of spin delocalization, and the ability to couple.



**Scheme A.1.** Terminal Mo(V) phosphide coupling.

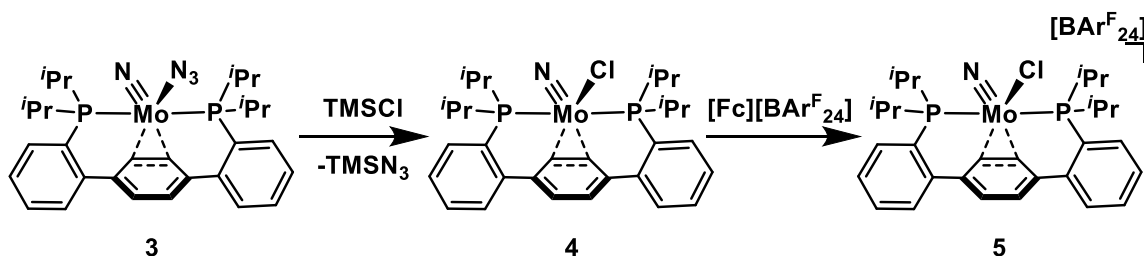
Oxidatively induced bimetallic coupling is invoked in both ammonia<sup>1</sup> and water<sup>2</sup> oxidation chemistries. Within this context, understanding the factors that govern these reactions would insight new transformations relevant to energy conversion. A recent report from the Storr group has shown that the spin leakage onto a terminal Mn nitrido dictates its ability to undergo N–N coupling.<sup>3</sup> In these systems, the spin delocalization was controlled by ligand electronics. To our knowledge, no systematic studies have been conducted to examine radical character as a function of the multiply bonded element, leaving the metal center and ancillary ligand unperturbed. A significant challenge in undertaking such an investigation is finding a suitable system capable of supporting open-shell complexes with different multiply bonded ligands. Open-shell nitrides are known,<sup>3-4</sup> alkylidyne are rare,<sup>5</sup> and prior to our studies, phosphides<sup>6</sup> and carbides had yet to be reported. Herein we scrutinize the oxidative activation of a series of Mo(IV) complexes, probing their electronic structures and the effects they have on E–E



bond formation.

## RESULTS AND DISCUSSION

In an effort to prepare an isoelectronic series of  $\text{Mo}\equiv\text{E}$  complexes that vary only in the identity of E, a synthetic route to Mo nitride chloride **4** was developed (Scheme A.2.). Addition of an excess of TMSCl to a benzene solution of **3** resulted in the desired ligand substitution reaction as evidenced by a subtle shift in the  $^{31}\text{P}\{^1\text{H}\}$  NMR spectrum (35.01 to 33.29 ppm). The  $^1\text{H}$  NMR spectrum of complex **1** is qualitatively similar to that of the azide precursor, except the resonances are slightly shifted. Most notably, one of the isopropyl methine resonances shifts 0.8 ppm upfield, resonating at 3.79 ppm.



**Scheme A.2.** Synthesis of Mo(IV) and Mo(V) nitride chloride complexes.

Analogously to the phosphide congener, **1**, complex **4** can be chemically oxidized by  $[\text{Fc}][\text{BARF}_{24}]$  ( $\text{Fc} = \text{Cp}_2\text{Fe}$ ). Addition of one equiv. of oxidant to a thawing solution of **1** resulted in an immediate color change to deep purple, a hue that persisted upon warming to room temperature. Crystallization confirmed the formation of the desired Mo(V) nitride cation (Figure A.1., right). Though we have elected to forgo a diffraction study of **4**, the similarity of the solution spectroscopies suggests crystallized **3** can act as a suitable surrogate for a metrical comparison. Upon oxidation, the Mo–N distance contracts (1.663(4) Å); assuming a similar electronic structure for **5** and its phosphide congener, **2**, this effect is likely a manifestation of the smaller ionic radius of Mo(V) as the SOMO is strictly non-bonding with respect to the nitride. A significant difference is observed in the Mo–C bonds (ave. 2.461(4) Å) of the  $\eta^2$  metal-arene interaction and the C2–C3 bond (1.395(6) Å). Again consistent with the molecular orbital picture developed for **2**, these changes are attributed to removing an electron from a Mo d-orbital that backbonds into the C2–C3  $\pi^*$  orbital.

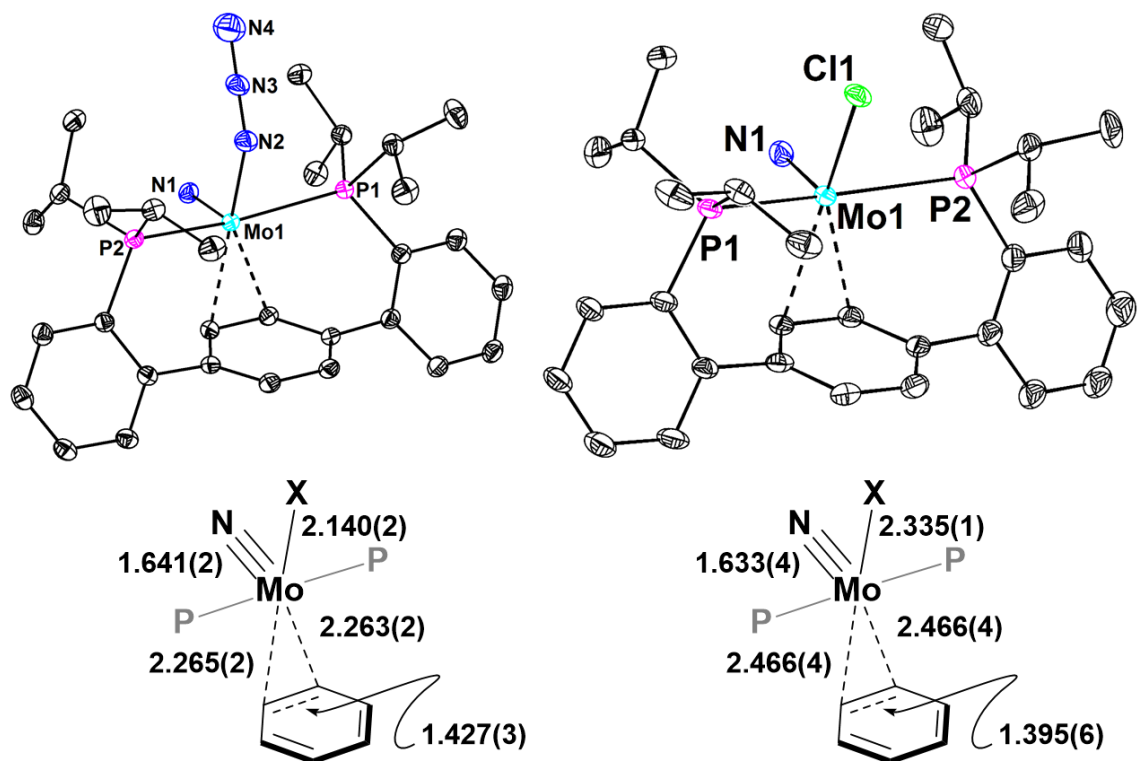


**Figure A.1.** Solid state structures of nitrides **1** (left) and **3** (right). Thermal anisotropic displacement ellipsoids are shown at the 50% probability level and hydrogen atoms have been omitted for clarity. Pertinent metrical parameters [ $\text{\AA}$ ] are shown below each structure.

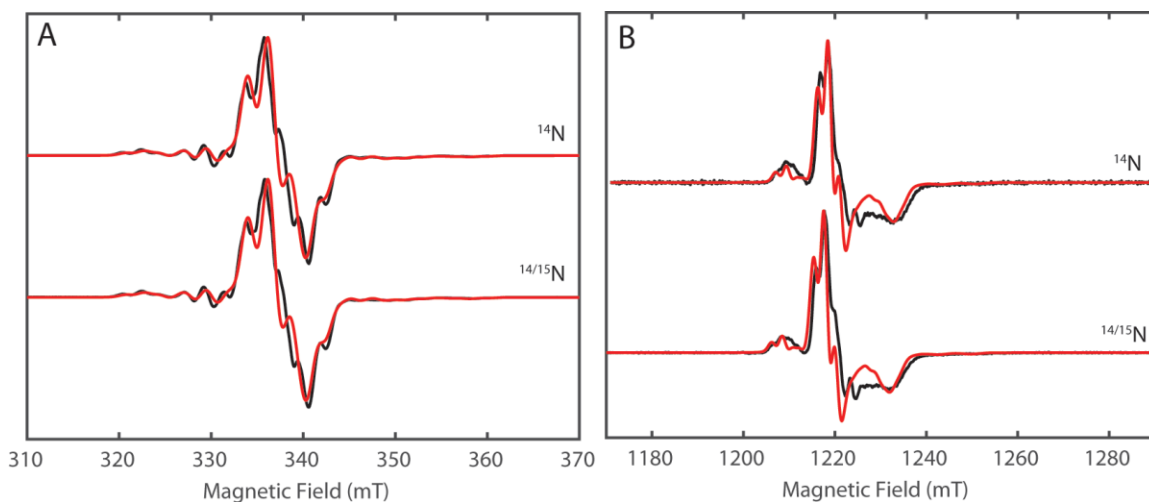


**Figure A.2.** A) X-band CW-EPR spectra of nitride **4** generated with natural abundance N (top trace) and 50%  $^{15}\text{N}$  (bottom trace) represented in black with simulations using parameters in Table A.1 displayed in red. B) Pseudomodulated Q-band ESE-EPR spectra of nitride **4** generated with natural abundance N (top trace) and 50%  $^{15}\text{N}$  (bottom trace) represented in black with simulations using parameters in Table A.1.

The X-band CW spectrum of a frozen 2Me-THF glass of **4** displays a complex, primarily axial signal (Figure A.2.). To aid in parsing the multifaceted hyperfine coupling to the Mo, Cl, N, and proximal arene H nuclei, a series of pulse EPR experiments were conducted. To further aid with hyperfine coupling assignments, a 50%  $^{15}\text{N}$  enriched sample was prepared from **3- $^{15}\text{N}$** .

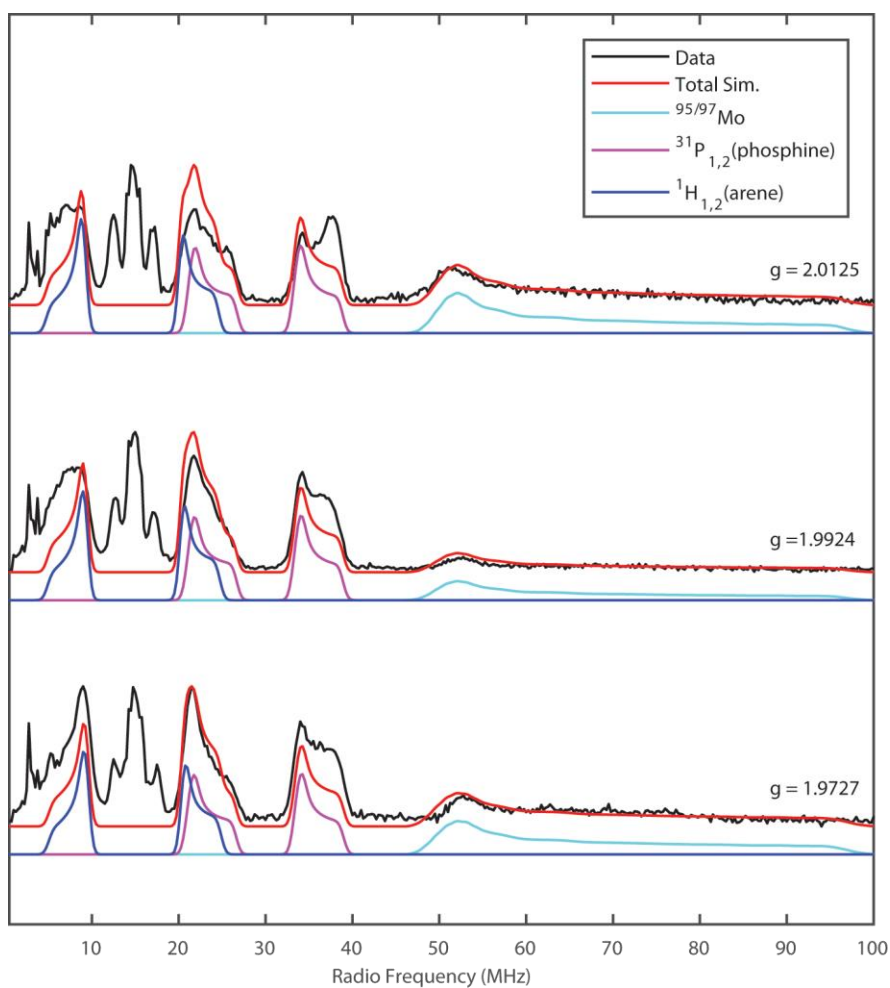


**Figure A.3.** X-band Davies ENDOR of nitride **4** generated with natural abundance N with simulations of using parameters in Table A.1.

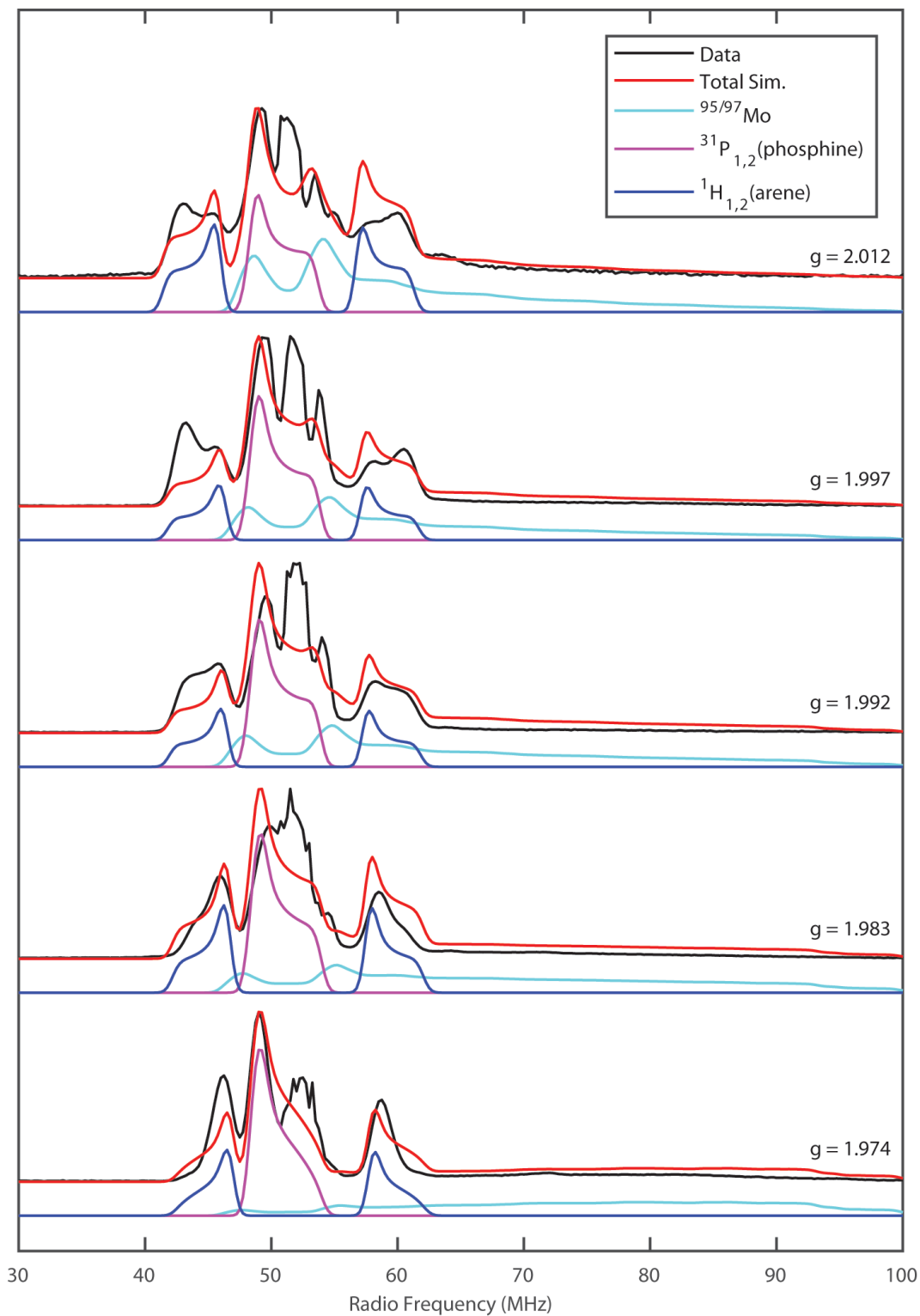


**Figure A.4.** Q-band Davies ENDOR of nitride **4** generated with natural abundance N with simulations of using parameters in Table A.1.

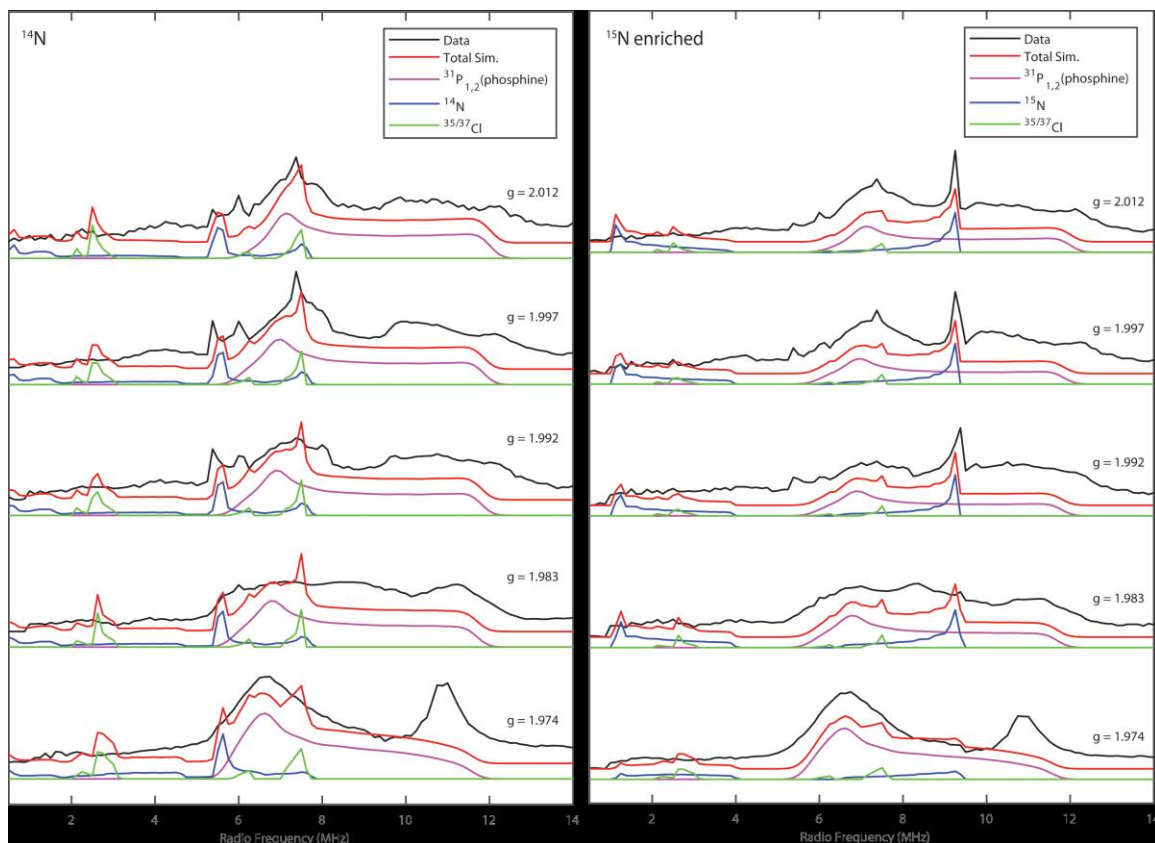


**Figure A.5.** Field-dependent Q-band Davies ENDOR of nitride **4** generated with natural abundance N (left panel) and 50%  $^{15}\text{N}$  (right panel) with simulations using parameters in Table A.1.

**Table A.1.** EPR fit parameters for nitrides **4/4- $^{15}\text{N}$** .

	$g$	[1.997 1.997 1.974]
$A$ (MHz)	$^{95,97}\text{Mo}$ ( $I = 5/2$ , 24%)	[100 100 194]
	$^{31}\text{P}$ ( $I = 1/2$ , 100%)	[56 66 54]
	$^1\text{H}$ ( $I = 1/2$ , 100%)	[20 11 11]
	$^{35,37}\text{Cl}$ ( $I = 3/2$ , 100%)	[5 5 4]
	$^{15}\text{N}$ ( $I = 1/2$ , 100%)	[8.2 8.2 2.5]
	$^{14}\text{N}$ ( $I = 1$ , 100%) <sup>‡</sup>	[5.85 5.85 1.78]

<sup>‡</sup> $^{14}\text{N}$   $e^2Qq/b = 2.8$  MHz;  $\eta = 0.1$

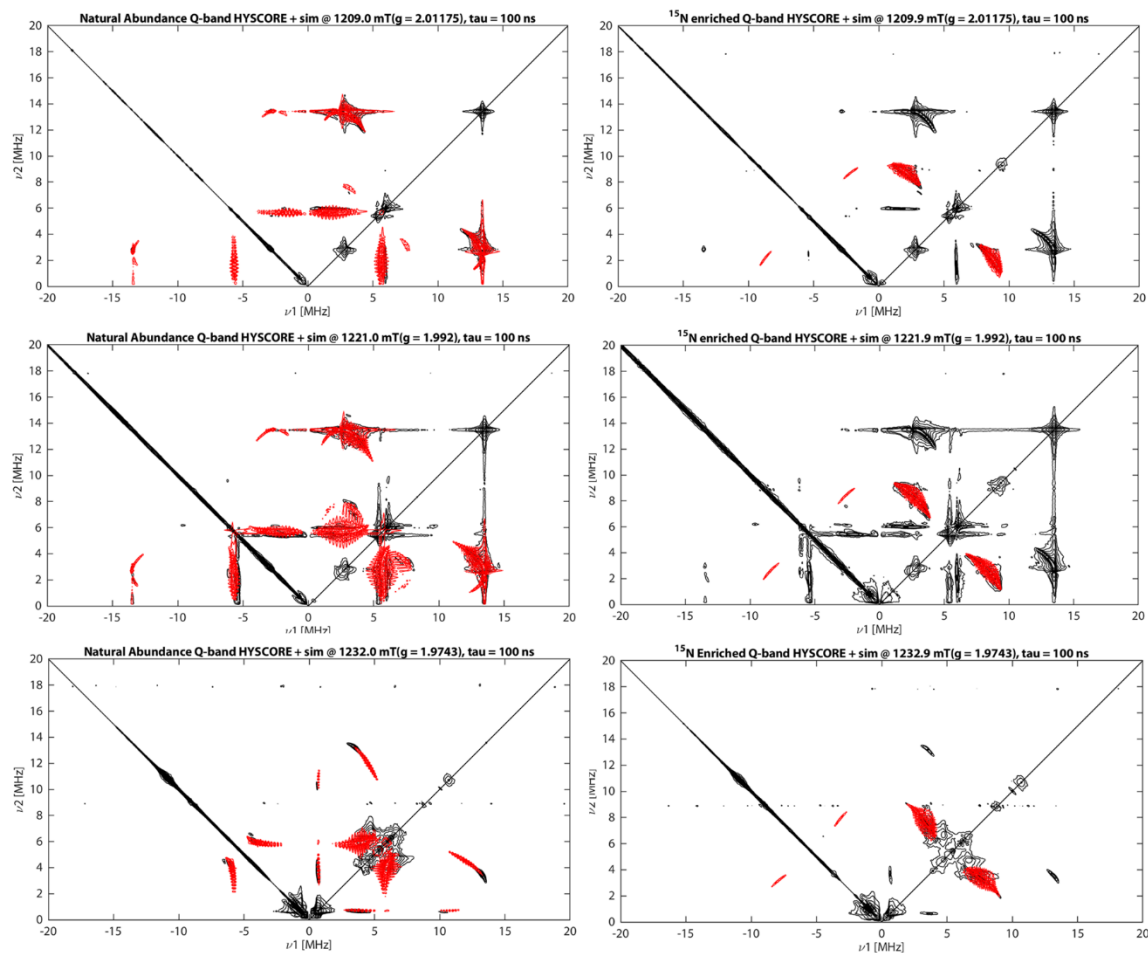
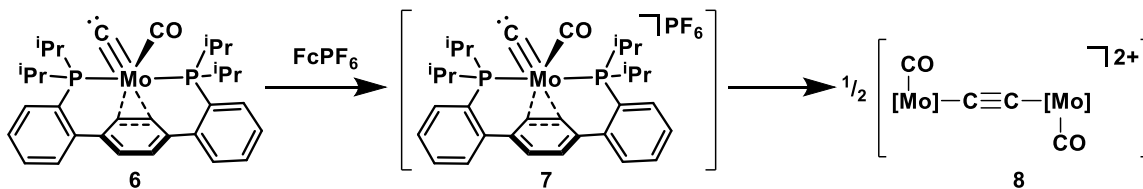


**Figure A.6.** Field-dependent Q-band HYSCORE of nitride **4** generated with natural abundance N (left panel) and 50%  $^{15}\text{N}$  (right panel) with simulations using parameters in Table A.1. Experimental data are displayed as black contour maps, with simulations of  $^{14}\text{N}$  and  $^{15}\text{N}$  displayed in red.

Compiling the data, satisfactory fit parameters were obtained, as shown in Table A.1. Using a hyperfine decomposition process like that applied to terminal phosphide **2**, we see that the majority of anisotropic hyperfine is purely from through space dipolar interaction ( $\mathbf{T}_{nloc}^Z = [1.4 \ 1.4 \ -2.8]$  MHz) due to very short Mo–N bond distance (1.633 Å). This leaves  $\mathbf{T}_{loc} = [-0.47 \ -0.47 \ 0.49]$  MHz which corresponds to  $\rho_{p_z} \approx 0.006 e^-$ . Contrasting the phosphide case, in which the EPR data suggested between 0.10 and 0.15  $e^-$  delocalized onto the terminal P, the nitride case shows significantly diminished spin.

In line with the attenuated spin leakage to the nitride ligand in **4**, heating solutions of **4** to 100 °C showed no evidence of formation of a Mo(II) dication, the expected product of N–

N coupling. Further support for the inability of **4** to couple comes from computation, which predicts both a lessened percentage of unpaired spin on the nitride and does not find an energetically favorable pathway to N–N bond formation.



**Scheme A.3.** *In situ* oxidation of terminal carbide **6**.

Another congener of phosphide **1** is terminal carbide **6**. The instability of **6** necessitates *in situ* synthesis (Chapter 3), which further complicates attempts to prepare and characterize a reactive open-shell complex. As a starting point, the chemical oxidation of **6**-<sup>13</sup>C was attempted (Scheme A.X.). Low temperature (-78 °C) addition of FcPF<sub>6</sub> resulted in conversion to a new major species, as evidenced by disappearance of the carbidic resonance and growth of two signals at 268.86 and 239.45 ppm (Figure A.7.). These shifts are in the range of ethynediyl<sup>7</sup> and CO carbons, respectively. Warming to room temperature provides two major species, evinced by both <sup>13</sup>C{<sup>1</sup>H} and <sup>31</sup>P{<sup>1</sup>H} NMR, which may be isomers of a C–C coupled species, **8**, but further characterization this product is needed. Again, computation agrees with the experimental data, suggesting favorable C–C bond formation from **7**.

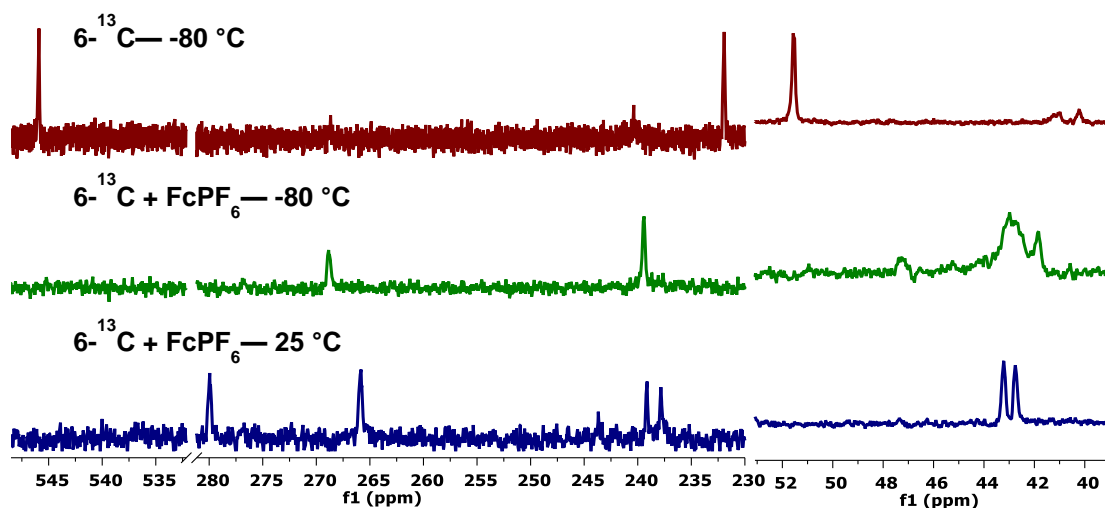


**Figure A.7.** Partial <sup>13</sup>C{<sup>1</sup>H} (126 MHz, THF) and <sup>31</sup>P{<sup>1</sup>H} (202 MHz, THF) NMR spectra following the oxidation of terminal carbide **6**-<sup>13</sup>C.



As  $6\text{-}^{13}\text{C}$  promptly reacted at  $-78^\circ\text{C}$  to form a putative C–C coupled product, we anticipated that an open-shell intermediate would be exceedingly fleeting. To provide a spectroscopic benchmark, should such a species be obtained, we synthesized alkylidyne analog **10**, which, bearing a  $\text{Me}_3\text{Si}$  group on the alkylidyne, should be unable to couple. Addition of  $\text{FcBAR}^{\text{F}}_{24}$  to a 2Me-THF solution of Mo(IV) complex **9** led to a deep red solution that was silent by  $^{31}\text{P}\{^1\text{H}\}$  NMR (Figure A.8.). Crystallization of this species confirmed successful preparation of carbyne cation **10** (Figure A.8., right). Unfortunately, positional disorder of the CO and Cl ligands makes detailed structural analysis precarious, but the Mo–CSiMe<sub>3</sub> bond (1.762 Å) remains unchanged upon oxidation. Dissimilar to **2** and **5**, **10** shows no significant metal-arene interaction in the solid-state; the five-coordinate *pseudo*-square pyramidal geometry is maintained.

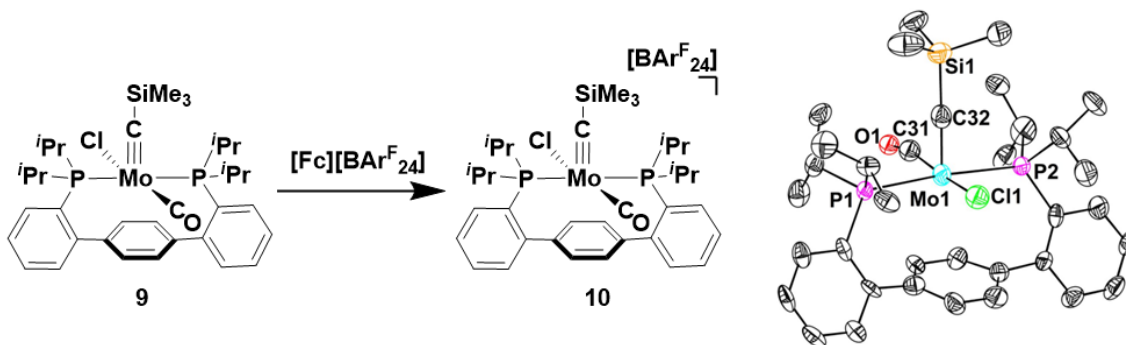


**Figure A.8.** Synthesis and solid-state structure of alkylidyne cation **10**. Thermal anisotropic displacement ellipsoids are shown at the 50% probability level and hydrogen atoms and counterions are omitted for clarity. The CO (C31 and O1) and Cl (Cl1) ligands are positionally disordered and cannot be modeled satisfactorily without the use of restraints. The present rendering refined these atoms isotropically, without restraints, with only the major population shown.

With access to both **10** and  $10\text{-}^{13}\text{C}$ , we undertook detailed EPR studies of these cations. CW, Davies ENDOR, and HYSOCORE data, like that presented for **3**, has been collected. Satisfactory fitting is underway.

## CONCLUSION

Oxidation of well-characterized  $d^2$   $\text{Mo}\equiv\text{E}$  complexes afford access to the corresponding  $\text{Mo(V)}$  cations, in the case of  $\text{E} = \text{P}, \text{N},$  and  $\text{CSiMe}_3$ . Computation and EPR studies demonstrate that the degree of radical character at E dictates coupling chemistry. Attempts to access the carbide congener are ongoing, but preliminary experimentation and computation suggest that it is capable of facile C–C bond formation.

## EXPERIMENTAL SECTION

### *Synthesis of 4*

A 20 mL scintillation vial was charged with **3** (750 mg, 1.23 mmol) and a stir bar. C<sub>6</sub>H<sub>6</sub> (6 mL) was added and stirring initiated, providing a homogenous burgundy solution. TMSCl (670 mg, 6.17 mmol) was added dropwise, causing a slight lightening of the solution. The vial was sealed and left to stir for 8 h. At this time, the vial was placed in a -35 °C freeze and the contents frozen solid. Following lyophilization, the resulting red powder was suspended in cold (-35 °C) hexanes (4 mL) and filtered through a medium porosity fritted funnel. The solids were dried *in vacuo*, providing **4** as pale red free-flowing solids (611 mg, 1.01 mmol, 82%). Samples of **4** synthesized in this manner showed a slight free-ligand impurity (<3%), but were used without further purification. <sup>1</sup>H NMR (400 MHz, C<sub>6</sub>D<sub>6</sub>, 23 °C) δ: 7.31 (dd, *J* = 7.46, 1.76 Hz, 2H, aryl-*H*), 7.26 (br d, *J* = 7.23 Hz, 2H, aryl-*H*), 7.05-7.08 (m, 4H, aryl-*H*), 6.01 (s, 2H, central arene-*H*), 4.44 (t, *J* = 2.35 Hz, 2H, central arene-*H*), 3.74-3.85 (m, 2H, CH(CH<sub>3</sub>)<sub>2</sub>), 2.51-2.61 (m, 2H, CH(CH<sub>3</sub>)<sub>2</sub>), 1.87-1.93 (m, 6H, CH(CH<sub>3</sub>)<sub>2</sub>), 1.41-1.47 (m, 6H, CH(CH<sub>3</sub>)<sub>2</sub>), 0.71-0.75 (m, 6H, CH(CH<sub>3</sub>)<sub>2</sub>), 0.30-0.36 (m, 6H, CH(CH<sub>3</sub>)<sub>2</sub>). <sup>31</sup>P{<sup>1</sup>H} NMR (162 MHz, C<sub>6</sub>D<sub>6</sub>, 23 °C) δ: 33.29 (s).

### *Synthesis of 5*

A 20 mL scintillation vial was charged with a 2Me-THF (8 mL) solution of **4** (80 mg, 0.132 mmol) and a stir bar. The vial was placed in an LN<sub>2</sub> chilled cold well and the contents frozen solid. Immediately upon thawing, a 2Me-THF (4 mL) solution of FcBAR<sub>24</sub><sup>F</sup> (140 mg, 0.132 mmol) was added dropwise, with stirring. Upon addition of the oxidant, the deep red color of **4** darkened to a blue/purple. After warming to room temperature, volatiles were removed *in vacuo*, providing a dark purple residue. Extraction with hexanes (3 x 10 mL) removed the Fc byproduct. Sequential trituration of the remaining solids with Et<sub>2</sub>O (4 mL) and pentane (4 mL) provided **5** as a dark blue powder (159 mg, 0.108 mmol, 82%). X-ray quality single crystals of **5** were grown via vapor diffusion of pentane into a saturated Et<sub>2</sub>O solution at -35 °C.

*In Situ Oxidation of 6-<sup>13</sup>C*

A sample of **6-<sup>13</sup>C** (0.028 mmol) in THF solution (0.4 mL) in a J. Young style NMR tube was prepared as reported previously (Chapter 3). The tube was cooled to -78 °C via submersion in a dry ice/acetone slush bath. A solution of FcPF<sub>6</sub> (10 mg, 0.031 mmol) in THF (0.3 mL) was added with a heavy argon counterflow. The tube was sealed and transferred to an NMR probe, pre-chilled to -80 °C. <sup>13</sup>C{<sup>1</sup>H} and <sup>31</sup>P{<sup>1</sup>H} NMR spectra were recorded. The sample was warmed, gradually, in the probe, collecting spectra at 10 °C intervals. Upon warming to 25 °C, a final set of spectra were obtained.

*Synthesis of 10*

A 20 mL scintillation vial was charged with a 2Me-THF (8 mL) solution of **9** (200 mg, 0.282 mmol) and a stir bar. The vial was placed in an LN<sub>2</sub> chilled cold well and the contents frozen solid. Immediately upon thawing, a 2Me-THF (4 mL) solution of FcBAR<sup>F</sup><sub>24</sub> (297 mg, 0.282 mmol) was added dropwise, with stirring. Upon addition of the oxidant, the light red color of **4** darkened. After warming to room temperature, volatiles were removed *in vacuo*, providing a maroon residue. Extraction with hexanes (3 x 10 mL) removed the Fc byproduct. Sequential trituration of the remaining solids with Et<sub>2</sub>O (4 mL) and pentane (4 mL) provided **10** as a dark red powder (394 mg, 0.251 mmol, 89%). X-ray quality single crystals of **10** were grown via vapor diffusion of pentane into a saturated Et<sub>2</sub>O solution at -35 °C.

## REFERENCES

- (1) a) Ware, D. C.; Taube, H. *Inorg. Chem.* **1991**, *30*, 4605; b) Seymore, S. B.; Brown, S. N. *Inorg. Chem.* **2002**, *41*, 462.
- (2) Betley, T. A.; Wu, Q.; Van Voorhis, T.; Nocera, D. G. *Inorg. Chem.* **2008**, *47*, 1849.
- (3) Clarke, R. M.; Storr, T. J. *Am. Chem. Soc.* **2016**, *138*, 15299.
- (4) a) Gloaguen, Y.; Rebreyend, C.; Lutz, M.; Kumar, P.; Huber, M.; van der Vlugt, J. I.; Schneider, S.; de Bruin, B. *Angew. Chem. Int. Ed.* **2014**, *53*, 6814; b) Scheibel, M. G.; Wu, Y.; Stückl, A. C.; Krause, L.; Carl, E.; Stalke, D.; de Bruin, B.; Schneider, S. *J. Am. Chem. Soc.* **2013**, *135*, 17719; c) Scheibel, M. G.; Askevold, B.; Heinemann, F. W.; Reijerse, E. J.; de Bruin, B.; Schneider, S. *Nature Chemistry* **2012**, *4*, 552; d) Margulieux, G. W.; Bezdek, M. J.; Turner, Z. R.; Chirik, P. J. *J. Am. Chem. Soc.* **2017**, *139*, 6110.
- (5) a) van der Eide, E. F.; Piers, W. E.; Parvez, M.; McDonald, R. *Inorg. Chem.* **2007**, *46*, 14; b) Manna, J.; Gilbert, T. M.; Dallinger, R. F.; Geib, S. J.; Hopkins, M. D. *J. Am. Chem. Soc.* **1992**, *114*, 5870; c) Carter, J. D.; Kingsbury, K. B.; Wilde, A.; Schoch, T. K.; Leep, C. J.; Pham, E. K.; McElwee-White, L. *J. Am. Chem. Soc.* **1991**, *113*, 2947; d) Felixberger, J. K.; Kiprof, P.; Herdtweck, E.; Herrmann, W. A.; Jakobi, R.; Gütlich, P. *Angew. Chem. Int. Ed.* **1989**, *28*, 334.
- (6) Buss, J. A.; Oyala, P. H.; Agapie, T. *Angew. Chem. Int. Ed.* **2017**, *56*, 14502.
- (7) Colebatch, A. L.; Cordiner, R. L.; Hill, A. F.; Nguyen, K. T. H. D.; Shang, R.; Willis, A. C. *Organometallics* **2009**, *28*, 4394.



## Appendix B

### Terphenyl Diphosphine Molybdenum Complexes Bearing a Central Phenol: Towards Bifunctional Catalysis

**ABSTRACT**

Thus far, this dissertation has focused on Mo coordination complexes of a single *para*-terphenyl diphosphine ligand (**P2**). The rich chemistry exhibited by this system often involves the transfer of hydrogen atoms (*cf.* Chapter 2, Chapter 7, Chapter 8), and during its development, the incorporation of acid/base non-innocent motifs in the secondary coordination sphere of teraryl ligands was an area of intense research in the group. In this vein, Mo complexes of a teraryl diphosphine ligand bearing a central phenol, **P2<sup>OH</sup>**, were explored. Precursory results reporting two distinct metalation routes for this proligand and preliminary demonstrating both acid/base non-innocence and potential redox isomerization are reported.



## GENERAL INTRODUCTION

The development of so-called “metal-ligand bifunctional” catalysts is a topical area of both fundamental chemical research<sup>1</sup> and industrial application.<sup>2</sup> In a broad sense, bifunctional catalysts poise reactive functional groups in close proximity to a metal center, engendering new reactivity and/or selectivity in desirable transformations.<sup>3</sup> From early examples with pendant acidic protons (A<sup>4</sup> & B,<sup>5</sup> Figure B.1.), to more nuanced cooperativity (C,<sup>6</sup> Figure B.1.), the design, study, and implementation of these catalysts is of inherent interest.

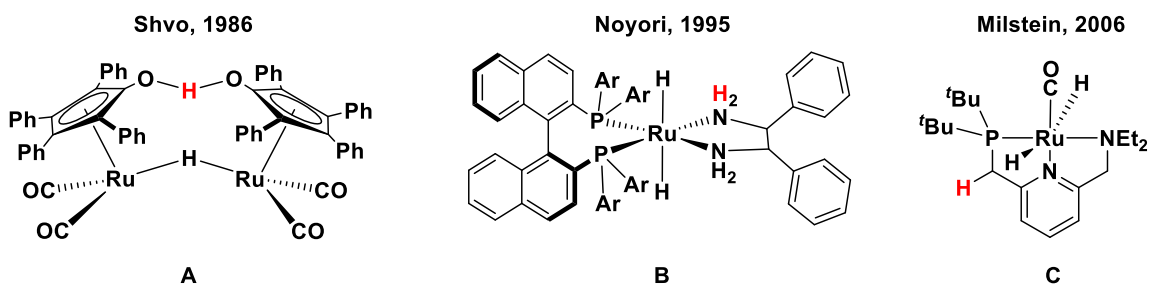
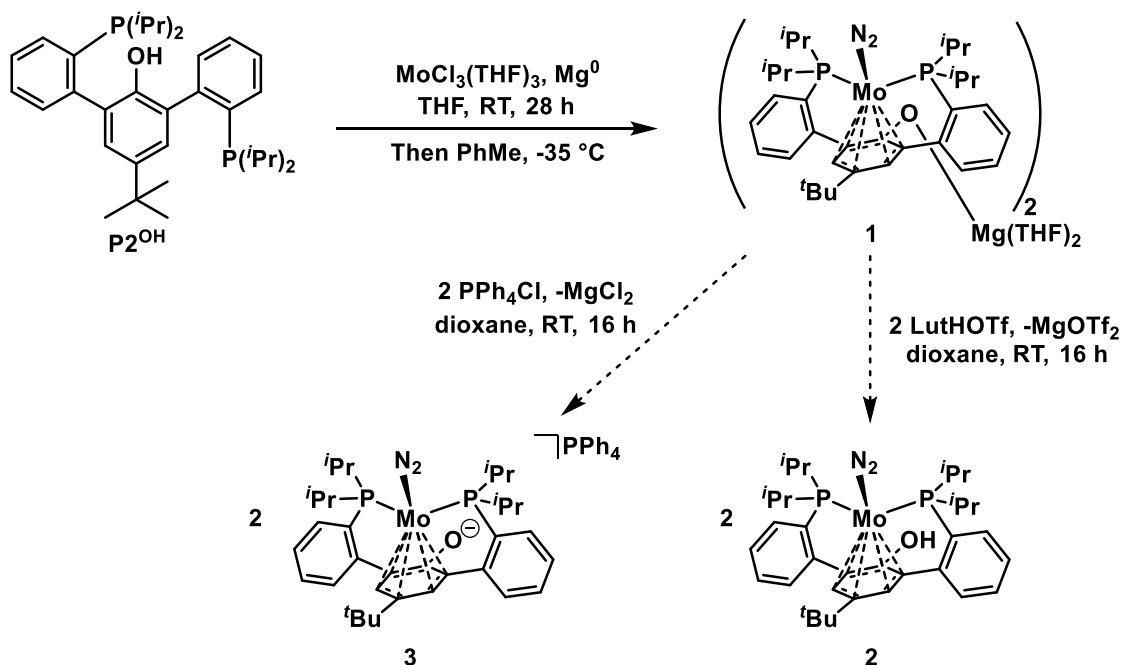


**Figure B.1.** Literature examples of metal-ligand bifunctional catalysts with the non-innocent H-atoms highlighted in red.

In the course of pursuing the chemistry outlined in the body of this dissertation, inspiring literature examples of bifunctional catalysts capable of mediating the types of transformations explored—AB dehydrogenation,<sup>7</sup> CO reduction,<sup>8</sup> CO<sub>2</sub> hydrogenation/FA dehydrogenation<sup>9</sup>—were identified. These, reports, in addition to concurrent work in the group studying diphosphine ligands decorated with catechol/quinone,<sup>10</sup> hydroquinone/*para*-quinone,<sup>11</sup> and bis(arylamino)phenol moieties,<sup>12</sup> motivated work towards Mo complexes supported by proligand **P2<sup>OH</sup>**. With a proximal phenol/phenoxide, **P2<sup>OH</sup>** Mo compounds would provide insight into the role of pendant acid in the chemistries developed for the parent **P2** ligand.

## RESULTS AND DISCUSSION

Proligand **P2<sup>OH</sup>** can be prepared in five steps from commercial materials, following a preparation previously reported by our group.<sup>13</sup> Seeking direct access to a low-valent Mo complex, metalation with Mo halide precursors was explored. MoCl<sub>3</sub>(THF)<sub>3</sub><sup>14</sup> has been shown to coordinate phosphine ligands; subsequent reduction under N<sub>2</sub> can provide the desired low-valent metal compounds.<sup>14-15</sup> Addition of MoCl<sub>3</sub>(THF)<sub>3</sub> to a solution of **P2<sup>OH</sup>** in THF afforded a dark brown homogeneous solution (Scheme B.1.). Stirring this solution for 28 h over activated Mg<sup>0</sup> turnings, under an N<sub>2</sub> atmosphere, did not change the appearance of the solution. However, a new diamagnetic resonance was observed at 81.57 ppm by <sup>31</sup>P{<sup>1</sup>H} NMR spectroscopy, a signal shifted slightly downfield from the Mo(0) N<sub>2</sub> adduct on **P2**. This new species was isolated as a red/orange powder that showed limited solubility in common organic solvents, prohibiting further NMR characterization. Consistent with the proposed assignment as an N<sub>2</sub> adduct, the solid-state IR spectrum demonstrated a strong band at 1951 cm<sup>-1</sup>.<sup>16</sup>



**Scheme B.1.** Synthesis of **P2<sup>OH</sup>**-supported Mo(0) N<sub>2</sub> adducts.

The solid-state structure of the aforementioned species, as determined by single-crystal XRD, confirmed its identity as a Mo(0) N<sub>2</sub> complex (Figure B.2.). **1** crystallizes as a Mg-bridged

dimer; the metrical parameters are consistent with a central phenoxide assignment; the C1–O1 distance, at 1.339(17) Å, corresponds to a single bond.<sup>10a</sup>  $\eta^6$  Mo-arene binding is corroborated by the equivalent C–C bonds around the phenoxide ring. The Mo–N and N–N distances (2.001(13) and 1.119(12) Å, respectively) are similar to those of phosphine-bound Mo N<sub>2</sub> complexes.<sup>16b</sup>

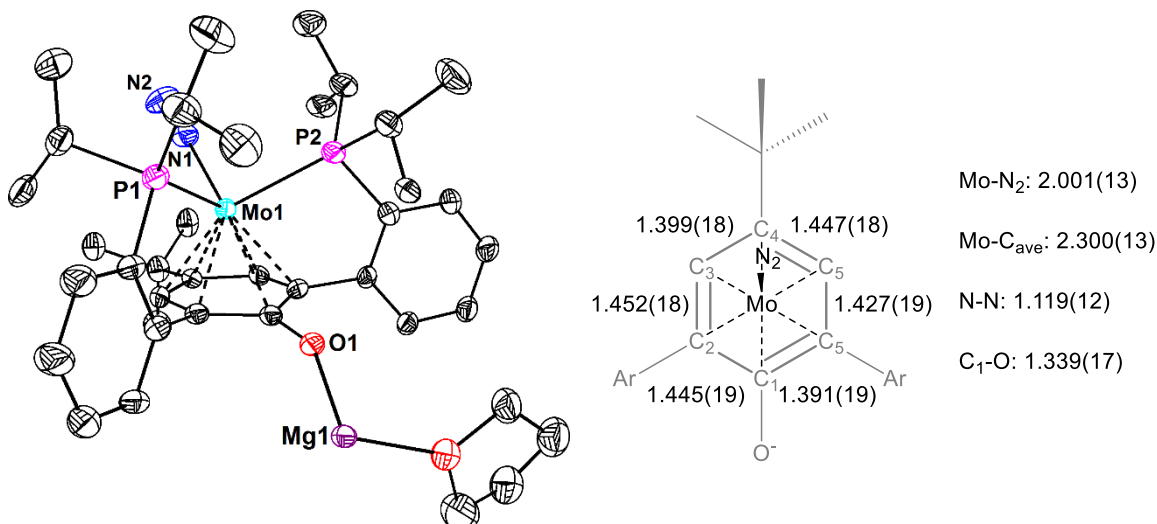


**Figure B.2.** Preliminary solid-state structure and relevant metrical parameters for Mo(0) N<sub>2</sub> adduct, **1**. Thermal anisotropic displacement ellipsoids are shown at the 50% probability level. Half of the dinuclear structure, sans hydrogen atoms, is shown for clarity.

Though fortuitous for its isolation, the insolubility of **1** proves problematic for reactivity testing. Both salt metathesis and protonation were explored in attempts to access mononuclear complexes (Scheme B.2). Addition of LutHOTf afforded a soluble species with no observable hydride signal in the <sup>1</sup>H NMR spectrum (Scheme B.1). A single central arene signal at 4.07 ppm, consistent with a C<sub>s</sub> solution structure, was observed; the <sup>31</sup>P{<sup>1</sup>H} NMR spectrum showed a singlet centered at 78.52 ppm, close to that attributed to **1**. The IR spectrum displayed a strong N<sub>2</sub> stretch at 1932 cm<sup>-1</sup>, signifying retention of the N<sub>2</sub> ligand. Based on these data, a tentative assignment for the product of protonation, phenol complex **2**, is proposed.

Addition of PPh<sub>4</sub>Cl to a dioxane suspension of **1** likewise afforded a more soluble Mo diphosphine compound (Scheme B.1). The <sup>31</sup>P{<sup>1</sup>H} NMR spectrum showed a broad resonance ( $\Delta f_{\text{FWHM}} = 108$  Hz) at 81.23 ppm with a relative integration of two versus a sharp

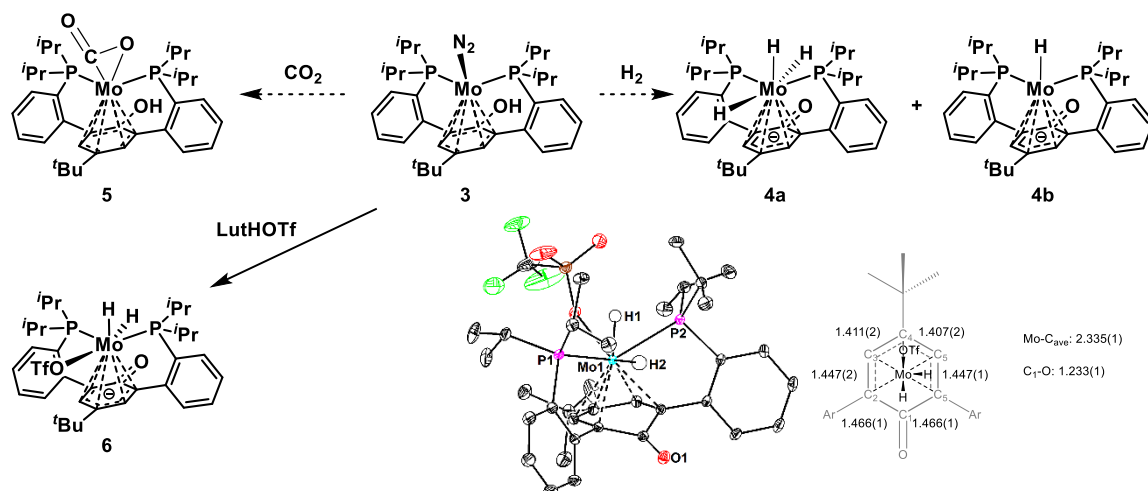


**Figure B.3.** Small molecule reactivity from putative  $\eta^6$ -phenol Mo N<sub>2</sub> adduct **3**. The solid-state structure and pertinent metrical parameters of protonation product **6** are shown, with thermal anisotropic displacement ellipsoids at the 50% probability level and non-hydride H-atoms omitted for clarity.

singlet at 22.40 ppm, assigned to the ligand phosphine and phosphonium, respectively. The <sup>1</sup>H NMR spectrum displays a central arene signal at 4.26 ppm, similar to that of **1** and **2**. The IR spectrum of this complex displays an N<sub>2</sub> stretch at 1989 cm<sup>-1</sup>, consistent with preliminary assignment as the  $\eta^6$ -phenoxide N<sub>2</sub> adduct **3**.

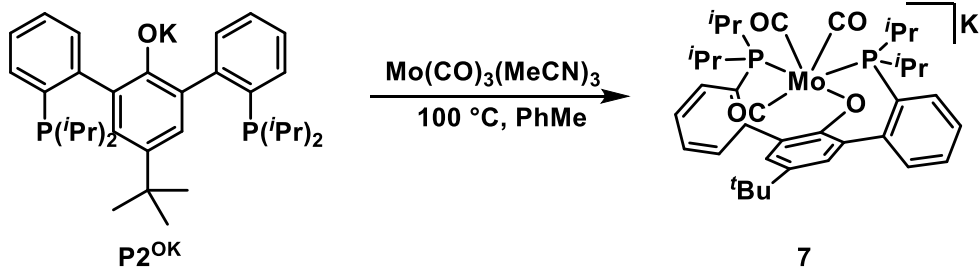
With soluble low-valent complexes in hand, reactivity with small molecules was explored. In line with reactivity seen for the **P2** analog, H<sub>2</sub> and CO<sub>2</sub> addition were studied (see Chapters 2, 7, and 8). Treating a C<sub>6</sub>D<sub>6</sub> solution of **3** with 1 atm of H<sub>2</sub> resulted in the formation of two species, as evidenced by multinuclear NMR spectroscopy (Figure B.3.). The <sup>1</sup>H NMR spectrum displayed two central phenol resonances—5.47 and 4.83 ppm—in a relative ratio of 0.4 : 1. Three high-field triplets were also present: -1.31 (t, <sup>2</sup>J(P,H) = 47.4 Hz), -3.65 (tt, <sup>2</sup>J(P,H) = 42.8 & <sup>2</sup>J(H,H) = 8.6 Hz), and -5.19 (br t, <sup>2</sup>J(P,H) = 37.23 Hz, consistent with formation of tri- and monohydride complexes, **4a** and **4b**. The <sup>31</sup>P{<sup>1</sup>H} NMR spectrum showed two resonances; collecting <sup>1</sup>H{<sup>31</sup>P} spectra associated the <sup>31</sup>P resonances 92.55 and 70.51 ppm to the putative trihydride and monohydride, respectively. The reorganization of the phenoxide to a cyclohexadienonyl motif, electronically similar to a Cp ligand, is proposed based off of the maintenance of downfield shifted <sup>1</sup>H protons for the C3 and C5 carbons of the central arene,

and structural data for a related molecule (*vide infra*). X-ray diffraction studies are necessitated to confirm the ligand structure in **4a/b**, but the seeming reluctance of Mo, typically regarded as oxophilic, to coordinate an O<sup>-</sup> donor (phenoxide) is surprising and likely speaks to the electronic character of the low-valent metal center.

Addition of CO<sub>2</sub> (1 atm) to a C<sub>6</sub>D<sub>6</sub> solution of **3** likewise afforded a new species (Figure B.3.). With a <sup>31</sup>P{<sup>1</sup>H} resonance at 65.92 ppm, a single arene resonance in the <sup>1</sup>H NMR spectrum at 4.38 ppm, and no indication of hydride formation, this new species is putatively assigned as CO<sub>2</sub> adduct **5**. Having studied the protonation (Chapter 7) and hydrogenation (Chapter 8) of CO<sub>2</sub> in detail on the related **P2** system, the possibility of incorporating a proton in the secondary coordination sphere of a low-valent CO<sub>2</sub> complex is enticing. However, this tentative assignment is currently no more than a promising lead.

Unfortunately, synthesis of phenol-bound **2** proved challenging to reproduce. Addition of acid often resulted in formation of a complex with hydride resonances, inconsistent with formation of **3**. Considering that low-valent **3** may react with acid, insoluble **1** was treated with two equiv. of LutHOTf (Figure B.3.). A new complex with a high field triplet at -3.71 ppm (<sup>2</sup>J(P,H) = 64.01 Hz, <sup>1</sup>H NMR) integrating one-to-one relative to a single arene resonance at 5.20 ppm (<sup>1</sup>H NMR) was formed. A corresponding broad singlet at 78.54 ppm in the <sup>31</sup>P{<sup>1</sup>H} NMR was observed. Crystallization of this species confirmed its structure as dihydride triflate complex **6**. Long C1–C2 and C6–C1 distances in the central ring (1.466(1) Å) and a short C1–O1 contact of 1.233(1) Å are consistent with predominance of a cyclohexenonyl resonance contributor for the arene ring. This is further supported by slight puckering of the ketone below the C2–C3–C4–C5–C6 plane (Figure B.3.). The interplay between this strong L<sub>2</sub>X donor and the η<sup>6</sup>-phenoxide binding mode in proton transfer reactions is of significant interest, but at this time, remains unexplored.

While working with Bogdan Dimitriui, an undergraduate SURF student in the Agapie group, we developed an alternative route to metallate **P2**<sup>OH</sup>. Targeting CO complexes in line with those explored in Chapters 2 and 3 of this thesis, Bogdan developed a high-yielding route to



**Scheme B.2.** Synthesis of Mo tricarbonyl anion **7**.

coordinate a  $\text{Mo}(\text{CO})_3$  fragment to  $\text{P2}^{\text{OH}}$ . Initial ligand deprotonation affords the potassium phenoxide salt,  $\text{P2}^{\text{OK}}$  (Scheme B.2.). Refluxing  $\text{Mo}(\text{CO})_3(\text{MeCN})_3$  and  $\text{P2}^{\text{OK}}$  in PhMe affords a new species with a peak in the  $^{31}\text{P}\{^1\text{H}\}$  NMR spectrum at 38.35 ppm. The  $^1\text{H}$  NMR of this complex shows no resonances from 4 to 6 ppm, suggesting phenoxide oxygen, rather than phenoxide  $\pi$ -system binding. Bogdan crystallized this compound; the solid state structure corroborates the clues from solution spectroscopy, showing a phenoxide diphosphine Mo tricarbonyl anion, **7** (Figure B.4). Pursuits to oxidize this complex, hoping to access a cationic

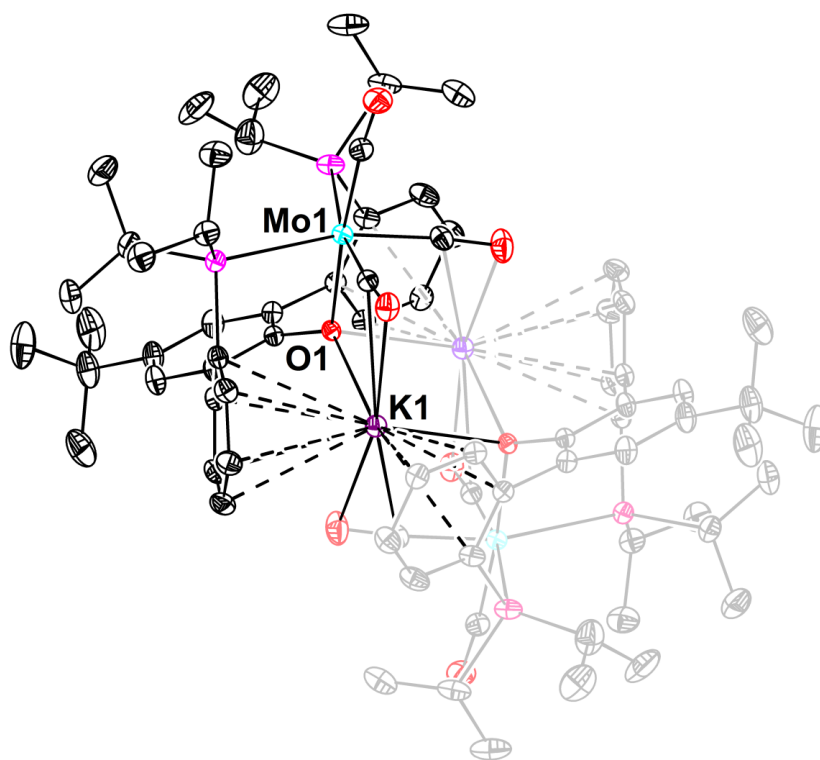


**Figure B.4.** Solid-state structure of **7**. Thermal anisotropic displacement ellipsoids are shown at the 50% probability level. H-atoms are omitted for clarity.

dicarbonyl en route to reductive CO coupling chemistry, were unproductive. Ag-based oxidants led to extensive transmetallation. Reactions with I<sub>2</sub> seemed most promising, but no definitive data suggesting successful oxidation have been collected to date. Synthesis of a dicarbonyl complex on this scaffold and exploration of reductive coupling chemistry would provide an insightful structure/function comparison to the **P2** system discussed in Chapters 2 and 3 of this thesis.

## CONCLUSION

Two disparate metalation routes were developed for the preparation of Mo complexes supported by the **P2<sup>OH</sup>** pro-ligand. The first affords direct access to N<sub>2</sub> complexes, which have subsequently been explored for reactivity with protons, H<sub>2</sub>, and CO<sub>2</sub>. Preliminary results suggest that a low-valent, electron-rich Mo center will preferentially coordinate the  $\pi$ -system of the phenoxide, favoring a cyclohexenonyl structure over the naked phenoxide. These compounds offer intriguing entries to small molecule activation chemistry in which a proximal proton-donor or proton-relay has been incorporated into the secondary coordination sphere of the metal. A second metalation route affords an anionic Mo tricarbonyl from the pro-ligand salt **P2<sup>OK</sup>**.



## EXPERIMENTAL SECTION

### *Synthesis of 1*

A 200 mL RB flask was charged with **P2<sup>OH</sup>** (500 mg, 0.970 mmol), THF (40 mL), and a stir bar. Stirring was initiated, providing a very pale yellow homogeneous solution. MoCl<sub>3</sub>(THF)<sub>3</sub> (420 mg, 0.100 mmol) was added in a single portion as a solid. Following stirring for 30 mins, Mg<sup>0</sup> turnings (800 mg, 32.9 mmol) were added to the dark brown mixture. Stirring under N<sub>2</sub> continued to 28 h. At this time, volatiles were removed *in vacuo*, providing a brown residue. The residue was extracted with pentane; the red/orange pentane solution was stripped of solvent, giving a red residue. Minimal PhMe was added to completely dissolve the residue (ca. 4 mL) and the PhMe solution was cooled to -35 °C for 12 h, precipitating **1** as a red/orange powder (117 mg, 0.079 mmol, 16%). IR (Diamond ATR, cm<sup>-1</sup>) ν<sub>N=N</sub>: 1951.

### *Reaction of 1 with LutHOTf*

A 20 mL scintillation vial was charged with **1** (20mg, 0.013 mmol), LutHOTf (7 mg, 0.026 mmol), dioxane (2 mL), and a stir bar. The resulting suspension was stirred for 16 h. The reaction mixture was filtered through celite and the filtrate dried under reduced pressure, affording a red residue. <sup>1</sup>H NMR (300 MHz, C<sub>6</sub>D<sub>6</sub>, 23 °C) δ: 7.64 (d, *J* = 7.26 Hz, 2H, aryl-*H*), 7.37 (br, 2H, aryl-*H*), 7.02-7.13 (m, 4H, aryl-*H*), 4.07 (s, 2H, central arene-*H*), 2.61-2.67 (m, 2H, CH(CH<sub>3</sub>)<sub>2</sub>), 2.26-2.35 (m, 2H, CH(CH<sub>3</sub>)<sub>2</sub>), 1.34-1.41 (m, 6H, CH(CH<sub>3</sub>)<sub>2</sub>), 1.13-1.19 (m, 6H, CH(CH<sub>3</sub>)<sub>2</sub>), 1.02-1.08 (m, 6H, CH(CH<sub>3</sub>)<sub>2</sub>), 0.78-0.85 (m, 6H, CH(CH<sub>3</sub>)<sub>2</sub>). <sup>31</sup>P{<sup>1</sup>H} NMR (121 MHz, C<sub>6</sub>D<sub>6</sub>, 23 °C) δ: 78.52 (s).

### *Reaction of 1 with PPh<sub>4</sub>Cl*

A 20 mL scintillation vial was charged with **1** (40mg, 0.027 mmol), PPh<sub>4</sub>Cl (20 mg, 0.054 mmol), dioxane (2 mL), and a stir bar. The resulting suspension was stirred for 16 h. The reaction mixture was filtered through celite and the filtrate dried under reduced pressure, affording an orange powder. The NMR spectrum for this reaction was not particularly clean, but the following resonances could be assigned unambiguously: <sup>1</sup>H NMR (300

MHz, C<sub>6</sub>D<sub>6</sub>, 23 °C)  $\delta$ : 7.41 (d,  $J$  = 5.55 Hz, 2H, aryl-*H*), 4.26 (br s, 2H, central arene-*H*), 2.89 (br s, 2H, CH(CH<sub>3</sub>)<sub>2</sub>), 2.49 (br s, 2H, CH(CH<sub>3</sub>)<sub>2</sub>), 1.64 (br m, 6H, CH(CH<sub>3</sub>)<sub>2</sub>), 1.30-1.40 (br m, 12H, CH(CH<sub>3</sub>)<sub>2</sub>), 1.06 (br m, 6H, CH(CH<sub>3</sub>)<sub>2</sub>). <sup>31</sup>P{<sup>1</sup>H} NMR (121 MHz, C<sub>6</sub>D<sub>6</sub>, 23 °C)  $\delta$ : 81.23 (2P, **P2**<sup>OH</sup>), 22.40 (1P, PPh<sub>4</sub>).

*Reaction of “2” with H<sub>2</sub>*

A J. Young tube was charged with a solution of **2** (15 mg, 0.022 mmol) in C<sub>6</sub>D<sub>6</sub> (0.5 mL). The reaction mixture was degassed via three freeze-pump-thaw cycles and the tube backfilled with H<sub>2</sub> (1 atm). The tube was sealed and reaction progress monitored by NMR spectroscopy. This reaction provided a mixture of species, but the salient NMR features corresponding to the major species are as follows: <sup>1</sup>H NMR (300 MHz, C<sub>6</sub>D<sub>6</sub>, 23 °C)  $\delta$ : 5.46 (s, 2H, central arene-*H*, monohydride), 4.83 (s, 2H, central arene-*H*, trihydride), -1.31 (t,  $J$  = 49.56 Hz, 1H, Mo-*H*, monohydride), -3.68 (tt,  $J$  = 42.31, 7.67 Hz, 1H, Mo-*H*, trihydride), -5.20 (br t,  $J$  = 36.34 Hz, 2H, Mo-*H*, trihydride). <sup>31</sup>P{<sup>1</sup>H} NMR (121 MHz, C<sub>6</sub>D<sub>6</sub>, 23 °C)  $\delta$ : 92.55 (s, trihydride), 70.51 (s, monohydride).

*Reaction of “2” with CO<sub>2</sub>*

A J. Young tube was charged with a solution of **2** (15 mg, 0.022 mmol) in C<sub>6</sub>D<sub>6</sub> (0.5 mL). The reaction mixture was degassed via three freeze-pump-thaw cycles and the tube backfilled with CO<sub>2</sub> (1 atm). The tube was sealed and reaction progress monitored by NMR spectroscopy. <sup>1</sup>H NMR (300 MHz, C<sub>6</sub>D<sub>6</sub>, 23 °C)  $\delta$ : 7.44-7.47 (m, 2H, aryl-*H*), 7.21-7.24 (m, 2H, aryl-*H*), 6.99-7.02 (m, 4H, aryl-*H*), 4.38 (s, 2H, central arene-*H*), 3.13-3.22 (m, 2H, CH(CH<sub>3</sub>)<sub>2</sub>), 2.54-2.62 (m, 2H, CH(CH<sub>3</sub>)<sub>2</sub>), 1.42-1.44 (br m, 6H, CH(CH<sub>3</sub>)<sub>2</sub>), 1.14-1.16 (br m, 6H, CH(CH<sub>3</sub>)<sub>2</sub>), 0.93-0.99 (br m, 12H, CH(CH<sub>3</sub>)<sub>2</sub>). <sup>31</sup>P{<sup>1</sup>H} NMR (121 MHz, C<sub>6</sub>D<sub>6</sub>, 23 °C)  $\delta$ : 92.55 (s). 65.92 (s).

*Reaction of 1 with Excess LutHOTf*

A 20 mL scintillation vial was charged with **1** (20mg, 0.013 mmol), LutHOTf (14 mg, 0.052 mmol), dioxane (2 mL), and a stir bar. The resulting suspension was stirred for 16 h. The reaction mixture was filtered through celite and the filtrate dried under reduced

pressure, affording a red residue. This reaction provided a mixture of species, but the salient NMR features corresponding to the major species are as follows:  $^1\text{H}$  NMR (300 MHz,  $\text{C}_6\text{D}_6$ , 23 °C)  $\delta$ : 5.20 (s, 2H, central arene-*H*), -3.71 (t,  $J = 64.05$  Hz, 2H, Mo-*H*).  $^{31}\text{P}\{^1\text{H}\}$  NMR (121 MHz,  $\text{C}_6\text{D}_6$ , 23 °C)  $\delta$ : 78.54 (s).

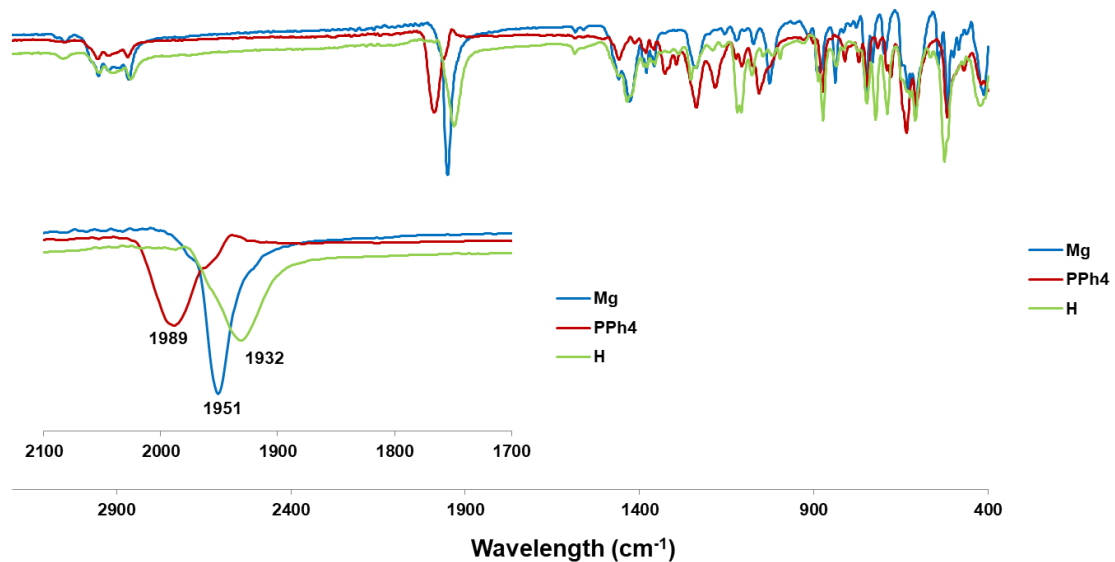


**Figure B.5.** ATR IR Spectra of  $\text{N}_2$  Complexes Supported by the  $\text{P2}^{\text{OH}}$  Ancillary Ligand. The inset shows an enlargement of the relevant N–N stretches.

## REFERENCES

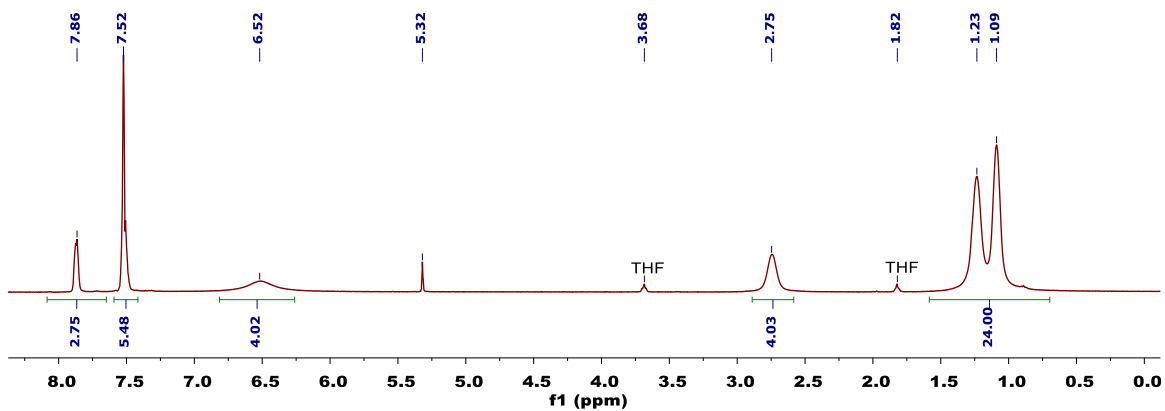
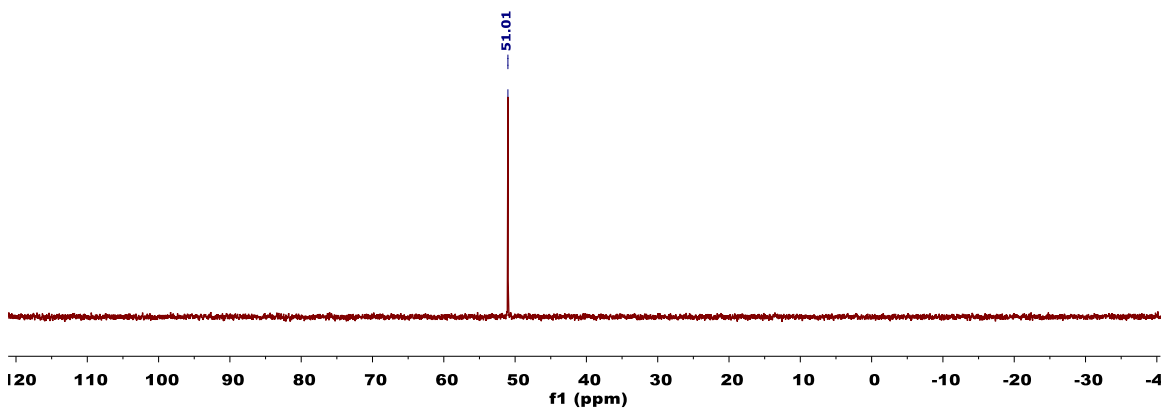
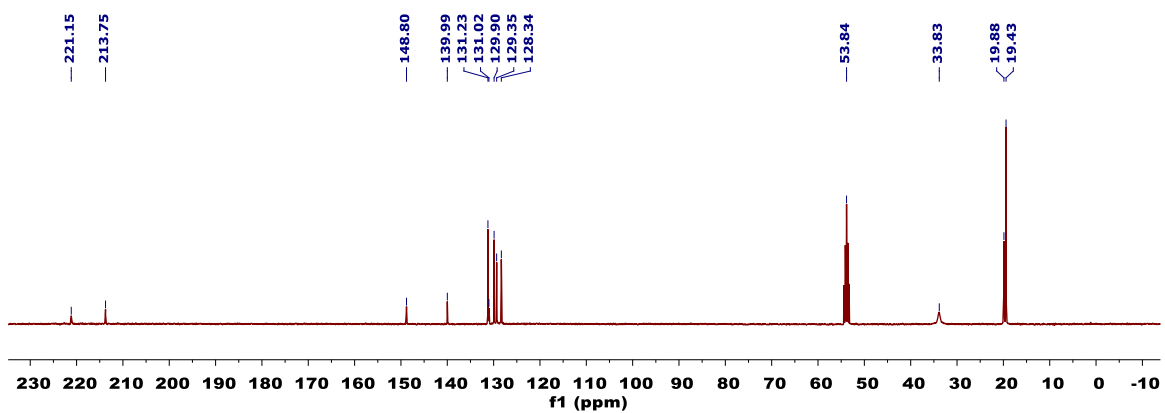
- (1) a) Morris, R. H. *Acc. Chem. Res.* **2015**, *48*, 1494; b) Conley, B. L.; Pennington-Boggio, M. K.; Boz, E.; Williams, T. J. *Chem. Rev.* **2010**, *110*, 2294; c) Khusnutdinova, J. R.; Milstein, D. *Angew. Chem. Int. Ed.* **2015**, *54*, 12236; d) Friedrich, A.; Schneider, S. *ChemCatChem* **2009**, *1*, 72.
- (2) a) Brands, K. M. J.; Payack, J. F.; Rosen, J. D.; Nelson, T. D.; Candelario, A.; Huffman, M. A.; Zhao, M. M.; Li, J.; Craig, B.; Song, Z. J.; Tschaen, D. M.; Hansen, K.; Devine, P. N.; Pye, P. J.; Rossen, K.; Dormer, P. G.; Reamer, R. A.; Welch, C. J.; Mathre, D. J.; Tsou, N. N.; McNamara, J. M.; Reider, P. J. *J. Am. Chem. Soc.* **2003**, *125*, 2129; b) Otsuka, T.; Ishii, A.; Dub, P. A.; Ikariya, T. *J. Am. Chem. Soc.* **2013**, *135*, 9600; c) Saudan, L. A.; Saudan, C. M.; Debieux, C.; Wyss, P. *Angew. Chem. Int. Ed.* **2007**, *46*, 7473; d) Touge, T.; Nara, H.; Fujiwhara, M.; Kayaki, Y.; Ikariya, T. *J. Am. Chem. Soc.* **2016**, *138*, 10084.
- (3) Dixon, D. J. *Beilstein J. Org. Chem.* **2016**, *12*, 1079.
- (4) Blum, Y.; Czarkie, D.; Rahamim, Y.; Shvo, Y. *Organometallics* **1985**, *4*, 1459.
- (5) Ohkuma, T.; Ooka, H.; Hashiguchi, S.; Ikariya, T.; Noyori, R. *J. Am. Chem. Soc.* **1995**, *117*, 2675.
- (6) Zhang, J.; Leitus, G.; Ben-David, Y.; Milstein, D. *Angew. Chem. Int. Ed.* **2006**, *45*, 1113.
- (7) a) Lu, Z.; Conley, B. L.; Williams, T. J. *Organometallics* **2012**, *31*, 6705; b) Conley, B. L.; Williams, T. J. *Chem. Commun.* **2010**, *46*, 4815; c) Glüer, A.; Förster, M.; Celinski, V. R.; Schmedt auf der Günne, J.; Holthausen, M. C.; Schneider, S. *ACS Catalysis* **2015**, *5*, 7214; d) Marziale, A. N.; Friedrich, A.; Klopsch, I.; Drees, M.; Celinski, V. R.; Schmedt auf der Günne, J.; Schneider, S. *J. Am. Chem. Soc.* **2013**, *135*, 13342.
- (8) a) Miller, A. J. M.; Labinger, J. A.; Bercaw, J. E. *Organometallics* **2010**, *29*, 4499; b) Miller, A. J. M.; Labinger, J. A.; Bercaw, J. E. *J. Am. Chem. Soc.* **2008**, *130*, 11874.
- (9) a) Bernskoetter, W. H.; Hazari, N. *Acc. Chem. Res.* **2017**, *50*, 1049; b) Bielinski, E. A.; Lagaditis, P. O.; Zhang, Y.; Mercado, B. Q.; Würtele, C.; Bernskoetter, W. H.; Hazari, N.; Schneider, S. *J. Am. Chem. Soc.* **2014**, *136*, 10234; c) Mills, M. R.; Barnes, C. L.; Bernskoetter, W. H. *Inorg. Chem.* **2018**, *57*, 1590.
- (10) a) Henthorn, J. T.; Agapie, T. *Inorg. Chem.* **2016**, *55*, 5337; b) Henthorn, J. T.; Lin, S.; Agapie, T. *J. Am. Chem. Soc.* **2015**, *137*, 1458.
- (11) Horak, K. T.; Agapie, T. *J. Am. Chem. Soc.* **2016**, *138*, 3443.
- (12) Marcus Low--unpublished results.
- (13) Edouard, G. A.; Kelley, P.; Herbert, D. E.; Agapie, T. *Organometallics* **2015**, *34*, 5254.
- (14) Anker, M. W.; Chatt, J.; Leigh, G. J.; Wedd, A. G. *J. Chem. Soc., Dalton Trans.* **1975**, 2639.
- (15) a) George, T. A.; Tisdale, R. C. *Inorg. Chem.* **1988**, *27*, 2909; b) Bernskoetter, W. H.; Tyler, B. T. *Organometallics* **2011**, *30*, 520.
- (16) a) Green, M. L. H.; Silverthorn, W. E. *J. Chem. Soc., Dalton Trans.* **1973**, 301; b) Buss, J. A.; Edouard, G. A.; Cheng, C.; Shi, J.; Agapie, T. *J. Am. Chem. Soc.* **2014**, *136*, 11272.



## Appendix C

### Nuclear Magnetic Resonance Spectra for Characterization of Isolated and *in situ* Generated Complexes

## CHAPTER 2

Figure C.1.  $^1\text{H}$  NMR Spectrum (500 MHz,  $\text{CD}_2\text{Cl}_2$ ) of **2**.Figure C.2.  $^{31}\text{P}\{^1\text{H}\}$  NMR Spectrum (121 MHz,  $\text{CD}_2\text{Cl}_2$ ) of **2**.Figure C.3.  $^{13}\text{C}\{^1\text{H}\}$  NMR Spectrum (101 MHz,  $\text{CD}_2\text{Cl}_2$ ) of **2**.

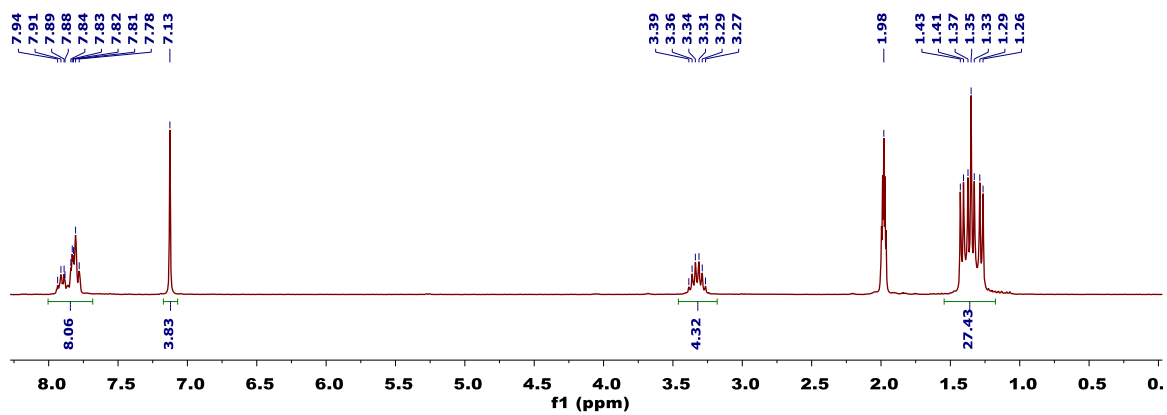


Figure C.4.  $^1\text{H}$  NMR Spectrum (300 MHz,  $\text{CD}_3\text{CN}$ ) of **3**.

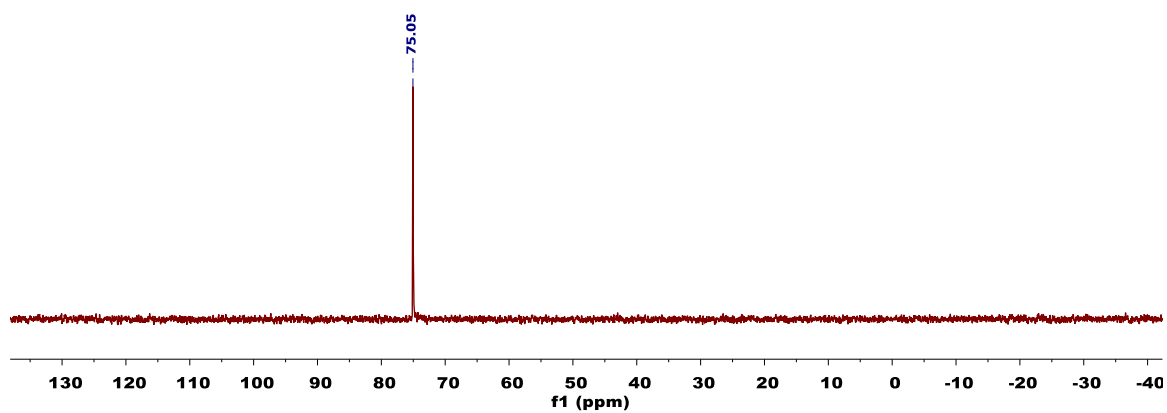


Figure C.5.  $^{31}\text{P}\{^1\text{H}\}$  NMR Spectrum (121 MHz,  $\text{CD}_3\text{CN}$ ) of **3**.

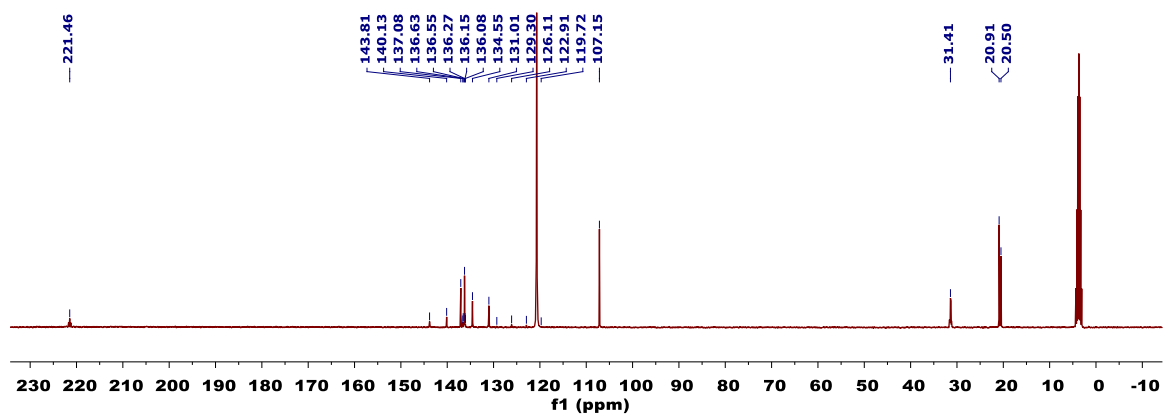
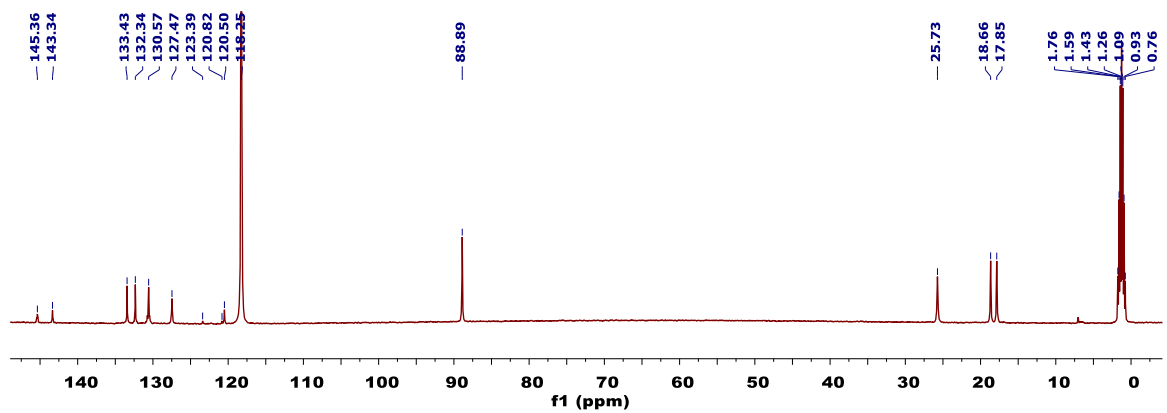
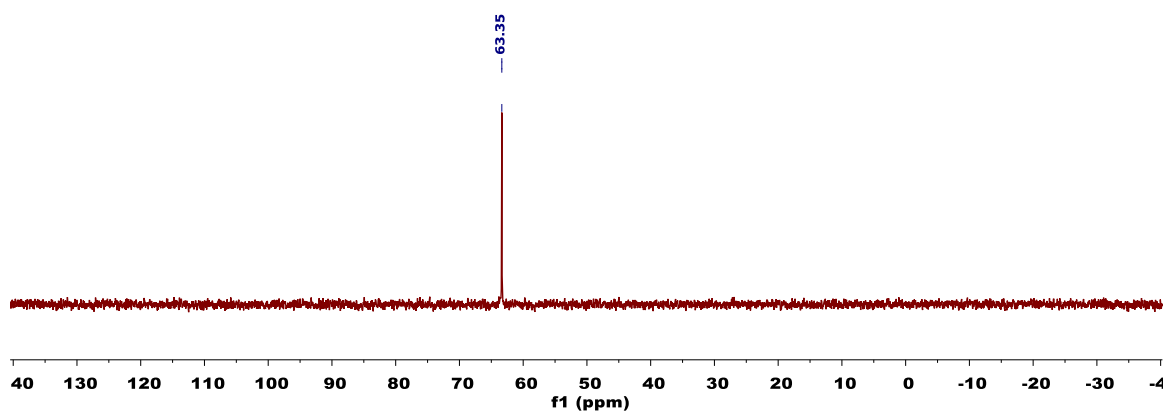
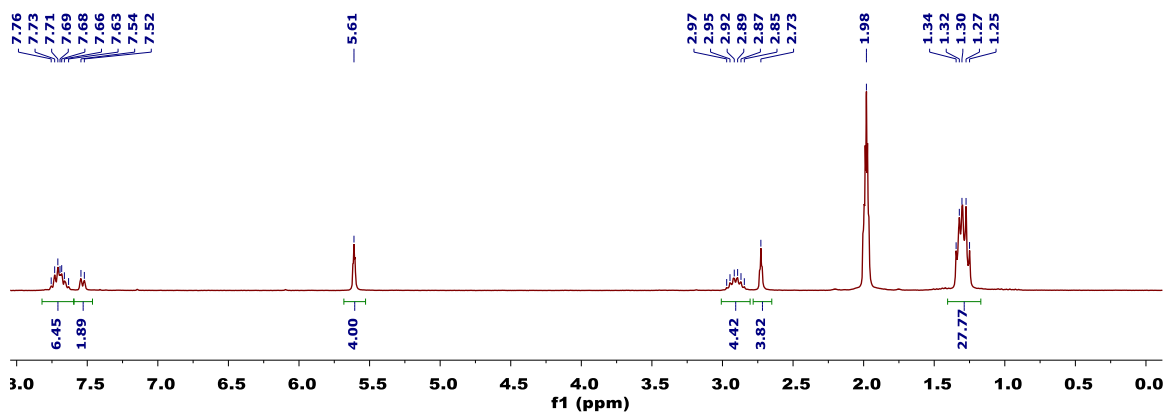


Figure C.6.  $^{13}\text{C}\{^1\text{H}\}$  NMR Spectrum (101 MHz,  $\text{CD}_3\text{CN}$ ) of **3**.





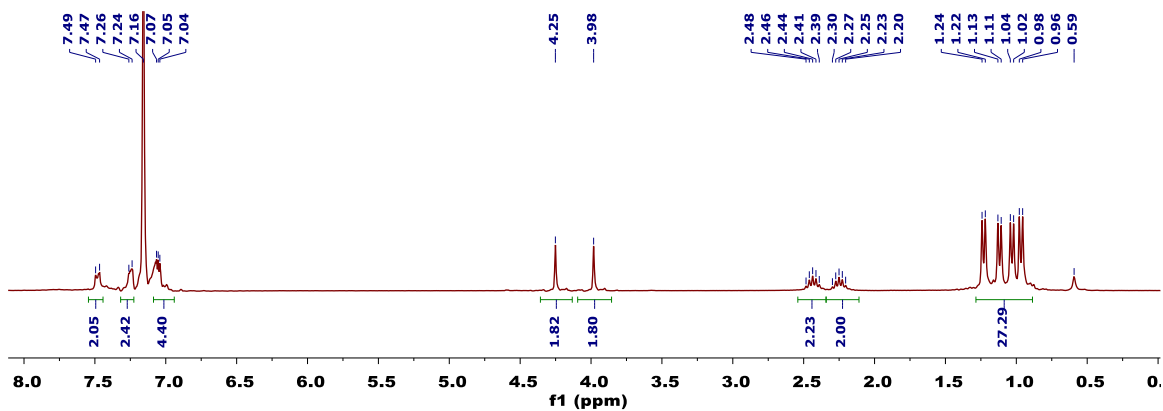


Figure C.10.  $^1\text{H}$  NMR Spectrum (300 MHz,  $\text{C}_6\text{D}_6$ ) of 5.

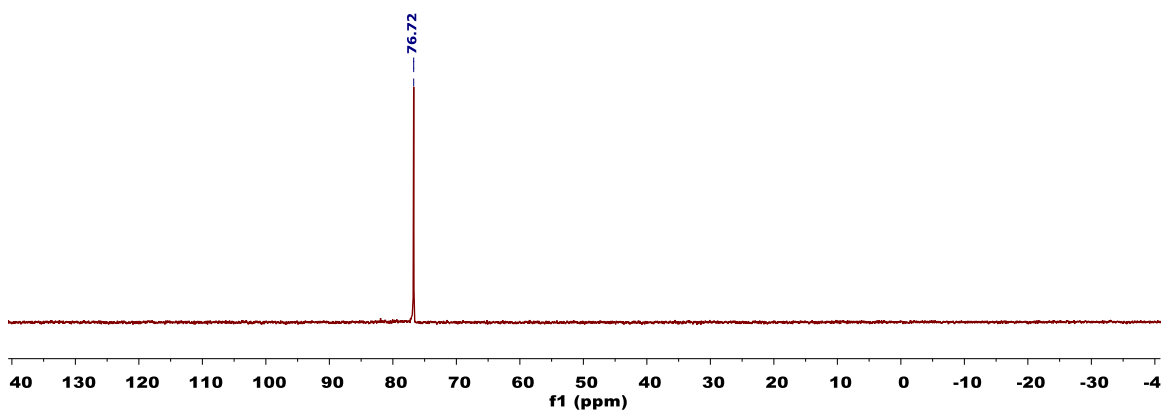


Figure C.11.  $^{31}\text{P}\{^1\text{H}\}$  NMR Spectrum (121 MHz,  $\text{CD}_2\text{Cl}_2$ ) of 5.

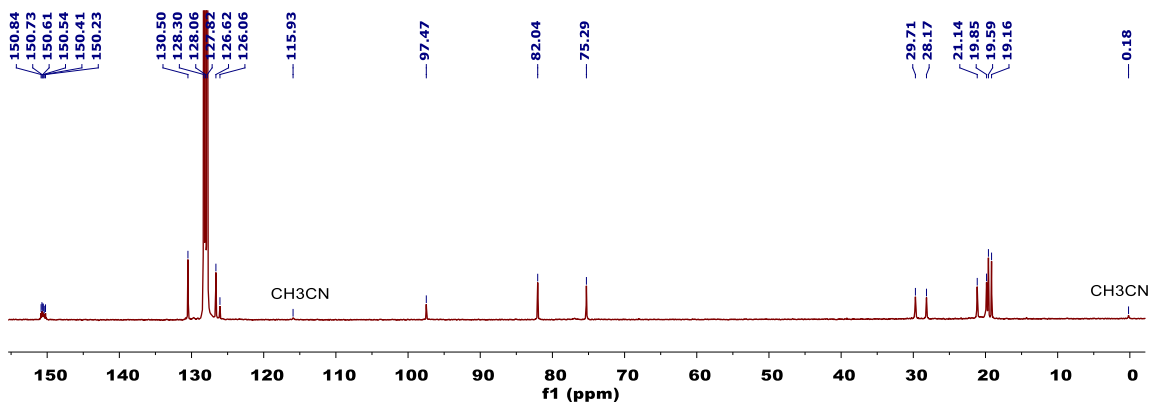


Figure C.12.  $^{13}\text{C}\{^1\text{H}\}$  NMR Spectrum (101 MHz,  $\text{C}_6\text{D}_6$ ) of 5.

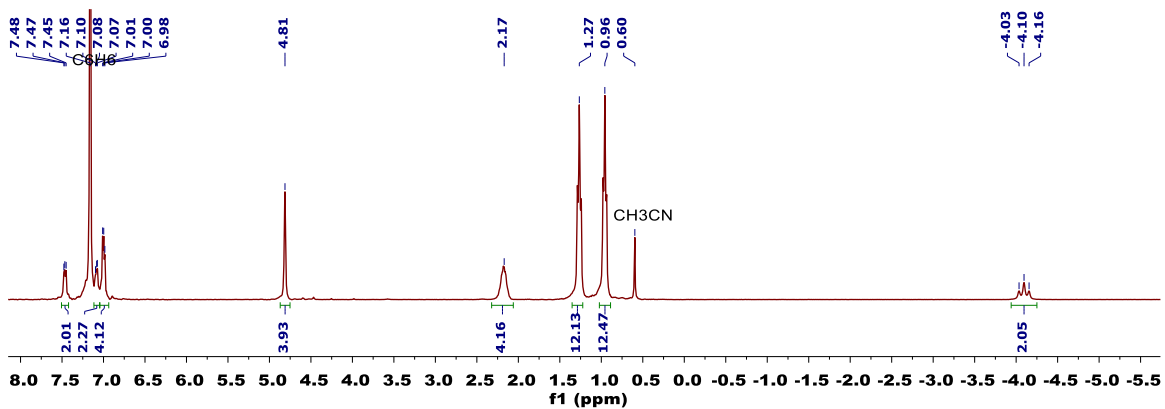


Figure C.13.  $^1\text{H}$  NMR Spectrum (300 MHz,  $\text{C}_6\text{D}_6$ ) of **6**.

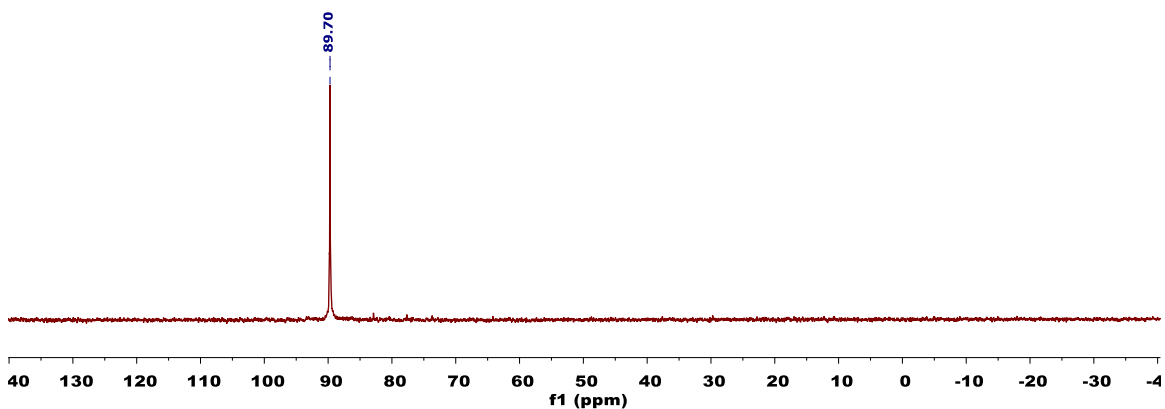


Figure C.14.  $^{31}\text{P}\{^1\text{H}\}$  NMR Spectrum (121 MHz,  $\text{C}_6\text{D}_6$ ) of **6**.

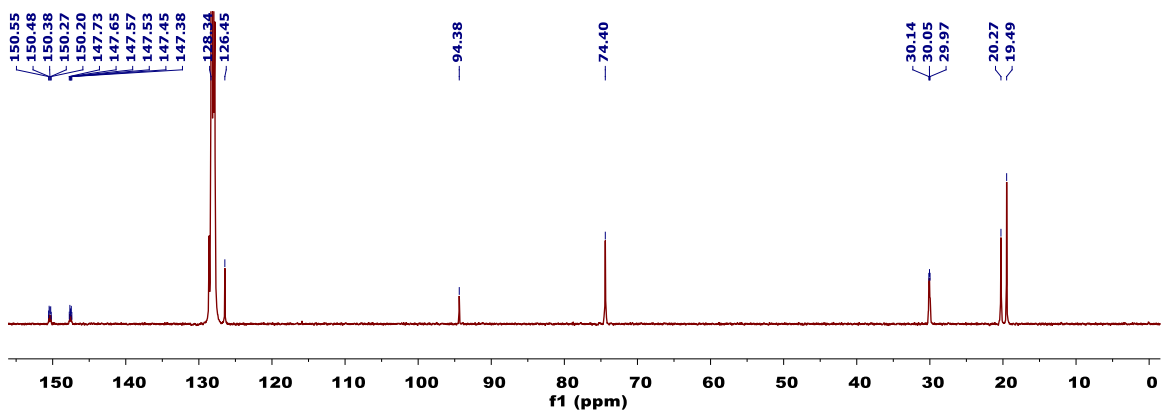


Figure C.15.  $^{13}\text{C}\{^1\text{H}\}$  NMR Spectrum (126 MHz,  $\text{C}_7\text{D}_8$ ) of **6**.

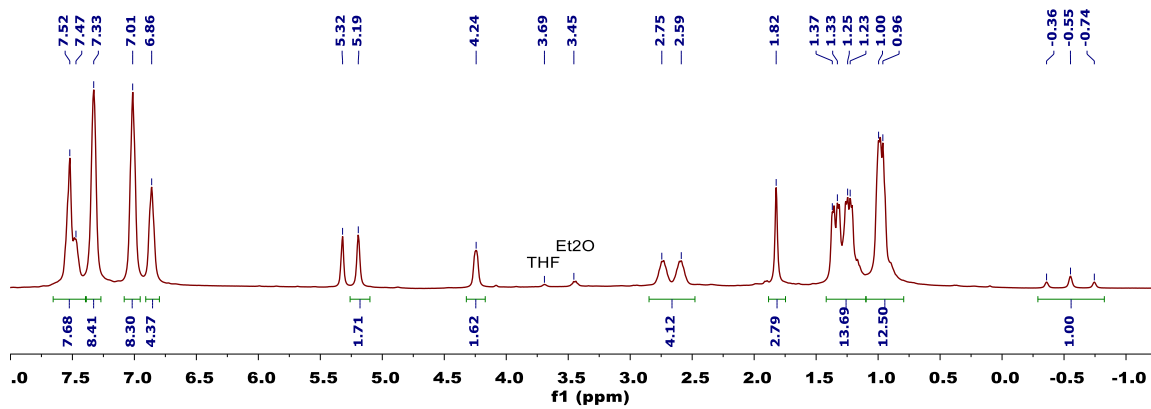


Figure C.16.  $^1\text{H}$  NMR Spectrum (400 MHz,  $\text{CD}_2\text{Cl}_2$ ) of 7.

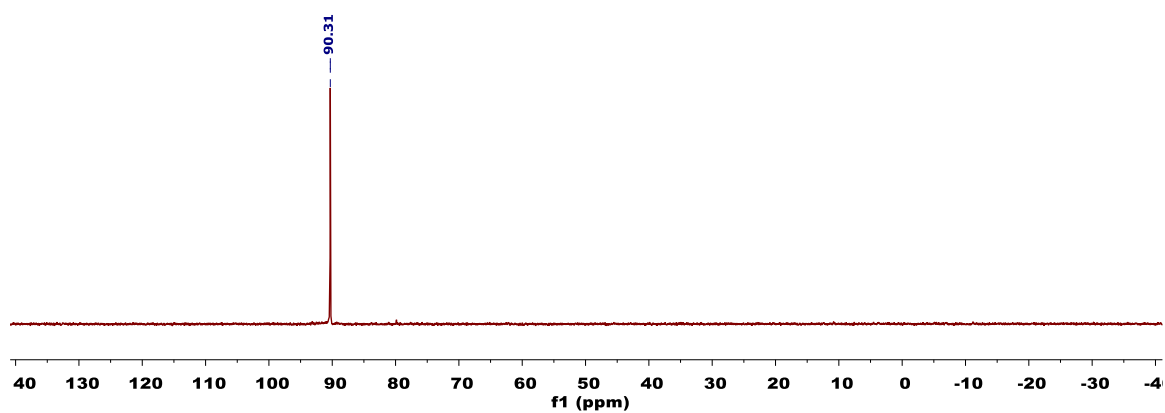


Figure C.17.  $^{31}\text{P}\{^1\text{H}\}$  NMR Spectrum (162 MHz,  $\text{CD}_2\text{Cl}_2$ ) of 7.

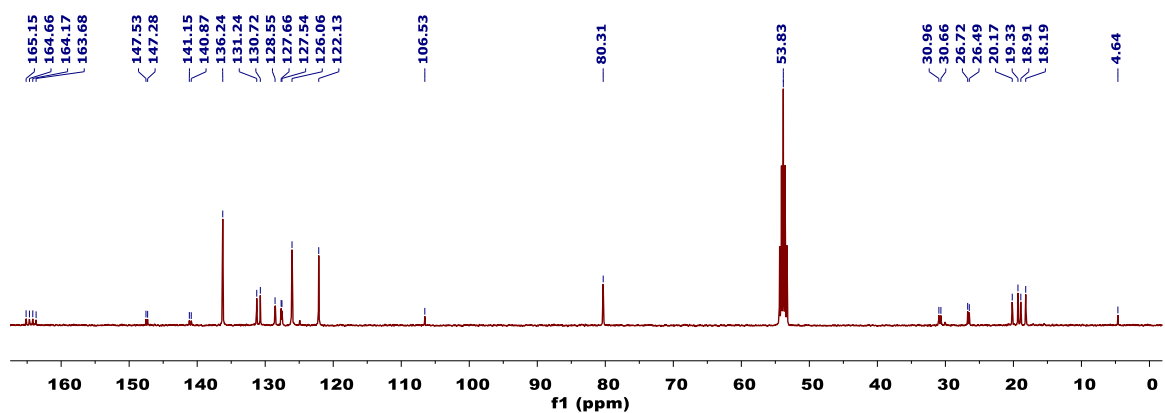


Figure C.18.  $^{13}\text{C}\{^1\text{H}\}$  NMR Spectrum (101 MHz,  $\text{CD}_2\text{Cl}_2$ ) of 7.

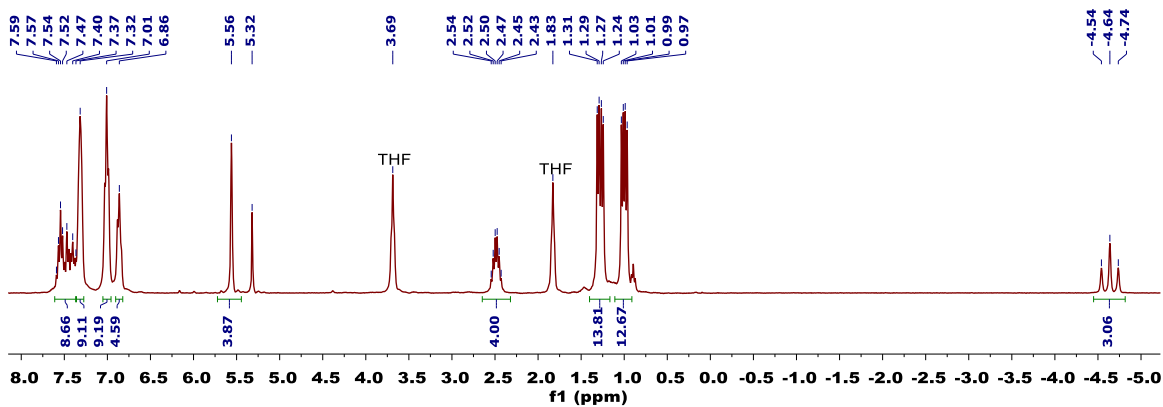


Figure C.19.  $^1\text{H}$  NMR Spectrum (300 MHz,  $\text{CD}_2\text{Cl}_2$ ) of **8**.

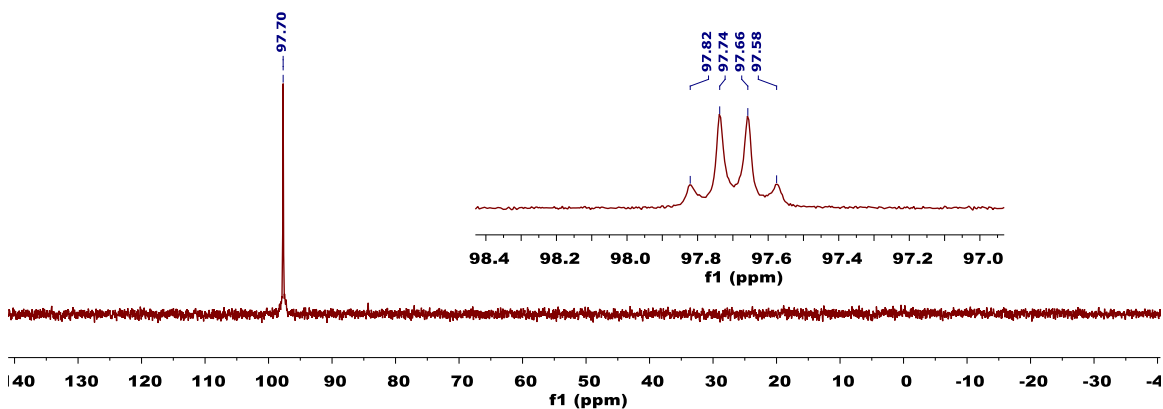


Figure C.20  $^{31}\text{P}\{^1\text{H}\}$  NMR Spectrum (121 MHz,  $\text{CD}_2\text{Cl}_2$ ) of **8**. Inset:  $^{31}\text{P}\{^1\text{H}\}$  NMR Spectrum (162 MHz,  $\text{CD}_2\text{Cl}_2$ ) of **8** with the proton decoupler centered at 7.0 ppm (selective hydride coupling).

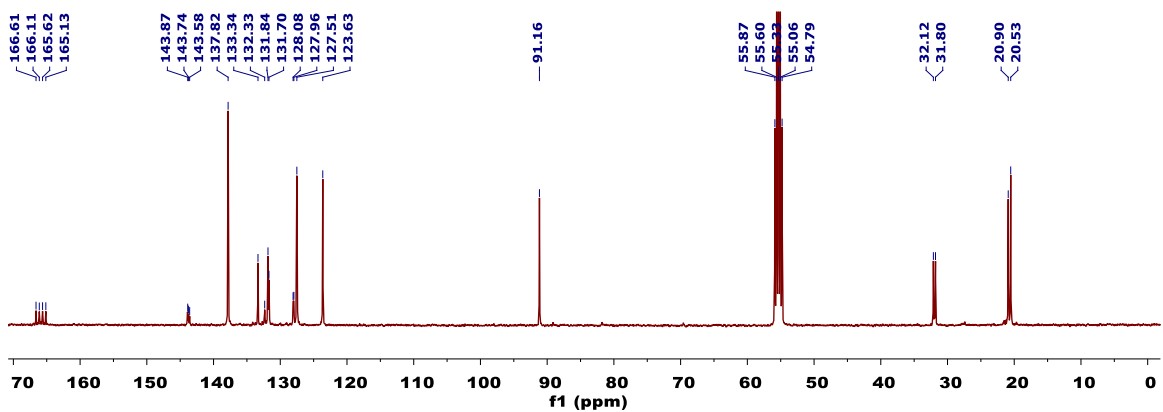
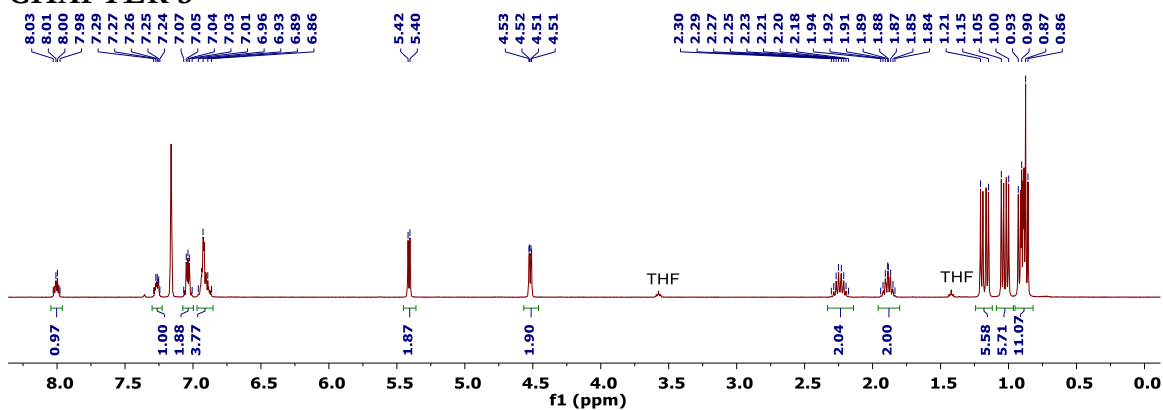
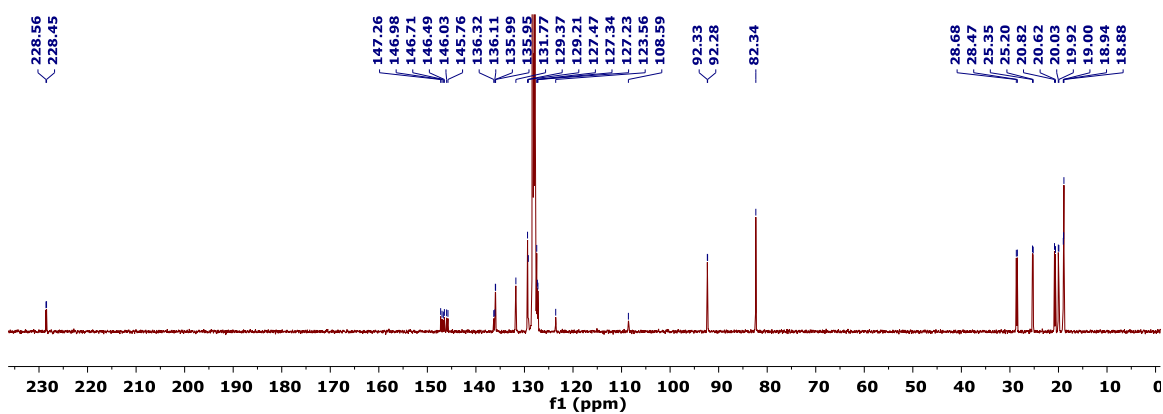
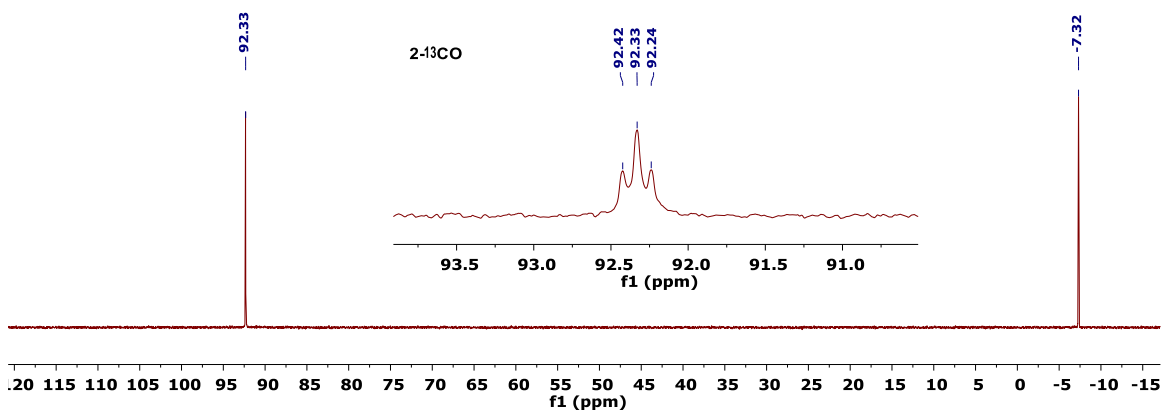


Figure C.21.  $^{13}\text{C}\{^1\text{H}\}$  NMR Spectrum (101 MHz,  $\text{CD}_2\text{Cl}_2$ ) of **8**.

## CHAPTER 3

Figure C.22.  $^1\text{H}$  NMR Spectrum (400 MHz,  $\text{C}_6\text{D}_6$ , 25°C) of **2**.Figure C.23.  $^{13}\text{C}\{^1\text{H}\}$  NMR Spectrum (101 MHz,  $\text{C}_6\text{D}_6$ , 25°C) of **2**.Figure C.24.  $^{31}\text{P}\{^1\text{H}\}$  NMR Spectrum (162 MHz,  $\text{C}_6\text{D}_6$ , 25°C) of **2**. The inset shows a partial  $^{31}\text{P}\{^1\text{H}\}$  NMR spectrum for **2**- $^{13}\text{CO}$ .

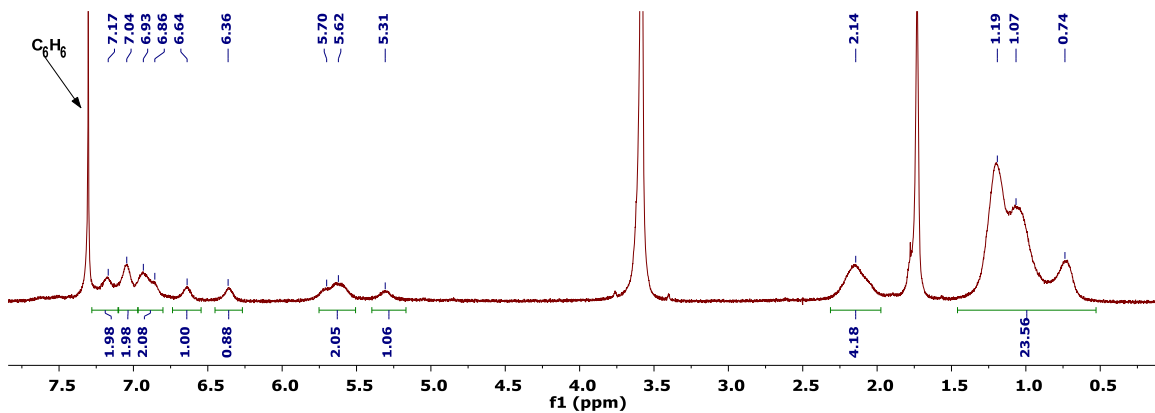


Figure C.25.  $^1\text{H}$  NMR Spectrum (400 MHz,  $\text{THF-}d_8$ ,  $25^\circ\text{C}$ ) of **3**.

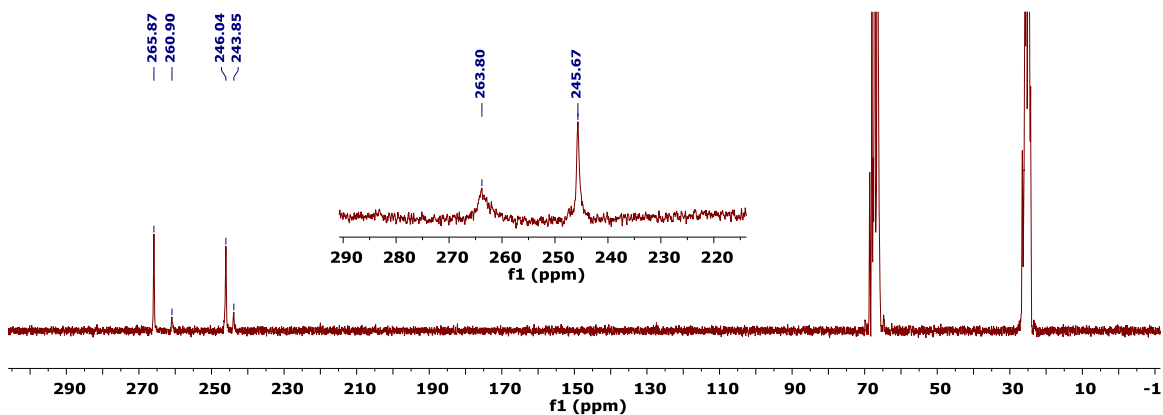


Figure C.26.  $^{13}\text{C}\{^1\text{H}\}$  NMR Spectrum (126 MHz,  $\text{THF-}d_8$ ,  $-80^\circ\text{C}$ ) of **3- $^{13}\text{C}$ O**. The inset shows the downfield region of a  $^{13}\text{C}\{^1\text{H}\}$  NMR spectrum of the same sample collected at  $25^\circ\text{C}$ .

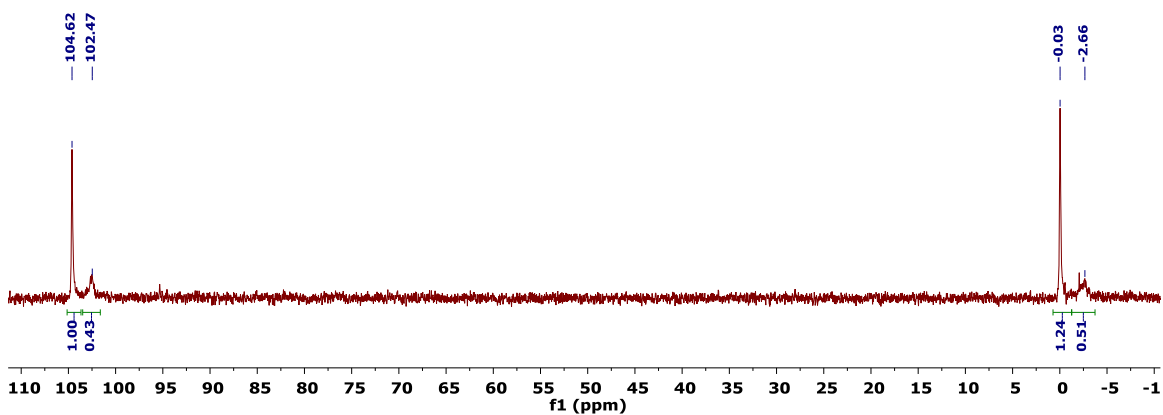


Figure C.27.  $^{31}\text{P}\{^1\text{H}\}$  NMR Spectrum (162 MHz,  $\text{THF-}d_8$ ,  $25^\circ\text{C}$ ) of **3**.

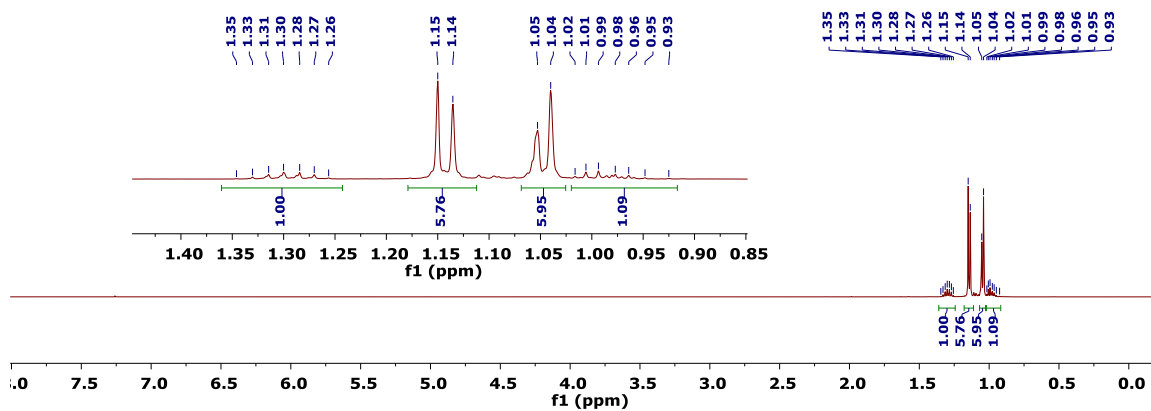


Figure C.28.  $^1\text{H}$  NMR Spectrum (500 MHz,  $\text{CDCl}_3$ ,  $25^\circ\text{C}$ ) of **6a**. The inset contains and enlargement of the 0.85-1.45 ppm region.

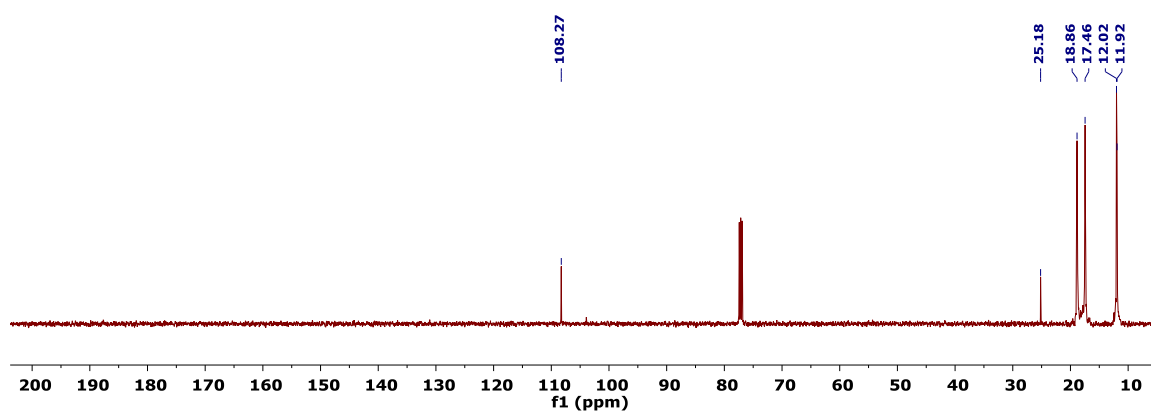


Figure C.29.  $^{13}\text{C}\{^1\text{H}\}$  NMR Spectrum (126 MHz,  $\text{CDCl}_3$ ,  $25^\circ\text{C}$ ) of **6a**.

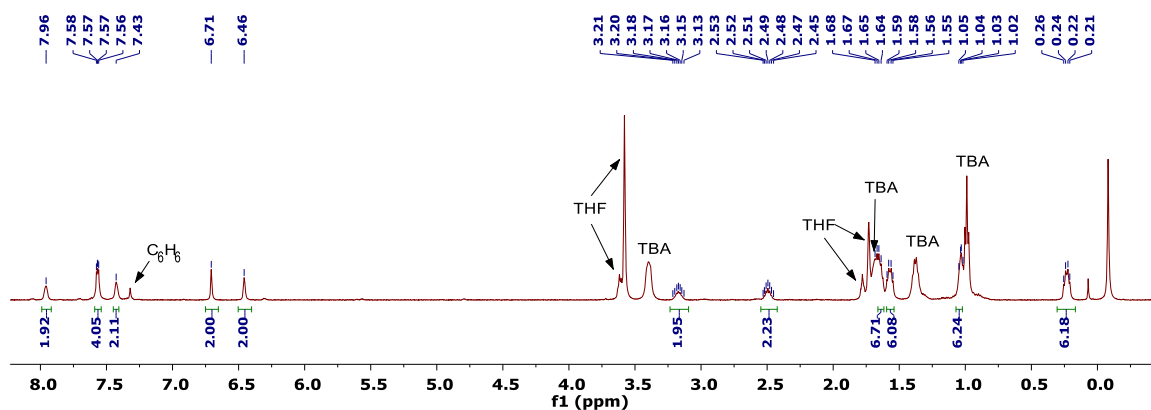
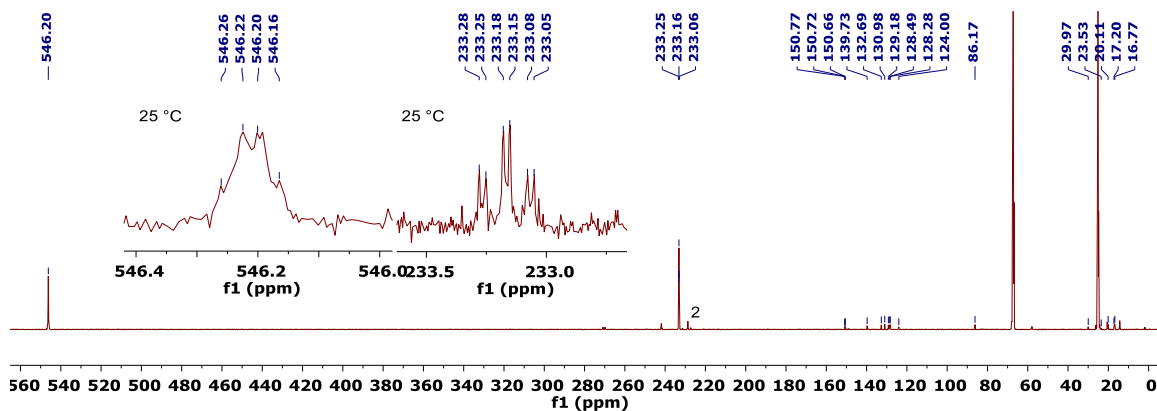
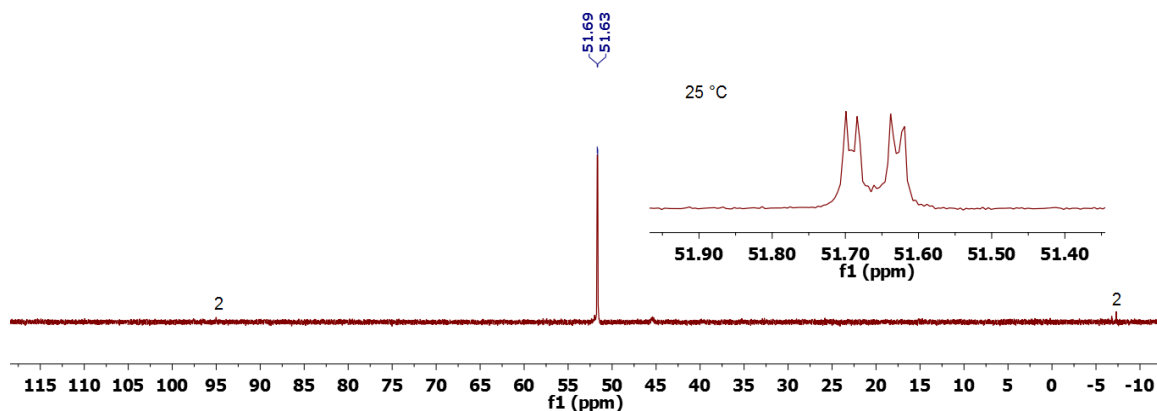


Figure C.30.  $^1\text{H}$  NMR Spectrum (500 MHz,  $\text{THF-}d_8$ ,  $-20^\circ\text{C}$ ) of **7- $^{13}\text{C}$ O**.





**Figure C.31.**  $^{13}\text{C}\{^1\text{H}\}$  NMR Spectrum (126 MHz,  $\text{THF-}d_8$ ,  $-20^\circ\text{C}$ ) of  $7\text{-}^{13}\text{CO}$ . The inset shows a  $^{13}\text{C}\{^1\text{H}\}$  NMR spectrum taken at  $25^\circ\text{C}$ , demonstrating well resolved  $^2J_{PC}$  and  $^2J_{CC}$ .



**Figure C.32.**  $^{31}\text{P}\{^1\text{H}\}$  NMR Spectrum (202 MHz,  $\text{THF-}d_8$ ,  $-20^\circ\text{C}$ ) of  $7\text{-}^{13}\text{CO}$ . The inset shows a  $^{31}\text{P}\{^1\text{H}\}$  NMR spectrum taken at  $25^\circ\text{C}$ , demonstrating well resolved  $^2J_{PC}$ .

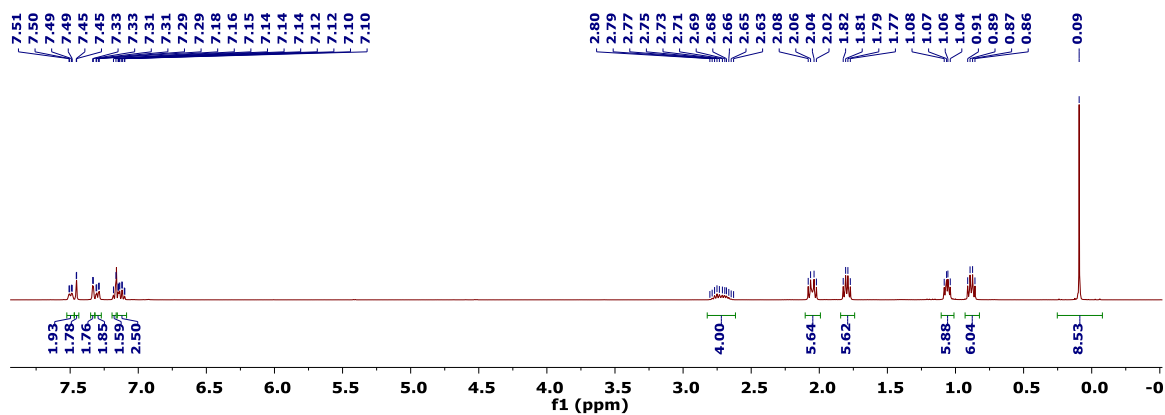


**Figure C.33.**  $^1\text{H}$  NMR Spectrum (400 MHz,  $\text{C}_6\text{D}_6$ ,  $25^\circ\text{C}$ ) of **8**.

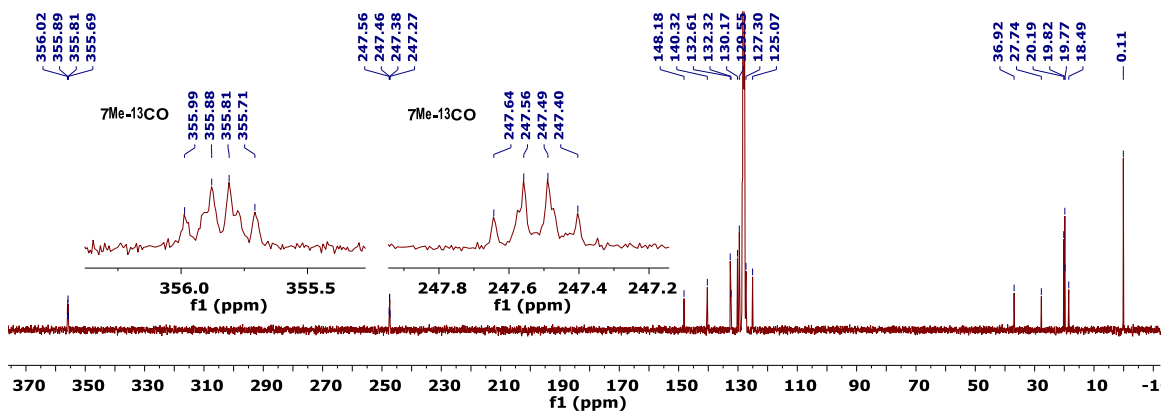


**Figure C.34.**  $^{13}\text{C}\{^1\text{H}\}$  NMR Spectrum (101 MHz,  $\text{C}_6\text{D}_6$ ,  $25^\circ\text{C}$ ) of **7**. The inset shows the enhanced  $^{13}\text{C}$  signals for **8- $^{13}\text{C}$ O**.

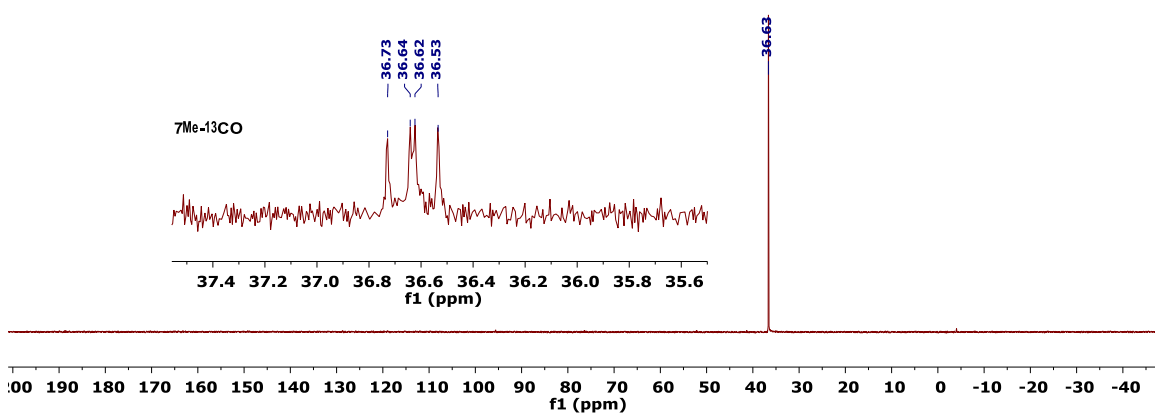


**Figure C.35.**  $^{31}\text{P}\{^1\text{H}\}$  NMR Spectrum (162 MHz,  $\text{C}_6\text{D}_6$ ,  $25^\circ\text{C}$ ) of **7**. The inset shows a partial  $^{31}\text{P}\{^1\text{H}\}$  NMR spectrum for **8- $^{13}\text{C}$ O**.

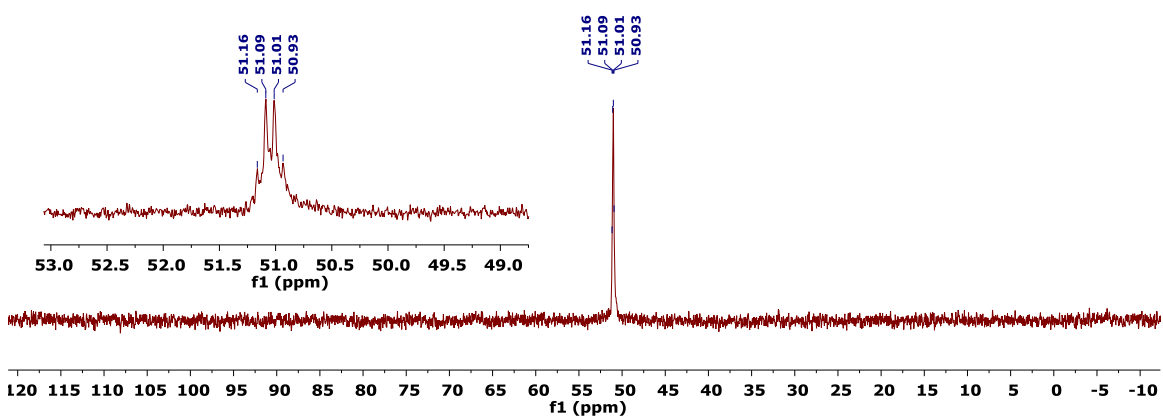


**Figure C.36.**  $^{31}\text{P}\{^1\text{H}\}$  NMR Spectrum (300 MHz,  $\text{C}_6\text{D}_6$ ,  $25^\circ\text{C}$ ) of  $\text{P}_2\text{Mo}(^{13}\text{CO})_3$ . The inset contains an enlargement of the quartet at 51.01 ppm.

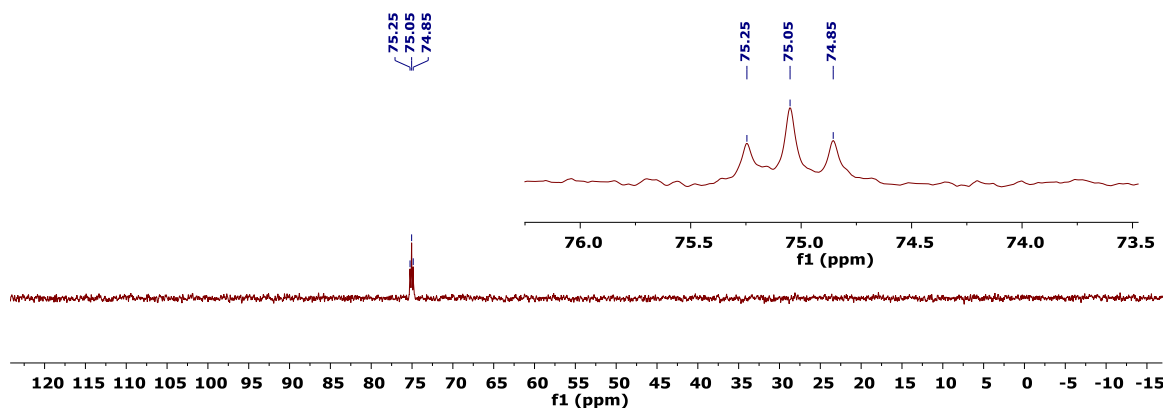


**Figure C.37.**  $^{31}\text{P}\{^1\text{H}\}$  NMR Spectrum (300 MHz,  $\text{CD}_3\text{CN}$ ,  $25^\circ\text{C}$ ) of  $1\text{-}^{13}\text{C}\text{O}$ . The inset contains an enlargement of the triplet at 75.05 ppm.

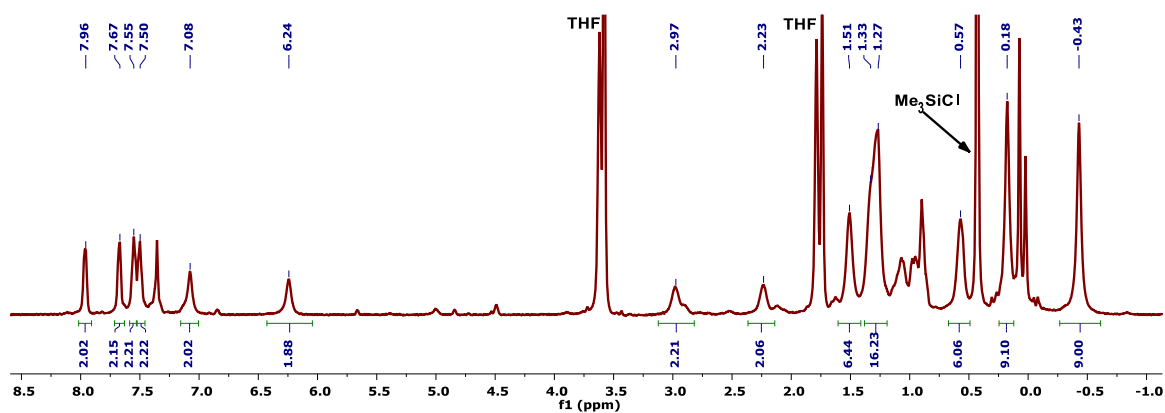


**Figure C.38.**  $^1\text{H}$  NMR spectrum (500 MHz,  $\text{THF-}d_8$ ,  $-80^\circ\text{C}$ ) of a mixture of  $2\text{-}^{13}\text{C}$  (3%),  $9\text{-}^{13}\text{C}$  (87%), and  $10\text{-}^{13}\text{C}$  (10%).

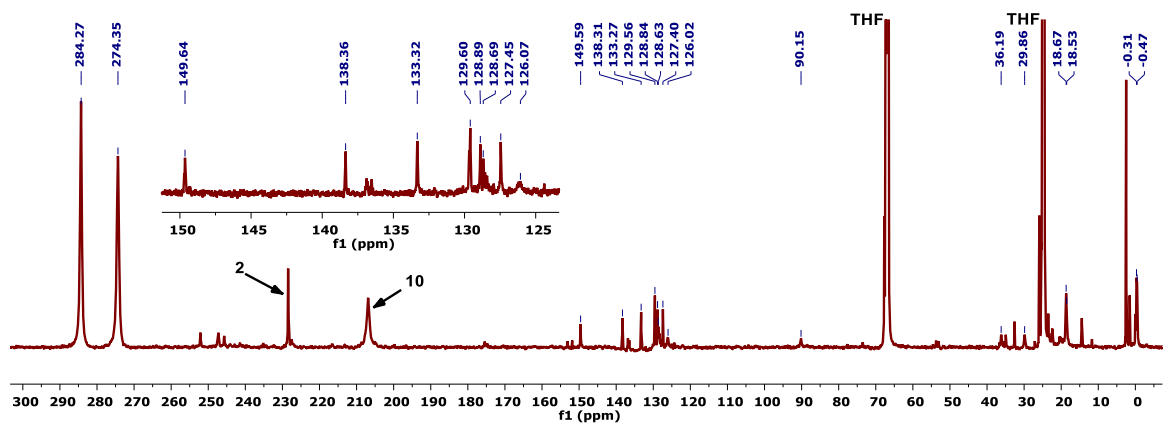


**Figure C.39.**  $^{13}\text{C}\{^1\text{H}\}$  NMR spectrum (126 MHz,  $\text{THF-}d_8$ ,  $-80^\circ\text{C}$ ) of a mixture of  $2\text{-}^{13}\text{C}$  (3%),  $9\text{-}^{13}\text{C}$  (87%), and  $10\text{-}^{13}\text{C}$  (10%). The inset shows an enlargement of the aryl region.

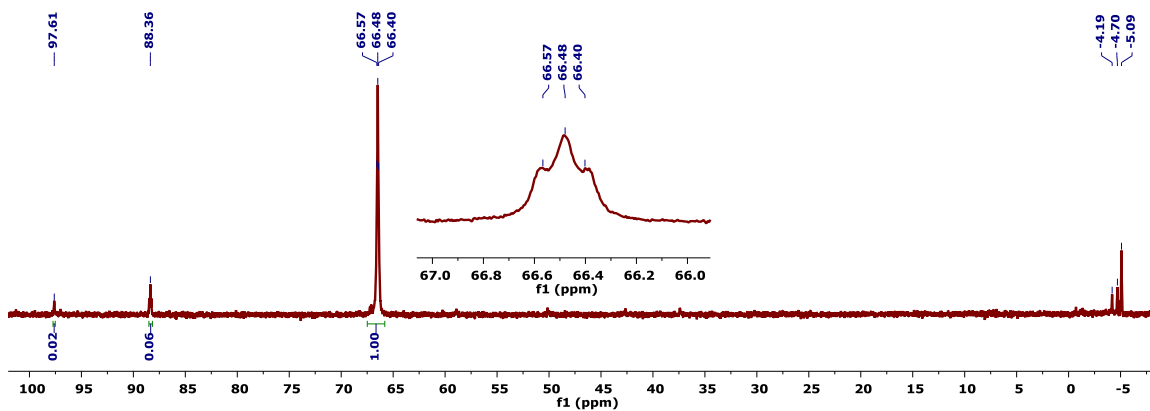


**Figure C.40.**  $^{31}\text{P}\{^1\text{H}\}$  NMR spectrum (202 MHz,  $\text{THF-}d_8$ ,  $-80^\circ\text{C}$ ) of a mixture of  $2\text{-}^{13}\text{C}$  (3%),  $9\text{-}^{13}\text{C}$  (87%), and  $10\text{-}^{13}\text{C}$  (10%). The inset shows an enlargement of the doublet assigned to  $9\text{-}^{13}\text{C}$ .

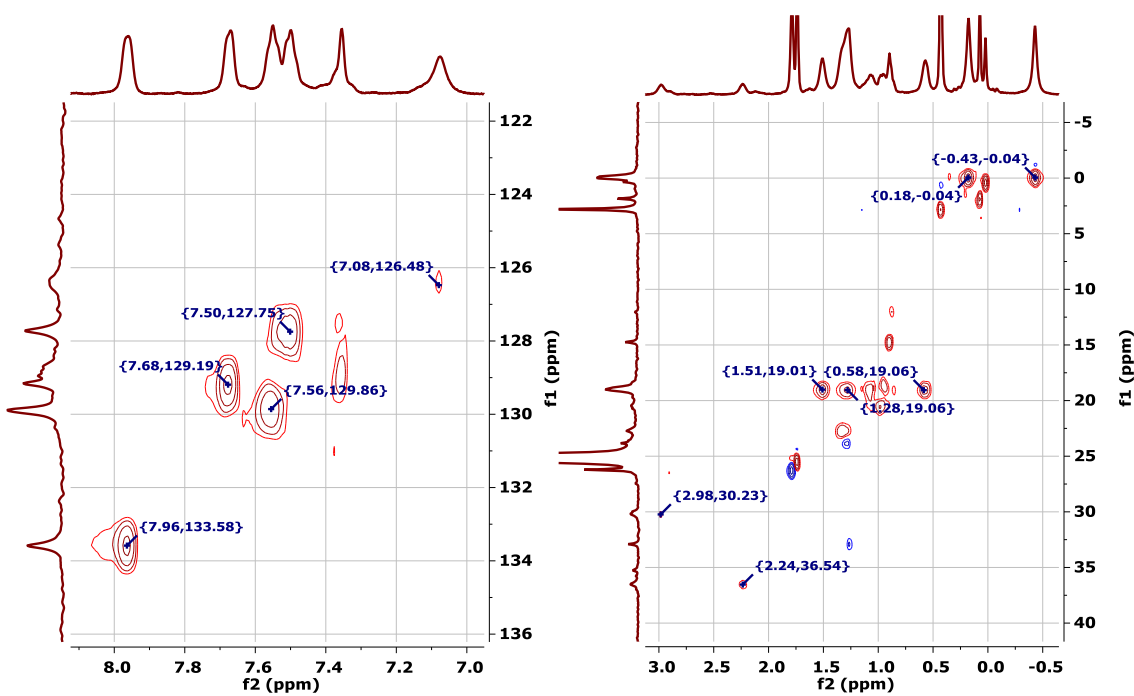


**Figure C.41.** Partial  $^1\text{H}/^{13}\text{C}$  HSQC NMR spectra (500/126 MHz,  $\text{THF-}d_8$ ,  $-80^\circ\text{C}$ ) of a mixture of  $2\text{-}^{13}\text{C}$  (3%),  $9\text{-}^{13}\text{C}$  (87%), and  $10\text{-}^{13}\text{C}$  (10%). The cross peaks attributable to the aryl (left) and alkyl (right) resonances of  $9\text{-}^{13}\text{C}$  are labeled.

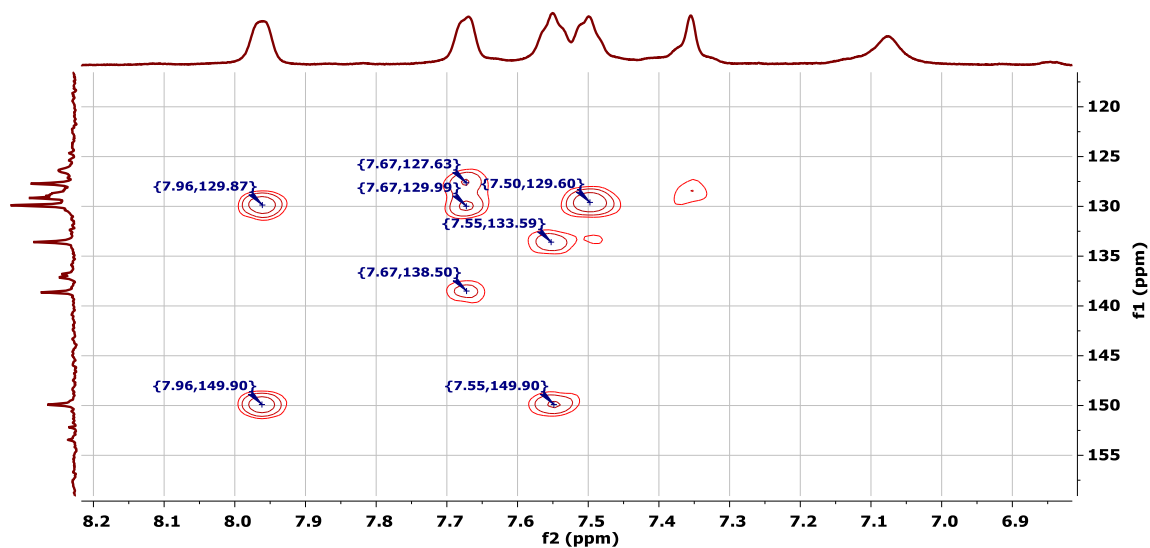


**Figure C.42.** Partial  $^1\text{H}/^{13}\text{C}$  HMBC NMR spectrum (500/126 MHz,  $\text{THF}-d_8$ ,  $-80^\circ\text{C}$ ) of a mixture  $2\text{-}^{13}\text{C}$  (3%),  $9\text{-}^{13}\text{C}$  (87%), and  $10\text{-}^{13}\text{C}$  (10%). The cross peaks attributable to the aryl resonances of  $9\text{-}^{13}\text{C}$  are labeled.

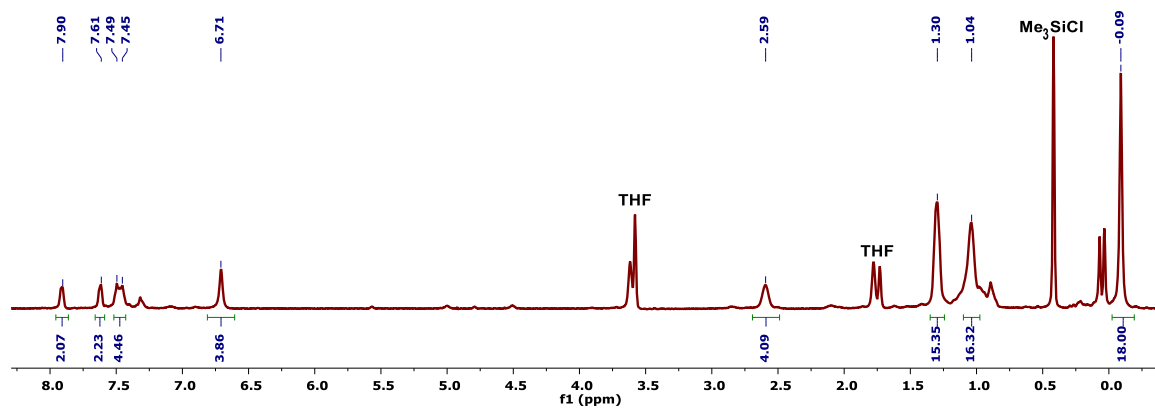


**Figure C.43.**  $^1\text{H}$  NMR Spectrum (500 MHz,  $\text{THF}-d_8$ ,  $-20^\circ\text{C}$ ) of a mixture of  $2\text{-}^{13}\text{C}$  (5%),  $9\text{-}^{13}\text{C}$  (82%), and  $10\text{-}^{13}\text{C}$  (13%).

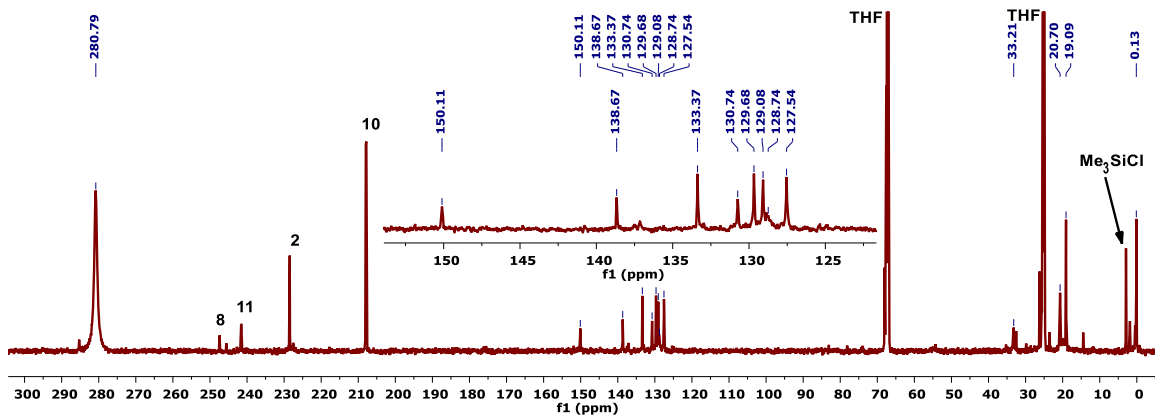


**Figure C.44.**  $^{13}\text{C}\{^1\text{H}\}$  NMR Spectrum (126 MHz, THF- $d_8$ ,  $-20^\circ\text{C}$ ) of a mixture of  $2\text{-}^{13}\text{C}$  (5%),  $9\text{-}^{13}\text{C}$  (82%), and  $10\text{-}^{13}\text{C}$  (13%). Over the course of the NMR experiment, trace amounts of  $11\text{-}^{13}\text{C}$  and  $8\text{-}^{13}\text{C}$  were formed. The inset shows an enlargement of the aryl region.

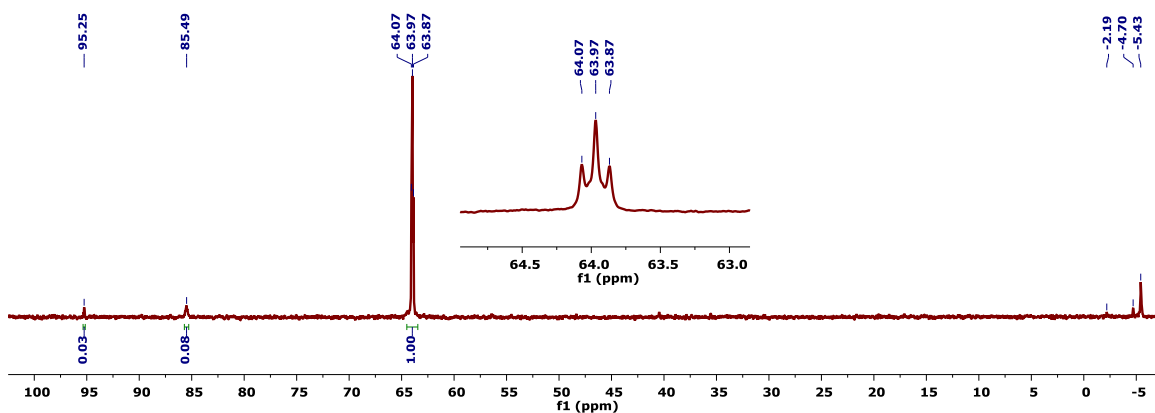


**Figure C.45.**  $^{31}\text{P}\{^1\text{H}\}$  NMR Spectrum (202 MHz, THF- $d_8$ ,  $-20^\circ\text{C}$ ) of a mixture of  $2\text{-}^{13}\text{C}$  (5%),  $9\text{-}^{13}\text{C}$  (82%), and  $10\text{-}^{13}\text{C}$  (13%). The inset shows an enlargement of the triplet assigned to  $9\text{-}^{13}\text{C}$ .

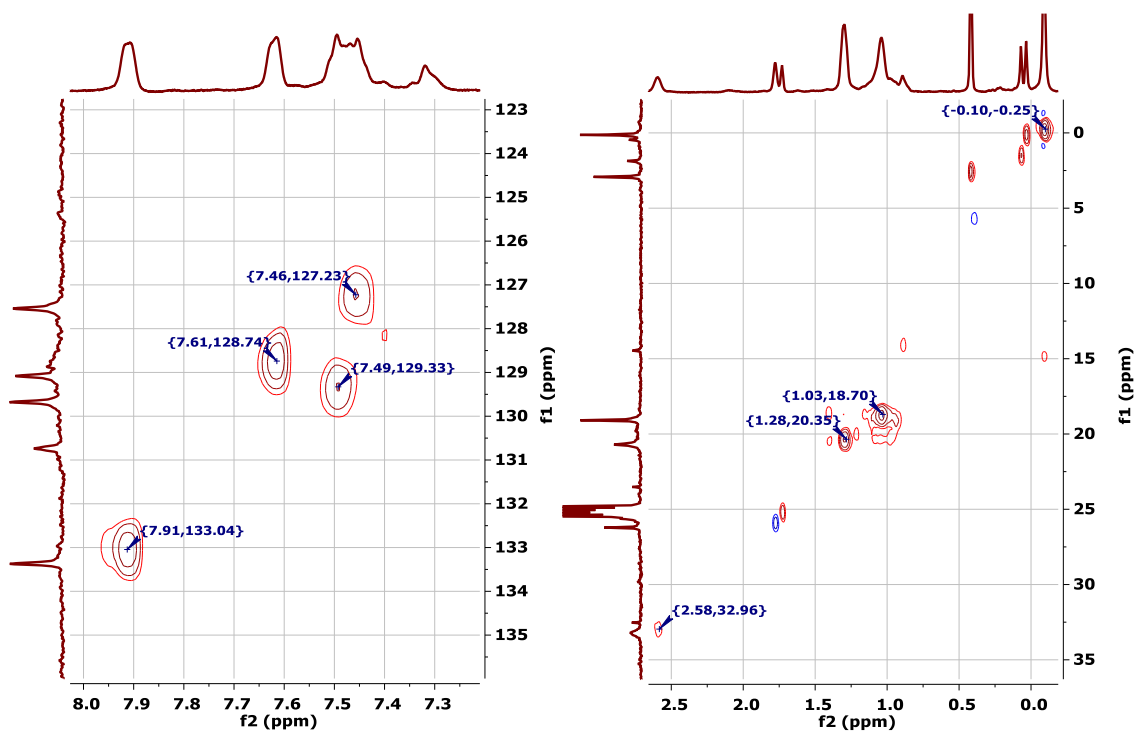


**Figure C.46.** Partial  $^1\text{H}/^{13}\text{C}$  HSQC NMR spectra (500/126 MHz,  $\text{THF-}d_8$ ,  $-80^\circ\text{C}$ ) of a mixture of  $2\text{-}^{13}\text{C}$  (5%),  $9\text{-}^{13}\text{C}$  (82%), and  $10\text{-}^{13}\text{C}$  (13%). The cross peaks attributable to the aryl (left) and alkyl (right) resonances of  $9\text{-}^{13}\text{C}$  are labeled.

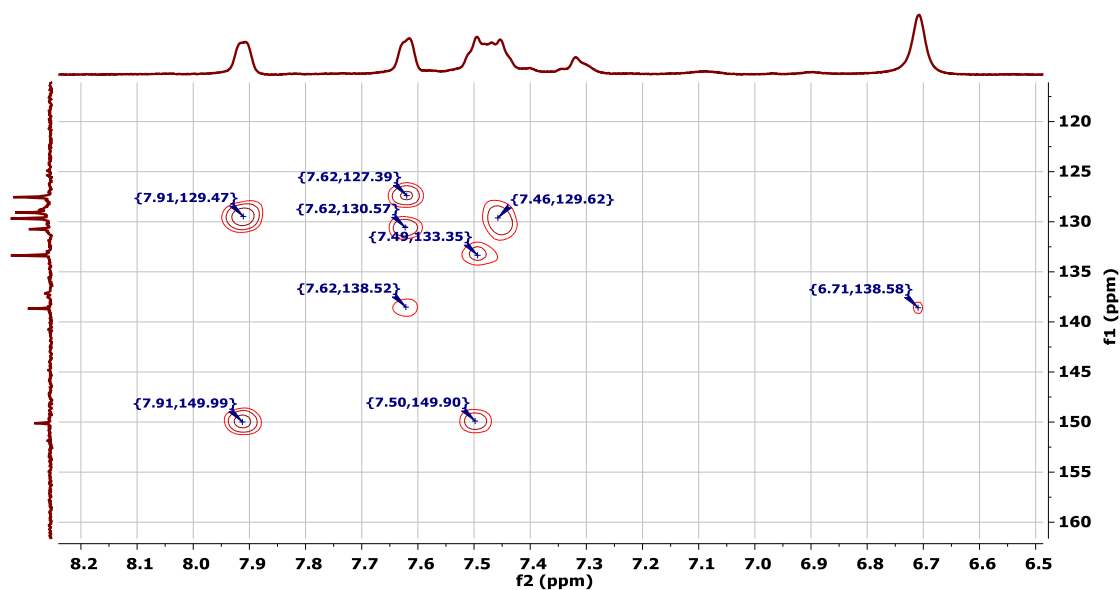


**Figure C.47.** Partial  $^1\text{H}/^{13}\text{C}$  HMBC NMR spectrum (500/126 MHz,  $\text{THF-}d_8$ ,  $-80^\circ\text{C}$ ) of a mixture of  $2\text{-}^{13}\text{C}$  (5%),  $9\text{-}^{13}\text{C}$  (82%), and  $10\text{-}^{13}\text{C}$  (13%). The cross peaks attributable to the aryl resonances of  $9\text{-}^{13}\text{C}$  are labeled.

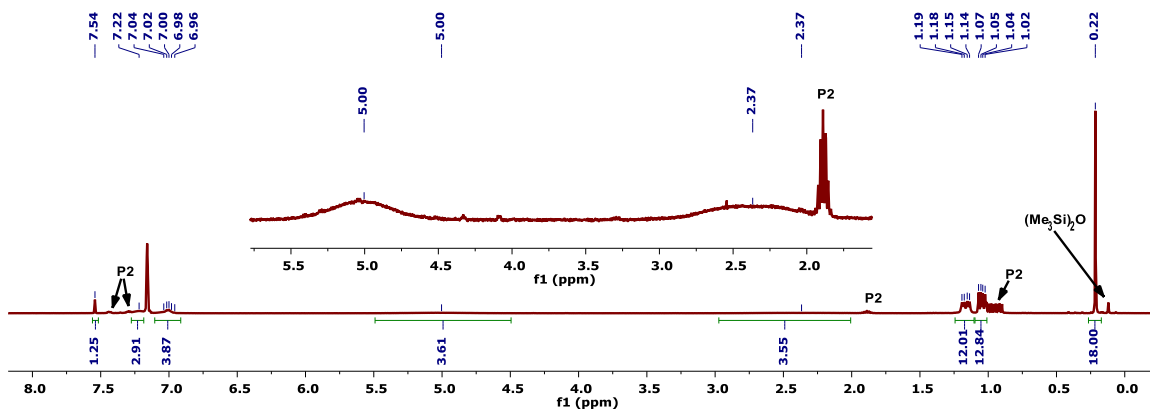


**Figure C.48.**  $^1\text{H}$  NMR Spectrum (400 MHz,  $\text{C}_6\text{D}_6$ ,  $23^\circ\text{C}$ ) of a 75:25 mixture of **10** and free diphosphine (P2). The inset shows broad resonances associated with the central arene and isopropyl methine resonances of **10** at 5.00 and 2.37 ppm, respectively. The sharper multiplet centered at 1.89 ppm is the isopropyl methine resonance of the free diphosphine ligand.

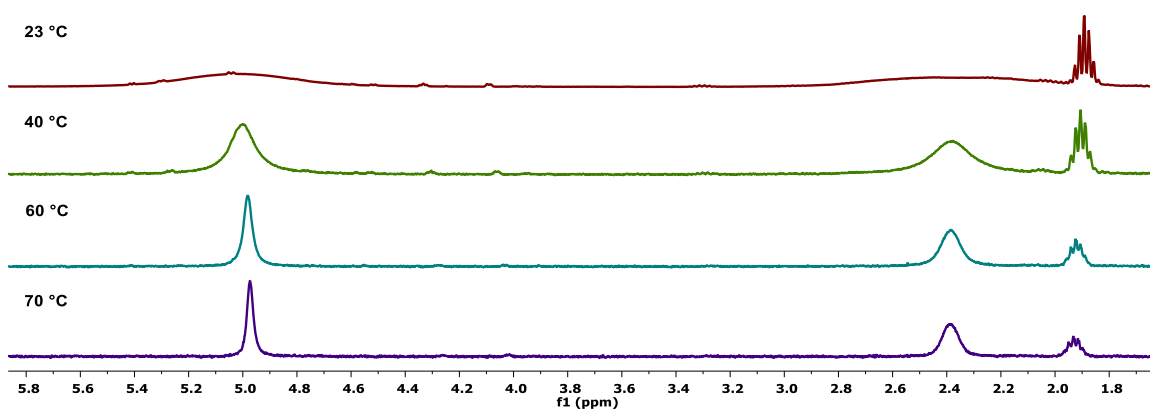


**Figure C.49.** Partial  $^1\text{H}$  NMR Spectra (400 MHz,  $\text{C}_6\text{D}_6$ ) of a 75:25 mixture of **10** and free diphosphine (P2) from 23 to  $70^\circ\text{C}$ ., showing the temperature dependent breadth of the central arene and isopropyl methine resonances.

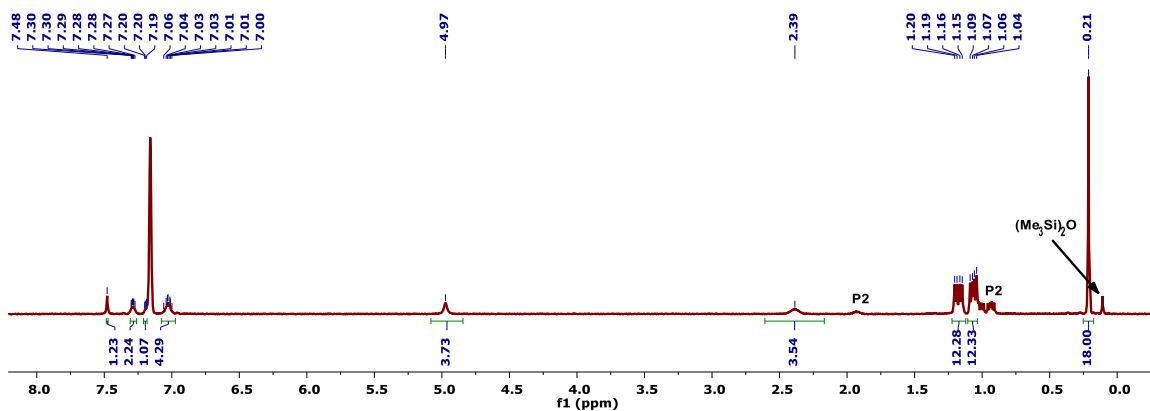


**Figure C.50.**  $^1\text{H}$  NMR Spectrum (400 MHz,  $\text{C}_6\text{D}_6$ ,  $70^\circ\text{C}$ ) of a 75:25 mixture of **10** and free diphosphine (P2).



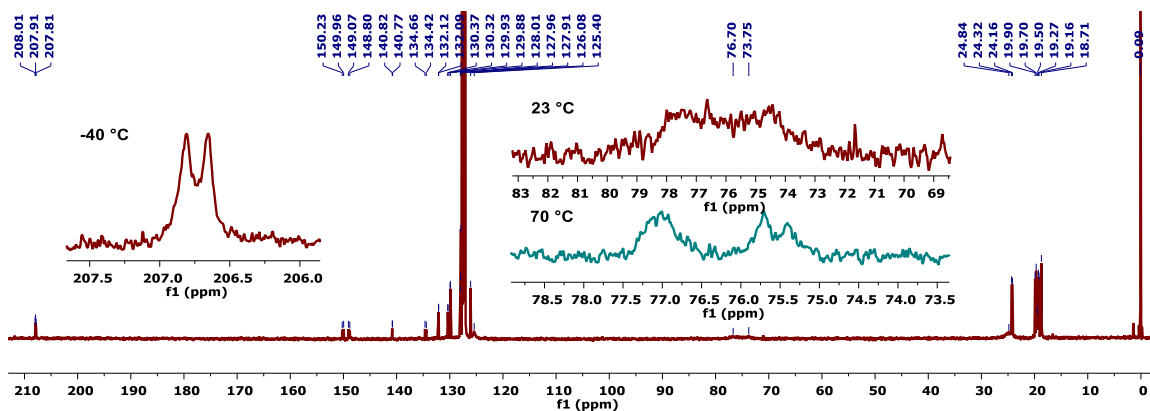


**Figure C.51.**  $^{13}\text{C}\{^1\text{H}\}$  NMR Spectrum (162 MHz,  $\text{C}_6\text{D}_6$ ,  $23^\circ\text{C}$ ) of a 75:25 mixture of **10** and free diphosphine (P2). The left inset shows the resolved  $^{31}\text{P}/^{13}\text{C}$  scalar coupling in  $^{10}\text{-}^{13}\text{C}$  at  $-40^\circ\text{C}$ . The right inset shows the central arene carbon resonances of **10** at  $23$  (top right) and  $70$  (bottom right)  $^\circ\text{C}$ .

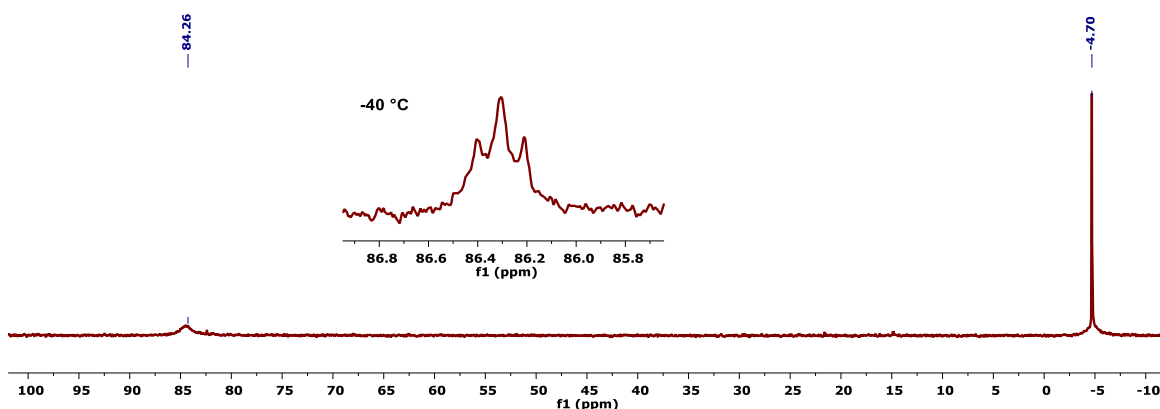


**Figure C.52.**  $^{31}\text{P}\{^1\text{H}\}$  NMR Spectrum (162 MHz,  $\text{C}_6\text{D}_6$ ,  $23^\circ\text{C}$ ) of a 75:25 mixture of **10** and free diphosphine (P2). The resonance for the free phosphine arm of **10** coincides with that of the free ligand. The inset shows the triplet assigned to the bound phosphine arm of  $^{10}\text{-}^{13}\text{C}$  ( $202.4$  MHz, THF,  $-40^\circ\text{C}$ ) displaying a  $^2J(\text{P,C})$  of  $19.57$  Hz.

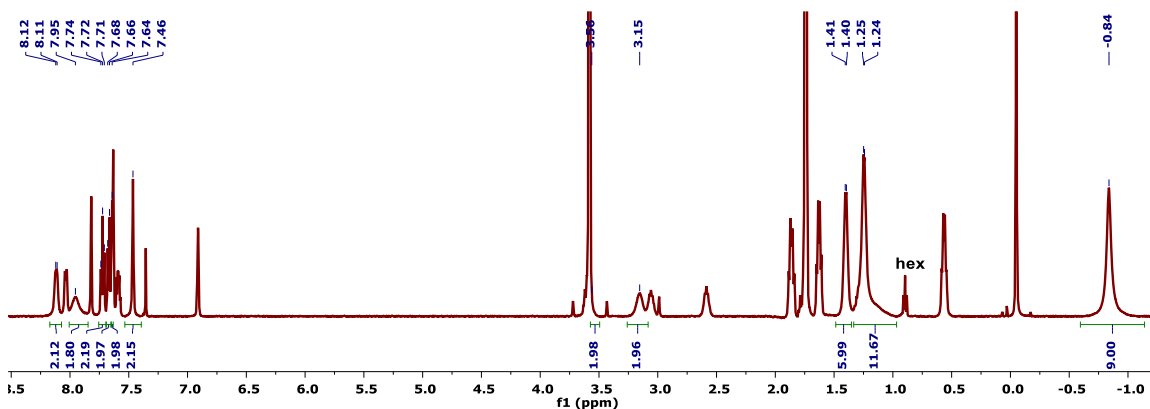


**Figure C.53.**  $^1\text{H}$  NMR Spectrum (500 MHz,  $\text{THF-}d_8$ ,  $-80^\circ\text{C}$ ) of a mixture of **11** (56%) and **8** (44%).

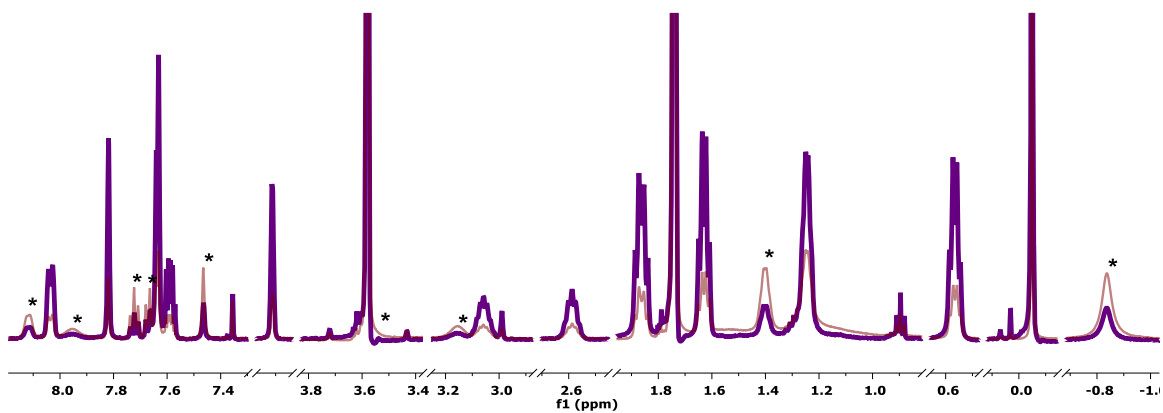


**Figure C.54.** Stacked  $^1\text{H}$  NMR Spectrum (500 MHz,  $\text{THF-}d_8$ ,  $-80^\circ\text{C}$ ) of the same mixture of **11** (56%) and **8** (44%) after 30 minutes at room temperature (14% **11**/86% **8**). The asterisks denote peaks unambiguously assigned to **11**.

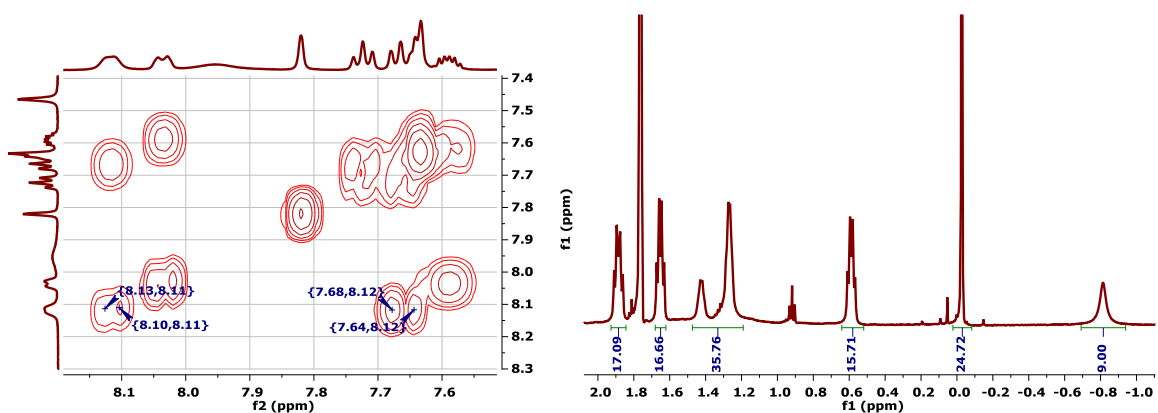


**Figure C.55.** Partial  $^1\text{H}/^1\text{H}$  COSY NMR spectrum showing a correlation between the aryl proton signal of **11** at 8.12 ppm and a proton resonance of **11** at 7.64 ppm; this proton's chemical shift coincides with that of an aryl proton in **8** (7.63 ppm) (left). Partial  $^1\text{H}$  NMR spectrum showing that the isopropyl methyl protons of **11** resonate as two multiplets (1.42 and 1.27 ppm). The integration of these resonances sums to *ca.* 18H relative to the trimethylsilyl group after subtracting the coincidental isopropyl methyl resonance of **8** at 1.27 ppm (16-17H in the same relative integration scale, right).

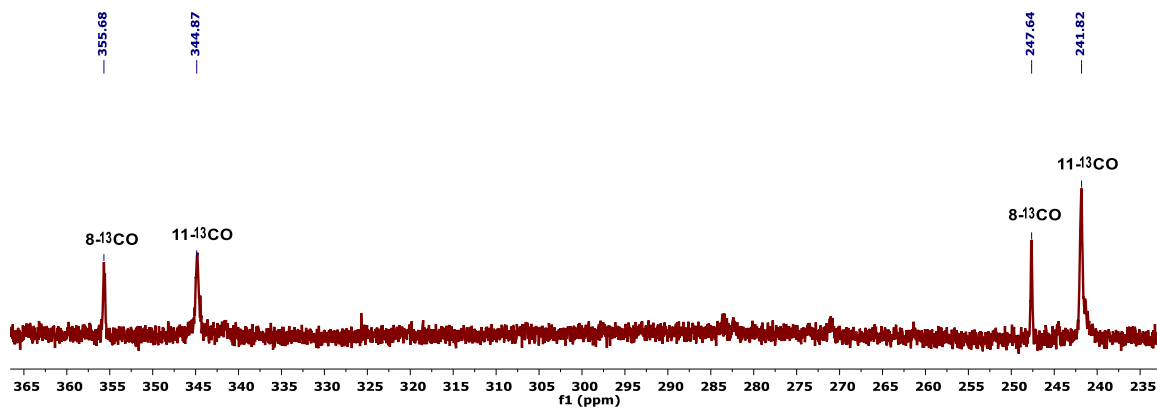


**Figure C.56.** Partial  $^{13}\text{C}\{^1\text{H}\}$  NMR Spectrum (202 MHz, THF,  $-80^\circ\text{C}$ ) of a mixture of **11** (74%) and **8** (26%). At this temperature, the resonances are broad and the  $^2J(\text{P},\text{C})$  cannot be resolved.

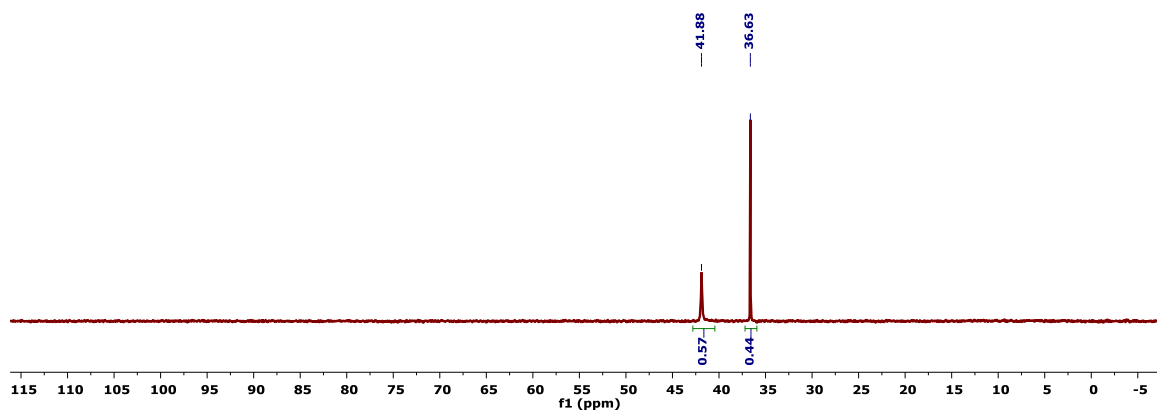


**Figure C.57.**  $^{31}\text{P}\{^1\text{H}\}$  NMR Spectrum (202 MHz, THF- $d_8$ ,  $-80^\circ\text{C}$ ) of a mixture of **11** and **8**.

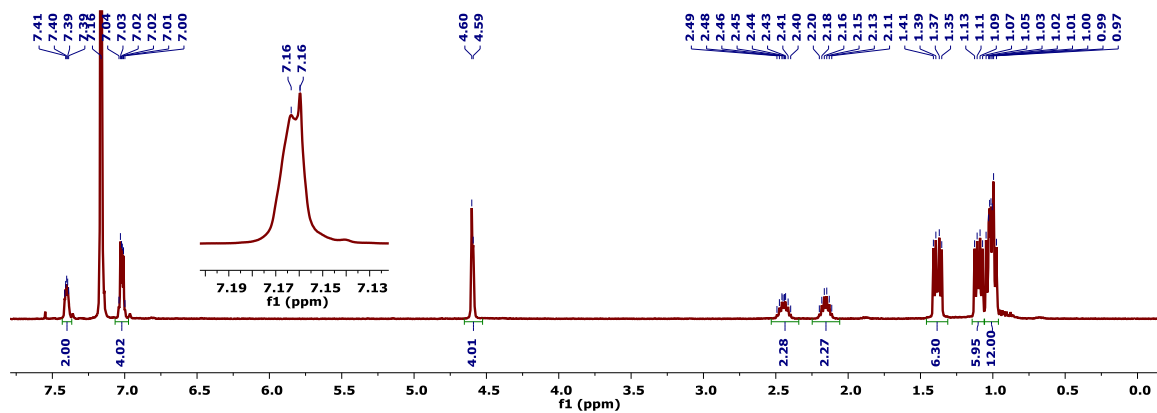


**Figure C.58.**  $^1\text{H}$  NMR Spectrum (400 MHz,  $\text{C}_6\text{D}_6$ ,  $23^\circ\text{C}$ ) of **16**. The inset shows a phenylene proton resonance that coincides with residual  $\text{C}_6\text{D}_5\text{H}$  at 7.16 ppm.

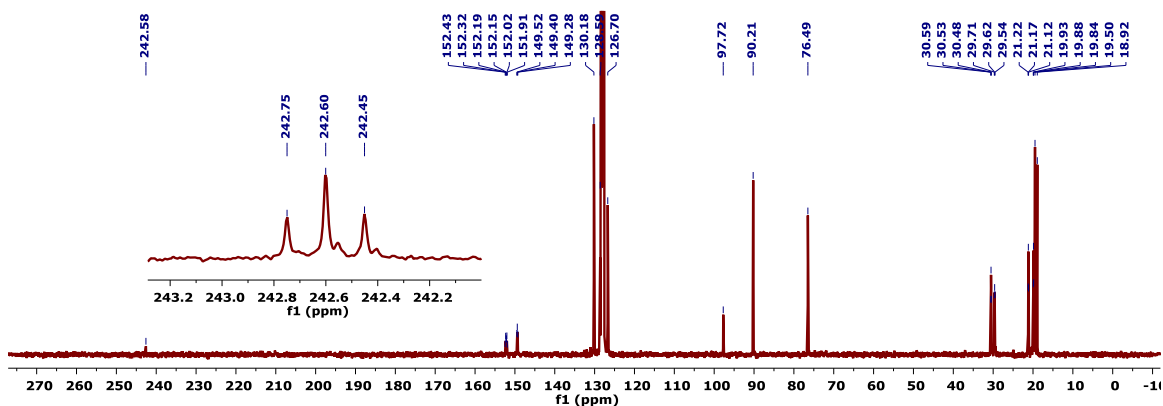


**Figure C.59.**  $^{13}\text{C}\{^1\text{H}\}$  NMR Spectrum (101 MHz,  $\text{C}_6\text{D}_6$ , 25°C) of **16**. The inset shows the enhanced  $^{13}\text{C}$  signals for  $16\text{-}^{13}\text{C}$ .

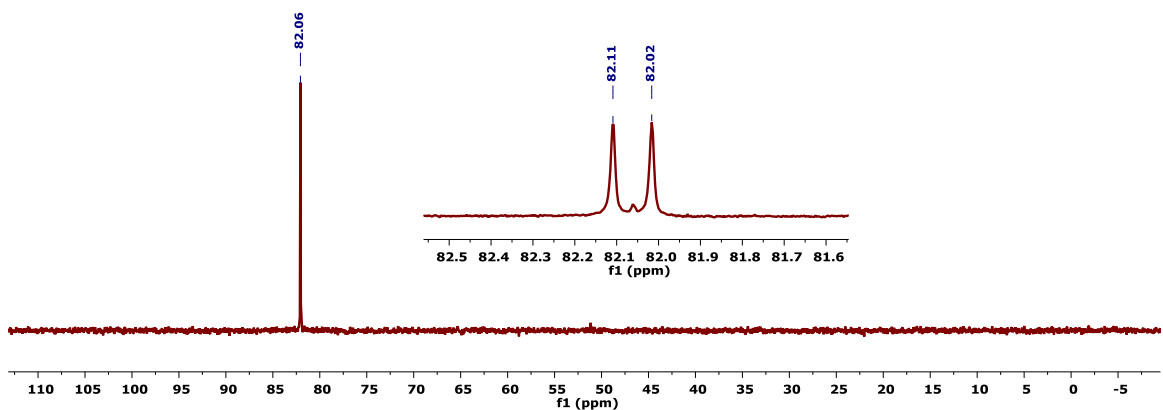


**Figure C.60.**  $^{31}\text{P}\{^1\text{H}\}$  NMR Spectrum (162 MHz,  $\text{C}_6\text{D}_6$ , 25°C) of **16**. The inset shows a partial  $^{31}\text{P}\{^1\text{H}\}$  NMR spectrum for  $16\text{-}^{13}\text{C}$ .

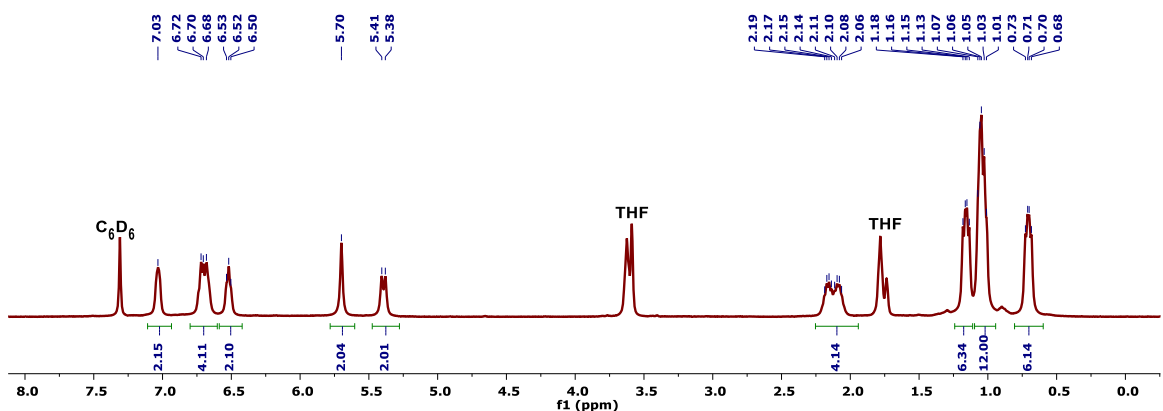


**Figure C.61.**  $^1\text{H}$  NMR Spectrum (400 MHz,  $\text{THF}\text{-}d_8$ , 23°C) of  $17\text{-}^{13}\text{C}$ .

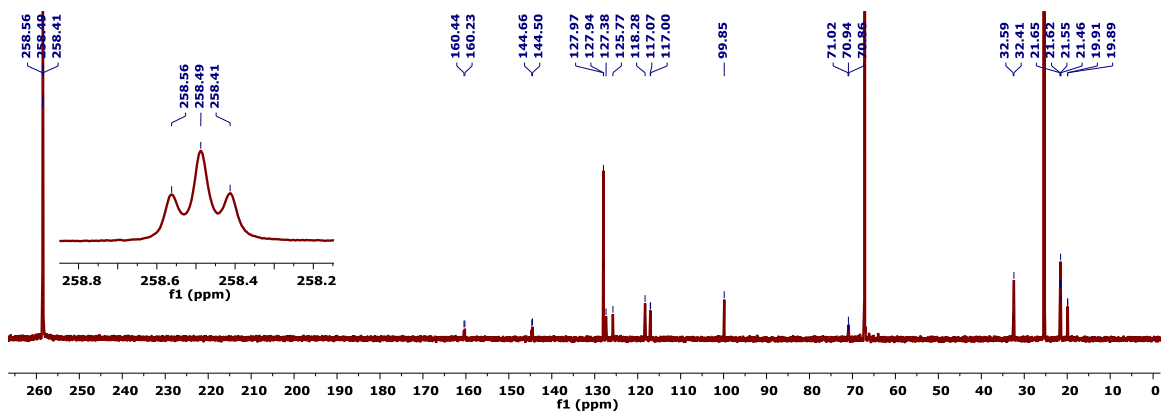


**Figure C.62.**  $^{13}\text{C}\{^1\text{H}\}$  NMR Spectrum (101 MHz, THF, 23°C) of  $17\text{-}^{13}\text{C}$ . The inset shows an enlargement of the resonance corresponding to the isotopically enriched carbonyl carbon.

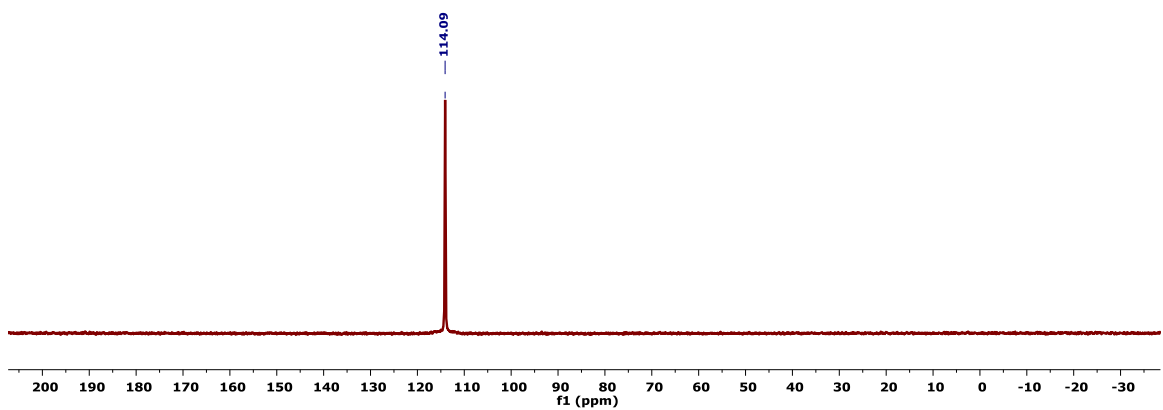


**Figure C.63.**  $^{31}\text{P}\{^1\text{H}\}$  NMR Spectrum (162 MHz, THF, 23°C) of  $17\text{-}^{13}\text{C}$ .

## CHAPTER 4

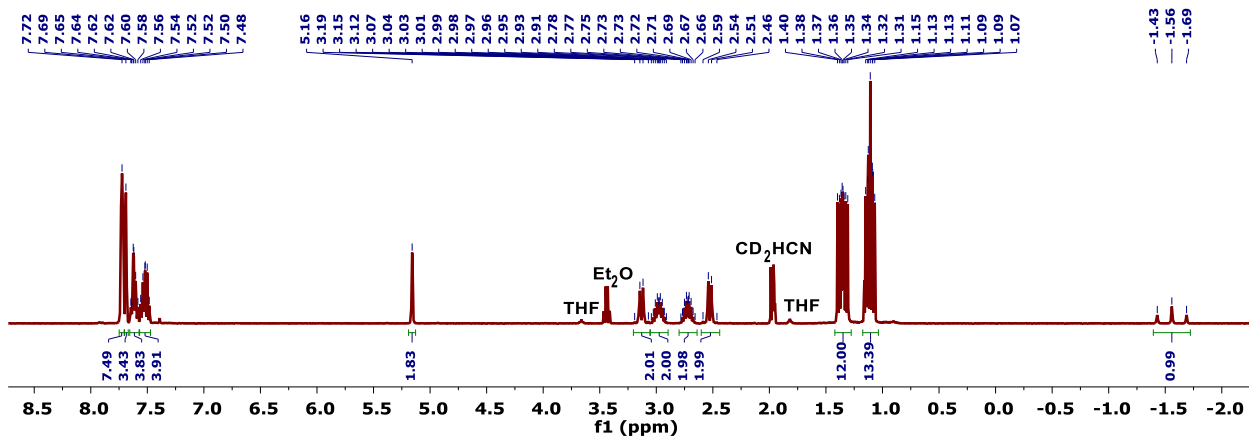


Figure C.64. <sup>1</sup>H NMR Spectrum (400 MHz, CD<sub>3</sub>CN, 23°C) of 2.

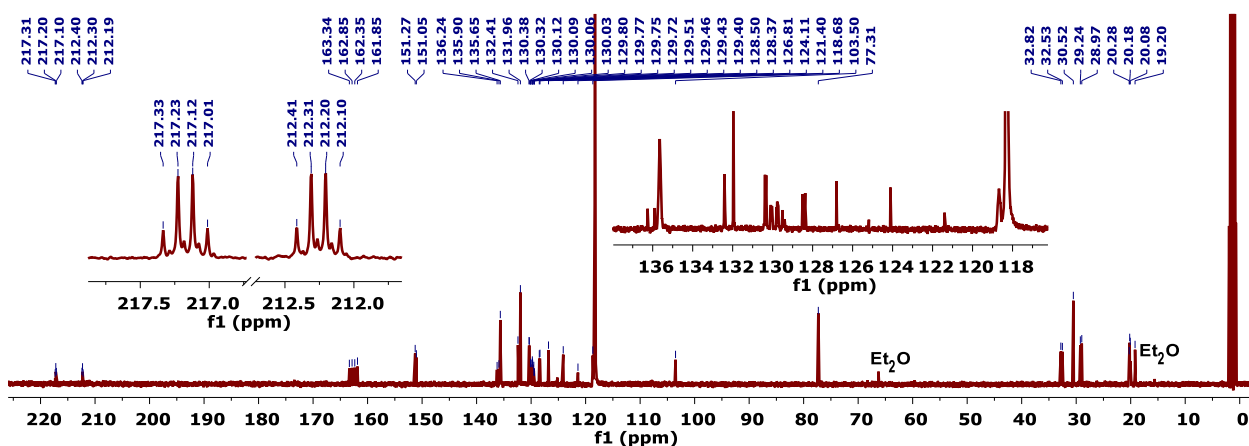


Figure C.65. <sup>13</sup>C{<sup>1</sup>H} NMR Spectrum (101 MHz, CD<sub>3</sub>CN, 23°C) of 2. The insets show the CO resonances of 2-<sup>13</sup>C (left) and an enlargement of the aryl region (right).

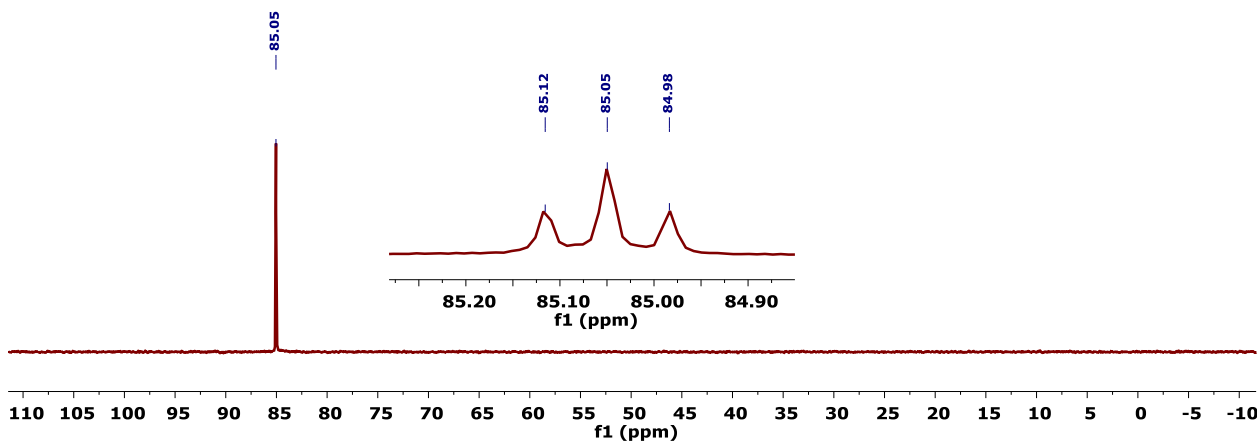
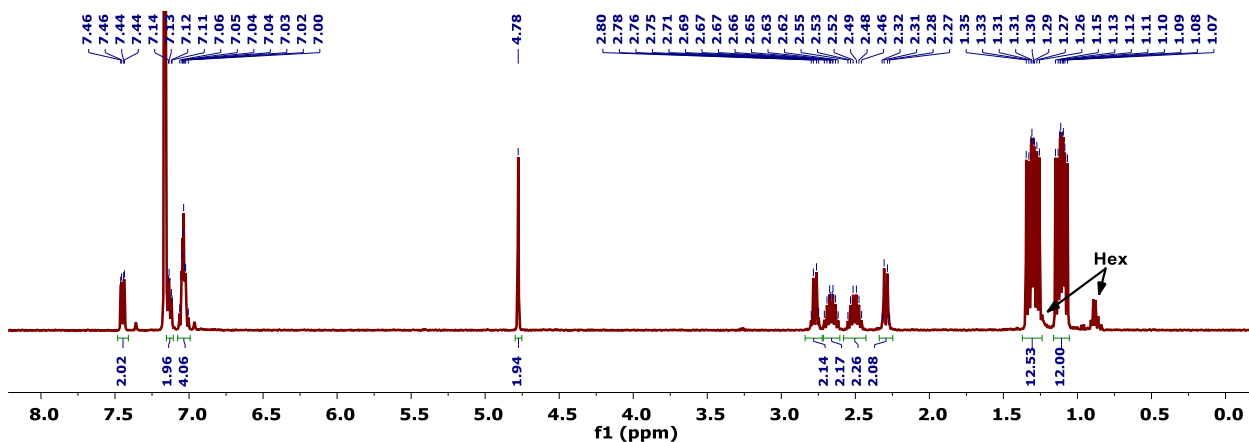
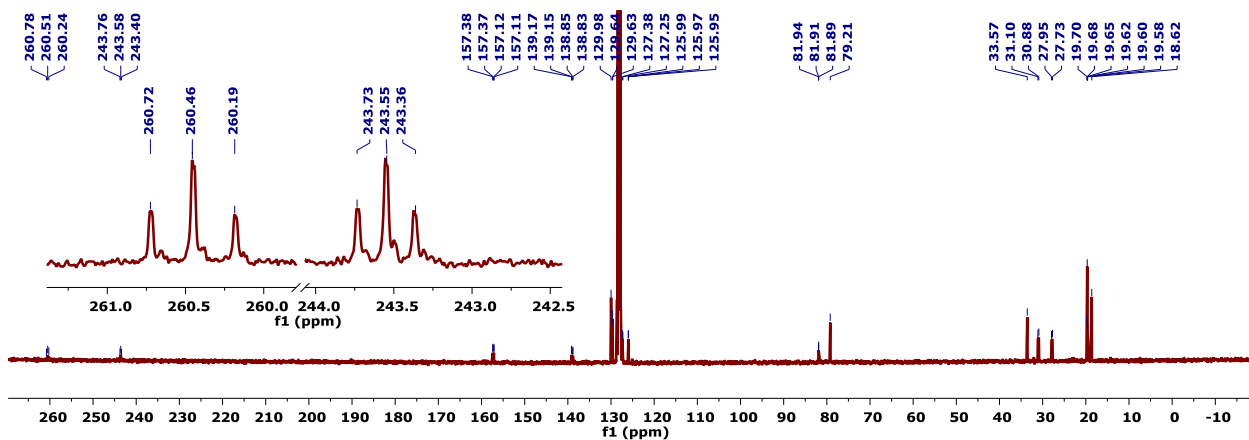


Figure C.66. <sup>31</sup>P{<sup>1</sup>H} NMR Spectrum (162 MHz, C<sub>6</sub>D<sub>6</sub>, 23°C) of 2. The inset shows the partial <sup>31</sup>P{<sup>1</sup>H} NMR spectrum of 2-<sup>13</sup>C.



**Figure C.67.**  $^1\text{H}$  NMR Spectrum (400 MHz,  $\text{C}_6\text{D}_6$ , 23  $^\circ\text{C}$ ) of **3**. An *n*-hexane solvent impurity coincides with the upfield portion of the downfield isopropyl methyl multiplets, resulting in an inflated integral for these resonances.



**Figure C.68.**  $^{13}\text{C}\{^1\text{H}\}$  NMR Spectrum (101 MHz,  $\text{C}_6\text{D}_6$ , 25 $^\circ\text{C}$ ) of **3**. The inset shows the enhanced  $^{13}\text{C}$  signals for **3**- $^{13}\text{C}$ .

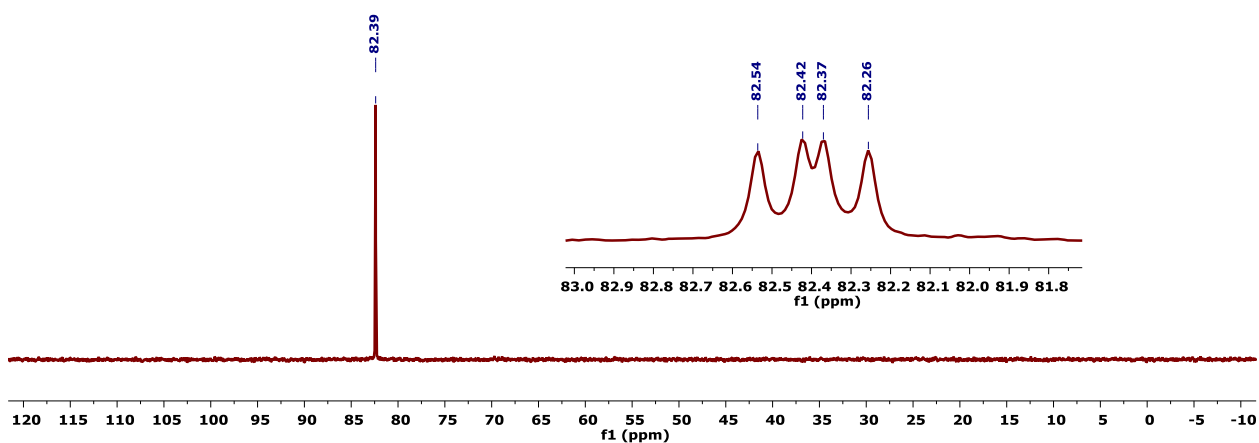


**Figure C.69.**  $^{31}\text{P}\{^1\text{H}\}$  NMR Spectrum (162 MHz,  $\text{C}_6\text{D}_6$ , 25 $^\circ\text{C}$ ) of **3**. The inset shows a partial  $^{31}\text{P}\{^1\text{H}\}$  NMR spectrum for **3**- $^{13}\text{C}$ .

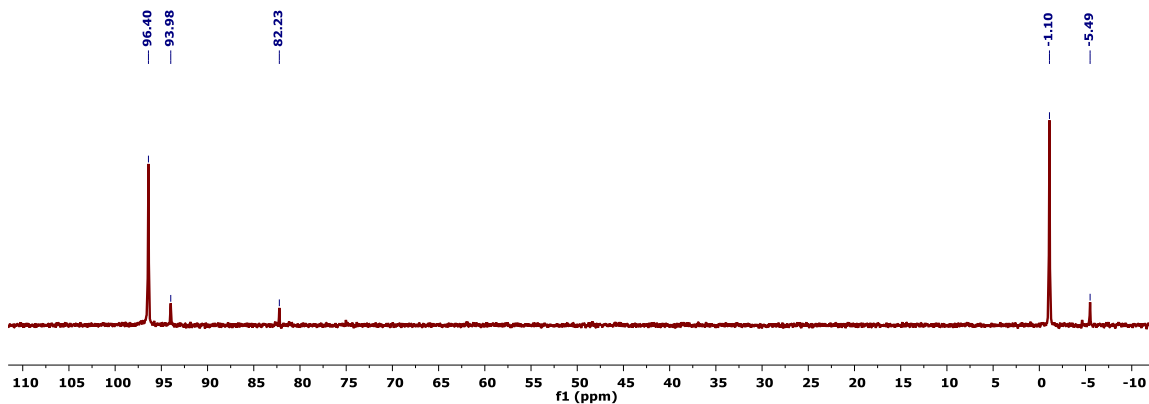


Figure C.70.  $^{31}\text{P}\{^1\text{H}\}$  NMR Spectrum (162 MHz,  $\text{C}_6\text{D}_6$ , 25°C) of 4.

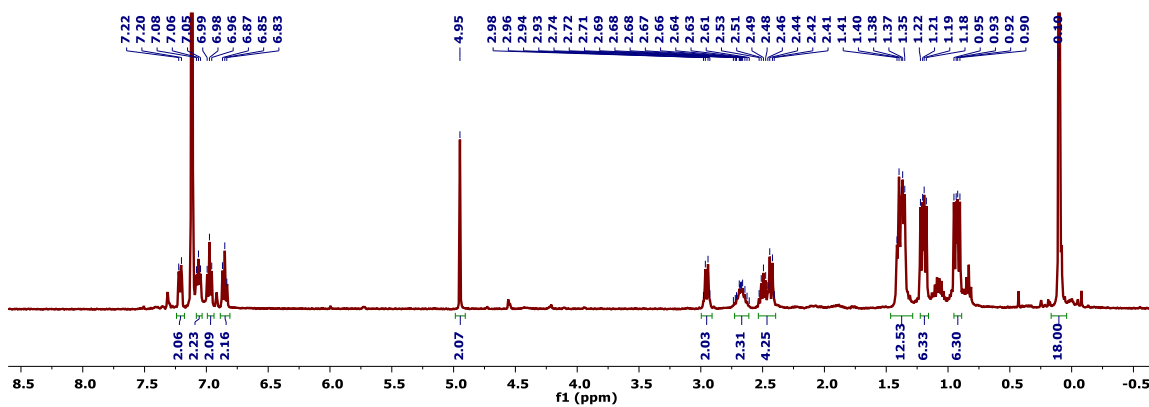


Figure C.71.  $^1\text{H}$  NMR Spectrum (400 MHz,  $\text{C}_6\text{D}_6$ , 23 °C) of 5.

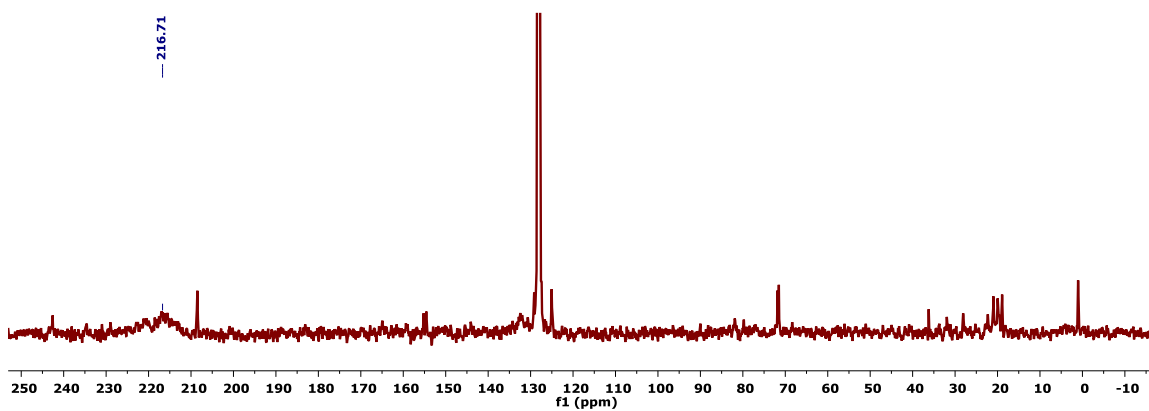


Figure C.72.  $^{13}\text{C}\{^1\text{H}\}$  NMR Spectrum (101 MHz,  $\text{C}_6\text{D}_6$ , 25°C) of 5.



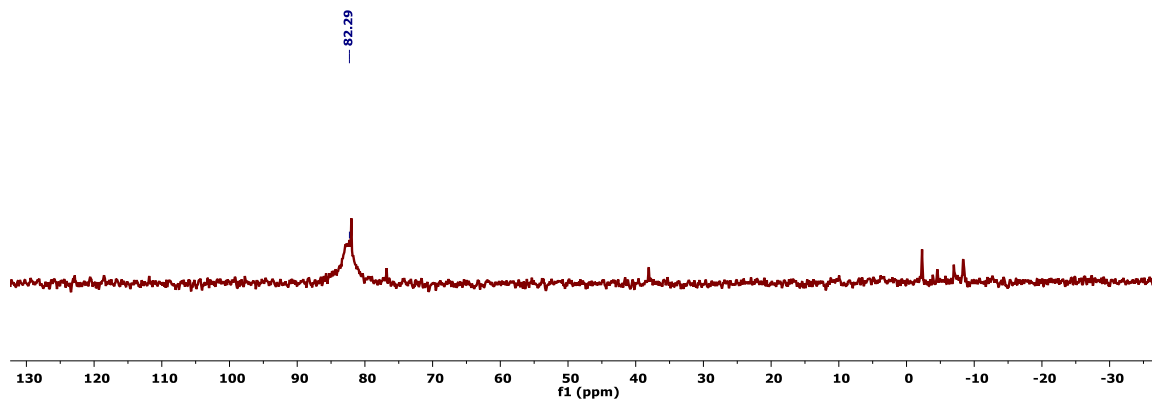


Figure C.73.  $^{31}\text{P}\{^1\text{H}\}$  NMR Spectrum (162 MHz,  $\text{C}_6\text{D}_6$ , 25°C) of **5**.

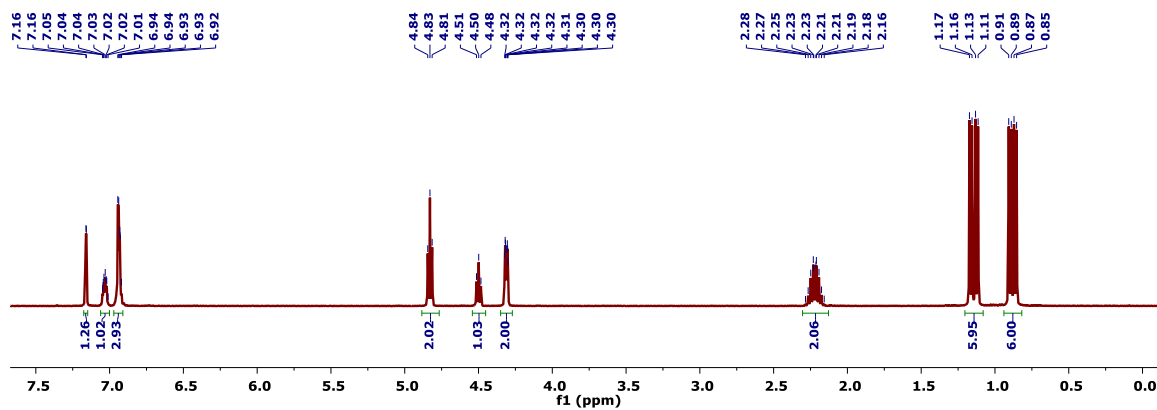


Figure C.74.  $^1\text{H}$  NMR Spectrum (400 MHz,  $\text{C}_6\text{D}_6$ , 23 °C) of **9**.

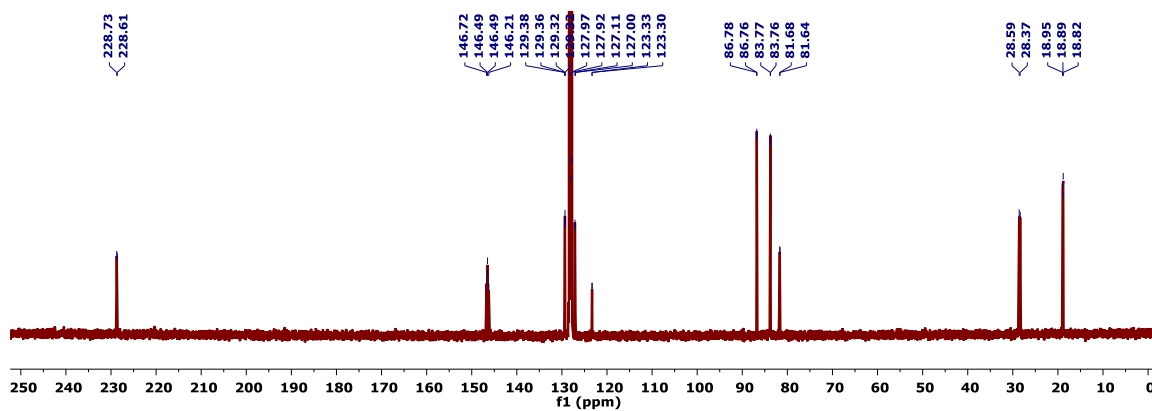


Figure C.75.  $^{13}\text{C}\{^1\text{H}\}$  NMR Spectrum (101 MHz,  $\text{C}_6\text{D}_6$ , 23°C) of **9**.

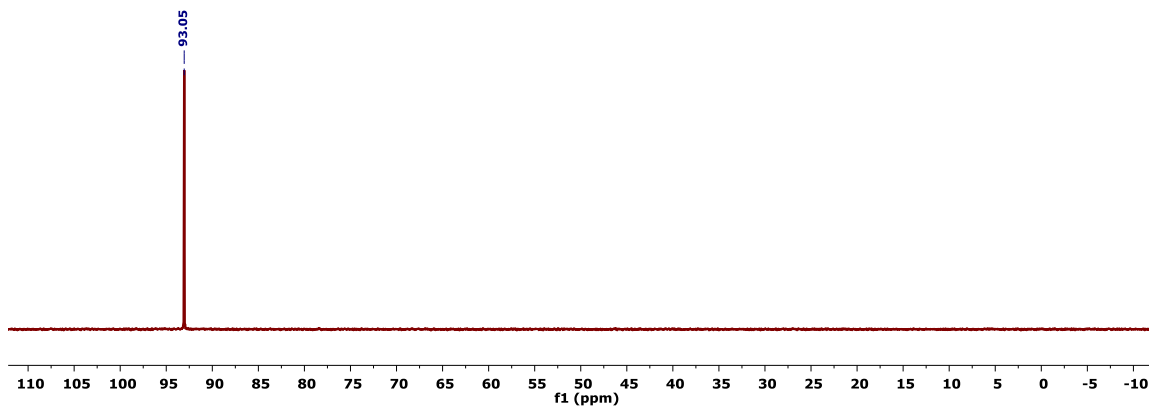


Figure C.76.  $^{31}\text{P}\{^1\text{H}\}$  NMR Spectrum (162 MHz,  $\text{C}_6\text{D}_6$ , 23°C) of **9**.

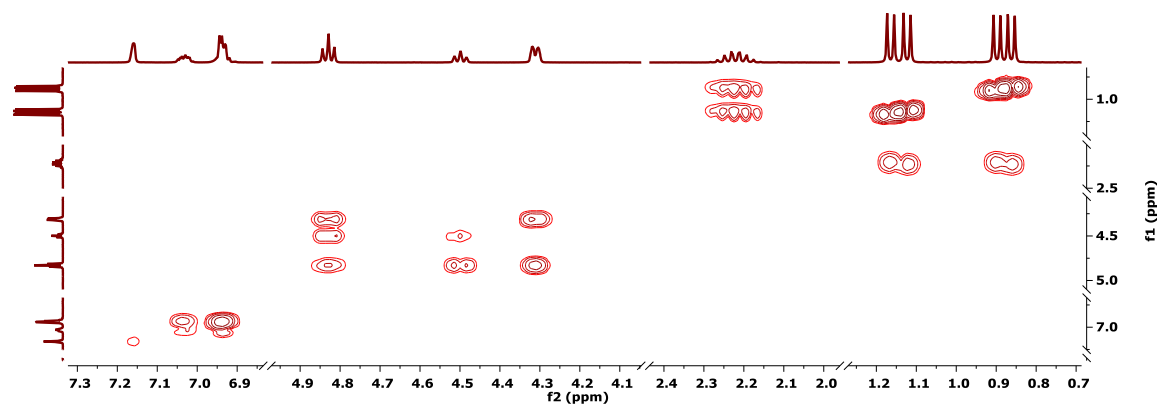


Figure C.77.  $^1\text{H}/^1\text{H}$  COSY NMR Spectrum (400 MHz,  $\text{C}_6\text{D}_6$ , 23°C) of **9**.

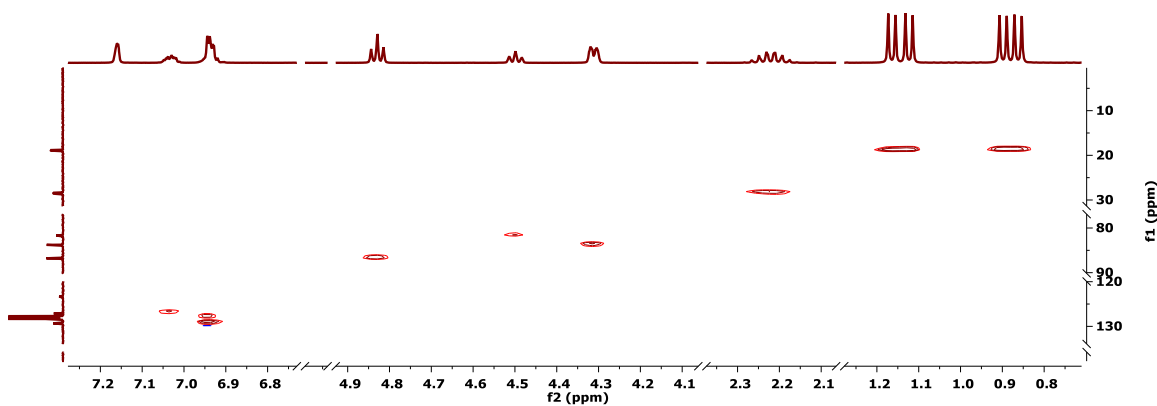


Figure C.78.  $^1\text{H}/^{13}\text{C}$  HSQC NMR Spectrum (400/101 MHz,  $\text{C}_6\text{D}_6$ , 23°C) of **9**.

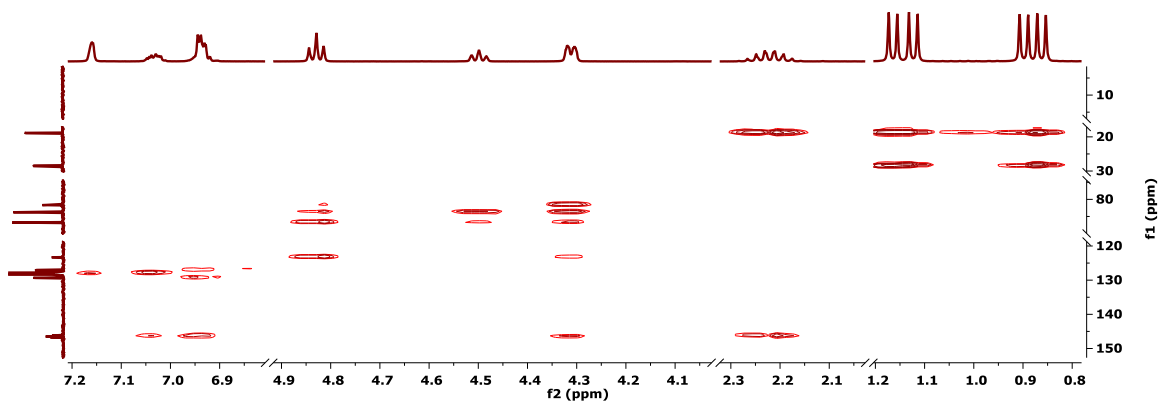


Figure C.79.  $^1\text{H}/^{13}\text{C}$  HMBC NMR Spectrum (400/101 MHz,  $\text{C}_6\text{D}_6$ , 23°C) of **9**.

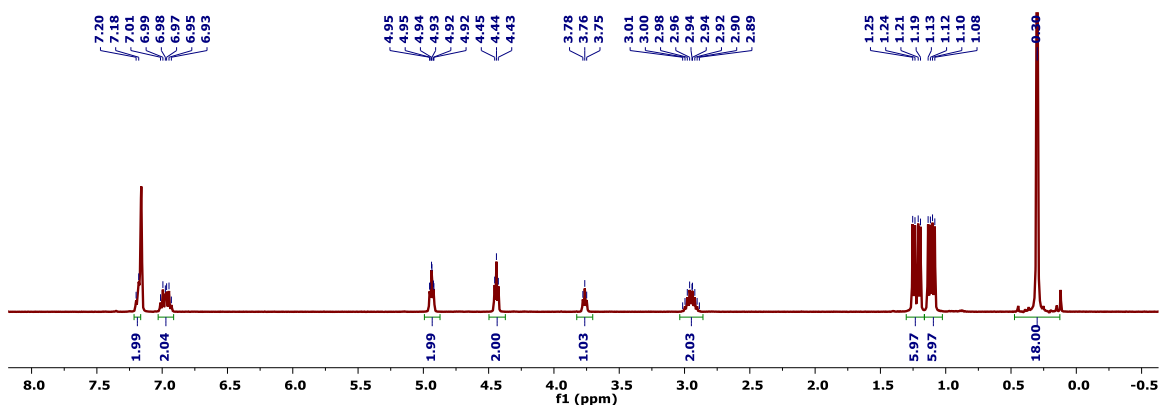


Figure C.80.  $^1\text{H}$  NMR Spectrum (400 MHz,  $\text{C}_6\text{D}_6$ , 23 °C) of **10**.

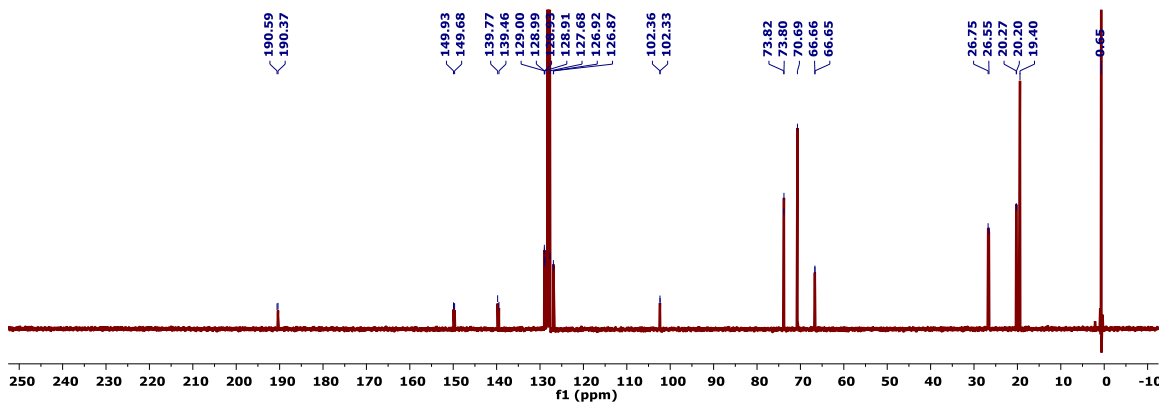


Figure C.81.  $^{13}\text{C}\{^1\text{H}\}$  NMR Spectrum (101 MHz,  $\text{C}_6\text{D}_6$ , 23°C) of **10**.

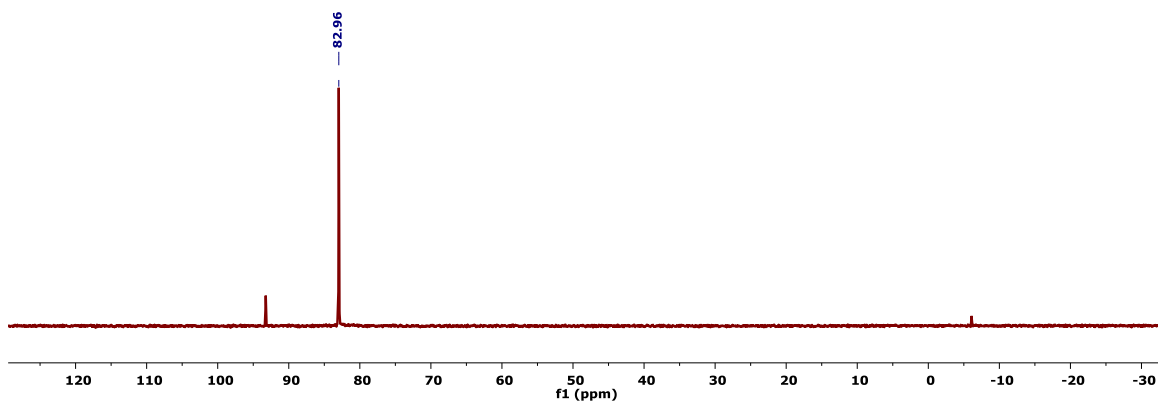


Figure C.82.  $^{31}\text{P}\{^1\text{H}\}$  NMR Spectrum (162 MHz,  $\text{C}_6\text{D}_6$ , 25°C) of **10**.

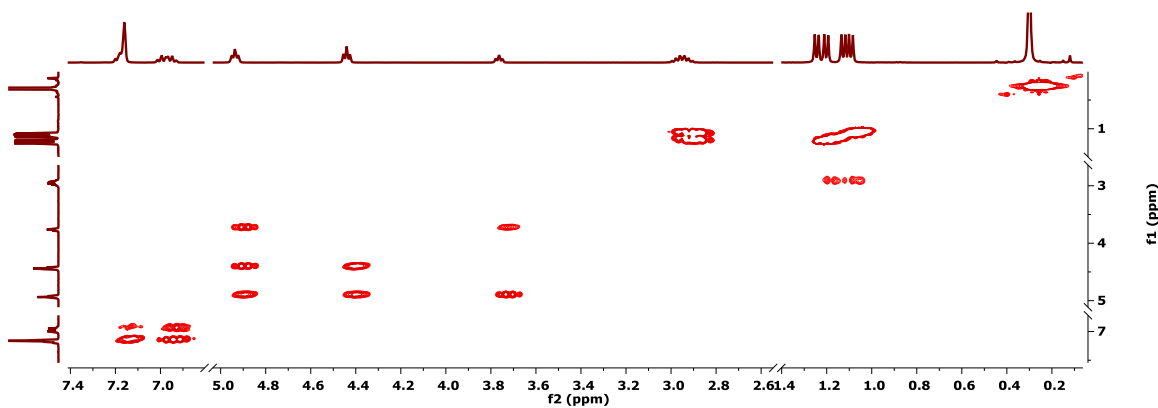


Figure C.83.  $^1\text{H}/^1\text{H}$  COSY NMR Spectrum (400 MHz,  $\text{C}_6\text{D}_6$ , 23°C) of **10**.

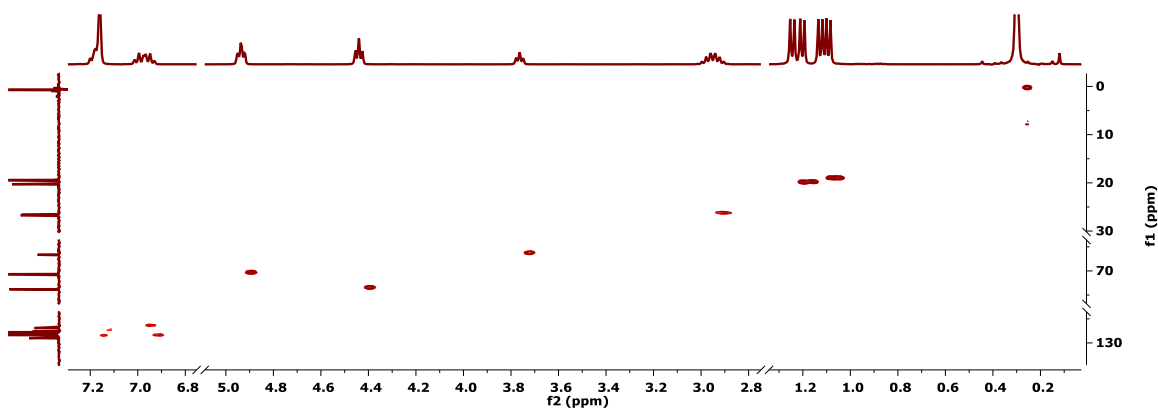


Figure C.84.  $^1\text{H}/^{13}\text{C}$  HSQC NMR Spectrum (400/101 MHz,  $\text{C}_6\text{D}_6$ , 23°C) of **10**.

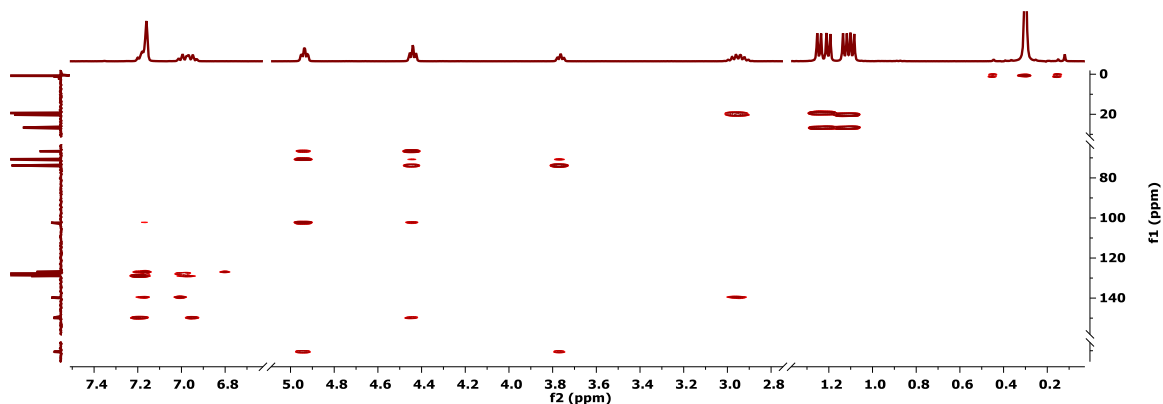


Figure C.85.  $^1\text{H}/^{13}\text{C}$  HMBC NMR Spectrum (400/101 MHz,  $\text{C}_6\text{D}_6$ , 23°C) of **10**.

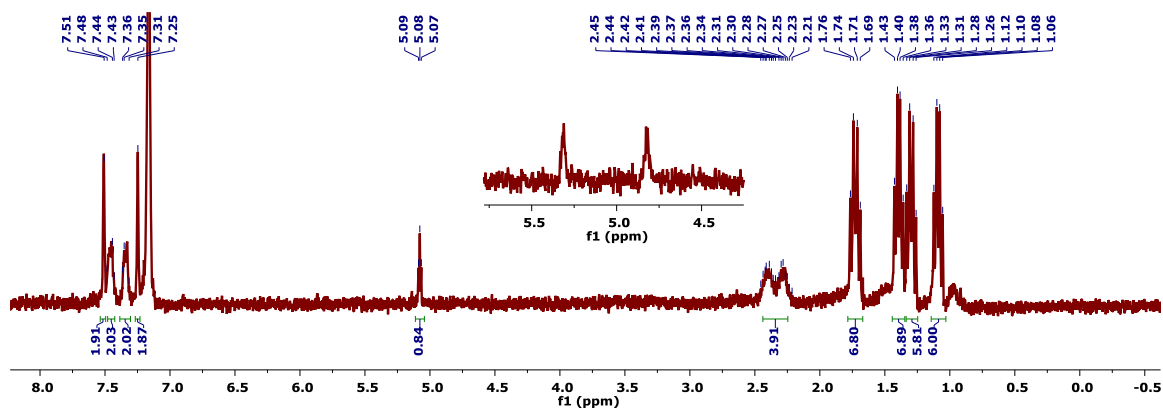


Figure C.86.  $^1\text{H}$  NMR Spectrum (300 MHz,  $\text{C}_6\text{D}_6$ , 23 °C) of **19**.

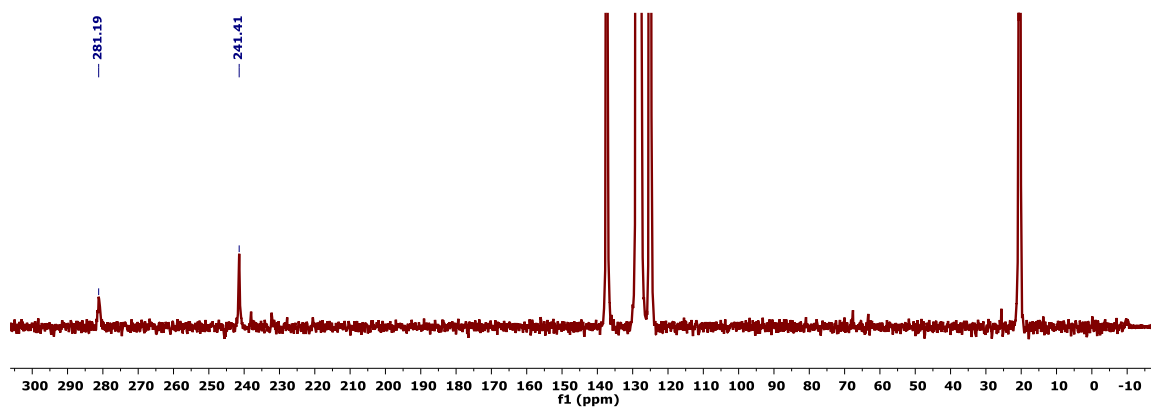


Figure C.87.  $^{13}\text{C}\{^1\text{H}\}$  NMR Spectrum (126 MHz,  $\text{C}_7\text{D}_8$ , -78 °C) of **19- $^{13}\text{C}$** .

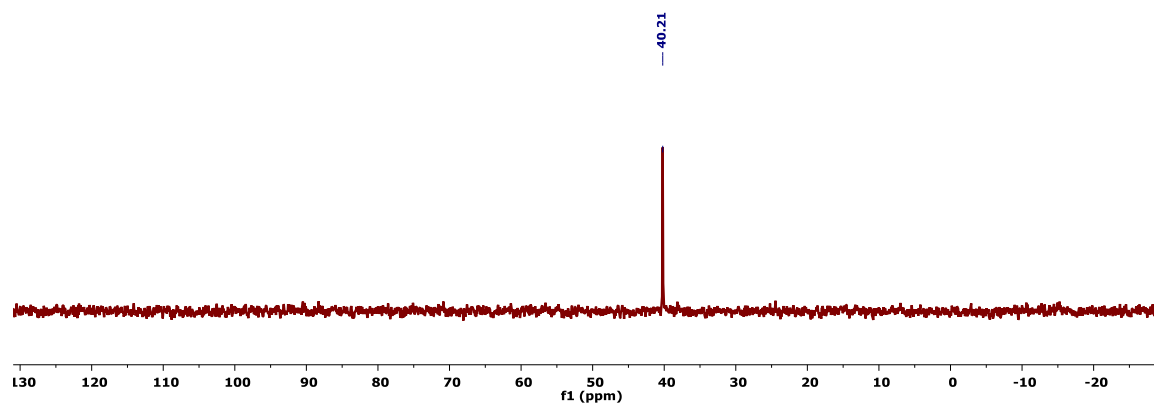


Figure C.88.  $^{31}\text{P}\{^1\text{H}\}$  NMR Spectrum (162 MHz,  $\text{C}_6\text{D}_6$ , 25°C) of **19**.

## CHAPTER 5

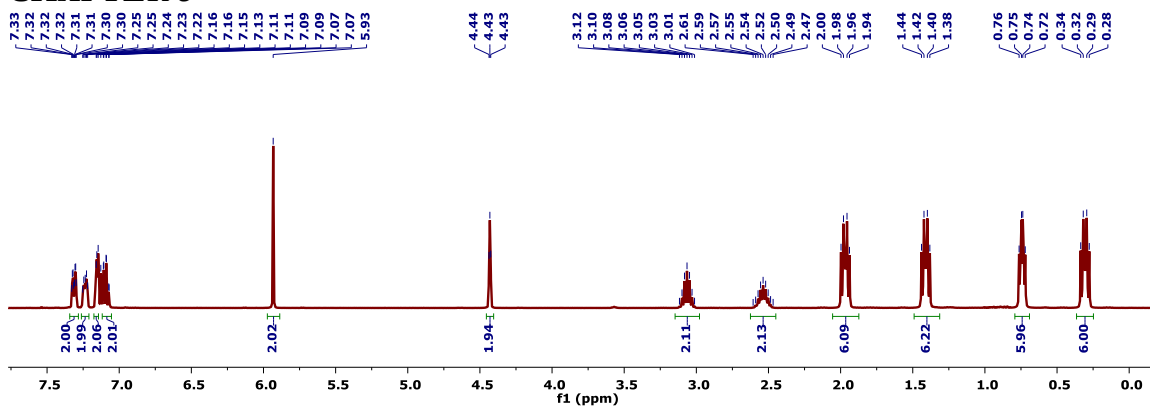


Figure C.89.  $^1\text{H}$  NMR spectrum (400 MHz,  $\text{C}_6\text{D}_6$ , 23  $^\circ\text{C}$ ) of **2**.

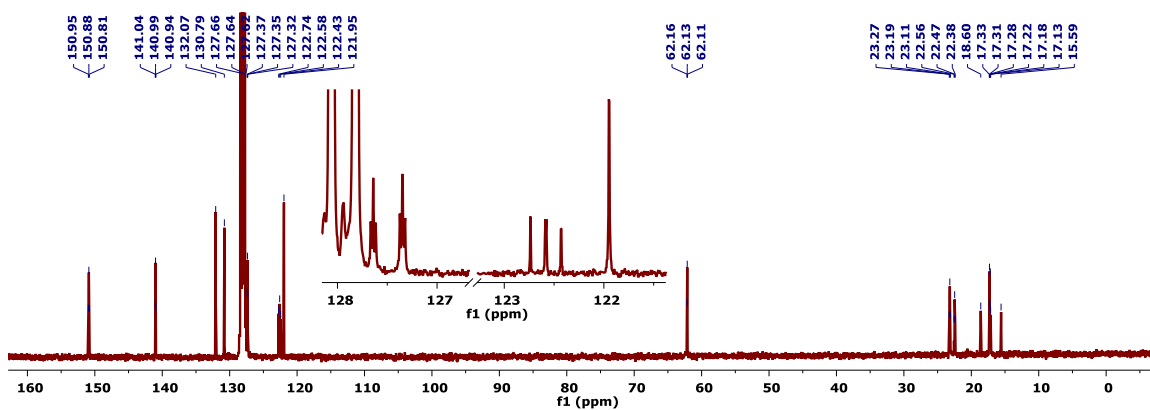


Figure C.90.  $^{13}\text{C}\{^1\text{H}\}$  NMR spectrum (101 MHz,  $\text{C}_6\text{D}_6$ , 23  $^\circ\text{C}$ ) of **2**. The inset depicts and enlargement of the aromatic region.

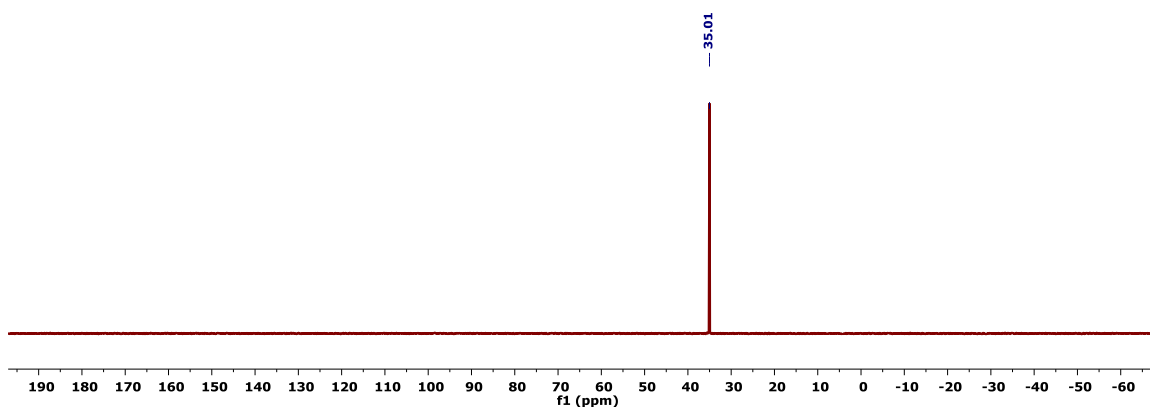


Figure C.91.  $^{31}\text{P}\{^1\text{H}\}$  NMR spectrum (162 MHz,  $\text{C}_6\text{D}_6$ , 23  $^\circ\text{C}$ ) of **2**.

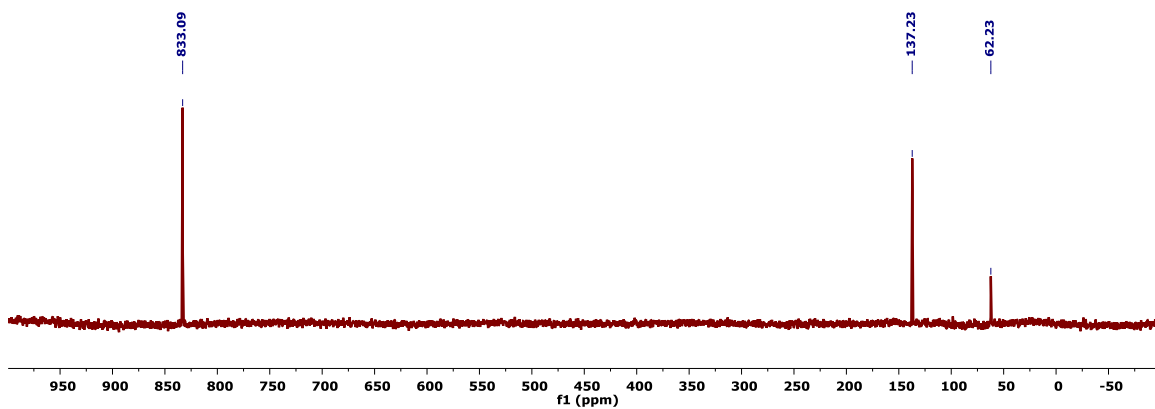


Figure C.92.  $^{15}\text{N}\{^1\text{H}\}$  NMR spectrum (51 MHz,  $\text{C}_6\text{D}_6$ , 25 °C) of **2**.

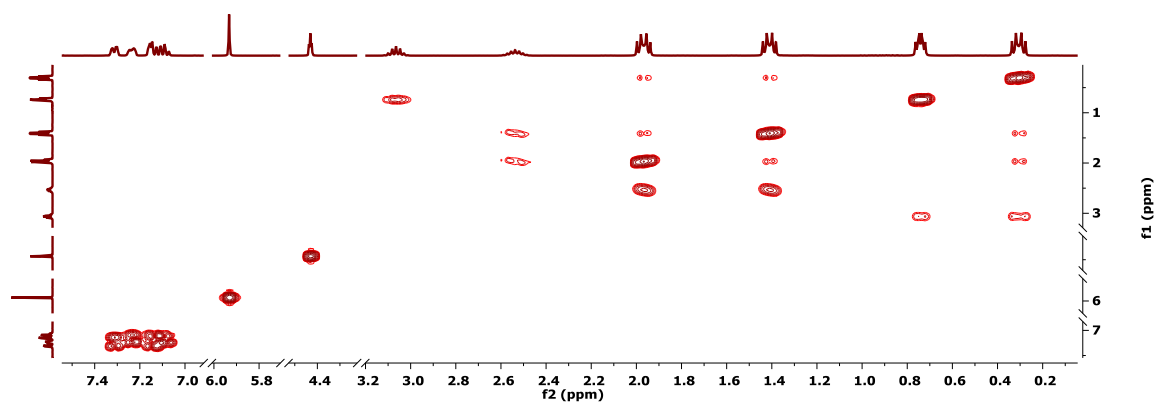


Figure C.93.  $^1\text{H}/^1\text{H}$  COSY NMR spectrum (400 MHz,  $\text{C}_6\text{D}_6$ , 23 °C) of **2**.

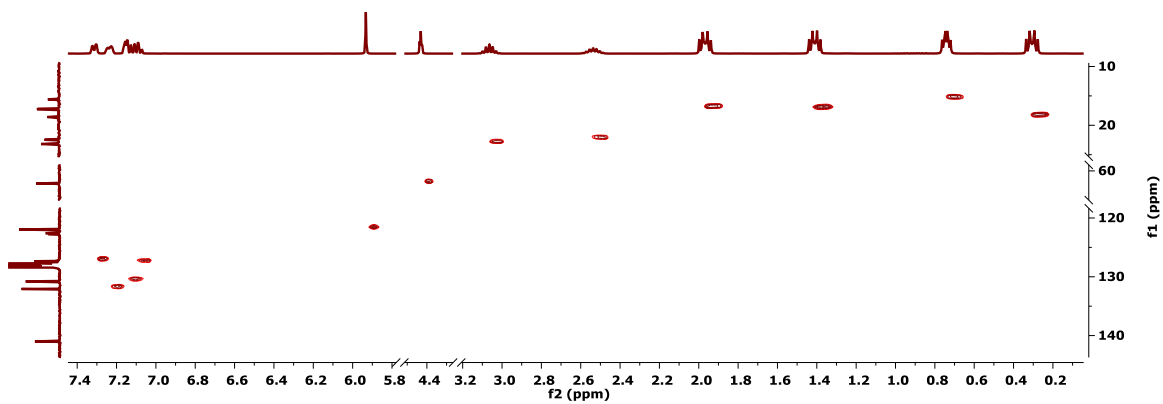


Figure C.94.  $^1\text{H}/^{13}\text{C}$  HSQC NMR spectrum (400/101 MHz,  $\text{C}_6\text{D}_6$ , 23 °C) of **2**.



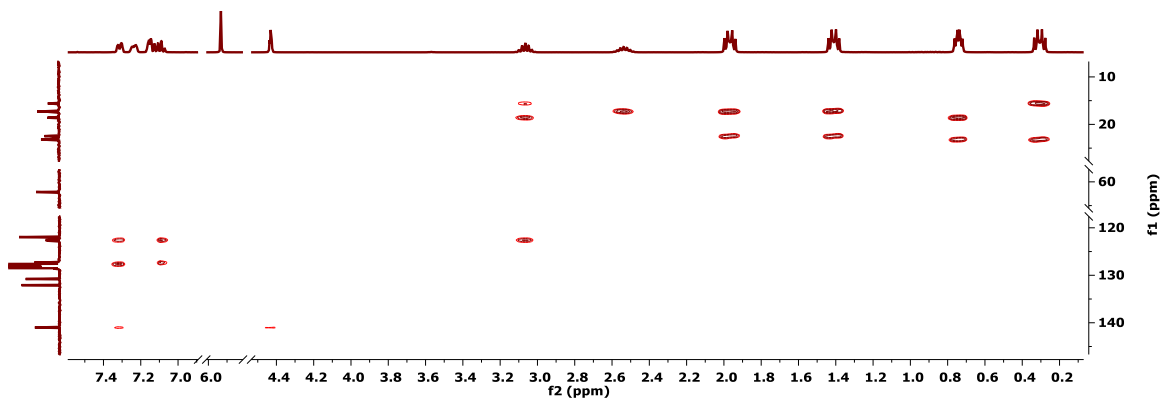


Figure C.95.  $^1\text{H}/^{13}\text{C}$  HMBC NMR spectrum (400/101 MHz,  $\text{C}_6\text{D}_6$ , 23 °C) of **2**.

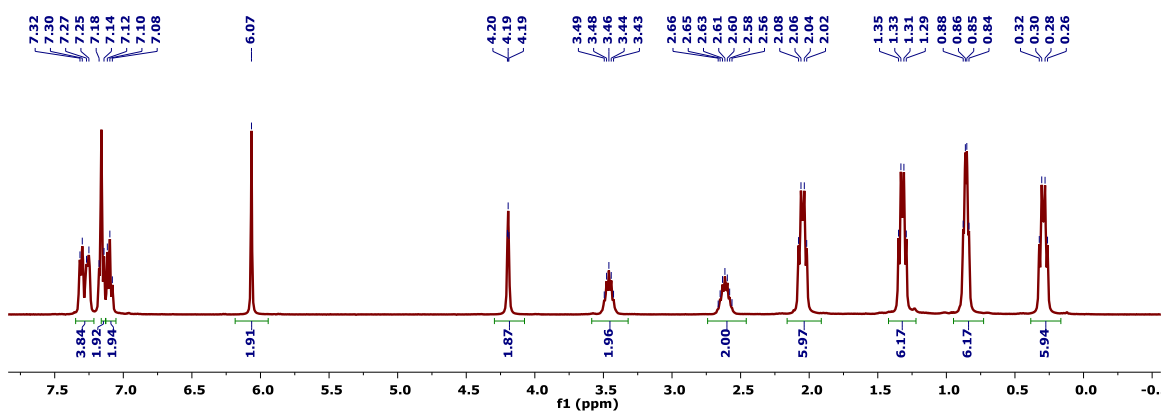


Figure C.96.  $^1\text{H}$  NMR spectrum (400 MHz,  $\text{C}_6\text{D}_6$ , 23 °C) of **3**.

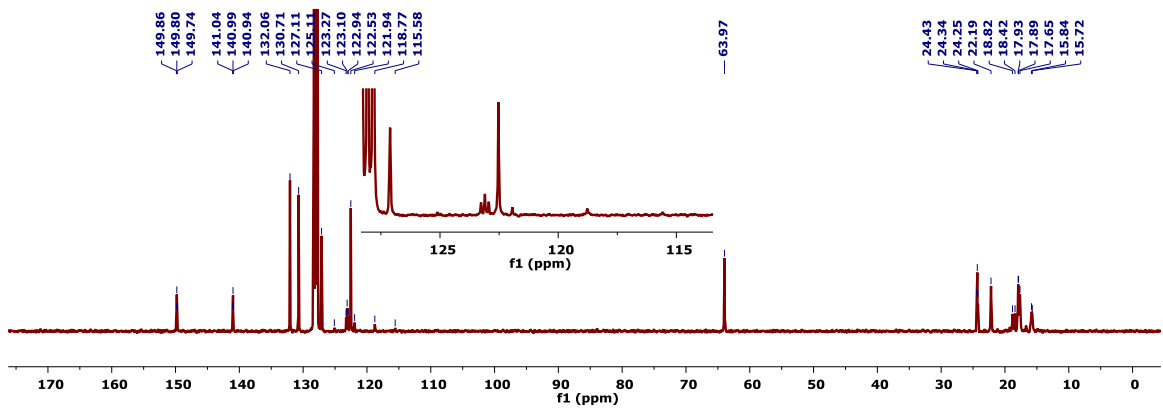


Figure C.97.  $^{13}\text{C}\{^1\text{H}\}$  NMR spectrum (101 MHz,  $\text{C}_6\text{D}_6$ , 23 °C) of **3**. The inset depicts and enlargement of the aromatic region.

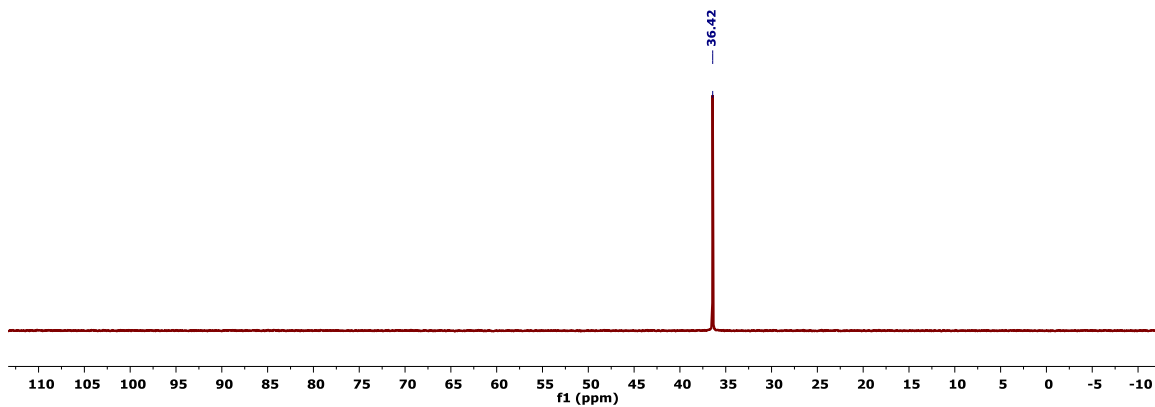


Figure C.98.  $^{31}\text{P}\{^1\text{H}\}$  NMR spectrum (162 MHz,  $\text{C}_6\text{D}_6$ , 23 °C) of **3**.

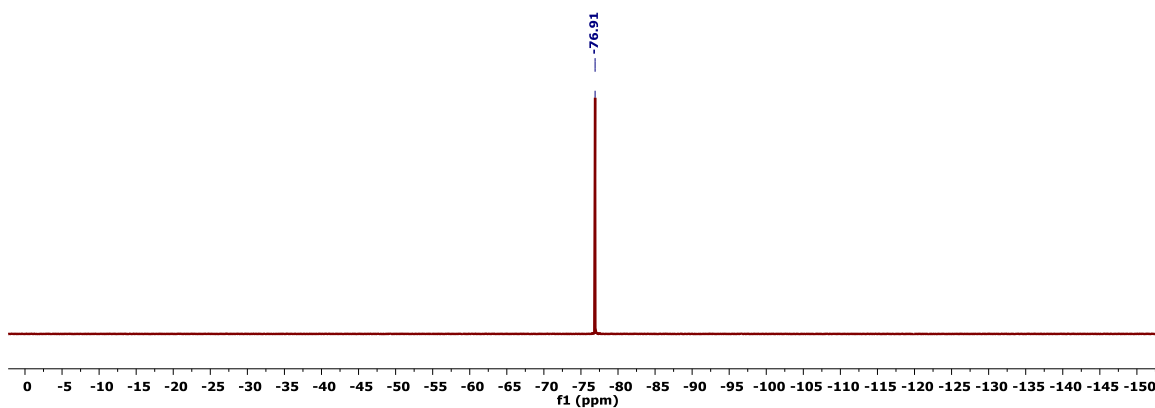


Figure C.99.  $^{19}\text{F}$  NMR spectrum (376 MHz,  $\text{C}_6\text{D}_6$ , 23 °C) of **3**.

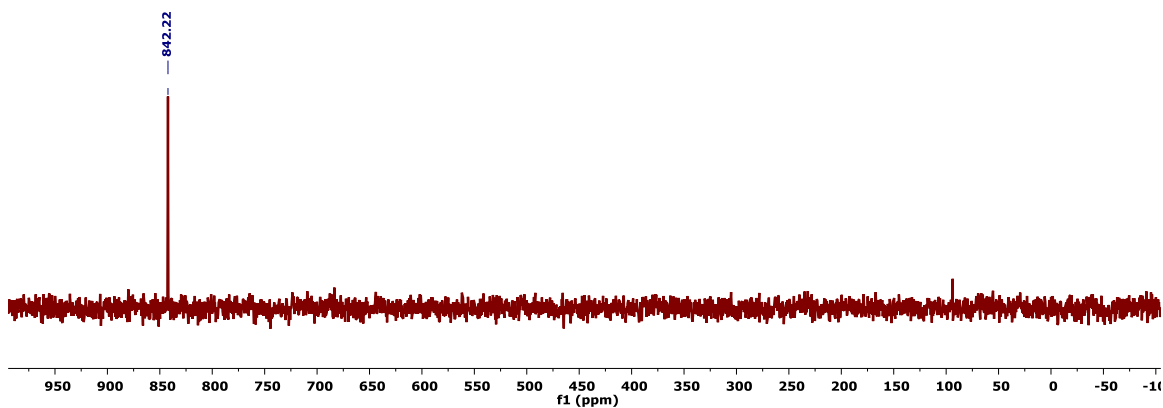


Figure C.100.  $^{15}\text{N}\{^1\text{H}\}$  NMR spectrum (51 MHz,  $\text{C}_6\text{D}_6$ , 25 °C) of **3**.

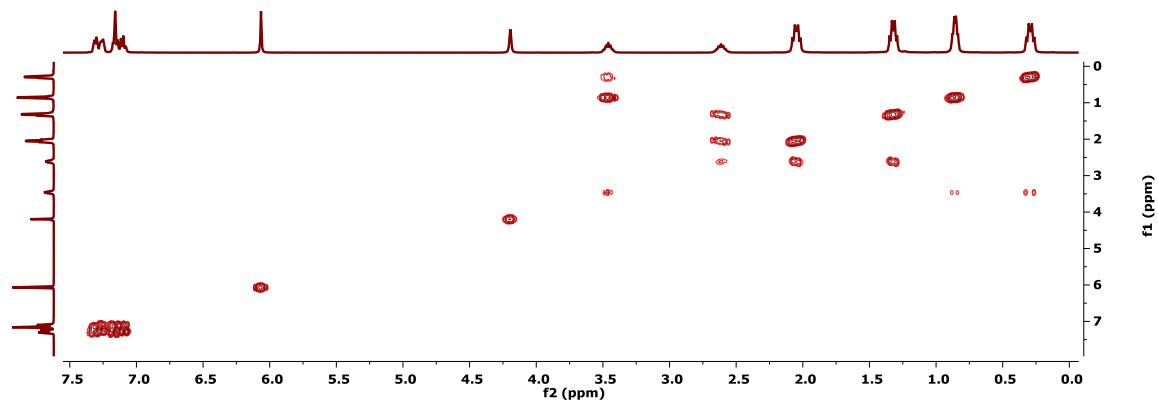


Figure C.101.  $^1\text{H}/^1\text{H}$  COSY NMR spectrum (400 MHz,  $\text{C}_6\text{D}_6$ , 23  $^\circ\text{C}$ ) of **3**.

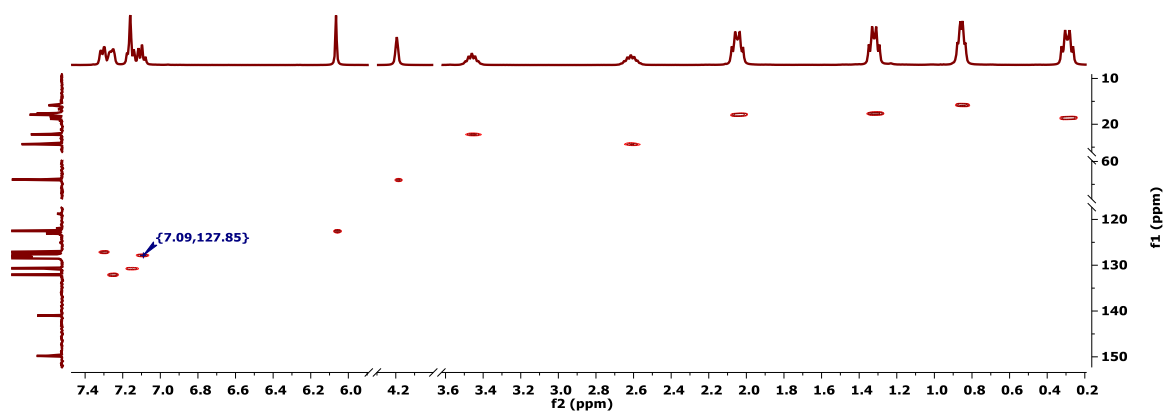


Figure C.102.  $^1\text{H}/^{13}\text{C}$  HSQC NMR spectrum (400/101 MHz,  $\text{C}_6\text{D}_6$ , 23  $^\circ\text{C}$ ) of **3**. The  $^{13}\text{C}$  resonance that coincides with the  $\text{C}_6\text{D}_6$  solvent residual is labeled.

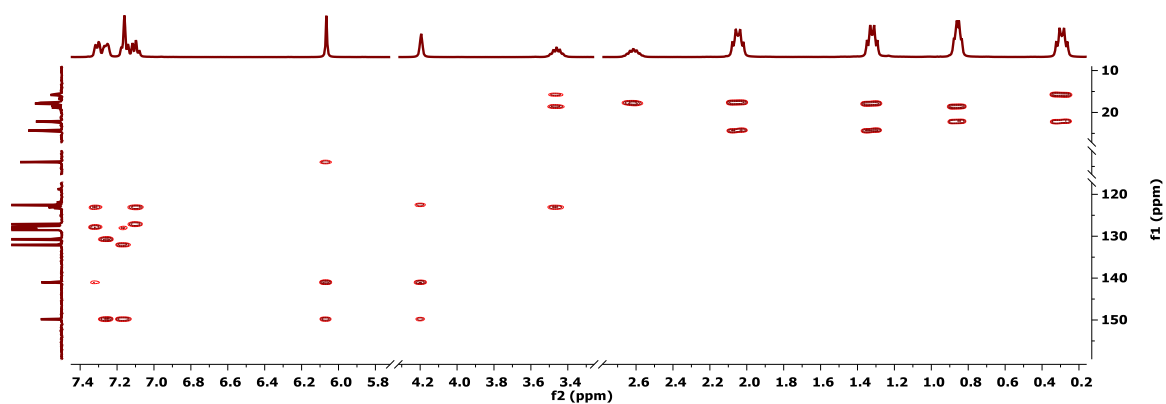
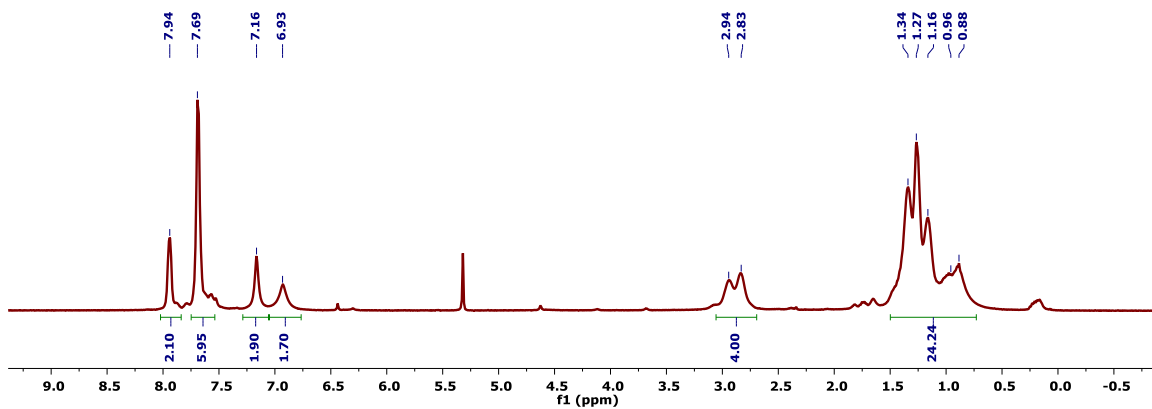
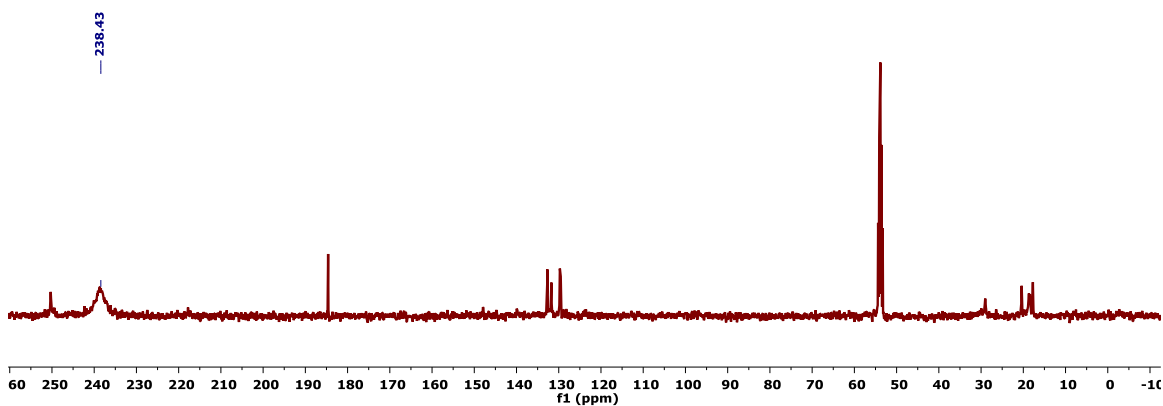


Figure C.103.  $^1\text{H}/^{13}\text{C}$  HMBC NMR spectrum (400/101 MHz,  $\text{C}_6\text{D}_6$ , 23  $^\circ\text{C}$ ) of **3**.



**Figure C.104.**  $^1\text{H}$  NMR spectrum (400 MHz,  $\text{CD}_2\text{Cl}_2$ , 23 °C) of a reaction mixture comprised primarily of  $4\text{-}^{13}\text{C}$ .



**Figure C.105.**  $^{13}\text{C}\{^1\text{H}\}$  NMR spectrum (101 MHz,  $\text{CD}_2\text{Cl}_2$ , 23 °C) of a reaction mixture comprised primarily of  $4\text{-}^{13}\text{C}$ . The sufficient spectral signal to noise was obtained to validate the broad resonance for the isotopically enriched carbonyl.

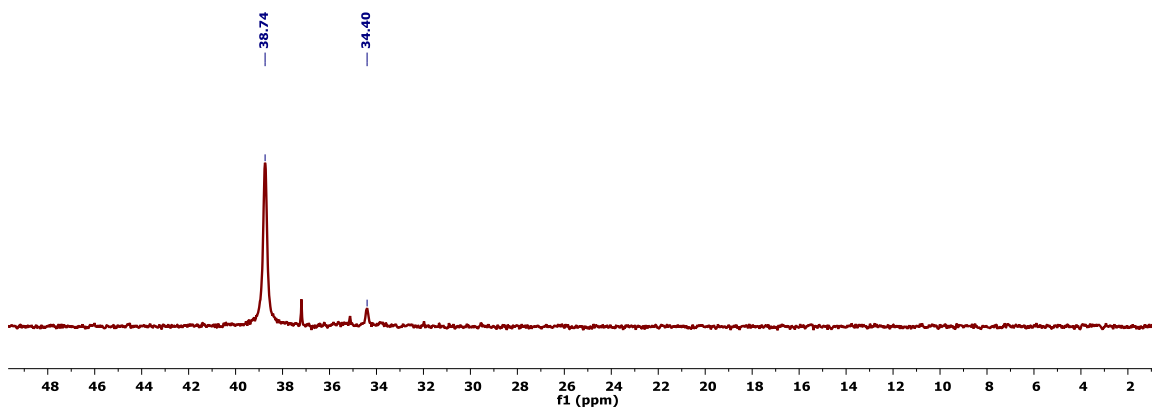


**Figure C.106.**  $^{31}\text{P}\{^1\text{H}\}$  NMR spectrum (162 MHz,  $\text{CD}_2\text{Cl}_2$ , 23 °C) of a reaction mixture comprised primarily of  $4\text{-}^{13}\text{C}$ .

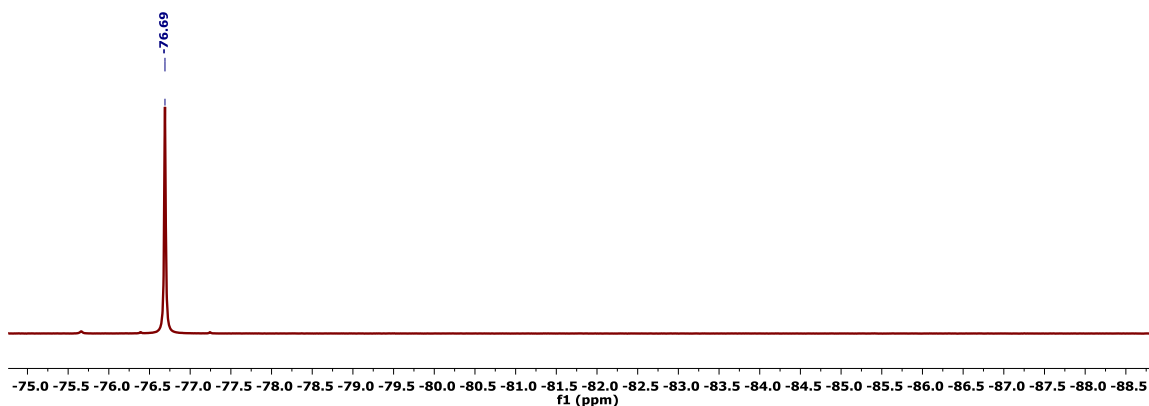


**Figure C.107.**  $^{19}\text{F}$  NMR spectrum (376 MHz,  $\text{CD}_2\text{Cl}_2$ , 23 °C) of  $4\text{-}^{13}\text{C}$ .

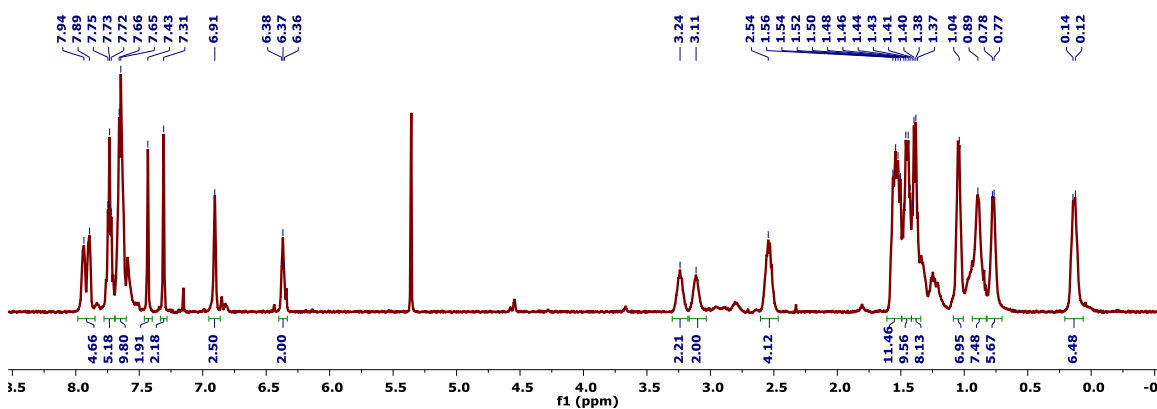


**Figure C.108.**  $^1\text{H}$  NMR spectrum (500 MHz,  $\text{CD}_2\text{Cl}_2$ , -65 °C) of a reaction mixture comprised primarily of  $4\text{-}^{13}\text{C}$ .

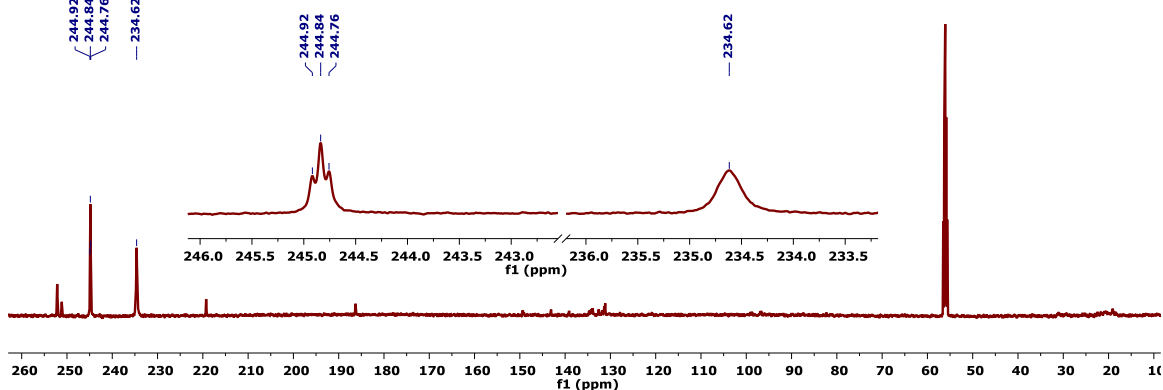


**Figure C.109.**  $^{13}\text{C}\{^1\text{H}\}$  NMR spectrum (126 MHz,  $\text{CD}_2\text{Cl}_2$ , -65 °C) of a reaction mixture comprised primarily of  $4\text{-}^{13}\text{C}$ . The sufficient spectral signal to noise was obtained to validate the broad resonance for the isotopically enriched carbonyl. The inset shows enlargements of the CO resonances of the two isomers of  $4\text{-}^{13}\text{C}$ .

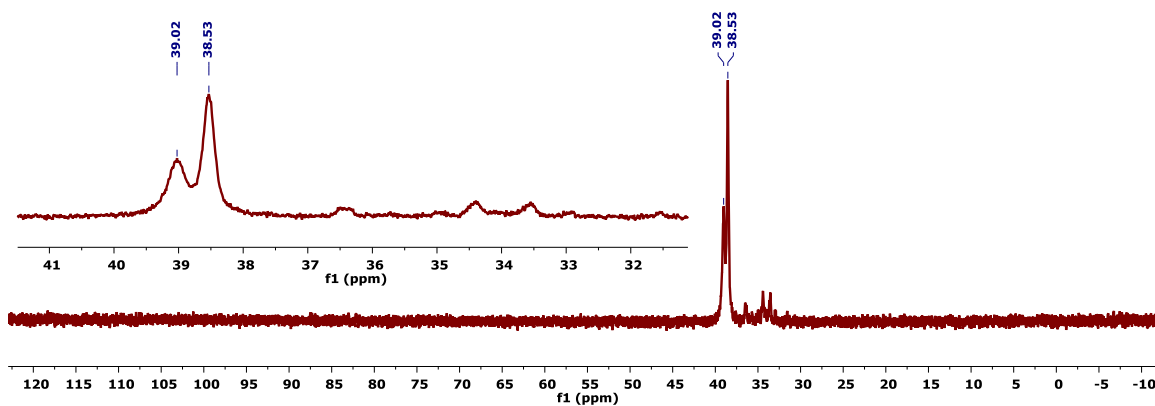


**Figure C.110.**  $^{31}\text{P}\{^1\text{H}\}$  NMR spectrum (202 MHz,  $\text{CD}_2\text{Cl}_2$ ,  $-65^\circ\text{C}$ ) of a reaction mixture comprised primarily of  $4\text{-}^{13}\text{C}$ . The inset highlights the two resonances attributable to  $4\text{-}^{13}\text{C}$ .

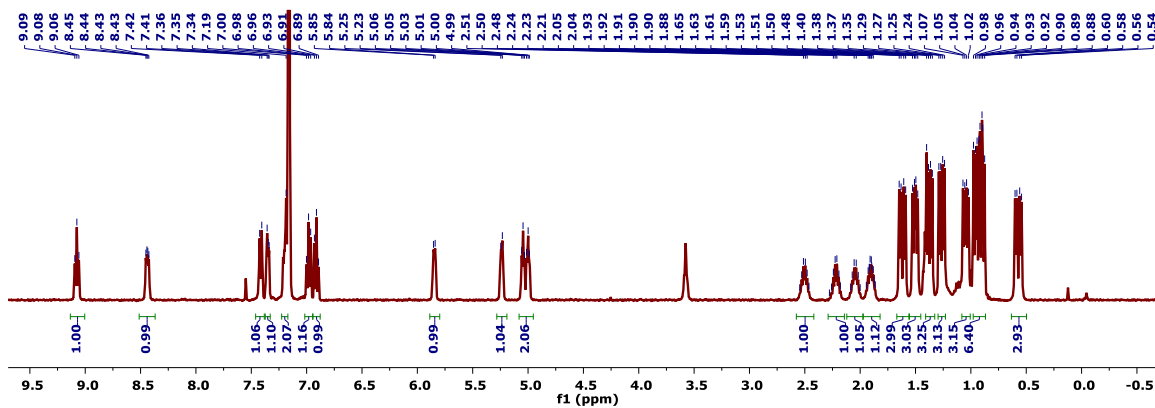


**Figure C.111.**  $^1\text{H}$  NMR spectrum (400 MHz,  $\text{C}_6\text{D}_6$ ,  $23^\circ\text{C}$ ) of **5**.

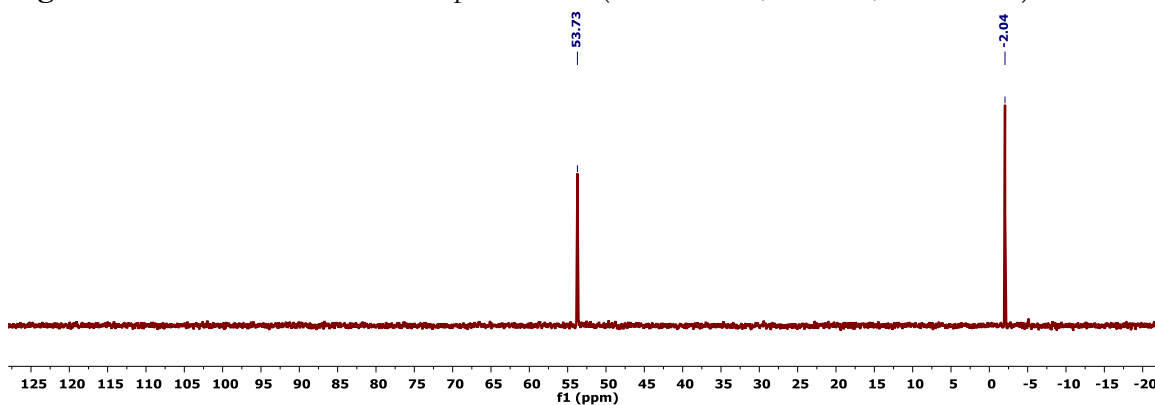


**Figure C.112.**  $^{31}\text{P}\{^1\text{H}\}$  NMR spectrum (162 MHz,  $\text{C}_6\text{D}_6$ ,  $23^\circ\text{C}$ ) of **5**.

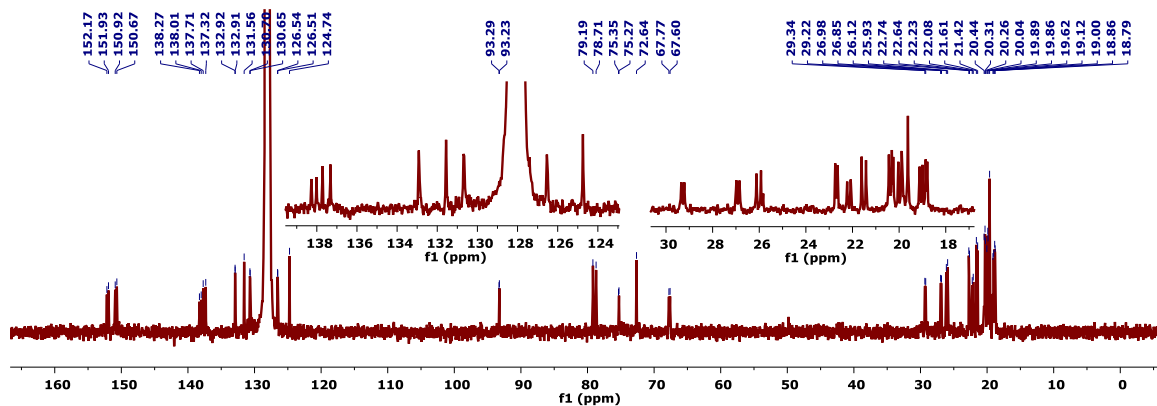


**Figure C.113.**  $^{13}\text{C}\{^1\text{H}\}$  NMR spectrum (101 MHz,  $\text{C}_6\text{D}_6$ , 23 °C) of **5**. The insets show the enlargements of the aromatic (left) and aliphatic (right) regions of the spectrum.

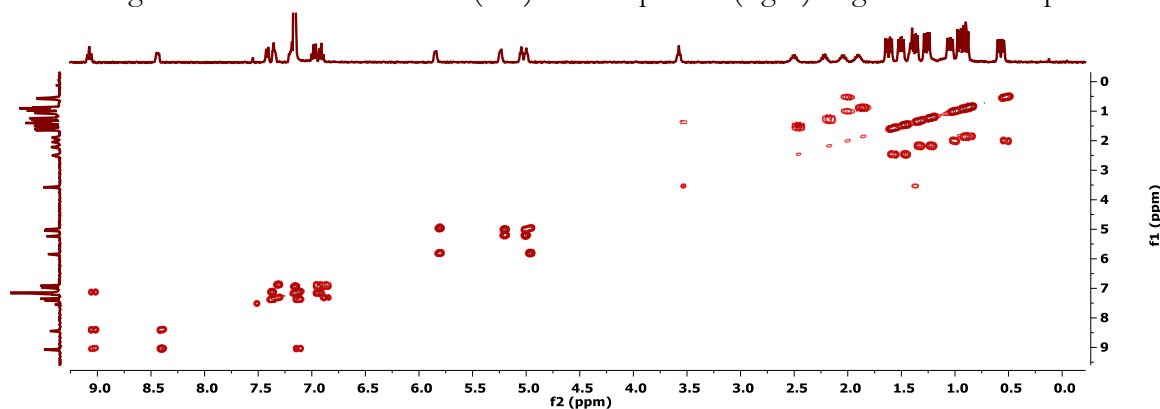


**Figure C.114.**  $^1\text{H}/^1\text{H}$  COSY NMR spectrum (400 MHz,  $\text{C}_6\text{D}_6$ , 23 °C) of **5**.

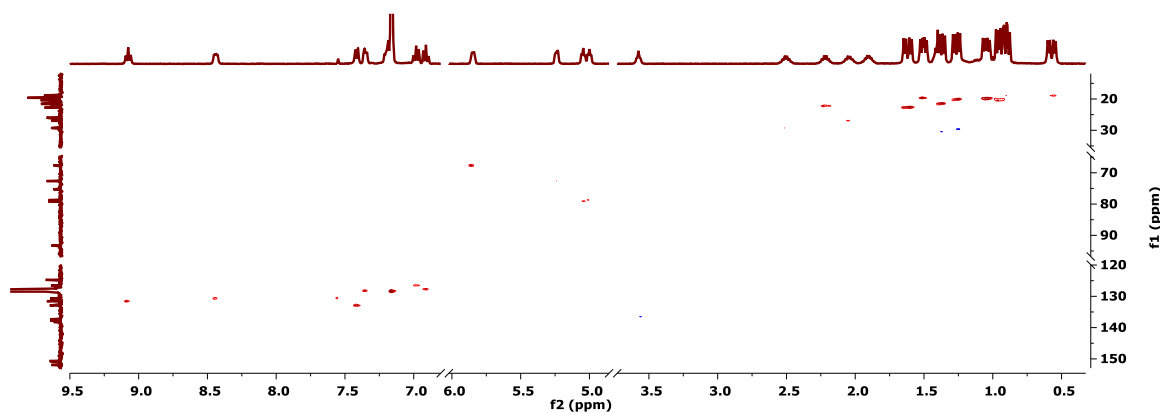


**Figure C.115.**  $^1\text{H}/^{13}\text{C}$  HSQC NMR spectrum (400/101 MHz,  $\text{C}_6\text{D}_6$ , 23 °C) of **5**.

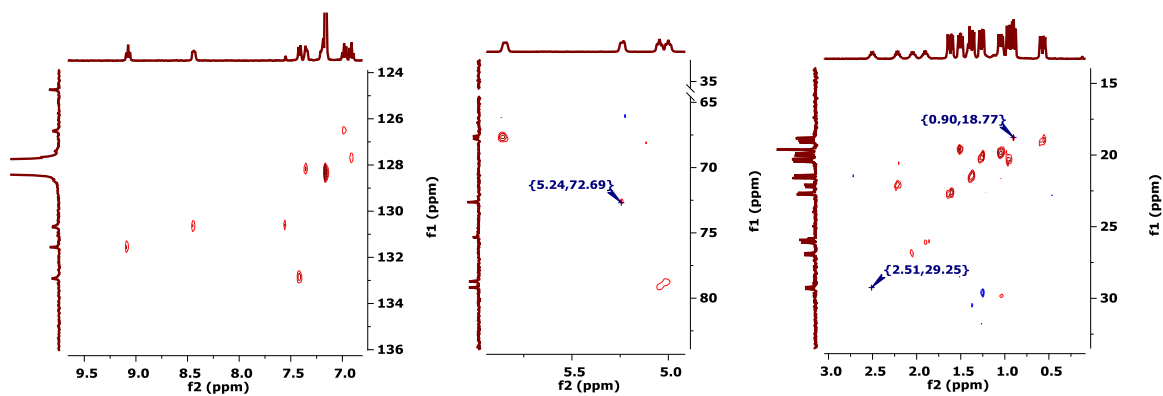


Figure C.116. Partial  $^1\text{H}/^{13}\text{C}$  HSQC NMR spectra (400/101 MHz,  $\text{C}_6\text{D}_6$ , 23 °C) of 5.

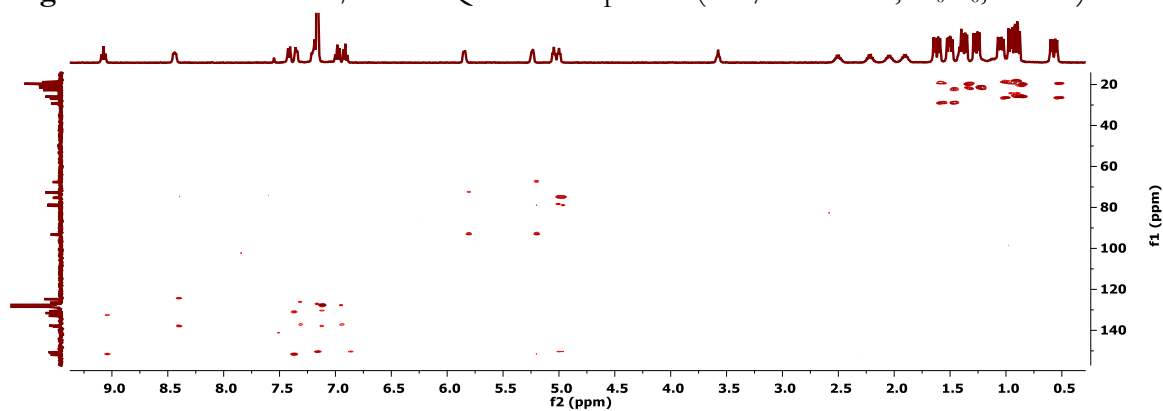


Figure C.117.  $^1\text{H}/^{13}\text{C}$  HMBC NMR spectrum (400/101 MHz,  $\text{C}_6\text{D}_6$ , 23 °C) of 5.



## CHAPTER 6

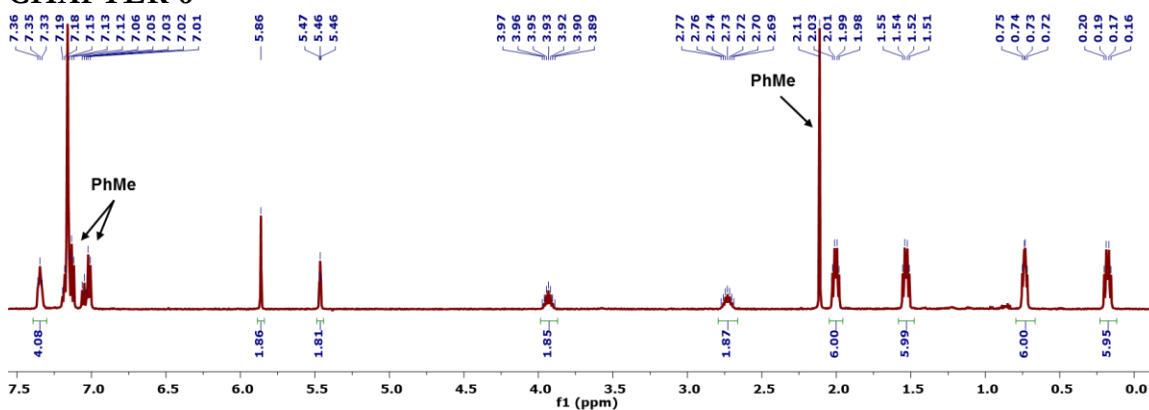


Figure C.118.  $^1\text{H}$  NMR Spectrum (500 MHz,  $\text{C}_6\text{D}_6$ ,  $25^\circ\text{C}$ ) of **2**.

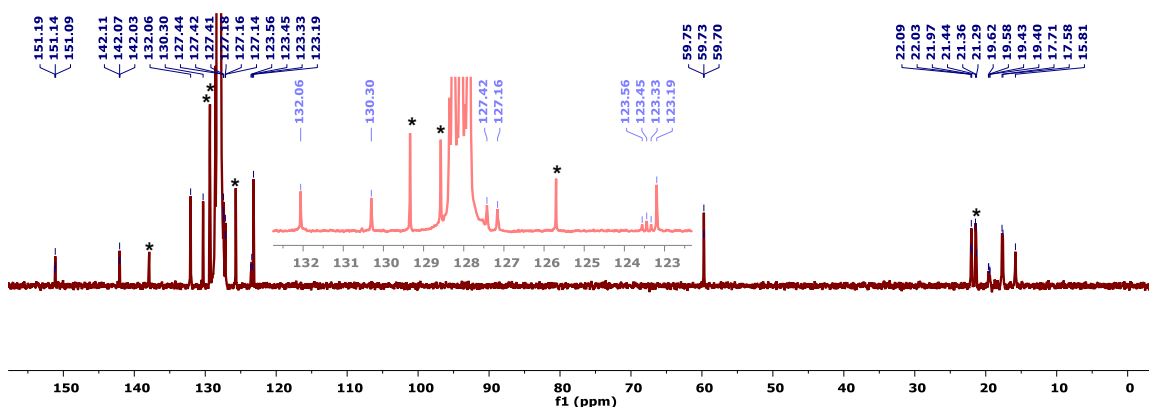


Figure C.119.  $^{13}\text{C}\{^1\text{H}\}$  NMR Spectrum (126 MHz,  $\text{C}_6\text{D}_6$ ,  $25^\circ\text{C}$ ) of **2**. The inset shows an enlargement of the aryl resonances near the  $\text{C}_6\text{D}_6$  solvent residual.  $^{13}\text{C}$  NMR signals corresponding to toluene are denoted with an asterisk.

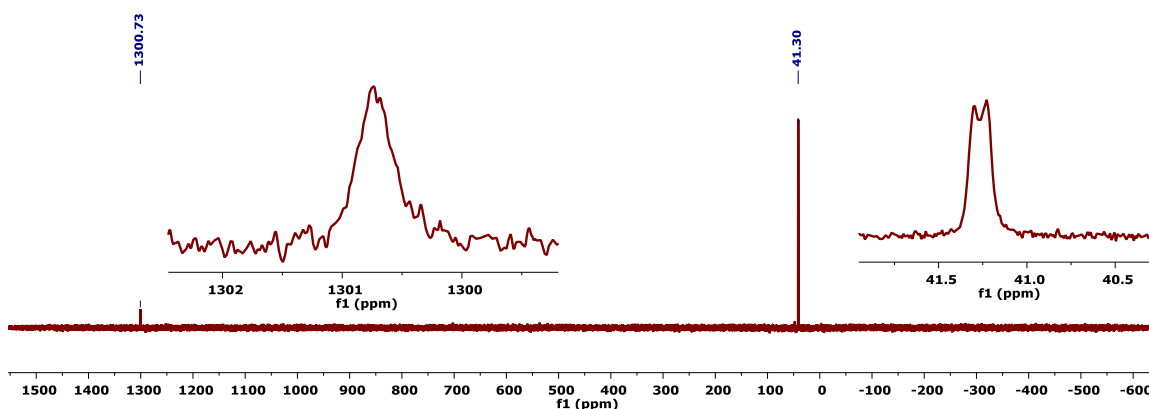


Figure C.120.  $^{31}\text{P}\{^1\text{H}\}$  NMR Spectrum (162 MHz,  $\text{C}_6\text{D}_6$ ,  $23^\circ\text{C}$ ) of **2**. The insets show enlargements of the phosphide (left) and phosphine (right) resonances, demonstrating a broad signal for the former and a broad, but resolved, doublet for the latter.

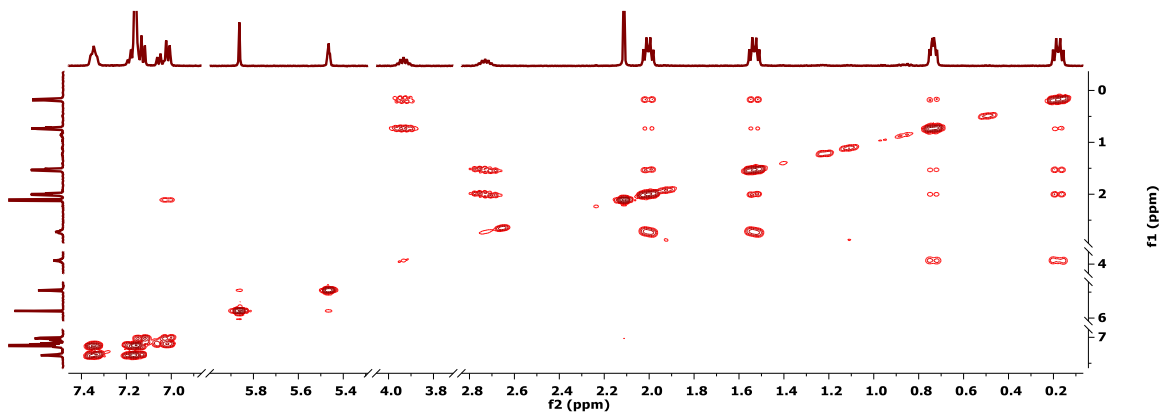


Figure C.121. Partial  $^1\text{H}/^1\text{H}$  COSY NMR Spectrum (500 MHz,  $\text{C}_6\text{D}_6$ , 25°C) of **2**.

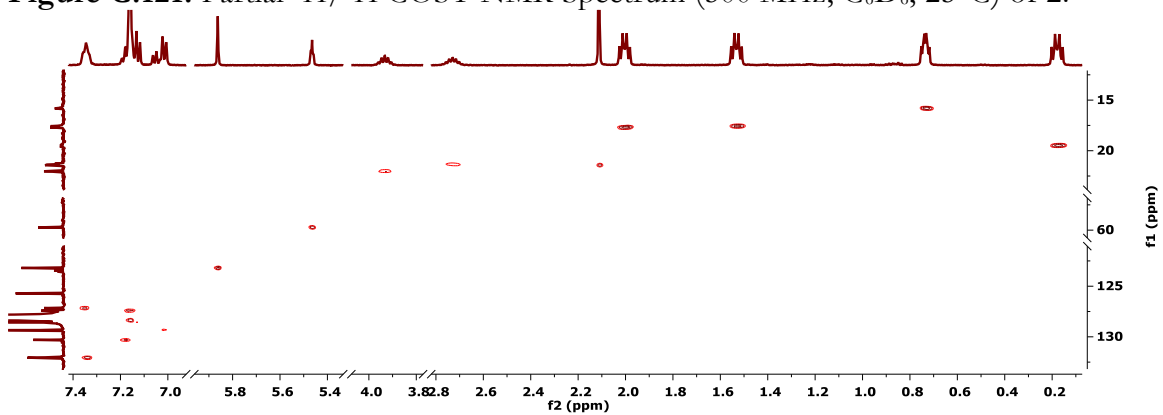


Figure C.122. Partial  $^1\text{H}/^{13}\text{C}$  HSQC NMR Spectrum (500/126 MHz,  $\text{C}_6\text{D}_6$ , 25°C) of **2**.

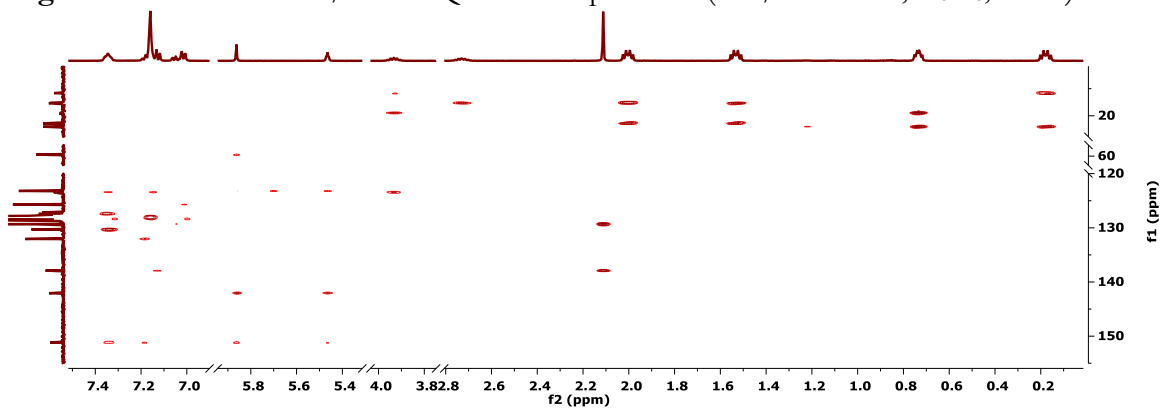


Figure C.123. Partial  $^1\text{H}/^{13}\text{C}$  HMBC NMR Spectrum (500/126 MHz,  $\text{C}_6\text{D}_6$ , 25°C) of **2**.

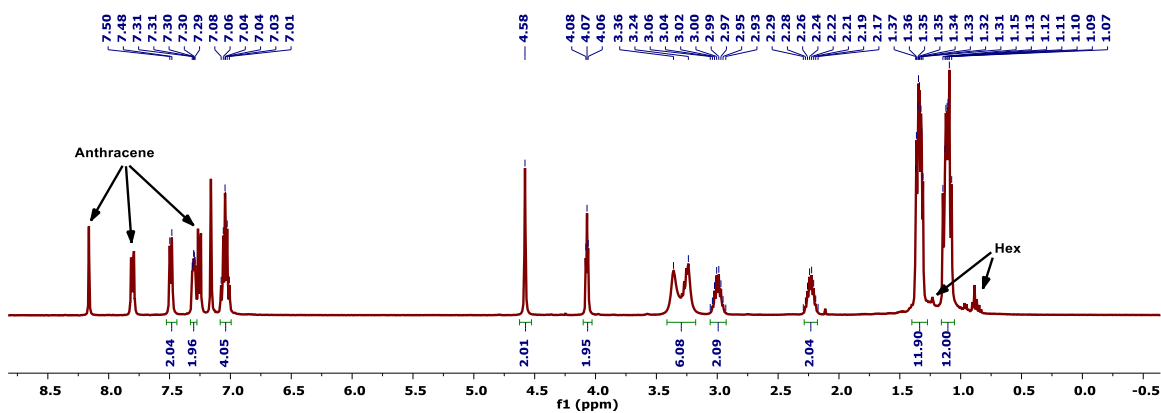


Figure C.124.  $^1\text{H}$  NMR Spectrum (400 MHz,  $\text{C}_6\text{D}_6$ ,  $23^\circ\text{C}$ ) of **3**.

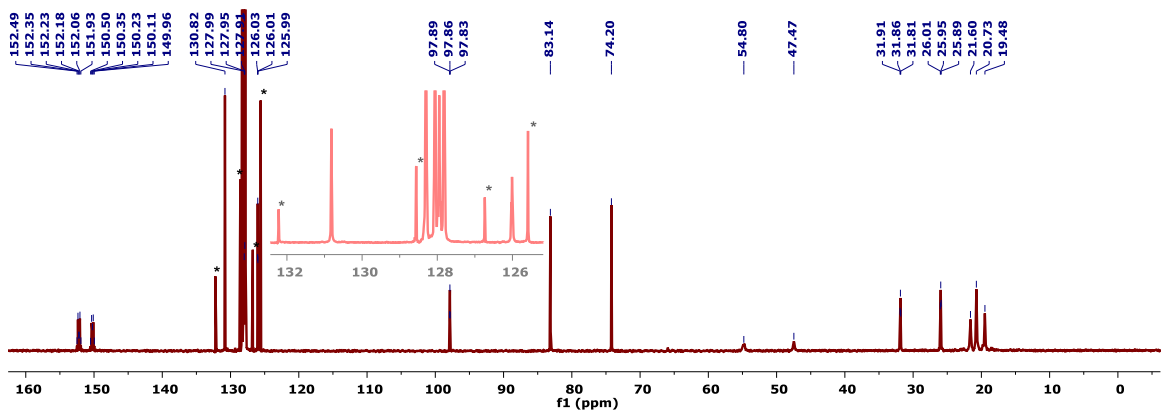


Figure C.125.  $^{13}\text{C}\{^1\text{H}\}$  NMR Spectrum (101 MHz,  $\text{C}_6\text{D}_6$ ,  $23^\circ\text{C}$ ) of **3**. The inset shows an enlargement of the aryl resonances near the  $\text{C}_6\text{D}_6$  solvent residual.  $^{13}\text{C}$  NMR signals corresponding to anthracene are denoted with an asterisk.

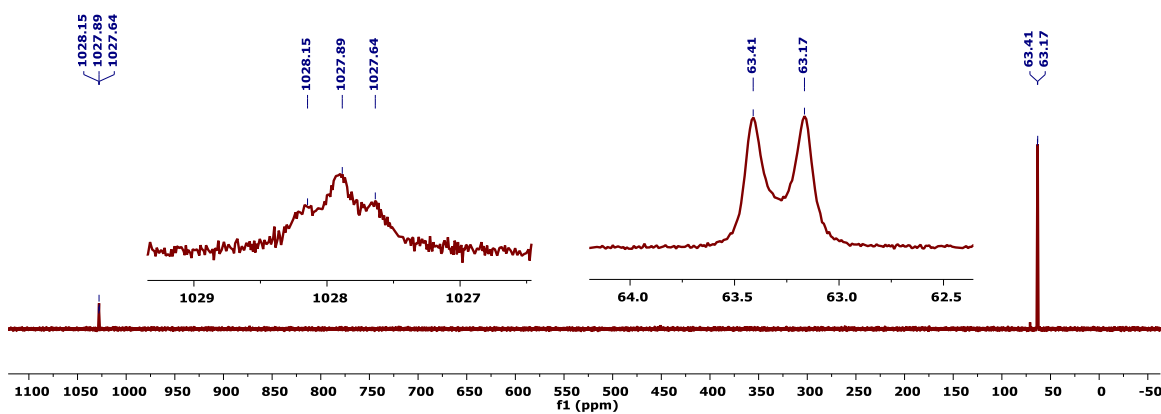


Figure C.126.  $^{31}\text{P}\{^1\text{H}\}$  NMR Spectrum (162 MHz,  $\text{C}_6\text{D}_6$ ,  $23^\circ\text{C}$ ) of **3**. The insets show enlargements of the phosphinidene (left) and phosphine (right) resonances.

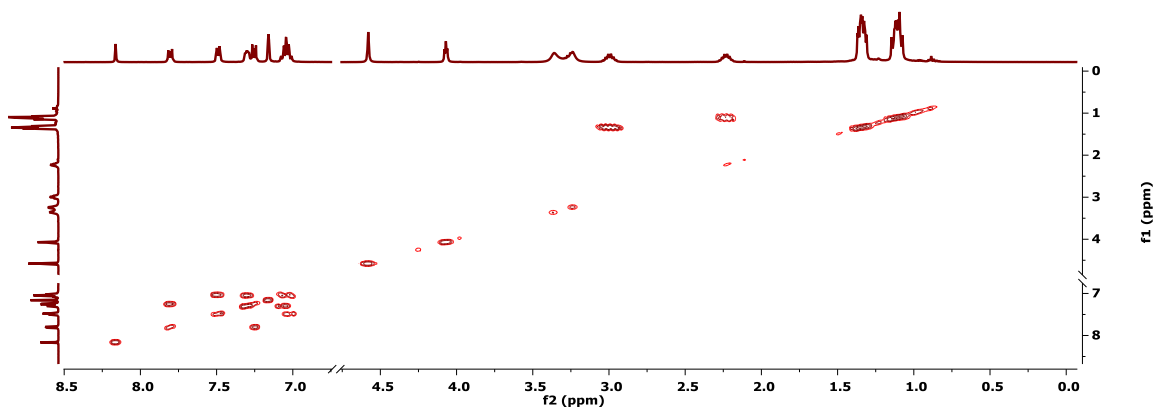


Figure C.127. Partial  $^1\text{H}/^1\text{H}$  COSY NMR Spectrum (400 MHz,  $\text{C}_6\text{D}_6$ , 23°C) of **3**.

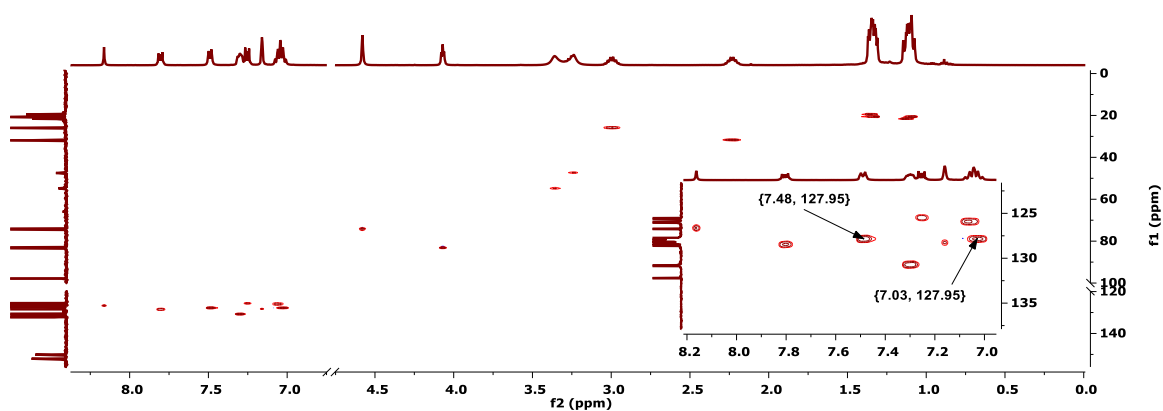


Figure C.128. Partial  $^1\text{H}/^{13}\text{C}$  HSQC NMR Spectrum (400/101 MHz,  $\text{C}_6\text{D}_6$ , 23°C) of **3**. The inset shows an enlargement of the aromatic region.

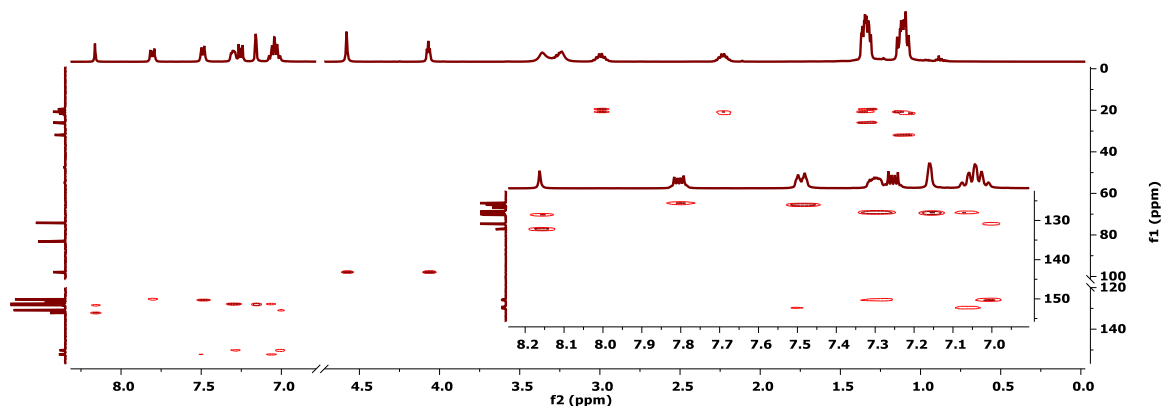


Figure C.129. Partial  $^1\text{H}/^{13}\text{C}$  HMBC NMR Spectrum (400/101 MHz,  $\text{C}_6\text{D}_6$ , 23°C) of **3**. The inset shows an enlargement of the aromatic region.

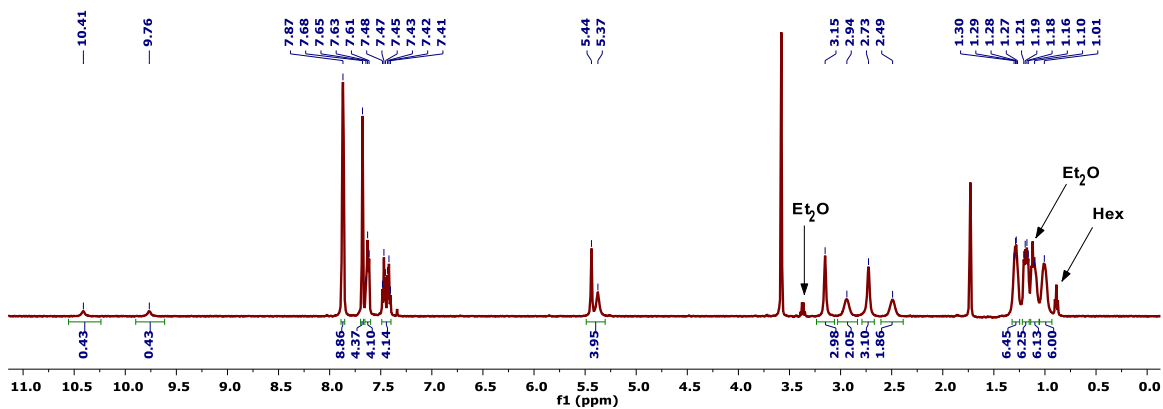


Figure C.130. <sup>1</sup>H NMR Spectrum (500 MHz, THF-*d*<sub>8</sub>, -50°C) of 4.

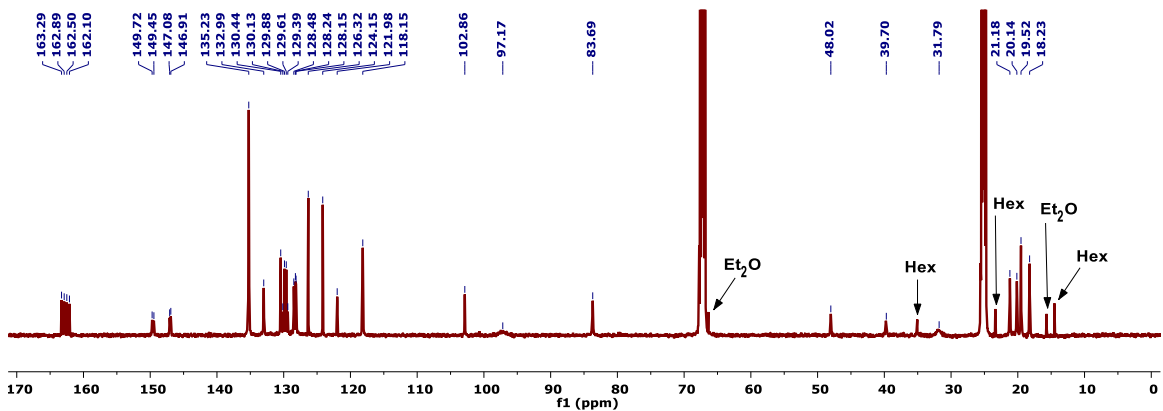


Figure C.131. <sup>13</sup>C {<sup>1</sup>H} NMR Spectrum (126 MHz, THF-*d*<sub>8</sub>, -50°C) of 4.

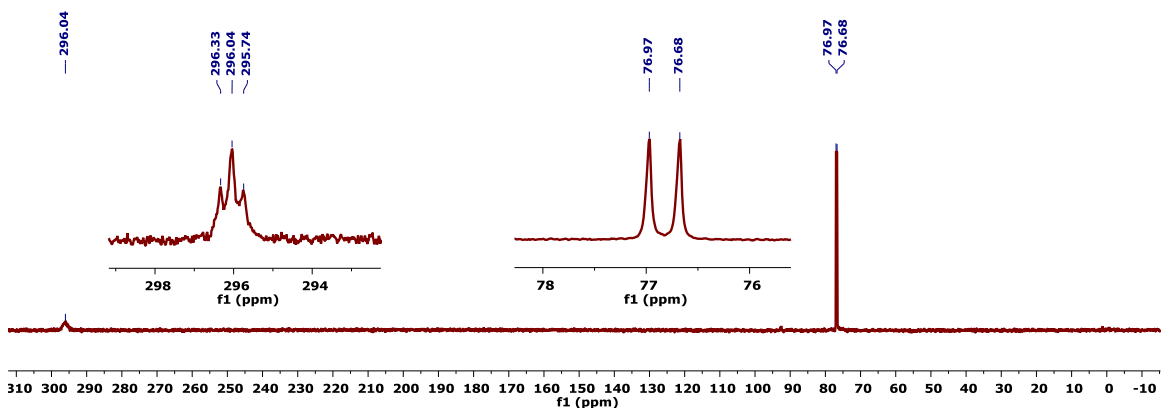


Figure C.132. <sup>31</sup>P {<sup>1</sup>H} NMR Spectrum (162 MHz, THF, 23°C) of 4. The insets show enlargements of the dimethylamino phosphide (left) and phosphine (right) resonances.

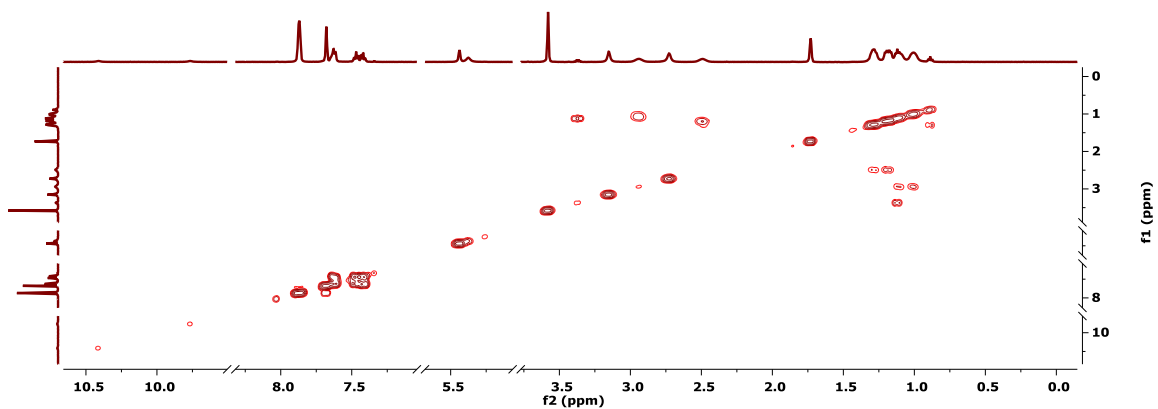


Figure C.133. Partial  $^1\text{H}/^1\text{H}$  COSY NMR Spectrum (500 MHz,  $\text{THF-}d_8$ ,  $-50^\circ\text{C}$ ) of **4**.

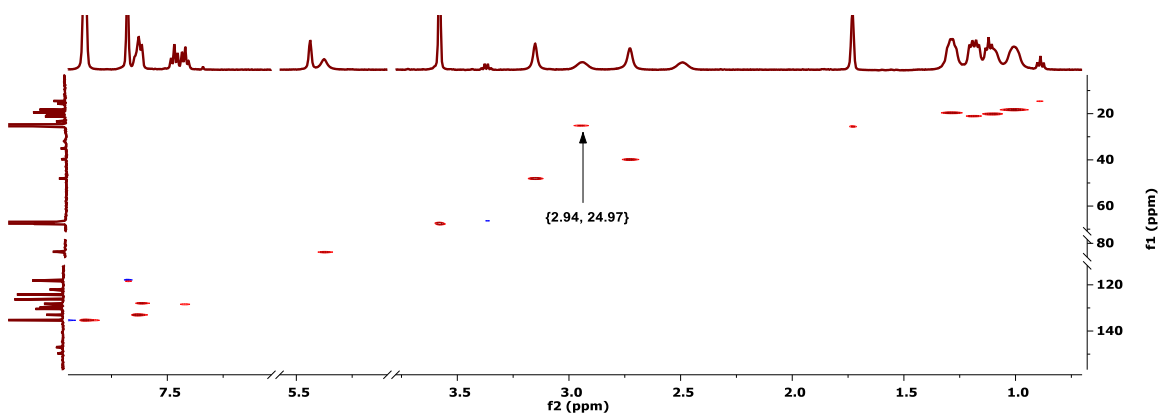


Figure C.134. Partial  $^1\text{H}/^{13}\text{C}$  HSQC NMR Spectrum (500/126 MHz,  $\text{THF-}d_8$ ,  $-50^\circ\text{C}$ ) of **4**.

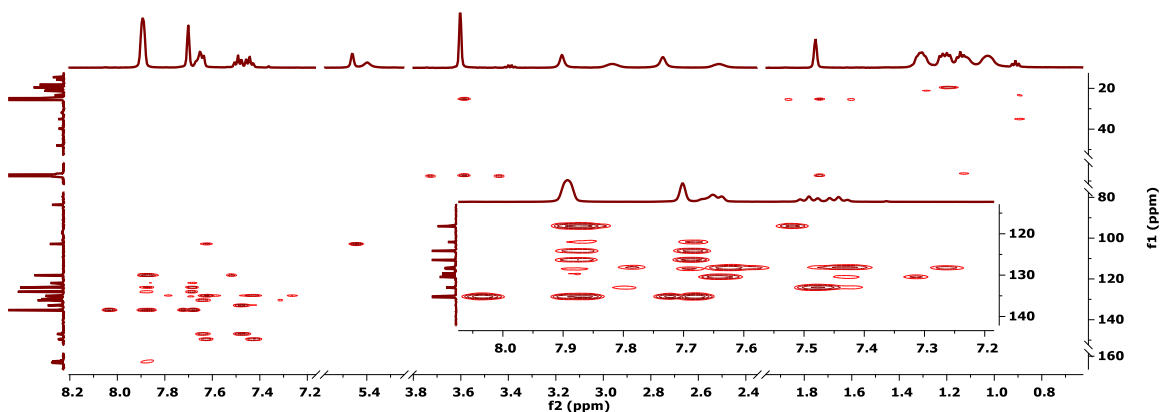


Figure C.135. Partial  $^1\text{H}/^{13}\text{C}$  HMBC NMR Spectrum (500/126 MHz,  $\text{THF-}d_8$ ,  $-50^\circ\text{C}$ ) of **4**. The inset shows an enlargement of the aromatic region.

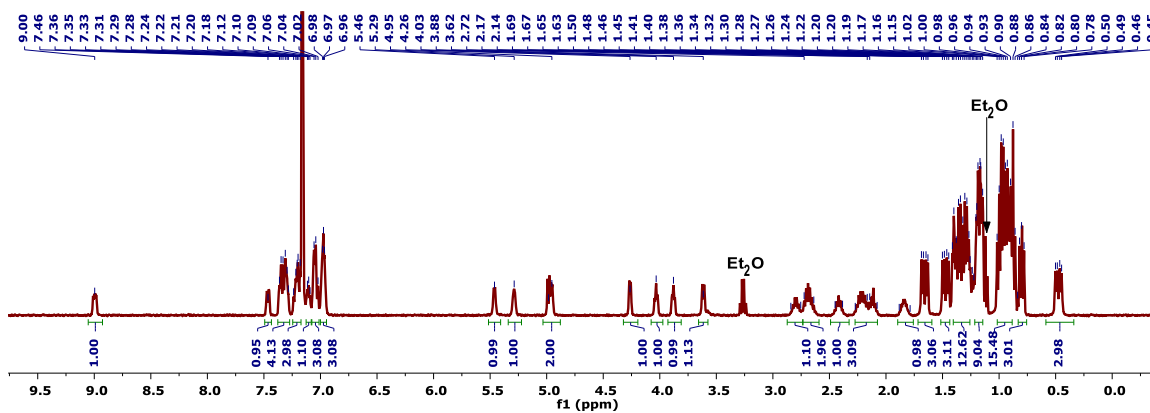


Figure C.136.  $^1\text{H}$  NMR Spectrum (400 MHz,  $\text{C}_6\text{D}_6$ ,  $23^\circ\text{C}$ ) of 5.

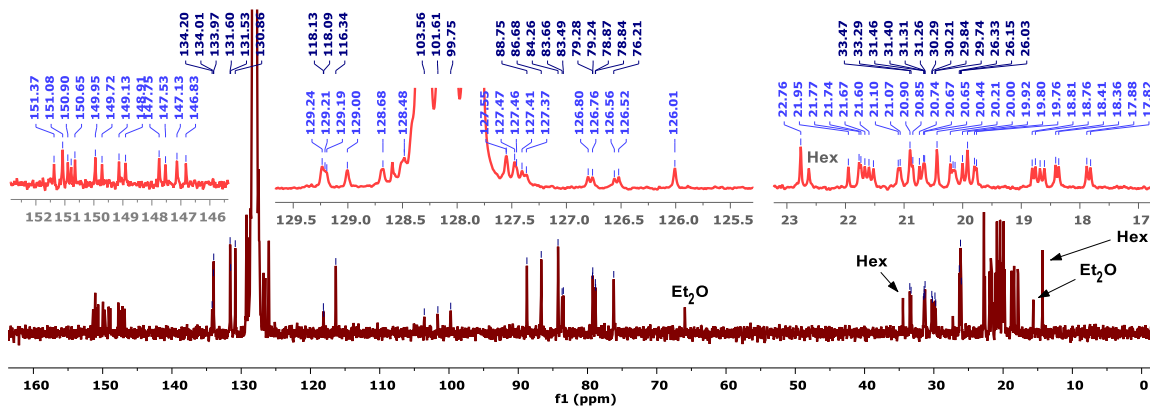


Figure C.137.  $^{13}\text{C}\{^1\text{H}\}$  NMR Spectrum (101 MHz,  $\text{C}_6\text{D}_6$ ,  $23^\circ\text{C}$ ) of 5. The insets show enlargements of the aromatic and aliphatic regions of the spectrum, including chemical shift labels.

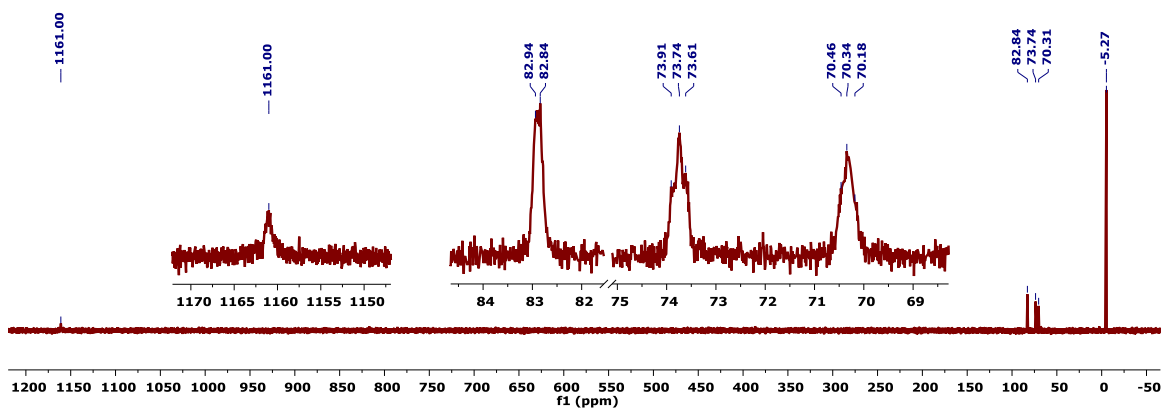
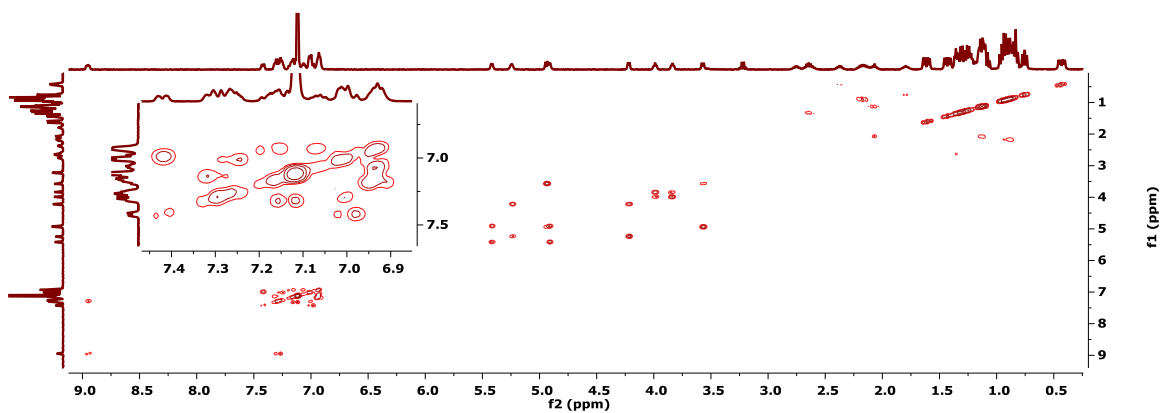
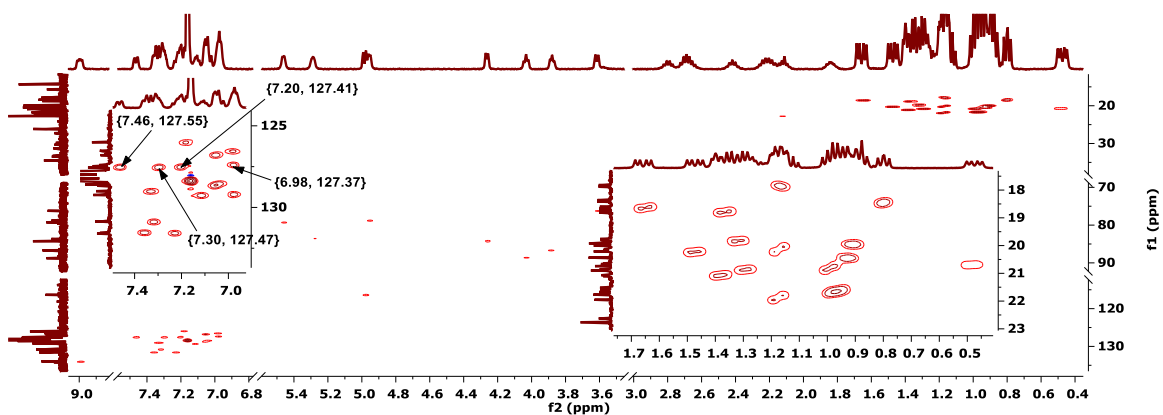


Figure C.138.  $^{31}\text{P}\{^1\text{H}\}$  NMR Spectrum (162 MHz,  $\text{C}_6\text{D}_6$ ,  $23^\circ\text{C}$ ) of 5. The insets show enlargements of the bridging phosphide (left) and Mo-bound phosphine (right) resonances.



**Figure C.139.**  $^1\text{H}/^1\text{H}$  COSY NMR Spectrum (400 MHz,  $\text{C}_6\text{D}_6$ ,  $23^\circ\text{C}$ ) of **5**. The inset shows an enlargement of the aromatic region of the spectrum.



**Figure C.140.** Partial  $^1\text{H}/^{13}\text{C}$  HSQC NMR Spectrum (400/101 MHz,  $\text{C}_6\text{D}_6$ ,  $23^\circ\text{C}$ ) of **5**. The insets show enlargements of the aromatic (left) and aliphatic (right) regions.

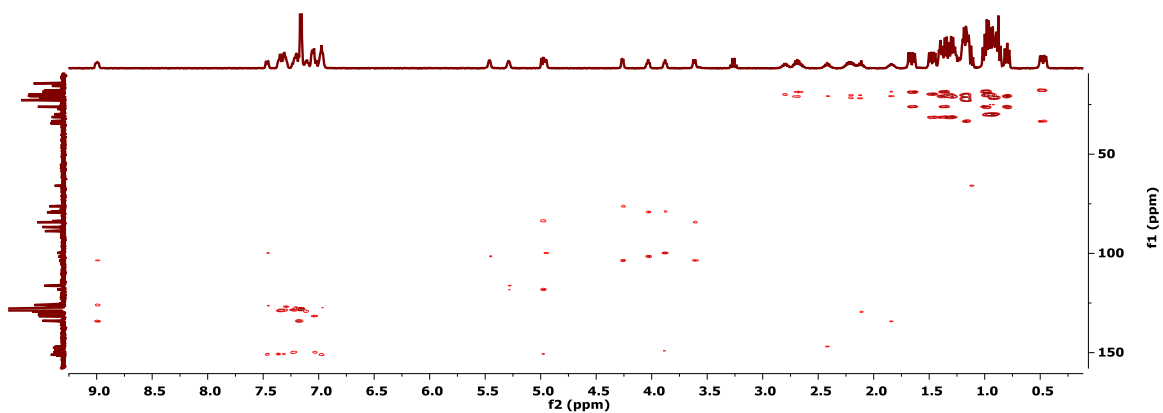


**Figure C.141.**  $^1\text{H}/^{13}\text{C}$  HMBC NMR Spectrum (400/101 MHz,  $\text{C}_6\text{D}_6$ ,  $23^\circ\text{C}$ ) of **5**.



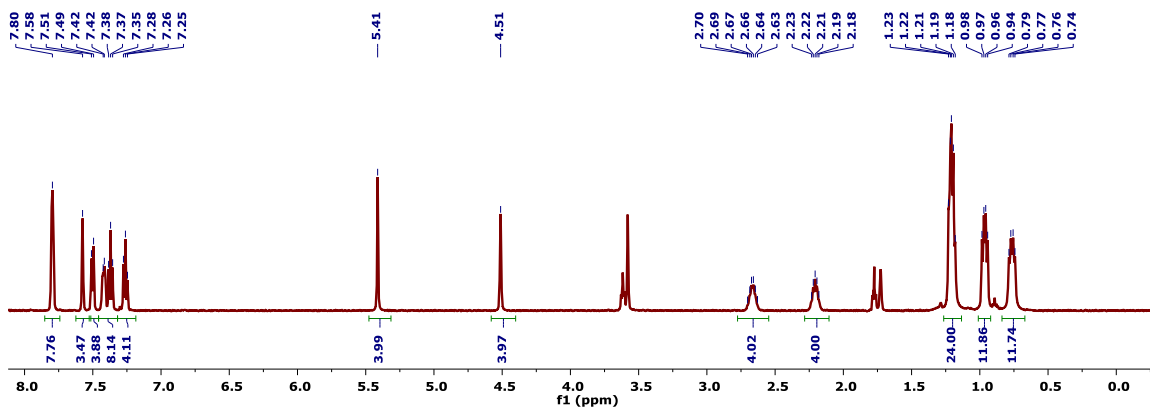


Figure C.142.  $^1\text{H}$  NMR Spectrum (500 MHz,  $\text{C}_6\text{D}_6$ ,  $25^\circ\text{C}$ ) of **6**.

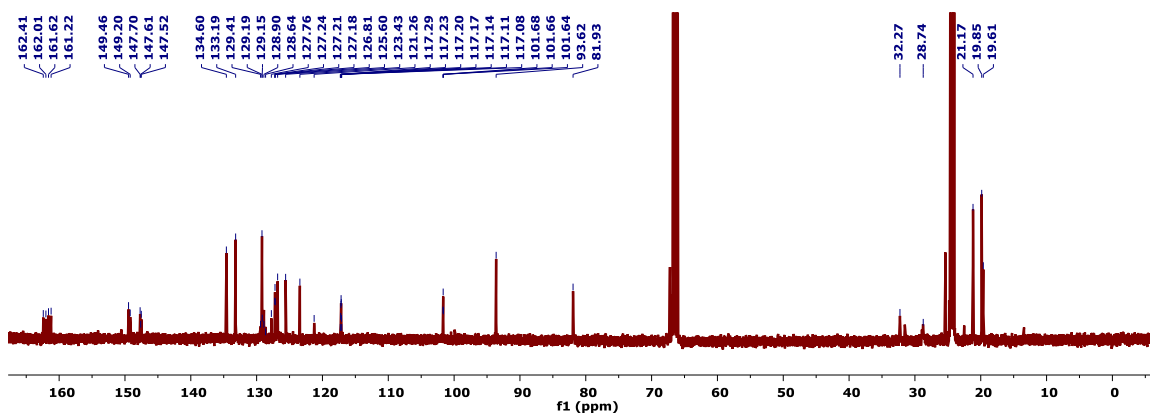


Figure C.143.  $^{13}\text{C}\{^1\text{H}\}$  NMR Spectrum (126 MHz,  $\text{C}_6\text{D}_6$ ,  $25^\circ\text{C}$ ) of **6**.

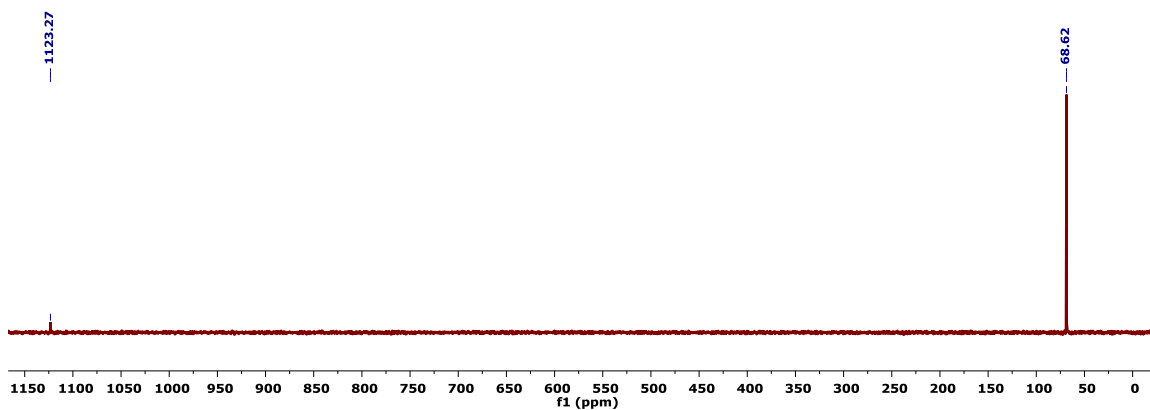


Figure C.144.  $^{31}\text{P}\{^1\text{H}\}$  NMR Spectrum (162 MHz, THF,  $23^\circ\text{C}$ ) of **6**.

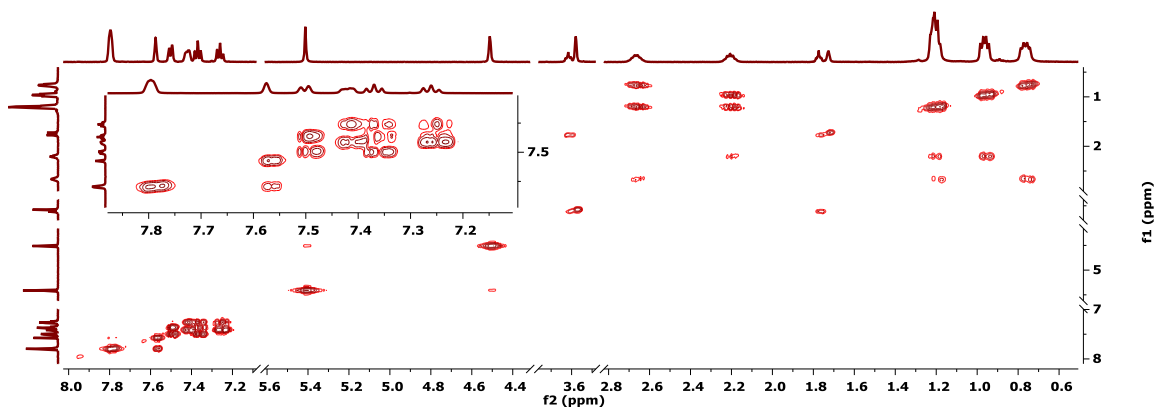


Figure C.145. Partial  $^1\text{H}/^1\text{H}$  COSY NMR Spectrum (500 MHz,  $\text{THF-}d_8$ ,  $23^\circ\text{C}$ ) of **6**.

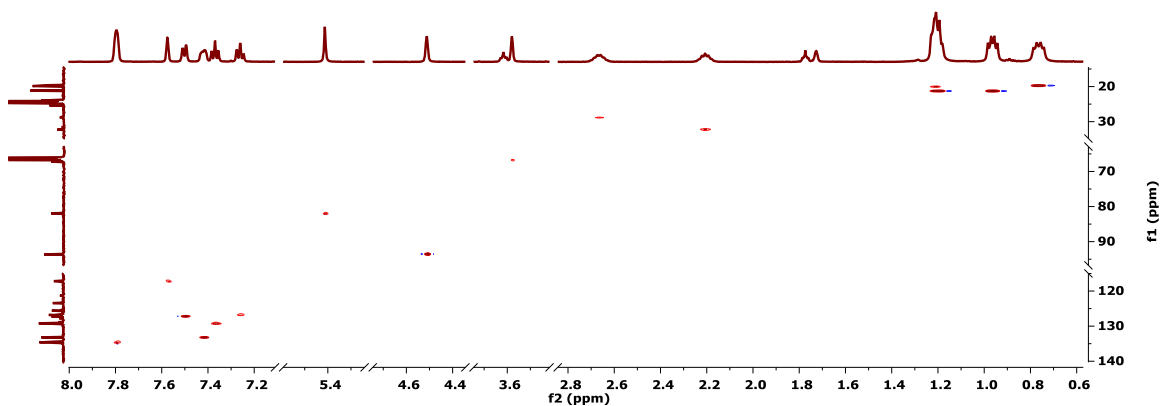


Figure C.146. Partial  $^1\text{H}/^{13}\text{C}$  HSQC NMR Spectrum (500/126 MHz,  $\text{THF-}d_8$ ,  $23^\circ\text{C}$ ) of **6**.

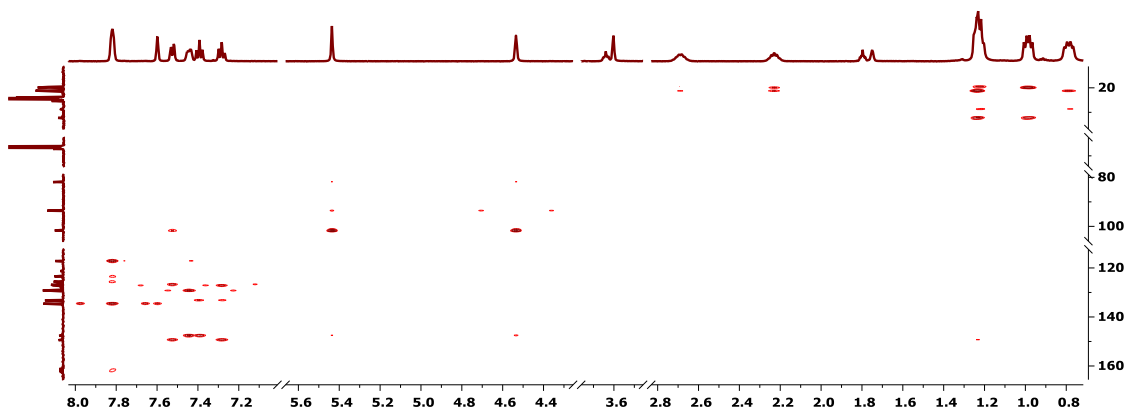
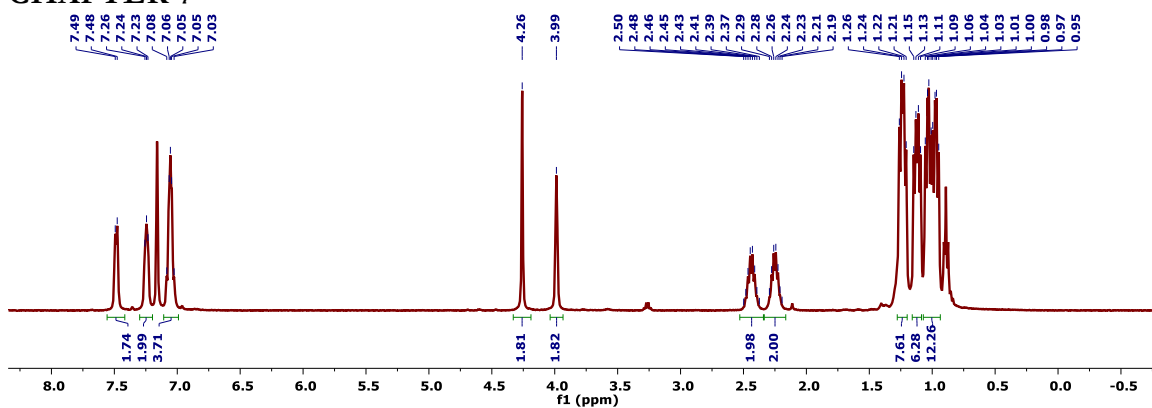
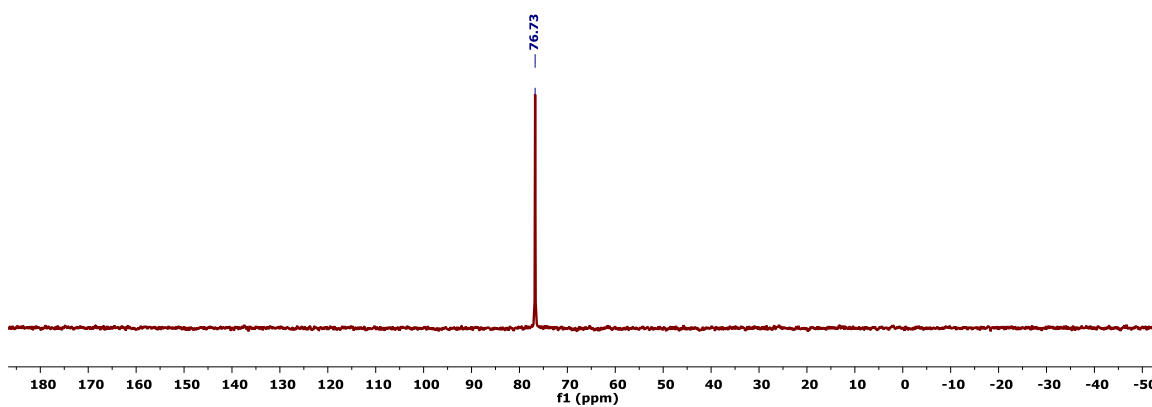
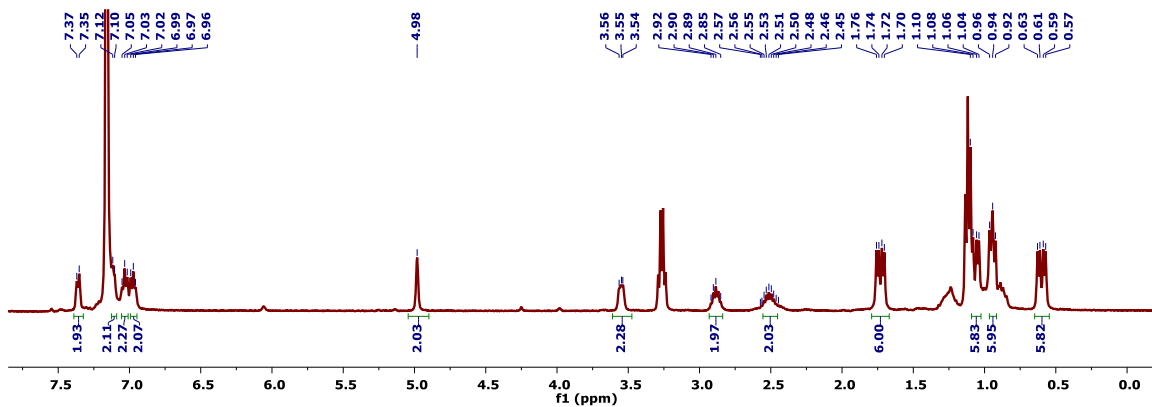


Figure C.147. Partial  $^1\text{H}/^{13}\text{C}$  HMBC NMR Spectrum (500/126 MHz,  $\text{THF-}d_8$ ,  $23^\circ\text{C}$ ) of **6**.

## CHAPTER 7

Figure C.148. <sup>1</sup>H NMR Spectrum (400 MHz, C<sub>6</sub>D<sub>6</sub>, 23°C) of as prepared 1.Figure C.149. <sup>31</sup>P{<sup>1</sup>H} NMR Spectrum (162 MHz, C<sub>6</sub>D<sub>6</sub>, 23°C) of as prepared 1.Figure C.150. <sup>1</sup>H NMR spectrum (400 MHz, C<sub>6</sub>D<sub>6</sub>, 23 °C) of 2.

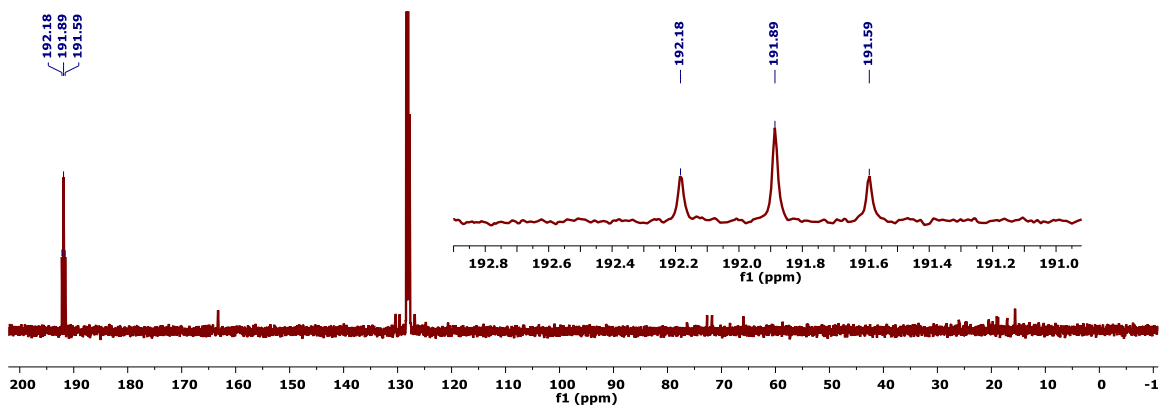


Figure C.151.  $^{13}\text{C}$  NMR spectrum (400 MHz,  $\text{C}_6\text{D}_6$ , 23  $^\circ\text{C}$ ) of **2**.

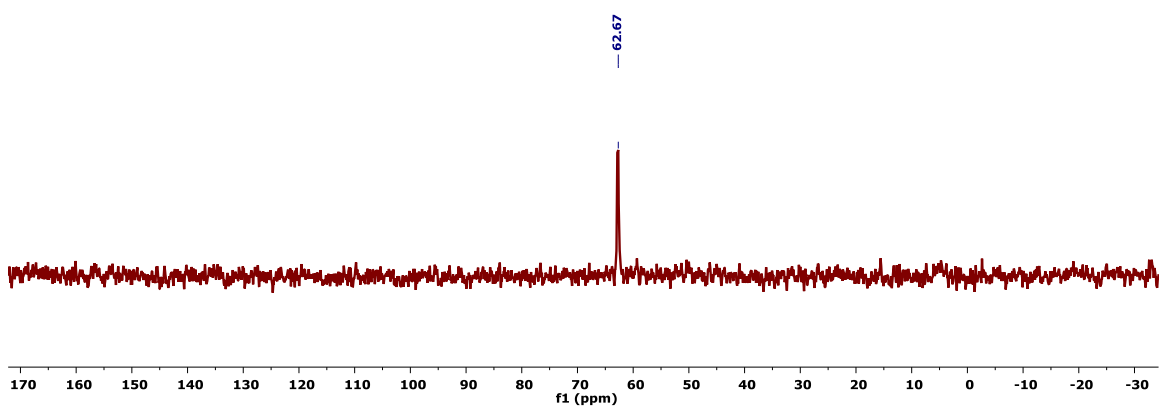


Figure C.152.  $^{31}\text{P}\{^1\text{H}\}$  NMR spectrum (162 MHz,  $\text{C}_6\text{D}_6$ , 23  $^\circ\text{C}$ ) of **2**.

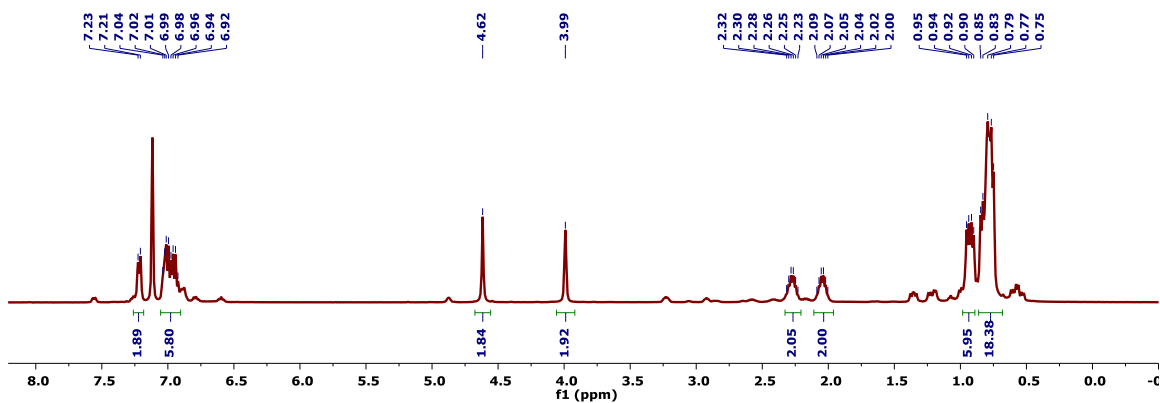
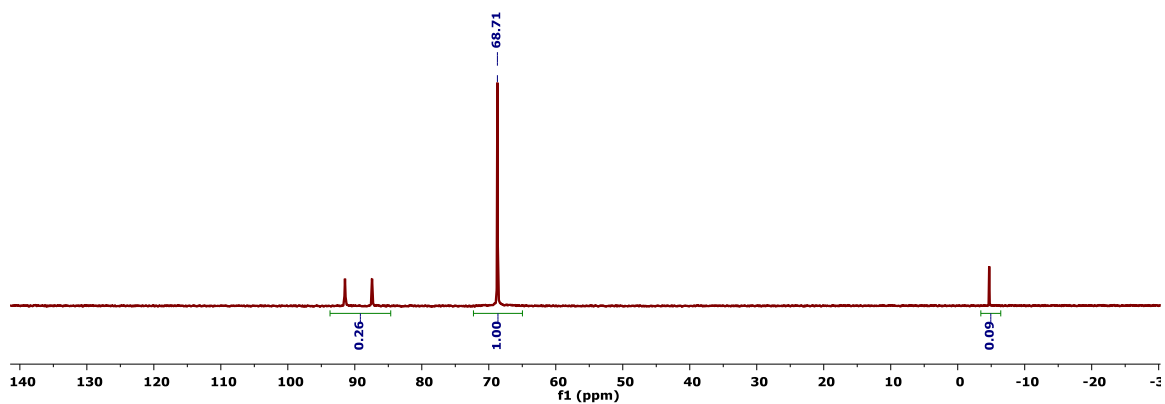
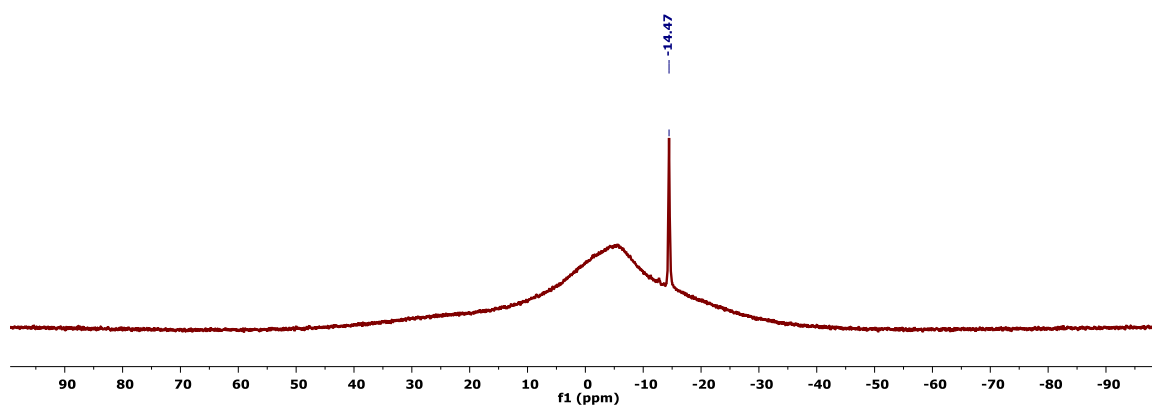


Figure C.153.  $^1\text{H}$  NMR spectrum (400 MHz,  $\text{C}_6\text{D}_6$ , 23  $^\circ\text{C}$ ) of a reaction mixture comprised primarily of **3**.



**Figure C.154.**  $^{31}\text{P}\{^1\text{H}\}$  NMR spectrum (162 MHz,  $\text{C}_6\text{D}_6$ , 23 °C) of a reaction mixture comprised primarily of **3**.



**Figure C.155.**  $^{11}\text{B}\{^1\text{H}\}$  NMR spectrum (128 MHz,  $\text{C}_6\text{D}_6$ , 23 °C) of a reaction mixture comprised primarily of **3**.

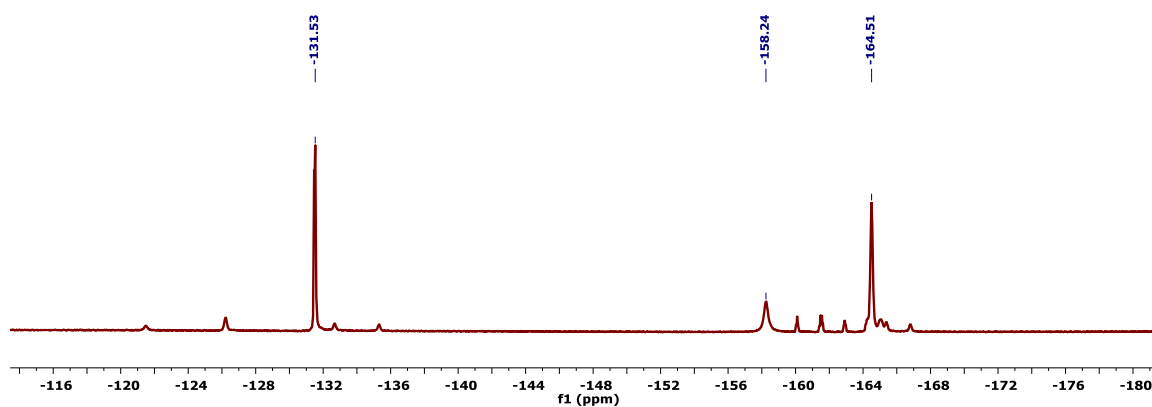


**Figure C.156.**  $^{19}\text{F}$  NMR spectrum (376 MHz,  $\text{C}_6\text{D}_6$ , 23 °C) of a reaction mixture comprised primarily of **3**.

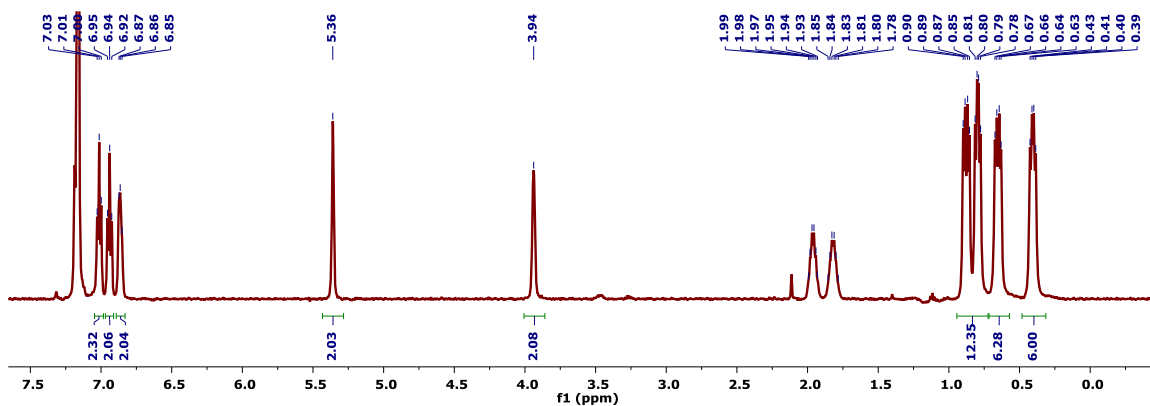


Figure C.157.  $^1\text{H}$  NMR Spectrum (400 MHz,  $\text{C}_6\text{D}_6$ ,  $23^\circ\text{C}$ ) of 4.

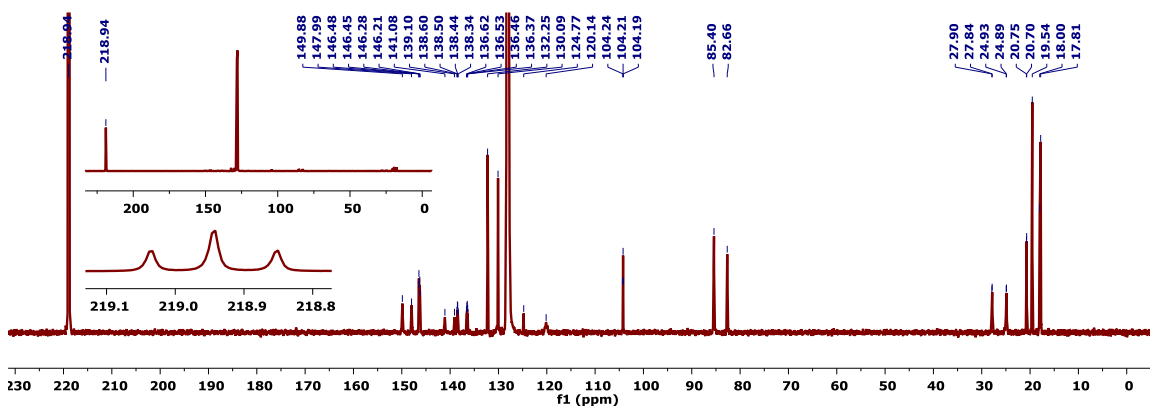


Figure C.158.  $^{13}\text{C}\{^1\text{H}\}$  NMR Spectrum (101 MHz,  $\text{C}_6\text{D}_6$ ,  $23^\circ\text{C}$ ) of 4- $^{13}\text{C}$ . The insets show an untopped spectrum (top) and an enlargement of the  $^{13}\text{CO}_2$  resonance.

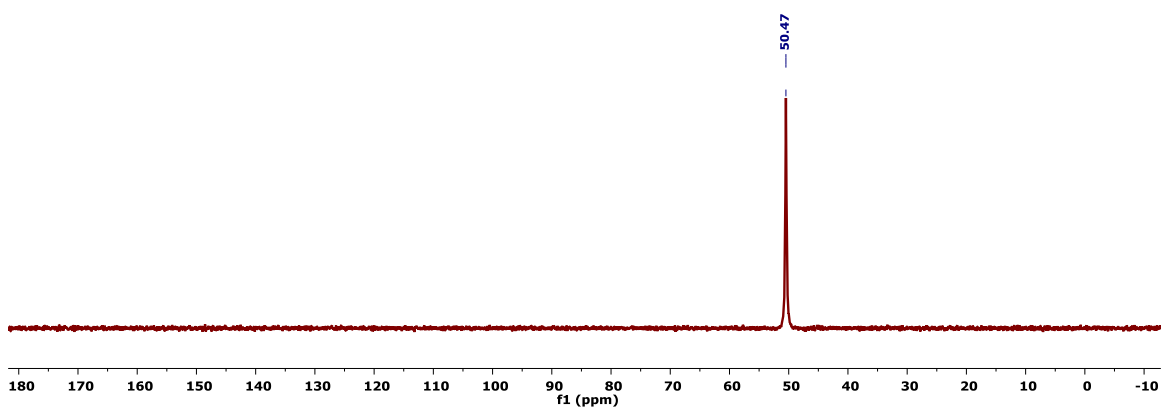


Figure C.159.  $^{31}\text{P}\{^1\text{H}\}$  NMR Spectrum (162 MHz,  $\text{C}_6\text{D}_6$ ,  $23^\circ\text{C}$ ) of 4.

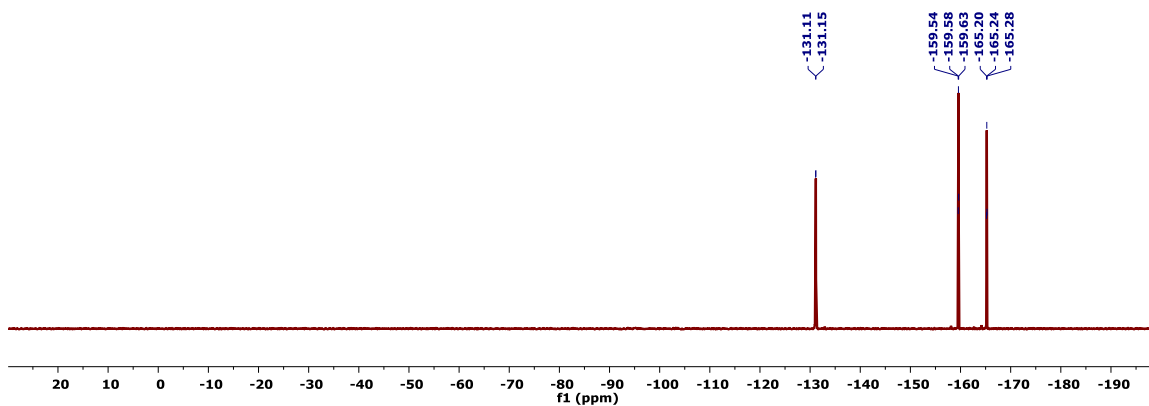


Figure C.160.  $^{19}\text{F}$  NMR spectrum (376 MHz,  $\text{C}_6\text{D}_6$ , 23 °C) of 4.

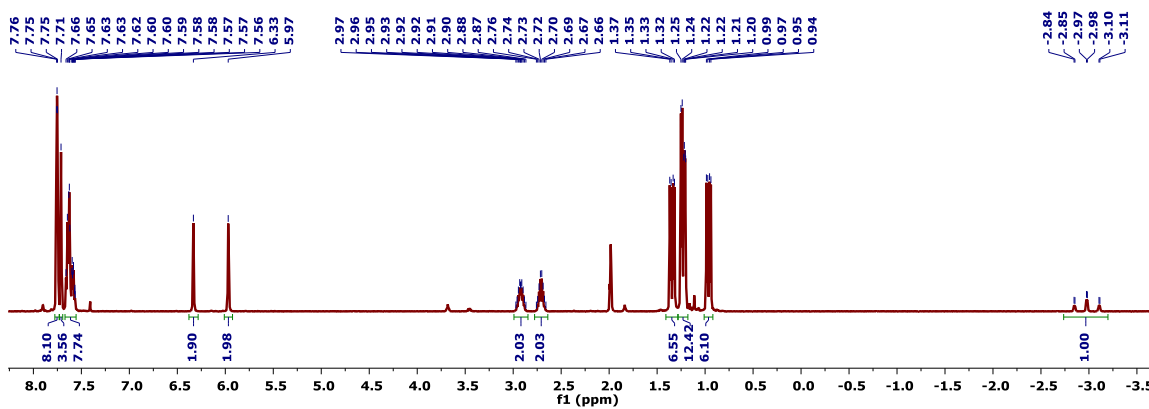


Figure C.161.  $^1\text{H}$  NMR Spectrum (400 MHz,  $\text{C}_6\text{D}_6$ , 23 °C) of 6- $^{13}\text{C}$ .

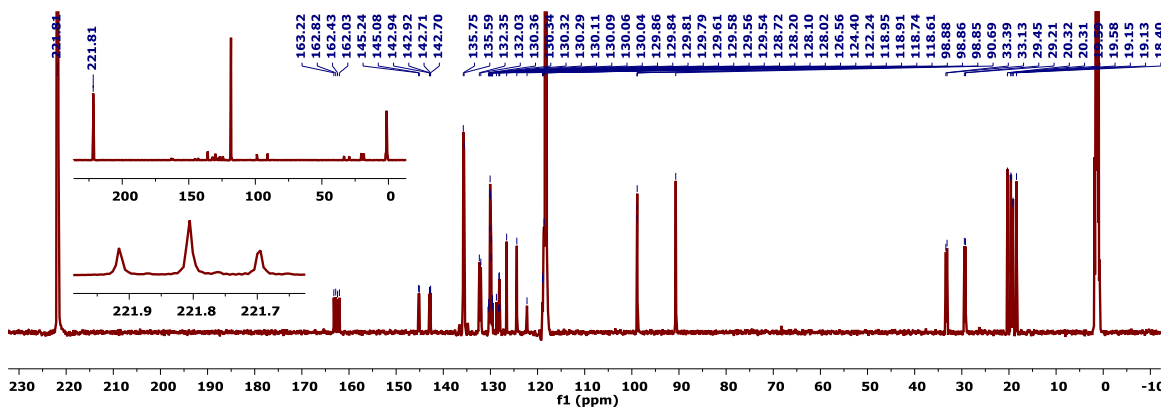
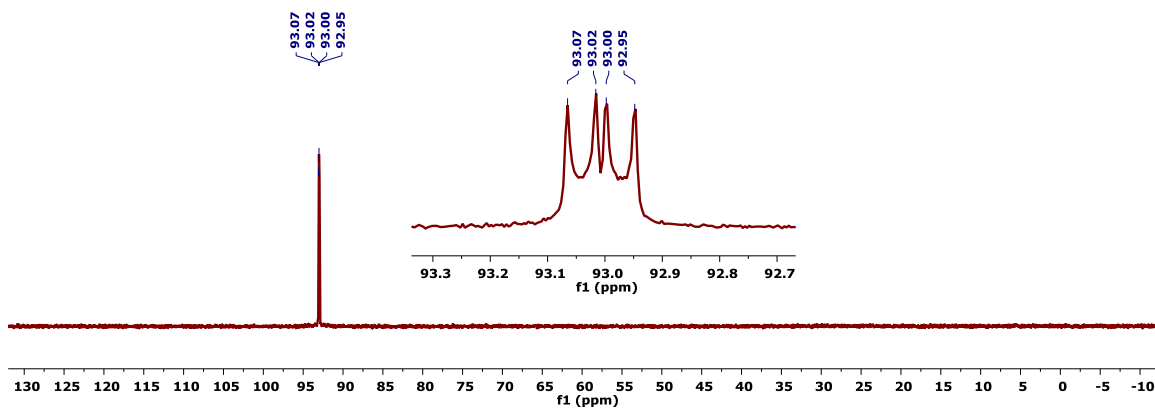


Figure C.162.  $^{13}\text{C}\{^1\text{H}\}$  NMR Spectrum (101 MHz,  $\text{C}_6\text{D}_6$ , 23 °C) of 6- $^{13}\text{C}$ .



**Figure C.163.**  $^{31}\text{P}\{^1\text{H}\}$  NMR Spectrum (162 MHz,  $\text{C}_6\text{D}_6$ , 23°C) of  $6\text{-}^{13}\text{C}$ . The inset shows an enlargement of the relevant resonance, with well-defined  $^2J(\text{P,C})$  and  $^2J(\text{P,H})$  scalar coupling.



## CHAPTER 8

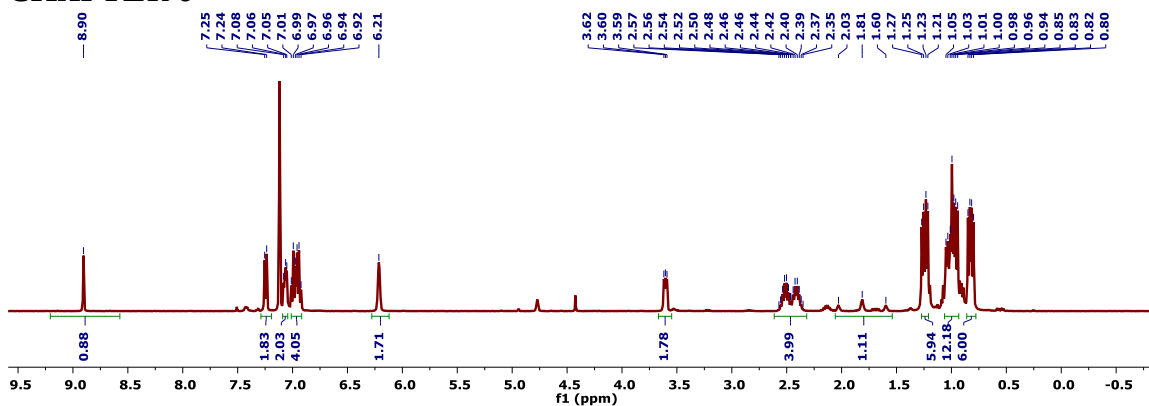


Figure C.164.  $^1\text{H}$  NMR Spectrum (400 MHz,  $\text{C}_6\text{D}_6$ ,  $23^\circ\text{C}$ ) of **4**.

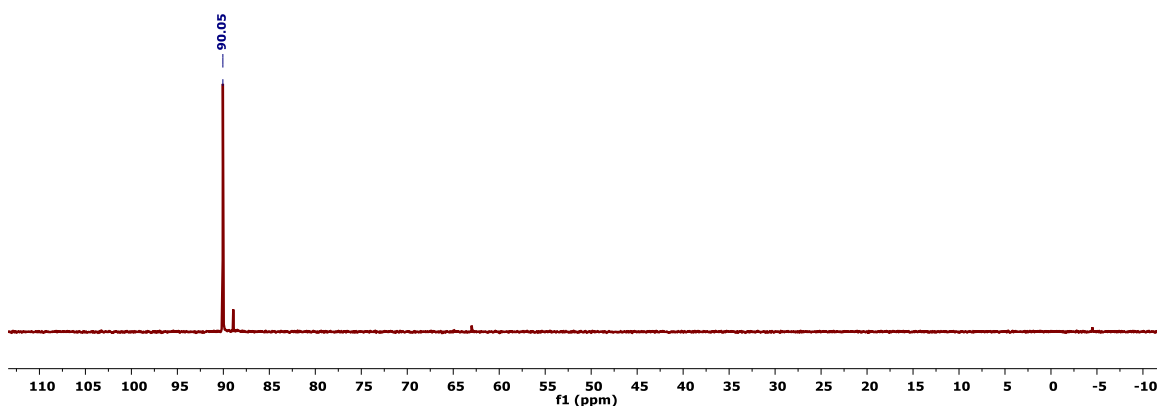


Figure C.165.  $^{31}\text{P}\{^1\text{H}\}$  NMR Spectrum (162 MHz,  $\text{C}_6\text{D}_6$ ,  $23^\circ\text{C}$ ) of **4**.

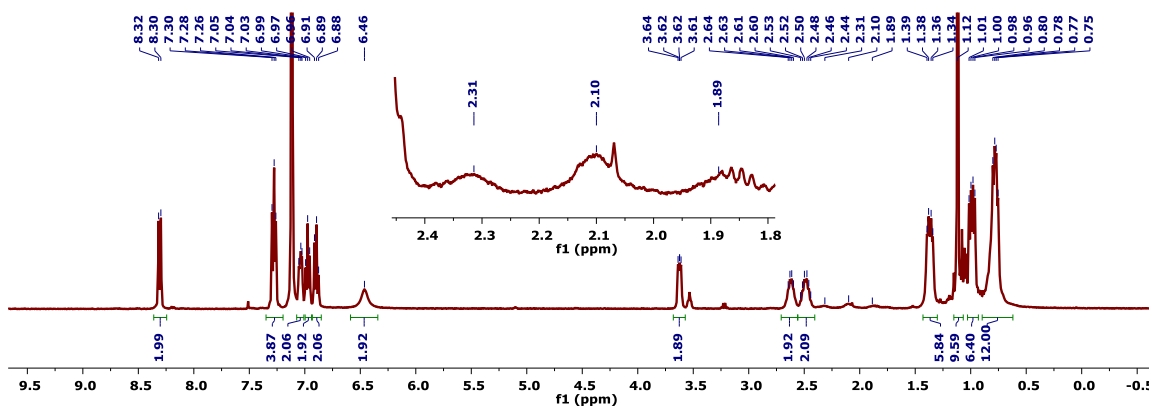


Figure C.166.  $^1\text{H}$  NMR Spectrum (400 MHz,  $\text{C}_6\text{D}_6$ ,  $23^\circ\text{C}$ ) of **5**. The inset shows an enlargement of the hydride resonance at 2.10 ppm.

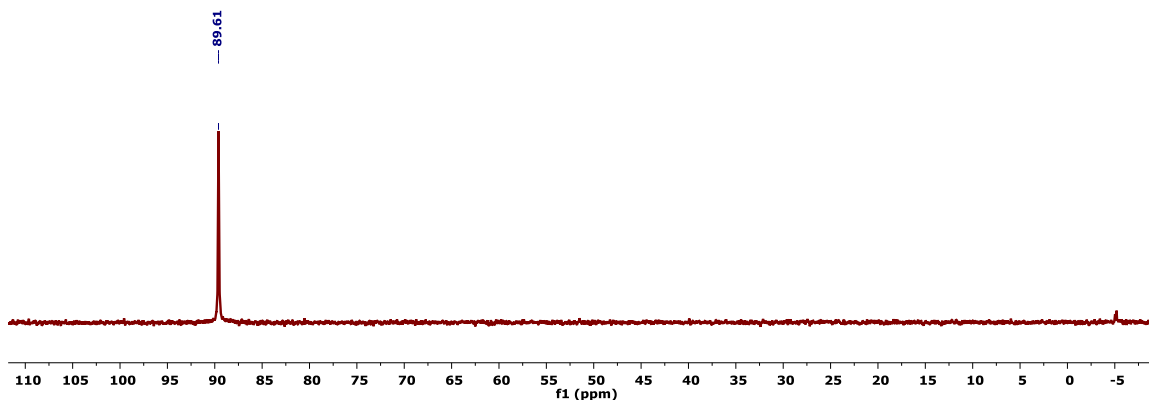


Figure C.167. <sup>31</sup>P{<sup>1</sup>H} NMR Spectrum (162 MHz, C<sub>6</sub>D<sub>6</sub>, 23°C) of 5.

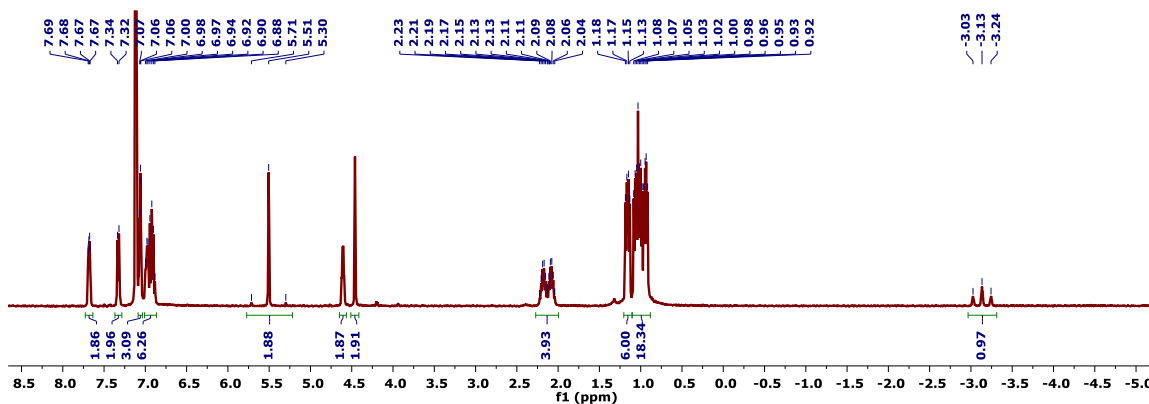


Figure C.168. <sup>1</sup>H NMR Spectrum (400 MHz, C<sub>6</sub>D<sub>6</sub>, 23°C) of 6<sup>PhH</sup>.

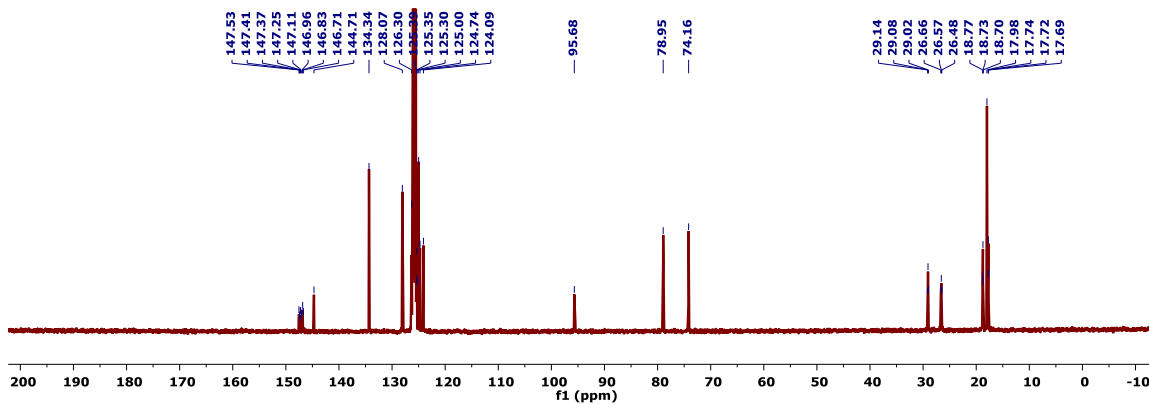


Figure C.169. <sup>13</sup>C{<sup>1</sup>H} NMR Spectrum (101 MHz, C<sub>6</sub>D<sub>6</sub>, 23°C) of 6<sup>PhH</sup>.

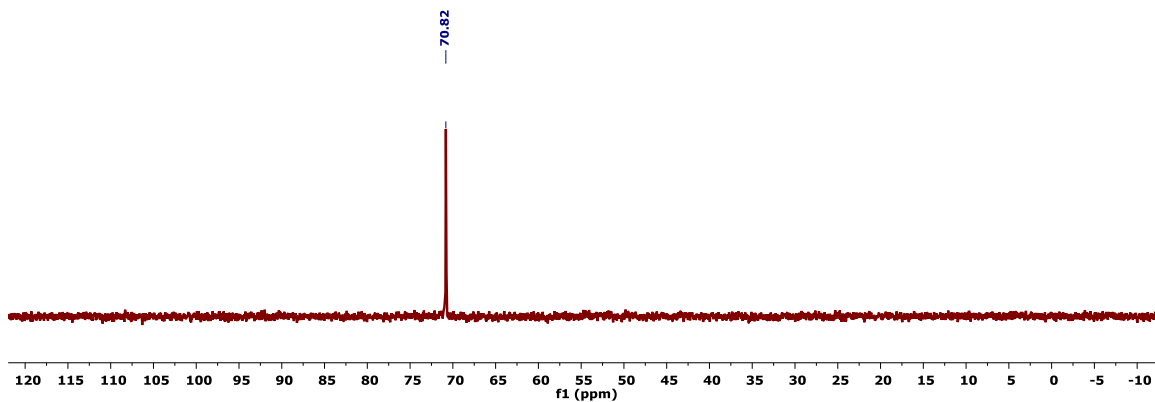


Figure C.170.  $^{31}\text{P}\{^1\text{H}\}$  NMR Spectrum (162 MHz,  $\text{C}_6\text{D}_6$ ,  $23^\circ\text{C}$ ) of  $6^{\text{PhH}}$ .

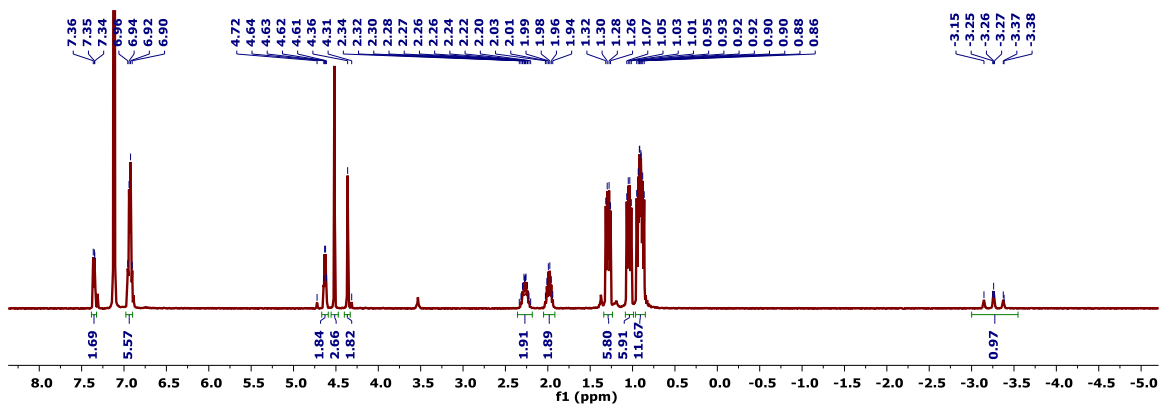


Figure C.171.  $^1\text{H}$  NMR Spectrum (400 MHz,  $\text{C}_6\text{D}_6$ ,  $23^\circ\text{C}$ ) of  $6^{\text{HH}}$ .

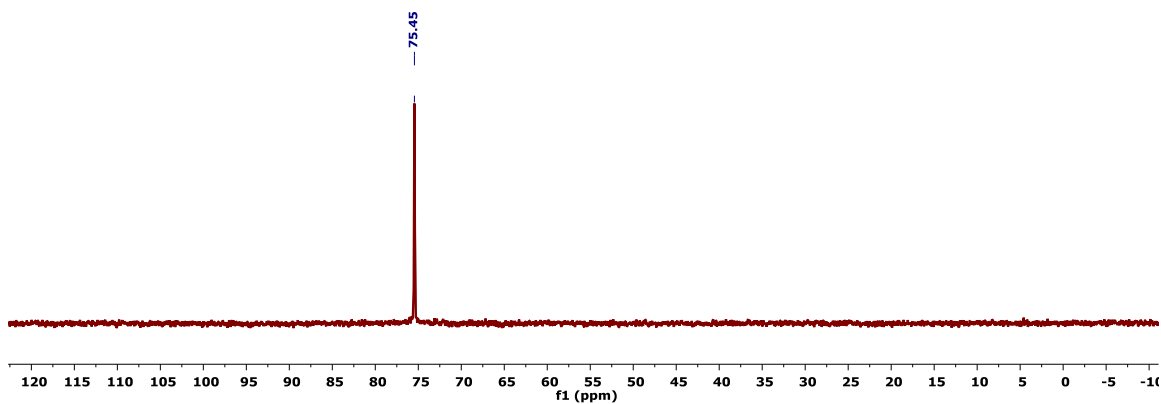


Figure C.172.  $^{31}\text{P}\{^1\text{H}\}$  NMR Spectrum (162 MHz,  $\text{C}_6\text{D}_6$ ,  $23^\circ\text{C}$ ) of  $6^{\text{HH}}$ .

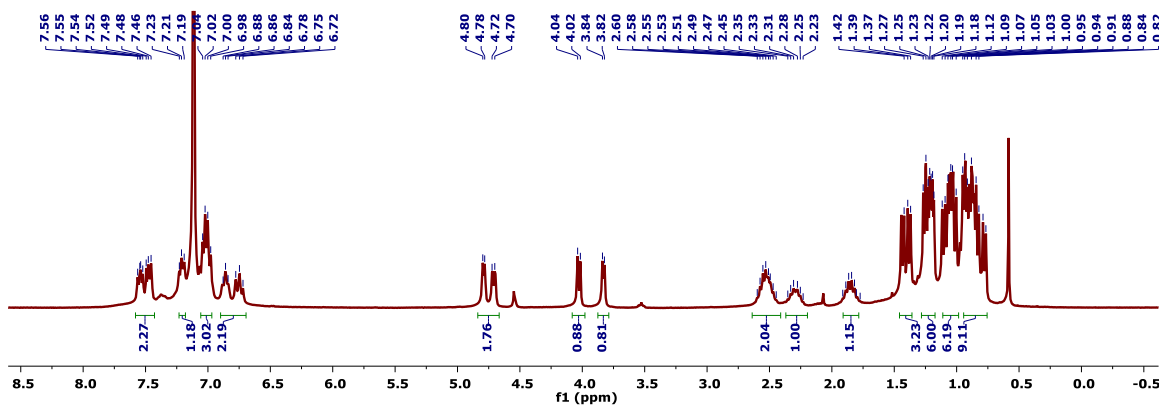


Figure C.173.  $^1\text{H}$  NMR Spectrum (300 MHz,  $\text{C}_6\text{D}_6$ ,  $23^\circ\text{C}$ ) of *in situ* generated **11**.

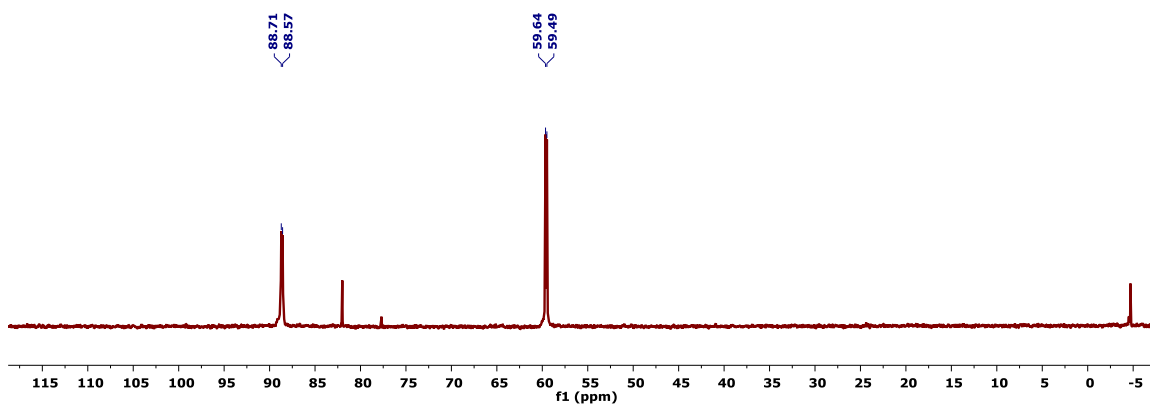
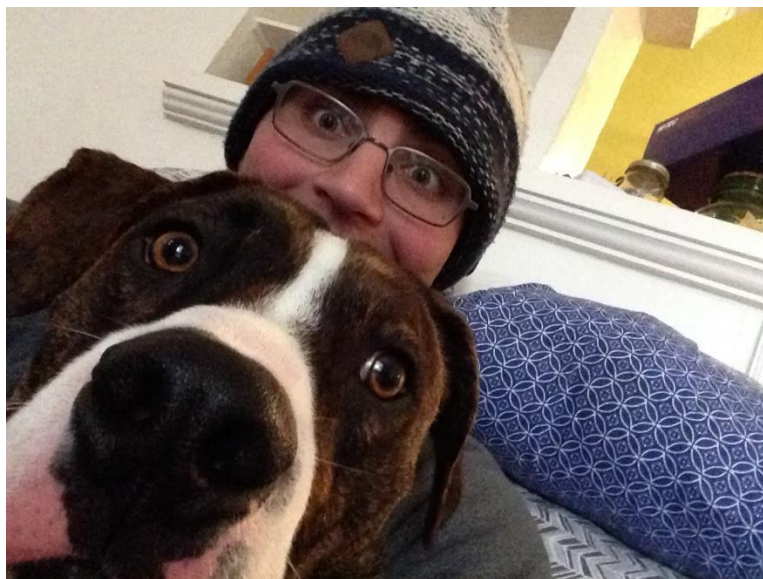


Figure C.174.  $^{31}\text{P}\{^1\text{H}\}$  NMR Spectrum (110 MHz,  $\text{C}_6\text{D}_6$ ,  $23^\circ\text{C}$ ) of *in situ* generated **11**.



## ABOUT THE AUTHOR



Joshua Alan Buss was born in Las Vegas, NV on New Year's Eve, 1989, to Otto and Serena Buss, thirty minutes before the stroke of midnight. His family moved when he just a wee three-year old, and he and his older sister Etta Suzanne Buss, were raised spending summers in Sterling, Alaska and winters in Patagonia, Arizona. He attended Patagonia Union High School, an underfunded public school of about 100 students, where he played three sports, learned to play jazz trombone, and developed an appreciation for chess. On Friday nights and Saturdays, Josh developed his skills as a professional dishwasher, a background that has served him well in the lab. After graduating in 2008, Josh attended Claremont McKenna College as a Questbridge Scholar. He conducted original research both at his home institution under the guidance of Prof. Anna Wenzel and through a CENTC REU appointment at the University of Washington mentored by Mike Heinekey. Though his time in the Wenzel group directed Josh toward a career in chemistry, it was in Seattle that he became enamored with organometallic synthesis, potent chemical reductants, and amateur glassblowing. Josh was granted a B.A. in Chemistry from CMC in 2012 and he moved down the street soon after. He completed his Ph.D. studies, as an NSF fellow, in the laboratories of Prof. Theodor Agapie at the California Institute of Technology in 2018. He plans to move north to Madison, Wisconsin, accepting a post-doctoral appointment in the research group of Prof. Shannon Stahl. Winter is coming! When he is not in lab, Josh enjoys wandering around in the woods, drinking strong coffee, and dogs.

## Joshua Alan Buss

Curriculum Vitae

[jbuss@caltech.edu](mailto:jbuss@caltech.edu)

520.604.6473

---

### EDUCATION

- **California Institute of Technology, Division of Chemistry and Chemical Engineering (2012 – present)**

Ph.D. candidate in chemistry

Areas of concentration: Inorganic/Organometallic Chemistry

GPA: 4.0/4.0

- **Claremont McKenna College (2008 – 2012)**

B.A. in chemistry

Areas of concentration: General Chemistry and Mathematics

Overall GPA: 3.9/4.0; Major GPA: 3.9/4.0

### AWARDS and HONORS

- **National Science Foundation Graduate Research Fellowship (2014 – 2017)**

*California Institute of Technology*

- **DIC Travel Award: 251<sup>st</sup> ACS National Meeting (2016)**

*American Chemical Society*

- **Dow Chemical Company Graduate Fellowship in Chemistry and Chemical Engineering (2014 – 2015)**

*California Institute of Technology*

- **Exemplary Teaching Assistant (2013)**

*California Institute of Technology* – Award criterion: anonymous student reviews

- **Magna Cum Laude (2012)**

*Claremont McKenna College*

- **Best Senior Thesis in Physical Science (2012)**

*Claremont McKenna College*

- **John Stauffer Memorial Scholarship (2012)**

*W.M. Keck Science Center* – Award criterion: top senior science student

- **ACS Undergraduate Award in Inorganic Chemistry (2012)**

*W.M. Keck Science Center* – Award criterion: faculty vote

- **Barry M. Goldwater Scholar in Mathematics, Science, and Engineering (2011)**

*Claremont McKenna College*

- **ACS Undergraduate Award in Analytical Chemistry (2011)**

*W.M. Keck Science Center* – Award criterion: faculty vote

- **Dean's List (2008-2011)**

*Claremont McKenna College*

- **Questbridge Scholar (2008 – 2012)**

*Claremont McKenna College*

### RESEARCH EXPERIENCE

- **Graduate Research (Prof. Theo Agapie) (2012 – present)**

1) Synthesis and study of super-reduced molybdenum complexes demonstrating stabilizing metal-arene interactions and investigation of their activation of challenging small molecule substrates.

- 2) Mechanistic interrogation of a carbon monoxide reductive coupling scheme demonstrating C–O cleavage, terminal carbide intermediacy, C–C bond formation, and product release—a net four electron process.
  - 3) Preparation of molybdenum complexes bearing multiply-bonded ligands and the assessment of the group transfer reactivity of those moieties.
  - 4) Investigation of ammonia borane dehydrogenation catalysis by low-valent molybdenum catalysts for hydrogen-based energy storage applications.
  - 5) Development of two modes of stoichiometric carbon dioxide reduction from an  $\eta^2$ -CO<sub>2</sub> complex of molybdenum.
  - 6) Exploration of terphenyl diphosphine ligands bearing a pendant phenol as a proton relay and potential redox-active ligand moiety.
- **Center for Enabling New Technologies Through Catalysis (Prof. D. Michael Heinekey) (2011)**
    - 1) Elaborated iridium C–H bond activation catalysts bearing N-heterocyclic carbene ligands.
    - 2) Refractory synthesis of a practical rhodium chloride precursor from the raw metal.
  - **Undergraduate Research (Prof. Anna Wenzel) (2010 – 2012)**
    - 1) Designed and executed the preparation of *ortho*-substituted (*R*)-5,5',6,6',7,7',8,8'-octahydro-[1,1'-binaphthalene]2,2'-diols to test as helical twist agents in nematic liquid crystals.
    - 2) Surveyed the efficacy of established oxidative coupling methodologies in comparison to a novel microwave-promoted, *tert*-butyl peroxide-catalyzed approach.
    - 3) Explored imidazoles as substrates for a Lewis-acid assisted sequential Michael-Aldol synthesis of dihydroquinolines.

## MENTORING EXPERIENCE

- **Ruomeng Wan**—Caltech Undergraduate (Spring 2015 – present)
  - 1) Oversaw the synthesis and coordination chemistry of a teraryl diphosphine ligand bearing a central pyridine motif that displays binding to either the pyridine N or  $\pi$ -system as a function of the metal center's oxidation state and primary coordination sphere.
  - 2) Targeted the preparation and characterization of indium phosphide nanomaterials via the electrodeposition of well-defined molecular precursors.
- **Yohei Ueda**—Visiting Scholar, Osaka University (Spring 2017 – Fall 2017)
  - 1) Assisted in the synthesis of a Mo nitride/amide complex toward the oxidation and coupling of the nitrogenous ligands.
  - 2) Prepared well-defined molecular phosphide complexes to attempt protonation and measure BDEs of P–H bonds in metal phosphide model systems.
- **Bogdan Dimitriu**—Caltech Undergraduate (Winter 2014 – Spring 2015)
  - 1) Synthesized a rare Mo hydride/hydrosulfide complex and explored its potential as an intermediate relevant to proton reduction catalysis.

## TEACHING EXPERIENCE

- **Head Teaching Assistant:** Inorganic Synthesis Laboratory with Prof. Theo Agapie (Fall 2013)  
*California Institute of Technology*
- **Teaching Assistant:** Introductory Inorganic Chemistry with Prof. Theo Agapie (Spring 2013)  
*California Institute of Technology*
- **Teaching Assistant:** Solar Energy Conversion Laboratory with Prof. Jeff Mendez (Fall 2012 – Winter 2012)  
*California Institute of Technology*



- **Teaching Assistant:** Organic Chemistry Laboratory with Prof. Robert Iafe (Fall 2011 – Spring 2012)

*W.M. Keck Science Department*

## PUBLICATIONS

- 1) “Electrochemical Synthesis of Metal Phosphides Under Mild Conditions: Mechanistic Insights and Application for Proton Reduction” Naoki Shida, **Joshua A. Buss**, and Theodor Agapie, *Chem. Commun.* **2018**, *54*, 767.
- 2) “Terminal Molybdenum Phosphides with *d*-Electrons: Radical Character Promotes Coupling Chemistry” **Joshua A. Buss**, Paul H. Oyala, and Theodor Agapie, *Angew. Chem. Int. Ed.* **2017**, *56*, 14502.
- 3) “Ethylene Tetramerization Catalysis: Effects of Aluminum-Induced Isomerization of PNP to PPN Ligands” Alejo M. Lifschitz, Nathanael A. Hirscher, Heui Beom Lee, **Joshua A. Buss**, and Theodor Agapie, *Organometallics*, **2017**, *36*, 1640.
- 4) “Mechanism of Molybdenum Mediated Carbon Monoxide Deoxygenation and Coupling: Mono- and Dicarbyne Complexes Precede C–O Bond Cleavage and C–C Bond Formation” **Joshua A. Buss** and Theodor Agapie, *J. Am. Chem. Soc.*, **2016**, *138*, 16466.
- 5) “Four-Electron Deoxygenative Reductive Coupling of Carbon Monoxide at a Single Metal Site.” **Joshua A. Buss** and Theodor Agapie, *Nature*, **2016**, *529*, 72.
- 6) “Molybdenum Catalyzed Ammonia Borane Dehydrogenation: Oxidation State Specific Mechanisms.” **Joshua A. Buss**, Guy A. Edouard, Christine Cheng, Jade Shi, and Theodor Agapie, *J. Am. Chem. Soc.*, **2014**, *136*, 11272.
- 7) “Efficient Microwave Method for the Oxidative Coupling of Phenols.” Sharday Grant-Overton, **Joshua A. Buss**, Eva H. Smith, Elisa G. Gutierrez, Eric J. Moorhead, Vivian S. Lin, and Anna G. Wenzel, *Synth. Commun.*, **2014**, *45*, 331.
- 8) “A Copper(II)-Catalyzed, Sequential Michael-Aldol Reaction for the Preparation of 1,2-Dihydroquinolines.” Anna M. Wagner, Claire E. Knezevic, Jessica L. Wall, Victoria L. Sun, **Joshua A. Buss**, LeeAnn T. Allen, and Anna G. Wenzel, *Tetrahedron Lett.*, **2012**, *53*, 833.

### *Manuscripts in Preparation*

- 9) “Selective Two-Electron Reduction of Carbon Monoxide Mediated by a Molybdenum Phenol Phosphine Complex” Siti Nurhanna Riduan, **Joshua A. Buss**, and Theodor Agapie, *manuscript in preparation*.
- 10) “Lewis-Acid Stabilization and Activation of Small Molecules: C–O Bond Cleavage of CO<sub>2</sub> with Protons Facilitated by Borane Coordination” **Joshua A. Buss**, David VanderVelde, and Theodor Agapie, *manuscript in preparation*.
- 11) “Extending the Carbon Chain: C<sub>3</sub> Oxygenates Derived from the Reductive Coupling of CO” Choon Heng Low, **Joshua A. Buss**, and Theodor Agapie, *manuscript in preparation*.
- 12) “Cyanate Formation from an Anionic Mo Nitride” **Joshua A. Buss**, Christine Cheng, and Theodor Agapie, *manuscript in preparation*.
- 13) “Bimodal CO<sub>2</sub> Reduction: Formate and Silanol Formation Following E–H Bond Activation” **Joshua A. Buss** and Theodor Agapie, *manuscript in preparation*.
- 14) “Variable Binding Modes of Pyridine in Molybdenum Complexes Supported by a P-pyridine-P Ligand” Ruomeng Wan, **Joshua A. Buss**, Kyle T. Horak, and Theodor Agapie, *manuscript in preparation*.

## PRESENTATIONS

- **Joshua A. Buss** and Theodor Agapie “Molybdenum-Mediated Carbon Monoxide Reduction, Deoxygenation, and Coupling.” Organometallic Chemistry Gordon Research Conference, Salve Regina University, Newport, RI, USA 7/10-14/2017 (poster)

- **Joshua A. Buss** and Theodor Agapie “Molybdenum-Mediated Carbon Monoxide Reduction, Deoxygenation, and Coupling.” Organometallic Chemistry Gordon Research Seminar, Salve Regina University, Newport, RI, USA **7/8/2017** (oral)
- **Joshua A. Buss** and Theodor Agapie “Four-Electron Reductive Coupling of Carbon Monoxide.” SoCal Organometallics Meeting, University of California Irvine, Irvine, CA, USA **4/23/2016** (oral)
- **Joshua A. Buss** and Theodor Agapie “Four-Electron Reductive Coupling of Carbon Monoxide: Evidence for Dicarbyne and Terminal Carbide Reaction Intermediates.” 251<sup>st</sup> ACS National Meeting, San Diego, CA, USA **3/2016** (oral)
- **Joshua A. Buss** and Theodor Agapie “Four-Electron Reductive Coupling of Carbon Monoxide.” Division of Chemistry and Chemical Engineering Seminar Day, California Institute of Technology, Pasadena, CA, USA **10/16/2015** (oral)
- **Joshua A. Buss** and Theodor Agapie “Super Reduced Molybdenum Complexes: Carbon Monoxide Deoxygenation and Coupling.” SoCal Organometallics Meeting, California Institute of Technology, Pasadena, CA, USA **2/22/2015** (poster)
- **Joshua A. Buss**, Guy A. Edouard, Christine Cheng, Jade Shi, and Theodor Agapie “Molybdenum Catalyzed Ammonia Borane Dehydrogenation.” 248<sup>th</sup> ACS National Meeting, San Francisco, CA, USA **8/14/2014** (oral)
- **Joshua A. Buss**, Guy A. Edouard, Christine Cheng, Jade Shi, and Theodor Agapie “*Para*-Terphenyl Diphosphine Molybdenum Complexes: Synthesis and Reactivity.” 248<sup>th</sup> ACS National Meeting, San Francisco, CA, USA **8/10/2014** (poster)
- **Joshua A. Buss** and Theodor Agapie “Molybdenum Terphenyl Diphosphine Ammonia Borane Dehydrogenation Catalysts.” SoCal Organometallics Meeting, University of Southern California, Los Angeles, CA, USA **11/17/2013** (oral)
- **Joshua A. Buss**, Anna G. Wenzel, and James A. Rego “Cholesteric Induction in Nematic Liquid Crystals: Applications of H<sub>8</sub>-BINOL Analogs as Chiral Dopants.” 243<sup>rd</sup> ACS National Meeting, San Diego, CA, USA **9/26/2012** (poster)
- **Joshua A. Buss**, Robert Robertson Jr., and D. Michael Heinekey “Progress Toward Efficient C-H Activation with Iridium(III) N-Heterocyclic Carbene Complexes.” NSF Center for Enabling New Technologies Through Catalysis Annual Meeting, Seattle, WA, USA **9/12/2011** (poster)
- Sharday Grant-Overton, **Joshua A. Buss**, and Anna G. Wenzel “Microwave-Assisted Oxidative Coupling of Phenols.” 241<sup>st</sup> ACS National Meeting, Anaheim, CA, USA **3/28/2011** (poster)

*“I do believe that the measure of a man  
Is the length he will go from the place he began”*

*~Bronze Radio Return*